

Lecture Notes in Mechanical Engineering

Md. Abdul Maleque

Ahmad Zahirani Ahmad Azhar

Norshahida Sarifuddin

Sharifah Imihezri Syed Shaharuddin

Afifah Mohd Ali

Nor Farah Huda Abdul Halim *Editors*

Proceeding of 5th International Conference on Advances in Manufacturing and Materials Engineering


ICAMME 2022, 9–10 August, Kuala Lumpur, Malaysia

 Springer

Lecture Notes in Mechanical Engineering


Series Editors

Fakher Chaari, National School of Engineers, University of Sfax, Sfax, Tunisia

Francesco Gherardini , Dipartimento di Ingegneria “Enzo Ferrari”, Università di Modena e Reggio Emilia, Modena, Italy

Vitalii Ivanov, Department of Manufacturing Engineering, Machines and Tools, Sumy State University, Sumy, Ukraine

Editorial Board

Francisco Cavas-Martínez , Departamento de Estructuras, Construcción y Expresión Gráfica Universidad Politécnica de Cartagena, Cartagena, Murcia, Spain

Francesca di Mare, Institute of Energy Technology, Ruhr-Universität Bochum, Bochum, Nordrhein-Westfalen, Germany

Mohamed Haddar, National School of Engineers of Sfax (ENIS), Sfax, Tunisia

Young W. Kwon, Department of Manufacturing Engineering and Aerospace Engineering, Graduate School of Engineering and Applied Science, Monterey, CA, USA

Justyna Trojanowska, Poznan University of Technology, Poznan, Poland

Jinyang Xu, School of Mechanical Engineering, Shanghai Jiao Tong University, Shanghai, China

Lecture Notes in Mechanical Engineering (LNME) publishes the latest developments in Mechanical Engineering—quickly, informally and with high quality. Original research reported in proceedings and post-proceedings represents the core of LNME. Volumes published in LNME embrace all aspects, subfields and new challenges of mechanical engineering.

To submit a proposal or request further information, please contact the Springer Editor of your location:

Europe, USA, Africa: Leontina Di Cecco at Leontina.dicecco@springer.com

China: Ella Zhang at ella.zhang@springer.com

India: Priya Vyas at priya.vyas@springer.com

Rest of Asia, Australia, New Zealand: Swati Meherishi at swati.meherishi@springer.com

Topics in the series include:

- Engineering Design
- Machinery and Machine Elements
- Mechanical Structures and Stress Analysis
- Automotive Engineering
- Engine Technology
- Aerospace Technology and Astronautics
- Nanotechnology and Microengineering
- Control, Robotics, Mechatronics
- MEMS
- Theoretical and Applied Mechanics
- Dynamical Systems, Control
- Fluid Mechanics
- Engineering Thermodynamics, Heat and Mass Transfer
- Manufacturing
- Precision Engineering, Instrumentation, Measurement
- Materials Engineering
- Tribology and Surface Technology

Indexed by SCOPUS and EI Compendex.

All books published in the series are submitted for consideration in Web of Science.

To submit a proposal for a monograph, please check our Springer Tracts in Mechanical Engineering at <https://link.springer.com/bookseries/11693>

Md. Abdul Maleque ·
Ahmad Zahirani Ahmad Azhar ·
Norshahida Sarifuddin ·
Sharifah Imihezri Syed Shaharuddin ·
Afifah Mohd Ali · Nor Farah Huda Abdul Halim
Editors

Proceeding of 5th International Conference on Advances in Manufacturing and Materials Engineering

ICAMME 2022, 9–10 August, Kuala Lumpur,
Malaysia

 Springer

Editors

Md. Abdul Maleque
Department of Manufacturing
and Materials Engineering
Kulliyyah of Engineering
International Islamic University Malaysia
Jalan Gombak, Kuala Lumpur, Malaysia

Ahmad Zahirani Ahmad Azhar
Department of Manufacturing
and Materials Engineering
Kulliyyah of Engineering
International Islamic University Malaysia
Jalan Gombak, Kuala Lumpur, Malaysia

Norshahida Sarifuddin
Department of Manufacturing
and Materials Engineering
Kulliyyah of Engineering
International Islamic University Malaysia
Jalan Gombak, Kuala Lumpur, Malaysia

Sharifah Imihezri Syed Shahrudin
Department of Manufacturing
and Materials Engineering
Kulliyyah of Engineering
International Islamic University Malaysia
Jalan Gombak, Kuala Lumpur, Malaysia

Afifah Mohd Ali
Department of Manufacturing
and Materials Engineering
Kulliyyah of Engineering
International Islamic University Malaysia
Jalan Gombak, Kuala Lumpur, Malaysia

Nor Farah Huda Abdul Halim
Department of Manufacturing
and Materials Engineering
Kulliyyah of Engineering
International Islamic University Malaysia
Jalan Gombak, Kuala Lumpur, Malaysia

ISSN 2195-4356

ISSN 2195-4364 (electronic)

Lecture Notes in Mechanical Engineering

ISBN 978-981-19-9508-8

ISBN 978-981-19-9509-5 (eBook)

<https://doi.org/10.1007/978-981-19-9509-5>

© The Editor(s) (if applicable) and The Author(s), under exclusive license to Springer Nature Singapore Pte Ltd. 2023

This work is subject to copyright. All rights are solely and exclusively licensed by the Publisher, whether the whole or part of the material is concerned, specifically the rights of translation, reprinting, reuse of illustrations, recitation, broadcasting, reproduction on microfilms or in any other physical way, and transmission or information storage and retrieval, electronic adaptation, computer software, or by similar or dissimilar methodology now known or hereafter developed.

The use of general descriptive names, registered names, trademarks, service marks, etc. in this publication does not imply, even in the absence of a specific statement, that such names are exempt from the relevant protective laws and regulations and therefore free for general use.

The publisher, the authors, and the editors are safe to assume that the advice and information in this book are believed to be true and accurate at the date of publication. Neither the publisher nor the authors or the editors give a warranty, expressed or implied, with respect to the material contained herein or for any errors or omissions that may have been made. The publisher remains neutral with regard to jurisdictional claims in published maps and institutional affiliations.

This Springer imprint is published by the registered company Springer Nature Singapore Pte Ltd. The registered company address is: 152 Beach Road, #21-01/04 Gateway East, Singapore 189721, Singapore

Preface

The 5th International Conference on Advances in Manufacturing and Materials Engineering (ICAMME 2022) is organized as a part of KOE IIUM Congress 2022 with the aim to provide a platform for knowledge sharing and interchange among researchers, academicians, and industrial expertise in terms of current research and development especially in the advancement of knowledge in Manufacturing Engineering and Materials Engineering.

This conference provides state-of-the-art information on traditional materials and manufacturing technology that are currently placed having limited applications in the industries and/or not meeting the Industry 4.0 on digital technology. This conference, thus, gives opportunity for senior as well as young scientists and academics from different parts of the world who are actively involved with the research in advanced and sustainable material, smart manufacturing, simulation, modeling and management to come together and share their experience on the latest advancements.

We would like to take this opportunity to thank most sincerely the co-organizers, supporters, sponsors, whose support made it possible to success the event and also to award prizes. Many thanks go to the members of the Organizing Committee and the International Advisory Committee and Reviewers who reviewed the conference paper and refereed the papers for the 'Lecture Notes in Mechanical Engineering' (indexed by SCOPUS) for publication.

Finally, sincere thanks go to the authors of the papers. Without their timely submission of manuscripts of high quality, publication of these proceedings would not have been possible.

August 2022

Publication Team
ICAMME 2022

Contents

Investigating the Synthesis of Activated Carbon from Carbon Chips of Carbon Fibre Reinforced Polymer for the Removal of Methylene Blue	1
Farhah Rusyda Fathi, Dzilal Amir, Nor Farah Huda Abd Halim, and Ricca Rahman Nasaruddin	
The Influence of Glycerol on Physical and Mechanical Properties of Mango Seed Starch Film	9
Nur' Aishah Ahmad Shahrin, Norshahida Sarifuddin, Farah Diana Mohd Daud, and Hafizah Hanim Mohd Zaki	
Influence of Cutting Edge Radius (CER) and Width of Cut (WOC) on Tool Wear in Milling SUS 316 Stainless Steel	17
N. F. H. Abd Halim, A. N. Dahnel, Umma Sankar Gunasegaran, Lim Joo Eng, M. S. Mohamad Amiruddin, and S. H. Tomadi	
Influence of Milling Parameters on the Characteristics of Alumina-Titania Nanocomposite Prepared by High-Energy Ball Milling	25
Siti Atikah Mohammad Asari, Mahani Yusoff, Mohamad Najmi Masri, Hidayani Jaafar, Mohd Hasmizam Razali, and Wan Mohd Norsani Wan Nik	
ANFIS Domestic Water Consumption Model Before and During Covid19 Pandemic in Tangerang Indonesia	33
Diah Septiyana, Mohamed Abd. Rahman, Tasnim Firdaus Binti Mohamed Ariff, Nor Aiman Sukindar, and Erry Yulian T. Adesta	
Microstructure and Mechanical Properties of Porous Aluminium Composites Reinforced with Diamond Particles	41
Bisma Parveez, Nur Ayuni Jamal, Syazwan b Mohamad Kadri, Hafizah Hanim Mohd Zaki, and Ahmad Zahirani Ahmad Azhar	

Improving Bending Deformation Behavior of Superelastic NiTi Archwire by Ageing Treatment	47
N. A. N. I. Latiffi, N. S. S. Khairi, M. F. Razali, and M. H. Hassan	
A Short Review on Diamond Reinforced Aluminium Composites	55
Nur Izzah Nazurah Kusuadi, Nur Ayuni Jamal, and Yusilawati Ahmad	
Amperometric Study of P3HT/Multi-walled Carbon Nanotubes Composite for Malathion Sensing	63
Nurul Syahirah Nasuha Sa'aya, Siti Zulaikha Ngah Demon, Norli Abdullah, Ahmad Farid Mohd Azmi, and Norhana Abdul Halim	
Force Deflection Behaviors of NiTi Archwires at Different Bending Conditions: A Mini Review	71
A. Munir and M. F. Razali	
Effect of Carbon Dioxide Gas Flow Rate on Production of PCC from Carbide Lime Waste	77
Emee Marina Salleh, Rohaya Othman, Siti Noorzidah Mohd Sabri, and Zawawi Mahim	
Surface Wettability of Treated Quartz Substrates and Their Optical Characterization of Deposited Reduced Graphene Oxide	85
Nurul Farhana Abu Kasim, Norhana Abdul Halim, Ahmad Farid Mohd Azmi, Norli Abdullah, Keat Khim Ong, and Siti Zulaikha Ngah Demon	
Development of Regression Model Between Driving Comfort Perception and Muscle Contraction	93
Darliana Mohamad, Baba Md Deros, Dian Darina Indah Daruis, and Ahmad Rasdan Ismail	
Comparative Study on Performance Characteristics of Modified Alloy Steels by TIG and Water Jet Peening Processes	101
A. Azhari, A. N. Md Idriss, and M. A. Maleque	
Signal Improvement on Fibre Optic Evanescent Wave Sensor Based Polymeric Sensitive Coating of Chitosan-Agarose Hydrogel	109
Muhammad Haziq Noor Akashah, Siti Rabizah Makhsin, Rozina Abdul Rani, Nor Hayati Saad, Khairunisak Abdul Razak, Peter Gardner, and Patricia J. Scully	
Tribological Behavior of Cartilage Replacement with the Presence of Bio-Lubrication	117
Farah Nabillah Kazwa, Salmiah Kasolang, and M. Mazwan Mahat	
The Physical Activation and Chemical Activation Reaction During Synthesis of Activated Carbon from Empty Fruit Bunch	123
Hasan Marzuki, Alya Naili Rozhan, and Hadi Purwanto	

Heterotrigona Itama Kelulut Honey Dehydration Process to Prolong Shelf Life 131
 Mohd Amirul Ashraf Muhammad, Adibah Amir,
 and Abdul Rahman Abdul Razak

The Future Directions of IBS Prefabrication Implementation in the Construction Industry 139
 Hassan Ismail, Suaathi Kaliannan, and Mohd Ruzi Hamzah

Effect of Zirconia Doping on the Sintering and Mechanical Properties of Hydroxyapatite Bioceramic 147
 S. Sivakumar, C. H. C. Alexander, H. L. Teow, M. Yeakub Ali,
 and S. Ramesh

Properties of Alumina–Zirconia Composites Prepared by Slip-Casting Method 155
 K. Y. Sara Lee, S. Ramesh, L. F. Siah, A. K. Nor Azmah, W. D. Teng,
 N. M. Mubarak, and D. Kurniawan

Mechanical and Thermal Properties of 3D Printed Polylactic Acid Reinforced Alkaline Lignin with Epoxidized Palm Oil Bio-Composites 161
 Nurul Amirah Abd Rahman, Hazleen Anuar, Fathilah Ali,
 and Jonghwan Suhr

Effect of Supercritical Carbon Dioxide Pressure on Foamed PolyLactic Acid Biocomposite 169
 Nurfarahin Mohd Nordin, Hazleen Anuar, and Yose Fachmi Buys

Characteristics of Zinc-Doped Hydroxyapatite Prepared Using Biogenic and Synthetic Calcium Precursor 175
 C. M. Mardziah, N. R. N. Masdek, N. M. Mubarak, and S. Ramesh

Energy Cost Characteristics of a Micro-Wind Power System Based on Different Capacity Factor: A Case Study of Locations in Nigeria 183
 Bashir Isyaku Kunya, Yusuf Alhassan, S. T. Auwal, Magaji Tambaya,
 D. Kurniawan, and S. Ramesh

Parametric Study on Abrasive Wear of Reinforced Polytetrafluoroethylene Composites Using Taguchi Model 191
 Musa Alhaji Ibrahim, Magaji Tambaya, Auwalu Gidado Yusuf,
 S. T. Auwal, D. Kurniawan, and S. Ramesh

Electric Vehicle Modeling: A Review 199
 Ibraheem. S. M. Alzehawi, Waleed F. Faris, Fadly Jashi Darsivan,
 and Mohammed Rafeeq

Wear and Corrosion of Ceramic Coated Metallic Surface in Presence of Biodiesel	207
Md Abdul Maleque, Masjuki Hassan, Safa Yusuf Cetin, Ihsan Efeoglu, and Md Mustafizur Rahman	
Linear Shrinkage of ZTA–TiO₂–Cr₂O₃ Ceramic Cutting Tool	215
Raqibah Najwa Mudzaffar, Ahmad Zahirani Ahmad Azhar, Hanisah Manshor, Nik Akmar Rejab, and Afifah Mohd Ali	
The Effect of LaB₆ Target Current on Mechanical and Tribological Properties LaB₆ Doped TiBCN Based Films Deposited by CFUBMS-HiPIMS	221
Nuriye Aksakalli, Ihsan Efeoglu, Berkay Gumus, and Evren Tan	
Enhancing the Tool Life of Aluminium Oxide (Al₂O₃) Inserts Using Hybrid Microwave Energy in Dry Machining of High Strength Steel (KRUPP 6582)	229
Rakan Hatem Alawbali and Tasnim Firdaus Ariff	
A Comparative Study of Additively Manufactured Nickle Titanium (NiTi) Shape Memory Alloy (SMA)	237
Sivasanghari Karunakaran, Dayang Laila Abang Abdul Majid, Che Nor Aiza Jaafar, Muhammad Hussain Ismail, and Husam Yahya Imran	
The Mechanical and Tribological Properties of LaB₆ Thin Films Deposited by Closed-Field Unbalanced Magnetron Sputtering	245
Gökhan Gülten, Mustafa Yeşilyurt, Banu Yaylalı, Yaşar Totik, and İhsan Efeoglu	
Deposition of Nb Doped CrYN Thin Films: Investigation of Structural, Mechanical and Tribological Properties	251
Furkan Yüksel, Gokhan Gulden, Banu Yaylalı, Yasar Totik, and Ihsan Efeoglu	
Annealing Effect on Nb Additive CrYN Thin Films Deposited by Magnetron Sputtering	259
Banu Yaylalı, Gökhan Gülten, Mustafa Yeşilyurt, Furkan Yüksel, M. Alperen Polat, and İhsan Efeoglu	
Structural, Optical, and Photocatalytic Performance of ZnO Particles Synthesized via Direct Heating Technique for Rhodamine B Removal	267
Chee Meng Koe, Swee-Yong Pung, and Sumiyah Sabar	

Synthesis and Characterization of Ta/TaN Coatings with CFUBMS-HiPIMS Technology 273
 Muhammed Alperen Polat, Gökhan Gülten, Yaşar Totik, Md. Abdul Maleque, Haji Hassan Masjuki, Safa Yusuf Çetin, and İhsan Efeoglu

Enablers and Barriers of Lean Manufacturing Implementation in Indonesian Manufacturing Companies 281
 Herry Agung Prabowo, Erry Yulian Triblas Adesta, Farida, and Avicenna

Study on the Challenges of Implementing Industry 4.0 in UAE Using Analytical Hierarchy Process AHP Method 289
 Muataz Al Hazza, Hamdah Al Dahmani, Fatmah Alyammahi, and Amel Al Naqbi

Surface Treatment of Polyethylene Terephthalate Substrate by Sodium Hydroxide 297
 Najwa Ibrahim and Mariatti Jaafar

Enhancement of Fenton Process Using High Entropy Alloy Powder as Catalyst 305
 Nur Hudawiyah Abu Hassan, Mohammed Saedi Jami, Farah Diana Mohd Daud, Nur Ayuni Jamal, and Norhuda Hidayah Nordin

Analysis of the Adjusting Bolts System’s Contribution to Levelling Error of the Heated Bed in FDM 3D Printer 313
 Rudi Kurniawan Arief, Nor Aiman Sukindar, Irfan Hilmy, and Erry Yulian T. Adesta

Failure Mechanism on Ti-6Al-4V Material Processed Using Selective Laser Melting (SLM) 321
 Sukri Mubarak, Poppy Puspitasari, Andoko Andoko, Abdul Munir Hidayat Syah Lubis, Avita Ayu Permanasari, and Muhammad Ilman Hakimi Chua Abdullah

Lean Manufacturing and Six Sigma Principles Implementation in the Industry: Case Study 327
 Muataz Hazza Al Hazza, Syahir Zahari, Islam Bourini, Md Yusof Bin Ismail, Mohammad Yeakub Ali, and Erry Y. T. Adesta

Study of Burrs in Milling of Marine Grade AISI 316 Stainless Steel with Minimum Quantity Lubrication 337
 Muhammad Haziq Bin Haji Awang Jaafar, Mohammad Yeakub Ali, Maziri Bin Morsidi, S. Ramesh, Erry Yulian T. Adesta, and Seri Rahayu Ya’akub

Friction Welding of Similar and Dissimilar Materials: Analysis of Tensile Strength	343
Ak. Md. Asyraf Aditya, Mohammad Yeakub Ali, S. Ramesh, Ahmad Shamil Abd Rahman, and Muataz Al Hazza	
Performance of Graphite Based Nanofluid in MQL Grinding of Mild Steel	351
M. R. Hasmizuan Rais, Mohammad Yeakub Ali, S. Ramesh, Seri Rahayu Ya'akub, and Zunaidi Ibrahim	
Study of Surface Integrity in Turning Ti-Alloy Using Optimal Depth of Cut	359
Dinesh Reddy Nallagangula, Abdul Md Mazid, Neamul Khandoker, and Mohammad Yeakub Ali	
Tribology Properties of Titanium Alloy (Ti-6Al-4V) at Various Temperature on α/β Solution Treatment and Aging Condition	367
Poppy Puspitasari, Muhammad Raffli Putra Wardana, Diki Dwi Pramono, Abdul Munir Lubis, Avita Ayu Permanasari, Muhammad Ilman Hakimi Chua Abdullah, and Puput Risdanareni	
Experimental and Thermal Modeling of Beeswax-Filled Extruder via Solidwork for Batik Printing	373
Sharifah Imihezri Syed Shaharuddin, Sharifah Nur Balqis Syed Azman, Norhashimah Shaffiar, M. K. Nor Khairusshima, and Nor Aiman Sukindar	
Electrical Resistance of Fabric Immersed with PEDOT:PSS Doped Ag NPs and DMSO Solution	381
Nur'Aishah Ahmad Shahrim, Zuraida Ahmad, Wan Nur' Alia Nadhirah Wan Solah, Amelia Wong Azman, Norshahida Sarifuddin, and Yose Fachmi Buys	
An Experimental Study on the Tensile Strength of Friction Stir Welded AA5052 Aluminum Alloy	389
Ky-Thanh Ho, Ba-Hoi Nguyen, Ngoc-Tuan La, Thai-Son Le, and Van-Thong Pham	
Palladium/Lathanum Cobaltite Catalyst Polymer Exchange Membrane Fuel Cell for Electric Vehicle	397
Ataur Rahman, Sany Ihsan, and Ali Momoud	
Review on Fused Deposition Modelling Extruder Types with Their Specialities in Filament Extrusion Process	407
Muhammad Afif Md Azhar, Nor Aiman Sukindar, Mohd Hanafi Ani, Hazleen Bt Anuar, Shafie Bin Kamaruddin, Sharifah Imihezri Syed Shaharuddin, Mohd Yusry Mustafa, Erry Yulian Triblas Adesta, Rudi Kurniawan Arief, and Mohd Hafis Sulaiman	

Extrusion Temperature and Viscosity of Various Soy Wax/Beeswax Blends 415
 Sharifah Imihezri Syed Shaharuddin, Nur Amalina Mustafa,
 Norhashimah Shaffiar, M. K. Nor Khairusshima,
 and Nor Aiman Sukindar

Investigation Study on Risk Management Practices in Adding Value to the New Product Development 421
 Muataz Hazza Al Hazza, Nasuha Bt Mohd Nasir, Islam Bourini,
 Zubaidah M. Hazza, Atiah Abdullah Sidek, and Mohammad Yeakub Ali

A Comparison of the Thermal Conductivity of 3D Printed ABS and ABS/Graphite at Various Infill Patterns and Densities 429
 Ahmad Amri Nordin, Siti Nazehah Mohd Sofian,
 Sharifah Imihezri Syed Shaharuddin, Norhashimah Shaffiar,
 Abd Malek Abdul Hamid, and Nor Aiman Sukindar

Optimizing Tensile Strength of PLA-Lignin Bio-composites Using Machine Learning Approaches 437
 Mohd Romainor Manshor, Amjad Fakhri Kamarulzaman,
 Hazleen Anuar, Siti Fauziah Toha, Fathilah Ali, Nor Aiman Sukindar,
 Jonghwan Suhr, and Nursyam Dzuha Haris

Detection Method of *Kelulut* Honey Adulteration 445
 Nurul Zafiq Jefferi, Adibah Amir, and Hadi Purwanto

Investigation of the Wear Behavior of Forging Tool by Ball on Disc and Impact Sliding Tribometer 451
 Yaşar Sert, Tevfik Küçükömeroğlu, Hüccet Kahramanzade,
 and İhsan Efeoğlu

Towards Whole Day Thermoelectric Energy Scavenging from Solar Using Carbon Based Photothermal Nanofluid 461
 Penzi Panguot, Abdah Nadhirah Khamis,
 Mohd Aszwan Jimal, Nur Natasha Erna Herman, Lily Yong,
 and Megat Muhammad Ikhsan Megat Hasnan

Diffusion, Seebeck and Conductivity of Spin Crossover Complexes Towards Thermoelectric Power Generation 469
 Megat Muhammad Ikhsan Megat Hasnan, Chai Chang Yei,
 Nur Aqilah Mohamad, Ahmad Razani Haron, Pungut Ibrahim,
 Herwansyah Lago, Ismail Saad, and Hazlihan Haris

In Situ Measurement and Remediation of Condensation Issue in Sarawak General Hospital Molecular Lab During COVID 19 477
 Muhammad Syukri Imran Abdullah, Azhaili Baharun,
 Abdul Malik Zainal Abidin, Noor Muhammad Abd Rahman,
 and Nyuk Yen Chin

Cement-Based with Partial Replacement of Nano-Silica for Improvement in Compressive Strength	483
Mudrikah Sofia Mahmud, Aina Fadzleen Aadnan, Farah Diana Mohd Daud, Norshahida Sarifuddin, Hafizah Hanim Mohd Zaki, Norhuda Hidayah Nordin, and Nur Farahiyah Mohammad	
Effect of Oxygen Gas Exposure on T91 Alloy at High Temperature Oxidation of Steam Reformer	491
Muhammad Rafiq Haikal Rosdin, Ahmad Abdul Mun'im Ismail, Abd Malek Abdul Hamid, Hadi Purwanto, Suhaimi Illias, Syed Noh Syed Abu Bakar, and Mohd Hanafi Ani	
Effect of Zn Content on Biodegradable Mg Alloy Synthesized via Mechanical Alloying for Biomedical Application	501
Emee Marina Salleh and Zuhailawati Hussain	
Effect of Pore Forming Agent on Phase Transformation Behavior of Porous NiTi Shape Memory Alloy	509
Hafizah Hanim Mohd Zaki, Nur Amanina Abd Kadir, Nur Ayuni Jamal, M. Abd. Maleque, Farah Diana Mohd Daud, Norshahida Sarifuddin, and Jamaluddin Abdullah	
Nano-Structured Zinc Oxide/Silicon Dioxide Thermoelectric Generator: A Waste Heat Harvesting Technology	517
Ataur Rahman, Yusuf Abdi, Kyaw Myo Aung, and Sany Ihsan	
Mechanical and Structural Properties of Epoxy Bio-Composite Using Fish Bones as Bio-Filler	525
Azriena Nathasa Zakaria and Tasnim Firdaus Ariff	
Characterization of New Biofluid Lubrication Formulation Using Castor Oil with Hyaluronic Acid Additive for Artificial Joints	533
Amira Atikah Suhairi, M. Mazwan Mahat, and Nurul Nadiyah Mohd Kamaldin	
Blast Furnace Slag Cement Clinker Production Using Limestone-Hot Blast Furnace Slag Mixture	539
Ahmad Abdul Mun'im Ismail, Muhammad Rafiq Haikal Rosdin, Alya Naili Rozhan, Hadi Purwanto, Abd Malek Abdul Hamid, Muhamad Faiz Md. Din, Mohd Fairus Mohd Yasin, and Mohd Hanafi Ani	
A Quad Band Negative Permittivity Microwave Metamaterial Design for Satellite Applications with Wider Bandwidth	547
Md. Bellal Hossain, Mohammad Rashed Iqbal Faruque, and Muhamad Roszaini Roslan	

Fabrication of Plaque Using Hot Press Method for Recycling Plastic Material 555
 Haszeme Bin Abu Kasim, Mohamad Faizuddin Bin Hashim, Ab Aziz Bin Mohd Yusof, Noor Hafiz Bin Noodin, Hazim Sharudin, and Mohamad Hussain Bin Ismail

A Case Study on Exploring the Benefits and Challenges Influencing the Implementation of Life Cycle Assessment as a Design Tool in an Air Filter Manufacturing Industry 563
 Abu Sadik Billahil Waasi, Atiah Abdullah Sidek, Afiqah Alias, and Muataz Hazza Al Hazza

Characterization of Poly(vinyl) Alcohol Based Aerogel Assisted by Cellulose Nanocrystal 571
 Raimi Fariz Nasrudin, Noorasikin Samat, and Nurul Sakinah Engliman

Perforation Size Effect on Lotus Leaf Based Oil/Water Separator 579
 Muhammad Hariz Ahat, Fethma M. Nor, S. Ramesh, and Denni Kurniawan

Investigation of Chip Formation During Turning of Aluminum Alloys 7075-T651 in Dry and Chilled Air Condition 585
 Muhammad Izzat Amin Bin Rosli, Natasha A. Raof, Aishah Najiah Dahnel, Suhaily Mokhtar, and Nor Khairusshima Muhamad Khairussaleh

The Influence of Cutting Parameters and Chilled Air on the Tool Wear of Uncoated Solid Carbide Cutting Tool During Milling CFRP ... 591
 R. Muhammad Nabil, M. K. Nor Khairusshima, R. Siti Fatirah, and Sharifah Imihezri Syed Shaharuddin

Study on the Hardness of Uncoated Carbide Cutting Tool at Different Cutting Parameters 599
 K. Muhammad Irfan, M. K. Nor Khairusshima, A. R. Natasha, D. Aishah Najiah, and M. Suhaily

Cutting Temperatures and Their Effects on Drilling of NFRP Composites Using Taguchi Method 605
 Muhammad ‘Izzudin Mohd Zaid, Suhaily Mokhtar, Aishah Najiah Dahnel, Natasha A. Raof, and Nor Khairusshima Muhamad Khairussaleh

Investigation of Microgels and Double Crosslinked Microgels Containing 2-Carboxyethyl Acrylate (CEA) 613
 Syazwani Mohd Zaki and Sharan Musa

Magnetic Properties of High Entropy Alloys as Electromagnetic Wave Absorber 621
Ain Najwa Md Saupi, Norhuda Hidayah Nordin, Nur Azam Abdullah, and Muhammad Hanafi Azami

The Latching Performance of Soy Wax/Beeswax Prints in Alkaline Dye Solution and Heated Water 629
Sharifah Imihezri Syed Shaharuddin, Muhammad Rizal bin Saidi, Norhashimah Shaffiar, M. K. Nor Khairusshima, and Hazlina Md. Yusof

Analysis and Optimum Machining Parameters on Surface Roughness and Material Removal Rate for Titanium Alloy in Milling Machining with MQL 637
Siti Haryani Tomadi, Nor Farah Huda Abd Halim, H. Mas Ayu, R. Daud, and Muhammad Ariff Zakaria

Thermoelectric Properties of B-FeSi₂ Thermoelectric Module Utilizing Cast-Iron Scrap Chips 645
Assayidatul Laila Nor Hairin, Muhammad Haziq Hakmal Jailani, and Megat Muhammad Ikhsan Megat Hasnan

Mechanical Properties of Magnesium Hydroxide/Halloysite Nanotubes Reinforced Polyamide 11 Nanocomposites 653
Nur Najma Athirah Azahari, Hazleen Anuar, Azman Hassan, Mohammed Jawaaid, Zahurin Halim, and Sani Amril Samsudin

Two-Stage Sintering of Zirconia Toughened Alumina Composite (ZTA) Doped with Copper Oxide 661
S. Sivakumar, C. H. C. Alexander, H. L. Teow, M. Yeakub Ali, and S. Ramesh

Investigating the Synthesis of Activated Carbon from Carbon Chips of Carbon Fibre Reinforced Polymer for the Removal of Methylene Blue



Farhah Rusyda Fathi, Dzilal Amir, Nor Farah Huda Abd Halim, and Ricca Rahman Nasaruddin

Abstract The milling operation of carbon fibre reinforced polymers (CFRP) generates waste named carbon chips (CC) which could be converted into value-added products such as activated carbon (AC). In this study, we synthesized AC from the CC of CFRP. The effects of mass ratio of raw materials and activating agent, reaction temperature, and the concentration of acid in the washing step, to the yield of AC and the removal of methylene blue in solution, were investigated. The results show that CC from CFRP gave higher yield and performance when compared to AC produced from durian skin (DS) and CC-DS mixture. Higher reaction temperature (600 °C) and 5% concentration of nitric acid (HNO₃) resulted in the highest yield and methylene blue (MB) adsorption percentage of the AC. As AC is widely used in many applications such as water and air remediations, this study can significantly promote the use of CC, the CFRP waste as raw materials for the AC synthesis.

Keywords Carbon fibre reinforced polymer · Carbon chips · Durian skin · Activated carbon · Methylene blue removal

1 Introduction

Carbon fibre reinforced polymer (CFRP) is a composite that has excellent tensile strength, modulus, and fatigue strength. It is widely used for aircraft and automotive structural applications [1]. During the process of making products from CFRP such as milling and grinding, the waste of CFRP, commonly called as carbon chips (CC) are generated. Recycling of CC is difficult due to the resin composition and CFRP complex structures [2, 3]. As the annual worldwide demand for CFRP has increased,

F. R. Fathi · D. Amir · R. R. Nasaruddin (✉)

Department of Chemical Engineering and Sustainability, Kulliyah of Engineering, International Islamic University Malaysia, Jalan Gombak, Kuala Lumpur, Malaysia
e-mail: riccanasaruddin@iium.edu.my

N. F. H. A. Halim (✉)

Department of Materials and Manufacturing Engineering, Kulliyah of Engineering, International Islamic University Malaysia, Jalan Gombak, Kuala Lumpur, Malaysia
e-mail: farahudahalim@iium.edu.my

the CC generation from CFRP is also increasing. Other than recycling, this waste could be converted into value-added product, such as activated carbon (AC) due to its high carbon content. To the best of our knowledge, there is still lack of study that investigate the use of CC of CFRP as raw material for the AC synthesis.

On the other hand, durian skin (DS) has been increasingly converted into AC as one of its solid-waste management strategies [4, 5]. Comparing the AC synthesized from CC of CFRP with the AC synthesized from DS could determine the potential of the CC of CFRP as raw material for the AC synthesis. Thus, in this study, we investigated the yield percentage and adsorption performances of the AC synthesized from CC of CFRP and compared the results with the AC produced from DS. The effects of activating agent, reaction temperature and concentration of nitric acid in the washing step were also studied. Understanding the effects of synthesis parameters is helpful to further optimize the synthesis of AC from CC of CFRP [6].

2 Materials and Methods

2.1 Materials

Carbon fibre reinforced polymer (CFRP) was collected from the Department of Materials and Manufacturing, Kulliyah of Engineering (KOE), International Islamic university Malaysia (IIUM), meanwhile the DS was collected from the local seller. Potassium hydroxide (KOH) and nitric acid (HNO_3) were obtained from the Department of Chemical Engineering, KOE, IIUM. Methylene blue (MB) of aquarium application grade was purchased from local seller.

2.2 Synthesis of AC

Pretreatment Of Raw Materials With Activating agent

The collected CC of CFRP and DS were first cleaned, washed, and dried to remove some external impurities and remaining durian flesh, respectively. Then, they were grinded into small sizes (about 1-2 mm). The raw materials were then weighted (*parameter a*) and put into conical flask and mixed with certain amount of activating agent, KOH (*parameter b*) for 2 h. Then the mixture was dried in oven at 80 °C for 3 h. The mass of the treated raw materials was recorded as the initial mass (m_0).

Calcination of Raw Materials to Synthesize AC

The pre-treated raw materials were put into porcelain crucible and calcined in a Carbolite furnace for 1 h at desirable temperature (*parameter c*). After the synthesized AC cooled down, the acid-washing step took place whereby the AC was soaked in HNO_3 with certain concentration (*parameter d*) for 5 min and then it was washed

Table 1 Variation of parameters in the synthesis of AC

#	Parameter a Raw materials (g of CC: g of DS)	Parameter b Amount of KOH (g of a: mL of KOH)	Parameter c Temperature (°C)	Parameter d Acid Conc. (%)
1	<ul style="list-style-type: none"> • 0.6: 0.0 (1:0) • 0.3: 0.3 (1:1) • 0.0: 0.6 (0.1) 	1: 2	200	5
2	*(1:0)	<ul style="list-style-type: none"> • 0.25: 0.5 (2:1) • 0.5: 0.5 (1:1) • 0.5: 1 (1:2) 	200	5
3	*(1:0)	*(1:1)	<ul style="list-style-type: none"> • 200 • 400 • 600 	5
4	*(1:0)	*(1:1)	*(600)	<ul style="list-style-type: none"> • 3 • 5 • 10

* The values are selected from previous experiment

with distilled water several times until the pH of the discarded water becomes neutral. Next, the synthesized AC was dried in the oven for 3 h. The final mass of the AC (m_f) was recorded. Yield of AC was calculated as in Eq. 1, where m_o was the initial mass of the raw materials and m_f is the mass of the synthesized AC.

$$\text{Yield}(\%) = \frac{m_f}{m_o} 100 \quad (1)$$

Variation of Parameter

The effects of each parameter (*parameter a, b, c* and *d*) to the yield of AC and to the MB adsorption percentage were investigated using one-factor-at-a time (OFAT) method. The values of *parameter a, b, c* and *d* were varied as in Table 1. Other parameters (i.e., reaction time and drying time) were kept constant as stated previously.

2.3 Methylene Blue (MB) Removal in Solution

MB removal in solution by its adsorption onto the AC was selected to indicate the adsorption percentage of AC because it is simple and can be observed easily by the colour change from bright blue to colourless (indicating the adsorption had occurred) [6]. The adsorption of MB onto AC was also compared by using UV–Vis spectroscopy JASCO V780 series by analysing the UV–Vis absorption at wavelength of 600 nm for MB characteristic peak. The UV–Vis absorption is directly proportional to the concentration of MB in the solution. Briefly, 0.018 mg/L MB was prepared using

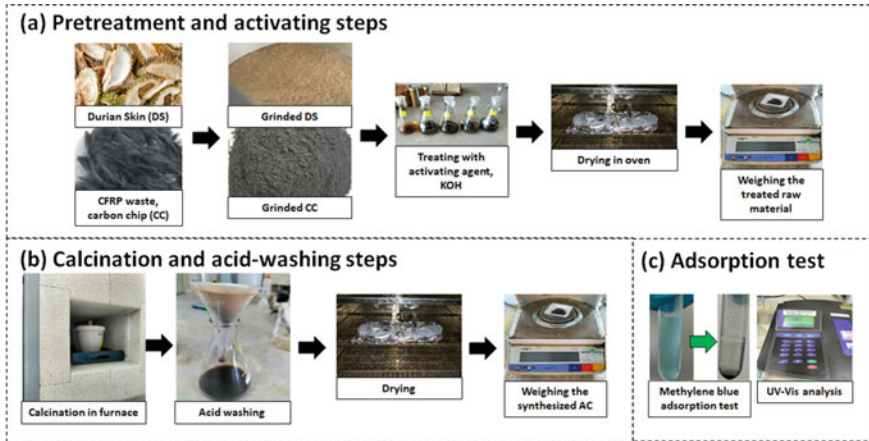


Fig. 1 Images of **a** pre-treatment and activating steps, **b** calcination and acid-washing steps and **c** adsorption test

distilled water and its UV–Vis absorption was determined and recorded (A_0). Then, 1 mL of the solution was put inside a 3 mL cuvette containing 0.01 g of synthesized AC. The mixture was left at room temperature for 24 h without stirring. After that, the final UV–Vis absorption of the MB solution (A_f) in the cuvette was determined and recorded. The MB adsorption percentage was determined as in Eq. 2:

$$\text{Adsorption percentage (\%)} = \frac{A_o - A_f}{A_o} \times 100 \quad (2)$$

All the procedures are summarized in following Fig. 1(a–c). All experimental runs were done in duplicates and the average of the data was taken for further analyses.

3 Results and Discussion

Figure 2a shows the yield percentage and MB adsorption percentage of AC from different sources of raw material. The highest yield percentage is AC from CC which is 45.80% and the highest MB adsorption percentage is 72.90%. The weight of all synthesized ACs decreased because the calcination process removed most organic compounds in the carbonaceous structure of the precursor. The yield percentage of AC synthesized from CC of CFRP was higher than AC synthesized with DS because CFRP contains more carbon materials than DS. DS contains more organic compounds, especially sulfur-containing molecules which easily removed during the calcination process via hydrogenation, desulfurization, and condensation processes [7]. Meanwhile, AC synthesized from the mixture of CC and DS gave an intermediate yield percentage.

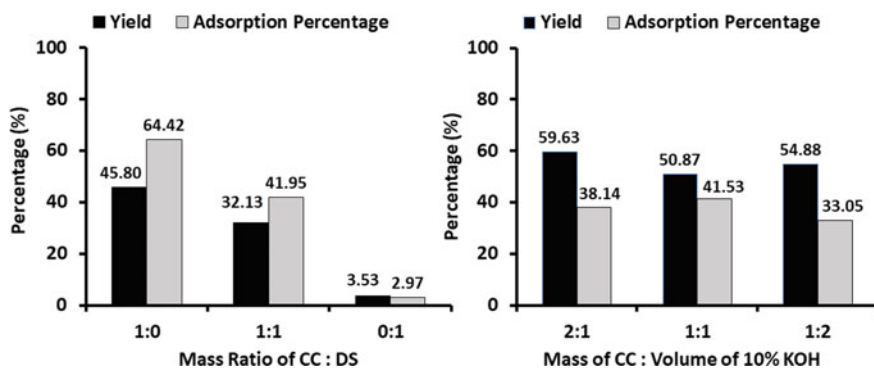


Fig. 2 Yield and MB adsorption percentages synthesized by **a** different mass ratio of CC (from CFRP) and DS, and **b** different ratio of mass of CC to volume of 10% KOH

Results in Fig. 2a also show that the MB adsorption percentage follows the same trend of the yield percentage. Adsorption percentage of AC is influenced by the size and volume of AC pores and the presence of carboxyl or hydroxyl groups on the AC surface. The high MB adsorption percentage might indicate the presence of larger pore sizes and volumes, thus more active sites for adsorption of MB on the AC [8] which can be further confirmed by Breunauer-Emmet-Teller (BET) and scanning electron microscopy (SEM) analyses. Based on the results in Fig. 2a, AC synthesized from 100% CC of CFRP was used for further study.

Graph in Fig. 2b shows that the highest yield was obtained when the ratio of mass of CC-to-the volume of KOH ($R_{\text{massCC}/\text{volumeKOH}}$) was 2:1. However, in terms of MB adsorption percentage, the best performance was obtained when $R_{\text{massCC}/\text{volumeKOH}}$ was 1:1. It was found that MB adsorption percentage increases with the increase of KOH as more pores were formed. However, an excess amount of KOH could damage the pores and reduce its adsorption capacity. Hence, the $R_{\text{massCC}/\text{volumeKOH}}$ of 1:1 was selected for further study.

Effects of other important parameters which are reaction temperature and concentration of acid for the washing step in the synthesis of AC are shown Fig. 3a, b, respectively. Based on graph in Fig. 3a, calcination at 600 °C resulted in the medium yield percentage (44.4%) but the highest MB adsorption percentage (74.58%). It was also found that lower temperature at 200 °C produced the highest yield of AC but its MB adsorption percentage is comparably high with the MB adsorption percentage of AC synthesized at 600 °C. The highest yield may be due to less removal of organic compounds from the resins in CFRP at lower temperature, thus giving more mass to the synthesized AC. Therefore, it is hard to tell that the AC produced with this low calcination temperature is the best as some uncalcined carbon materials might still exist. Although, in terms of cost benefit, lower temperature is preferable to reduce the cost of production, the selected temperature used for further study was 600 °C because of the highest MB adsorption percentage and it is confirmed that most of the carbon materials have been calcined at high temperature and converted into AC [9].

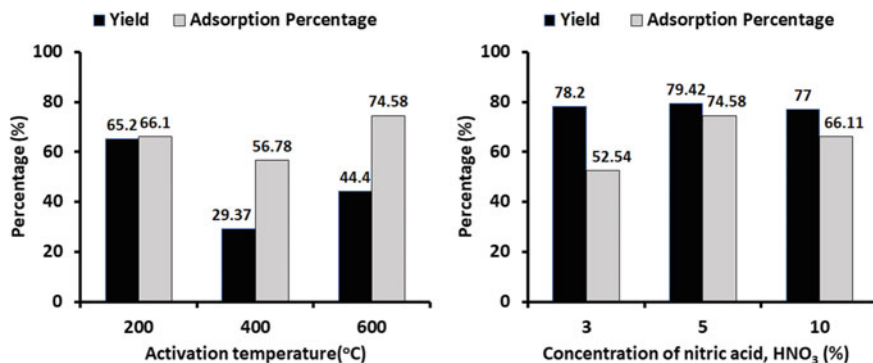


Fig. 3 Yield and MB adsorption percentages synthesized by **a** different reaction temperature, and **b** different concentration of HNO₃ in acid-washing step

Acid washing steps is important in the synthesis of AC because the process can increase the carboxyl and hydroxyl functional groups on the AC surface, for a better adsorption capacity. Based on the graph in Fig. 3b, the concentration of acid did not affect the yield of AC as acid-washing was done after the calcination process. 5% concentration of acid improved the MB adsorption percentage as compared to lower concentration (3%). However, when the concentration is further increased to 10%, the MB adsorption percentage decreased, probably due to damages to the pore structures of AC caused by the too acidic condition.

4 Conclusion

In conclusion, 1:1 ratio of mass-to-volume of 10% KOH, 600 °C reaction temperature and 5% acid washing were found to be the parameters that produced the highest yield (~ 80%) of AC from CFRP waste with the highest MB adsorption percentage (>70%). The yield and adsorption capacity of AC from CFRP waste was also found to be better than AC produced from durian skin, a common biomass waste used in the synthesis of AC. Therefore, CFRP waste has a promising potential as raw materials for the AC synthesis and in the removal of methylene blue in the treatment of wastewater from textile industry.

References

1. Mustafa AM, Suhaimi ABA, Shahrudin NS, Halim NFHA (2021) An experimental investigation on surface quality of CFRP after milling in cutting fluid environment. *J Phys Conf Ser* 2051:02053
2. Soraia P, Silvestre TP (2011) Recycling carbon fibre reinforced polymers for structural applications: technology review and market outlook. *Waste Manage* 31(2):378–392
3. Witik RA, Teuscher R, Michaud V, Ludwig C, Månson J-AE (2013) Carbon fibre reinforced composite waste: an environmental assessment of recycling, energy recovery and landfilling. *Compos A Appl Sci Manuf* 49:89–99
4. Mokhtar MF, Latib EHA, Sufian S, Ku Shaari KZ (2012) Preparation of activated carbon from Durian shell and seed. *Adv Mater Res* 626:887–891
5. Foo KY, Hameed BH (2012) Textural porosity, surface chemistry and adsorptive properties of durian shell derived activated carbon prepared by microwave assisted NaOH activation. *Chem Eng J* 187:53–62
6. Arcibar-Orozco JA, Barajas-Elías BS, Baltazar-Campos H, Rangel-Mendez R (2022) Preparation of carbon materials from chromium-tanned leather shavings for the removal of dyes from aqueous solution. *Appl Water Sci* 12:213
7. Desa SS, Ishii T, Nueangnoraj K (2021) Sulfur-doped carbons from Durian peels, their surface characteristics, and electrochemical behaviors. *ACS Omega* 6(38):24902–24909
8. Mangun CL, Daley MA, Braatz RD, Economy J (1998) Effect of pore size on adsorption of hydrocarbons in phenolic-based activated carbon fibers. *Carbon* 36(1–2):123–129
9. Chandra TC, Mirna MM, Sunarso J, Sudaryanto Y, Ismadji S (2009) Activated carbon from durian shell: preparation and characterization. *J Taiwan Inst Chem Eng* 40(4):457–462

The Influence of Glycerol on Physical and Mechanical Properties of Mango Seed Starch Film



Nur'Aishah Ahmad Shahrim , Norshahida Sarifuddin ,
Farah Diana Mohd Daud , and Hafizah Hanim Mohd Zaki 

Abstract Films made of thermoplastic starch indicate the potential for usage as packaging materials. These films' mechanical qualities, however, are poor. Therefore, the purpose of this research was to determine how different plasticizer concentrations, such as glycerol, in starch, affected the physical and mechanical characteristics of the films. By using the solution casting process, 3 wt.% mango seed starch was produced and combined with 5–30 wt.% glycerol. The addition of 5 wt.% glycerol contributed by the well-dispersed starch molecules was found to increase the film's tensile strength (TS) to 3.26 MPa as shown by scanning electron microscopy (SEM). In mango seed starch, more glycerol addition lowers the TS but considerably raises the elongation at break (E%). Additionally, the glycerol-plasticized mango seed starch films showed greater solubility when the glycerol content was increased. The mechanical characteristics of mango seed starch films changed significantly depending on the amount of glycerol present for use in packaging.

Keywords Mango seed · Starch · Glycerol · Plasticizer · Thermoplastic film

1 Introduction

Academics and industries are working harder to preserve the sustainability of material systems. This includes making thermoplastic starch using biodegradable biopolymers. A polysaccharide known as thermoplastic starch is frequently utilized as a matrix for green composites to create biodegradable plastic packaging. Additionally, compared to other bio-based polymers, starch-based materials are easily developed by plasticizing a renewable resource, which is native starch, without the use of an expensive synthesis method, which is why they are extensively explored [1]. Very few studies have been published to far on starch from unconventional sources like mango seeds (*Mangifera indica*). Since mango seeds have a high starch yield (74–81%) and amylose content (21%) that contribute to the ability to produce films and

N. A. Shahrim (✉) · N. Sarifuddin · F. D. M. Daud · H. H. M. Zaki
Department of Manufacturing and Materials Engineering, Kulliyah of Engineering, International Islamic University Malaysia, 53100 Kuala Lumpur, Malaysia
e-mail: nuraishah.shahrim@live.iium.edu.my

the characteristics of films [2]. Mango seeds are therefore used in this study as a source of starch.

However, due to its robust intra- and intermolecular hydrogen bonds, starch often cannot function as a thermoplastic, leading to high moisture sensitivity and brittleness [3]. Hence, plasticizers such as glycerol and water must be added between 60 °C and 180 °C, commonly known as the gelatinization process, in order to modify the shape and enable it to be used similarly to the majority of conventional synthetic thermoplastic polymers [4]. The limitations of starch could be overcome by adding glycerol as a plasticizer to mango seed starch. The addition of the polyol should create structural changes in the polymer chain that will improve the tensile strength and elongation at break of the glycerol-plasticized mango seed starch film [5]. However, research on the impact of glycerol addition in the cotyledon (inner) region of mango seeds is rare. Utilizing a cheap supply of starch for the production of biodegradable thermoplastic film was the goal of the current investigation. Mango seed starch (MSS) film's mechanical and physical characteristics were examined in relation to its glycerol content.

2 Materials and Methods

2.1 Materials

Mango seeds were purchased at the neighborhood market, where the seeds are regarded as trash. Glycerol was purchased from Merck and is 84.5–85.5% pure according to the European Pharmacopoeia (Ph. Eur.).

2.2 Preparation of Thermoplastic Starch Film with Glycerol

The starch from mango seeds was extracted before creating thermoplastic (TPS) film in accordance with the method described in our earlier research [3, 7]. Then, using solution casting, the fabrication of TPS incorporation with glycerol was done. The film samples' components are abbreviated in Table 1. On a heated plate at 85 ± 5 °C, a 3 wt.% mango seed starch aqueous suspension was gelatinized while being continuously stirred. The gelatinized suspensions were given a plasticizer addition of 5 to 30 wt.% glycerol, which was agitated for 20 min at 250 rpm. After that, the slurries were cast on acrylic trays and left to dry in a 40 °C oven overnight. Films were carefully taken out of the trays and put in a desiccator for 24 h at 30% relative humidity (RH) before more testing.

Table 1 Used symbols and corresponding compositions of each film sample

Materials	Abbreviations	Samples (weight proportions, gram)		
		Starch	Glycerol	Distilled water
GTPS1	G05	3.0	0.5	96.5
GTPS2	G10	3.0	1.0	96.0
GTPS3	G15	3.0	1.5	95.5
GTPS4	G20	3.0	2.0	95.0
GTPS5	G25	3.0	2.5	94.5
GTPS6	G30	3.0	3.0	94.0

2.3 Characterization and Testing

A Scanning Electron Microscope (JEOL, JSM-IT 100; Japan) operating at an acceleration voltage of 10 kV with a magnification of 500 was used to analyze the morphology of the film surfaces. With an accuracy of 0.01 mm, a digital electronic caliper was used to measure the thickness of the film. A 20 × 20 mm² film sample was dried for 24 h at 105 °C to determine the amount of moisture in the film. Equation 1 was used to compute the weight variation of the film. Film samples were submerged in 30 mL of distilled water, stored in a sealed conical flask at 23 ± 2 °C, and intermittently swirled for 24 h to assess the film solubility. Using filter paper, the insoluble portion of the film sample was separated from the soluble components in distilled water before being dried for 24 h at 105 °C. Using Eq. 2, the solubility of the film was calculated.

$$\text{Moisture content}(\%) = \frac{\text{Mass of film} - \text{Mass of dried film}}{\text{Mass of film}} \times 100 \quad (1)$$

$$\text{Solubility}(\%) = \frac{\text{Mass of film} - \text{Mass of residue}}{\text{Mass of film}} \times 100 \quad (2)$$

The tensile strength and elongation characteristics of film were investigated using an ASTM D882-02-compliant Shimadzu MTS tensile tester.

3 Results and Discussion

3.1 Morphological Properties

The smooth surface of the G05 film as seen in the micrograph in Fig. 1a suggested that the starch molecules had been evenly distributed and that the structural integrity was being maintained because few granules were exposed in the low glycerol level.

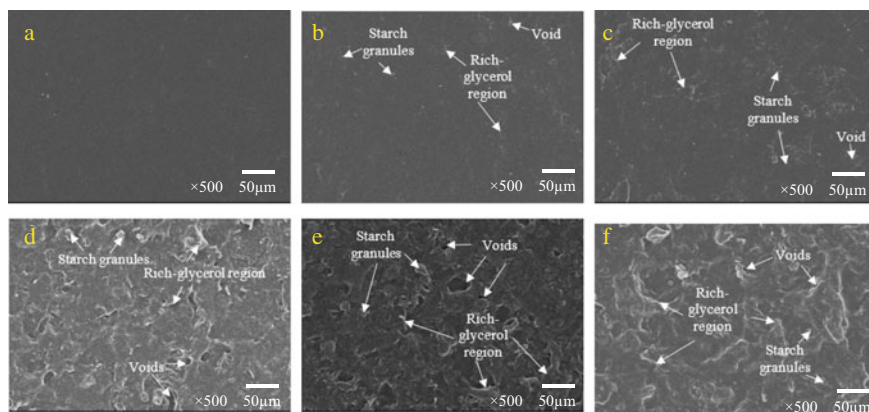


Fig. 1 SEM micrographs at $500\times$ magnification for plasticized mango seed starch films with various glycerol concentrations **a** 5, **b** 10, **c** 15, **d** 20, **e** 25, and **f** 30 wt. %

The surface appears to get rougher when glycerol content rises over 5 wt.%, and phase separation between starch and glycerol in blend films can be seen clearly as illustrated in Fig. 1b–f. The mango seed starch granules still had traces of their oval or cuboidal-like forms in the SEM, as indicated by the arrows in the micrographs.

3.2 Physical Properties

Table 2 displays the physical characteristics of mango seed starch films with glycerol contents ranging from 5 to 30 wt.%, including thickness, moisture content, and solubility.

With the addition of glycerol content from 5 to 30 wt.%, the thickness of the starch film increased from 0.187 to 0.262 mm. The tiny molecular size of glycerol and its function as a plasticizer in creating hydrogen bonds with starch chains and

Table 2 Physical properties of glycerol-plasticized mango seed starch films^a

Samples	Film thickness (mm)	Moisture content (%)	Film solubility (%)
G05	0.187 ± 0.018	14.13	20.25
G10	0.200 ± 0.009	25.00	21.21
G15	0.206 ± 0.010	36.21	24.32
G20	0.212 ± 0.012	42.86	27.50
G25	0.238 ± 0.008	49.65	27.78
G30	0.262 ± 0.005	54.36	27.94

^a Mean value ± standard deviation of triplicates

increasing free volume in the blended film may be responsible for the thicker film [7]. Because more hydrophilic groups interact with water molecules, thicker starch films with glycerol added cause the film's moisture content solubility to increase [8].

As the starch film becomes more hydrophilic with an increase in glycerol concentration, plasticization of mango seed starch films from 5 to 30 wt.% considerably increases the moisture content from 14.13 to 54.36% [9]. Higher glycerol concentration results in a greater capacity to absorb water due to the accessible hydroxyl group's strong hygroscopic character, which can interact with water by hydrogen bonds ($-\text{OH}$) [10].

Due to the hydrophilicity of glycerol as a plasticizer, which facilitated the absorption of water molecules, film solubility improved from 20.25 to 27.94% when glycerol content increased from 5 to 30 wt.%. Additionally, because glycerol's hydroxyl groups are highly affine to water molecules, glycerol-plasticized starch-based films may readily hold onto water in their matrix and create hydrogen bonds, acting as a water-holding agent [7].

3.3 Mechanical Properties

The starch-based films were found to be fragile because they had low glycerol contents—less than 5 wt.%. As a result, the minimal glycerol content in this investigation was fixed at 5 wt.%.

The incorporation of 5 wt% glycerol content in mango seed starch films exhibits the maximum tensile strength value of 3.26 MPa, as illustrated in Fig. 2. This may be explained by the dominance of the starch-starch intermolecular attraction over the strong hydrogen bonds created by that interaction [11]. The homogeneity of the G05 film's surface indicated by the well-dispersed starch molecules observed by SEM was also contributed to the obtained value of tensile strength [12]. Additional glycerol addition, from 5 to 30 wt.%, drastically reduced the film's tensile strength, which was linked to the existence of free volume or voids, as shown by SEM. The hydrogen bonds that had been created between starch molecules and plasticizers were weakened as a result of the plasticization mechanism's reduction in the intermolecular contacts and cohesion forces between the starch chains [13].

Furthermore, the glycerol content was increased from 5 to 25 wt.%, which significantly improved the mango seed starch film elongation from 8.99 to 10.82%. By facilitating the movement of molecules between the chains as the glycerol level rises, starch molecules become more mobile, which reduces their rigidity and increases their flexibility, leading to an increase in film elongation [14]. However, when the glycerol concentration was increased from 25 to 30 wt.%, the elongation of the film was dramatically reduced, going from 10.82 to 10.12%. The anti-plasticization activity of highly plasticized starch might be explained by the fact that water or plasticizer molecules were able to remove the D-glucosyl residues of amylose or amylopectin from the starch polymers as a result of the vibration or movement of the starch polymer chains [15].

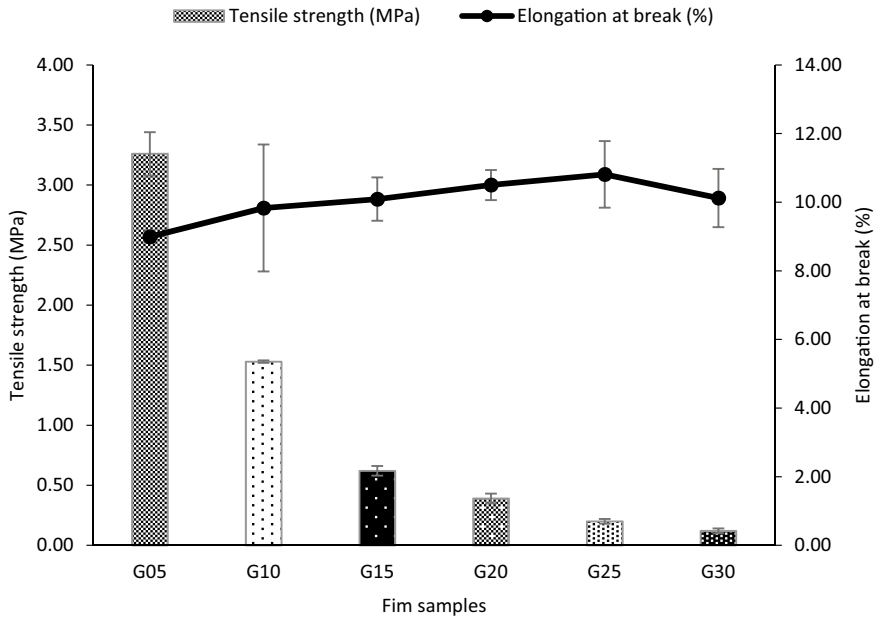


Fig. 2 Influence of glycerol content on tensile strength and elongation at break of mango seed starch films

4 Conclusion

Glycerol was studied for its effects on the physical and mechanical properties of mango seed starch films. The mango seed starch formed a thicker film with a higher moisture content and film solubility when more than 5% glycerol was added. Increased glycerol content in mango seed starch caused the film's surface to become rougher, which decreased tensile strength and increased elongation at break. The research findings are anticipated to aid in the creation of thermoplastic starch-based packaging films.

References

1. Soulestin J, Prashantha K, Lacrampe MF, Krawczak P (2011) Bioplastics based nanocomposites for packaging applications in handbook of bioplastics and biocomposites engineering applications. pp 76–119
2. Shahrin NA, Sarifuddin N, Ismail H (2018) Extraction and characterization of starch from mango seeds. *J Phys Conf Ser* 1082:012019
3. Jiugao Y, Ning W, Xiaofei M (2005) The effects of citric acid on the properties of thermoplastic starch plasticized by glycerol. *Starch/Staerke* 57(10):494–504
4. Rodriguez-Gonzalez FJ, Ramsay BA, Favis BD (2004) Rheological and thermal properties of thermoplastic starch with high glycerol content. *Carbohydr Polym* 58(2):139–147

5. Shahrin NA, Sarifuddin N, Zaki HHM, Azhar AZA (2018) The effects of glycerol addition to the mechanical properties of thermoplastic films based on jackfruit seed. *Malaysian J Anal Sci* 22(5):892–898
6. Ahmad Shahrin N, Sarifuddin N, Mohd Zaki HH, Ahmad Azhar AZ (2020) Estimating suitable starch extraction from mango seeds using analytical hierarchy process (AHP) method. *Mater Sci Forum* 1010:471–476
7. Sanyang ML, Sapuan SM, Jawaid M, Ishak MR, Sahari J (2015) Effect of glycerol and sorbitol plasticizers on physical and thermal properties of sugar palm starch based films. *Recent Adv Environ Ecosyst Dev* 157–162
8. Mali S, Grossmann MVE, García MA, Martino MN, Zaritzky NE (2004) Barrier, mechanical and optical properties of plasticized yam starch films. *Carbohydr Polym* 56(2):129–135
9. Shekarabi AS, Oroiehie AR, Vaziri A, Ardjmand M, Safekordi AA (2014) Effect of glycerol concentration on physical properties of composite edible films prepared from plums gum and carboxy methyl cellulose. *Indian J Fundam Appl Life Sci* 4:1241–1248
10. Farahnaky A, Saberi B, Majzoobi M (2013) Effect of glycerol on physical and mechanical properties of wheat starch edible films. *J Texture Stud* 44(3):176–186. Soulestin J, Prashantha K, Lacrampe MF, Krawczak P (2011) Bioplastics based nanocomposites for packaging applications. In: *Handbook of bioplastics and biocomposites engineering applications*, pp 76–119
11. Abdullah AHD, Putri OD, Sugandi WW (2019) Effects of starch-glycerol concentration ratio on mechanical and thermal properties of cassava starch-based bioplastics. *J Sains Mater Indones* 20(4):162–167
12. Tarique J, Sapuan SM, Khalina A (2021) Effect of glycerol plasticizer loading on the physical, mechanical, thermal, and barrier properties of arrowroot (*Maranta arundinacea*) starch biopolymers. *Sci Rep* 11(1):1–17
13. Zhang Y, Han JH (2006) Plasticization of pea starch films with monosaccharides and polyols. *J Food Sci* 71(6):253–261
14. Sothornvit R, Krochta J (2005) Plasticizers in edible films and coatings. *Innov Food Packag* 403–433
15. Zhang Y, Rempel C (2012) Retrogradation and antiplasticization of thermoplastic starch. *InTech* 117–135

Influence of Cutting Edge Radius (CER) and Width of Cut (WOC) on Tool Wear in Milling SUS 316 Stainless Steel



N. F. H. Abd Halim, A. N. Dahnel, Umma Sankar Gunasegaran,
Lim Joo Eng, M. S. Mohamad Amiruddin, and S. H. Tomadi

Abstract The application of stainless steel, especially SUS 316 have been significantly increasing especially in manufacturing area. However, problems such as rapid tool wear and poor surface roughness are a major problem when machining SUS316. The geometry and type of materials of cutting tool during machining SUS 316 plays a significant role in determining the outcome of the machining. This study was conducted to investigate the effect of cutting-edge radius (CER) and width of cut (WOC) on tool wear in milling SUS316 stainless steel. 6 mm diameter of uncoated tungsten carbide having three different values of CER which are 30, 40 and 50 and WOC of 0.1, 0.6 and 1.2 mm were selected as cutting tool in this study. A cutting speed of 4500 RPM, feed rate of 350 mm/min were kept constant throughout this experiment. It has been found that the cutting edge radius of the cutting tools plays a significant impact on the tool life and the surface roughness. It is proved that different CER and WOC values have significant influence on the tool wear and surface roughness while milling SUS 316 and it is concluded that the most optimum parameter combination is between 30 μm CER and 0.1 mm WOC based on the experimental data collected. It executes lower readings for both the imposed wear on cutting tool and the surface roughness of machined SUS 316 after 4400 mm machining length compared to other data of different combinations.

Keywords Edge radius · Width of cut · SUS316 · Tool wear

N. F. H. Abd Halim (✉) · A. N. Dahnel · M. S. M. Amiruddin · S. H. Tomadi
Department of Manufacturing and Materials Engineering, Kulliyyah of Engineering, International Islamic University Malaysia, Kuala Lumpur, Malaysia
e-mail: farahudahalim@iiu.edu.my

U. S. Gunasegaran · L. J. Eng
Department of Mechanical Engineering, Faculty of Engineering and Technology, Tunku Abdul Rahman University College, Kuala Lumpur, Malaysia

1 Introduction

Application of industry in automotive and medical industries have been increasingly applied nowadays. The properties of stainless steel such as good in corrosion resistance and varieties of strength made them always chosen as the main materials in a certain application. The most common and frequent machined stainless steels are the austenitic types, such as grades 304 and 316. These are characterized by their high work hardening rates and poor chip breaking properties during machining. In medical industries for example, stainless steel has been chosen as main materials especially for surgical equipment and apparatus. The most preferable type of stainless steel is the austenitic type due to its ability to endure extreme temperature operation and it possesses higher corrosion resistance properties [1]. Although stainless steel is always chosen as a main material due to the non-corrosion properties, machining stainless steel is not easy due to its properties. For instance, to enhance the hardness of the stainless steel, the addition of molybdenum in the stainless-steel composition made them difficult to machine. Also, the addition of chromium in stainless steel composition aided in resistivity to corrosion and scratch made several problems such as rapid tool wear and poor surface roughness a major concern when machining them. In medical field, fine surface finish which is approximately $0.2\ \mu\text{m}$ is broadly utilized normal surface roughness in making the surgical devices and it is necessary to anticipate the grinding and scratching amid surgery. Scratch marks will be a source of living microscopic organisms and infections. Poor surface finish and brief apparatus life are a major issue within the machining of stainless steel [2]. Other than the composition of the stainless steel that affects the machinability of the stainless steel, other parameters and concerns also contributed to the machining outcomes. It is recommended to use an uncoated carbide tool for this project since the milling process will be operating with moderate cutting parameters metal-working industry is broadly utilized the coated and uncoated carbide tools as the best alternative for most turning or milling operations. Cutting edge radius (CER) is an important cutting geometry that significantly affects the performance of the machining in terms of tool wear as well as the surface quality after machining. Several research has been carried out to investigate the effect of CER on tool wear. It was reported that the combination of low cutting edge radius with minimum feed rate and depth of cut will improve the performance of the cutting tool as well as produce better surface quality. When comparing cutting tools having lower CER of $0.03\ \text{mm}$ with $0.05\ \text{mm}$ CER, the tool life increases in a range of 48–80% when milling AISI H13 [3]. It was also reported that when comparing between 20, 30 and $40\ \mu\text{m}$, lowest CER resulted in highest tool wear, and it is recommended to machine with $30\ \mu\text{m}$. They mentioned that the tool wear increased as the CER value decreased as well as the tool wear increased as the cutting speed increased from 120 to $200\ \text{m/min}$ when machining AISI 52,100 steels [4]. The uncoated carbide tool is best fitted for moderate cutting parameters in terms of tool life and cost wise and it is true to this project as moderate cutting parameters such as the cutting speed, feed rate and others are being utilized [5]. In addition, numerous factors could also influence the machinability of stainless steel

such as the geometry of the cutting tool, microstructure of workpiece, cutting speed, depth of cut, feed rate, and unbending nature of the machine [6].

Therefore, this research was carried out to investigate the effect of different cutting edge radius (CER) on tool wear during milling AISI 316.

2 Research Methodology and Experimental Set Up

Milling of SUS 316 stainless steel were carried out on Vertical Centre Nexus 410A from Yamazaki Mazak Singapore Pte Ltd. SUS 316 stainless steel having a hardness of 17 HRC and a dimension of $200 \times 200 \times 100$ mm supplied by HPMT industries was used as a main workpiece during this study. 6 mm uncoated tungsten carbide end mill with 4 flutes and 30° rake angle were used throughout the experiment. Three different cutting edge radius (CER) which are 30, 40 and $50 \mu\text{m}$ and width of cut (WOC) of 0.1, 0.6 and 1.2 mm were tested in this study. The spindle speed of 4500 RPM and feed rate of 350 mm/min were kept constant throughout the experiment for all combination of CER and WOC. The cutting parameters selected for this study were tabulated in Table 1. The tool wear was measured at every 400 to 600 mm machining length. Dinolite portable USB microscope was utilized to measure the tool wear. The tool wear for each flute was measured and the average was taken for data analysis (Fig. 1).

Table 1 Cutting parameters during milling of SUS 316 using uncoated tungsten carbide end mill

Parameter	Value
Spindle speed (rpm)	4500
Feed rate (mm/min)	350
Depth of cut (mm)	6.0
Width of cut (mm)	0.1
	0.6
	1.2
Cutting edge radius (μm)	30
	40
	50
Cutting condition	Dry

Fig. 1 Dinolite dino-lite portable microscope used for tool wear measurement



3 Result and Discussion

3.1 *The Effect of CER and WOC in Milling of SUS 316*

Figure 2 shows the progression of tool wear when milling SUS316 stainless steel with different CER and WOC. From Fig. 2 it shows that the tool wear increased as the machining length increased for all CER and WOC. When milling SUS 316 with cutting tool having a CER $30\ \mu\text{m}$, it was observed that when milling with 1.2 mm WOC, the cutting tool failed after milling 600 mm. The tool wear measured when the tool failed was 0.107 mm. It is expected that combination of lower CER of $30\ \mu\text{m}$ with high width of cut of 1.2 mm produced higher cutting forces that lead to the premature failure of the cutting tool. It was also found that there was dislodgement of cutting tool materials on the flank surface as shown in Fig. 4. It is expected that when applying higher WOC, the chip contact area between the cutting tools and the workpiece increased. Thus, it would lead to greater stress and cutting forces to be incorporated into the operation and increases the tool wear [7]. In contrast when applying low WOC of 0.1 mm least wear was measured for 30 and $50\ \mu\text{m}$ CER. It has been reported that when applying lower width of cut the tool wear measured will decrease as compared with when machining with higher depth of cut [8]. Overall, it can be inferred that large WOC is not favorable to work with small CER tool as it will reduce the cutting tool lifespan due to increasing of the friction between the cutting tool and the workpiece thus increase the tool wear and shorten the tool life.

In case of $50\ \mu\text{m}$ CER, using 0.6 mm WOC has speeded up the tool failure by 80% whereby the tool could only cut through 880 mm instead of 4400 mm of total machining length as in Fig. 2c. Whereas the tool wear rate is lower for 0.1 and 1.2 mm WOC and as expected the least wear is shown when the smallest WOC, 0.1 mm is

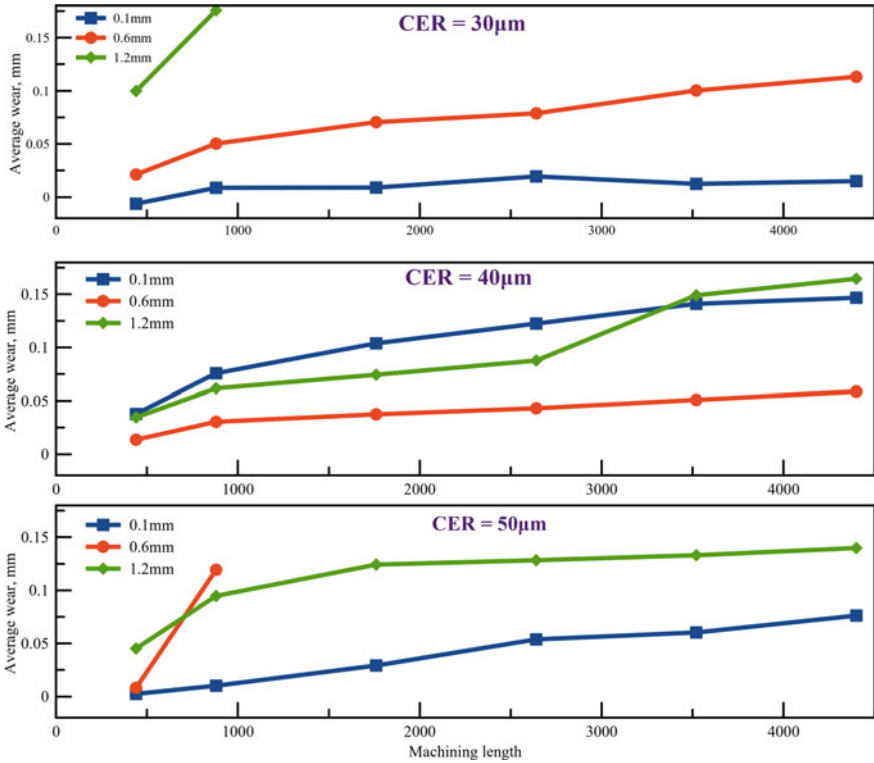


Fig. 2 Tool wear vs machining length for cutting tool with different cutting edge radius during milling SUS316

utilized, which is 0.0790 mm. Referring to Fig. 2a and c, for 30 and 50 μm CER lower WOC resulted in lower tool wear, however, for 40 μm CER, the lowest tool wear was obtained when milling with 0.6 WOC. It was mentioned by Chuangwen et. al [9] that the increase in cutting width could reduce chip deformation and result in a lower friction coefficient. This occurrence reduced the force applied by the tool, hence reduced the tool wear rate. Chip deformation is generated by high temperature and pressure at the cutting zone that would cause the tool to have a built-up edge.

Figure 3 shows the images of the cutting tool after machining with 1.2 mm WOC obtained from the Dinolite USB microscope. It was found that the chipping and dislodgement of cutting tool materials was severe especially for 30 and 50 CER. Figure 4 shows the images taken by SEM and found that some of the cutting tool materials were removed from the flank surface of the cutting tools.

wear was obtained rather than 0.0594 mm and 0.0790 mm when milling with 40 μm and 50 μm CER with 0.6 mm and 0.1 mm WOC respectively.

Acknowledgements The authors would like to thank HPMT Industries SDN BHD for supporting this research.

References

1. Zumelzu E, Sepúlveda J, Ibarra M (1999) Influence of microstructure on the mechanical behaviour of welded 316 L SS joints. *J Mater Process Technol* 94(1):36–40
2. Abdullah M, Chua MIH, Bakar A, Ghani J (2010) Effects of insert nose radius and processing cutting parameter on the surface roughness of Aisi 316 stainless steel. *Key Eng Mater* 447–448:51–54
3. Bakar HNA, Ghani JA, Haron CHC (2020) Influence of rounded cutting-edge radius and machining parameters on surface roughness and tool wear in milling AISI H13 steel under dry and cryogenic machining. *J Tribol* 24:52–64
4. Zhao T, Zhou JM, Bushlya V, Ståhl JE (2017) Effect of cutting edge radius on surface roughness and tool wear in hard turning of AISI 52100 steel. *Int J Adv Manuf Technol* 91(9):3611–3618
5. Saravanan Lakshmanan M, Xavio A (2014) Performance of coated and uncoated inserts during intermittent cut milling of AISI 1030 steel. *Proc Eng* 97:372–380
6. Gökkaya H, Nalbant M (2007) The effects of cutting tool geometry and processing parameters on the surface roughness of AISI 1030 steel. *Mater Des* 28(2):717–721
7. El-Hossainy TM, El-Zoghby AA, Badr MA, Maalawi KY, Nasr MF (2010) Cutting parameter optimization when machining different materials. *Mater Manuf Processes* 25(10):1101–1114
8. Okokpujie P, Ohunakin OS, Bolu CA, Okokpujie KO (2018) Experimental data-set for prediction of tool wear during turning of Al-1061 alloy by high speed steel cutting tools. *Data Brief* 18:1196–1203
9. Chuangwen X, Jianming D, Yuzhen C, Huaiyuan L, Zhicheng S, Jing X (2018) The relationships between cutting parameters, tool wear, cutting force and vibration. *Adv Mech Eng* 10(1)

Influence of Milling Parameters on the Characteristics of Alumina-Titania Nanocomposite Prepared by High-Energy Ball Milling



Siti Atikah Mohammad Asari, Mahani Yusoff, Mohamad Najmi Masri, Hidayani Jaafar, Mohd Hasmizam Razali, and Wan Mohd Norsani Wan Nik

Abstract High energy ball milling (HEBM) is a simple mechanical technique used for particle size reduction and mixing different materials from bulk to nanostructured materials. It is able to produce nano-size grains of ceramic-based composite and sometimes with sufficient energy new phase can be formed through the diffusion process. The present study focuses on the effect of HEBM on the structure, microstructure, and properties of alumina—titania ($\text{Al}_2\text{O}_3\text{-TiO}_2$) nanocomposite. Elemental powders of Al_2O_3 and TiO_2 were milled in a planetary ball mill at different milling times and milling speeds, then heated to $600\text{ }^\circ\text{C}$. The composites were characterized for phase identification, structural properties, morphology, and compaction behavior. The peak broadening was significant with increasing milling time. The unstable Al_2TiO_5 was formed at a lower milling time for 300 rpm but diminished after heat treatment. The lowest crystallite size was obtained after 10 h milling time and with the speed of 300 rpm which originated from grain refinement due to a large amount of defects generation during milling. Increasing milling time and milling speed influenced the green density as a result of fine composite particle size and TiO_2 particles.

Keywords High-energy ball milling · $\text{Al}_2\text{O}_3\text{-TiO}_2$ · Coating

S. A. M. Asari · M. Yusoff (✉) · M. N. Masri · H. Jaafar
Faculty of Bioengineering and Technology, Universiti Malaysia Kelantan, 17600 Jeli, Kelantan, Malaysia
e-mail: mahani@umk.edu.my

M. H. Razali
Faculty of Science and Marine Environment, Universiti Malaysia Terengganu, 21030 Kuala Nerus, Terengganu, Malaysia

W. M. N. W. Nik
Faculty of Ocean Engineering Technology and Informatics, Universiti Malaysia Terengganu, 21030 Kuala Nerus, Terengganu, Malaysia

1 Introduction

Ball milling is a technique subjecting the powder to a container with grinding media for particle size reduction. Meanwhile, high-energy ball milling (HEBM) involves heavy deformation of the powder through a collision between ball-powder-container walls. The collisions trapped powder between colliding balls and/or balls and wall containers. The entrapped powder becomes severely deformed when a very large amount of stress is introduced. However, the nature of milled composite powder is greatly influenced by milling parameters such as milling time, milling speed, size of balls, and ball-to-powder ratio. HEBM is often used to synthesize nanostructured materials, composites, and alloys. Ceramic matrix composite is also produced by this method. Alumina-titania ($\text{Al}_2\text{O}_3\text{-TiO}_2$) composites are well known for their low thermal expansion, high toughness, and low thermal conductivity [1, 2]. These composites are used in the construction and coating of high-performance applications especially when a thermal barrier is needed [3, 4]. In coating application, fine $\text{Al}_2\text{O}_3\text{-TiO}_2$ composite particle size is required. The current processing technique such as spray drying [4–6], sol-gel [7, 8], and sintering [9] of $\text{Al}_2\text{O}_3\text{-TiO}_2$ composites requires a long period of time to achieve fine size owing to complicated equipment setup, slow processing, and inadequate control of processing parameters. Furthermore, coatings made of nanostructured materials have a uniform microstructure and excellent interfacial adhesion between steel substrates. These features also can be fulfilled by $\text{Al}_2\text{O}_3\text{-TiO}_2$ nanocomposite coating produced by HEBM [10, 11].

Obtaining fine particle size and good distribution of TiO_2 reinforcement within Al_2O_3 matrix requires a high energy impact to be transferred to a composite powder mixture. The main purpose of choosing the optimum milling time and milling speed is to reach a steady state condition between fracturing and cold welding. However, if the milling time exceeded the maximum, contamination may occur. Hence, investigating the effects of milling time and speed on the cold welding, fracturing, and re-welding of milled $\text{Al}_2\text{O}_3\text{-TiO}_2$ powder particles will be beneficial. The purpose of this research is to evaluate the structure, morphology, and density of $\text{Al}_2\text{O}_3\text{-TiO}_2$ nanocomposite synthesized by HEBM and sintering at various milling times and speeds.

2 Materials and Method

Al_2O_3 ($\geq 98\%$ purity, 70% volume, average particle size $> 20 \mu\text{m}$) powder and TiO_2 powder. Al_2O_3 and TiO_2 ($> 99.5\%$ purity, average particle size $> 21 \text{nm}$) were used in this study and were purchased from Sigma Aldrich. The composition used in this study was $\text{Al}_2\text{O}_3\text{-30wt\%TiO}_2$. The powder mixture was milled for 2, 4, 8, 10 h at 200, 250, and 300 rpm in a planetary ball milling (DECO-PBM-V-0.4L) using a container made by zirconia with a 5 mm diameter size of zirconia balls. The ball-to-powder ratio used was 1:5. The phase identification and structural properties of

Al_2O_3 - TiO_2 nanocomposites were characterized using the X-ray Diffraction technique (Bruker D2 Phaser). The step size was fixed at 0.02° with 2θ angle from 20° to 90° . The crystallite size and internal strain were analyzed using the Williamson-Hall method. The morphology of the nanocomposite was determined by scanning electron microscope (SEM) (JEOL JSM-IT100) with energy dispersive spectroscopy attachment for a composite milled at 300 rpm. After milling, the as-milled powder was then compacted at 400 MPa using uniaxial single action hydraulic press in a 10 mm diameter cylindrical die and heat treated at 600°C for 1 h. The green density of nanocomposites was measured using Archimedes' principle.

3 Results and Discussion

Figure 1 shows the XRD pattern of Al_2O_3 - TiO_2 nanocomposite powder milled at different times of 2, 4, 8 and 10 h and milling speeds of 200, 250, and 300 rpm. The broadening of Al_2O_3 peak started after 4 h of milling and become more pronounced when reaching 10 h of milling. The intensity reduction of TiO_2 is higher than Al_2O_3 peaks for all composites. When milling time is extended, rapid internal refinement occurs, resulting in a large number of defects due to larger powder particles and powder particle/container collisions. There was a new phase existing in the composite other than Al_2O_3 and TiO_2 peaks which were identified as Al_2TiO_5 for composite milled for 2 and 4 h with 300 rpm. The formation of Al_2TiO_5 is attributed to sufficient energy during milling due to excess TiO_2 in the composite. Dissolution of Al into the TiO_2 lattice forms an extended solid-solution that plays a part in reducing the scattering factor of the TiO_2 phase which establishes a metastable structure at the grain boundary [12]. The presence of Al_2TiO_5 precludes adequate densification of the composite [13]. However, in this study, Al_2TiO_5 peaks disappeared after 8 h of milling. It could be because unstable Al_2TiO_5 spontaneously decomposes at temperatures lower than 1280°C [14].

Figure 2 shows the Al_2O_3 crystallite size and internal strain of Al_2O_3 - TiO_2 nanocomposite powder milled at different times of 2, 4, 8 and 10 h and milling speeds of 200, 250, and 300 rpm. The Al_2O_3 crystallite size falls below 20 nm for all milling times and milling speeds, indicating that the produced is nanostructured materials. Increasing milling time reduced the Al_2O_3 crystallite size and increased the Al_2O_3 internal strain. Continuous deformation of the composite powder throughout the milling process creates an accumulation of defects such as dislocations, leading to continuous refinement of Al_2O_3 crystallite size. In the case of powder milled at 300 rpm, a slight decrease of Al_2O_3 crystallite size from the speed of 2–8 h has been observed compared to that of the powder milled at 200 and 250 rpm. It's possible that higher milling speeds produce more kinetic energy each hit, allowing for faster solid solubility.

The morphology of Al_2O_3 - TiO_2 nanocomposite milled at different milling times and 300 rpm is shown in Fig. 3. In all milling times, the microstructure consists of uniformly distributed particle distribution with different shapes and particle sizes.

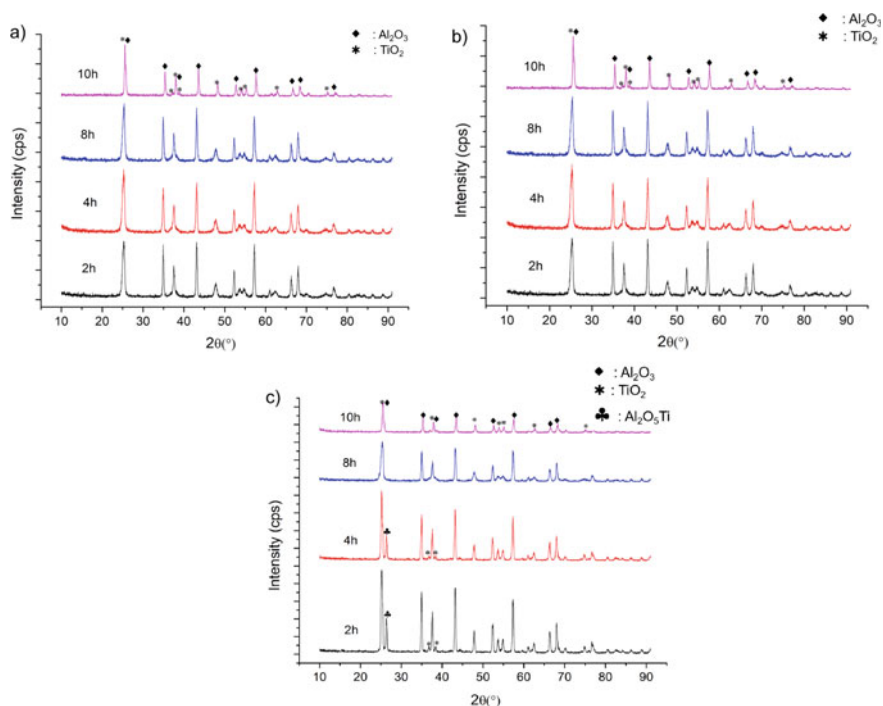


Fig. 1 XRD patterns of Al₂O₃-TiO₂ nanocomposite milled at different milling times with milling speeds of **a** 200 rpm, **b** 250 rpm and **c** 300 rpm

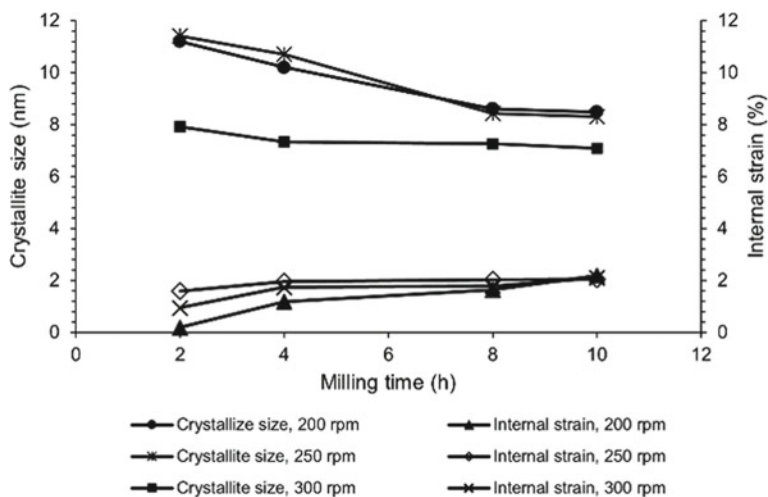


Fig. 2 Al₂O₃ crystallite size and internal strain of Al₂O₃-TiO₂ nanocomposite milled at different times with milling speeds of **a** 200 rpm, **b** 250 rpm and **c** 300 rpm

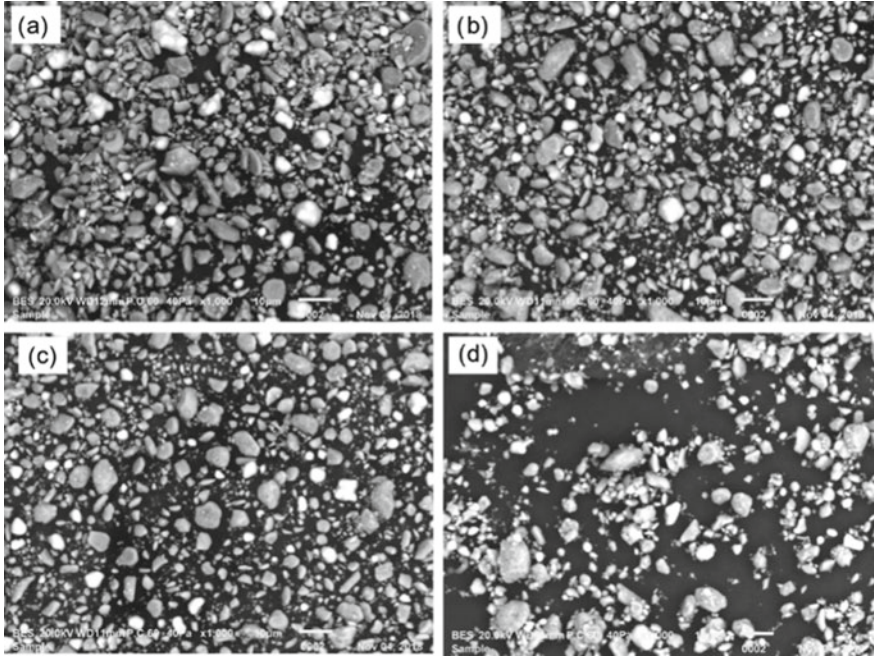


Fig. 3 SEM images of $\text{Al}_2\text{O}_3\text{-TiO}_2$ nanocomposite milled at **a** 2 h **b** 4 h **c** 8 h and **d** 10 h at 300 rpm

At 2 and 4 h milling time, the powder particles appear flattened and cold welding caused the composite particle size to increase. At 8 h milling time, the powder shape becomes spherical and reduced to a smaller size due to the predominant mechanism in this stage being plastic deformation and cold welding. Then, after 10 milling, the particles turn to become flake-like and agglomerated.

Figure 4 shows the green density of $\text{Al}_2\text{O}_3\text{-TiO}_2$ nanocomposite powder milled at different milling times and milling speeds. The composite milled of 300 rpm has the lowest density for all milling times. A higher density is attained by a longer milling time because of homogeneous distribution and finer particles of the nanocomposite that was produced from continuous impact energy. Moreover, the presence of homogenous distribution and small particle size of TiO_2 might restrict the composite powder from being significantly deformed during compaction. Such observation is related to the hardening effect that hinders the dislocation movement.

XRD patterns of sintered $\text{Al}_2\text{O}_3\text{-TiO}_2$ nanocomposite milled at different milling times and 300 rpm are shown Fig. 5. Heating was performed in order to confirm whether the Al_2TiO_5 phase is formed by the milling process or could be induced during heat treatment. Meybodi et al. [15] suggested that Al_2TiO_5 was formed after sintering. In this study, heat treated did not produce Al_2TiO_5 but only produced more crystalline Al_2O_3 and TiO_2 peaks. The Al_2TiO_5 formed in this work was unstable, and it could spontaneously dissociate due to a number of conditions including phase purity, grain size, environment, and additives.

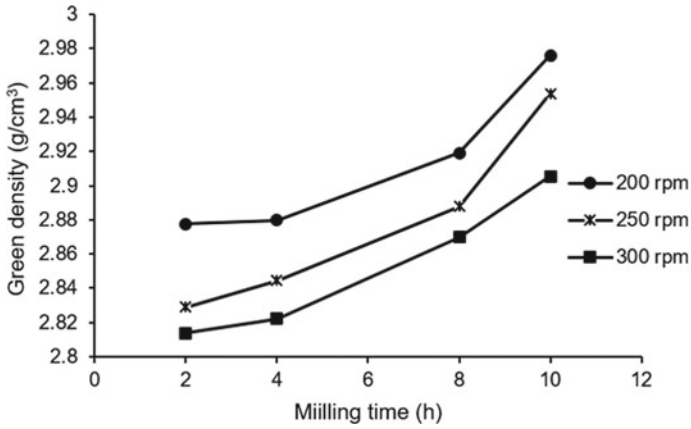


Fig. 4 Green density of Al₂O₃-TiO₂ nanocomposite milled at different milling times with milling speeds of 200, 250, and 300 rpm

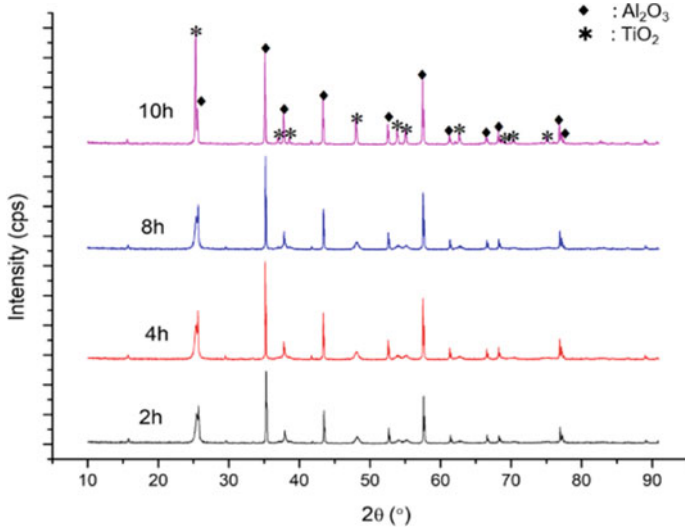


Fig. 5 XRD patterns of sintered Al₂O₃-TiO₂ nanocomposite milled at different milling times with a milling speed of 300 rpm

4 Conclusions

Al₂O₃-TiO₂ nanocomposite has been successfully produced using high energy ball milling. Increasing milling time and milling speed induce the internal structure changes of the composite. The crystallite size was in the nanoscale indicating that the Al₂O₃-TiO₂ was nanocomposite. The energy from milling drives the formation

metastable phase (Al_2TiO_5) but disappeared at 10 h of milling and after sintering. The micro-features of the Al_2O_3 - TiO_2 nanocomposite consist of fine TiO_2 particles around the Al_2O_3 that effects the green density of the nanocomposites.

Acknowledgements The authors would like to thank the Faculty of Bioengineering and Technology, Universiti Malaysia Kelantan for providing research materials and equipment.

References

1. Jia SK, Zou Y, Xu JY, Wang J, Yu L (2015) Effect of TiO_2 content on properties of Al_2O_3 thermal barrier coatings by plasma spraying. *Trans Nonferrous Metals Soc of China* 25:175–183
2. Ali S, Juntunen T, Sintonen S, Ylivaara O, Puurunen R, Lipsanen H, Hannula SP (2016) Thermal conductivity of amorphous $\text{Al}_2\text{O}_3/\text{TiO}_2$ nanolaminates deposited by atomic layer deposition. *Nanotechnology* 27:445704
3. Kovaleva M, Prozorova M, Arseenko M, Tyurin Y, Kolisnichenko O, Vasilik N, Sirota V, Pavlenko I (2015) Deposition and characterization of alumina–titania coating by multi-chamber gas-dynamic sprayer. *Results in Phys* 5:1–2
4. Bian H, Yang Y, Wang Y, Tian W, Jiang H, Hu Z, Yu W (2013) Effect of microstructure of composite powders on microstructure and properties of microwave sintered alumina matrix ceramics. *J Mater Sci Technol* 29(5):429–433
5. Marra F, Baiamonte L, Bartuli C, Valente M, Valente T, Pulci G (2016) Tribological behaviour of alumina-titania nanostructured coatings produced by air plasma spray technique. *Chem Eng Trans* 47:127–132
6. Michalak M, Łatka L, Sokołowski P, Niemiec A, Ambroziak A (2020) The microstructure and selected mechanical properties of Al_2O_3 + 13 wt% TiO_2 plasma sprayed coatings. *Coatings* 10(2):173
7. Dascalescu T, Todan L, Rusu A, Preda S, Andronescu C, Culita DC, Munteanu C, Zaharescu M (2014) Nanosized Al_2O_3 - TiO_2 oxide powder with enhanced porosity obtained by sol-gel method. *Rev Roum Chim* 59(2):125–134
8. Akkaya Arer UO, Tepehan FZ (2014) Influence of Al_2O_3 : TiO_2 ratio on the structural and optical properties of TiO_2 - Al_2O_3 nano-composite films produced by sol gel method. *Compos B Eng* 58:147–151
9. Bian H, Yang Y, Wang Y, Tian W (2012) Preparation of nanostructured alumina–titania composite powders by spray drying, heat treatment and plasma treatment. *Powder Technol* 219:257–263
10. Coste S, Bertrand G, Coddet C, Gaffet E, Hahn H, Sieger H (2007) High-energy ball-milling of Al_2O_3 - TiO_2 powders. *J Alloy Compd* 434–435:489–492
11. Šuopys A, Marcinauskas L, Grigaitienė V, Kėželis R, Aikas M, Uscila R, Tučkutė S, Lelis M (2021) The effect of heat treatment on the microstructure and phase composition of plasma sprayed Al_2O_3 and Al_2O_3 - TiO_2 coatings for applications in biomass firing plants. *Coatings* 11(11):1289
12. Yang Y, Chang Q, Hu Z, Zhang X (2018) A comparative study on the addition methods of TiO_2 sintering aid to the properties of porous alumina membrane support. *Membranes* 8(3):49
13. Guidara A, Chaari K, Fakhfakh S, Bouaziz J (2017) The effects of MgO , ZrO_2 and TiO_2 as additives on microstructure and mechanical properties of Al_2O_3 -fap composite. *Mater Chem Phys* 202:358–368

14. Rendtorff N, Suárez G, Aglietti EF (2014) Non isothermal kinetic study of the aluminium titanate formation in alumina-titania mixtures. *Cerâmica* 60(355):411–416
15. Meybodi S, Barzegar-Bafrooei H, Ebadzadeh T, Tazike M (2013) Microstructure and mechanical properties of Al_2O_3 -20wt% Al_2TiO_5 composite prepared from alumina and titania nanopowders. *Ceram Int* 39:977–982

ANFIS Domestic Water Consumption Model Before and During Covid19 Pandemic in Tangerang Indonesia



Diah Septiyana, Mohamed Abd. Rahman,
Tasnim Firdaus Binti Mohamed Ariff, Nor Aiman Sukindar,
and Erry Yulian T. Adesta

Abstract WHO has declared Covid-19 disease as a pandemic on a global scale. The Indonesian government had announced a physical distancing & movement control order (PSBB) to combat Covid-19 transmission. The effect of PSBB caused many factories to stop operating and forced workers to work from home. This event had resulted in the increase in domestic water consumption. In this paper, we analyze the increased domestic water consumption using ANFIS mathematical model. The model shows the increase in domestic water consumption three months before and the first three months of the Covid-19 pandemic, due to PSBB, Moslem religious rituals such as fasting in Ramadhan, and the ban of Homecoming in Eid Fitr. We can see the model shows significant increases in domestic water consumption from 3 constant variables such as: A from 1,243,000 to 1,288,000, B from 1,303,000 to 1,410,000, and C from 1,279,000 to 1,340,000.

Keywords Water consumption · ANFIS · PSBB · Covid-19 · Modeling

1 Background

On March 11, 2020, the number of covid cases outside China has increased 13-fold, and the number of countries with cases increased threefold, therefore the WHO declared the Covid-19 disease a pandemic on a global scale. This pandemic has created many problems ranging from production to distribution and had given a heavy blow to the industry. To combat Covid-19 pandemic transmission in Indonesia, the

D. Septiyana (✉) · M. Abd. Rahman · T. F. B. M. Ariff · N. A. Sukindar
Department of Manufacturing and Material Engineering, Kulliyah of Engineering (KOE),
International Islamic University Malaysia (IIUM), 53100 Kuala Lumpur, Selangor, Malaysia
e-mail: dee.septie@gmail.com

D. Septiyana
Department of Engineering, Faculty of Industrial Engineering, Universitas Muhammadiyah
Tangerang, Banten 15118, Indonesia

E. Y. T. Adesta
Department of Industrial Engineering Safety and Health, Faculty of Engineering, Universitas Indo
Global Mandiri (UIGM), Palembang 30129, Indonesia

Indonesian government has declared PSBB regulation (physical distancing & movement control order) [1]. Even though the Covid-19 pandemic started in November 2019 in Wuhan, China [2], the Indonesian government only declared PSBB at the end of March 2020 [3]. The effect of PSBB caused many factories to stop operating [2], resulting in a significant decline in production utilization followed by a reduction of workers [4].

This PSBB aimed to reduce mobility and activities [1], office or school, and work from home or online learning [5]. Another approach to combat Covid-19 was to practice hygiene culture such as washing hand and washing every item that was exposed to many people's hands [6]. This hygiene culture had caused an increase in domestic water consumption [7]. An increase in water consumption means an increase in domestic water production capacity, and thus increasing the risks management of chemical materials, customer bills, and others. This increase in water production has its challenge for water companies: maintaining supply while reducing water production costs. Despite its excellence in modeling phenomena, ANFIS had not been used in modeling increasing domestic water consumption. Therefore, in this paper, we use ANFIS model to analyze the increase in domestic water consumption three months before Covid-19 and the first three months of Covid-19 pandemic and thus we can analyze the risks management concerning the increasing water production.

2 ANFIS Method

Our approach was to build a mathematical model of water consumption during Covid-19 pandemic using ANFIS and analyze it to see whether there is an increase in water consumption or not. This need to be done so we can further analyze it for risk assessment during the pandemic. This approach can be done because ANFIS was considered as a universal estimator [8]. ANFIS has been developed to solve real world problems, such as electromagnetic wave channel model [9], control problem, forecasting, and others. ANFIS was developed by Jang in 1993 [10], based on fuzzy if-then rules from Takagi and Sugeno [11]. We can write ANFIS algorithm based on Jang's paper below. For step one, each output is symbolized by O_i^1 , which serves to raise the degree of membership.

$$O_i^1 = \mu A_i(x) \text{ and } O_i^1 = \mu B_i(x), \quad i = 1, 2 \quad (1)$$

Where

i—each node in ANFIS architecture.

x—input to node i.

A, B—the linguistic label (such as small, large, etc.).

In this step, every membership function type can be used, but in Jang's method, generalized bell membership functions were used to provide two outputs: maximum equal to 1 and minimum equal to 0. Therefore, we obtain:

$$\mu A_i(x) = \frac{1}{1 + \left(\frac{x-c_i}{a_i}\right)^{2*b_i}} \quad (2)$$

where a, b, c—the parameter set.

The second step is constructed by multiplying the two input signals. Every node represents the firing strength of fuzzy inference.

$$O_i^2 = \mu A_i(x) \cdot \mu B_i(x), \quad i = 1, 2 \quad (3)$$

For the next step, normalization was applied for each firing of fuzzy inference.

$$O_i^3 = \overline{W}_i = \frac{W_i}{W_1 + W_2}, \quad i = 1, 2 \quad (4)$$

where

w —the firing strength of node

\overline{W}_i —the normalized firing strength of node.

Next step contains the calculation of the output based on parameters of rule consequent.

$$O_i^4 = \overline{W}_i \cdot F_i = W_i \cdot (P_i x + Q_i x + R_i x), \quad i = 1, 2 \quad (5)$$

where P, Q, R—the parameter set

Finally, the last step computes the overall output as the summation of all input signals.

$$O_i^5 = \text{Overall Output} = \sum_{k=0}^n \overline{W}_i \cdot F_i = \frac{\sum_{k=0}^n W_i \cdot F_i}{\sum_{k=0}^n W_i} \quad (6)$$

Because ANFIS learns from gradient descent and chain rule, error rate needs to be known for data training for each node output. Assuming i -th position node outputs as O_i the training data set has P number input, and the error function can be measured as:

$$E_p = \sum_{m=1}^{\#L} (T_{mp} - O_{mp}^L)^2 \quad (7)$$

where

E_p —error measure which is the sum of squared errors

T_{mp} —m component from P output target vector

O_{mp}^L —m component from output vector that has produced by P input vector.

Hence, the error rate can be calculated as:

$$\frac{\partial E_p}{\partial O_{ip}^k} = \sum_{m=1}^{\#k+1} \frac{\partial E_p}{\partial O_{mp}^{k+1}} \frac{\partial O_{mp}^{k+1}}{\partial O_{ip}^k} \quad (8)$$

where $1 \leq k \leq L-1$ is error rate of internal node, its expressed as linear combination error rate of nodes in the next stages. Therefore, for all $1 \leq k \leq L$ and $1 \leq i \leq \#(k)$, we can find $\frac{\partial E_p}{\partial O_{ip}^k}$, with Eqs. 7 and 8. we have α as a parameter of adaptive network.

$$\frac{\partial E}{\partial \alpha} = \sum_{O^* \in S} \frac{\partial E_p}{\partial O^*} \frac{\partial O^*}{\partial \alpha} \quad (9)$$

where S—shows the set of nodes whose output depends on α .

Derivative for overall error measurement E with respect to α is:

$$\frac{\partial E}{\partial \alpha} = \sum_{p=1}^p \frac{\partial E_p}{\partial \alpha} \quad (10)$$

Therefore, we can write the updated formula for generic parameter α as follows:

$$\Delta \alpha = -\eta \frac{\partial E}{\partial \alpha} \quad (11)$$

where η —learning rate.

The learning rate can be written as

$$\eta = \frac{k}{\sqrt{\sum_{\alpha} \left(\frac{\partial E}{\partial \alpha}\right)^2}} \quad (12)$$

where k- the step size of length each gradient transition in the parametric space.

3 Result and Discussion

Using machine learning such as ANFIS we derive the domestic water consumption model for three months before Covid-19 and the first three months covid-19. Table 1 shows data from the Water Company in the Tangerang district, while Fig. 1 show the model.

Using Eq. 6, we can build mathematical model three months before Covid-19 and the first three months of Covid-19. The domestic water consumption Model for 3 months before Covid-19 (before PSBB was applied or restricted movement) can be seen on Eq. 13. The domestic water consumption Model for the first 3 months during Covid-19 (PSBB applied or restricted movement) can be seen on Eq. 14.

$$\frac{\left(\left(\frac{1}{1+\left|\frac{x-0.99}{0.488}\right|^{2*2}}\right)A\right) + \left(\left(\frac{1}{1+\left|\frac{x-1.99}{0.51}\right|^{2*1.99}}\right)B\right) + \left(\left(\frac{1}{1+\left|\frac{x-3}{0.49}\right|^{2*1.99}}\right)C\right)}{\left(\left(\frac{1}{1+\left|\frac{x-0.99}{0.488}\right|^{2*2}}\right)\right) + \left(\left(\frac{1}{1+\left|\frac{x-1.99}{0.51}\right|^{2*1.99}}\right)\right) + \left(\left(\frac{1}{1+\left|\frac{x-3}{0.49}\right|^{2*1.99}}\right)\right)} \tag{13}$$

where the constant parameter is A = 1,243,000, B = 1,303,000, C = 1,279,000.

$$\frac{\left(\left(\frac{1}{1+\left|\frac{x-3.98}{0.477}\right|^{2*2}}\right)A\right) + \left(\left(\frac{1}{1+\left|\frac{x-4.99}{0.54}\right|^{2*1.99}}\right)B\right) + \left(\left(\frac{1}{1+\left|\frac{x-6}{0.48}\right|^{2*2}}\right)C\right)}{\left(\left(\frac{1}{1+\left|\frac{x-0.99}{0.488}\right|^{2*2}}\right)\right) + \left(\left(\frac{1}{1+\left|\frac{x-1.99}{0.51}\right|^{2*1.99}}\right)\right) + \left(\left(\frac{1}{1+\left|\frac{x-3}{0.49}\right|^{2*1.99}}\right)\right)} \tag{14}$$

Table 1 Domestic water consumption 3 months before & 3 months with PSBB applied

Month	Domestic	Remarks	Month	Domestic	Remarks
Dec-19	1,247,216	Before Covid-19	Mar-20	1,296,576	During Covid-19
Jan-20	1,298,774	Before Covid-19	Apr-20	1,400,947	During Covid-19
Feb-20	1,280,983	Before Covid-19	May-20	1,345,001	During Covid-19



Fig. 1 Membership function input for domestic water consumption three months before Covid-19 and the first three months of Covid-19 with PSBB applied (restricted movement)

where the constant parameter is $A = 1,288,000$, $B = 1,410,000$, and $C = 1,340,000$.

The model shows us the increasing domestic water consumption in the first 3 months during Covid-19. We can be seen this from variable A, B, and C which is variable for exact month that occurs, while non equation variable was the exact water consumption. To simplify our analysis, we plot the mathematical model into matlab. In Fig. 2 we can see the model in domestic water consumption for three months before Covid-19 and the first 3 months Covid-19.

On Table 2, we can see that this mathematical model shows us an indication that there is an increase in water consumption that is caused by PSBB (restricted movement). The PSBB causes too many people to work in their houses, thus increasing domestic water consumption. From analysis, even though Indonesia has religious rituals such as fasting in the Full month of Ramadan and the culture of Mudik (homecoming ritual) for Eid Fitr, due to the Covid-19 pandemic, there is PSBB which includes the ban on Mudik. Therefore, the increase in water consumption in the Tangerang happens on Ramadhan 2020 and Eid Fitr 2020 compared to Ramadhan 2019 and Eid Fitr 2019, before the Covid-19 pandemic.

Fig. 2 Domestic water consumption modelling three months before Covid-19 and the first three months Covid-19 with PSBB applied (restricted movement). where “x” is the month and “y” is the total volume (m³)

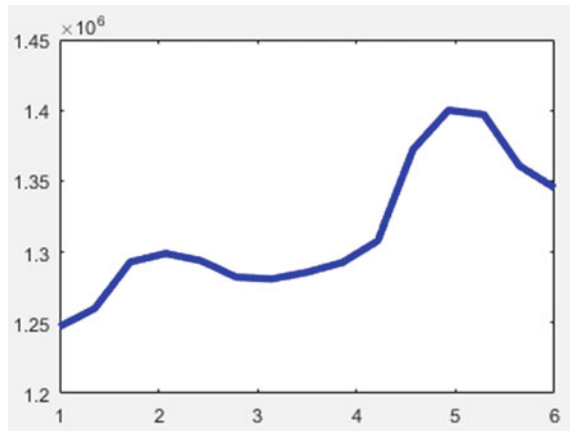


Table 2 Domestic water consumption 3 months before, In, after Ramadhan. Comparison in 2019 (Before pandemic) and 2020 (during pandemic)

Month	Domestic	Remark
May-19	1,225,890	Ramadhan before pandemic (May 5–June 4)
Jun-19	1,144,995	Mudik Eid Fitri
Jul-19	1,227,219	Normal condition
Mar-20	1,296,576	During pandemic (PSBB 1st)
Apr-20	1,400,947	Ramadhan In Covid-19 pandemic (April 23–May 23)
May-20	1,345,001	Stay at home in Eid Fitri (without Mudik In Indonesia)

In order to provide a good risk analysis in drinking water during the covid-19 pandemic, we must understand the nature of water consumption during the covid-19 pandemic. Because most people think that water consumption will be decreased during the covid-19 pandemic the cause of the PSBB effect (which is the ban of almost all activities), however, this opinion wasn't true. We have validated this hypothesis using a ANFIS mathematical model and compare it with actual data that shows the increase of water consumption in the first 3 months of a covid-19 pandemic.

4 Conclusion

In this paper, a mathematical model using ANFIS was developed to see whether the Covid-19 Pandemic has impacted domestic water consumption in Tangerang Indonesia. Using 6-month worth of actual data (three months before and three months after Covid-19 Pandemic), the ANFIS model shows significant increases in domestic water consumption. This hypothesis can be seen from 3 constant ANFIS variables that increase in value such as A from 1,243,000 to 1,288,000, B from 1,303,000 to 1,410,000, and C from 1,279,000 to 1,340,000. The analysis indicated that the increase in water consumption during the Covid-19 pandemic in April and May 2020 was due to Ramadan and the decreased mobility of people because of PSBB, which included the ban of Mudik on Eid Fitr 2020 in Indonesia. Therefore, we conclude that ANFIS model was reliable and valid to be used in similar situations.

References

1. Andriani H (2020) Effectiveness of large-scale social restrictions (PSBB) toward the new normal era during COVID-19 outbreak: a mini policy review. *J Indonesian Health Policy and Admin* 5(2):61–65
2. Yang Q, Zhou Y, Ai J, Ma J, Cao F, Cao W, Zhang W, Wang S, Chen W, Ma X, Zhang W, Li W (2020) Collaborated effort against SARS-CoV-2 outbreak in China. *Clin Transl Med* 10(1):13–16
3. Pati UK (2020) Indonesian government policy in mitigating economic risks due to the impact of the Covid-19 outbreak. *J Law and Legal Reform* 1(4):577–590
4. Yang MG, Paul H, Sachin BM (2011) Impact of lean manufacturing and environmental management on business performance: an empirical study of manufacturing firms. *Int J Prod Econ* 129(2):251–261
5. Dwi Putri Robiatul A, Iklima S (2020) Kebijakan PSBB Pemerintah Kota Surabaya dalam Menyegah Penyebaran Virus Covid-19. *Sahafa J Islamic Commun* 3(1)
6. Escobar-Escobar MB, García-García N (2020) Knowledge of COVID-19 and hand washing. *Revista de Salud Publica* 22(3)
7. Ratna Septi H (2020) Study of increasing demand for clean water during the Covid 19 pandemic in Yogyakarta City. In: *Prosiding Seminar Nasional Unimus, Yogyakarta*
8. Valcic SB, Samodol A, Valcic M (2020) Applying adaptive neuro-fuzzy inference system (ANFIS) while analysing interdependencies of tax burden and capital structure of croatian hotel companies. In: *2020 43rd international convention on information, communication and electronic technology (MIPRO), Croatia*

9. Galang PNH, Hadi MH, Fauziah ST, Rafiqul MI, Hajar Binti SY, Yulian Triblas EA, Rabeya A (2022) Near ground Pathloss propagation model using adaptive neuro fuzzy inference system for wireless sensor network communication in forest, jungle, and open dirt road environments. *Sensors* 22(9):3267–3285
10. Jyh-Shing RJ (1993) ANFIS: adaptive-network-based fuzzy inference system. *IEEE Trans Syst Man Cybernet* 23(3): 665–685
11. Tomohiro T, Michio S (1985) Fuzzy identification of system and its application to modeling and control. *IEEE Trans Syst Man Cybern* 15(1):116–132

Microstructure and Mechanical Properties of Porous Aluminium Composites Reinforced with Diamond Particles



Bisma Parveez, Nur Ayuni Jamal, Syazwan b Mohamad Kadri, Hafizah Hanim Mohd Zaki, and Ahmad Zahirani Ahmad Azhar

Abstract In the present work, diamond particles with various contents (5, 10 and 15 wt. %) were reinforced in porous aluminium (Al) composite via powder metallurgy technique. The desirable porous structure was designed by incorporating polymethylmethacrylate (PMMA) as a space holder material at fixed content of 30 wt. % in all the composites. Morphology of the resultant porous Al composite demonstrated the formation of uniform closed-cell macropores and diamond particles that are well bonded within the Al matrix. However, higher weight percentage (wt.%) of diamond content resulted in appearances of agglomeration and improper pore. X-ray diffraction (XRD) analysis confirmed strengthening intermetallic phases at the interfaces, thus improving the bonding strength and wetting action. The composites with 5wt.% and 10wt.% diamond content exhibited better compressive properties.

Keywords Porous aluminium · Polymethylmethacrylate · Diamond · Powder metallurgy · Space holder

1 Introduction

Porous metals have been the subject of research for development over the past two decades and are being applied in engineering fields. These lightweight materials have exceptional physical, thermal, and mechanical properties [1]. Porous Al composites are highly considered a structural material for aircraft and automobiles due to their lightweight, excellent compressibility, and high strength-to-weight ratio. Incorporating the ductile Al matrix with second-phase reinforcements that are stronger and stiffer has improved the physical and mechanical properties of the composites [2]. Considering the excellent properties of diamond particles, they have the potential to be employed as a reinforcement material in strengthening porous Al composite. Al matrix composite reinforced diamond is drawing more attention due to its low density and ease of fabrication [3].

B. Parveez · N. A. Jamal (✉) · S. M. Kadri · H. H. M. Zaki · A. Z. A. Azhar
Department of Manufacturing and Materials Engineering, Kulliyah of Engineering, International Islamic University Malaysia, P. O. Box 10, 50728 Kuala Lumpur, Malaysia
e-mail: ayuni_jamal@iium.edu.my

The porosity in Al foams is achieved through foaming agents or space holders such as titanium hydride (TiH_2), CaMg (CaCO_3)₂, and calcium carbonate (CaCO_3) [4]. However, they have certain limitations. An alternative space holder material that can overcome these limitations is PMMA due to its excellent formability, good biocompatibility, and low decomposition temperature of around 360–400 °C, leaving no residue as it decomposes completely [5]. This study investigated the effects of diamond particles in strengthening porous Al composites via the powder metallurgy technique. The impact of diamond particles on microstructure, density, porosity, and compressive properties of the porous Al composites was examined using SEM, XRD, and compression testing.

2 Materials and Method

The materials used in this study were Aluminium (Al), magnesium (Mg), tin (Sn), boron (B), polymethylmethacrylate (PMMA,) and diamond powder of average size 45 μm , 10 μm , 45 μm , 10 μm , 150 μm and 45 μm respectively. These powders had 99.9% purity and were acquired from Sigma Aldrich, Malaysia. The composites consisted of 2wt.%Mg, 3wt.% Sn, 4wt.% B, 30wt.% PMMA and various contents of diamond particles (5, 10 and 15 wt.%). Porous Al composites were fabricated using the powder metallurgy technique. Firstly, metallic powders were mixed at 250 rpm for 12 h. Next, metallic powders were mixed with PMMA and diamond particles, which were then compacted at 250 MPa. Lastly, they were sintered at 580 °C for 2 h in an argon atmosphere using a tube furnace. The morphology and density of the samples were analyzed via (JEOL JSM-6300F) Scanning Electron Microscopy (SEM) and Archimedes principle, respectively. The X-ray diffraction (XRD) analysis and compression testing were performed via X-ray diffractometer (PAN analytical empyrean 1032) in the range of 30–85° and uniaxial compression at a constant crosshead speed of 0.5 mm/min at room temperature.

3 Result and Discussion

3.1 Morphology of Diamond Reinforced Porous Al Composite

The microstructure of the porous Al composite with various contents (5, 10 and 15 wt. %) of diamond particles is shown by SEM in Figs. 1 and 2. The porous composites are composed of the structure of a closed macro-pore. The spherical-shaped PMMA particles form homogeneously distributed macro-pores throughout the composite, which provide better pore interconnectivity. The diamond particles were distributed uniformly in porous Al composites with 5 and 10 wt % diamond particle content, as

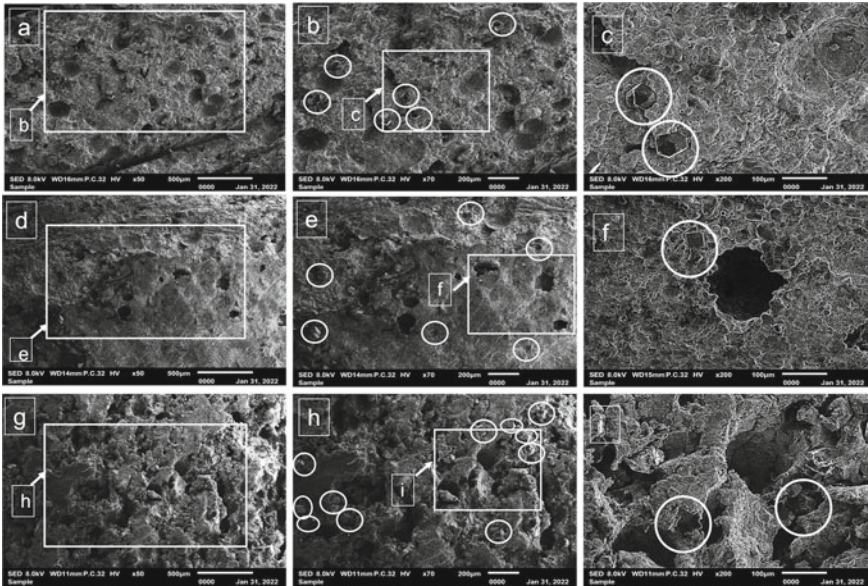


Fig. 1 SEM micrography of cross-section of sintered porous Al composite with **a, b, c** 5, **d, e, f** 10 and **g, h, i** 15 wt.% diamond particle content

shown in Fig. 1. However, in porous Al composites with 15wt.%, the higher diamond content resulted in the formation of agglomeration and incomplete wetting action between reinforcements and metal matrix, causing the formation of micropores and cracks in the cell walls, as shown in Fig. 1g, h, i. Figure 2 portrays the porosity with various diamond particle contents. Figure 2a and b exhibit open pores, and Fig. 2c shows constituents of closed pores. As evident from Fig. 2a and b pores exhibit darker pores, it signifies open pores, while in case of Fig. 2c, pores are gray colored showing closed pores (i.e. pores filled with PMMA particles). The closed pores may be due to the higher content of diamond particles which leads to the formation of carbides with matrix materials. These carbides act as a thermal barrier [6], thereby preventing the decomposition of PMMA particles. Other diamond particles do not seem to be well bonded with the Al matrix, as shown in Fig. 1c, f, i, due to more significant differences in their thermal conductivity.

3.2 Density and Porosity of Sintered Diamond Reinforced Porous Al Composite

The sintered densities of diamond reinforced porous Al composite with various diamond particle contents (5, 10, and 15 wt. %) are shown in Fig. 2d. The sintered densities of porous Al composites increased when the diamond content increased.

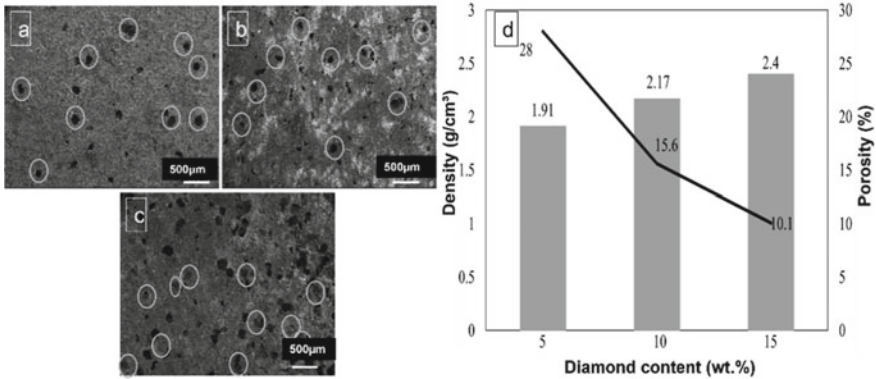


Fig. 2 Surface morphology of sintered porous Al composite foam with **a** 5, **b** 10, **c** 15 wt. % diamond particle content and **d** Relative densities and porosities of diamond reinforced composite

As shown in Fig. 2d, the porosities decreased when the diamond particle content increased due to the existence of open porosities (5 and 10wt.%) and closed pores (15wt.%). The presence of closed pores as a result of higher diamond content, offering thermal barrier to PMMA particle decomposition, thus porosity decreases thereby increasing the densities. Figure 2d clearly shows 28% porosity; consequently, decomposition of 28wt.% PMMA out of 30% was added into the composite with 5wt.% diamond content. For composites with 10wt.% diamond content decreased to 15% only in the composite with 15wt.% diamond content was found to be the least (around 10%) due to a higher thermal barrier due to a higher percentage of carbide formation, as shown in Fig. 3b.

3.3 X-Ray Diffraction (XRD) of Porous Al Composite

Figure 3b displays the XRD patterns of diamond reinforced porous Al composites with various diamond contents (5, 10, and 15wt.%). Apart from the four typical Al peaks at 38.5, 44.7, 65.1 and 82.3°, low intensity of diamond peak was detected at 43.9 and 78° [7]. The intensities of main peaks for all samples increased with increasing diamond content. The peak of intermetallic compound ($\text{Al}_{17}\text{Mg}_3$) at $2\theta = 38.156^\circ$ and (B_{13}C_2) at $2\theta = 36.242^\circ$ was also observed in all the composites [8].

These intermetallic phases further improve the wetting action between the Al matrix and diamond particles, thus improving interfacial bonding between the matrix and the reinforcements and strengthening the composites [9]. The formation of Al_2C_3 [7] occurs in all composites. However, in the composite with 15wt.% diamond content was found to be higher, as shown in Fig. 3a. The peak height increases with increasing diamond particle content.

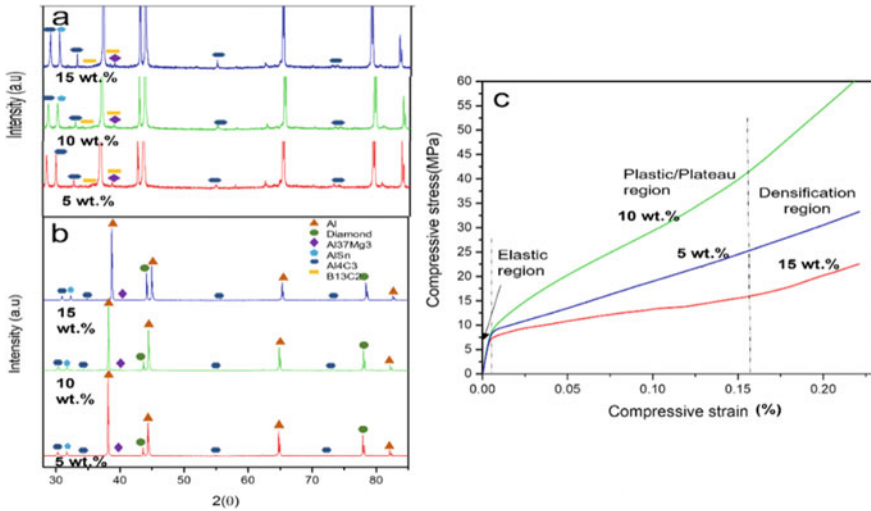


Fig. 3 a XRD patterns with 5 wt. %, 10 wt. %, and 15 wt. %, diamond particles content, b Magnified XRD pattern and c Stress–strain diagram of diamond particles reinforced porous Al composite

3.4 Compressive Properties

The deformation behavior and compressive properties of diamond reinforced porous Al composites with different diamond content are shown in Fig. 3c. All curves in Fig. 3c exhibited the typical Gibbs-Ashby deformation pattern, which included three distinct stages: (1) linear elastic region, which occurred at the beginning due to face stretching and cell wall bending; (2) plateau region, which was characterized by plastic deformation at nearly constant stress; and (3) final densification region where the stress suddenly increased [10]. The plateau stress and energy absorption increased for composites with diamond content up to 10wt.%; however, it decreased when the composite of 15wt.% diamond content was used.

Also, from Table 1 it is evident that the highest value of energy absorption capacity of 3.6 MJ/m³ was obtained for the composite with 10wt.% diamond content, while the lowest value (1.8 MJ/m³) was attained for the composite with 15wt.% diamond content. Still, the importance of energy absorption for diamond particle reinforced composites was more as compared to composites without reinforcement (1.41 MJ/m³) in the previous literature [5]. The increase in compressive properties was due to a well-defined porous structure and uniform distribution of diamond particles in composites with 5 and 10 wt.% diamond content, which aided in more energy absorption under compressive stress. However, for the composite with 15wt.% diamond content, the reduced values of compressive properties were most probably due to the closed pore structure and agglomeration of diamond particles.

4 Conclusion

The fabrication of diamond reinforced porous Al composites with various diamond contents was achieved successfully by powder metallurgy technique, which led to better distribution of diamond particles. The addition of Mg, B, and Sn resulted in formation of intermetallic phases that enhance wettability and bonding strength between matrix and diamond particles. As a result, the densities, porosities, and compressive properties improved—the porous composite with 10wt.% exhibited better properties; however, the porous composite with 5wt.% diamond particles revealed efficient sintering resulting into almost complete removal of PMMA particles leading to formation of well defined porous structure. In this case, a stress–strain curve showed more constant plateau stress suitable for porous materials. However, there was insufficient bonding between Al matrix and diamond particles, which could be improved via coated diamond particles as reinforcement and various processing parameters.

Acknowledgements The current work was supported by the Ministry of Higher Education (MOHE) of Malaysia and International Islamic University Malaysia (IIUM) (FRGS/1/2019/TK08/UIAM/02/5).

References

1. Kondoh K (2012) In: Kondoh K (ed)
2. Parveez B, Jamal NA, Maleque A, Yusof F, Jamadon NH, Adzila S (2021) Review on advances in porous Al composites and the possible way forward. *J Mater Res Technol* 14:2017–2038
3. Tan Z, Chen Z, Fan G, Ji G, Zhang J, Xu R, Shan A, Li Z, Zhang D (2016) Effect of particle size on the thermal and mechanical properties of aluminum composites reinforced with SiC and diamond. *Mater Des* 90:845–851
4. Paulin I (2014) Synthesis and characterization of Al foams produced by powder metallurgy route using dolomite and titanium hydride as a foaming agents. *Mater Tehnol* 48:943–947
5. Jamal NA, Tan AW, Yusof F, Katsuyoshi K, Hisashi I, Singh S, Anuar H (2016) Fabrication and compressive properties of low to medium porosity closed-cell porous aluminum using PMMA space holder technique. *Materials (Basel)*. 9:1–13
6. Yang W, Peng K, Zhu J, Li D, Zhou L (2014) Enhanced thermal conductivity and stability of diamond/aluminum composite by introduction of carbide interface layer. *Diam Relat Mater* 46:35–41
7. Monje IE, Louis E, Molina JM (2013) Optimizing thermal conductivity in gas-pressure infiltrated aluminum/diamond composites by precise processing control. *Compos Part A Appl Sci Manuf* 48:9–14
8. Akinwekomi AD, Tang C, Chi-pong G, Law W, Chen L, Yang X (2018) Synthesis and characterisation of floatable magnesium alloy syntactic foams with hybridised cell morphology. *Mater Des*
9. Fan YM, Guo H, Xu J, Chu K, Zhu XX, Jia CC (2011) Effects of boron on the microstructure and thermal properties of Cu/diamond composites prepared by pressure infiltration. *Int J Miner Metall Mater* 18:472–478
10. Gibson LJ, Ashby MF (1997) In: Cellular solids, structure and properties. Cambridge University Press

Improving Bending Deformation Behavior of Superelastic NiTi Archwire by Ageing Treatment



N. A. N. I. Latiffi, N. S. S. Khairi, M. F. Razali, and M. H. Hassan

Abstract A rectangular superelastic NiTi archwire is always preferred during the teeth levelling stage of orthodontic treatment due to its capacity to transmit torque and straighten the malposed tooth's position. The early application of this archwire geometry is only applicable once the round archwire has leveled the teeth to a certain extent. This study investigates the applicability of ageing treatment in improving the bending deformation behavior of rectangular superelastic NiTi archwires. In this regard, the rectangular superelastic NiTi archwires were aged at various temperatures before their bending deformation is determined using a three-point bending test. The ageing treatment successfully reduced the bending force exerted by the superelastic NiTi archwire during the unloading cycle. The bending force decreased from 3.0 to 2.2 N when the archwires were aged at 490 °C, while the residual deflection remained unchanged. This research indicates that ageing may be utilised to reduce the bending force of commercial NiTi archwires, resulting in a more comfortable orthodontic experience.

Keywords Superelastic · NiTi archwires · Orthodontic treatment · Bending force · Three-point bending

1 Introduction

The force necessary to move teeth during orthodontic treatment is generated by the spring-back potential of the bent archwire. Numerous studies have been carried out to better understand the force–deflection behaviours of archwire materials, and orthodontists have determined that the optimal orthodontic material has a high elastic limit, a low force–deflection rate (stiffness), and a wide activation range [1]. Archwires are made of a range of materials, ranging from stainless steel and nickel-titanium to cobalt-chromium and beta-titanium, and are used to exert biomechanical stresses during orthodontic treatment [2]. Superelastic NiTi archwires are widely

N. A. N. I. Latiffi · N. S. S. Khairi · M. F. Razali (✉) · M. H. Hassan
School of Mechanical Engineering, Universiti Sains Malaysia, Engineering Campus, 14300
Nibong Tebal, Penang, Malaysia
e-mail: mefauzinzam@usm.my

© The Author(s), under exclusive license to Springer Nature Singapore Pte Ltd. 2023
Md. A. Maleque et al. (eds.), *Proceeding of 5th International Conference on Advances in Manufacturing and Materials Engineering*, Lecture Notes in Mechanical Engineering,
https://doi.org/10.1007/978-981-19-9509-5_7

used for levelling and alignment, whereas beta titanium and stainless-steel wires are frequently utilised for space closure and detailing. This is because the superelastic nature of NiTi archwires enables the wire to be bent at huge deflections with minimal effort needed from the orthodontist to insert the wire into the very irregular bracket system. In comparison to conventional alloy archwires, NiTi archwires promote a mild and steady force of 1–2.0 N during bending [1], which is preferable for optimal tooth movement.

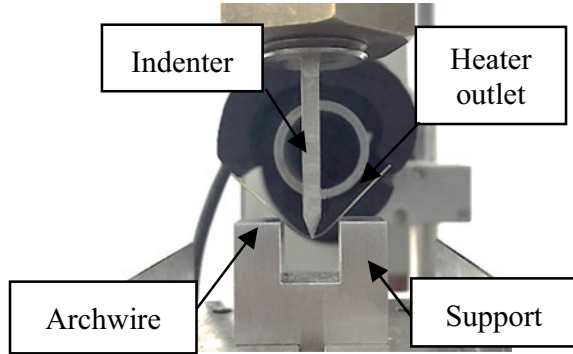
The superelastic NiTi alloy is frequently considered in the medical field for the manufacture of stents for the heart, bone staples, orthodontic archwire, and implants [3]. The superelastic properties of the NiTi alloy enable it to revert to its original shape following severe inelastic deformation strain. This immediate shape recovery is possible because of the alloy's reversible martensitic phase change ability. This superelastic characteristic is characterised during bending deformation by the production of force plateaus, both during loading and recovery of the alloy. Interestingly, with ageing treatment, this force plateau or the minimum force required to activate the alloy may be changed to satisfy application requirements [4].

Commercial NiTi archwires come in a variety of diameters and geometries. Typically, a round NiTi archwire with a diameter of 0.012–0.020 inch is used to align and level uneven teeth during the earliest phases of orthodontic therapy before switching to a rectangle wire with a size of 0.016×0.022 – 0.021×0.025 inch. This archwire sequence is required to keep an appropriate amount of biomechanical stress on the tooth throughout orthodontic treatment. While it is well established that rectangular archwires are superior to round archwires in terms of their capacity to transmit torque to the tooth, little effort has been done to lower their bending force. The purpose of this study is to investigate if ageing may be used to improve the flexural behaviour of commercial NiTi archwire. The outcomes of this study may persuade orthodontists to consider rectangular archwires early in orthodontic treatment, hence lowering the total number of clinical visits for archwire adjustments.

2 Methodology

This work considered a commercial 0.016×0.022 -inch superelastic NiTi archwire. This archwire size was chosen for its common use during the initial leveling stage in orthodontic treatment [1]. The archwire were cut into three different lengths of specimens: 50 mm for tensile testing, 2 mm for thermal transformation analysis, and 30 mm for three-point bending testing. The specimens were solution treated at 900 °C for 15 min in an argon environment using a single zone tube furnace (GSL-1100X). Following solution treatment, the specimens were aged for 30 min at four different ageing temperatures: 400, 430, 460, and 490 °C. This setting was chosen in light of the observed gradual changes in the thermal and mechanical properties of Ni-rich NiTi wires upon ageing [5].

Fig. 1 NiTi specimen bent on three-point bending setup



The thermal transformation temperature of the aged specimens was measured using differential scanning calorimeter (DSC) machine (TA-Q20). The thermal analysis temperature range was set at $-80\text{ }^{\circ}\text{C}$ to $80\text{ }^{\circ}\text{C}$ with a heating and cooling rate of $10\text{ }^{\circ}\text{C}/\text{min}$. The specimens' transformation temperatures were determined by the intersection of tangent lines drawn on their transformation peaks, such as described in ISO 15841: Dentistry-Wires for use in Orthodontics.

The bending deformation behavior of the aged specimens was assessed from the three-point bending test. This test was performed on a universal testing machine (Instron 3367), by following the testing procedures and settings suggested in ISO 15841. The test was conducted at a temperature of $36\text{ }^{\circ}\text{C}$, using a chamber with a constant flow of warm air supplied by a heater. The three-point bending test was performed by using the compressive jig as shown in Fig. 1. The test was started by placing the 30 mm long specimen on a jig with a 10 mm gap between supports. Then, at a rate of $1\text{ mm}/\text{min}$, the centrally located indenter pushed the wire's centre part downward by 3.1 mm, before returning to its original location with the same speed. This displacement setting enables the archwire specimen's bending force to be measured throughout the loading and unloading cycle. The bending deflection was performed in the direction of the height (0.016 inch) of the specimen.

3 Results and Discussions

Figure 2 shows the differential scanning calorimetry (DSC) plot of the NiTi archwires aged at different temperatures for 30 min. The peaks represent the temperature at which the phase transition occurs between austenite (A), martensite (M), and rhombohedral (R) structure. For example, at around $20\text{ }^{\circ}\text{C}$, the as-received NiTi archwire exhibited as a complete austenite structure. Overall, it is seen that when the archwires were heat treated at various temperatures, the thermal transformation temperature varied and the number of transformation peaks increased. For instance, the temperature required for complete austenite transformation has risen from $-18\text{ }^{\circ}\text{C}$ for solution treated specimens to $32\text{ }^{\circ}\text{C}$ for $490\text{ }^{\circ}\text{C}$ aged specimens. This observation

is consistent with recent work [6], which describes the change in peak number and temperature as a result of the precipitate particles' heterogeneous distribution inside the alloy matrix. Additionally, the thermal transformation peaks for specimens aged at 400 and 430 °C are not clearly visible on the DSC curves. This is because the phase transformation of the specimens occurred across a large temperature range, hence decreasing the peak intensity.

Figure 3 shows the force–deflection curve of the NiTi archwires after aged at different temperatures for 30 min. It is observed that the ageing treatment effectively altered the superelastic NiTi archwire's bending deformation. The solution treated archwire displayed the greatest force of 5.6 N when loaded to 3.1 mm deflection, above the 4.8 N force of the as-received archwire. It's worth noting that archwires aged at 490 °C promoted the lowest force during loading to 3.1 mm and unloading to 2.0 mm, respectively, with force magnitudes of 3.9 and 2.2 N. The observed changes in mechanical deformation after ageing treatment are consistent with the findings in [7], and this observation may be related to the decrease in the critical stress required for martensitic transformation as a result of Ti_3Ni_4 precipitate production [8].

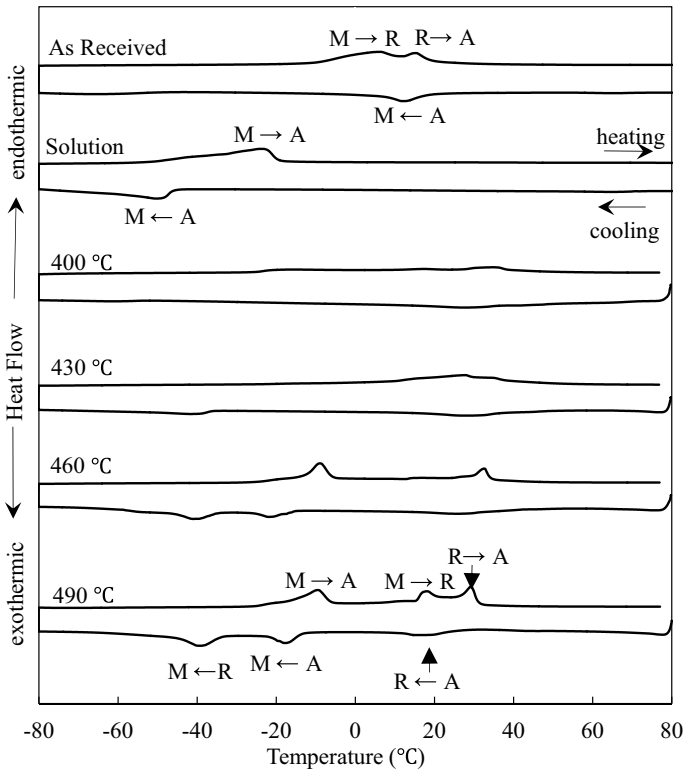


Fig. 2 Thermal transformation behavior of the NiTi specimen after ageing at different temperatures for 30 min

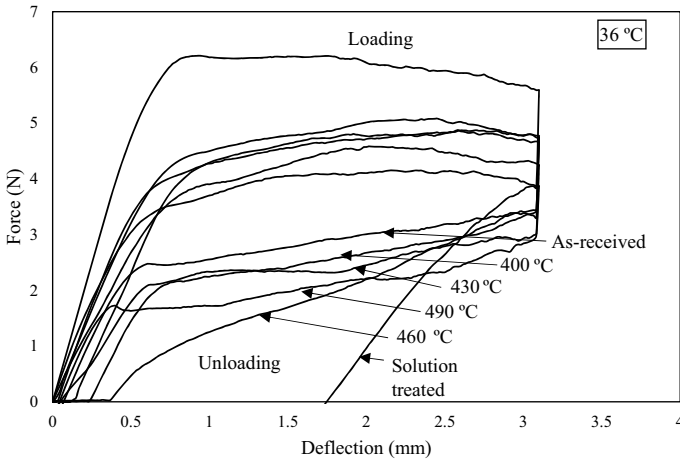


Fig. 3 Force–deflection behavior of superelastic NiTi archwires after ageing at different temperature for 30 min

The influence of ageing temperature on the bending deformation behaviour of rectangular NiTi archwires is shown in Fig. 4. The unloading force and residual deflection were determined using the data in Fig. 3. The magnitude of the unloading force was determined at 2.0 mm deflection, whereas the residual deflection value was determined when the unloading force reached zero. For comparison, the bending force and residual deflection data from the as-received were also included in the figure. When deformed in a 36 °C environment, the as-received NiTi archwire showed the greatest force magnitude of 3.0 N and residual deflection of 0.08 mm. In general, ageing effectively decreased the unloading force of the rectangular NiTi archwire from 3.0 to 2.2 N when the as-received archwire was aged at 490 °C. In contrast, there are little variations in the residual deflection, which ranges between 0.01 and 0.05 mm.

The unloading force and the residual deflection are essential factors in determining which archwires to employ during orthodontic therapy. This is because the unloading force dictates the amount of biomechanical stress applied to the patient tooth, while the residual deflection dictates the archwire's capacity to recover after being significantly bent during installation. The present findings from this study indicate that thermal and bending deformation behaviour of commercial NiTi archwires can be further adjusted by ageing treatments. Additional study is necessary to determine the ideal ageing environment; the optimal temperature and duration of ageing that would enhance the flexibility of the rectangular NiTi archwire, allowing it to be considered for teeth levelling as soon as feasible.

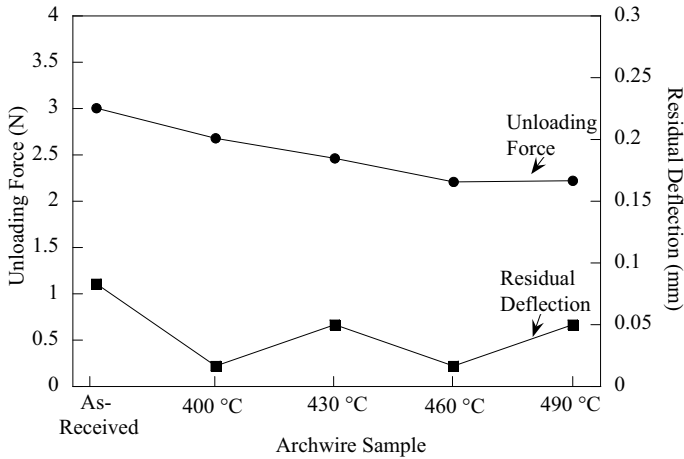


Fig. 4 Effect of ageing temperature on the unloading force and residual deflection of superelastic NiTi archwires

4 Conclusion

The thermal transformation and bending deformation behaviour of commercial superelastic NiTi archwires varied after 30 min of exposure to a range of various ageing temperatures. The bending force steadily decreased from 3.0 to 2.2 N while the archwires were aged at temperatures ranging from 400 to 490 °C. The impact of ageing on the amount of deflection residual in the NiTi archwire after recovery is negligible. For a 30-min ageing duration, 490 °C is an appropriate temperature to consider in order to minimise the bending force of the commercial superelastic NiTi archwires.

Acknowledgements The authors are grateful for the financial support provided by the Ministry of Higher Education Malaysia for Fundamental Research Grant Scheme with Project Code: FRGS/1/2020/TK0/USM/03/5

References

1. Proffit WR, Fields Jr HW, Sarver DM (2014) Contemporary orthodontics. Elsevier Health Sciences
2. Fujiyama K, Kera Y, Yujin S, Tanikawa C, Yamashiro T, Guo X, Ni A, Deguchi T (2022) Comparison of clinical outcomes between Invisalign and conventional fixed appliance therapies in adult patients with severe deep overbite treated with nonextraction. *Am J Orthod Dentofac Orthop* 161(4):542–547
3. Asgarinia F, Parvizi S (2022) Biomedical applications of NiTi alloys. In: Nickel-titanium smart hybrid materials. Elsevier, pp 297–325

4. Romanò J, Lazzari F, Garavaglia L, Pittaccio S (2022) Short duration heat treatments before aging increase mechanical hysteresis of pseudoelastic NiTi alloy. *J Mater Eng Perform* 1–7
5. Liu X, Wang Y, Yang D, Qi M (2008) The effect of ageing treatment on shape-setting and superelasticity of a nitinol stent. *Mater Charact* 59(4):402–406
6. Asgarinia F, Hashemi SM, Parvizi S (2022) Heat treatment of NiTi alloys. In: *Nickel-titanium smart hybrid materials*. Elsevier, pp 69–101
7. Manchuraju S, Kroeger A, Somsen C, Dlouhy A, Eggeler G, Sarosi PM, Anderson PM, Mills MJ (2012) Pseudoelastic deformation and size effects during in situ transmission electron microscopy tensile testing of NiTi. *Acta Mater* 60(6–7):2770–2777
8. Timofeeva EE, Panchenko EY, Zherdeva MV, Eftifeeva AS, Surikov NY, Tagiltsev AI, Chumlyakov Y (2022) Effect of one family of Ti_3Ni_4 precipitates on shape memory effect, superelasticity and strength properties of the B2 phase in high-nickel [001]-oriented Ti-51.5 at.% Ni single crystals. *Mater Sci Eng A* 832:142420

A Short Review on Diamond Reinforced Aluminium Composites



Nur Izzah Nazurah Kusuadi, Nur Ayuni Jamal, and Yusilawati Ahmad

Abstract Diamond, which is a type of carbon material, is an attractive reinforcement material for aluminium matrix composites due to its excellent properties such as high hardness, high thermal conductivity and low coefficient of thermal expansion. Diamond reinforced aluminium (diamond/Al) composite is a promising candidate material for applications of thermal management and electronic packaging. However, there are some major issues between Al metal matrix and diamond reinforcement that limit the utilization of the composites such as poor wettability and low interfacial bonding. This review discusses the challenges in diamond/Al composites, initiatives taken to solve the issues and processing techniques used to fabricate diamond/Al composites along with related advantages and limitations.

Keywords Diamond reinforcement · Aluminium matrix · Manufacturing process · Coating · Interfacial bonding

1 Introduction

Metal matrix composite (MMC) is made up from the combination of a continuous matrix of metal or alloy with a reinforcement of particle, short fibre or continuous fibre. The matrix is the dominating material that produces the shape of the composites and transfers the load between the metal and reinforcement, while reinforcement is a stronger substance used in composites and is distributed throughout the matrix material [1]. The development of MMC was motivated by the insufficient strength and stiffness of metals and alloys [2]. Combination of metal matrix and reinforcement for MMC can be developed to form excellent properties such as high young's

N. I. N. Kusuadi · N. A. Jamal (✉)

Department of Manufacturing and Materials Engineering, Kulliyyah of Engineering, International Islamic University Malaysia, P.O BOX 10, 50728 Kuala Lumpur, Malaysia
e-mail: ayuni_jamal@iium.edu.my

Y. Ahmad

Department of Chemical Engineering and Sustainability, Kulliyyah of Engineering, International Islamic University Malaysia, P.O BOX 10, 50728 Kuala Lumpur, Malaysia

modulus, high thermal conductivity, good wear resistance and low coefficient of thermal expansion.

Nowadays, aluminium metal matrix composite is a highly demanding material and has various applications in engineering field such as automotive sector, aerospace industry, construction materials, marine transport and off-shore applications. Aluminium metal matrix composites are becoming increasingly popular in the transportation sector due to their lower noise and fuel consumption as compared to other materials. The increasing applications are due to enhanced properties of aluminium metal matrix composite such as high strength, wear resistant, high specific modulus and good wear resistance.

There are a number of literatures which have successfully fabricated Aluminium MMC with reinforcements such as SiC [3], Al₂O₃ [4], CNT [2], diamond particles [5], TiB₂ [6] and B₄C [7]. Reinforcements such as SiC, Al₂O₃ and B₄C are commonly used due to their low cost and excellent properties. Diamond is preferred to be used since remarkable properties are required and cost is not a problem. Among the reinforcements, diamond has the highest thermal conductivity compared to any material available at an industrial scale of up to 2200 W/mK at 25 °C, which makes it a suitable candidate for thermal management applications. The exceptional thermal properties of diamond can be transferred to bulk engineering components by reinforcing diamond particles in a second material, preferably a metallic matrix such as Al [8]. Diamond reinforced metals have exceptionally high Young's moduli, which are 3 to 4 times higher than those of unreinforced matrix materials [9]. On the other hand, diamond reinforced metal composites have high thermal conductivity and low thermal expansion, making them ideal for heat sink applications [10]. Therefore, the intent of this review is to study the challenges and common problems induced in diamond/Al composites, ways to minimize the problems and processing techniques available to fabricate diamond/Al composites.

2 Diamond/Aluminium Composites

Nowadays, diamond reinforced Al matrix (diamond/Al) composites have been widely used for applications in the areas of thermal management, electronic packaging and semiconductor processing equipment due to their excellent properties of high thermal conductivity, low density and low coefficient of thermal expansion [11–13].

Previous extensive findings on diamond/Al composites have highlighted the major issue of poor wetting property between Al matrix and diamond particles, which is of great importance in order to obtain desirable properties of the composite. Sun et al. [14] found that there are large amounts of wide gap around diamond particles when they are reinforced with Al matrix under SEM images, which highlight the poor wetting property between diamond particles and Al matrix.

To overcome this drawback, in-depth researches have been carried out to study methods in improving interfacial bonding, which involve the addition of alloying

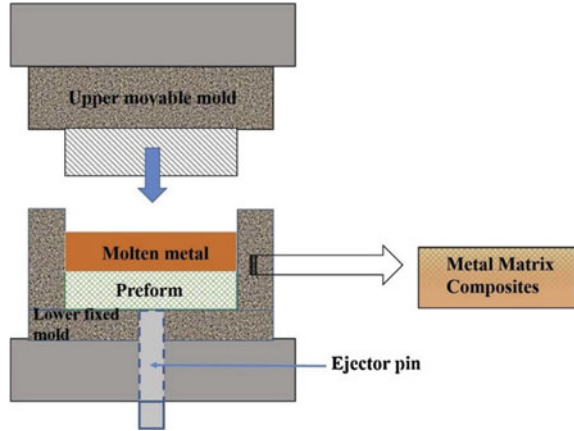
elements and diamond coating treatments [15]. Xue and Yu [16] found that addition of Ti into Al matrix increased the interfacial bonding and thermal conductivity of the composite. Wu et al. [17] added Cu as an alloying element in the Al matrix and found that the Al₂Cu phase was formed at the interface, resulting in strong interfacial bonding and increased thermal conductivity. However, method of coating treatment appears to be more effective than adding alloying element [16]. Guo et al. [18] compared both methods of adding Si into Al matrix and coating diamond surfaces with Ti and found out that both methods relatively improved the interfacial bonding of diamond/Al composite and increased the thermal conductivity. However, Ti coating layer was found to have more interfacial thermal barriers at the diamond/Al interface compared to adding Si into Al matrix. Yang et al. [15] found that coating diamond particles with tungsten (W) coatings via magnetron sputtering method improved the interfacial bonding and increased TC values of diamond and Al. Zhou et al. [19] improved the interface characteristics and higher TC of diamond/Al composites by coating diamond particles with Cr. In another study conducted by Sun et al. [14], they found that diamond/Al composites with B₄C-coated diamond enhanced the interfacial bonding between Al and diamond, exhibiting higher thermal conductivity and a rise in the density of the composite.

By improving the interfacial bonding between Al matrix and diamond particles, the mechanical properties of the composite are also improved. In a study conducted by Zhang et al. [20], they found that W-coated/Al diamond composites exhibit higher bending strength compared to uncoated diamond/Al composites. Sun et al. [14] found that the bending strength of B₄C-coated diamond/Al composites was about twice that of uncoated diamond/Al composites. The coated layer, which is made up of carbides and metal, works as a crack propagation layer by transferring diamond strength to the aluminium matrix while allowing good adhesion between diamond and Al matrix, which results in higher density and lower porosity, thus forming a stronger composite. These findings showed that coating of diamond particles with carbide element material improves the adhesion of Al matrix to the diamond particle surfaces, which contributes to the significant increase in TC and bending strength of diamond/Al composites.

3 Manufacturing Processes of Diamond/Aluminium Composites

There are various manufacturing processes to fabricate diamond/Al composites based on available literatures. Each process has their own merits and demerits. The selection of appropriate process is crucial in order to understand the desired features of resultant diamond/Al composites.

Fig. 1 Schematic diagram of squeeze casting infiltration [21]



3.1 Squeeze Casting Infiltration

Squeeze casting is a combination of casting and forging process. In general, metal solidifies under pressure when a closed die is used. Pressure is applied to the molten metal as shown in Fig. 1 due to the movement of the mould parts, and it penetrates over the dispersed phase. Squeeze casting produces products with high weldability, good surface finish, high corrosion resistance, high temperature resistance and high dimensional accuracy [1]. Khalid et al. successfully fabricated diamond/Al composite through squeeze casting method and found that the produced composites are free from voids and microcracks [8]. Jiang et al. also successfully developed diamond/Al composites via squeeze casting method. However, the interfacial reaction appears to be the main issue of squeeze casting method [13].

3.2 Gas Pressure Infiltration

The process of gas pressure infiltration uses pressurized gas to apply pressure on the molten metal and force the molten metal into a preform in vacuum condition as shown in Fig. 2. Ruch et al. [22] fabricated Al(Si)-diamond composites using gas pressure infiltration method and found that longer exposure time of diamond crystals to the aluminium melt results in a reaction between aluminium and carbon, which produces Al_4C_3 . However, violent interfacial reactions may occur at high temperature of infiltration. Optimizing the fabrication parameters of gas pressure infiltration may solve the interfacial reactions problems.

Fig. 2 Schematic diagram of gas pressure infiltration [21]

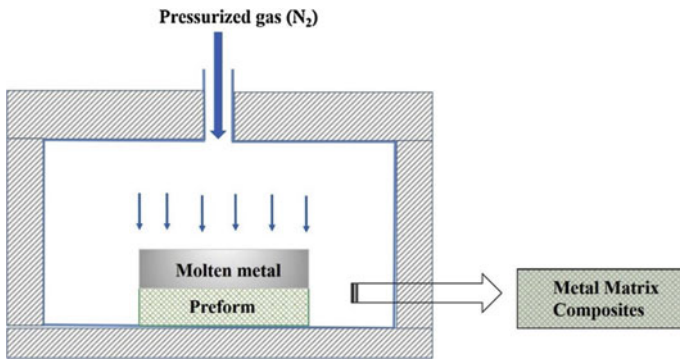
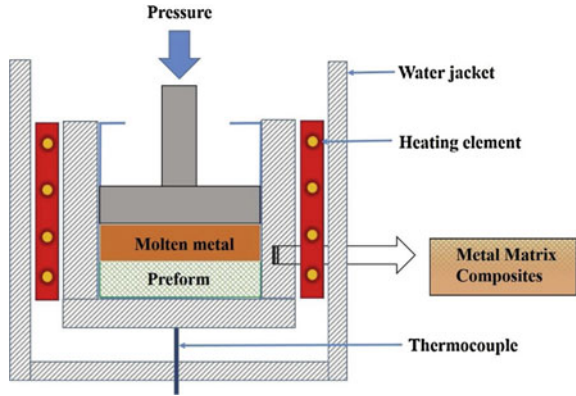


Fig. 3 Schematic diagram of pressure infiltration process [21]

3.3 Pressure Infiltration

Pressure infiltration is a technique used to make high reinforcement content by solidifying molten metal or alloy in a mould that is filled with reinforcement material as shown in Fig. 3. Pressure infiltration method is able to produce MMCs with low coefficient of thermal expansion by allowing for very high particle volume fractions. Guo et al. [18] obtained Ti-coated diamond/Al composites and diamond/Al-Si composites by optimizing the fabrication parameters of pressure infiltration.

3.4 Powder Metallurgy

Powder metallurgy is a solid-state process that is widely used in fabricating diamond/Al composite in order to reduce interfacial reactions. This relatively low

temperature process involves the mixing of Al metal powder and diamond reinforcement particles in a rotary mill, which is then followed by compaction and sintering. Zhang et al. [20] successfully fabricated W-coated diamond/Al composites through powder metallurgy method and found that diamond particles are homogeneously distributed in the diamond/Al composites. Sun et al. systematically studied the bending strength and thermal conductivity in uncoated diamond/Al composites and B4C-coated diamond/Al composites via powder metallurgy method [14].

4 Conclusion

This review summarized drawbacks in developing diamond/Al composites and the methods employed to minimize the issue. Various manufacturing processes of diamond/Al composites were also discussed along with their pros and cons. Diamond/Al composites are promising materials that can be used in the applications of thermal management due to their excellent thermal conductivity. In future, researchers are required to find solutions to overcome issues such as cost of reinforcement, development of new manufacturing techniques and improved properties of diamond/Al composites.

Acknowledgements The authors are thankful for the sponsorship provided by the Ministry of Higher Education of Malaysia and International Islamic University Malaysia (IIUM) under the Grant Number of FRGS/1/2019/TK08/UIAM/02/5 to ensure the completion of the current project.

References

1. Senthil S, Raguraman M, Manalan DT (2020) Materials today : proceedings manufacturing processes and recent applications of aluminium metal matrix composite materials : a review. *Mater Today Proc*
2. Bakshi SR, Lahiri D, Agarwal A (2010) Carbon nanotube reinforced metal matrix composites—a review. *Int Mater Rev* 55:41–64
3. Chandio AD, Ansari MB, Hussain S, Siddiqui MA (2019) Silicon carbide effect as reinforcement on aluminium metal matrix composite. *J Chem Soc Pakistan* 41:650–654
4. Narayana Murty SVS, Nageswara Rao B, Kashyap, BP (2003) On the hot working characteristics of 6061Al–SiC and 6061–Al₂O₃ particulate reinforced metal matrix composites. *Compos Sci Technol* 63:119–135
5. Yang W, Peng K, Zhou L, Zhu J, Li D (2014) Finite element simulation and experimental investigation on thermal conductivity of diamond/aluminium composites with imperfect interface. *Comput Mater Sci* 83:375–380
6. Suresh S, Moorthi NSV (2012) Aluminium-titanium diboride (Al–TiB₂) metal matrix composites: challenges and opportunities. *Procedia Eng* 38:89–97
7. Maramreddy RT, Rao SR, Padmanabhan G (2012) Fabrication and mechanical properties of aluminium-boron carbide composites. *Int J Mater Biomater Appl* 2:15–18
8. Khalid FA, Beffort O, Klotz UE, Keller BA, Gasser P (2004) Microstructure and interfacial characteristics of aluminium–diamond composite materials. *Diam Relat Mater* 13:393–400

9. Weidenmann KA, Tavangar R, Weber L (2009) Mechanical behaviour of diamond reinforced metals. *Mater Sci Eng A* 523:226–234
10. Sun Y, He L, Zhang C, Meng Q, Liu B, Gao K, Wen M, Zheng W (2017) Enhanced tensile strength and thermal conductivity in copper diamond composites with B4C coating. *Sci Rep* 7:2–11
11. Huang Y, Ouyang Q, Zhang D, Zhu J, Li R, Yu H (2014) Carbon materials reinforced aluminum composites: a review. *Acta Metall Sin (English Lett)* 27:775–786
12. Tong Z, Shen Z, Zhang Y (2007) Aluminum/diamond composites and their applications in electronic packaging. *Proc Electron Packag Technol Conf EPTC*
13. Jiang L, Wang P, Xiu Z, Chen G, Lin X, Dai C, Wu G (2015) Materials characterization Interfacial characteristics of diamond/aluminum composites with high thermal conductivity fabricated by squeeze-casting method. *Mater Charact* 106:346–351
14. Sun Y, Zhang C, He L, Meng Q, Liu BC, Gao K, Wu J (2018) Enhanced bending strength and thermal conductivity in diamond/Al composites with B4C coating. *Sci Rep* 8:1–12
15. Yang W, Chen G, Wang P, Qiao J, Hu F, Liu S, Zhang Q, Hussain M, Dong R, Wu G (2017) Enhanced thermal conductivity in diamond/aluminum composites with tungsten coatings on diamond particles prepared by magnetron sputtering method. *J Alloys Compd* 726:623–631
16. Xue C, Yu JK (2013) Enhanced thermal conductivity in diamond/aluminum composites: comparison between the methods of adding Ti into Al matrix and coating Ti onto diamond surface. *Surf Coatings Technol* 217:46–50
17. Wu J, Zhang H, Zhang Y, Li J, Wang X (2012) Effect of copper content on the thermal conductivity and thermal expansion of Al-Cu/diamond composites. *Mater Des* 39:87–92
18. Guo CY, He XB, Ren SB, Qu XH (2016) Thermal properties of diamond/Al composites by pressure infiltration: comparison between methods of coating Ti onto diamond surfaces and adding Si into Al matrix. *Rare Met* 35:249–255
19. Zhou H, Ran M, Li Y, Yin Z, Tang Y, Zhang W, Zheng W, Liu J (2021) Improvement of thermal conductivity of diamond/Al composites by optimization of liquid-solid separation process. *J Mater Process Technol* 297:117267
20. Zhang C, Cai Z, Wang R, Peng C, Qiu K, Wang N (2016) Microstructure and thermal properties of Al/W-coated diamond composites prepared by powder metallurgy. *Mater Des* 95:39–47
21. Ramanathan A, Krishnan PK, Muraliraja R (2019) A review on the production of metal matrix composites through stir casting—furnace design, properties, challenges, and research opportunities. *J Manuf Process* 42:213–245
22. Ruch PW, Beffort O, Kleiner S, Weber L, Uggowitzer PJ (2006) Selective interfacial bonding in Al(Si)-diamond composites and its effect on thermal conductivity. *Compos Sci Technol* 66:2677–2685

Amperometric Study of P3HT/Multi-walled Carbon Nanotubes Composite for Malathion Sensing



Nurul Syahirah Nasuha Sa'aya, Siti Zulaikha Ngah Demon, Norli Abdullah, Ahmad Farid Mohd Azmi, and Norhana Abdul Halim

Abstract Novel electronic nanomaterial, the carbon nanotube (CNT) has emerged in many sensor applications because of large surface area, functional electronic and chemical properties. In this paper, functionalized MWCNT and polymer semiconductor, poly(3-hexylthiophene-2,5-diyl), (P3HT) were introduced to assist analyte anchoring and improving sensitivity performance of organophosphate sensor. The amperometric measurement of nanocomposite sensor shows the electrical properties of P3HT/MWCNT-OH increased by 85% compared to pristine MWCNT sensor. Implying a better charge carrier pathway present in MWCNT-OH composite upon malathion exposure, the change of current, ΔI of P3HT/MWCNT-OH were way larger compared to pristine device. The origin of conductivity in P3HT/MWCNT-OH thin film was filament-like structure due to non-covalent wrapping as observed from electron microscope. The origin of π - π interaction between P3HT and MWCNT was also detected in UV-visible absorption. In conclusion, the proposed P3HT/MWCNT-OH sensor device demonstrated good sensitivity (~ 0.1 –500 ppb) with limit of detection of 0.07 ppb towards malathion.

Keywords P3HT · Carbon nanotube · Malathion · Amperometric · Sensing

1 Introduction

A large number of functional materials have been investigated for gas sensing applications owing to the fact that when a particular gas interacts with these surfaces,

N. S. N. Sa'aya

Faculty of Defence Science and Technology, National Defence University of Malaysia, Sungai Besi Camp, 57000 Kuala Lumpur, Malaysia

S. Z. N. Demon

Centre for Tropicalization, National Defence University of Malaysia, Sungai Besi Camp, 57000 Kuala Lumpur, Malaysia

N. Abdullah · A. F. M. Azmi · N. A. Halim (✉)

Centre for Defence Foundation Studies, National Defence University of Malaysia, Sungai Besi Camp, 57000 Kuala Lumpur, Malaysia

e-mail: norhana@upnm.edu.my

some alteration in its properties can be observed. As a result, these functional materials might be thought of as sensing films [1]. Organic and polymer semiconductors have gained a lot of research attention for usage in next-generation electronics and optoelectronics because of their flexibility and ease of processing. Carbon nanotubes (CNT) have piqued the interest of researchers all over the world due to their pseudo-1D structure and exceptional mechanical, electrical, and thermal properties. CNT materials are being used in nanoelectronics devices, chemical sensors, solar cells, and other applications. CNTs have a large specific surface area and can absorb a large amount of gas, making them a potential candidate for chemical sensors with high sensitivity [2]. Liu et al. shows the importance of using functionalized CNT in sensing applications. Hydroxyl functionalized CNT has been reported to perform better compared to pristine CNT due to its more efficient charge transfer [3]. In proposing CNT nanocomposite sensing material, non-covalent interaction is essentially advantageous as it does not affect the porous textural properties of CNT [4]. Because the π graphene sheet system will not be disturbed, meaning that it will not impact the exterior surface area of the tubes.

Typically, the purpose of CNT functionalization is to improve its water solubility so that it can be used for many practical applications. CNT sidewalls/end caps are bound to other novel materials, such as semiconducting polymer. Because of its ease of solution processability in various solvents. Poly (3-hexyl thiophene) or widely abbreviated as P3HT has been the most extensively investigated conjugated polymer for the development of organic semiconductor devices [5]. When the conducting polymer is non-covalently attached to the CNT surface, van der Waals forces are reduced and CNT dispersion is improved, improving the processability of CNT devices [6].

Therefore, we believe a combination of P3HT and MWCNTs can produce promising nanocomposites for organophosphate (Malathion) sensor applications. From the author's knowledge, only a few studies have been reported on the amperometric studies and origin of electrical signal due to material interaction in using conducting polymer, P3HT and multi walled carbon nanotubes (MWCNT) for malathion detection.

2 Materials and Methods

Regio-regular poly(3-hexylthiophene-2,5-diyl) (Sigma Aldrich, purity: > 99%, molecular weight, $M_w \sim 50,000\text{--}100,000$) was used in this work. Multi-walled carbon nanotubes and hydroxylated multiwalled carbon nanotubes were purchased from Sigma Aldrich (purity: > 95% carbon basis). Tetrahydrofuran (THF) was used as a suspension agent and purchased from Sigma Aldrich. All materials and reagents were used as received. Nanocomposite films were prepared according to the following procedures; MWCNT and P3HT were dispersed in THF solution and magnetically stirred at a constant temperature of 50 °C for 96 h with a consistent speed of 650 rpm. The mixture was then ultra-sonicated ($f = 50/60$ Hz) for 2 h to form

a well-dispersed MWCNT suspension. The supernatant of the mixture solution was collected after centrifuged for 1 h at 4500 rpm. The films were filtrated, drop-casted and subsequently spin coated on the α -quartz and ITO substrates at 500 rpm for 3 s and then allowed to dry at room temperature. Pristine P3HT, P3HT/MWCNT and P3HT/MWCNT-OH were characterized using UV-Vis spectrophotometer, (Lambda 750, PerkinElmer). The nanostructures morphology of the samples and I-V measurement were studied by field emission scanning electron microscopy (FESEM) on a Gemini SEM500 instrument machine and Metrohm Autolab B. V (PGSTAT204) potentiostat, respectively.

3 Result and Discussion

The amperometric characteristics of P3HT, MWCNT, MWCNT-OH, P3HT/MWCNT and P3HT/MWCNT-OH obtained in the current-voltage measurement were tabulated in Table 1.

The electrical conductivity for P3HT was measured to be around 7.2×10^{-6} S/cm while pristine MWCNT and hydroxylated-MWCNT demonstrate higher electrical conductivity at 7.16×10^{-3} S/cm and 3.22×10^{-3} S/cm, respectively. The electrical conductivity can be measured using formula $s = \frac{l}{RA}$ where, l is the length, A is the sectional area and R , is the resistance. The values are agreeable and of range of semiconducting materials. Generally, conductivity in conductive polymer and CNT can be attributed to carbon atom sp^2 hybridization due to π - π interactions [7, 8]. However, parameters of sample preparation such as dispersion, homogeneity and close pack structure can also affect the overall conductivity performance. P3HT/MWCNT nanocomposite showed electrical conductivity of 4.8×10^{-7} S/cm. This low value of electrical conductivity implied that P3HT only acts as a binder to the MWCNT, but its stabilized aromatic ring is incapable to facilitate charge conductivity [8]. On the other hand, P3HT/MWCNT-OH nanocomposite shows outstanding conductivity that is 6.0×10^{-3} S/cm. The reason behind this good electrical behaviour can be explained in the UV-Vis and morphology of the nanocomposite later.

Table 1 Amperometric characteristics of P3HT, P3HT/MWCNT, P3HT/MWCNT-OH before and after addition of malathion

Sample	Conductivity, s (S/cm)	Conductivity after the addition of malathion (S/cm)	Change of current, ΔI (A)
P3HT	7.2×10^{-6}	7.38×10^{-7}	6.46×10^{-6}
MWCNT	7.16×10^{-3}	–	–
MWCNT-OH	3.22×10^{-3}	–	–
P3HT/MWCNT	4.8×10^{-7}	5.19×10^{-8}	4.28×10^{-7}
P3HT/MWCNT-OH	6.0×10^{-3}	2.53×10^{-9}	5.9×10^{-3}

Figure 1 shows UV–Vis absorption spectra of P3HT, P3HT/MWCNT and P3HT/MWCNT-OH. Interaction between P3HT and MWCNT mainly occurred at π - π^* interaction between the conjugated double bond of graphite ring and conjugated double bond of P3HT and also from van der Waals interaction from other sites [9]. In Fig. 1, B should be at 570, while C should be at 620 nm. Peak labelled with B originated from van der Waals hairy chain of alkyl in P3HT, appeared very prominent on all spectra. Peak labelled C represents electronic transition attributed to an interchain absorption, is shown to diminish upon becoming composite. Its absorption edge indicated optical band gap of the polymer corresponding to the formation of an excitation delocalized over multiple P3HT chains. Peak C in P3HT/MWCNT-OH has red shifted relative to P3HT/MWCNT spectrum indicating slight difference in P3HT and MWCNT ordered structures. Our calculation shows the bandgap energy is 2.06 eV and 2.04 eV for P3HT/MWCNT and P3HT/MWCNT-OH.

Fig. 1 UV–Vis spectra of P3HT, P3HT/MWCNT and P3HT/MWCNT-OH

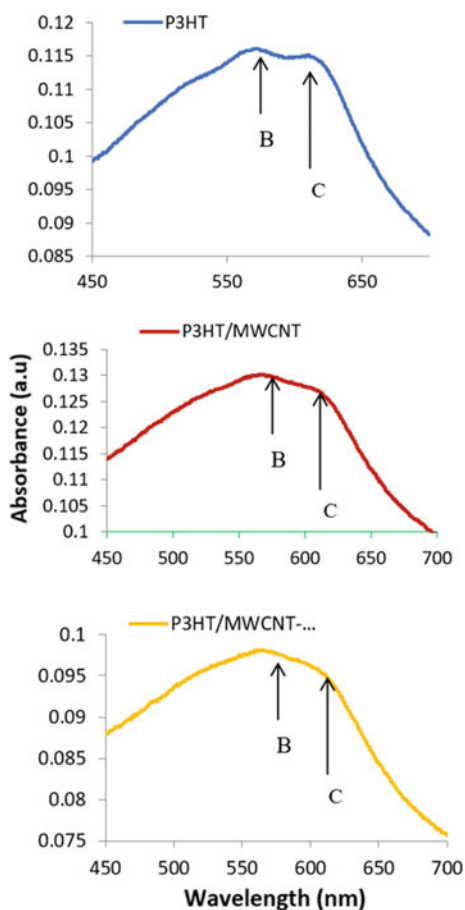


Figure 2 shows, proposed mechanism of P3HT/MWCNT-OH nanocomposite (a) before (b) after exposure to malathion that result into drastic change in electrical characteristics. Initially, P3HT/MWCNT-OH has π - π interaction and π -H interaction which effectively increases charge hopping mobility as well as better dispersion quality. However, upon exposure of malathion, we observed large change of current, ΔI compared to other devices (Refer Table 1). This can be explained by additional mechanism that disrupt charge carrier pathway present in MWCNT-OH composite. As seen in Fig. 2b, the MWCNT-OH will form H-bonding with oxygen atoms in the pesticide. Malathion has rich high electronegativity O atoms that can compete with π - π stacking aromatic rings to form interaction. This way, malathion interaction reduced pancake bonding by π - π stacking materials, which effectively limits charge transfers within the nanocomposite. Hence, causing drastic drop of conductivity. We observed this H-bond with malathion acts temporarily due to the close pack structure between the P3HT and MWCNT-OH as we can see in Fig. 2a. In such a closed system, π - π stacking aromatic rings are close enough to the OH group to regain its ability to transfer charges after desorption of malathion. This will be an advantage to the P3HT/MWCNT-OH as a reusable sensing material with cyclic capability. The diameter size of MWCNT-OH was found to be larger than the MWCNT, thus explained better interaction with the polymer and amperometric characteristics of MWCNT-OH sensing material. In our previous publication [10], we discussed that the P3HT managed to non-covalently wrapped around MWCNT, covering efficiently large enough surface area for malathion sensing. It is highly desirable since the P3HT has larger affinity to organophosphate compound [10] (Fig. 3).

Finally, the limit of detection (LOD) and limit of quantitation (LOQ) of P3HT/MWCNT-OH were defined. The LOD and LOQ need to be distinguished to show the analyte can be quantitated at defined levels for imprecision and accuracy [11]. Our measurement was established using 3:1 and 10:1 noise for LOD and LOQ respectively [12]. Table 2 shows the LOD and LOQ in the study resistivity towards the analyte of malathion on P3HT/MWCNT-OH nanocomposite. The LOD obtained in the study revealed that the P3HT/MWCNT-OH has the potential to perform ultra-trace analysis of malathion using two-point probe measurement. The estimated limit of detection of malathion by P3HT/MWCNT-OH nanocomposite was 0.07 ppb which demonstrates good sensitivity compared to other examples [13]. Figure 4 shows adsorption and desorption measurement of P3HT/MWCNT-OH with 0.1 ppb malathion and water. It was seen that a change of current with a 0.1 ppb dropped. The current was recovered after four minutes of malathion introduction. There is no change in the current if water is adsorbed into the sample. This proved the P3HT/MWCNT-OH can be selective towards malathion.

4 Conclusion

In our study, the P3HT/MWCNT-OH is shown with better amperometric property compared to P3HT/MWCNT, for the application detecting malathion. This is evident

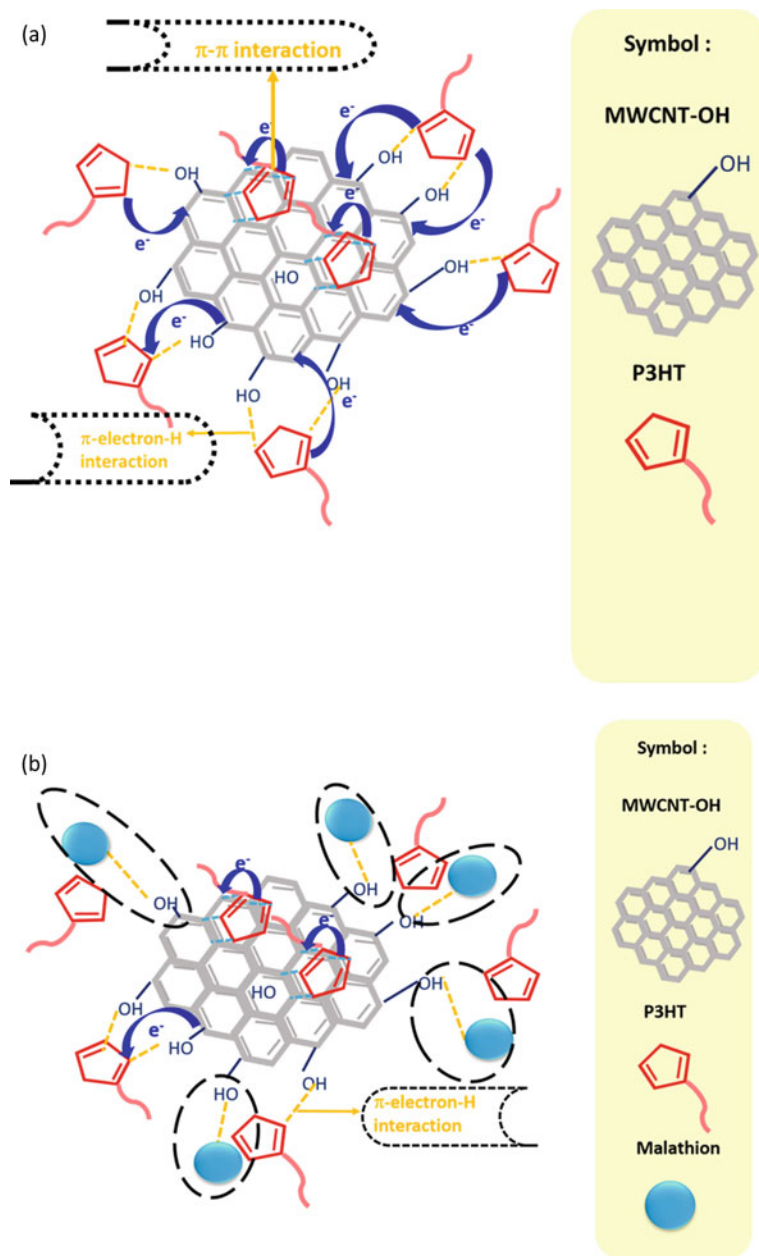


Fig. 2 Proposed mechanism of P3HT/MWCNT-OH nanocomposite **a** before **b** after exposure to malathion

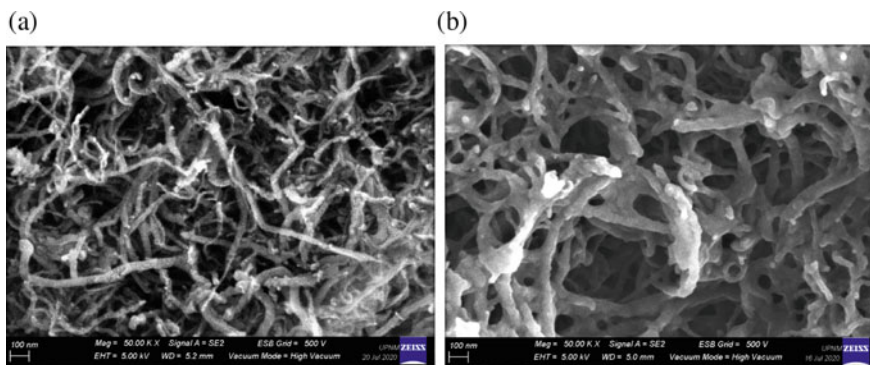


Fig. 3 Morphology of **a** MWCNT-OH and **b** P3HT/MWCNT-OH using HR-TEM

Table 2 LOD and LOQ for malathion towards P3HT/MWCNT-OH

Parameter	Concentration of malathion (ppb)
LOD	0.07
LOQ	0.70

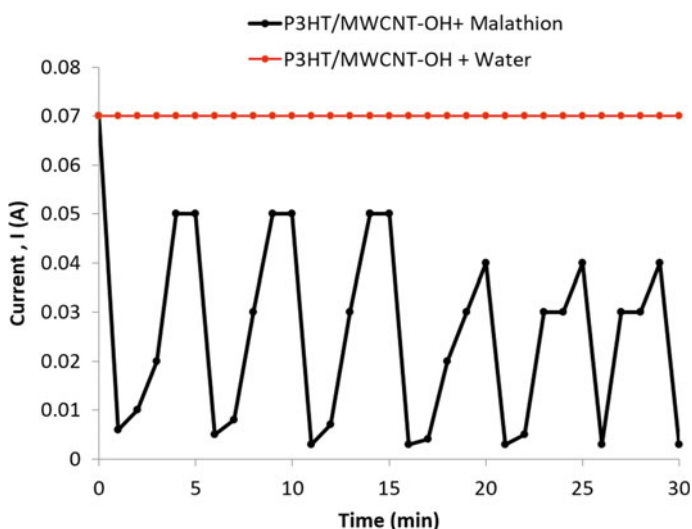


Fig. 4 Adsorption and desorption measurement of P3HT/MWCNT-OH with 0.1 ppb malathion (black) and water (red)

by lower bandgap energy and increased diameter of MWCNT-OH after P3HT is wrapped around the nanotube through π - π interaction. It is proposed the π electron-H interaction between π -conjugated at P3HT and MWCNT-OH is responsible in increasing charge carrier conductivity. Upon malathion exposure, the electron will

make a temporary H-interaction with malathion which reduced carrier mobility. P3HT/MWCNT-OH demonstrates good sensitivity (0.1 ppb to 500 ppb) with a limit of detection is 0.07 ppb as good for sensor devices. The π electron-H interaction helps to regain its ability to transfer charges and gives an advantage to the P3HT/MWCNT-OH as a reusable sensing material with cyclic capability.

Acknowledgements The authors acknowledged the financial support from the Ministry of Education (MoE) and Research Centre for Chemical Defence, National Defence University of Malaysia (grant no. UPNM/2018/CHEMDEF/ST/03).

References

1. Giulianini M, Motta N (2012) Polymer self-assembly on carbon nanotubes. In: Self-assembly of nanostructures: the INFN lectures, vol 3. Springer, New York, pp 1–72
2. Avouris P, Appenzeller J, Martel R, Wind SJ (2003) Carbon nanotube electronics. *Proc IEEE* 91(11):1772–1783
3. Liu Y, Pei Z, Zhang Q, Ge Y, Zhang R, Wang B, Sang S (2021) Electronic properties of OH-CNT-Ag composite: a combined first-principles and experimental study. *Appl Nanosci* 11(3):737–749
4. Liu SF, Petty AR, Sazama GT, Swager TM (2015) Single-Walled carbon nanotube/metalloporphyrin composites for the chemiresistive detection of amines and meat spoilage. *Angewandte Chemie International Edition* 54(22):6554–6557
5. Kanai Y, Grossman JC (2008) Role of semiconducting and metallic tubes in P3HT/carbon-nanotube photovoltaic heterojunctions: density functional theory calculations. *Nano Lett* 8(3):908–912
6. Song JP, Choi SH, Chung DW, Lee SJ (2021) Latex-based polystyrene nanocomposites with non-covalently modified carbon nanotubes. *Polymers* 13(7):1168
7. Lee KM, Huang CH, Chang CY, Chang CC (2020) The optical and microstructural characterization of the polymeric thin films with self-assembly nanoparticles prepared by spin-coating techniques. *Crystals* 10(5)
8. Breslow R (2014) Novel aromatic and antiaromatic systems. *Chem Record* 14(6):1174–1182
9. Giulianini M, Waclawik ER, Bell JM, Scarselli M, Castrucci P, de Crescenzi M (2011) Microscopic and spectroscopic investigation of poly(3-hexylthiophene) interaction with carbon nanotubes. *Polymers* 3(3):1433–1446
10. Sa'aya NSN, Demon SZN, Abdullah N, Abd Shatar VFKE, Halim NA (2019) Optical and morphological studies of multiwalled carbon nanotube-incorporated poly(3-hexylthiophene-2, 5-diy) nanocomposites. *Sens Mater* 31:2997–3006
11. Jannetto PJ (2017) Therapeutic drug monitoring using mass spectrometry. In: *Mass spectrometry for the clinical laboratory*, pp 165–179
12. Şengül Ü (2016) Comparing determination methods of detection and quantification limits for aflatoxin analysis in hazelnut. *J Food Drug Anal* 24(1):56–62
13. Ebrahim S, El-Raey R, Hefnawy A, Ibrahim H, Soliman M, Abdel-Fattah TM (2014) Electrochemical sensor based on polyaniline nanofibers/single wall carbon nanotubes composite for detection of malathion. *Synth Metals* 190:13–19

Force Deflection Behaviors of NiTi Archwires at Different Bending Conditions: A Mini Review



A. Munir and M. F. Razali 

Abstract This study's objective is to describe the force–deflection behaviour of NiTi archwires when bent into different configurations. NiTi archwires revolutionised orthodontics by generating light, constant force across a larger displacement range than conventional stainless steel archwires. This capacity to provide constant mild force during orthodontic treatment improves treatment efficacy, especially during the aligning and levelling phase. In order to comprehend the force–deflection behaviour of NiTi archwires in bracket settings in light of the varied malocclusion statuses of different patients, several settings have been studied. It is observed that the force behaviour of NiTi archwires varies with the extent of bending, distances specified between brackets, bracket material and ligation technique. This knowledge on the magnitude and trend of force variation is essential for orthodontists to identify archwires and brackets according to the irregularity state of the teeth, hence enhancing the patient's treatment experience.

Keywords Force–deflection behavior · Orthodontic bracket · Bending · NiTi archwires

1 Fixed Appliance Therapy

Fixed appliance therapy is utilised in most orthodontic treatment as it improves proper tooth alignment [1]. The archwire and the metal bracket are the primary components of the fixed appliance utilised in this treatment. After attaching the dental brackets to the tooth, an archwire is carefully positioned inside the bracket slot by following the irregularity of the bracket location, causing local bending along the length of the archwire. The archwires are then locked inside the slot using small rubber rings, fine archwires, or a metal door, depending on the chosen bracket's ligation type. Throughout the length of therapy, as the archwires attempt to restore their straight shape, the

A. Munir · M. F. Razali (✉)

School of Mechanical Engineering, Universiti Sains Malaysia, Engineering Campus, 14300 Nibong Tebal, Penang, Malaysia
e-mail: mefauzinizam@usm.my

malpositioned tooth is gradually dragged downwards in the bending recovery direction. For the initial and alignment phases of orthodontic treatment using edgewise appliances, it is believed that the shape memory and superelastic properties of NiTi alloy archwires correspond to physical properties that provide light, continuous force for tooth movement [2].

2 Application of NiTi Archwires in Orthodontic Levelling Treatment

Orthodontic therapy is provided in stages. First, the teeth are aligned and levelled, next the bite is corrected (the upper and lower teeth are made to fit together), and last, the spaces between the teeth are closed. The superelastic NiTi archwires have been a popular option for the alignment and levelling stage of orthodontic treatment, as this material offers an extraordinarily broad activation range at a lower and more consistent force magnitude. Most research on the biomechanics of orthodontic therapy have focused on the early stage of treatment. The most often replicated scenario is the levelling treatment of a severely misplaced canine [3, 4].

After being engaged to each bracket, the unloading of the archwires, accompanied with tooth movement, causes a sliding motion of the archwires within the neighboring bracket slot. Figure 1 depicts the friction component formed at the archwires-bracket interface during the recovery of archwire curvature in the bracket system. The NiTi archwires' force is dependent on the strength of both resistance components encountered during sliding mechanics because of the requirement of sliding motion during levelling [5]. Additionally, the NiTi application proved safe and facilitated long-term oral intake in patients with difficult-to-treat hypopharyngeal or cervical esophageal strictures, hence eliminating the need for periodic dilations [6].

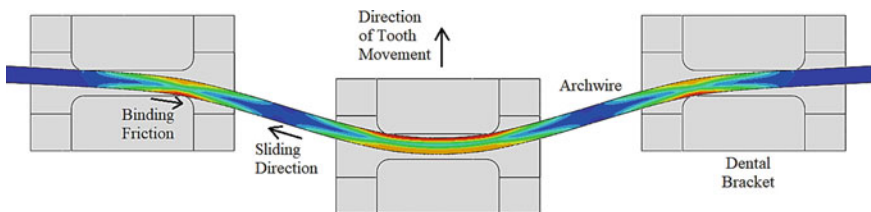


Fig. 1 Schematic representation of sliding friction component in a three-bracket system

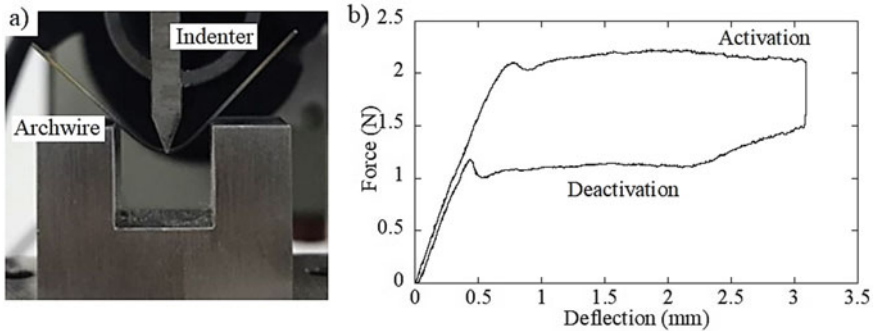


Fig. 2 Simple bending of orthodontic archwires: **a** three-point bending model and **b** force–deflection of NiTi archwire in a three-point bending model

3 Archwires Bending in Three-Point Bending System

Figure 2a illustrates how the force–deflection of orthodontic archwires has been tested for years using a standard three-point bending test. Even though this test does not reflect the actual bending environment in the mouth, it has been utilised extensively for the convenience of comparison between research. Figure 2b shows the force–deflection characteristics of nickel titanium (NiTi), as determined by a standard three-point bending test. Observations indicate that NiTi archwires produce a lighter, more consistent force over a broad deflection range. Despite the existence of two force levels on the force–deflection curve, the section of interest is the unloading course because it indicates the amount of the force transferred by the archwires to the teeth [7, 8].

4 Archwires Bending in Bracket System

After discovering the significance of contact friction during levelling treatment, researchers began including brackets into bending study experimental setups. Figure 3a depicts the typical three-bracket bending arrangement used to examine the force deflection of archwires. Most of the research performed for the wire bending test in bracket arrangement has concentrated on minor archwire deflection, often 2.0 mm or less. Research work considering the small deflection bending reported that the NiTi archwires exhibited a consistent force throughout the deactivation course [9]. Recent expansion of bending testing to accommodate deflections greater than 3.0 mm such reported in [10] is a relatively latest improvement. As seen in Fig. 3b, the force of the archwires varied throughout the activation and deactivation of the bending load. This trend in gradient force was attributed to the sequential production of binding friction in relation to the rise in archwire deflection.

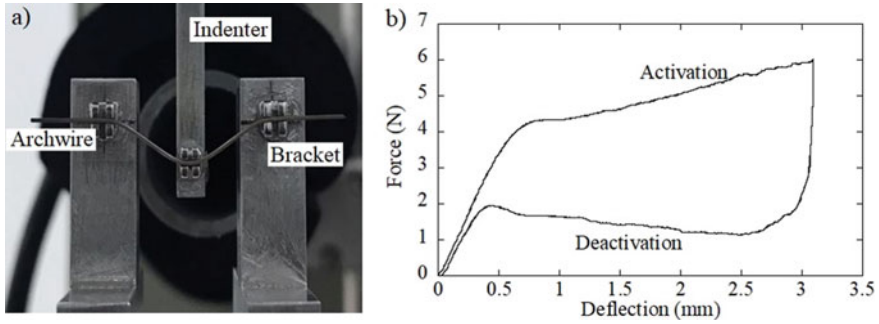


Fig. 3 Modified bending of orthodontic archwires: **a** three bracket bending model and **b** force–deflection of NiTi archwires in a three-bracket bending model

Early archwire force evaluation is essential to measure the amount of force being transferred to the teeth during orthodontic treatment. In order to move the misaligned teeth effectively, force must be used within an appropriate force range. Because the friction of the bracket changes the continuous force behaviour into a slope, this force prediction method is more difficult in bracket systems. Archwires can vary substantially in their ability to exert force during the course of therapy, which is not ideal for tooth movement.

4.1 Archwires Deflection

In-vitro experiments on the vertical displacement of dental brackets have been conducted at numerous deflection magnitudes ranging from 0.5 to 6.0 mm [11]. According to studies, the bracket displacement magnitude modifies the interaction between the archwires and the bracket slot, hence altering the force–deflection trend. Razali et al. [12], who investigated the force–deflection behavior of NiTi archwires at different deflections, found that the archwires exhibited variation in unloading force magnitude as it recovered from 3.0 and 4.0-mm deflections.

4.2 Inter-Bracket Distance

Inter-bracket distance is an additional component that is frequently overlooked while studying the force–deflection behaviour of NiTi archwires [13]. Inter-bracket distance is the distance between the midpoints of the teeth over which the bracket is placed during the installation of a fixed appliance system. Sathler et al. [14], who studied the force deflection of NiTi archwires at various inter-bracket intervals, discovered that the deactivation force varied between 66.34 and 179.28 cN. The

author drew the conclusion that force deflection was not highly reliant on inter-bracket distance after seeing a narrow force fluctuation during testing.

4.3 Bracket Material

The rising popularity of aesthetic brackets in orthodontic treatments, especially among young adult patients, is due to their natural appearance. The functionality of beautiful brackets has been the subject of fewer investigations than that of ordinary brackets. Baccetti et al. [15] found that bending 0.36 mm-NiTi archwires in the presence of ceramic brackets required a larger activation force of 1.10–1.20 N than bending the same archwires in the presence of stainless-steel brackets (0.10–1.20 N). Even though the difference in force was not statistically significant, the increased activation force needed when employing ceramic brackets at each tested deflection of 1.50, 3.0, 4.5, and 6.0 mm underlined the significance of binding friction to the archwires forces.

4.4 Ligation Technique

Several researches have considered the influence of ligation on the force released to the teeth by NiTi archwires. Baccetti et al. [16] examined the pressures released by 0.3-mm NiTi archwires prior to bending while utilising self-ligating and traditionally ligated brackets. At a minor deflection magnitude of 1.5 mm, the differences between the two bracket systems' deactivation forces were minimal. At 4.5 mm of archwire deflection, the self-ligating system produced a positive force of 1.2 N whereas the traditional system produced zero force. The author noted that the added friction from the elastic ties increased the total sliding resistance, hence decreasing the springback potential of the archwires.

5 Conclusion

The force magnitude and behaviour of NiTi archwires are contingent on the bending test configuration. In a three-point bending arrangement where the influence of friction on force magnitude is negligible, NiTi archwires can only generate a light and continuous force. In the bracket system, the force released by the archwires is dependent on the characteristics and arrangement of the brackets, with a greater force anticipated in cases requiring greater archwire deflection, smaller distances between brackets, the use of conventional ligation technique, and the application of ceramic-based brackets.

Acknowledgements The authors are grateful for the financial support provided by the Ministry of Higher Education Malaysia for Fundamental Research Grant Scheme with Project Code: FRGS/1/2020/TK0/USM/03/5

References

1. Proffit WR, Fields Jr HW, Sarver DM (2014) Contemporary orthodontics. Elsevier Health Sciences
2. Tochigi K, Oda S, Arai K (2015) Influences of archwire size and ligation method on the force magnitude delivered by nickel-titanium alloy archwires in a simulation of mandibular right lateral incisor linguoversion. *Dent Mater J* 34(3):388–393
3. Montasser MA, El-Bialy T, Keilig L, Reimann S, Jäger A, Bourauel C (2013) Force levels in complex tooth alignment with conventional and self-ligating brackets. *Am J Orthod Dentofac Orthop* 143(4):507–514
4. Montasser MA, Keilig L, El-Bialy T, Reimann S, Jäger A, Bourauel C (2015) Effect of archwire cross-section changes on force levels during complex tooth alignment with conventional and self-ligating brackets. *Am J Orthod Dentofac Orthop* 147(4):S101–S108
5. Vartolomei AC, Serbanoiu DC, Ghiga DV, Moldovan M, Cuc S, Pollmann MCF, Pacurar M (2022) Comparative evaluation of two bracket systems' kinetic friction: conventional and self-ligating. *Materials* 15(12):4304
6. Conio M, Filiberti RA, Siersema PD, Manta R, Bianchi S, De Ceglie A (2022) A new designed self-expandable metal stent for the management of benign radiotherapy-induced hypopharyngeal or cervical esophageal strictures. *Surg Endosc* 36(4):2290–2299
7. Alobeid A, Dirk C, Reimann S, El-Bialy T, Jäger A, Bourauel C (2017) Mechanical properties of different esthetic and conventional orthodontic wires in bending tests. *J Orofacial Orthopedics/Fortschritte der Kieferorthopädie* 78(3):241–252
8. Maizeray R, Wagner D, Lefebvre F, Lévy-Bénichou H, Bolender Y (2021) Is there any difference between conventional, passive and active self-ligating brackets? A systematic review and network meta-analysis. *Int Orthod* 19(4):523–538
9. Jaeger R, Schmidt F, Naziris K, Lapatki BG (2021) Evaluation of orthodontic loads and wire-bracket contact configurations in a three-bracket setup: comparison of in-vitro experiments with numerical simulations. *J Biomech* 121:110401
10. Lefebvre C, Saadaoui H, Olive JM, Renaudin S, Jordana F (2019) Variability of slot size in orthodontic brackets. *Clin Experimental Dental Res* 5(5):528–533
11. Ramezannejad A, Xu W, Xiao WL, Fox K, Liang D, Qian M (2019) New insights into nickel-free superelastic titanium alloys for biomedical applications. *Curr Opin Solid State Mater Sci* 23(6):100783
12. Razali MF, Mahmud AS, Mokhtar N (2018) Force delivery of NiTi orthodontic arch wire at different magnitude of deflections and temperatures: a finite element study. *J Mech Behav Biomed Mater* 77:234–241
13. Kato M, Namura Y, Yoneyama T, Shimizu N (2018) Effect of the vertical position of the canine on the frictional/orthodontic force ratio of Ni–Ti archwires during the levelling phase of orthodontic treatment. *J Oral Sci* 17–0356
14. Sathler R, de Freitas MR, Soufen CA, Zanda M, Fernandes TMF, Maranhão OBV, Garib DG, Janson G (2020) Elastic deflection study of nickel-titanium orthodontic wires: 3-point bending test X clinical simulation device. *J Interdisc Dent* 10(1):29
15. Baccetti T, Franchi L, Camporesi M (2008) Forces in the presence of ceramic versus stainless steel brackets with unconventional vs conventional ligatures. *Angle Orthod* 78(1):120–124
16. Baccetti T, Franchi L, Camporesi M, Defraia E, Barbato E (2009) Forces produced by different nonconventional bracket or ligature systems during alignment of apically displaced teeth. *Angle Orthod* 79(3):533–539

Effect of Carbon Dioxide Gas Flow Rate on Production of PCC from Carbide Lime Waste



Emee Marina Salleh, Rohaya Othman, Siti Noorzidah Mohd Sabri, and Zawawi Mahim

Abstract Carbide lime or lime sludge is a by-product of acetylene manufacturing through a hydrolysis of calcium carbide (CaCl_2). In Malaysia, carbide lime is classified as a scheduled waste under Environmental Quality Act: EQA 1974 (SW 427). This industrial waste is frequently rich in calcium hydroxide ($\text{Ca}(\text{OH})_2$), rendering it a substitute potential precursor for producing marketable precipitated calcium carbonate (PCC). In addition to the abundant carbide lime waste, the acetylene production has also increased carbon dioxide (CO_2) gas emission that traps heat in the atmosphere. This phenomenon has become a crucial environmental concern as the rise of CO_2 gas emission leads to global warming. In order to overcome this environmental issue, the pair of carbide lime waste and CO_2 gas were utilized as primary precursors in producing commercial-grade PCC. The precipitation process was achieved via feasible carbonation approach promoted using natural sucrose solution in extracting Ca^{2+} ions from the carbide lime waste. In investigating the effect of CO_2 supply on the PCC formation, CO_2 gas flow rate was varied i.e. 200, 400, 600, 800 and 1000 ml/min. Increasing the CO_2 flow rate resulted in significant time reduction (from 33 min at 200 ml/min to only 9 min at 1000 ml/min) and particle refinement (from 5.28 μm at 200 ml/min to 1.16 μm at 1000 ml/min). Production of PCC with purity 96–98% suggested that the carbide lime waste was successfully transformed into marketable PCC, thus may help in preserving environmental sustainability.

Keywords Precipitated calcium carbonate · Carbide lime waste · Carbon dioxide · Carbonation · Sucrose solution

1 Introduction

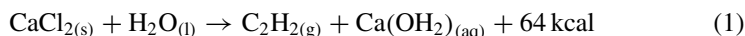
The global acetylene gas market is currently beholding stable growth. Owing to its high flame temperature properties, acetylene gas is extensively used for numerous

E. M. Salleh (✉) · R. Othman · S. N. M. Sabri · Z. Mahim
Mineral Research Centre, Department of Mineral and Geoscience Malaysia, Jalan Sultan Azlan Shah, 31400 Ipoh, Perak, Malaysia
e-mail: emeemarina@jmg.gov.my

© The Author(s), under exclusive license to Springer Nature Singapore Pte Ltd. 2023
Md. A. Maleque et al. (eds.), *Proceeding of 5th International Conference on Advances in Manufacturing and Materials Engineering*, Lecture Notes in Mechanical Engineering,
https://doi.org/10.1007/978-981-19-9509-5_11

77

metalworking applications including oxy-acetylene cutting, heat treating, soldering, brazing and welding [1, 2]. However, the production of acetylene results in a formation of massive carbide lime by-product via hydrolysis of calcium carbide (CaC_2) as shown in Eq. 1 [3]. The waste is generated as an aqueous slurry containing substantial calcium hydroxide (Ca(OH)_2) up to 60–70% with slight content of calcium carbonate (CaCO_3) up to 1–10% and 1–3% of unreacted carbon and silicates [4, 5].



In Malaysia, the carbide lime waste is classified as a scheduled waste under the Environmental Quality Act; EQA 1974 (SW 427). The carbide lime waste is environmentally hazardous which is attributable to its high alkalinity with a pH of ~12.5, unpleasant odour and it can cause irritation to skin and throat [6, 7]. In 2018, almost 20,000 tons of carbide lime has been produced from the Malaysian acetylene gas industry and this statistic keeps increasing year by year. This scenario makes the carbide lime an avoided by-product where the industry has to pay high cost for water treatment in disposing the scheduled waste. Currently, the carbide lime has been recycled for agricultural purposes, sewage and water treatments and in several industrial processes [8, 9], hence mitigating waste disposal concerns and degraded zones by limestone exploitation (used as a raw material for calcium oxide and hydroxide production) [4]. In addition to this application and attributable to its high-calcium content, this waste was targeted to be transformed into a more marketable product i.e. precipitated calcium carbonate (PCC). Commercially, the high purity, well-ordered particle size and morphology makes PCC as the white filler of choice for numerous industrial applications including in papermaking, paint, sealant, plastics, rubbers, paints, drugs and textiles [7].

In this current work, the production of PCC was performed by carbonation reaction through bubbling CO_2 gas approach. Effect of CO_2 flow rates (200, 400, 600, 800 and 1000 ml/min) on a formation of PCC was investigated. By utilizing the carbide lime waste as one of the main precursors, it not only increases the production of a marketable product via feasible technique, however it also can preserve environmental sustainability by transforming the industrial waste into secondary profit.

2 Research Methodology

Carbide lime waste as a calcium (Ca)-based starting material was supplied from MCB Industries Sdn. Bhd., one of the main Malaysian local manufacturer of acetylene gas. Sucrose granules that acted as a promoter agent was purchased from a local company and compact CO_2 gas of 99% purity was procured from Linde Malaysia Sdn. Bhd. In this current work, the precipitation of CaCO_3 was conducted via carbonation of Ca-rich ionic solution under continuous flow of CO_2 gas. Prior to a preparation of Ca-rich ionic solution, natural sucrose solution as a promoter agent was prepared in

order to extract calcium ions (Ca^{2+}) from a starting material i.e. low-grade carbide lime waster. About 7 wt% of carbide lime was added into 1 L of sucrose solution. This Ca-containing solution was mixed vigorously and left overnight in order to allow the optimum extraction the of Ca^{2+} ions into the solution. Afterward, the Ca-ionic solution was filtered in acquiring a clear Ca^{2+} -rich ionic solution and eliminating any residue.

Subsequently, CO_2 gas was continuously introduced into the Ca^{2+} -rich ionic solution to provide an effective carbonation process. The effect of the CO_2 supply on the carbonation and production of PCC was investigated by varying the CO_2 flow rate, i.e. 200, 400, 600, 800 and 1000 ml/min. The carbonation process was performed under atmospheric condition and mechanically stirred at constant rotational speed of 1000 rpm. The additional mechanical disturbance might increase the precipitation mechanism of PCC and avoid an excessive growth of PCC particles. The carbonation process was monitored due to pH value and the process was stopped at \pm pH 8 where a complete precipitation of the CaCO_3 was considerably achieved. The synthesized PCC was filtered and washed using warm water to remove any excess promoter agent. The filtrate was oven-dried at 60 °C for 24 h. The time taken for the carbonation process and weight of the PCC yield was measured. Morphology of the synthesized PCC was evaluated using Field Emission Scanning Electron Microscope (FESEM) Supra 40 V Zeiss, Germany. Particle size distribution of the PCC was measured using Laser Particle Size Analyzer. Presence of the oxide element in PCC was analyzed using X-Ray Fluorescence Spectrometer, XRF-1700, Shimadzu, Japan.

3 Research Findings

3.1 Carbonation Time and PCC Yield

Figure 1 displays carbonation time and weight of PCC produced at different CO_2 gas flow rates. Apparently, a duration for the precipitation of calcium carbonate was substantially reduced with increasing CO_2 flow rate which was from 33 min at 200 ml/min to only 9 min at 1000 ml/min. This significant time reduction at higher CO_2 flow rate suggested that higher content of CO_3^{2-} ions enhanced the carbonation activity, thus shortened the required time for a complete precipitation mechanism of PCC. Concurrently, there was no observable change in PCC yield produced at various CO_2 flow rates. This phenomenon signified that the CO_2 supply during the precipitation provided significant effect on the carbonation activity rather than on the production of PCC yield.

Fig. 1 Carbonation time and PCC yield at different CO₂ flow rates

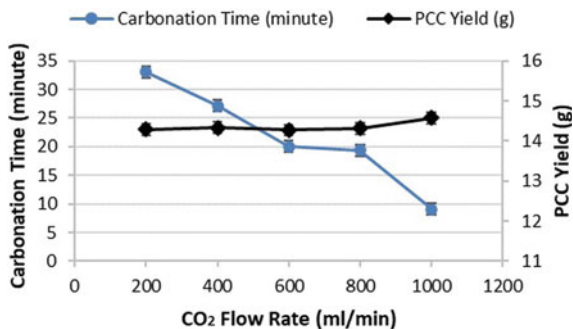
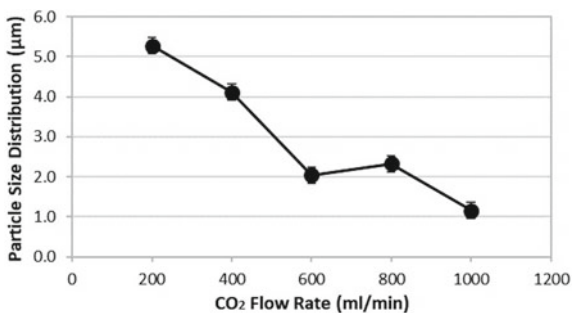


Fig. 2 Particle size distribution of PCC at various CO₂ flow rates



3.2 Particle Size Distribution

Figure 2 shows a distribution of PCC particle size evaluated using Laser Particle Size Analyzer as a function of CO₂ flow rate. The size of PCC particles decreased from 5.28 μm to 1.16 μm with increasing CO₂ flow rate from 200 ml/min to 1000 ml/min, respectively. This significant particle size reduction at high CO₂ flow rate was attributable to the high concentration of CO₃²⁻ ions that rapidly encouraged a large number of nuclei formation thus providing limited space for the particles to grow during the recrystallization mechanism. The self-force between the formed particles during carbonation reaction hindered the particle enlargement [4]. In addition, the high content of CO₃²⁻ ions due to continuous CO₂ supply at higher flow rate led to high-rate precipitation of the PCC. This rapid precipitation completion resulted in a formation of stable PCC particles without extensive enlargement or any indication of intergrowth phenomenon.

3.3 Morphology Evaluation

Figure 3 illustrates the morphologies of PCC particle distribution at various CO₂ flow rates. At 200 ml/min of CO₂ flow rate, the distribution of irregular-structured

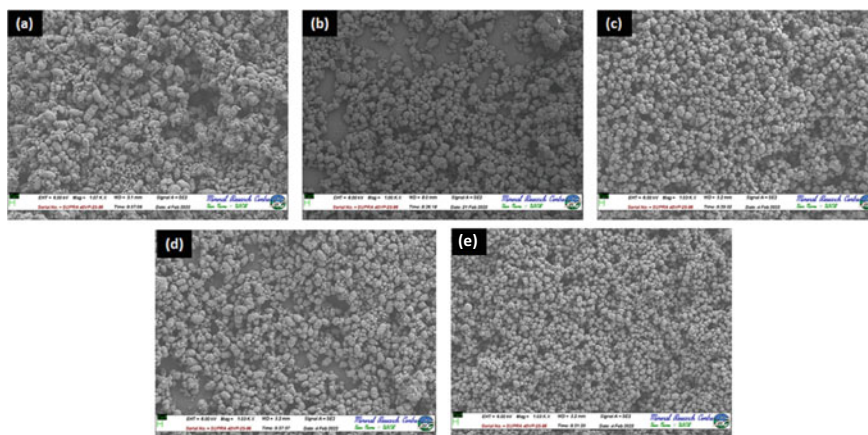


Fig. 3 Micrograph of PCC particles produced at **a** 200, **b** 400, **c** 600, **d** 800 and **e** 1000 ml/min of CO_2 gas flow rate

PCC particles was not entirely uniform. As can be seen, there was finer particles that attached to the coarser particles. The attachment of finer PCC particles ($1.1\text{--}1.7\ \mu\text{m}$) to the coarser particles ($\sim 5.3\ \mu\text{m}$) so-called agglomeration occurred in order to increase their particle stability [7]. Increasing CO_2 flow rate up to 400 ml/min induced a formation of finer and more uniform PCC particle distribution. Uniform distribution of rhombohedral PCC particles that was observed at 600 ml/min of CO_2 supply suggested a stable carbonation was initiated at this flow rate. Particle intergrowth started to occur with increasing CO_2 supply up to 800 ml/min. This phenomenon was attributed to the high content of CO_3^{2-} ions that induced high rate of carbonation activity, thus resulted in the enlargement of PCC particles. Interestingly, well-dispersed of fine cubicle PCC particles was achieved at 1000 ml/min of CO_2 supply. At this condition, the Ca^{2+} ions were sufficiently reacted with CO_3^{2-} ions within short period of carbonation time, thus promoting non-intergrowth of PCC particles. This finding suggested that a control of CO_2 flow rate was necessary in producing PCC particles with required morphology and particle size distribution.

3.4 X-Ray Fluorescence (XRF)

Table 1 displays calcium oxide (CaO) content of PCC samples produced at different CO_2 flow rates was from 53.86% to 55.08%. The relatively high CaO content approaching 56% signified that the produced PCC might be categorized in medium to high grade PCC as the purity of PCC sample referring to CaCO_3 percentage was calculated according from CaO content. This current finding suggested this carbonation technique using natural promoter agent might offer high potential for

Table 1 The purity of CaCO₃ produced

CO ₂ Flow rate (ml/min)	200	400	600	800	1000
CaO (%)	54.73	53.86	54.94	55.08	54.97
CaCO ₃ (%)	97.7	96.2	98.1	98.4	98.2

transforming low-grade carbide lime waste into medium-to-high-grade PCC for commercialization in a wide range of industrial applications.

4 Conclusion

This current work demonstrated the low-grade carbide lime waste was successfully transformed into medium-to-high-grade PCC with 96–98% via the developed carbonation approach using natural promoter agent. Effectively, a substantial time reduction in producing PCC was achieved by increasing the CO₂ supply from 200 ml/min to 1000 ml/min with 33 min to only 9 min, respectively. There was no apparent change of PCC yield with increasing CO₂ flow rate. The size of PCC particles decreased from 5.28 μm to 1.16 μm with increasing CO₂ flow rate from 200 ml/min to 1000 ml/min, respectively. The non-uniform irregular PCC particles at low CO₂ flow rate transformed into homogenous rhombohedral-structured PCC particles at higher CO₂ supply up to 400 ml/min and above.

Acknowledgements This work was supported by the Ministry of Energy and Mineral Resources. The authors would like to thank Mineral Research Centre, Department of Mineral and Geoscience Malaysia and Rock Based Technology Section for the fund and technical supports.

References

1. Erdogan N, Eken HA (2017) Precipitated calcium carbonate production, synthesis and properties. *Physicochemical Probl Mineral Process* 53:57–68
2. Ana MLP, Roberta P, Carlos GG, Lourdes FV, Domingo C (2010) A breakthrough technique for the preparation of high-yield precipitated calcium carbonate. *J Supercrit Fluids* 52:298–305
3. Onimisi JA, Roniza I, Kamar SA, Norlia B, Hashim H (2016) A novel rapid mist spray technique for synthesis of single-phase precipitated calcium carbonate using solid-liquid-gas process. *Korean J Chem Eng* 34:1–5
4. Sun J, Wang L, Zhao D (2017) Polymorph and morphology of CaCO₃ in relation to precipitation conditions in a bubbling system. *Chin J Chem Eng* 25:1335–1342
5. Walsh D, Mann S (1995) Fabrication of hollow porous shells of calcium carbonate from self organizing media. *Nature* 377:320–323
6. Santos RM, Pieter C, Tom VG (2012) Synthesis of pure aragonite by sonochemical mineral carbonation. *Chem Eng Res Des* 90:715–725
7. Ligia MMC, Gabriel MO, Rafael S (2017) Precipitated calcium carbonate nano-microparticles: applications in drug delivery. *Adv Tissue Eng Regenerative Med* 3:336–340

8. Salleh EM, Othman R, Mahim Z, Sabri SNM (2021) Effect of liquid feeding rate on carbonation of precipitated calcium carbonate via continuous method. *J Phys Conf Ser* 2080 (1):012017
9. Zevenhoven R, Legendre D, Said A, Jarvinen M (2019) Carbon dioxide dissolution and ammonia losses in bubble columns for precipitated calcium carbonate (PCC) production. *Energy* 175:1121–1129

Surface Wettability of Treated Quartz Substrates and Their Optical Characterization of Deposited Reduced Graphene Oxide



Nurul Farhana Abu Kasim, Norhana Abdul Halim,
Ahmad Farid Mohd Azmi, Norli Abdullah, Keat Khim Ong,
and Siti Zulaikha Ngah Demon

Abstract Broadly researched graphene materials as thin films and coatings have high interest in electronics and optoelectronics application. Here, we addressed the challenge of coating colloidal graphene produced by chemical reduction of graphene oxide (GO) onto quartz substrates. Silane-treated substrates are known for their effectiveness in producing high quality coating, therefore their effect on optical property of the coating must be investigated as such for fiber optic sensor application. L-ascorbic acid, a green reducing agent was used to obtain reduced graphene oxide (RGO) that was spun on bare and treated substrates. Wettability study of bare, piranha treated and silane treated surfaces using water contact angle measurement shows piranha treated surface possessed lowest hydrophobicity among all surfaces. We found that the presence of O–H and N–H chemical species on silane treated substrate rendered the surfaces hydrophilic compared to bare substrate. Our result also shows the silane treated surface produced more effective RGO coating after 25 times colloid sample deposition. The optical spectrum measured from the thin film shows there is proportional increase of the absorbance with the amount of RGO content on substrate. These findings can be used to understand the coating effectiveness of colloid samples thus giving better quality RGO films for various application.

Keywords Reduced graphene oxide · Silane · Contact angle · Optical · Surface

N. F. A. Kasim

Faculty for Defence Science and Technology, National Defence University of Malaysia, Kem Sungai Besi, 57000 Sungai Besi, Kuala Lumpur, Malaysia

N. A. Halim · A. F. M. Azmi · N. Abdullah · K. K. Ong

Centre for Defence Foundation Studies, National Defence University of Malaysia, Kem Sungai Besi, 57000 Sungai Besi, Kuala Lumpur, Malaysia

S. Z. N. Demon (✉)

Centre for Tropicalization, National Defence University of Malaysia, Kem Sungai Besi, 57000 Sungai Besi, Kuala Lumpur, Malaysia

e-mail: zulaikha@upnm.edu.my

1 Introduction

Graphene and graphene-based materials exhibit interesting electrical, optical, mechanical, and chemical properties which make them good candidates for important applications such as transistors, sensors, transparent electrode, and solar cell devices [1]. Due to its atomic thinness, graphene must be bound to a substrate making the adhesion between graphene and other materials critical for device fabrication [2]. Graphene oxide (GO) is a form of graphene that includes oxygen functional groups, give interesting capabilities that can be superior than those of graphene in some area. For example, structural defects in GO allow engineered control over optical transparency, electrical and chemical conductance of graphene achieved by various chemical and physical functionalities. By reducing graphene oxide, these oxidized functional groups are removed, a graphene material can be obtained [3]. This so-called reduced graphene oxide, often abbreviated as RGO. RGO possessed almost similar high conductivity of graphene, high surface area, and at the same time available for various chemical or biological anchoring. Naturally, GO are hydrophilic but with reduction in its oxygen containing functionalities its nature changes from hydrophilic to hydrophobic [4]. Thus, having hydrophobic RGO, one must put up with the difficulty in creating hybrid structures or composite materials such as films coating [5]. RGO colloid will result into non-homogenous RGO film and significant disparity of electrical or optical characteristics across the film. In our interest of fabricating fiber optic based chemical sensor, the inhomogeneity of the coating may cause inconsistency in optical signal detection.

One method to improve RGO film deposition is via surface substrate's treatment as such using silanes functional groups. The reaction with the substrate's surface will result into maximum number of accessible sites with appropriate surface energies that allow binding of the molecules with the substrates [6]. Typically, the silanes materials act as initial point for substrate modification and has a favor as polymeric films, in terms of total coverage and organic functionality. They are the primary materials utilized in composites, adhesives, sealants and coatings. Previously, the silane pre-treatment was also used for Surface Enhanced Raman Scattering (SERS) in the optical study of metals [7].

In this work, we demonstrate a simple surface treatment method on quartz substrate in order to enhance the RGO surface coverage after spin coating of RGO colloidal solution. Wettability comparison using water contact angle measurement between the bare and treated quartz substrates obtained using piranha solution and silane solution will be shown. The optical and compositional of RGO films after the surface treatment will be analyzed. The relationship between surface wettability and the optical characteristics can be used to determine effectiveness of the RGO coverage for future application of RGO coatings.

2 Experimental

2.1 Materials

Graphene oxide (GO dispersion in H₂O, 4 mg/ml), L-ascorbic acid (L-AA), hydrogen peroxide (30% H₂O₂), methanol (99.8% CH₃OH), hydrochloric acid (37% HCl), (3-aminopropyl)triethoxysilane (97% APTES) were purchased from Sigma Aldrich. Sulphuric acid (95.98% H₂SO₄) and nitric acid (69% HNO₃) was obtained from R&M Chemicals, Malaysia and used as received.

2.2 RGO Synthesis and Spin Coating

RGO was prepared by using L-AA as reducing agent in GO solution. Quartz substrate were cleaned in a piranha solution of H₂SO₄ and H₂O₂ (4:1) at 70 °C for 60 min. After being rinsed in H₂O, substrates were soaked in aqua regia solution of HCl and HNO₃ (3:1). Substrates were rinsed in H₂O and then immersed in 2% of APTES and methanol solution. The solution was stirred vigorously and left for 24 h. Silanised substrates were finally removed and rinsed and stored in H₂O. The RGO solution were spin coated at 1000 rpm speed. The bare substrates are used as it is.

3 Result and Discussion

3.1 Silane Activation on Quartz Surface

Water contact angle measurements were performed to study the difference in wettability of the surfaces in absence and presence of treatment. As observed in Fig. 1a, the contact angle measured from the bare surface is 51.22°, dropped to 22.49° for piranha-treated surface. Piranha surface treatment caused removal of surface contaminants and OH-groups formation, hence, introducing hydrophilization of the surface. It is understood that bare quartz surface gives hydrophobic interaction upon water contact but drastically becoming hydrophilic after 30 min of piranha treatment etching. Further introduction of silane groups by immersing the piranha-treated substrates into aqueous APTES solution for 24 h resulted in small increase in contact angle to 28.42°. This angle increment is anticipated due to formation of a silane layer on the substrate that is now terminated with free hydrophilic amine groups. The APTES causes slight reduction in hydrophilicity of the quartz surface.

To support this chemical functionalization occurring during silane activation, we produced infrared transmittance spectra measured from bare and treated quartz substrates. It can be observed from Fig. 2a, appearance of N–H vibrational mode

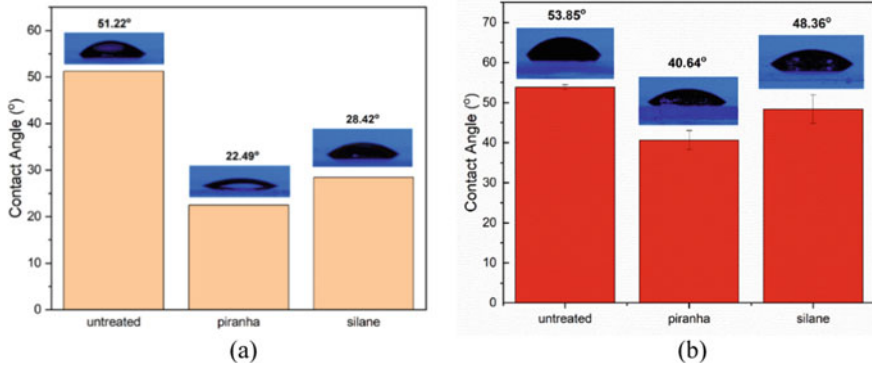


Fig. 1 a Water and b RGO contact angles measured on pristine glass, piranha-treated glass and silane-treated glass

located at 1548 cm^{-1} signifies amines functionalization on treated surface. Meanwhile, slight change in vibrational region belongs to symmetric hydrogen-bonded Si-OH stretching mode are observed after the silane treatment [8]. As the result of hydroxyl group treatment, the vibrational peak at 3130 cm^{-1} becomes more prominent compared to 3266 cm^{-1} peak detected from untreated surface. On the other hand, no significant changes is detected in Si-H vibrational region from both spectra. The appearance of 1548 cm^{-1} and 3130 cm^{-1} peaks proved the hydroxyl groups and amine groups were successfully grafted onto quartz which compliment hydrophilic characteristics measured from water contact angle measurements. The optical transmittance of the bare and treated quartz substrates are shown in Fig. 2b where there is no change in transmittance at visible range from 300 to 800 nm wavelengths. We dictated small decrease transmittance reduction of lower wavelengths is due to absorbance by organic matter after the functionalization.

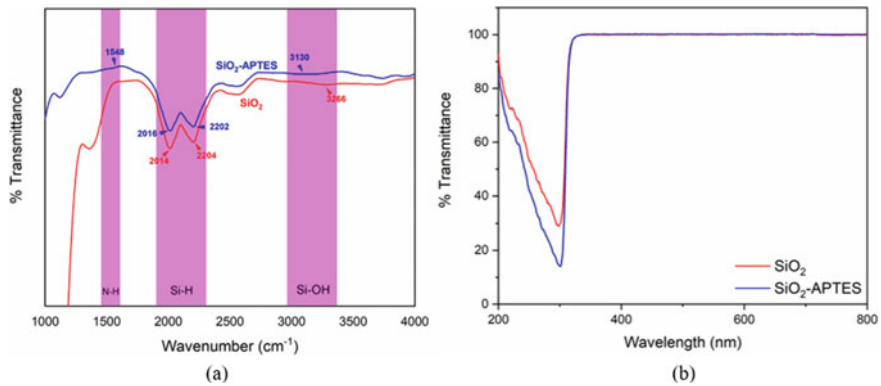


Fig. 2 Comparison analysis using a FTIR spectra and b UV-Vis transmittance spectra of treated and bare quartz, SiO_2

The contact angle measurements with RGO suspensions dropped onto bare substrate, piranha treated substrate and silane treated substrate. This investigation allows us to get a rough idea on the difference of hydrophobicity between water and RGO suspensions. Our result is shown in Fig. 1b. Upon initial drop of the RGO colloid suspension on the untreated surface, the contact angle is 53.85°, slightly higher from the one measured using droplet. Interestingly, the RGO contact angle measured from both piranha treated substrate and silane treated substrate are still quite large, at 40.64° and 48.36° respectively. Similar trend of contact angle depreciation was observed meaning the silane activation is still effective on RGO droplet. It is inferred that the colloid RGO suspension is more hydrophobic compared to water but the effectiveness of the surface wettability maybe improved when the RGO is spin-coated on the quartz afterwards.

3.2 Effect of Surface Treatment on Spin Coated RGO Film

Figure 3 shows the reflection and transmission surface of RGO films from both quartz substrates as function of wavelength in comparison with bare substrates. The spectrum of RGO film deposited on silane treated surface shows an increase in overall optical transparency indicating higher RGO content compared to bare surface. For the determination of reflection and absorption coefficient of the films, Kirchoff’s law states that the sum of the absorbance, reflectance and transmittance of a surface in a particular wavelength equal to one [9]:

$$A + T + R = 1 \tag{1}$$

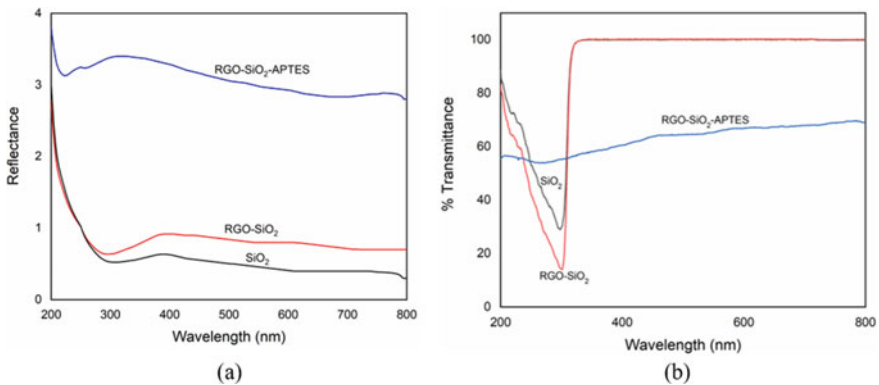


Fig. 3 Comparison analysis of **a** reflectance and **b** transmittance from UV-Vis for RGO films deposited on untreated and treated quartz substrates (inset: microscope images)

where A is Absorbance, T is Transmittance and R is reflectance of the surface. If the surfaces are opaque the transmittance equal to zero and higher reflectance value will be obtained. From both data in Fig. 3, treated substrates were showing highest reflectance value where transmittance has the lowest %. Thus, both results for RGO treated films shows decrease in transparency, which indicated a good deposition coverage.

4 Conclusion

In this study, silane surface modification was employed to produce effective RGO film coating on quartz substrates. L-AA was used to synthesize the hydrophobic RGO colloid solution where it was later spin coated onto quartz substrates. The water contact angle shows the transformation of surface wettability after piranha and silane treatments were done on the quartz substrate. Successful surface modification was shown by depreciation of water contact angle in order of bare substrate > silane treated substrate > piranha treated substrate indicating quartz surface becoming more hydrophilic after treatment. The FTIR analysis confirmed the presence of amine functional group on silane treated quartz substrate. Other than proven effectiveness in producing better coverage RGO films, the method also has significant impact on optical property of RGO due to primary concern of having functional groups introduced to the substrate. The method of silane surface modification is rather scalable and can be easily applied to produce high quality RGO thin films.

Acknowledgements We acknowledged financial assistance from Fundamental Research Grant Scheme from Ministry of Higher Education Malaysia, FRGS/1/2020/STG07/UPNM/03/1. We also like to thank Centre for Defence Foundation Studies, UPNM and Centre for Chemical Defence, UPNM for characterization facilities.

References

1. Tiwari SK, Sahoo S, Wang N, Huczko A (2020) Graphene research and their outputs: status and prospect. *J Sci Adv Mater Devices* 5:10–29
2. Akinwande D, Huyghebaert C, Wang CH, Serna MI, Goossens S, Li LJ, Wong HSP, Koppens FHL (2019) Graphene and two-dimensional materials for silicon technology. *Nature* 573:507–518
3. Saleem H, Haneef M, Abbasi HY (2018) Synthesis route of reduced graphene oxide via thermal reduction of chemically exfoliated graphene oxide. *Mater Chem Phys* 204:17
4. Wang F, Wu Y, Huang Y (2018) Novel application of graphene oxide to improve hydrophilicity and mechanical strength of aramid nanofiber hybrid membrane. *Compos Part A Appl Sci Manuf* 110:126–132
5. Smith AT, LaChance AM, Zeng S, Liu B, Sun L (2019) Synthesis, properties, and applications of graphene oxide/reduced graphene oxide and their nanocomposites. *Nano Mater Sci* 1:31–47
6. Wang L, Schubert US, Hoepfener S (2021) Surface chemical reactions on self-assembled silane based monolayers. *Chem Soc Rev* 50:6507–6540

7. Bright RM, Walter DG, Musick MD, Jackson MA, Allison KJ, Natan MJ (1996) Chemical and electrochemical Ag deposition onto preformed Au colloid monolayers: Approaches to uniformly-sized surface features with Ag-like optical properties. *Langmuir* 12:810–817
8. Velmuzhov AP, Sukhanov MV, Churbanov MF, Kotereva TV, Shabarova LV, Kirillov YP (2018) Behavior of hydroxyl groups in quartz glass during heat treatment in the range 750–950°C. *Inorg Mater* 54(9):925–930. <https://doi.org/10.1134/S0020168518090169>
9. Bayati MR, Shariat MH, Janghorban K (2005) Design of chemical composition and optimum working conditions for trivalent black chromium electroplating bath used for solar thermal collectors. *Renew Energy* 30:2163–2178

Development of Regression Model Between Driving Comfort Perception and Muscle Contraction



Darlina Mohamad , Baba Md Deros , Dian Darina Indah Daruis , and Ahmad Rasdan Ismail 

Abstract Fatigue has been strongly linked to posture comfort, and it has contributed to 15.7% of the total road accidents in Malaysia. This study aimed to develop a linear model to illustrate the relationship between the perception of driving comfort (subjective assessment) and muscle contraction (objective measurement) of the most comfortable and optimal driving posture angle for drivers. The sEMG tool was used to conduct the objective measurement on 14 respondents for assessing the upper muscle activity of the body, that are the Biceps Brachii (BB), Anterior Deltoid (AD), and Upper Trapezius (UT) which involved in controlling the car steering wheel. The measurement observed three driving posture parameters according to the angle of the elbow. Multiple linear regression (stepwise) was used to develop the linear model. Three linear models were developed for each of the postures involved and results showed that posture B with an angle at 134° is considered as the most comfortable posture position for driving with the lowest muscle contraction value at $15.67 \mu\text{V}$ (BB), $19.31 \mu\text{V}$ (AD), and $12.36 \mu\text{V}$ (UT) compared to the other two measured postures. A linear regression model was developed to show the cause and effect between subjective evaluation for the comfort level and the objective measurement for the muscle RMS value while driving. The linear regression is $55.858 + 1.384$ (Muscle RMS) mm in μV . The regression model showed that only AD muscle is significant in influencing the respondent's comfort level. This linear regression model will help researchers and vehicle manufacturers to develop a more comfortable and suitable driver seating area.

Keywords Ergonomic · Driving posture · Surface electromyography · Linear regression

D. Mohamad (✉) · A. R. Ismail

Department of Creative Technology, Faculty of Creative Technology and Heritage, Universiti Malaysia Kelantan, Kota Bharu, Malaysia

e-mail: darliana.m@umk.edu.my

B. M. Deros

Alfa Persada Sdn Bhd, Klang, Selangor, Darul Ehsan, Malaysia

D. D. I. Daruis

Department of Mechanical Engineering, Faculty of Engineering, Universiti Pertahanan Nasional, Kuala Lumpur, Malaysia

1 Introduction

With the rising number of car users on the road, which causes congested traffic and more time on the road, car owners are more likely to purchase a vehicle that can offer optimal comfort while driving. Demand for ergonomic features from the buyers has influenced the car manufacturer to include ergonomic criteria in the designing and manufacturing process of the car, especially the driver's space. Usually, the input in the vehicle study is on the car steering wheel angle and the car pedals placement [1].

The interaction between the car that is the machine and human is important in ensuring the driving process running efficiently and smoothly [2]. Drivers will spend much time controlling and navigating the steering wheel where muscle activity varies according to movement and grip of the steering wheel, and the activity can either enhance the driving comfort or fatigue experience while driving [3]. A report on road accident factors released by MIROS [4] explained that fatigue is the third highest cause of road accidents.

The development of a linear model can help to predict the relationship between muscle activity and fatigue [5]. The multiple linear regression calculation is capable of providing accurate analysis due to its flexibility [6]. Most of the calculations of linear regression from the previous studies were done in predicting the relationship model of shoulder movement through sEMG (Surface Electromyography) measurements such as studies from Brookham, Wong, and Dickerson [7] and McDonald et al. [8]. Several studies also published findings on the linear models of subjective evaluation relationship and objective measurement in experiments involving the comfort of driving posture. Daruis et al. [9] discovered a relationship model of subjective assessment and objective measurement. However, the objective measurement only used measurement of interface pressure. Yusoff [10] came out with a linear model of subjective evaluation relationship and objective measurement, which the author included sEMG measurement, but it only focused on the lower part of the human body. Through these studies, the importance of combining these two types of assessment can be distinguished. Thus, this study aimed to propose and develop a relationship model on most comfort posture angle for car drivers by using sEMG measurement and subjective assessment.

2 Materials and Methods

2.1 Procedures

Prior to the start of the experiment, 14 selected respondents with at least one year driving experienced were briefed on the objectives and procedures of the experiment. The number of respondents between 10 and 20 samples is already sufficient for experimental studies [11]. Then, respondents were instructed to sit on the driver's seat attached with a special simulator with the driver's hand condition on the steering

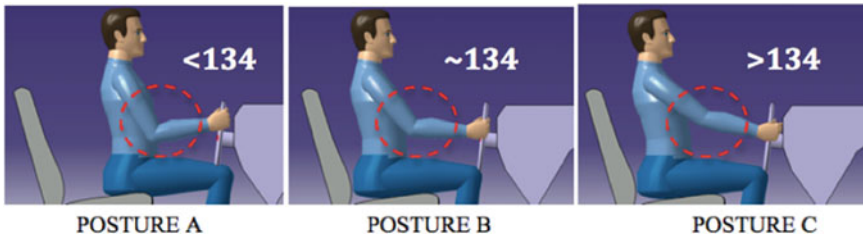


Fig. 1 Three driving postures in the experiment

wheel of the car was at 2 o'clock and 10 o'clock position [12]. The position of the seat distance, as well as the angle of the driver's backrest, is adjustable. Respondents had to conduct the steering wheel for 30 s as directed with the steering wheel rotation angle rate between 45° and 90° after 25–30 min using the simulator. This steering control activity is repeated for three postures that were distinguished through different angles of the elbow which are Posture A (<134), Posture B ($=134$) and Posture C (>134) that were referred from Mohamad et al. [13] as in Fig. 1.

2.2 Objective Measurement Research Design (sEMG)

The sEMG signal measurement experiment utilized Delsys Trigno wireless system equipment that obtained raw data with sampling rate was at 2000 Hz. The frequency signal from the muscles was extracted by the device on the surface of the skin and accepted by Trigno's mobile device as an interface between the device and the computer. EMGWorks software[®] was used to download the signal data. For every posture position, there were three muscle contraction readings produced which are Biceps Brachii (BB), Anterior Deltoid (AD), and Upper Trapezius (UT). Reference signal measurement, i.e., Maximum Voluntary Contraction (MVC), is also collected for the normalization of sEMG data. Procedures for sEMG and MVC measurement were carried out in accordance with procedures from Surface Electromyography for the Non-Invasive Assessment of Muscles (SENIAM) [14]. The experimental data obtained will be processed by MATLAB software version and analyzed through Microsoft Excel software. These sEMG signal data values were used as an independent variable to develop a linear regression model.

2.3 Subjective Assessment Research Design

The subjective assessment was designed by using the Visual Analogue Scale (VAS) to gather information on the comfort rate of driving posture according to different postures. The total reading scale of response is 100 mm [15]. Each 20 mm scale

reading was divided into five different levels of comfort starting from the left, which are uncomfortable, moderately uncomfortable, moderately comfortable, comfortable, and most comfortable. The scores accumulated by respondents were measured using rulers to obtain VAS scores. This information was used as a dependent variable to develop a linear regression model.

2.4 Calculation of Double Linear Regression Model

The final data from subjective assessment and objective measurement were grouped for statistical calculation processes, which included the data of subjective assessment in millimeter unit of the comfort assessment scale and data from objective measurement in millivolt units of sEMG signal data. The data statistical calculation process was carried out using SPSS software. The calculation for the relationship model between objective measurement and subjective assessment was performed through the calculation of a double linear regression model with the stepwise method.

3 Results

3.1 Driver's Comfort Linear Modelling

The linear model of driver's comfort level developed in this study can predict the relationship between subjective assessments, which is the driver's perceptual rating data on comfort, with objective measurement of the value of muscle contraction obtained from the sEMG experiment. Table 1 shows the summary of multiple regression results for each posture.

From Table 1, there are three models produced with R-values of 0.705, 0.739, and 0.727, respectively. A previous study from Laursen et al. [16] also found an average R score in a range of approximately 0.776. The average R^2 for all three muscles is 0.524, and the score is in line with a previous study by Xu et al. [17] in relation to shoulder movement with the control of shoulder and hand muscles that the study figured an average value of R^2 of 0.510. In addition, according to Piaw [18], an R-value of more than 0.71 indicates that there is a strong correlation between the variables involved.

Table 1 Summary of multiple regression results for postures

Comfort model	R	R^2	R^2 Adjustment	Standard error for estimation
Posture A	0.705	0.497	0.455	16.116
Posture B	0.739	0.546	0.509	11.547
Posture C	0.727	0.529	0.444	19.194

Table 2 Coefficient values and significant levels of linear model comfort posture B

Posture B Comfort model	Non-uniformity coefficient		Uniformity coefficient	T	Significance level
	B	Default error	Beta		
Constants	55.858	7.674		7.279	0
Muscle activity AD posture B	1.384	0.364	0.739	3.802	0.003

Thus, the equation chosen to represent the relationship between subjective assessment and objective measurement in this study is the one that successfully extracted the highest R-value, which is the posture B comfort model of 0.739.

To determine the significance level of variables contributing to the linear model of Posture B, a table of conformity is drawn in Table 2. From Table 2, the significance value of constant and muscle AD posture B is less than 0.05. This value translates that the probability of getting a T value for a constant is 7.279, and the gradient for muscle activity AD posture B is 3.802. In addition, for posture B only AD muscle activity that contributes to the driving comfort level.

Also, in Table 2, a linear model equation of posture B comfort to estimate the perception of posture comfort B (y) refers to the value of B from the non-uniformity coefficient of constant (c) and muscle activity of AD for posture B ($\times 1$) as shown in the following equation;

$$y = 1.384x_1 + 55.858 \quad (1)$$

Based on the results, there is strong evidence to conclude that muscle activity from AD muscle during Posture B is a significant predictor when estimating the perception of driver's comfort in Posture B. Muscle activity of AD during Posture B can explain 54.6% of variances that exist in the perception level of driving comfort in Posture B. This conclusion is made at a significance level of $\alpha = 0.05$ (5%) or at a confidence level of 95%.

4 Conclusions

In conclusion, this study has successfully achieved the main objective of this study that is to develop a driver's comfort linear model to demonstrate the relationship between subjective assessment and objective measurement. The linear model developed in this study has been verified from the value of R^2 . Besides that, the significance level of all the predictors is less than the value of $\alpha = 0.05$. The best linear model to describe the relationship between objective measurement and subjective assessment is the linear model produced through the highest Pearson R correlation coefficient, the linear model for posture B ($R = 0.739$). The calculations for the development

of linear models concluded that the linear relationship model of subjective evaluation and objective measurements produced from this study could be defined through collected data from AD muscle activity during posture B, where the angle of the elbow is placed at 134° . The driving posture of the affected position represents the relationship of the angular value model of the most comfortable and optimal driving posture. This study is expected to bridge the gap in research on the comfort of driving according to the proper driving posture, especially in controlling the steering wheel. The regression model can also be a predictor among independent and independent variables, which will facilitate experiments on sEMG measurement for future driving posture.

References

1. Gao Z, Fan D, Wang D, Zhao H, Zhao K, Chen C (2014) Muscle activity and co-contraction of musculoskeletal model during steering maneuver. *Bio-Med Mater Eng* 24(1):2697–2706
2. Abdul Ghani MSA, Wan Shamsuddin SN (2020) Definitions and concepts of user experience (UX): A literature review. *Int J Creative Future Heritage (TENIAT)* 8(1):130–143. <https://doi.org/10.47252/teniat.v8i1.292>
3. Jung NH, Kim H, Chang M (2015) Muscle activation of drivers with hemiplegia caused by stroke while driving using a steering wheel or knob. *J Phys Ther Sci* 27:1009–1011
4. Miros (2014) Road safety plan of Malaysia 2014–2020. Jabatan Keselamatan Jalan Raya, Kementerian Pengangkutan Malaysia. Putrajaya
5. Jia B, Nussbaum MA (2016) Development and evaluation of an EMG-based model to estimate lumbosacral loads during seated work. *Int J Ind Ergon* 55:96–102
6. Slinker BK, Glantz SA (2008) Statistical primer for cardiovascular research dependent variable. *Circulation* 117(13):1732–1737
7. Brookham RL, Wong JM, Dickerson CR (2010) Upper limb posture and submaximal hand tasks influence shoulder muscle activity. *Int J Ind Ergon* 40:337–344
8. McDonald A, Picco BR, Belbeck AL, Chow AY, Dickerson CR (2012) Spatial dependency of shoulder muscle demands in horizontal pushing and pulling. *Appl Ergon* 43:971–978
9. Daruis DDI, Deros BM, Nor MJM, Hosseini Fouladi M (2012) Relationship between objective and subjective methods in evaluating static discomfort of car driver seat. *Adv Mater Res* (433–440):4997–5003
10. Yusoff AR (2017) Permodelan ramalan ketidakselesaian pemandu ketika mengawal dan mengendali pedal minyak kereta. Thesis Dr. Fal, Jabatan Kejuruteraan Mekanik dan Bahan, Fakulti Kejuruteraan Dan Alam Bina. Universiti Kebangsaan Malaysia
11. Sekaran U, Bougie R (2016) Research methods for business: a skill building approach. Edisi ke-7. Wiley, UK
12. Walton D, Thomas JA (2005) Naturalistic observations of driver hand positions. *Transp Res F Traffic Psychol Behav* 8(3):229–238
13. Mohamad D, Deros BM, Dzuraidah AW, Daruis DDI, Ismail AR (2010) Integration of comfort into a driver's car seat design using image. *Analysis* 7(7):924–929
14. Surface ElectroMyoGraphy for the Non-Invasive Assessment of Muscles (SENIAM) (2005) Roessingh research and development. The Netherlands. www.seniam.com
15. Kumar P, Tripathi L (2014) Challenges in pain assessment: pain intensity scales. *Indian J Pain* 28(2):61–70
16. Laursen B, Sjøgaard K, Sjøgaard G (2003) Biomechanical model predicting electromyographic activity in three shoulder muscles from 3D kinematics and external forces during cleaning work. *Clin Biomech* 18:287–295

17. Xu X, Mcgorry RW, Lin J (2014) A regression model predicting isometric shoulder muscle activities from arm postures and shoulder joint moments. *J Electromyogr Kinesiol* 24:419–429
18. Piaw CY (2006) *Asas Statistik Penyelidikan*. Edisi Pertama. McGraw-Hill. Shah Alam

Comparative Study on Performance Characteristics of Modified Alloy Steels by TIG and Water Jet Peening Processes



A. Azhari , A. N. Md Idriss , and M. A. Maleque 

Abstract The objective of this work is to compare the available results of peened surfaces by water jet process against the TIG melted track on stainless steel and low alloy steel samples respectively. Surface topographies, size of formed geometries, microstructural features and surface roughness were investigated. Modified steel hardened by the TIG process exhibited the depth and width of the molten pool of 1.5 mm and 3.5 mm respectively which was higher than the waterjet eroded track up to 0.22 mm and 2.4 mm respectively. The localized heat above steel melting temperature gave molten pool with globular structure near the surface. The impacted waterjet pressure modified the surface of the steel associated with a thin deformed layer. The formation of crater on the water jet eroded track resulted surface roughness value near 3.3 micron while that by the TIG due to those rippling marks showed 1.29 micron. Ranges of surface roughness, hardness and geometrical features of alloy steel can be tailored according to special needs of application. in the dentistry, automotive, oil and gas or aerospace by these two techniques.

Keywords Performance properties · Water jet · TIG · Alloy steel

1 Introduction

Surface modification through cold working processes use high pressure to dislocate the affected area at depths. Till this day, the example of available processes to serve the purpose are either by grit blasting, ball shot peening, laser shock peening, ball or roller burnishing. However, they are adapted to singular processing which means they utilizes high pressure to give the surface friction followed by deformation to alter just the top surface of metallic or semi metallic components. Instead of cutting, water

A. Azhari (✉)

Faculty of Manufacturing and Mechatronic Engineering Technology, Universiti Malaysia Pahang, 26600 Pekan, Pahang, Malaysia
e-mail: azmir@ump.edu.my

A. N. M. Idriss · M. A. Maleque

Department of Manufacturing and Materials Engineering, Kulliyyah of Engineering, International Islamic University of Malaysia, P.O. Box 10, 50728 Kuala Lumpur, Malaysia

jetting with the addition of hard particulates and selective liquid were reported to have a similar capability to harden the surface layer making this process advantageous than those singular processing (ball burnishing, shot peening) [1, 2]. Dissimilar modification techniques via hot working which are the TIG, lasers or electron beam use high heat input to melt a thin layer of the sample whilst letting them to cool at a high solidification rate to produce a hard top layer [3]. Because of using high heat yield over than the melting temperature of the material, a worked component is transformed into the resolidified zone, heat affected zone and undisturbed zone. In comparison, only the deformed and undeformed layers were exhibited generally by the water jet peening processes. TIG process is cheaper, can be easily operated, flexible and low in operational cost compared to the lasers or that of electron beam technique while water jetting is safe against creating hazardous environment due to created smoke or radiation and do not involve high heat to distort samples [4]. The water jet and TIG techniques share the same common energy inputs character involving used power, torch or head inclined angle, traverse speed and working distances. Highly pressurized streamed water peened for cavities along deformed surface can be made either in a singular direction or by overlapping [5–8]. The made layers by the TIG and waterjet were both found to develop higher hardness than the underneath undisturbed substrate [7, 9, 10]. No work was found to compare altered surface geometry, surface roughness, microstructural feature and microhardness from both the waterjet peening processes and TIG on the modified alloy steel surfaces. Several aspects that lead to these changes were discussed.

2 Experimental Work

2.1 TIG Process

In this work, the used substrate was the AISI 4340 low alloy steel that was cut to the dimension of $40 \times 100 \times 15 \text{ mm}^3$. The produced block was cleaned until surfaces were free from the dirt and debris using detergent and washed under the running water. Telwin and Miller 165 welding machine was used to produce a traverse track of 38 mm length. The processing condition that was used to produce this layer was at the heat input (HI) of 1344 J/mm which was calculated using Eq. 1 denoting V as used voltage while I and S were the applied current and torch travelling speed respectively. η at 48% is considered as heat absorption efficiency for TIG [9].

$$HI = \frac{VI}{s} \eta \quad (1)$$

Inert gas, the argon, was used to shroud the arc from excessive oxidation at the rate of 20 l/min. The produced track was sectioned perpendicularly to the direction of the travelling arc torch followed by metallographic grinding and polishing to remove the

Table 1 The water jet processing conditions [8]

Traverse rate (mm/min)	Pressure (MPa)	Standoff distance (mm)
50, 150	40, 80	2, 10

scratches. Nital was used to reveal the microstructures. DINO and NIKON optical scopes were used to examine the geometry and microstructural features of the surface while the Alicona Infinite 200 was used to measure the surface roughness of the topography at the distance of 2 mm across of the melted track. Wilson Wolpert machine was used for the hardenability test of 500 gf at 10 s indentation delay.

2.2 Waterjet Process

This experimental work used the SS400 substrate that was cut to the dimension of $25 \times 25 \times 4 \text{ mm}^3$. Garnet particles at the size of 75 to 106 micron was added with the water followed by streaming or jetting the liquid containing abrasive particles to the surface of the substrate. The processing condition used for peening the stainless steel surface is depicted in Table 1.

3 Results and Discussions

The micrograph of the surface topography, cross sectioned area and microstructures of the sample produced by the TIG and waterjet processes are shown in Fig. 1. The topography observed in Fig. 1a resembling arrays of half-moon shape are the rippling marks caused by melt solidification. In Fig. 1b, arc at the heat input of 1344 J/mm successfully produced a molten depth of 1.5 mm and width at 3.5 mm. Underneath is the HAZ that spreads before reaching the undisturbed substrate. The topography of the track produced by the waterjet abrasive technique is shown in Fig. 1c. Evident of waterjet impingement on the surface of the stainless steel as the head moved along its trajectory is shown by the dark contrast (Fig. 1c). When the same sample is viewed from the side in Fig. 1a, d channel corresponding to that dark contrast was observed. In this work the water added with garnet abrasive successfully erode the surface between 0.12 and 0.22 mm depth and from 1.1 to 2.4 mm width as highly pressurized liquid passes along the track. Using pulsed water jet technique, a channel depth of 2.2 mm was created [8, 10]. The consequent from the ploughing action using that highly pressurized liquid added garnet gave distribution of craters along the trough. Likewise, the solidified melt pool fused by the TIG process (Fig. 1b), the water jet sample was observed near hemispherical shape as shown in Fig. 1d. High melting and erosion in the middle of the track compared to the edges could be explained from the difference of energy densities which both the TIG and water jet processes had,

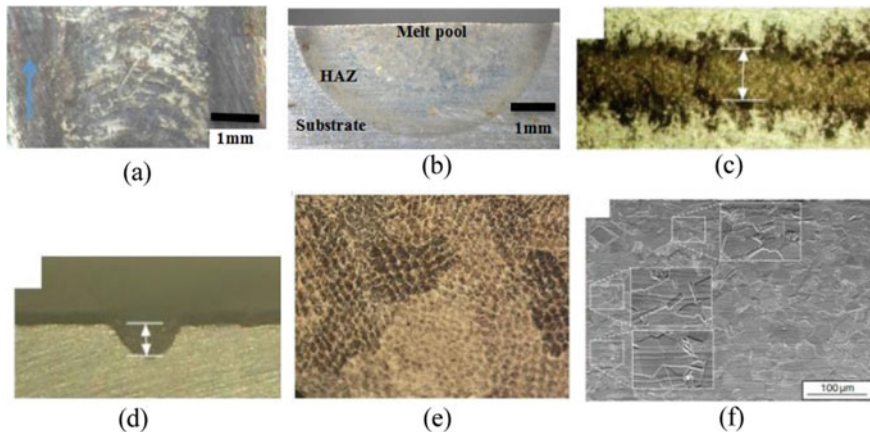


Fig. 1 The topographies, cross sectioned areas and microstructures of the TIG and waterjet surfaces. The micrograph of the surface topography consisting of rippling marks in Fig. 1a with an arrow depicting the torch travelling direction. The cross sectioned surface of the track noting the melted, HAZ and substrate regions in Fig. 1b. The abrasive water jet surface topography with a white arrow showing the average eroded valley width in Fig. 1c with its trough depth in Fig. 1d [8]. TIG equiaxed structure near the arc source in 1e. Prominent grain deformation (Fig. 1f) near the surface than the bottom by the water jet [7]

having highest in the middle and less at the edges. The trough creations using that abrasive water jet were associated with weight losses unlike under the TIG where weight losses are presumed not to take place.

In this work a single pass from the waterjet with garnet brought surface roughness to 3.3 micron which in comparison needed 2 passes to produce about 1 micron roughness without abrasive additions [7]. The results showed that adding the hard garnet (1940 HV) with the water for jetting resulted enhanced of erosion about 3 times than without adding that particulate. It had been explained that the first pass from the waterjet work left less pronounced surface roughness. Subsequently, the second overlapped pass did not remove that the 1st layer minimal rough trough. Instead, this 2nd pass gouged deeper across the nozzle traverse travelling distance. Adding hard abrasive particulates enhances erosion. The result shows the suitability to use water jetting or adding abrasive for soft or hard materials erosion respectively.

In comparison with the TIG process, roughness developed due to those solidified melt waves forming ripples across the track. Due to the absorbed heat amount in the between the early and later stage differs, the surface roughness was seen lower at the end of the tracks than their beginning under the TIG layer in a single track. This is because of the preheating effect resulting more dilution as the torch travelled before reaching near the end of melting and so achieved a smoother topography compared during the beginning of melting process. The early stage of melting possessed low preheating temperature which did not help high dissolution leading for fast solidification hence gave the rougher topography. Another reason for TIG melted track surface roughness is the formation of many porosities. In fact, one work demonstrated that

difference of surface roughness is achievable using difference of shielding gases either helium, nitrogen or argon with TIG [11].

The roughness profile recorded from the TIG melted surface was at $1.29 \mu\text{m}$. This was slightly higher than with $1 \mu\text{m}$ without abrasion from the water jet process [7]. This suggest that the water jet process could be used to flatten the roughness curve for a smoother surface profile of the TIG clad track. Since water jetting either with or without addition of abrasive particles are known to deplete a little layer from the top forming a trough, a proper tailoring would be needed to ensure the right surface profile and tolerance are achievable. Adversely to obtain the rough modified surface, abrasive water jet would be preferably used. Rough surface is beneficial for reduction of asperity contact during friction and assures lubricant entrapment between the moving parts, instead of wheel grinding technique, ripples can be removed by either waterjet or abrasive water jet techniques [12]. The generation of rough surface helps to anchor plasma sprayed metal powder for quality adherence to the substrate [13]. Thin substrate at 4 mm was found successfully modified without succumbing to perforation with that of abrasive water jet showing the process suitability to modify thin metals. TIG may suit thick substrate for modification.

The microstructure in Fig. 1e shows the resolidified molten pool at the surface region. The solidification of liquid metal gave the equiaxed structure (Fig. 1e) near that surface region while just above the substrate, columnar prevailed [14]. The coexistence of columnar and equiaxed structures resulted hardness to develop near 600 HV with the sample that had Fe-Cr-B incorporated on the mild steel surface via TIG. The micrograph in Fig. 1f shows the cross section of the top layer formed by the abrasive water jet processed at 2000 mm/s of 4 overlapped passes under the pressure of 200 MPa [7]. Due to the peening process the top layer density and dislocation gradually decreases with increased of depth. This can be seen from a certain degree of grain deformation with slip band away to 150 microns of depth (top) than lesser deformation at about 250 microns to the bottom. The effect of dislocation from abrasive water jet bombardment are severe at the top layer than the bottom because of the dislocation resistance increases with depth. Not much microstructural changes found at the bottom. This is associated with built hardness at the top layer than the bottom at 265 HV and 230 HV respectively. The hardness at 265 HV was about 2.5 times lower than the hardenability developed by the TIG having 600 HV. It is anticipated that the erosion resistance is high with low developed roughness because of the high hardness value. This was explained by Murugan and co-authors where developed roughness would be less when modifying the hard material [15]. In general, more pressing or deformation is an ideal way to develop hardness by slow travelling speed, high pressure, selected working distances or adding abrasive. With TIG or other arcing processes can rely fast solidification by accelerating torch travelling speed, lessening current or volt or increasing the working distances.

4 Conclusion

Surface modification via waterjet process can be classified as reduction or subtractive process because the material removal is inevitable which is similar to grinding or metal cuttings. Not only hardening the layer, TIG process melts reinforcement in the form of powder or wire filaments to build thickness making this technique classified as additive process. With no heat being involved except a little of imposed deformation capability on the metal surface, waterjet may provide the desired specification via altering the modified surface. Surface roughness can be tailored either by using TIG or waterjet processes with both associated with increase of hardened depth layer.

Acknowledgements The authors greatly acknowledge Department of Manufacturing and Materials Engineering of IIUM for the technical support and the financial support from the Ministry of Higher Education Malaysia through FRGS/1/2019/TK03/UMP/02/25 (RDU1901161).

References

1. Krajcarz D (2014) Comparison metal water jet cutting with laser and plasma cutting. *Procedia Eng* 69:838–843
2. Kumar H, Singh S, Kumar P (2013) Modified shot peening processes—A review. *Int J Eng Sci Emerg Technol* 5:12–19
3. Azam FI, Rani AMA, Altaf K, Rao T, Zaharin HA (2018) An in-depth review on direct additive manufacturing of metals. In: *IOP Conference series: Materials science and engineering*. IOP Publishing, p 12005
4. Kadir MHA, Asmelash M, Azhari A (2021) Investigation on welding distortion in stainless steel sheet using gas tungsten arc welding process. *Mater Today Proc* 46:1674–1679
5. Yun ZOU, Zhenkuan S, Qilong W, Tingchao LI, Dalei LI, Yang LI (2020) Improving the mechanical properties of 304 stainless steel using waterjet peening. *Mater Sci* 26:161–167
6. Azhari A, Schindler C, Hilbert K, Godard C, Kerscher E (2014) Influence of waterjet peening and smoothing on the material surface and properties of stainless steel 304. *Surf Coat Technol* 258:1176–1182
7. Azhari A, Schindler C, Kerscher E, Grad P (2012) Improving surface hardness of austenitic stainless steel using waterjet peening process. *Int J Adv Manuf Technol* 63:1035–1046
8. Husin H, Nawi MNM, Gebremariam MA, Azhari A (2019) Investigation on the effect of abrasive waterjet parameter on machining stainless steel. In: *Proceedings of the international manufacturing engineering conference and the Asia Pacific conference on manufacturing systems*. Springer, Berlin, pp 544–549
9. Mridha S, Idriss AN, Baker TN (2012) Incorporation of TiC particulates on AISI 4340 low alloy steel surfaces via tungsten inert gas arc melting. *Adv Mater Res Trans Tech Publ* 655–660
10. Hloch S, Srivastava M, Krolczyk JB, Chattopadhyaya S, Lehocák D, Simkulet V, Krolczyk GM (2018) Strengthening effect after disintegration of stainless steel using pulsating water jet. *Tehnički vjesnik* 25:1075–1079
11. Muñoz-Escalona P, Mridha S, Baker TN (2015) Effect of shielding gas on the properties and microstructure of melted steel surface using a TIG torch. *Adv Mater Process Technol* 1:435–443
12. Srivastava M, Tripathi R, Hloch S, Chattopadhyaya S, Dixit AR (2016) Potential of using water jet peening as a surface treatment process for welded joints. *Procedia Eng* 149:472–480
13. O’Neil NRL (2020) Optimized surface roughening by pulsed waterjet for suitable adhesion strength of plasma transferred wire arc coating

14. Idriss ANM, Mridha S, Baker TN (2015) Laser and GTAW torch processing of Fe–Cr–B coatings on steel: part II–microstructure and hardness. *Mater Sci Technol* 31:355–360
15. Murugan M, Gebremariam MA, Hamedon, Z, Azhari A (2018) Performance analysis of abrasive waterjet machining process at low pressure. In: *IOP conference series: Materials science and engineering*. IOP Publishing, p 12051

Signal Improvement on Fibre Optic Evanescent Wave Sensor Based Polymeric Sensitive Coating of Chitosan-Agarose Hydrogel



Muhammad Haziq Noor Akashah, Siti Rabizah Makhsin,
Rozina Abdul Rani, Nor Hayati Saad, Khairunisak Abdul Razak,
Peter Gardner, and Patricia J. Scully

Abstract This study aimed to explore the correlation between mechanical and structural properties of chitosan (CH) and agarose (AG) hydrogel as a sensitive coating for single-mode optical fibre (SMF) sensors. CH hydrogel was first made without crosslinking as a stock solution at 0.25% w/v concentration before introducing it to AG as the matrix in the fabrication of hybrid-hydrogel (HH). CH was introduced to AG solution in ratio of 1, 2, 5 and 10% w/v concentration to 2% w/v of AG. The highest thickness was shown by a sample of 2% w/v CH to AG hydrogel with an increment of 2.21% from the bare exposed SMF. From the absorption signal measurement, the correlation can be seen as the signal obtained increases directly proportional to the thickness coating. The sensor generated significant signal improvement when HH used a sensitive coating with a refractive index (RI) sensitivity of 3658 ± 0.23352 RIU⁻¹ for glycerol detection.

Keywords Agarose · Chitosan · Biosensor · Hydrogel · Fibre optic · Photonics

1 Introduction

Hydrogels are known as polymers that can respond significantly via volume changes [1] as they react to alterations in their surrounding medium. In this study, chitosan

M. H. N. Akashah · S. R. Makhsin (✉) · R. A. Rani · N. H. Saad
School of Mechanical Engineering, College of Engineering, Universiti Teknologi MARA, 40450
Shah Alam, Selangor, Malaysia
e-mail: sitirabizah@uitm.edu.my

K. A. Razak
School of Materials and Mineral Resources Engineering, Universiti Sains Malaysia, 14300
Nibong Tebal, Malaysia

P. Gardner
School of Chemical Engineering and Analytical Science, Manchester Institute of Biotechnology,
The University of Manchester, Manchester M1 7DN, UK

P. J. Scully
NCLA, School of Physics, National University of Ireland, Galway, Ireland

(CH) and agarose (AG) were used as the polymer precursor for hybrid-hydrogel (HH). AG possessed mechanics of controlled self-gelling properties, tunable mechanical properties, hydrophilic and non-immunogenic properties which have been widely used in biomedical applications. Due to its stiffness and functional groups, it can sustain cellular adhesion, proliferation, and conduct bioactivity. It also able to adjust water adsorption rate which is highly suitable for cellular activity environment [2].

The purpose behind the hybridisation of hydrogels in this work is basically to harness the void AG-based hydrogel is lacking which is the absence of the ability to capture biomolecules. In comparison to other types of additives to be used with AG, CH is the best candidate for it as it naturally has a polycationic polymer that has one amino ($-NH_2$) group and two hydroxyls ($-OH$) groups on each of every glucosidic residue [3]. As a polysaccharide, CH is able to interact with amyloid molecules across glucosamine groups due to the glycosidic residue which makes it suitable potential for a sensor in biomedical applications. Furthermore, the amino group of CH makes CH, and its derivatives have a strong affinity binding towards the surface of SMF in this work. The fabricated sensor utilised the evanescent wave as the sensing technique which allows the light to interact with the molecules that are within the vicinity of the evanescent field.

This study opted for the idea of a fibre optic-based evanescence wave sensor which has been known for its advantages such as lightweight, high immunity towards electromagnetic wave interference and low-cost material for production [4]. However, a standalone fibre-based sensor is lacking in terms of signal output consistency and detection. Hence, in this case, we have demonstrated the effect of the concentration of polymeric sensitive coating materials made from AG and CH onto the SMF probe, which use for the detection of different refractive index (RI) of glycerol for fibre-optic sensor configuration as illustrated in Fig. 1. We also validated the signal of the SMF evanescent sensor was significantly enhanced when the hybrid hydrogel (AG + CH) was used as a coating material instead of a single coating layer of polymeric hydrogel.

2 Methodology

2.1 Materials

The material used to make the fibre optic probe was YP-Link, (SMF). Other chemicals that were used include glutaraldehyde solution (G7651), chitosan (448,869), acetic acid (A6283) purchased from Sigma-Aldrich, Agarose (16,520,050) was purchased from ThermoFisher Scientific and glycerol (1,922,421) was purchased from Fisher Chemical.

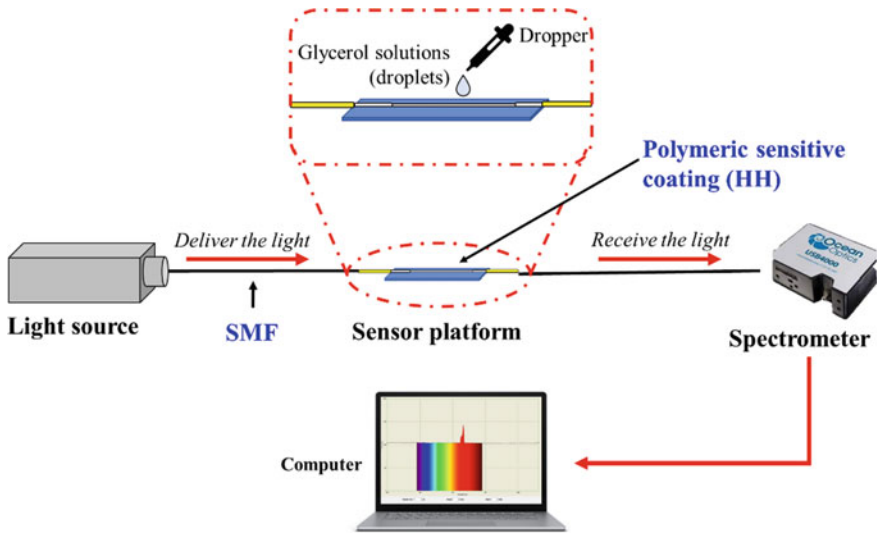


Fig. 1 SMF sensor configuration with HH as a polymeric sensitive coating material

2.2 Synthesis of AG and HH Hydrogels and Coating onto Fibre Optic

CH stock solution of 0.25% w/v was used as the additives for HH. The method to synthesis AG hydrogel and HH were expanded from the previous work [5]. The same procedures were applied to the synthesis of HH by introducing various concentrations of CH: sample ID (1%: CH-AG-1, 2%: CH-AG-2, 5%: CH-AG-5, 10%: CH-AG-10 v/v) in the mixing of AG with ultra-pure water. The priorly exposed core via method in [6] of the SMF cable was coated with HH via the dipping method. The dipping time was set to the optimum 5 min to get the desired thickness which has been optimized in our previous work [5] with the hydrogel remaining heated at 95 °C to avoid gel hardening. After the dipping process, the samples were let to be dried at room temperature (25 °C) overnight.

2.3 Characterisation of HH Hydrogel onto Fibre Optic and RI Sensing

The surface morphology of coated and the uncoated bare fibre optic core was investigated using scanning electron microscopy (SEM: HITACHI SU3500). The average size of the SMF probe before and after coating with AG hydrogel and HH was determined by measuring the SEM images of the probes using ImageJ software. The signal was obtained from Ocean optics spectrometer (USB4000).

3 Results and Discussions

The samples were observed using SEM (images not shown) to monitor their thickness measured using ImageJ software and the result is summarised in Table 1. In this work HH of CH-AG-2 showing the highest thickness of $122.18 \pm 0.312 \mu\text{m}$ from the bare SMF structure with increment of 2.21%. Moreover, the result showing a better coating coverage if compared to pure AG hydrogel as reported before [5]. From the FTIR spectra shown in Fig. 2, CH-based hydrogel possessed numerous functional groups compared to AG-based hydrogel. As seen in Fig. 2, as the amount of CH increases in the composition of AG, the functional group peaks of CH_3 (1386.58 cm^{-1}), CO-O-CO (1243.86 cm^{-1}), $\text{C}=\text{C}$ (1010.52 cm^{-1}) and C-H (879.39 cm^{-1}) starts to become more prominent. Whereas a major difference was seen on the AG peak that offers $\text{C}=\text{O}$ (1633.41 cm^{-1}) and OH (3305.39 cm^{-1}) only. As seen in the graph the peaks of chitosan at about 1300 cm^{-1} and 1100 cm^{-1} as per study conducted by [7] disappeared, indicating glutaraldehyde has successfully cross-linked CH structure. Figure 3a shows the signal obtained after coating the exposed SMF with HH and AG hydrogels. The highest signal produced was by sample CH-AG-2 which is $\sim 36.2\%$ increment from AG coated sample. This is due to the thickness of this sample being the highest compared to other coated samples (see Table 1), which proves the correlation between thickness and signal produced. Although as per sample AG hydrogels, despite reported [5] of having a thickness increment of 2.07% yet having low signal output could be due to the lack of pore structure which causes lesser volumetric change, hence giving a low signal.

It has been reported by having CH consisting of smaller particle nanostructure [8] would have led to a higher signal due to the suitability to mix well with AG. From sample CH-AG-2, it was proven with the amount of CH-AG used, it was able to achieve a stable state of HH.

Furthermore, CH has been reported to have high porosity [9] which allows higher penetration depth of the surrounding glycerol which had boosted the signal in sample CH-AG-2 compared to sample AG hydrogels despite having high almost the same range of thickness measurement and increment. The peak intensity was further refined in Fig. 3b against the contribution of CH in the HH composition. Hence the optimum sample CH-AG-2 was further tested with different RI of glycerol as shown in Fig. 3c.

Table 1 Summary of the coating samples; thickness, thickness increment and signal intensity

Sample ID	Thickness (μm)	Thickness increment (%)	Signal peak intensity (a.u.)
Bare SMF	119.54 ± 0.387	NA	NA
AG	122.02 ± 0.495	2.07	1520.76
CH-AG-1	119.37 ± 0.478	0.26	1674.55
CH-AG-2	122.18 ± 0.312	2.21	2071.03
CH-AG-5	120.01 ± 0.313	0.38	1549.74
CH-AG-10	120.73 ± 0.205	0.99	1369.65

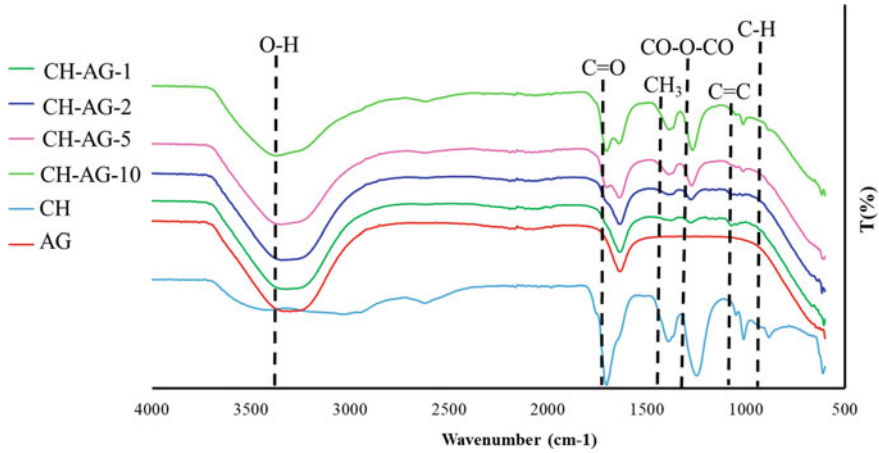


Fig. 2 FTIR of HH inclusive of their originated precursor CH and AG

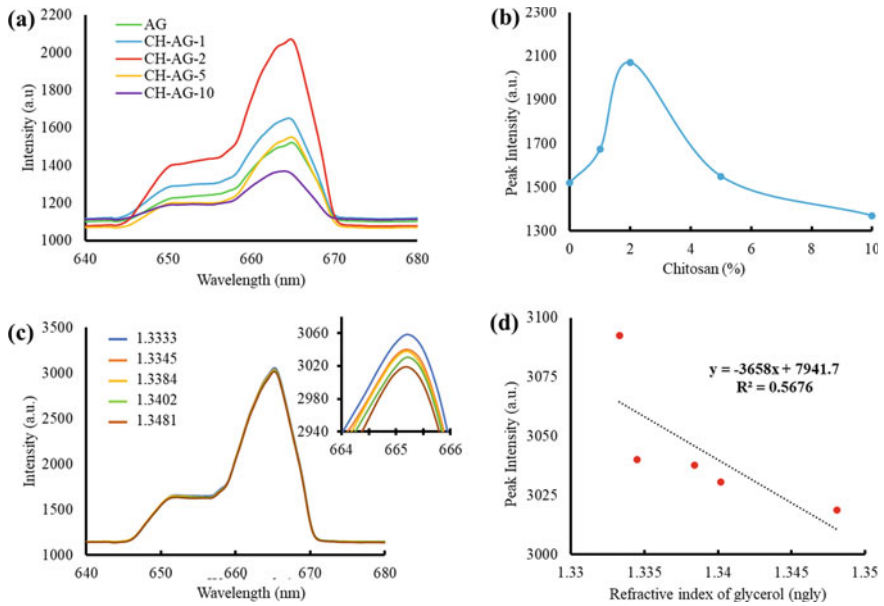


Fig. 3 Optical signal of coated SMF **a** with variations of HH and AG **b** intensity peak versus the percentage of CH in the HH composition, **c** signal obtained of sample CH-AG-2 tested with different RI of glycerol (inset shows the magnified intensity) and **d** peak intensity plotted against various RI of glycerol of the optimum sample CH-AG-2

The signal intensity was observed to drop as the concentration and RI of glycerol increased. This is mainly due to the reactivity of the coating layer with the light propagating through the layer and ability to penetrate different RI of the surrounding medium [10]. The RI sensitivity of sample CH-AG-2 was found at 3658 ± 0.23352 RIU⁻¹ for glycerol detection.

4 Conclusions

We have demonstrated a simple and less time-consuming method for producing HH. The integration of hydrogels combined from CH and AG were successfully embedded onto SMF. The result from the hybridisation of CH and AG as hydrogel has shown that the best of both characteristics was able to be obtained without losing each other signature identities. The analysis obtained from SEM has confirmed the presence of HH on SMF structure via thickness increment from bare structured SMF. Furthermore, it is confirmed that introducing CH in AG hydrogels has significantly increased the signal produced due to CH having smaller particles that act as a booster. The RI sensitivity was found at 3658 ± 0.23352 RIU⁻¹ for glycerol detection by the optimum sample CH-AG-2. Future work able to be carried out for biosensing applications as it is supported by the characteristics of AG and CH which are suitable for bioconjugations and bioactivity. The potential does not stop there, as this could be fundamental to integrate HH with other types of nanomaterials especially those that possess high biocompatibility.

Acknowledgements This research was funded by FRGS-Racer grant: 600-IRMI/FRGS-RACER5/3 (011/2019), Global Research Grant, UiTM (600-RMC 5/3/GRR (008/2020)) and FRGS grant 600-IRMI/FRGS 5/3(341/2019). The authors would like to thank all technical staff from the College of Engineering, UiTM Shah Alam for the technical support.

References

1. Fujiwara E, Cabral TD, Sato M, Oku H, Cordeiro CMB (2020) Agarose-based structured optical fibre. *Sci Rep* 10:1–8
2. Richter A, Paschew G, Klatt S, Lienig J, Arndt KF, Adler HJP (2008) Review on hydrogel-based pH sensors and microsensors. *Sensors* 8:561–581
3. Makhsin SR, Gardner P, Goddard NJ, Scully PJ (2020) Agarose-chitosan based hydrogel waveguide matrix: comparison synthesis and performance for optical leaky waveguide (OLW) biosensor. *Solid State Phenom* 301:87–96
4. Lee B (2003) Review of the present status of optical fiber sensors. *Opt Fiber Technol* 9:57–79
5. Noor Akashah MH, Rani RA, Saad NH, Rahman MKA, Scully PJ, Makhsin SR (2021) Facile microwave-assisted synthesis of agarose hydrogel for fibre optic biosensors application. In: *Proceedings—2021 regional symposium on micro and nanoelectronics, RSM 2021*. IEEE, Malaysia, pp 50–53

6. Akashah MHN, Rani RA, Saad NH, Rahman MKA, Makhsin SR (2019) Fabrication of sensing platform for single-mode-fibre (SMF) sensors. In: National symposium on micro-nano technology. NANO Kebangsaan, Cyberjaya, Malaysia, pp 45–46
7. Li B, Shan CL, Zhou Q, Fang Y, Wang YL, Xu F, Han LR, Ibrahim M, Guo LB, Xie GL, Sun GC (2013) Synthesis, characterization, and antibacterial activity of cross-linked chitosan-glutaraldehyde. *Mar Drugs* 11:1534–1552
8. Semwal V, Shrivastav AM, Gupta BD (2017) Surface plasmon resonance based fiber optic trichloroacetic acid sensor utilizing layer of silver nanoparticles and chitosan doped hydrogel. *Nanotechnology* 28
9. Chen LH, Chan CC, Yuan W, Goh SK, Sun J (2010) High performance chitosan diaphragm-based fiber-optic acoustic sensor. *Sens Actuators Phys* 163:42–47
10. Zhang ZF, Zhang Y (2015) Humidity sensor based on optical fiber attached with hydrogel spheres. *Opt Laser Technol* 74:16–19

Tribological Behavior of Cartilage Replacement with the Presence of Bio-Lubrication



Farah Nabillah Kazwa , Salmiah Kasolang , and M. Mazwan Mahat 

Abstract A healthy natural synovial joint is essential for the natural musculoskeletal system's painless active movements. The practical implementation of natural synovial joints enables well-lubricated contact surfaces with a very low friction coefficient and cartilage tissue wear. As is well known, cartilage replacement is a highly effective treatment; yet, there are still wear and fatigue issues with the materials utilized in the implants. So, the present paper focused on bio-lubricant performance and mechanical responses toward Poly Lactic Acid (PLA) as a tibial insert for cartilage replacement in Total Knee Replacement (TKR) with the presence of bio-lubricants. Canola oil, castor oil, and sunflower seed oil are considered vegetable oils, whereas Hyaluronic Acid (HA) is the friction modifier. The tribological behavior of selected vegetable oil with modifier was studied using a pin-on-disc tribometer. After tribological tests, the Coefficient of Friction (CoF) and wear rate were studied. The results showed that castor oil had a lower coefficient of friction than canola and sunflower seed oil. In conclusion, castor oil outperforms canola and sunflower seed oil in terms of friction reduction.

Keywords Polylactic acid · Friction coefficient · Vegetable oils · Pin-on-disc · Wear

1 Introduction

Every year, millions of individuals suffer from joint illness, such as osteoarthritis or joint damage, which has an impact on their daily lives. One in every four individuals in the United States (23.7%), or approximately 58.5 million people, has arthritis, according to the Centers for Disease Control and Prevention [1]. Arthritis is more prevalent in women (23.5%) than in males (18.1%), more common in adults with mediocre health (40.5%) than in those with great health (15.4%) [2]. Arthritis is becoming more common as people become older. When less-invasive treatments fail

F. N. Kazwa · S. Kasolang · M. M. Mahat (✉)
School of Mechanical Engineering, College of Engineering, Universiti Teknologi MARA, 40450
Shah Alam, Selangor, Malaysia
e-mail: mazwan@uitm.edu.my

© The Author(s), under exclusive license to Springer Nature Singapore Pte Ltd. 2023
Md. A. Maleque et al. (eds.), *Proceeding of 5th International Conference on Advances in Manufacturing and Materials Engineering*, Lecture Notes in Mechanical Engineering,
https://doi.org/10.1007/978-981-19-9509-5_16

117

to relieve severe joint dysfunction, the damage worsens. Joint replacement surgery may be able to resume their normal lives without discomfort. After a few years, particles of artificial joint material wear off, causing osteolysis and joint loosening.

Total knee replacement (TKR) performance is primarily influenced by their tribological characteristics since wear particles formed during the tribological process play an important role in the lifetime of the artificial joint system. Ultrahigh-molecular-weight polyethylene (UHMWPE), Co–Cr–Mo alloys, alumina (Al_2O_3), zirconia (ZrO_2), silica (SiO_2), and silicon nitride (Si_3N_4) [3]. The usual lifespan of UHMWPE is roughly 10 years, and patients may need to have surgery again for joint replacement. PLA has been proposed as an alternative replacement material for the TKR device. This study advocated investigating Poly-Lactic Acid (PLA) polymer, which may be utilized to replace present polymers [4].

Plant-based oils have improved lubricity, which results in longer equipment life and less corrosion of metal surfaces, and a high viscosity index. This is because they are non-toxic and non-harmful to the environment. The selection of lubricants in this research is based on their ability to alter certain characteristics such as friction, wear, oxidation, foaming, and corrosion. [5]. For example, the viscosity index for plant-based oil is around 220, whereas most mineral oils have a viscosity index in the range of 90–100 [6]. Biodegradable vegetable oils have a better lubricating ability than current mineral or synthetic oils because they contain a large amount of unsaturated and polar ester groups components that affect the conditions during reciprocating sliding. Their high viscosity also reduces operating temperature, resulting in up to 16 percent or more energy savings. Costel and Sorin [7] compared the tribological behavior of the two moving metals using bio-lubricant oil to mineral oil.

Based on preliminary studies, it is clear that lubricating processes inside TKR require additional investigation. Thus, the real objective for the current contribution was to experimentally assess the formation of the lubricating film, with a focus on the specific vegetable oils constituents concerning (i) speed, (ii) load, and (iii) lubricant concentration towards contact between a stainless-steel metal pin and a Polylactic acid polymer representing the tibial insert.

2 Methodology

This experiment began with the selection of a suitable material for the disc and pins that would be suitable for the human body. SOLIDWORKS software was used to create the 3D model of disc. Following that, select the best lubricants that meet the criterion of the knee condition, which includes other elements such as material, load, speed, and time.

Table 1 Material properties for disc material [8]

Material	Poisson ratio	Young modulus (N/mm ²)	Yield strength (MPa)
Polylactic acid (PLA)	0.36	3500	70

Table 2 Composition of lubricants oil [7, 9, 10]

Fatty acid percentage	Castor oil	Canola oil	Sunflower seed oil
Linoleic acid (%)	4–5	6–14	44–75
Oleic acid (%)	3–4	50–65	14–43

2.1 Materials

The standard pin used in this experiment is manufactured of SS316L stainless steel and has the following dimensions: 8 mm diameter and 25 mm length. The pin was cut into 25 mm using the abrasive cutter, then the pin is polished to achieve a mirror-like finishing. The pin was cleaned with acetone and wiped dry with a fresh lint-free industrial wipe before each subsequent test. PLA discs were printed using a 3D printing machine using material properties of PLA listed in Table 1.

2.2 Bio-Lubricants

The lubricants used in this paper are castor oil, canola oil, and sunflower seed oil. Vegetable-based oils are favored since they are biodegradable and non-toxic, making them safe for the environment and medicines. It has been discovered that the inclusion of modifiers such as friction modifiers (FMs) may significantly reduce friction. HA was used as a modifier in this study. Castor oil, canola oil, and sunflower seed oil were chosen for this investigation due to their refined state and oleic acid content, which appears to aid in minimizing friction. Table 2 shows the chemical composition of lubricant oil.

2.3 Test Procedure

The tribological characteristics of the produced lubricant were determined using a pin-on-disk tester. PLA discs with hardness ranging from 104 to 118R [11] are utilized. The pin is made of SS316L (95-887HV) [12] and is 8 mm in diameter by 25 mm in length. The track radius was 20 mm, the disc's rotational speed was 60, 90, and 360 rpm (walking, cycling, and running) at room temperature, and the

Table 3 Input parameters for pin-on-disc tribometer

Parameters	Input
Castor oil (L)	1.5
Canola oil (L)	1.5
Sunflower Seed oil (L)	1.5
Hyaluronic Acid (ml)	0, 5, 10
Pin hardness (HV) [12]	95–887
Disc hardness [11]	104–118
Track radius (mm)	20
Sliding distance (m)	1492.88
Sliding speed (m/s)	60, 90, 360

typical load was 45, 66, and 90 kg for walking, cycling, and running respectively. Before conducting the experiments, all of the samples were cleaned with acetone and dried. Table 3 shows input parameters for the pin-on-disc tribometer. A Pin-on-Disc machine was used to study the Coefficient of Friction and Wear Rate. When a pin made tangential contact with a revolving PLA disc, a sensor detected the friction between the sample and the disc. The test lasted 1800s, or 30 min, at a room temperature of 28 degrees Celsius.

3 Result and Discussion

3.1 Coefficient of Friction Behavior

Figure 1 depicts the development of the Coefficient of Friction (CoF) as a function of the number of cycles performed by the lubricants pair under varied retention circumstances. The CoF is high under dry circumstances. It reduces when bio-lubrication is used. The use of vegetable oils has resulted in a considerable reduction in the CoF.

Under dry conditions and in the presence of bio-lubricants, the CoF rises fast at the start of the test and exhibits considerable changes when compared to the response found when using bio-lubricants. These variations may indicate a change in contact. It shows that, with the presence of lubricants, the wear and fatigue issues with the materials utilized in the implants will be reduced. When compared to dry lubrication, the coefficient of friction for oil lubrication is quite low. As observed in Fig. 2, Castor oil shows the lowest CoF compared to Sunflower seed oil and Canola oil. It shows that castor oil shows the best result in reducing friction between pin and disc. In comparison to canola and sunflower seed oil, castor oil has the least fatty acids. The presence of thin lubricant coatings between the pin surfaces reduced material transfer and adhesion between the two surfaces. Castor oil has a lower friction torque than canola and sunflower seed oil because of this.

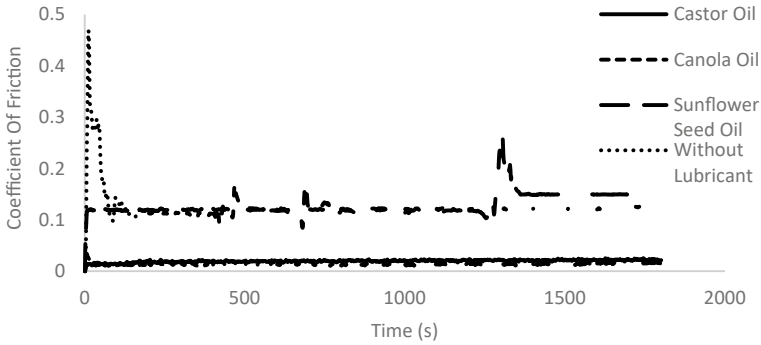


Fig. 1 The CoF of dry test vs bio-lubricants test

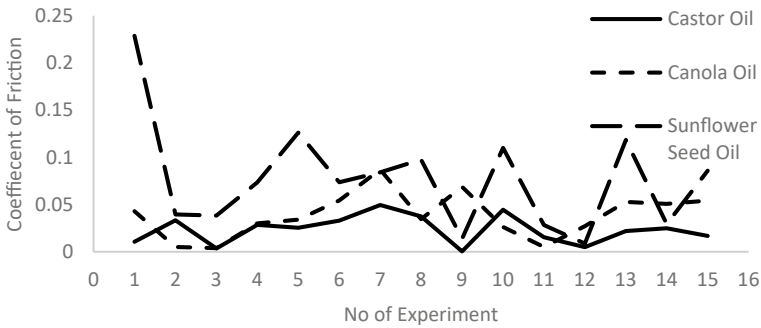


Fig. 2 CoF between castor, Canola, and sunflower seed oil

4 Conclusion

The current study demonstrates a successful tribological assessment of the presence of lubrication to reduce friction and wear in the human joint. Using a pin on disc tribometer, the influence of vegetable oils on the tribological reaction of lubricants with HA pair was investigated. When compared to the physiological disc without lubricants, vegetable oils resulted in a considerable drop in CoF. The most promising specific wear rate was found in the presence of castor oil, with a significant drop of around 98 percent as compared to the dry state.

The application of vegetable oils has resulted in a positive modification in the morphology of wear tracks. The ability of fatty acid molecules to adsorb on the surface of lubricants is an important aspect of the tribological effectiveness of vegetable oils. Vegetable oils with a high oleic acid concentration provide excellent friction and wear properties. The results showed that castor oil had a lower coefficient of friction and lower wear rate than canola and sunflower seed oil. In conclusion, castor oil outperforms canola and sunflower seed oil in terms of friction reduction. Finally, the findings of this study suggest that vegetable oils should be

given greater consideration by undertaking a series of further in vitro, in vivo, and clinical testing before final usage.

Acknowledgements The authors would like to thank the Ministry of Higher Education (MOHE) and the Research Management Centre of Universiti Teknologi MARA (UiTM) Shah Alam for funding this research via the Fundamental Research Grant Scheme (FRGS); grant number 600-IRMI/FRGS 5/3 (435/2019).

References

1. National Statistics CDC (2022) https://www.cdc.gov/arthritis/data_statistics/national-statistics.html, Last accessed 23Apr 2022
2. Barbour KE, Helmick CG, Boring M, Brady TJ (2017) Vital signs: prevalence of doctor-diagnosed arthritis and arthritis-attributable activity limitation—United States, 2013–2015. *Morb Mortal Wkly Rep* 66(9):246–253
3. Jasim HA (2019) Implant materials for knee and hip joint replacement: a review from the tribological perspective. *IOP Conf Ser Mater Sci Eng* 561(1):012007
4. Su CY, Huang SS, Fang HW (2018) Effects of major components of synovial fluid on the morphology and wear rate of polyetheretherketone (PEEK) particles under an accelerated wear process. *Polymers* 10(6):635
5. Chowdary K, Kotia A, Kotiya A (2020) Rheological properties of homeopathic preparation of animal and plant based synovial mimic fluid with MWCNT And alumina nanoparticles. *Plant Arch* 20(2):3507–3511
6. Heikal EK, Elmelawy MS, Khalil SA, Elbasuny NM (2017) Manufacturing of environment friendly biolubricants from vegetable oils. *Egypt J Pet* 26(1):53–59
7. Humelnicu C, Ciortan S, Amortila V (2019) Artificial neural network-based analysis of the tribological behavior of vegetable oil-diesel fuel mixtures. *Lubricants* 7(4)
8. Siakeng R, Jawaid M, Ariffin H, Sapuan SM, Asim M, Saba N (2019) Natural fiber reinforced poly(lactic acid) composites: a review. *Polym Compos* 40(2):446–463
9. Román-Figueroa C, Cea M, Paneque M, González ME (2020) Oil content and fatty acid composition in castor bean naturalized accessions under Mediterranean conditions in Chile. *Agronomy* 10(8):1145
10. Jabal MH, Abdulmunem AR, Abd HS (2019) Experimental investigation of tribological characteristics and emissions with nonedible sunflower oil as a biolubricant. *J Air Waste Manag Assoc* 69(1):109–118
11. Overview of Materials for Poly(lactic acid) (PLA) Biopolymer: <https://www.matweb.com/search/DataSheet.aspx?MatGUID=ab96a4c0655c4018a8785ac4031b9278&ckck=1>, Last accessed 29 Apr 2022
12. Jin W, Zhang C, Jin S, Tian Y, Wellmann D, Liu W (2020) Wire arc additive manufacturing of stainless steels: a review. *Appl Sci* 10(5)

The Physical Activation and Chemical Activation Reaction During Synthesis of Activated Carbon from Empty Fruit Bunch



Hasan Marzuki, Alya Naili Rozhan, and Hadi Purwanto

Abstract Empty fruit bunch (EFB) has a potential to be used as raw materials to produce activated carbon due to its low cost and high availability. A two-step activation process that consists of combination of carbonization and activation is one of the suitable methods to convert raw EFB into activated carbon. In this study, the two-step activation was employed by first conducting carbonization process at 500 °C under Argon gas flow for 1 h to convert it into biochar followed by physical and chemical activation. Physical activation was conducted at 500 and 800 °C under CO₂ gas flow for 1 h meanwhile chemical activation was done by mixing KOH with the carbon samples using weight ratios of 1:1 and 2:1 before it was heated at under Argon gas flow for 1 h. The resultant activated carbon samples were analyzed and characterized using weight loss analysis, Energy X-ray Spectroscopy (EDX), Raman Spectroscopy and Fourier Transfer Infrared (FTIR) spectroscopy to evaluate the physical characteristics. The result from these characterizations indicated that physical activation process yielded activated carbons with better physical characteristics compared to those of chemical activation process. This is mainly contributed by the facts that physical activation was conducted at a higher activation temperature.

Keywords Empty fruit bunch · Activated carbon · Pyrolysis

1 Introduction

Biomass consists of high composition of carbon and volatile matters, and it has been one of the raw materials that is being used for activated carbon production. This is due to its low cost, high availability and characteristics suitable to be used as activated carbons, such as high specific surface area and porosity. Empty fruit bunch

H. Marzuki · A. N. Rozhan (✉)

Kulliyah of Engineering, International Islamic University Malaysia, Jalan Gombak, 53100 Kuala Lumpur, Malaysia

e-mail: alyanaili@iium.edu.my

H. Purwanto

Kompleks PT. Semen Indonesia, Universitas Internasional Semen Indonesia, Jalan Veteran, Gresik, West Java 61122, Indonesia

(EFB) is one of the abundantly available biomass materials in Malaysia. This is due to Malaysia being one of the largest oil palm producers in the world [1, 2]. Majority of these EFB waste is left to be naturally decomposed, incinerated, or discarded in landfill. These biomass waste methods usually have low efficiency and would lead to environmental issues such as deterioration of air quality and emission of greenhouse gases. Thus, methods of converting these wastes into value-added products have attracted significant interests in order to curb the environmental issues [3].

The physical characteristics of EFB such as high carbon contents and large amounts of volatile matters make it an interesting material to be further explored for it to be used in the production of activated carbon [4]. Two-step activation process to synthesis activated carbon is regarded as the best synthesis route to convert EFB into activated carbon.

This study presents the comparison of these two types of activation methods—physical and chemical activation processes—on the EFB raw material. The point of interest in this research is to demonstrate the comparison of the effects of activation temperatures and the effects of the concentration of activation agent on the physical properties of the produced activated carbons. The chemical activation was carried out under various concentrations of activation agent under a constant temperature. Meanwhile, the physical activation was carried out under various activation temperatures with exposure to a constant activation agent.

2 Experimental

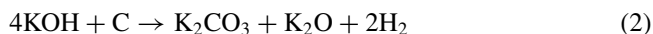
EFB used in this study was collected at Malaysian Palm Oil Board (MPOB), Bangi. The gross composition of EFB was 8.98% of fixed carbon, 83.94% of volatile matter, 6.8% of moisture content and 7.08% of ash. The elemental composition of EFB was 45.64% of carbon, 47.82% of oxygen, 6.19% of hydrogen and 0.35% of sulfur. Samples was defibrized and sieved with particle sizes ranging from 300–600 μm before drying at 105 °C for 24 h to remove moisture content. Two-step activation process was employed to synthesize activated carbons. First, carbonization process was conducted by heating the EFB at 500 °C for one hour under Argon gas flow to convert it into biochar before it could be activated into activated carbon samples. For physical activation, the biochar was heated under CO_2 gas flow for 1 h at temperature of 500 °C and 800 °C. The samples for physical activation were denoted as AC 500 and AC 800. For chemical activation, biochar was impregnated with KOH for one hour with the weight ratio of KOH to biochar of 1:1 and 2:1. The impregnated biochar underwent activation process under Argon gas flow for one hour at temperature of 500 °C. The samples for chemical activation is denoted as AC 1:1 and AC 2:1.

Raman spectroscopy was performed using instrument model Reinshaw inVia confocal Raman spectrometer with 532 nm excitation laser to observe the characteristics of the carbon material produced. The elemental composition of activated carbon was analyzed with Energy Dispersive X-Ray Spectroscopy (EDX) that were carried out using instrument model FESEM-ZEISS Supra 55VP. Fourier transform

infrared (FTIR) spectroscopy was carried out using instrument model Bruker Invenios instrument to detect the functional groups in the resultant products. The range of the FTIR spectra was from 500 cm^{-1} until 4000 cm^{-1} .

3 Result and Discussion

The reaction that took place during carbonization process was contributed from the heating process of the EFB at elevated temperatures. During this process, most of the volatile matters vaporized leaving networks of pores within the biochar bodies. The reaction between bio-char and the activation agent such as CO_2 and KOH will further create new smaller-sized pore formation through the reduction of carbon during activation process. The following Eqs. (1) to (4) describe the reaction that occur during the physical activation and chemical activation process [5, 6]. The weight loss analysis after the activation process further supported the theories of the carbon reduction during activation process. These processes mechanisms has allowed the formation of highly porous structure of the activated carbon.



Weight loss was measured after pyrolysis and activation process. The weight loss of 64% to 66.6% has been recorded during pyrolysis process. After activation process, AC 1:1 shows 10.9% of weight loss, AC 2:1 shows 13% of weight loss, AC 500 shows 9.7% of weight loss and AC 800 shows 30.7% of weight loss.

AC 800 has higher weight loss as compared to those of AC 1:1, AC 2:1 and AC 500. This may be contributed by the higher activation temperature of AC 800 compared to other samples. The higher weight loss indicates that there is a higher reaction that had occurred during the activation process in which it could be inferred that activation temperature plays a greater role during activation compared to the presence of activation agent. This is because, during physical activation, the activation temperature had been varied and the flow of CO_2 gas had been kept constant. In contrast with the chemical activation, the amount of activation agent, KOH was varied, and the activation temperature was kept constant.

Table 1 shows the elemental composition analysis for sample after chemical and physical activation process. In comparison with raw EFB, the percentage composition of carbon increase from 45% to around 80% and oxygen decreased from 47% to below

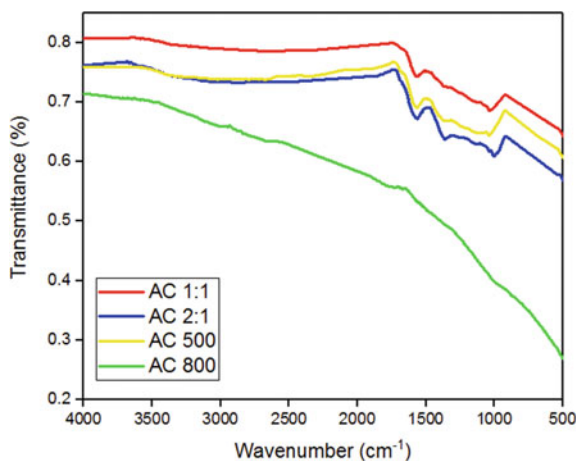
Table 1 EDX analysis

Sample	Carbon (wt%)	Oxygen (wt%)	Nitrogen (wt%)
AC 1:1	82.6	0.0	14.2
AC 2:1	83.6	10.3	1.0
AC 500	80.5	12.8	1.5
AC 800	76.6	16.0	1.2

20% after activation. These are contributed by the facts that more oxygen molecules bonded to the carbon during the carbonization and the activation process. In addition to that, oxygen molecules were also consumed in the carbonization process to produce the syngas [7].

Figure 1 shows the FTIR spectra that was performed to investigate the presence of the functional group on activated carbon after activation process. The peak at the 1500 cm^{-1} indicates that the presence of the $\text{C}=\text{C}$, which were contributed by the aromatic stretching of the activated carbon. There was also a presence of peak at 1000 cm^{-1} which represented the $\text{C}-\text{O}$ functional group [7]. The AC 1:1, AC 2:1 and AC 500 shows almost similar spectra with the same peak that present on these spectra, meanwhile for AC 800 there was almost no peak on those spectra which indicates that there was a low amount of functional group on the sample AC 800. This could be due to the factor of activation temperature, in which activation process of AC 1:1, AC 2:1 and AC 500 had been conducted at activation temperature of $500\text{ }^{\circ}\text{C}$ meanwhile activation process of AC 800 was conducted at $800\text{ }^{\circ}\text{C}$. This shows that activation temperature plays an important roles in building up the presence of the functional group on the activated carbon sample [7, 8]. The presence of oxygen surface functional group as indicated in the FTIR spectra has beneficial effect in terms increasing the adsorptive capacity of activated carbon [9].

Raman spectroscopy analysis of the activated carbon is shown in the Fig. 2. The D and G bands of activated carbon were expected to appear at 1348 cm^{-1} and 1600 cm^{-1}

Fig. 1 FTIR spectra of activated carbon

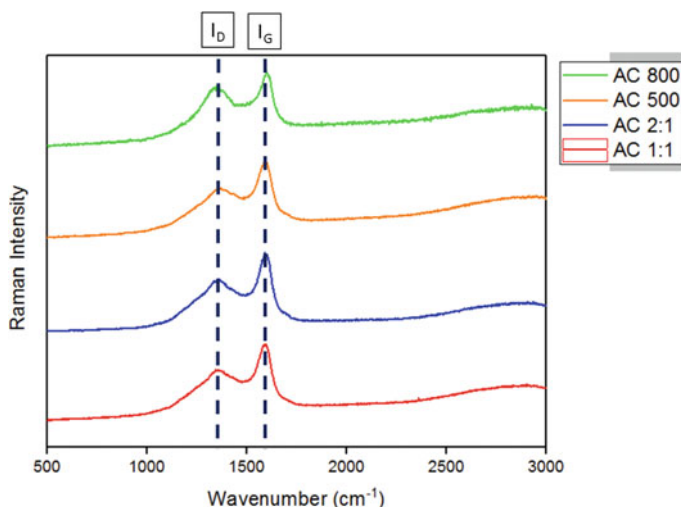


Fig. 2 Raman spectroscopy analysis of activated carbon

respectively [10, 11]. The G peak of Raman spectra represents the sp² carbon state meanwhile D peak of Raman spectra represents the disordered structure of the carbon materials [12]. The ratio between the D and G peak, I_D/I_G illustrates the degree of graphitization and defect structure present within the activated carbon sample.

Higher the value of I_D/I_G indicates the higher defect structure and higher degree of graphitization of the activated carbon materials. These two attributes are very essential for activated carbon as it can enhance its properties such as thermal stability, electrical conductivity and ion mobility within the pore network [12]. It can be observed that, AC 800 had the highest I_D/I_G intensity ratio at 0.84 meanwhile AC 1:1, AC 2:1 and AC 500 shows relatively similar value which were 0.71, 0.70 and 0.70 respectively. This shows that the activation temperature plays an essential role in developing the structure of activated carbon in which higher activation temperature will yield higher defect structure and high degree of graphitization.

4 Conclusion

This work demonstrates the comparison of the activated carbon that had undergone two types of reactions which were chemical and physical activations. Both methods utilized different types of parameters in which during chemical activation, the amount of activation agent, KOH, was varied and the activation temperature was kept constant. Meanwhile for physical activation, the activation temperature was varied and flow of CO₂ gas as the activation agent was kept constant. The following points summarize the conclusion that could be drawn from this study:

1. The weight loss analysis indicates that the activation temperature plays important roles in defining the rate of reaction during activation process compared to the amount of activation agent.
2. Carbon content percentage of the activated carbon sample increased after activation process meanwhile oxygen content decreased. The decreasing of oxygen content could be due to its consumption during carbonization and activation process as well as more oxygen bonded with the carbon during activation process.
3. Activation at higher temperatures yielded activated carbon with higher defect structure and higher degree of graphitization, it gives better properties to activated carbons in terms of their thermal stability, electrical conductivity and ion mobility.

Therefore, it can be concluded from this study that activation temperature plays an essential role in comparison to the concentration of the activation agent in synthesizing activated carbon.

Acknowledgements This research is supported by Ministry of Higher Education Malaysia through Fundamental Research Grant Scheme, FRGS/1/2019/TK07/UIAM/03/3.

References

1. Abas R, Kamarudin MF, Nordin AAB, Simeh MA (2011) A study on the Malaysian oil palm biomass sector—Supply and perception of palm oil millers. *Oil Palm Indus Econ J* 11(1):1–14
2. Faizi MK, Shahrman AB, Majid MSA, Shamsul BMT, Ng YG (2017) An overview of the oil palm empty fruit bunch (OPEFB) potential as reinforcing fibre in polymer composite for energy absorption applications. *MATEC Web Conf* 1064(90):1–9
3. Zhou C, Wang Y (2020) Recent progress in the conversion of biomass wastes into functional materials for value-added applications. *Sci Technol Adv Mater* 21(1):787–804
4. Samiran NA, Jaafar MNM, Chong CT, Han NJ (2015) A review of palm oil biomass as a feedstock for syngas fuel technology. *J Teknologi* 13–18
5. Lan X, Jiang X, Song Y, Jing X, Xing X (2019) The effect of activation temperature on structure and properties of blue coke-based activated carbon by CO₂ activation. *Green Process Synth* 8(1):837–845
6. Mopoung S, Moonsri P, Palas W, Khumpai S (2015) Characterization and properties of activated carbon prepared from tamarind seeds by KOH activation for Fe(III) adsorption from aqueous solution. *Sci World J*
7. Mahmud NA, Osman N, Md Jani AM (2018) Characterization of acid treated activated carbon from oil palm empty fruit bunches (EFB). *IOP Conf Ser J Phys* 1083
8. Osman NB, Shamsuddin N, Uemura Y (2016) Activated carbon of oil palm empty fruit bunch (EFB): core and shaggy. *Procedia Eng* 148:758–764
9. Charles HT, Radisav DV, Lois JU (1997) Impact of oxygen-containing surface functional groups on activated carbon adsorption of phenols. *Environ Sci Technol* 31:1972–1978
10. Singh A, Ghosh K, Kumar S, Agarwal AK, Jassal M, Goswami P, Chaturvedi H (2019) Interdigitated flexible supercapacitor using activated carbon synthesized from biomass for wearable energy storage. *arXiv preprint arXiv: 1903.02384*

11. Zheng Y, Deng T, Yue N, Zhang W, Zhu X, Yang H, Chu X, Zheng W (2021) Raman spectroscopy and correlative Raman technology excel as an optimal stage for carbon based electrode materials in electrochemical energy storage. *J Raman Spectrosc* 1–12
12. Cai P, Zou K, Deng X, Wang B, Zou G, Hou H, Ji X (2020) Defect rich hierarchical porous carbon for high power supercapacitors. *Frontiers Chem* 8(43)

Heterotrigena Itama Kelulut Honey Dehydration Process to Prolong Shelf Life



Mohd Amirul Ashraf Muhammad, Adibah Amir,
and Abdul Rahman Abdul Razak

Abstract One of the main challenges in the tropical honey industry such as *kelulut* honey is the naturally occurring high water content in the *kelulut* honey composition. If water content exceeds 22%, the fermentation process will occur at ambient temperature, spoiling the *kelulut* honey taste and reducing its shelf life. Therefore, the dehydration process is highly important to reduce the water content to less than 22% to halt the fermentation process in the *kelulut* honey. Nevertheless, the dehydration process has its own risk, it had been known that prolonged heating at elevated temperature has adverse effects on the quality of *kelulut* honey. In this study, a dehydration process was applied using indirect heating system to achieve a reduction of water content below 22% adhering to MS 2683:2017. The results have shown that for the lowest capacity of 1 kg *kelulut* honey, a reduction of water content below 22% was achieved in 2 hours while the highest capacity of 30 kg *kelulut* honey took 15 hours to achieve the reduction of water content below 22%. Finding from this study will benefit the small-scale *kelulut* breeders to prolong the *kelulut* honey shelf life via dehydration process.

Keywords *Kelulut* honey · Water content · Dehydration process · Shelf life

1 Introduction

A significant difference between honey produced from stingless bee meliponini or known as *kelulut* in Bahasa Melayu with the honey of honeybee *Apis mellifera* is higher water content, higher acidity and lower diastase activity [1]. Lockhead's study as cited by Subramanian et al. [2] reported that high water content is among the major challenge for tropical honey such as *kelulut* honey, the unprocessed honey containing

M. A. A. Muhammad · A. Amir (✉)

Department Manufacturing and Materials Engineering, , Kulliyah of Engineering, International Islamic University Malaysia, Kuala Lumpur, Malaysia

e-mail: adibah@live.iium.edu.my

A. R. A. Razak

My Iqra PLT, Selangor Fruit Valley, 45600 Rawang, Selangor, Malaysia

more than 20% water content readily undergoes fermentation. Almeida's study as cited by Martinez et al. [3] found the tropical humid made the water content in *kelulut* honey can be as high as 30%. This condition can cause fermentation to occur at ambient temperature because the liquid portion of the honey primarily consists of a concentrated mixture of fructose, acids and water, providing yeast with enough of an increase in the water percentage for growth and if the condition is prolonged can spoil the taste and texture of the *kelulut* honey, therefore reducing the quality. Therefore, *kelulut* honey is thermally treated to reduce water content for increasing shelf life and destroying spoilage microorganisms to prevent fermentation [2, 4]. A reduction in water content below 20% has been achieved after processing honey at 90 °C for 30 min [5], but this method is not suitable because at high-temperature caramelization of sugar will occur. Caramelization is an undesirable property in handling, processing and marketing. It also affects nutritional compositions that are lower in fat and protein [2, 5]. The heating temperature and duration must be controlled because overheating can result in product quality deterioration [4]. Overheating has been associated with increases in 5-hydroxymethylfurfural levels which resulted in darkening the honey's colouring and reducing its freshness [6]. The conventional heating process involves pre-heating to 40 °C, straining, filtering and indirect heating filtered honey at 60–65 °C for 25–30 min in a tubular heat exchanger followed by rapid cooling in order to protect its natural colour, flavour, enzyme content and other biological substance [7]. Other methods have been conducted to heat honey such as microwave, ultrasound and infrared to improve product quality [4].

In this study, an effective dehydration process for low capacity and medium capacity that utilized indirect heating method was applied to reduce the water content in *kelulut* honey from species *Heterotrigona Itama* below 22%.

2 Monofloral *Heterotrigona Itama*

The development of *kelulut* has recently become a popular source of income in Malaysia. *Heterotrigona Itama* is the most popular *kelulut* species for local *kelulut* breeders. It is contributed by the nature of *Heterotrigona Itama* which is a robust and easy adaptation to live in various habitats. This species is also known for its high disease resistance and ease of colony split [8]. The raw *kelulut* honey samples were collected from My Iqra PLT *kelulut* farm at Selangor Fruit Valley. The farm is a monofloral acacia mangium habitat for the *kelulut* species *Heterotrigona Itama*.

2.1 A Measure of Water Content

Nectar contains between 80 and 95% water and 5–20% sugar. As the bee carries nectar from the flower to the beehive colony, the sucrose component will be divided into two simple sugars. When the nectar is in the open cells, the working bees are supplied with

heat, which evaporates water in the nectar, resulting in pure sticky honey. According to Alimentarius Standard for Honey worldwide, the water content for Heather Honey (*Calluna*) and Clover Honey (*Trifolium*) must be less than 23%. For other honey, the water content must not exceed 21%. International Standard permissible level is 19% while the International Honey Commission and European Directive requirement is not more than 21% [9]. In 2017, the Malaysian Department of Standards established the standards of quality for *kelulut* honey, namely MS 2683:2017, according to this Malaysia Standard, the water content of an excellent grade processed *kelulut* honey should not exceed 22% [10].

3 Materials and Method

The components to set up the dehydration machine at a lower capacity (5 kg) were assembled using a temperature controller, dryer, cooler box, tray, chopstick, pressure pump, cooling fan, controller box and tube. Table 1 lists the specifications of each component.

3.1 Diagram of Dehydrator Machine Low Capacity

Figure 1 illustrated the schematic diagram of a low-capacity dehydration machine for 1, 3 and 5 kg capacity to perform the dehydration process for *kelulut* honey. All samples weight were measured using electronic scale 3SM M330 Series capacity 30 kg \times 1 g. The raw harvested *kelulut* honey sample was placed inside the cooler box, sucked into the tube by the pressure pump and pumped out of the cooler box. The *kelulut* honey will be pumped into the inclined tray and flows slowly to the bottom of the cooler box. A dryer supplied heat into the cooler box during the dehydration process. The cooling fan will maintain the temperature from overheating. The *kelulut* honey will flow onto the inclined tray continuously until the water content percentage has been reduced lower than 22%.

Table 1 List of components and specifications to assemble dehydration machine low capacity

No	Item	Specifications
1	Dryer power	1400 W
2	Dryer temperature	40–55 °C
3	Cooler box weight	10 kg
4	Pump power	72 W
5	Pump voltage	12 V
6	Cooling fan power supply	5v/0.5 A

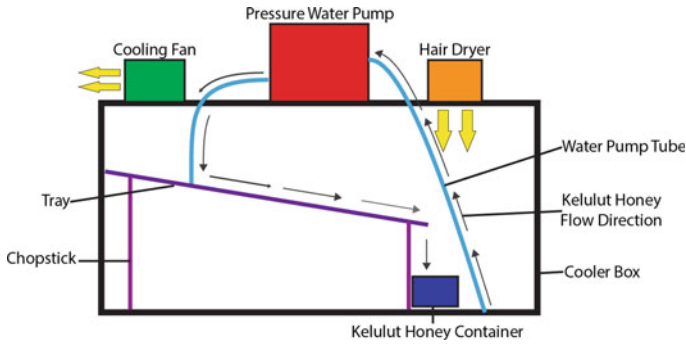


Fig. 1 Schematic diagram of low-capacity dehydration machine for 5 kg load

3.2 Diagram of Dehydrator Machine Medium Capacity

Figure 2 illustrated the schematic diagram of the medium capacity dehydration machine for 20 and 30 kg capacity to perform the dehydration process for *kelulut* honey. After the temperature is fixed at 40 °C, the stirring blade will rotate at a medium rate to ensure *kelulut* honey inside the container is uniformly stirred without spillage. Evaporated water from the *kelulut* honey will be absorbed by the humidifier to fasten the water absorption process. Excessive water will be stored in the water tank outside the dehydrator machine.

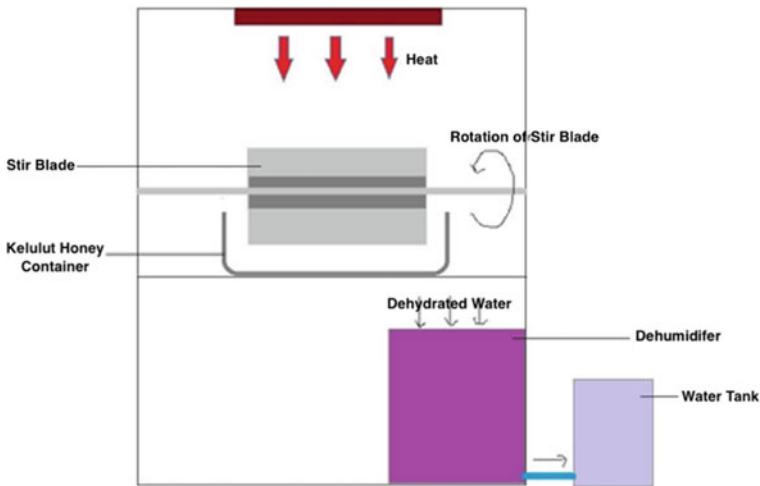


Fig. 2 Schematic diagram of medium capacity dehydration machine for 30 kg load

Table 2 Water content of *Heterotrigona Itama kelulut* honey before and after dehydration process

Capacity sample (kg)	Initial mass (kg)	Unprocessed water content (%)	Final mass (kg)	Final water content (%)	Time taken (Hours)
1	1.203	26.9	1.199	20.5	2
3	3.264	27.2	2.889	20.1	4
5	5.025	28.1	4.597	20.1	7
20	20.076	28.4	17.236	20.8	12
30	30.023	27.1	26.600	20.5	15

4 Results and Discussions

The findings from this study demonstrated that the dehydration process of *Heterotrigona Itama kelulut* honey can be successfully performed using indirect heating system. Table 2 showed as the capacity of the sample increased, a longer time was needed to reduce water content below 22%. It can be seen from Table 2, that for 1 kg of raw *Heterotrigona Itama kelulut* honey, it only took two hours to reduce the water content from 26.9% to 20.5% at a temperature below 45 °C. A sample of 3 kg has higher harvested water content, that is 27.2% while a sample of 5 kg has harvested water content of 28.1%. Respectively, it took 4 h and 7 h to complete the dehydration process at the same heating temperature. This result agrees with a previous study that suggested the best heating temperature for reduction of water content is between 40 and 60 °C. The same study found that at a higher temperature of 80 and 100 °C, for a duration between 3 and 5 hours, the diastase number in honey had reduced significantly [11]. Diastase number is an important indication of honey freshness. Mishandling in the thermal treatment process and poor storage may damage the honey since the activity of the enzyme decreases with the time of storage and heat level [3].

Figure 3 showed the longest time to reduce water content is for a sample of 30 kg, the dehydration process was completed after 15 hours to reduce the water content from 27.1% to 20.5%. This is because honey absorbs water easily from the air, especially in a tropical climate that has high humidity, it is difficult to harvest high-quality *kelulut* honey with low water content [12].

5 Conclusion

The significance outcome of this study demonstrated a green process that applies indirect heating method to reduce the water content of *kelulut* honey below 22% adhering to MS 2683:2017 to prolong the *kelulut* honey *Heterotrigona Itama* shelf life because without sufficient water content the fermentation process will stop.

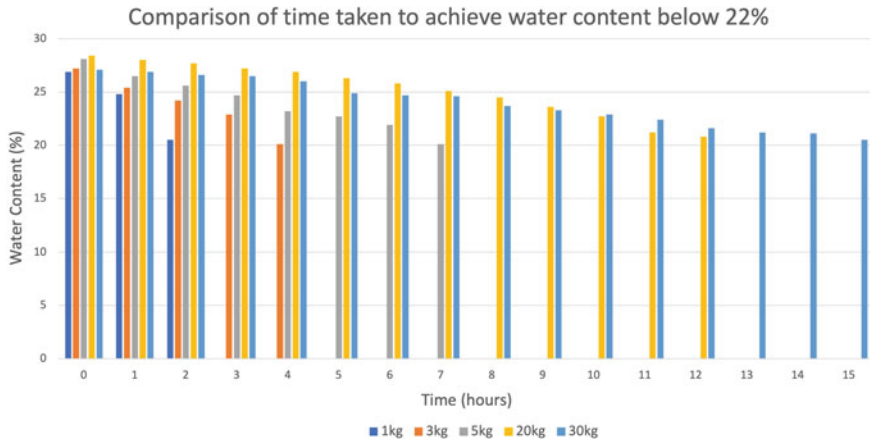


Fig. 3 Comparison of time taken to achieve water content below 22%

Acknowledgements The authors are thankful to My Iqra PLT for providing the samples and facilities to conduct this study.

References

1. Chong KY, Chin NL, Yusof YA (2017) Thermosonication and optimization of stingless bee honey processing. *Food Sci Technol Int* 23(7):608–622
2. Subramanian R, Hebbar HU, Rastogi NK (2007) Processing of honey: a review. *Int J Food Prop* 10(1):127–143
3. Martinez RA, Schvezov N, Brumovsky LA, Pucciarelli Roman AB (2018) Influence of temperature and packaging type on quality parameters and antimicrobial properties during Yatei honey storage. *Food Sci Technol Campinas* 38(Suppl. 1):196–202
4. Singh I, Singh S (2018) Honey moisture reduction and its quality. *J Food Sci Technol* 55(10):3861–3871
5. Chua LS, Adnan NA, Abdul-Rahaman N, Sarmidi MR (2014) Effect of thermal treatment on the biochemical composition of tropical honey samples. *Int Food Res J* 21:773–778
6. Han Z, Cai MJ, Cheng JH, Sun DW (2019) Effects of microwave and water bath heating on the interactions between myofibrillar protein from beef and ketone flavour compounds. *Int J Food Sci Technol* 54(5):1787–1793
7. Wakhle DM, Phadke RP (1995) Design for honey processing unit part I. *Indian Bee J* 57:144–146
8. Japar F, Mohd Sani Z, Reawrd NF, Yaakop S (2020) Pembangunan teknik penghasilan ratu kelulut secara massa dengan kaedah in vitro. *Buletin Teknologi MARDI (21) Khas Agrobiodiversiti* 59–70
9. Bogdanov S, D'Arcy BR, Mossel B, Marcazzan GL (1999) Honey quality and international regulatory standards: review by the international honey international honey standards are specified in a European honey. *Bee World* 80(2):61–69
10. Department of Standards Malaysian (2017) MS2683: 2017 Kelulut (Stingless bee) honey—specification. SIRIM Berhad Malaysia, Kuala Lumpur

11. Cozmuta AM, Cozmuta LM, Varga C, Marian M, Peter A (2011) Effect of thermal processing on quality of polyfloral honey. *Rom J Food Sci* 1(1):45–52
12. Abdullah I, Gary SR, Marla S (2007) Field trial of honey bee colonies bred for mechanisms of resistance against varroa destructor. *Apidologie* 38(July):67–76

The Future Directions of IBS Prefabrication Implementation in the Construction Industry



Hassan Ismail, Suaathi Kaliannan, and Mohd Ruzi Hamzah

Abstract Prefabrication in construction industry are defined as construction technique in which components are manufactured in a controlled environment (on or off site), transported, positioned and assembled into a structure with minimal additional site works. The adoption of prefabrication technology is a significant step toward a more sustainable construction process in the global industry. However, issues arise during implementation of this prefabrication technique, which currently underutilised in construction projects, as well as failures in construction due to poor quality and increased cost of construction. This study was conducted to examine the perceptions of the prefabrication practitioners in Malacca such as client, contractor and consultant in terms of quality, effectiveness and costing. A survey was conducted and 94 sets of questionnaire were analysed through Statistical Package for the Social Sciences (SPSS). Findings indicated that prefabrication technique assist firms in achieving their sustainable construction goals such as faster completion of construction project due to the usage of standard prefabricated components (effectiveness), less construction waste generation (cost) and quality of material (quality). This study implies that sustainable construction could be achieved by adopting the prefabrication technique compared to the conventional method.

Keywords Prefabrication · Industrialized building system (IBS) · Benefits · Future expectations · IBS application · Construction projects

H. Ismail

Department of Civil Engineering, Politeknik Merlimau, Karung Berkunci 1031 Pejabat Pos, 77300 Melaka, Malaysia

S. Kaliannan (✉)

School of Science and Technology, Wawasan Open University, 54, Jln Sultan Ahmad Shah, 10050 George Town, Pulau Pinang, Malaysia

e-mail: suaathik@wou.edu.my

M. R. Hamzah

Kolej Komuniti Selayang, Persiaran Pegawai, KM 16 Jalan Ipoh, 68100 Batu Caves, Selangor, Malaysia

1 Introduction

Prefabrication is a terminology used in the construction industry to depict components that are fabricated under processing factory conditions and thereafter transported to the construction site [1]. Adequate and affordable housing provision is a global problem challenging emerging economies and established economies, such as Malaysia. Prefabrication or industrialisation of construction is offered as one of the primary approaches to reduce the cost of delivering affordable housing. Further, building and construction industry likewise has significant energy, carbon, water, materials, waste and other environmental impacts. Prefabrication has been found to provide improved environmental outcomes in addition to having several other benefits, such as time, cost, construction quality, on-site safety and productivity. Although in the established markets such as Japan, Austria, Germany, Sweden and other European countries, the share of prefabrication in overall construction output remains strong, in many countries, including Australia, it still remains in its infancy [2].

Prefabrication is not a new construction technology in the global perspective, it is still uncommon in Malaysia's building construction industry due to various of factors [3]. The Malaysian construction industry is currently undergoing a transitional change from an industry employing conventional technology to more systematic and mechanised system. The new mechanised system is known as IBS (Industrialised Building System) or prefabricated method [4]. Prefabrication process was defined as a fabricated home one having walls, partitions, floors, ceiling and roof composed of sections of panels varying in size have been fabricated in a factory prior to erection on the building foundation [5].

2 Current IBS Approach in Malaysia

Malaysia considers the construction industry as one of the main contributors for the country's Gross Domestic Product (GDP) (Table 1).

In view of that, Malaysian Government proposed a new strategy through industrialization technology called Industrialized Building System (IBS) [10]. Construction of a project employing pre-fabrication may be finished in half the time it would take using typical construction methods; what should take 36 months can be completed in 18 months. Despite the fact that IBS has been around for 40 years, with well documented benefits and strong support from the Government, the pace of implementation and usage of IBS is still modest and falls short of the government's aim [11]. The application of IBS is to address the problem of high demand of housing in Malaysia. Malaysia's housing project has made a substantial contribution to the building industry and the country's economic growth [7].

Table 1 Factors of IBS application in Malaysia

Factors	Explanation
Quality, safety and professionalism	IBS should be approached as a holistic process rather than a set of technological solutions [6]. One of the main barriers of IBS implementation in the Malaysian construction industry is related to poor integration among stakeholders during the design stage [7]
Productivity	IBS involves prefabrication and installation of components at the construction site [8]. BIM is a process of producing and managing construction project information throughout the lifecycle of the project. BIM + IBS have proven to be productive and efficient for a construction project
Encourage the adoption of new technology	By using machines to develop components and other materials and then transferring them to the job site, the number of workers required is substantially decreased. Because the nature of construction necessitates the presence of a large number of personnel on-site [9]
Risk management in IBS	Technical and quality concerns in IBS generate aesthetic and practical flaws in completed buildings, including as cracks, blemishes, moisture infiltration, and inadequate thermal insulation. To mitigate such risks, a credible and effective risk management plan must be developed
Lack of expertise	Lack of competence is viewed as a major impediment to the construction of industrialised buildings. Wai et al. [9] and Mohd Nawi et al. [10] found that lack of expertise may result in severe conflicts between manufacturers and designers in the initial stage, failures in the production stage, and delays in delivering components to the construction site and in the erection schedule

3 Methodology

In order to acquire valid and relevant data, this study used three approaches. The following are the approaches: i. Distribution of questionnaires ii. Review of literature. The dissemination of questionnaires is a method of determining current awareness of IBS adoption. In a nutshell, the quantitative approach is a systematic method of presenting questions in which respondents are required to complete the questionnaire by selecting one or more questions from a list of options.

4 Results and Discussion

Respondents in this survey include all contractors, consultants, and clients involved in construction in the state of Malacca. Data was collected through email. A total of 200 sets of questionnaires were prepared and distributed to all the construction stakeholders as stated above. Only 47% (94) of questionnaires distributed were returned. The returned questionnaires were analysed using Statistical Package for Social Science (SPSS) version 21.0. Section 1 is divided into 7 parts which includes sector, role in company, qualification, working experience, project type and residential building.

5 Respondents' Background

Table 2 shows the majority of the respondents are contractor which represents 84% of total respondents. In reference of their working experience in construction industry, majority of respondents have 5–10 years' experience which is approximately 36.2% of respondents. On the other hand, 35.1% of the respondents hold position as project managers in the company.

Figure 1 shows the mean value the effectiveness of prefabricated construction method implementation in Malaysia.

Table 2 Respondents nature of business, experience and designation

Characteristics	Classification	Frequency	Percentage (%)
Nature of business	Contractor	79	84
	Client	7	7
	Consultant	8	9
Working experience	< 5 years	29	31
	5–10 years	34	36
	11–20 years	21	22
	> 21 years	10	11
Profession	Director	16	17
	Engineer	15	16
	Project Manager	33	35
	Others	30	32
Types of construction project	Residential	22	23
	Non-residential	11	12
	Industrial	6	6
	Social and amenities	22	23

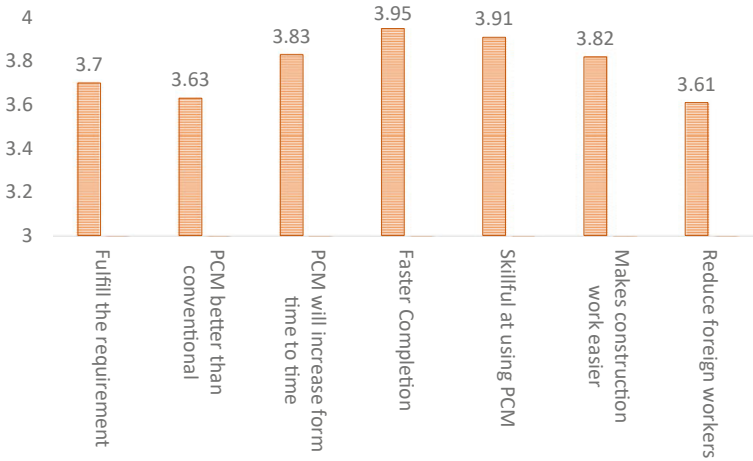


Fig. 1 Effectiveness of prefabricated construction method implementation in Malaysia

The mean value is around 3.61–3.95. Overall, respondents agreed that prefabrication technology resulted in speedier construction project completion due to the use of standard prefabricated components, with the mean value of 3.95 being the highest. Though some of them consider that the prefabrication construction method, with its lowest mean value of 3.61, is still unable to decrease the need for foreign employees as the contractor cannot afford to pay the salary for high-demand local workers [9].

Figure 2 indicates that respondents consider specialised imported machinery and equipment, as well as the necessity for capital investments, to be the most significant hurdles to the use of the prefabrication method in construction.

Fortunately, there is another advantage to using the prefabrication method, which is that respondent agreed it will produce less construction waste, resulting in lower waste management costs, as it states the same highest value of 3.85 in this section because the cost of investment for specialised imported equipment and machineries is high, respondents could presume it will produce less construction waste. Considering the effects of imported equipment and machineries as well as producing less building waste are interrelated, the question for both has the same highest mean. According to Fig. 3, the greatest mean value is 3.82, indicating that respondents agreed that the prefabrication approach can boost the pace and quality of the construction project.

The average range is between 3.36 and 3.82. More than half of respondents did not agree nor strongly agreed that the work of modifying is simple. Respondents believe that prefabricated building renovations are difficult to complete. The majority of them agree that prefabrication installation methods save time on the job site, resulting in higher material quality and greater efficiency during construction.

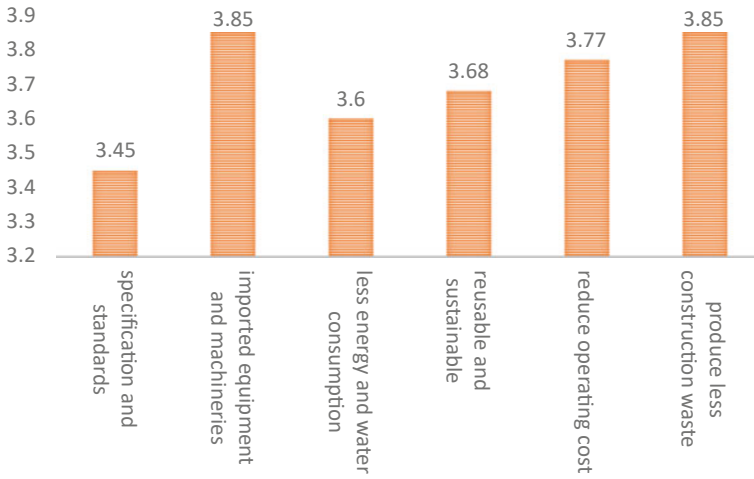


Fig. 2 Efficiency of prefabrication construction method compared to traditional methods in terms of costs

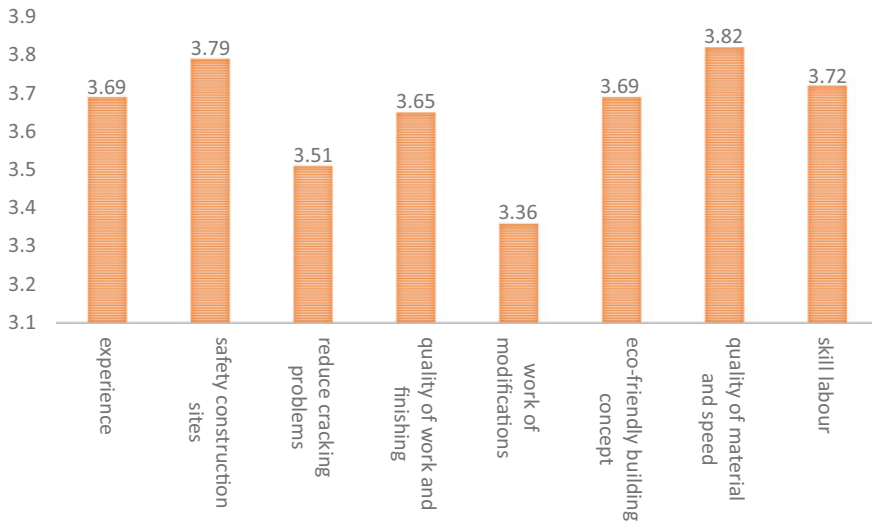


Fig. 3 Quality of prefabrication construction method

6 Conclusions

The comparatively low level of productivity and poor quality highlight the necessity for industry to adopt new technology and techniques in order to improve

Malaysia's construction sector. Positive consequences include a more skilled workforce, increased productivity, and a reduction in low-skilled workers, all of which contribute to greater end-product quality.

Hence, the government should expose the concept of prefabrication to contractors such as holding a seminar about prefabrication construction technology.

The incorporation of innovative manufacturing technology into the prefabrication process will not only boost productivity, but will also provide employees with a safer work environment, a stable work location, long-term growth prospects, and career advancement. Malaysia is currently experiencing issues with labour quality and retention. The increasing demand highlights the importance of preparing a multi-skilled work force for this industry. Prefabrication training available to locals in order to limit the use of foreigners and to give locals the opportunity to participate in constructions when there aren't enough locals to serve as general workers in the country.

The government should increase modular prefabrication production because Malaysia now has 257 factories producing modular prefabrication, which is insufficient to boost prefabrication implementation in Malaysia construction. The findings of this study assist readers comprehend the current state of prefabrication implementation compared to conventional construction method, impacts on the construction industry's long-term development, promotion initiatives, and future research directions. The study adds to the corpus of information as well as the many stakeholders.

References

1. Baghchesaraei A, Kaptan MV, Baghchesaraei OR (2015) Using prefabrication systems in building construction. *Int J Appl Eng Res* 10(24):44258–44262
2. Dave M, Watson B, Prasad D (2017) Performance and perception in prefab housing: an exploratory industry survey on sustainability and affordability. *Procedia Eng* 180:676–686
3. Jaffar Y, Lee CK (2020) Factors influencing industrialized building system (IBS) project performance: a systematic review. *J Gov Integrity* 3(2)
4. Pawar SR, Dhongade RR, Waje VV, Pande SM, Jadhav VS, Sangale YB (2017) Ibs as a sustainable building construction and management. *Int Res Adv Sci Eng* 6(3)
5. Arditi D, Ergin U, Günhan S (2000) Factors affecting the use of precast concrete systems. *J Archit Eng* 6(3):79–86
6. Azman MNA, Ahamad MSS, Hussin WMAW (2018) Comparative study on prefabrication construction process. *Int Surveying Res J* 2(1), 45–58. *IBS DIGEST, MIIIE 2018 Highlight. Issue 1. CIDB Malaysia*
7. Kamar KA, Azman MNA, Mohd Nawi MN (2014) IBS survey 2010: drivers, barriers and critical success factors in adopting industrialised building system (IBS) construction by G7 contractors in Malaysia. *J Eng Sci Technol* 9(4):490–501
8. Polat G (2008) Factors affecting the use of precast concrete systems in the United States. *J Constr Eng Manage-ASCE* 134(3):169–178

9. Wai FC, Mohd Amir Shazwan H, Abdolreza T (2018) Foreign workers reduction in Malaysian construction industry. *Int J* 2(8)
10. Mohd Nawi MN, Anuar HS, Lee A (2013) A review of IBS Malaysian current and future study. *Int J Eng Res Technol* 2(10):2378–2383
11. Le LJ, Zainal R (2021) The study of industrialized building system (IBS) implementation in terrace housing project. *Res Manag Technol Bus* 2.1:763–775

Effect of Zirconia Doping on the Sintering and Mechanical Properties of Hydroxyapatite Bioceramic



S. Sivakumar, C. H. C. Alexander, H. L. Teow, M. Yeakub Ali, and S. Ramesh

Abstract In the present study, varying amounts of zirconia (ZrO_2) (1, 2, 3 and 5 wt%) was doped with hydroxyapatite (HA) and their sintering behaviour was evaluated. A simple wet precipitation method was used to produce the HA and ZrO_2 powders. The ZrO_2 powder was added to the HA powder via a ball milling process. Green samples were prepared by powder pressing technique and pressureless sintered for 2 h at 750 °C, 1050 °C and 1250 °C. The Volume Fraction Porosity (VFP), Young's modulus and microhardness of sintered samples were measured. It was found that sample containing 1 wt% ZrO_2 sintered at 1250 °C exhibited the highest Young's modulus of 100 GPa and microhardness of 2.78 GPa, corresponding to the lowest VFP.

Keywords Zirconia · Hydroxyapatite · Sintering · Mechanical properties

1 Introduction

HA with chemical formula $Ca_{10}(PO_4)_6(OH)_2$ is a naturally occurring calcium phosphate mineral. The ratio of Ca/P in HA is 1.67 which is comparable to that of human bones which varies from 1.3 to 2.0 [1]. This makes implants and fillers manufactured from HA is biocompatible and bioactive [2]. Furthermore, HA is the only apatite

S. Sivakumar (✉) · C. H. C. Alexander
School of Engineering, Asia Pacific University Technology and Innovation, Jalan Teknologi 5,
Taman Teknologi Malaysia, 57000 Kuala Lumpur, Malaysia
e-mail: siva.kumar@staffemail.apu.edu.my

H. L. Teow
Taylor's University, No.1, Jalan Taylors, 47500 Subang Jaya, Selangor, Malaysia

M. Y. Ali · S. Ramesh
Faculty of Engineering, Universiti Teknologi Brunei, Tungku Highway, Gadong 1410, Brunei Darussalam

S. Ramesh
Department of Mechanical Engineering, Faculty of Engineering, Center of Advanced Manufacturing and Materials Processing, University of Malaya, 50603 Kuala Lumpur, Malaysia

member that is stable when it encounters human tissues. Unfortunately, owing to its low mechanical properties like fracture toughness and tensile strength [3], HA cannot largely and directly be used in biomedical field as transplant material in areas where large stress is applied like in hip joints. It is confined to areas where high stress is not needed like the auditory ossicles' fine bones in the middle ear and as implant materials to enhance bone growth [4].

Many studies have shown that proper control of material processing conditions including the use of dopants or additives could play a role in enhancing the properties of the material, enable the production of desired microstructure during sintering, joining or welding, and in the tailoring of projected microstructure-properties relationship for a host of engineering and biomedical applications [5–19].

For biomedical application, to capitalize the full potential of HA for bone related transplant materials, the mechanical characteristics of HA implants could be improved by doping with selective sintering additives without compromising the overall biocompatibility and bioactivity properties. On this note, zirconia (ZrO_2) ceramic has gained much interest as a dopant as it possesses high fracture toughness, high strength and are bioinert [20]. The major challenge, however in producing HA- ZrO_2 composites is that, the ZrO_2 normally requires high sintering temperature ($>1500\text{ }^\circ\text{C}$) [21] to fully densify which in turn would destabilise the HA phase to form α -tricalcium phosphate (α -TCP), β -tricalcium phosphate (β -TCP) and calcium phosphate (CaO) [22]. In this work, low-temperature sintering of HA containing small amounts of ZrO_2 as dopants were studied.

2 Methodology

HA was prepared by precipitation of calcium nitrate tetrahydrate with diammonium hydrogen phosphate at Ca/P ratio of 1.67, above pH of 10 [23]. The solution was stirred for 3 h at $60\text{ }^\circ\text{C}$ and let to settled for 24 h. This was followed by filtration to remove the precipitate. The HA was then washed and centrifuged to remove any residues. The remaining powder was then dried for 24 h at room temperature then calcined at $600\text{ }^\circ\text{C}$ for 4 h. Zirconium oxychloride was dissolved in distilled water and the transparent solution was mixed with dropwise ammonia solution [24, 25]. The precipitate was then let to settled for 24 h at room temperature, and then centrifuged at 8000 rpm. Pure zirconium dioxide was formed, and it was calcined at $600\text{ }^\circ\text{C}$ for 6 h to produce monoclinic zirconia. Various amount of ZrO_2 (1, 2, 3 and 5 wt%) was mixed with the HA powder via ball milling technique.

Fluid displacement method was applied to determine the volume fraction porosity (VFP) of the sample. First the dimensions of the sample were measured to calculate the bulk volume, V_b . Then the dry weight, W_d of the sample is measured in air. This is followed by vacuum saturation with water to ensure water fills up all the pore spaces and no air is trapped in the sample. The sample was measured again to obtain its saturated weight, W_s . Therefore, weight of water, W_w in pore spaces is given by $W_w = W_s - W_d$. To calculate the pore volume, V_p , Eq. (1) was used.

$$V_p = \frac{Ww}{\rho w} \quad (1)$$

where ρ_w is density of water since water was used as the soaking medium. The VFP was calculated by the Eq. (2).

$$VFP = \frac{Vp}{Vb} \quad (2)$$

Young's modulus was determined by using ultrasonic pulse-echo technique [26]. The hardness of all the samples were determined by using Vickers Hardness method. In this study, sintered samples were indented with a load varying from 80 to 120 N for 10 s. The surface characteristics of all the samples were investigated by using Philips XL30 scanning electron microscope (SEM).

3 Result and Discussion

Figure 1a indicates that the VFP increases with decreasing temperature regardless of dopant additions. All samples sintered at 750 °C showed the highest VFP with the maximum value of 0.54 was obtained for 5 wt% ZrO₂ addition. The lowest VFP of 0.10 was recorded for sample containing 1 wt% ZrO₂ sintered at 1250 °C. These results shows that sintering temperatures of 750 °C and 1050 °C are insufficient for densification [27]. These temperatures are still low for Ca²⁺ to be extracted from HA matrix by ZrO₂ which explains poor level of densification. At 1250 °C, Ca²⁺ of HA matrix diffuses well into ZrO₂ which causes VFP to be reduced.

An opposite trend was observed for the Young's modulus of HA as shown in Fig. 1b. It was noted that the higher sintering temperature, the higher is the Young's modulus and this can be associated with improved densification. The 1 wt% ZrO₂,

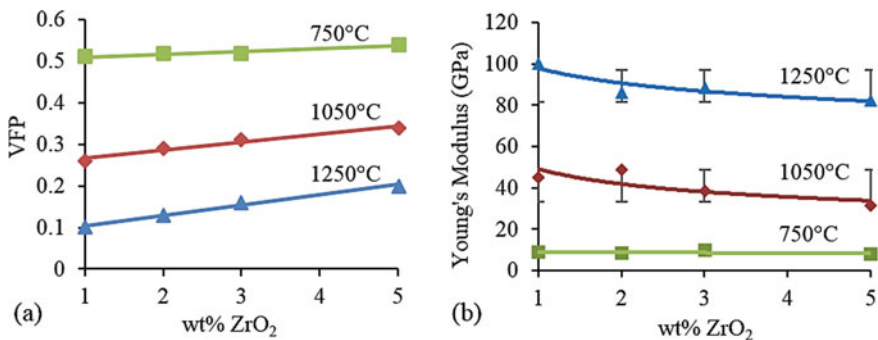
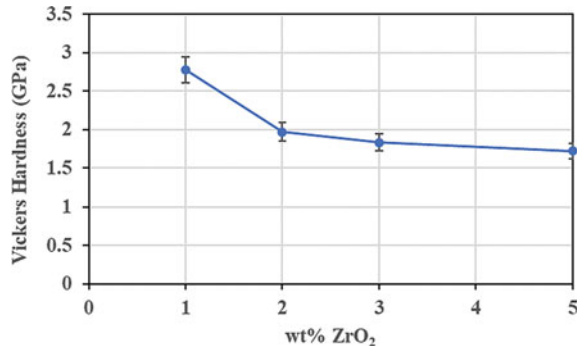


Fig. 1 Effect of zirconia content on **a** VFP and **b** Young's modulus of HA sintered at various temperatures

Fig. 2 Vickers hardness variation for samples sintered at 1250 °C



having a VFP of 0.10 at 1250 °C resulted in the highest modulus value of 100 GPa. At 750 °C, the Young's modulus remain low for all samples where densification did not take place. For temperatures 1050 °C and 1250 °C, the modulus decreases with increasing ZrO₂ content. This decrease could be mainly due to well exchange of Ca²⁺ and ZrO²⁺ ions between HA and ZrO₂ that causes decomposition of HA [28, 29].

As for the Vickers hardness (H_v), it was found that the highest value of 2.78 GPa was obtained for sample containing 1 wt% ZrO₂ sintered at 1250 °C as shown in Fig. 2. In general, all samples sintered at 1250 °C recorded higher H_v (> 1.5 GPa) compared to other samples. A declining hardness trend was noted for samples containing above 1 wt% zirconia which correlates with the increase in the VFP [30]. In general, the higher the VFP value, the lower the density and mechanical properties.

The Microstructural development of ZrO₂-doped HA sintered at 1250 °C is shown in Fig. 3.

The SEM result clearly shows the presences of equiaxed HA grain structure and that the porosity increases with the amount of ZrO₂ content. This was also accompanied by a reduction in the HA grain size as depicted in Fig. 3d for the 5 wt%-doped HA sample. The higher percentage of zirconia could have hindered full densification by disrupting the Ca²⁺ and PO₄³⁻ ions diffusion in the HA matrix [25].

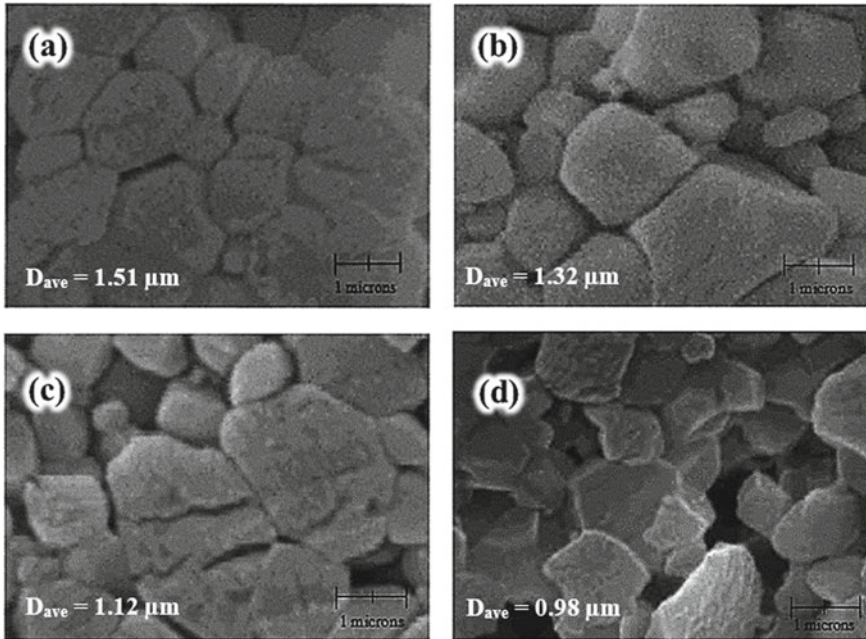


Fig. 3 Microstructural development of HA samples sintered at 1250 °C containing various amounts of ZrO₂: **a** 1 wt% **b** 2 wt% **c** 3 wt% and **d** 5 wt% (Mag. = × 10,000)

4 Conclusions

The effect of small amounts of ZrO₂ up to 5 wt% on the sintering properties of HA was investigated. The HA containing 1 wt% ZrO₂ sintered at 1250 °C showed desirable Young's modulus and hardness of 100 GPa and 2.78 GPa, respectively. Sintering temperatures of 750 °C and 1050 °C were insufficient to cause densification whereas increasing amount ZrO₂ resulted in higher porosity and lower HA grain size.

References

1. Gillman CE, Jayasuriya AC (2021) FDA-approved bone grafts and bone graft substitute devices in bone regeneration. *Mater Sci Eng, C* 130:112466
2. Hench LL (1998) Bioceramics. *J Am Ceram Soc* 81:1705–1728
3. Shamami DZ, Sayed MR, Mohsen S (2022) Characterization of magnesium-hydroxyapatite functionally graded composites prepared by rapid microwave sintering technique. *Ceram Int* 48(9):12641–12653
4. Wang Z, Zhang L, Zhang R, Wang M (2022) Design and fabrication of hydroxyapatite-carbon nanotubes-wood derived carbon composites. *Mater Lett* 315:131974
5. Ramesh S, Sara Lee KY, Tan CY (2018) A review on the hydrothermal ageing behaviour of Y-TZP ceramics. *Ceram Int* 44:20620–20634

6. Duraisamy N, Numan A, Ramesh K, Choi K-H, Ramesh S, Ramesh S (2015) Investigation on structural and electrochemical properties of binder free nanostructured nickel oxide thin film. *Mater Lett* 161:694–697
7. Bowen C, Ramesh S, Gill C, Lawson S (1998) Impedance spectroscopy of CuO-doped Y-TZP ceramics. *J Mater Sci* 33:5103–5110
8. Manladan SM, Yusof F, Ramesh S, Zhang Y, Luo Z, Ling Z (2017) Microstructure and mechanical properties of resistance spot welded in welding-brazing mode and resistance element welded magnesium alloy/austenitic stainless steel joints. *J Mater Process Technol* 250:45–54
9. Ramesh S, Zulkifli N, Tan CY, Wong YH, Tarlochan F, Ramesh S, Teng WD, Sopyan I, Bang LT, Sarhan AAD (2018) Comparison between microwave and conventional sintering on the properties and microstructural evolution of tetragonal zirconia. *Ceram Int* 44:8922–8927
10. Sampath Udeni Gunathilake TM, Ching YC, Chuah CH, Illias HA, Ching KY, Singh R, Nai-Shang L (2018) Influence of a nonionic surfactant on curcumin delivery of nanocellulose reinforced chitosan hydrogel. *Int J Biol Macromol* 118:1055–1064
11. Francis KA, Liew C-W, Ramesh S, Ramesh K, Ramesh S (2016) Ionic liquid enhanced magnesium-based polymer electrolytes for electrical double-layer capacitors. *Ionics* 22:919–925
12. Ramesh S, Amiriyani M, Meenaloshini S, Tolouei R, Hamdi M, Purboloksono J, Teng WD (2011) Densification behaviour and properties of manganese oxide doped Y-TZP ceramics. *Ceram Int* 37:3583–3590
13. Azim Jais A, Muhammed Ali SA, Anwar M, Rao SM, Muchtar A, Wan Isahak WNR, Tan CY, Singh R, Brandon NP (2017) Enhanced ionic conductivity of scandia-ceria-stabilized-zirconia (10Sc1CeSZ) electrolyte synthesized by the microwave-assisted glycine nitrate process. *Ceramics Int* 43:8119–8125
14. Misran H, Singh R, Yarmo MA (2008) Nonsurfactant route of fatty alcohols decomposition for templating of mesoporous silica. *Microporous Mesoporous Mater* 112:243–253
15. Barzani MM, Sarhan AAD, Farahany S, Ramesh S, Maher I (2015) Investigating the machinability of Al-Si-Cu cast alloy containing bismuth and antimony using coated carbide insert. *Measurement* 62:170–178
16. Yeo WH, Fry AT, Purboloksono J, Ramesh S, Inayat-Hussain JI, Liew HL, Hamdi M (2014) Oxide scale growth and presumed exfoliation in a 700 °C or higher steam condition: a simulation study for future operations of ultra-supercritical power plants. *J Supercrit Fluids* 92:215–222
17. Ching YC, Gunathilake TMSU, Chuah CH, Ching KY, Ramesh S, Liou N-S (2019) Curcumin/Tween 20-incorporated cellulose nanoparticles with enhanced curcumin solubility for nano-drug delivery: characterization and in vitro evaluation. *Cellulose* 26:5467–5481
18. Yee YY, Ching YC, Rozali S, Hashim NA, Ramesh S (2016) Preparation and characterization of poly(lactic acid)-based composite reinforced with oil palm empty fruit bunch fiber and nanosilica. *BioResources* 11(1):2269–2286
19. Ramesh S, Gill C (2001) Environmental degradation of CuO-doped Y-TZP ceramics. *Ceram Int* 27(6):705–711
20. Yin L, Nakanishi Y, Alao AR, Song XF, Abduo J, Zhang Y (2017) A review of engineered zirconia surfaces in biomedical applications. *Procedia Cirp* 65:284–290
21. Sivakumar S, Singh R, Teow HL, Chuan YL, Leong JKC (2014) Effect of short time sintering on the mechanical properties of undoped zirconia ceramics. *Appl Mech Mater* 629:420
22. Pokhrel S (2018) Hydroxyapatite: preparation, properties and its biomedical applications. *Adv Chem Eng Sci* 8(4):225
23. Piconi C, Maccauro G (1999) Zirconia as a ceramic biomaterial. *Biomaterial* 20(1):1–25
24. Vassal MF, Nunes-Pereira J, Miguel SP, Correia IJ, Silva AP (2019) Microstructural, mechanical and biological properties of hydroxyapatite-CaZrO₃ biocomposites. *Ceram Int* 45(7):8195–8203
25. Curran DJ, Fleming TJ, Towler MR, Hampshire S (2010) Mechanical properties of hydroxyapatite-zirconia compacts sintered by two different sintering methods. *J Mater Sci Mater Med* 21(4):1109–1120

26. Ren F, Case ED, Morrison A, Tafesse M, Baumann MJ (2009) Resonant ultrasound spectroscopy measurement of Young's modulus, shear modulus and Poisson's ratio as a function of porosity for alumina and hydroxyapatite. *Phil Mag* 89(14):1163
27. Naga SM, Hassan AM, Awaad M, Killinger A, Gadow R, Bernstein A, Sayed M (2020) Forsterite/nano-biogenic hydroxyapatite composites for biomedical applications. *J Asian Ceram Soc* 8(2):373–386
28. Nayak Y, Rana RP, Pratihar SK, Bhattacharyya S (2008) Pressureless sintering of dense hydroxyapatite–zirconia composites. *J Mater Sci Mater Med* 19(6):2437–2444
29. Cao Y, Li C, Xia Y, Ren K, Zhu S (2022) Study on the fabrication and mechanical properties of HAp-3YSZ composites by flash sintering. *Ceram Int* 48(11):16300–16305
30. Panda S, Biswas CK, Subhankar P (2021) A comprehensive review on the preparation and application of calcium hydroxyapatite: a special focus on atomic doping methods for bone tissue engineering. *Ceram Int* 47(20):28122–28144

Properties of Alumina–Zirconia Composites Prepared by Slip-Casting Method



K. Y. Sara Lee, S. Ramesh, L. F. Siah, A. K. Nor Azmah, W. D. Teng, N. M. Mubarak, and D. Kurniawan

Abstract The effect of zirconia concentrations on the properties of alumina–zirconia composites prepared by slip-casting method was studied. Varying amounts of yttria-tetragonal zirconia (Y-TZP) ranging up to 90 vol.% were added in alumina and sintered at 1450 °C. The sintered composites were then characterised in terms of bulk density, microstructure, Vickers hardness and bending strength. The calculated prepared bulk density of the green cast composites correlated well with the experimental values. The results showed that sintered bulk density improved with the increase of zirconia content. It was also revealed that the addition of about 60 vol.% of zirconia had contributed to maximum hardness and strength, up to 12 GPa and 708 MPa, respectively.

Keywords Slip-casting · Alumina–zirconia composites · Vickers hardness

1 Introduction

Alumina–zirconia composites, which are also known as alumina toughened zirconia (ATZ) or zirconia toughened alumina (ZTA) have been widely studied over the

K. Y. Sara Lee (✉)

Center of Systematic Innovation Research, Department of Mechanical Engineering, Faculty of Engineering and Technology, Tunku Abdul Rahman University of Management and Technology, 53300 Kuala Lumpur, Malaysia
e-mail: leeky@tarc.edu.my

S. Ramesh · N. M. Mubarak · D. Kurniawan

Faculty of Engineering, Universiti Teknologi Brunei, Tungku Highway, Gadong 1410, Brunei Darussalam

S. Ramesh

Center of Advanced Manufacturing and Materials Processing, Department of Mechanical Engineering, Faculty of Engineering, University of Malaya, 50603 Kuala Lumpur, Malaysia

L. F. Siah · A. K. Nor Azmah · W. D. Teng

Ceramics Technology Centre, SIRIM Berhad, 40911 Shah Alam, Malaysia

decades for manufacturing, biomedical and odontology applications. The composites combine the advantages of zirconia (high toughness and strength) and alumina (high hardness and stiffness), which results in superior biocompatibility, esthetic, and improved mechanical properties [1–3].

According to Lange [4], the selection of processing method is important in governing the densification and flaws in the green composites. It has been revealed by many authors that proper control of material processing conditions including the use of dopants or additives, play a role in determining the properties of the material, enable microstructure modification during joining or welding, and in the tailoring of suitable microstructure-properties for a host of applications [5–19].

Over the years, alumina–zirconia composites have been successfully prepared by numerous synthesis techniques, including classical mechanical mixing [20, 21], sol-gels [22], slip-casting [23, 24], hydro/solvothermal synthesis, co-precipitation and other colloidal techniques [25, 26]. For potential orthopedic applications, two different alumina–zirconia composites, ZTA-30 (30 wt% zirconia) and ZTA-60 (60 wt% zirconia) were consolidated by slip-casting method and sintered at 1600 °C. A high flexural strength of 509 MPa was reported for ZTA-60, with a bulk density of 4.95 g/cm³, as compared to ZTA-30 (409.9 Mpa and 4.34 g/cm³) [25]. The effects of zirconia content and slip-casting on mechanical strength and properties of alumina–zirconia composites are important in the fabrication process for orthopedic applications. Hence, the present work aimed to investigate the sintering characteristics of alumina–zirconia composites produced by slip-casting. The composites were sintered at 1450 °C and characterised in terms of bulk density, microstructural evolution, Vickers hardness, and bending strength.

2 Materials and Methods

In this study, 3 mol% Ytria-Tetragonal Zirconia Polycrystal (Y-TZP) and Alumina (Al₂O₃) powder were used as the starting powder. This commercially available powder was manufactured by Kyoritsu Co. Ltd., Japan with a mean particle size of about 0.3 μm. The detail preparation of the slip has been reported elsewhere [23]. The Y-TZP content was varied from 0 (Al₂O₃) to 100% (Y-TZP) with increments of 10 wt%. In this study, rectangular bar samples (5 × 15 × 50 mm) were prepared by slip casting and green samples were sintered in air at 1450 °C for 2 h at a ramp rate of 5 °C/min.

The bulk densities of the sintered composites were computed by the immersion method. The sintered composites were polished up to 1 μm prior to characterisation. Phase analysis of the polished composites was conducted by X-ray diffraction (XRD), where Cu-Kα served as the radiation source. Vicker's indentation technique was employed on the polished composites for microhardness measurements. The indentation load of 10 N was applied to each sample and remained constant for 15 s. Ten measurements were recorded for each sample and the average microhardness was calculated. A universal testing machine was used to measure the bending strength

of the composites, with a span of 30 mm and cross-head speed of 0.5 mm/min. Subsequently, scanning electron microscopy (SEM) was employed to examine the microstructure of the composites.

3 Results and Discussion

The XRD patterns of the sintered slip-cast Al_2O_3 -Y-TZP composites identified X-ray traces that attributed to tetragonal zirconia and Al_2O_3 phases. Generally, relevant peaks of Al_2O_3 decreased with a concomitant increase in the intensity of the tetragonal peaks, as the Y-TZP matrix content increased. Figure 1 shows the bulk density of sintered composites at different Y-TZP content. No improvement in bulk density was observed for the composites at the low content of Y-TZP (0–10 vol.%). However, the densification of the composites was enhanced effectively with the subsequent addition of Y-TZP content above 15 vol.%. The current results reveal that richer zirconia content (>15 vol.%) had improved densification in the composites. A similar trend was also reported by other authors for alumina–zirconia composites with higher zirconia content [27].

Figure 2 illustrates the microstructures of the sintered composites comprising 5 and 50 vol.% Y-TZP content, respectively. The SEM micrographs reveal distinctive bi-phase and equiaxed grain structures, containing alumina (dark phase) and tetragonal zirconia (light phase). The sizes of alumina grains had significantly reduced with richer Y-TZP content in the composite system, which correlates with the previous work [23]. The uniform distribution of the secondary phase had also demonstrated the high degree of homogeneity produced by slip-casting technique. The improved microstructural uniformity was also observed in other studies for alumina–zirconia composites obtained through slip-casting method [24, 25].

The Vickers hardness of the sintered composites had improved with the contribution of Y-TZP content, as shown in Fig. 3. The enhancement of Vicker hardness

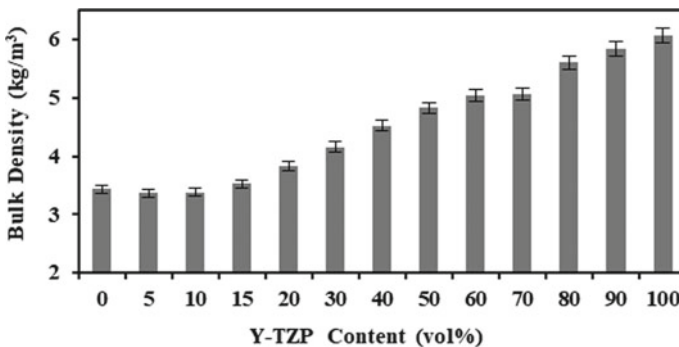


Fig. 1 Bulk density of sintered slip-cast Al_2O_3 -Y-TZP composites [23]

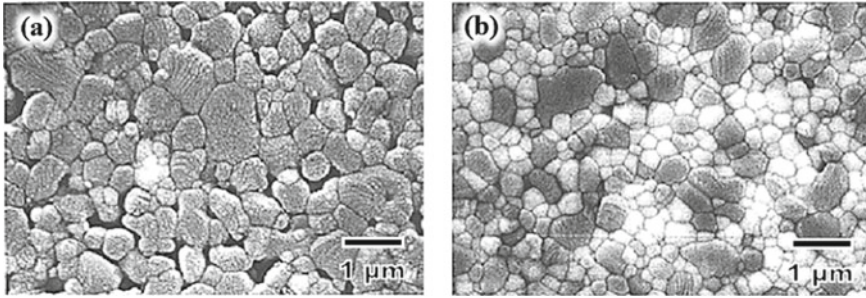


Fig. 2 Composites sintered at 1450 °C: **a** 5 vol.% Y-TZP and **b** 50 vol.% Y-TZP [23]. The brighter grain is zirconia and the darker is alumina

diminished once the value reached a maximum of about 12 GPa, for the composite comprising 60–70 vol.% Y-TZP. A similar trend was observed for the behaviour of bending strength as depicted in Fig. 4. Generally, maximum bending strength of about 708 MPa was achieved for the composite comprising 60 vol.% Y-TZP and the strength was maintained at about 500 MPa with the subsequent addition of Y-TZP. A similar observation was also reported for the composite comprising 60 wt% Y-TZP, where the flexural strength reached a maximum of 395 MPa [27]. In this study, the enhancement in bending strength could be attributed to the densification and homogeneity of microstructure produced by slip-casting technique.

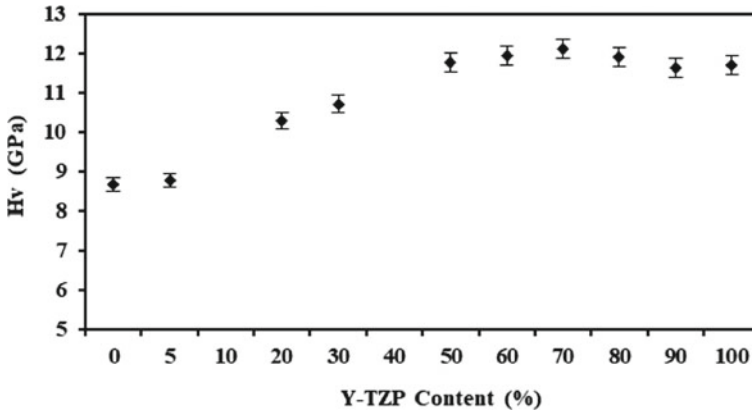


Fig. 3 Vickers hardness variations of Al_2O_3 —Y-TZP ceramics composite [23]

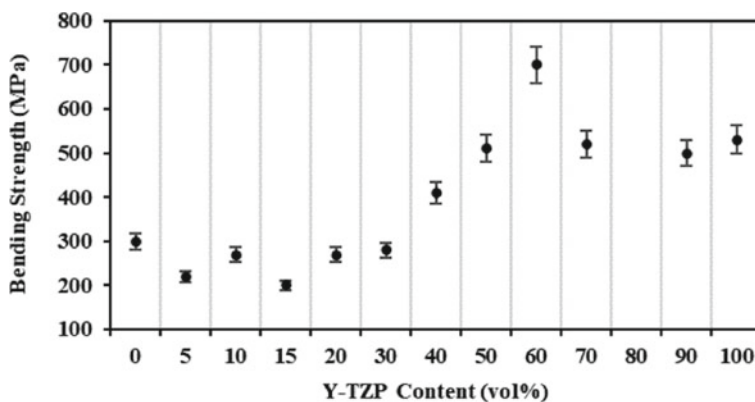


Fig. 4 Bending strength variations of Al_2O_3 —Y-TZP ceramics composite [23]

4 Conclusions

The current work had successfully demonstrated the viability of slip-casting technique in the fabrication of well-dispersed and homogeneous alumina–zirconia composite. The amount of Y-TZP addition had served as an important factor in governing the characteristics and properties of slip-cast composites. The bulk density in the composite system improved with the increase of Y-TZP content, which is directly dependent on the amount of retained tetragonal phase in the system. The current study also revealed a good correlation between Vickers hardness and bending strength, where maximum values were achieved for composites containing 60–70 vol.% of zirconia concentrations when sintered at 1450 °C.

References

1. Gautam C, Joyner J, Gautam A, Rao J, Vajtai R (2016) Zirconia based dental ceramics: structure, mechanical properties, biocompatibility and applications. *Dalton Trans* 45(48):19194–19215
2. Murti CFK, Maslakah U, Endarko E, Triwikantoro T (2022) Structural, physical and mechanical properties of zirconia-polymorph/alumina composites. *Mater Chem Phys* 285:126102
3. Magnani G, Fabbri P, Leoni E, Salernitano E, Mazzanti F (2021) New perspectives on zirconia composites as biomaterials. *J Compos Sci* 5(9):244
4. Lange FF (1983) Processing-related fracture origins: I, observations in sintered and isostatically hot-pressed $\text{Al}_2\text{O}_3/\text{ZrO}_2$ composites. *J Am Ceram Soc* 66(6):396–398
5. Ramesh S, Sara Lee KY, Tan CY (2018) A review on the hydrothermal ageing behaviour of Y-TZP ceramics. *Ceram Int* 44:20620–20634
6. Duraisamy N, Numan A, Ramesh K, Choi K-H, Ramesh S, Ramesh S (2015) Investigation on structural and electrochemical properties of binder free nanostructured nickel oxide thin film. *Mater Lett* 161:694–697
7. Bowen C, Ramesh S, Gill C, Lawson S (1998) Impedance spectroscopy of CuO-doped Y-TZP ceramics. *J Mater Sci* 33:5103–5110

8. Manladan SM, Yusof F, Ramesh S, Zhang Y, Luo Z, Ling Z (2017) Microstructure and mechanical properties of resistance spot welded in welding-brazing mode and resistance element welded magnesium alloy/austenitic stainless steel joints. *J Mater Process Technol* 250:45–54
9. Ramesh S, Zulkifli N, Tan CY, Wong YH, Tarlochan F, Ramesh S, Teng WD, Sopyan I, Bang LT, Sarhan AAD (2018) Comparison between microwave and conventional sintering on the properties and microstructural evolution of tetragonal zirconia. *Ceram Int* 44:8922–8927
10. Sampath Udeni Gunathilake TM, Ching YC, Chuah CH, Illias HA, Ching KY, Singh R, Nai-Shang L (2018) Influence of a nonionic surfactant on curcumin delivery of nanocellulose reinforced chitosan hydrogel. *Int J Biol Macromol* 118:1055–1064
11. Francis KA, Liew C-W, Ramesh S, Ramesh K, Ramesh S (2016) Ionic liquid enhanced magnesium-based polymer electrolytes for electrical double-layer capacitors. *Ionics* 22:919–925
12. Ramesh S, Amiriyani M, Meenaloshini S, Tolouei R, Hamdi M, Purboloksono J, Teng WD (2011) Densification behaviour and properties of manganese oxide doped Y-TZP ceramics. *Ceram Int* 37:3583–3590
13. Azim Jais A, Muhammed Ali SA, Anwar M, Rao SM, Mughtar A, Wan Isahak WNR, Tan CY, Singh R, Brandon NP (2017) Enhanced ionic conductivity of scandia-ceria-stabilized-zirconia (10Sc1CeSZ) electrolyte synthesized by the microwave-assisted glycine nitrate process. *Ceram Int* 43:8119–8125
14. Misran H, Singh R, Yarmo MA (2008) Nonsurfactant route of fatty alcohols decomposition for templating of mesoporous silica. *Microporous Mesoporous Mater* 112:243–253
15. Barzani MM, Sarhan AAD, Farahany S, Ramesh S, Maher I (2015) Investigating the machinability of Al-Si-Cu cast alloy containing bismuth and antimony using coated carbide insert. *Measurement* 62:170–178
16. Yeo WH, Fry AT, Purboloksono J, Ramesh S, Inayat-Hussain JI, Liew HL, Hamdi M (2014) Oxide scale growth and presumed exfoliation in a 700 °C or higher steam condition: a simulation study for future operations of ultra-supercritical power plants. *J Supercrit Fluids* 92:215–222
17. Ching YC, Gunathilake TMSU, Chuah CH, Ching KY, Ramesh S, Liou N-S (2019) Curcumin/Tween 20-incorporated cellulose nanoparticles with enhanced curcumin solubility for nano-drug delivery: characterization and in vitro evaluation. *Cellulose* 26:5467–5481
18. Yee YY, Ching YC, Rozali S, Hashim NA, Ramesh S (2016) Preparation and characterization of poly(lactic acid)-based composite reinforced with oil palm empty fruit bunch fiber and nanosilica. *BioResources* 11(1):2269–2286
19. Ramesh S, Gill C (2001) Environmental degradation of CuO-doped Y-TZP ceramics. *Ceram Int* 27(6):705–711
20. Daguano JKMF, Santos C, Souza RC, Balestra RM, Strecker K, Elias CN (2007) Properties of ZrO₂-Al₂O₃ composite as a function of isothermal holding time. *Int J Refract Metal Hard Mater* 25(5):374–379
21. Abbas MKG, Ramesh S, Sara Lee KY, Wong YH, Tan CY, Johnson Alengaram U, Ganesan P, Musharavati F, Zalnezhad E (2022) Densification of copper oxide doped alumina toughened zirconia by conventional sintering. *Ceram Int* 48(5):6287–6293
22. Hao Y, Li J, Yang X, Wang X, Lu L (2004) Preparation of ZrO₂-Al₂O₃ composite membranes by sol-gel process and their characterization. *Mater Sci Eng, A* 367(1):243–247
23. Ramesh S, Siah LF, Nor Azmah AK (2000) Sintering behaviour of slip-cast Al₂O₃-Y-TZP composites. *J Mater Sci* 35(21):5509–5515
24. Deville S, Chevalier J, Fantozzi G, Bartolomé JF, Requena J, Moya JS, Torrecillas R, Diaz LA (2003) Low-temperature ageing of zirconia-toughened alumina ceramics and its implication in biomedical implants. *J Eur Ceram Soc* 23(15):2975–2982
25. Olhero SM, Ganesh I, Torres PMC, Alves FJ, Ferreira JMF (2009) Aqueous colloidal processing of ZTA composites. *J Am Ceram Soc* 92(1):9–16
26. Basha MM, Basha SM, Singh BK, Mandal N, Sankar MR (2020) A review on synthesis of zirconia toughened alumina (ZTA) for cutting tool applications. *Mater Today Proc* 26:534–541
27. Abden MJ, Afroze JD, Qadir MR, Gafur MA, Chowdhury FUZ (2015) Correlation among composition, microstructure and mechanical properties of ZrO₂(Y₂O₃)/Al₂O₃ composite ceramics. *Inter J Mater Eng Innov* 6(2–3):170–184

Mechanical and Thermal Properties of 3D Printed Polylactic Acid Reinforced Alkaline Lignin with Epoxidized Palm Oil Bio-Composites



Nurul Amirah Abd Rahman, Hazleen Anuar, Fathilah Ali,
and Jonghwan Suhr

Abstract Fused deposition modeling (FDM), through 3D printing has an advantage of using thermoplastic polymers for fabrication of natural fiber reinforced composites (NFRC). Polylactic acid (PLA) is an extensively used thermoplastic in 3D printing application for its compatibility with the processing parameters. However, the uses of unfilled PLA will produce 3D printed parts with high brittleness, hence reinforcement with lignin from oil palm empty fruit bunches (OPEFB) was considered. Lignin, one of the major components in plant, was less utilized even though contains high aromatic compound that is crucial in the polymer industry. The effect of reinforcement capability of alkaline treated lignin in PLA matrix for fabrication of sustainable 3D printing material was studied where, the obtained alkaline lignin was reinforced in the PLA with various compositions (1, 3 and 5 phr). It has been found that the presence of lignin in the PLA improved the thermal properties as well as the mechanical properties of the PLA bio-composites. Nevertheless, addition of higher lignin load of more than 1 phr contributed to lower thermal and mechanical properties. Better thermal properties were found with addition of EPO, where the maximum degradation temperature and glass transition temperature of PLA bio-composite filaments (PLAE1) have been improved to 335 °C and 59 °C, respectively, instead of 330 °C and 62 °C for unfilled PLA.

Keywords 3D Printing · Fused deposition modeling · Alkaline lignin · Polylactic acid

N. A. A. Rahman · H. Anuar (✉)

Department of Manufacturing and Materials Engineering, Kulliyah of Engineering, International Islamic University Malaysia, Jalan Gombak, 53100 Kuala Lumpur, Malaysia
e-mail: hazleen@iium.edu.my

F. Ali

Department of Chemical Engineering and Sustainability, Kulliyah of Engineering, International Islamic University Malaysia, Jalan Gombak, 53100 Kuala Lumpur, Malaysia

J. Suhr

Faculty of Mechanical Engineering, College of Engineering, Sungkyunkwan University, Natural Sciences, Campus 2066, Seobu-Ro, Jangan-Gu, Suwon 16419, Gyeonggi-Do, Korea

1 Introduction

3D printing is a well-established form of manufacturing process that has revolved from prototyping method with limited mechanical properties of produced parts into versatile manufacturing technology to produce functional components. Additive manufacturing (AM) is a revolutionary manufacturing technology, also known as 3D printing through fused deposition modeling, that has been used for metal and polymer processing. FDM items are created by adding material layer by layer connected with adhesive bonding, whereas traditional methods create products through subtractive manufacturing methods [1].

Fused deposition modeling is a potential additive manufacturing (AM) technique today due to its ability to manufacture thermoplastics parts with advantages in the design and optimization of models with complex geometries, significant design flexibility, recyclability, and reduced material waste [2]. PLA (polylactic acid) is one of the most adaptable materials in 3D printing due to its strong reputation in traditional polymer processing good thermal stability. Regardless of the variety of printing polymers available, their mechanical properties of stiffness and strength are necessarily low due to the nature of printing. The main concern in the FDM process is the formation of void spaces between material deposition lines, which will impair the mechanical qualities and limit the applicability of printed components [3]. While there are various ways to improve the mechanical properties of the produced parts as well as the processing conditions, many studies were focusing on fabricating polymer matrix reinforced filaments [4]. Among the bio-based polymers considered, lignocellulosic polymers have attracted particular attention for AM over the past years.

Lignin is a key component of oil palm empty fruit bunches (OPEFB), which include a high concentration of aliphatic and aromatic chemicals. Lignin is distinguished from cellulose and hemicellulose by the presence of aromatic rings rather than lengthy polymer chains and well-known for its excellent thermal stability with the capability to improve interfacial adhesion during printing due to the hydrogen bond between lignin surface and PLA matrix.

In this work, analysis on thermal properties, mechanical properties and surface morphology of 3D printed PLA bio-composite reinforced with alkaline lignin from OPEFB has been made. Comparison was made with 3D printed alkaline lignin/PLA composite with addition of epoxidized palm oil (EPO) as plasticizer in order to improve processability. The aim of this study is to produce biodegradable printing material with improved mechanical and thermal properties compared to the pristine polymer. This is to motivate the uses of more sustainable polymer material in the high strength applications.

Table 1 Compositions of 3D printed PLA/alkaline lignin bio-composites

Material Designation	PLA (phr)	Lignin (phr)	EPO (phr)
PLA	100	–	–
PLAL1	100	1	–
PLAE1	100	1	5
PLAL3	100	3	–
PLAE3	100	3	5
PLAL5	100	5	–
PLAE5	100	5	5

2 Materials and Methods

2.1 Materials

PLA pellets, grade 2003D, with a density of 1.24 g/cm³ were supplied by Nature-Works Co. Ltd. Budi Oil Enterprise Sdn Bhd in Selangor, Malaysia, provided EPO with a density of 0.886 g/mL and a 2.84% oxirane oxygen content.

2.2 Methods

Preparation of PLA/alkaline lignin bio-composites. At first, the alkaline lignin powder was manually mixed with PLA pellets for the preparation of PLA/alkaline lignin bio-composites at various compositions (1 phr, 3 phr and 5 phr) with addition of 5% (w/w) EPO as plasticizer. Detailed were as presented in Table 1. Prior to the printing process, PLA/alkaline lignin filaments were extruded using Filabot EX6 with a temperature of 50 °C (feed), 180 °C (front), 190 °C (middle) and 180 °C (back) at different parts of the extruder. Consecutively, 3D CAD model was designed by Autodesk Fusion360, where the file was then converted to STL format for compatibility with Cura software for pre-printing and slicing. The G-code generated from the software was used in the Ender 3 Pro 3D printer. The printing speed was set at 50 mm/s bed temperature of 215 °C and 70 °C respectively. Using line pattern, the infill percentage of the 3D printed sample was 100%.

2.3 Analysis

Impact Test The Charpy impact strength was measured using a 7.5 J hammer on a Charpy impact machine (Dynisco Polymer Test, Advance Pendulum Impact (API)). The ASTM D256-compliant 3D printed bio-composite samples with thickness, width

and length of 3 mm, 12.5 mm and 65 mm respectively were prepared in a set of five for each composition. Before starting the test, the Dynisco Polymer Test, Automatic Sample Notcher (ASN) was used to notch the printed specimens.

Scanning Electron Microscopy (SEM) SEM was used to examine the fractured surfaces of the bio-composites caused by the impact test (JEOL, JSM-5600, UK). To achieve the conductive property, the samples were cut into smaller pieces and sputter coated with palladium. The photos were captured at magnifications of $500 \times$ at an accelerating voltage of 8.0 kV.

Thermogravimetry Analysis (TGA) The degradation behavior of PLA/alkaline lignin bio-composites was studied using a Perkin Elmer (TGA4000) instrument. The samples were heated using the platinum pan under a nitrogen environment at a rate of $10 \text{ }^\circ\text{C}/\text{min}$, ranging from $30 \text{ }^\circ\text{C}$ to $560 \text{ }^\circ\text{C}$.

3 Results and Discussions

3.1 Impact Test

Figure 1 shows the effects of varying lignin loads on the impact strength of 3D printed PLA bio-composites. The impact strength of pure 3D printed PLA was found to be around $8 \text{ kJ}/\text{m}^2$ with 0.30 J of adsorbed energy. PLAE1 had the strongest fracture resistance of $11 \text{ kJ}/\text{m}^2$, whereas PLAL1 had the lowest impact strength of $5 \text{ kJ}/\text{m}^2$ with adsorbed energy of 0.21 J and 0.35 J, respectively.

Aside from that, the inclusion of increased lignin content of more than 1 phr in 3D printed bio-composites resulted in a downward trend in impact strength. This suggested that the higher aspect ratio of the lignin filler in relation to the PLA matrix had caused higher rigidity in the bio-composites, consecutively caused poor interfacial bonding, which had created gaps between the lignin and matrix, resulting in micro-cracks prior to impact (see Fig. 2). The increased adsorbed energy of PLA bio-composites under higher lignin loads may also be noticed, where it was previously known that the impact strength of a composite was heavily dependent on the matrix's ability to absorb impact energy.

3.2 Scanning Electron Microscopy (SEM)

SEM analysis was performed on the cross-section of the fractured area, exhibited by interior and edge where the notches were made, to understand the impact strength of the printed PLA/lignin bio-composites. Figure 2d, f show that increased lignin

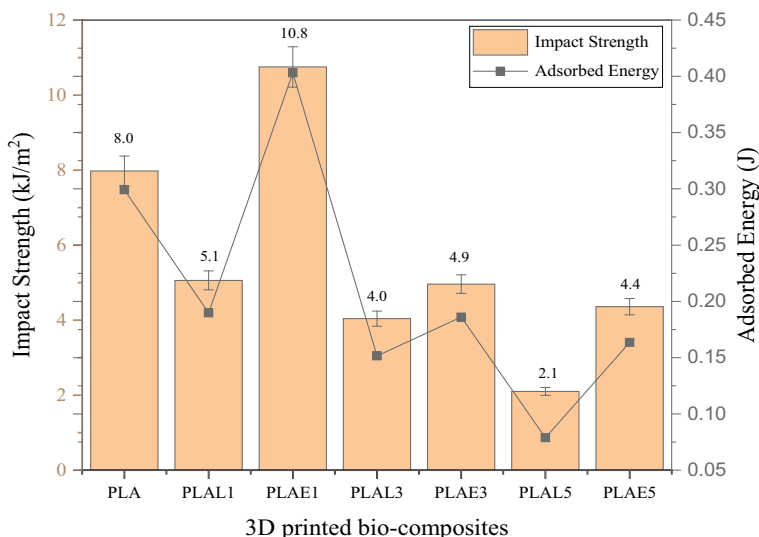


Fig. 1 Impact strength of the 3D printed PLA/lignin bio-composites

content of more than 1 phr without EPO addition (PLAL3 and PLAL5) resulted in weak adhesion between layers that may occur due to limited inter-filament polymer diffusion during the printing process.

PLAE3 on the other hand, exhibits improved filament adhesion compared to PLAL3 even though PLAE5 depicts a rougher fracture surface with more voids and apparent jagged edges in the area of direct impact force, these behaviors have been previously mentioned in Sect. 3.1, where more lignin load induced reduce interfacial bond due to high aspect ratio of lignin with respect to PLA matrix, hence more apparent gaps can be observed between layers (see Fig. 2f, g). Consecutively, these conditions had reduced the resistance to impact as explained in Sect. 3.1.

3.3 Thermogravimetry Analysis (TGA)

TGA was used to determine the thermal characteristics of 3D printed PLA/lignin bio-composites in order to observe the influence of lignin addition. Figure 3a, b depict the weight loss with rising temperature, TG, and the corresponding weight loss, DTG, of the printed PLA, PLAE1, and PLAL1.

The TG of these printed bio-composites shown in Fig. 3a exhibited a very similar thermal degradation behavior, with the on-set temperature (T_0) occurring at around 338 °C, 344 °C, and 340 °C for PLA, PLAE1, and PLAL1, respectively. The results showed that the T_0 of bio-composites containing lignin (PLAE1 and PLAL1) was higher than that of pure PLA. This has demonstrated that the addition of lignin results

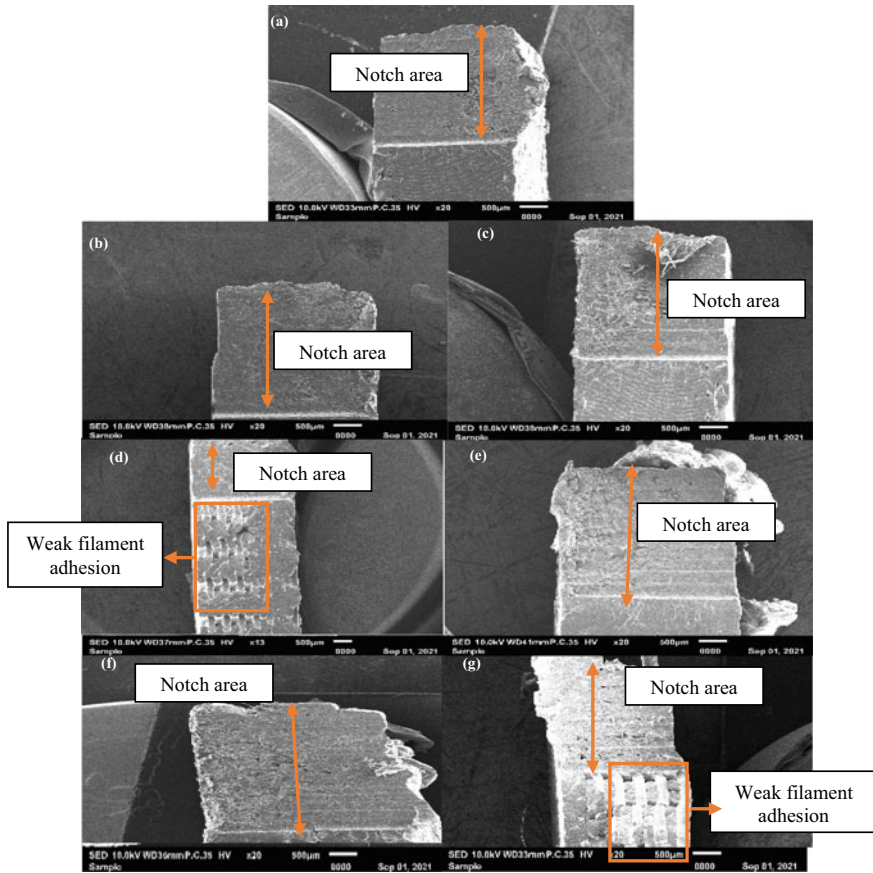


Fig. 2 Impact fracture of 3D printed bio-composites of **a** PLA, **b** PLAL1, **c** PLAE1, **d** PLAL3, **e** PLAE3, **f** PLAL5 and **g** PLAE5

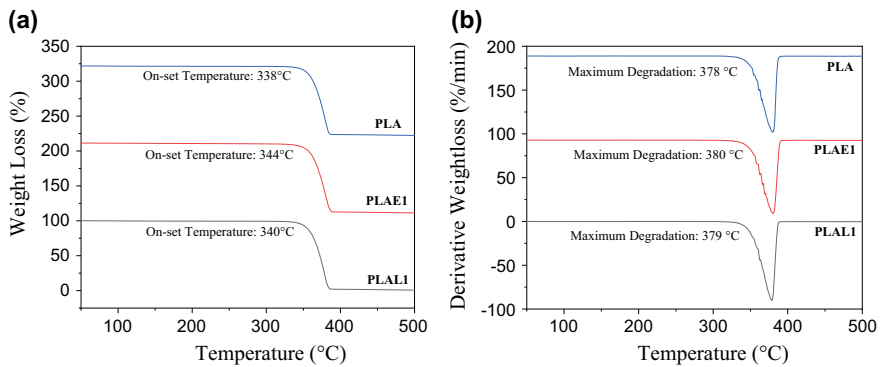


Fig. 3 **a** TG and **b** DTG curves of the 3D printed PLA/lignin bio-composites

in improved thermal stability, which is critical in lowering the rate of degradation during the 3D printing process. The DTG of the printed bio-composites shown in Fig. 3b exhibited similar behavior for all compositions, with maximum degradation temperature (T_{max}) observed to be higher with lignin addition compared to pure PLA. Based on these results, the addition of lignin provided better restriction on degradation at elevated temperatures due to the higher rigidity of the polymer chain. It can be seen that the presence of plasticizer in PLAE1 increased its ability to degrade.

4 Conclusion

In conclusion, PLAE1 had the best mechanical properties due to the addition of EPO, which allows interaction between the lignin and PLA matrix. Some future research ideas include optimizing the printing parameters such as temperature, printing orientation, infill pattern, and infill volume.

Acknowledgements The authors would like to thank Kulliyah of Engineering, International Islamic University Malaysia (IIUM), and the Asian Office of Aerospace Research and Development (AOARD) grant through collaborative research with Sungkyunkwan University (SPI20-009-0009) for the financial support.

References

1. Zhang S, Li M, Hao N, Ragauskas AJ (2019) Stereolithography 3D printing of lignin-reinforced composites with enhanced mechanical properties. *ACS Omega* 4(23):1–8
2. Chio C, Sain M, Qin W (2019) Lignin utilization: a review of lignin depolymerization from various aspects. *Renew Sustain Energy Rev* 107:232–249
3. Abd Rahman NA, Anuar H, Nordin NM, Asri SEAM, Ali F, Suhr J (2021) Mechanical and thermal properties of polylactic acid filled lignin powder biocomposite filaments with epoxidized palm oil for sustainable 3D printing application. *Perintis eJournal* 11(1):23–39
4. Pairon MS, Ali F, Ahmad F, Anuar H, Abdul Rahman NA, Saeed Mirghani ME, Suhr J, Thomas S (2022) Review on solvent extraction methods of lignin from oil palm empty fruit bunches (OPEFB). *J Nat Fibers* 1(17):1–18

Effect of Supercritical Carbon Dioxide Pressure on Foamed PolyLactic Acid Biocomposite



Nurfarahin Mohd Nordin, Hazleen Anuar, and Yose Fachmi Buys

Abstract The effect of Supercritical Carbon Dioxide (SCCO₂) pressure on foamed PolyLactic Acid (PLA) were studied in this work. Foamed PLA biocomposite thin film was created by combining PLA with Durian Skin Fibre (DSF) and Cinnamon Essential Oil (CEO) before being treated with supercritical carbon dioxide (SCCO₂). The morphological structure was studied to see the effect of pressure on the cell growth of the foamed polymer, later the correlation of morphology structure and tensile strength showing that the cell growth did hugely effect the tensile strength of the PLA biocomposite thin film.

Keywords Foamed biocomposite polymer · Supercritical carbon dioxide · Cell structure

1 Introduction

Environmental sustainable materials and processes have prompted an increase in interest in the creation of biocomposites created from natural fibres [1]. PLA is one of the most extensively researched and used biopolymers; it has garnered widespread attention for conventional applications such as packaging materials, fibre production, and, more recently, composites for a number of practical and mechanical purposes [2]. PLA holds a significant market share in the eco-friendly polymer market and is one of the most promising alternatives for future improvements [3].

Durio zibethinus Murray, generally known as durian, is a tropical fruit that is widely grown in Southeast Asia, particularly in Malaysia, Thailand, Indonesia, and the Philippines [4]. Assuming 60% of total durian fruit production is skin, the waste

N. M. Nordin (✉) · H. Anuar

Department of Manufacturing and Materials Engineering, Kulliyah of Engineering, International Islamic University Malaysia, Kuala Lumpur, Malaysia
e-mail: farahinnordin@rocketmail.com

Y. F. Buys

Department of Mechanical Engineering, Faculty of Industrial Technology, Universitas Pertamina, Jalan Teuku Nyak Arief, Simprung, Kebayoran Lama, Jakarta 12220, Indonesia

durian skins produced in 2020 is predicted to be 13,200 metric tonnes. Durian skins are often disposed of by open burning or landfilling, both of which pollute the environment [5]. DSF has a structure and qualities similar to other natural fibres, making it a good candidate for use as a filler in biocomposite materials [6]. The conventional ways of managing and tilizing durian fruit waste are not environmentally friendly; however, the use of durian skin fibre in composite is one of the most promising techniques of tilizing and managing durian fruit waste [7].

Natural biopolymer blends, in general, are appealing candidates for green synthesis of polymer-based nanocomposites due to numerous advantages of these polymers, such as low cost, accessibility, biodegradability, and flexible processability to improve and develop new sets of polymeric materials with desired properties [8]. Supercritical Carbon dioxide (SCCO₂) is a supercritical fluid which both pressure and temperature are above the critical value [9] SCCO₂ can be used to create cellular polymers. At constant temperature and pressure, the polymer is saturated with a gas or supercritical fluid (often CO₂ or N₂). The system is then brought to a supersaturated condition by either decreasing pressure (pressure induced phase separation) or increasing temperature (temperature induced phase separation), resulting in the nucleation and development of pores and cells within the polymer matrix [9, 10].

The focus of this work is to study the effect of varied pressure applied during SCCO₂ treatment on PLA biocomposite in term of its morphological structure and tensile strength.

2 Methodology

The PLA biocomposite thin films were process via solution casting, PLA, DSF and CEO will be placed in chloroform, which will serve as a reagent. The mixture will be quickly stirred on a hot plate with a magnetic stirrer until completely dissolved and casted into the mould. After the chloroform has fully evaporated and the sample has dried completely, the PLA biocomposite films will be treated to supercritical carbon dioxide (SCCO₂) at 80 °C but at a different pressure. Table 1 shows the variable parameter list.

The PLA biocomposite thin film will be created using the solution casting procedure. The PLA biopolymer resin (grade 4043D) supplied by NatureWorks® and chloroform must be mixed in a 1:10 ratio with 3% DSF content. 5% of Cinnamon Essential Oil from Tanamera, Kuala Lumpur were added into the solution casting,

Table 1 Parameter and samples abbreviation

Samples	Parameter		Samples
	Temperature	Pressure	Abbreviation
PLA-DSF 3%-CEO	80 °C	100	A10
		150	A15
		200	A20

to act as plasticizer and antimicrobial properties. DSF obtained from the discarded durian skin from a local market in Sungai Buloh. Durian skin was washed, chopped, dried, crushed, ground, and sieved through a 90 m sieve to obtain its fiber.

The morphology of foamed PLA biocomposite was observed using a scanning electron microscope (SEM) (JEOL 5600). The fracture surfaces of the composites from tensile tests were placed on an aluminum stub and sputter coated with palladium (Pd) to avoid electrostatic charge during scanning.

Tensile tests on foamed PLA biocomposite were performed using a Universal Testing Machine (Shimadzu Autograph AGS-X series) with a 10 mm/min crosshead and sample size according to ASTM D882. For each composition, five samples were evaluated, and the average was taken as the final result.

3 Results and Discussions

3.1 Cell Growth Structure

Through the SEM images, it can be seen that SCCO₂ has causing foamed PLA biocomposite to nucleated which indicated that foaming process is happening. Figure 1 is the SEM images of morphological structure for foamed PLA biocomposite. In Fig. 1 showed that distinct cell growth numbers as the pressure were increase, at 200 bar (A20) pressure more cell growth produced compare to at 100 bar (A10).

The pressure play an important role in producing foamed polymer [11], where the applied thermodynamic instability causes a pressure drop. The relief valve is opened in the vessel, the pressure drops quickly and the heated polymer quickly becomes supersaturated, which means that the solved gas withheld by the polymer. Phase separation is caused, and cells start to form and grow, which causes the sample to grow and creates a porous structure [12].

3.2 Tensile Strengths

The interrelation of foamed PLA composite structure with tensile strength can be seen through tensile strength results in Fig. 2. Through the tensile result, it shows that tensile strength highest at 150 bar pressure, by 47.29 MPa. At higher pressure, the tensile strength slightly drops which this is might due to the condition of the samples during testing that contribute to slightly lower tensile strength.

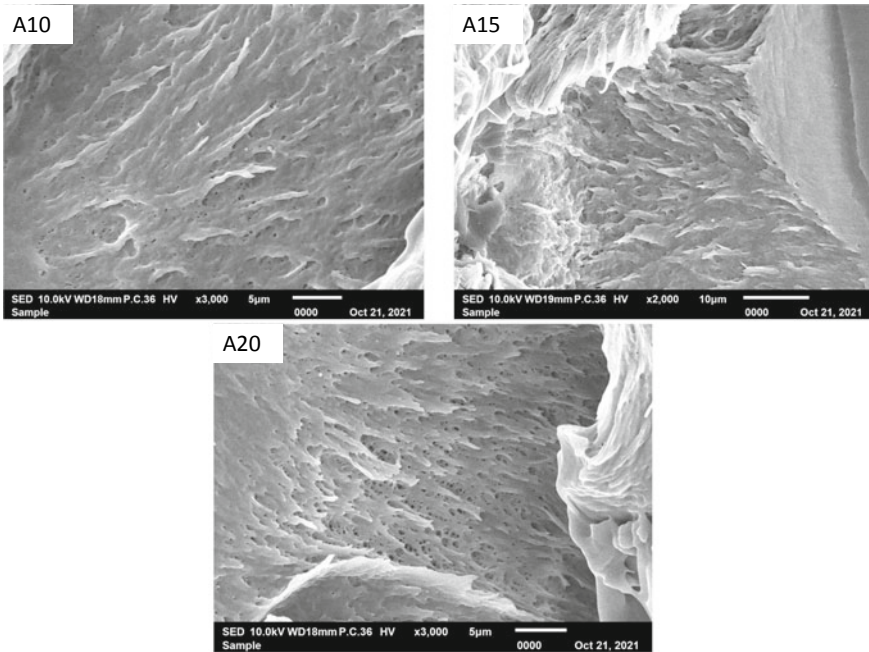


Fig. 1 Cells growth by different level of pressure applied during SCCO₂ treatment

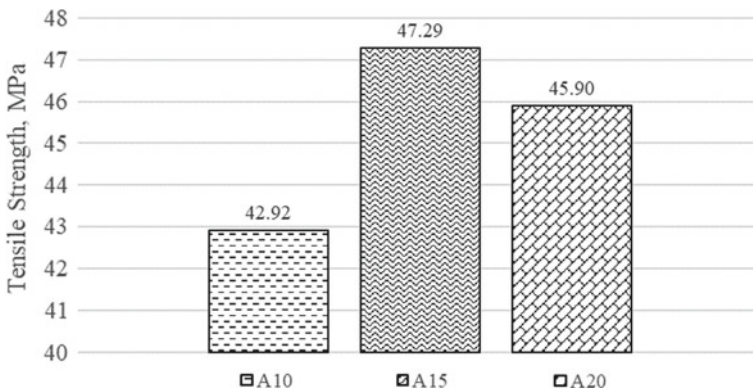


Fig. 2 Tensile strength of foamed PLA biocomposite

4 Conclusion

Conclusion made based on this work is higher pressure of SCCO₂ produced more cell growth in foamed PLA biocomposite. Tensile strength show that higher SCCO₂ pressure applied to the PLA biocomposite contribute to high tensile strength of foamed PLA biocomposite.

Acknowledgements The authors acknowledge the Ministry of Higher Education (MOE) for the funding provided through the Fundamental Research Grant Scheme (FRGS/1/2019/TK05/UIAM/02/2). The authors also would like to acknowledge International Islamic University Malaysia (IIUM), for the lab facilities.

References

1. Kaewpirom S, Worrarat C (2014) Preparation and properties of pineapple leaf fiber reinforced poly(lactic acid) green composites. *Fibers Polym* 15(7):1469–1477. <https://doi.org/10.1007/s12221-014-1469-0>
2. Sanjay MR, Siengchin S., Parameswaranpillai J, Jawaid M, Pruncu CI, Khan A (2019) A comprehensive review of techniques for natural fibers as reinforcement in composites: Preparation, processing and characterization. *Carbohydr Polym* 207:108–121. <https://doi.org/10.1016/J.CARBPOL.2018.11.083>
3. Turalija M, Bischof S, Budimir A, Gaan S (2016) Antimicrobial PLA films from environment friendly additives. *Compos Part B Eng* 102:94–99. <https://doi.org/10.1016/J.COMPOSITESB.2016.07.017>
4. Lee MC, Koay SC, Chan MY, Pang MM, Chou PM, Tsai KY (2018) Preparation and characterization of durian husk fiber filled polylactic acid biocomposites. *MATEC Web Conf* 152
5. Jun TY, Arumugam SD, Latip NHA, Abdullah AM, Latif PA (2010) Effect of activation temperature and heating duration on physical characteristics of activated carbon prepared from agriculture waste. *Environ Asia* 3:143–148
6. Mohd Nasir N et al. (2013) Tensile and morphological properties of durian skin nanobio fiber (DSnbF) filled of polylactic acid biocomposites
7. Busu WNW, Zakaria NE, Manshor MR, Khalid SE, Jaafar J, Abidin NFIZ (2015) Effect of fibre loading on mechanical properties of durian skin fibre composite. *J Trop Agric Food Sci* 42:169–174
8. Pinem MP, Wardhono EY, Nadaud F, Clause D, Saleh K, Guénin E (2020) Nanofluid to nanocomposite film: chitosan and cellulose-based edible packaging. *Nanomaterials* 10(4). <https://doi.org/10.3390/nano10040660>
9. Bocz K, Tábi T, Vadas D, Sauceau M, Fages J, Marosi G (2016) Characterisation of natural fibre reinforced PLA foams prepared by supercritical CO₂ assisted extrusion. *Express Polym Lett* 10(9):771–779
10. Kausar A et al. (2017) A conductive self-healing hybrid gel enabled by metal–ligand supramolecule and nanostructured conductive polymer. *J Appl Polym Sci* 6(1):n/a–n/a. <https://doi.org/10.1007/s10973-015-4393-7>
11. Monnereau L et al (2015) Gradient foaming of polycarbonate/carbon nanotube based nanocomposites with supercritical carbon dioxide and their EMI shielding performances. *Polymer (Guildf)* 59:117–123. <https://doi.org/10.1016/j.polymer.2014.11.063>
12. Singh I, Gandhi A, Mohanty S, Nayak SK (2020) Depressurization induced morphology control in solid-state microcellular batch foaming process. *J Macromol Sci Part A Pure Appl Chem* 57(6):409–420. <https://doi.org/10.1080/10601325.2019.1704178>

Characteristics of Zinc-Doped Hydroxyapatite Prepared Using Biogenic and Synthetic Calcium Precursor



C. M. Mardziah, N. R. N. Masdek, N. M. Mubarak, and S. Ramesh

Abstract Hydroxyapatite (HA) bioceramic has been used for clinical applications due mainly to its chemical similarity with human bones. However a major drawback with HA synthesized by using commercial sources is the absence of ions such as zinc which is normally found in natural bone. In this work, comparison between the characteristics of zinc HA powders synthesized using different source of calcium precursor (commercial and waste eggshells) were studied. Both powders were prepared through wet chemical precipitation method using the same phosphorous and zinc reagents, under the exact experimental conditions. The physicochemical properties of these powders before and after undergoing calcination at 700 °C were examined. This study demonstrated how the characteristics of the synthesized powders slightly differ in terms of their thermal stability and molecular structure due to the use of different calcium source. The study found that the addition of zinc ion in powders prepared using commercial calcium source led to higher formation of secondary phase, β -TCP than the powder prepared using eggshell calcium.

Keywords Calcium precursor · Chemical precipitation · Waste eggshell · Zinc hydroxyapatite

1 Introduction

Synthetic hydroxyapatite [HA, $\text{Ca}_{10}(\text{OH})_2(\text{PO}_4)_6$] has been widely used as implant material in biomedical field since many decades ago due to its chemical properties

C. M. Mardziah (✉) · N. R. N. Masdek
School of Mechanical Engineering, College of Engineering, Universiti Teknologi MARA,
Selangor Darul Ehsan, 40450 Shah Alam, Malaysia
e-mail: mardziah31@uitm.edu.my

N. M. Mubarak · S. Ramesh
Faculty of Engineering, Universiti Teknologi Brunei, Tunku Highway, Gadong 1410, Brunei Darussalam

S. Ramesh
Center of Advanced Manufacturing and Material Processing, Department of Mechanical Engineering, Faculty of Engineering, University of Malaya, 50603 Kuala Lumpur, Malaysia

that has close resemblance to the natural bone. One of the important features of HA is its capacity for ionic substitution. This means that the locations for hydroxyl, phosphate and calcium ions may be occupied by ions of a similar size and charge without disrupting the HA structure [1]. There has been a substantial effort made by numerous investigators to improve the overall properties of synthetic HA. One of the strategies is to introduce metallic ions into HA such as magnesium [2, 3], manganese [4], zinc [5], bismuth [6], and strontium [7].

Traces of metal ions can influence the lattice parameters, the crystallinity, the dissolution kinetics, increase chemical affinity and other physical properties of apatite [8]. They are also believed to have significant role towards improving cell-material interactions of HA and strengthening its mechanical properties, which is beneficial in the bone remodeling process. This strategy of incorporating metal ions and other minute dopants or additives, particularly that of transition metal oxides, during processing have also been shown to be successful and economical means of enhancing the properties of other materials during powder consolidation, promoting microstructure refinement during joining or welding, and in the tailoring of suitable microstructure-properties for a host of applications [9–17].

Amongst the transition metal oxides, zinc is recognized as an essential trace element in the human body due to its vital role in the development of skeletal system and normal biological growth. In addition, zinc inhibits osteogenic differentiation, stimulates osteoblasts activity and regulate cell biological response [18]. Zinc deficiency not only is associated with serious malnutrition problem but was also reportedly related to the impairment of maximal bone mass development [19], which increases the risk of osteoporotic bone. Zinc ions with approximately 0.012–0.025 wt% are found in all tissues of the human body, and most of them is stored in the skeleton [19]. It plays a major role in homeostasis, immune response, metabolic function, wound healing, oxidative stress and few other physiological systems in mammals.

Although several works on zinc substituted HA have been previously reported, they were mainly synthesized using commercial calcium sources. In this present study, zinc-doped HA (ZnHA-Es) bioceramic was prepared using waste chicken eggshells as its calcium precursor with 3 mol% of zinc ion incorporation. The samples were calcined at 700 °C and then compared to ZnHA, which was prepared using commercial calcium precursor under the same experimental conditions.

2 Materials and Method

For the preparation of ZnHA, commercial CaO powders (System Chemicals) and ammonium di-hydrogen phosphate ($\text{NH}_4\text{H}_2\text{PO}_4$) (R&M Chemicals) were used as a calcium and phosphorus precursor, respectively whilst the zinc ion source was zinc nitrate ($\text{Zn}(\text{NO}_3)_2$) from Sigma-Aldrich. On the other hand, for ZnHA-Es, the calcium eggshell (CaO-Es) was used in place of commercial CaO but for the other two precursors (phosphorous and zinc), the chemicals remained the same. It should

be noted that, the amount of zinc dopant incorporated in both type of samples was 3 mol%. In addition, ammonia solution (NH_4OH) from R&M Chemicals was used to increase the solution's pH.

In this work the eggshells were cleaned in hot water, crushed, and heat-treated at 700 °C for 1 h. The calcined powder was sieved to obtain the CaO-Es. Before the final mixing, each precursor was dissolved separately using distilled water on a hotplate magnetic stirrer until they became homogenous. $\text{NH}_4\text{H}_2\text{PO}_4$ and $\text{Zn}(\text{NO}_3)_2$ were slowly added into $\text{Ca}(\text{OH})_2$ solution and after that the NH_4OH was added little by little to increase the solution's pH to 10.5. The solution mixture was constantly stirred for 3 h while the reaction temperature was maintained at 90 °C. The precipitates were aged for 24 h, filtered and washed with deionized water to rinse away any contaminants that were still clinging on the precipitates. After that, they were dried overnight in an oven at 100 °C to remove excess water. All synthesized powders were subjected to calcination at 700 °C with a heating rate of 5 °C/min and a 2-h holding time. Calcination at this temperature was carried out to eliminate volatile substances present in the samples as well as to compare the powders characteristics between ZnHA-Es and ZnHA.

Phase identification and quantification in this study were conducted using X-Ray diffractometer (Rigaku Ultima IV) with a scan speed of 5°/min between 20 and 60°. The diffraction peaks were indexed according to International Centre for Diffraction Data (ICDD) PDF card number 01-079-5683, 01-086-1585, 01-080-2801, 01-077-9574 and 01-076-0571 for HA, β -TCP, CaCO_3 , CaO and $\text{Ca}(\text{OH})_2$, respectively.

For molecular structure identification, the IR spectra of the samples were recorded using a Fourier transform infrared (FTIR) spectrometer (Perkin Elmer) in a frequency range of 500–4000 cm^{-1} .

The microstructures of calcined samples were examined using field emission electron microscopy (FESEM) (FEI Quanta FEG450), which was also equipped with a built-in Energy Dispersive X-Ray (EDX) system to perform elemental analysis on the targeted samples. For clearer images, these samples were first coated with platinum (Pt) using sputter coater (Polaron, SC7620) prior observation under FESEM.

3 Results and Discussion

The XRD phase analysis of the commercial CaO and CaO-Es are shown in Fig. 1a. Both powders consist of three CaO signature peaks at 2θ degree of 32°, 37° and 54°. No other impurities were detected in both type of powders. It is crucial that the CaO-Es powders have excellent purity so that only an accurate amount of CaO-Es will be used as a reagent during the synthesis process.

The FTIR spectrum of CaO-Es shown in Fig. 1b, has close similarity with the spectrum of commercial CaO powders. Both indicate characteristic bands inherent to CaO structure, which contain carbonate and hydroxyl frequency bands. The broad carbonate bands at 2329, 1430 and 1056 cm^{-1} are associated with stretching mode

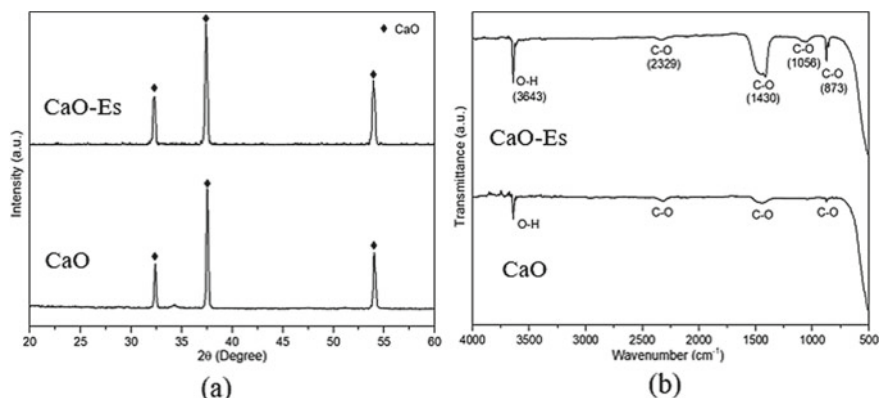


Fig. 1 Comparison between commercial CaO and eggshell derived CaO-Es in **a** XRD patterns and **b** FTIR spectrum

with respect to adsorbed CO_2 on the surface of CaO, while a sharp peak at 3643 cm^{-1} corresponds to hydroxyl band. Another sharp frequency band which also belongs to C–O group was observed at 873 cm^{-1} [20].

XRD patterns in Fig. 2 indicate that after calcination at $700\text{ }^\circ\text{C}$, both samples contain a mixture of HA and β -TCP phases. The main HA peaks were indexed at 32° , 32.3° and 33° in accordance to the ICDD standard for HA phase. Formation of β -TCP phase was confirmed by the appearance of a low intensity peak at approximately 31° , which is common when there is a presence of impurities like zinc ion in HA. Peak shifting was not observed in the present work. It is also evident that the ZnHA-Es was as crystalline as the ZnHA powders. However, the formation of secondary phase was apparently much higher in ZnHA compared to ZnHA-Es as indicated by the intensity of the β -TCP peak. Based on this calcination study, it can be deduced that HA phase for powders produced using commercial calcium most likely tend to decompose to β -TCP phase more rapidly compared to samples prepared using natural calcium.

The microstructure evolution of the ZnHA-Es and ZnHA calcined powders is presented in Fig. 3.

The SEM micrographs revealed that the powders consist of fine spherical-like particles of varying sizes. It was also observed that the microstructure of ZnHA-Es exhibited somewhat larger particles ($D_{\text{ave}} \sim 100\text{ nm}$) compared to the ZnHA ($D_{\text{ave}} \sim 40\text{--}50\text{ nm}$) samples. On the other hand, Ca/P ratio approximation based on EDX analysis shows that ZnHA-Es has Ca/P ratio 1.65 while for ZnHA, the ratio was 1.56.

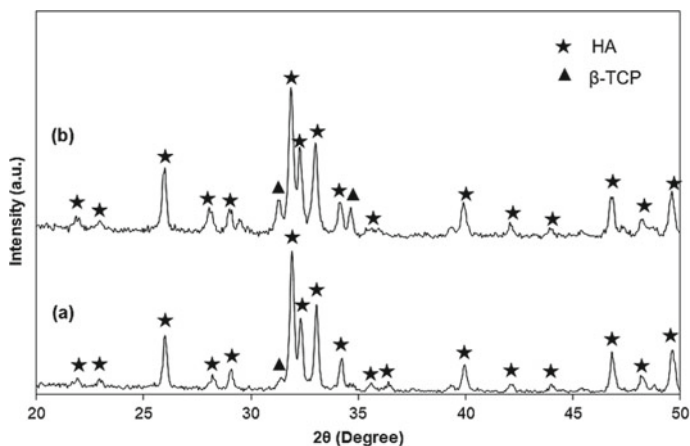


Fig. 2 XRD patterns of **a** ZnHA-Es and **b** ZnHA samples after calcination at 700 °C

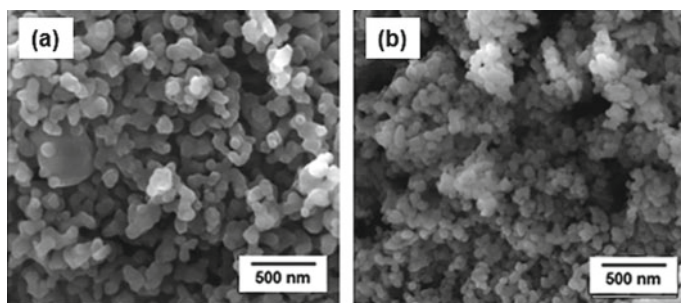


Fig. 3 FESEM micrographs (mag. \times 20 k) of **a** ZnHA-Es and **b** ZnHA powders

4 Conclusions

In this study, nanostructured ZnHA-Es and ZnHA powders were successfully prepared via precipitation method using calcium precursor derived from waste eggshells and commercial calcium, respectively. XRD results showed that the powders had become crystalline after calcination at 700 °C, with an apparent formation of biphasic mixture, HA and β -TCP in both samples. Agglomeration of powder aggregates (\sim 40 to 100 nm in size) was clearly noticed from FESEM images for both samples which is typical for nano-powders. Ca/P ratio of ZnHA-Es was found to be close to stoichiometric HA with 1.65 but on the contrary, the Ca/P ratio of ZnHA was much lower at 1.57, which indicates that it is calcium-deficient. The findings of this work suggested that ZnHA-Es and ZnHA has slightly different physicochemical properties, but both can still possibly be potential candidates as bio-implant material.

Acknowledgements This work was funded by Ministry of Higher Education Malaysia (MOHE) under Grant No. FRGS/1/2018/TK05/UITM/02/18 and FP020-2018A. We would also like to acknowledge Universiti Teknologi MARA (UiTM) and University of Malaya (UM) for providing laboratory facilities and technical supports.

References

1. Kolmas J, Groszyk E, Kwiatkowska-Rózycka D (2014) Substituted hydroxyapatites with antibacterial properties. *Biomed Res Int* 2014(2):178123
2. Antibyouni M, Ren Y, Bhaduri SB (2015) Magnesium substitution in the structure of orthopedic nanoparticles: a comparison between amorphous magnesium phosphates, calcium magnesium phosphates and hydroxyapatites. *Mater Sci Eng C* 52:11–17
3. Tan CY, Yaghoubi A, Ramesh S, Adzila S, Purbolaksono J, Hassan MA, Kutty MG (2013) Sintering and mechanical properties of MgO-doped nanocrystalline hydroxyapatite. *Ceram Int* 39:8979–8983
4. Pandya HM, Anitha P (2015) Influence of manganese on the synthesis of nano hydroxyapatite by wet chemical method for in vitro applications. *Am J Phytomedicine Clin Ther* 2(4):394–402
5. Tank KP, Chudasama KS, Thaker VS, Joshi MJ (2014) Pure and zinc doped nano-hydroxyapatite: synthesis, characterization, antimicrobial and hemolytic studies. *J Cryst Growth* 401:474–479
6. Ramesh S, Tan CY, Yeo WH, Tolouei R, Amiriyani M, Sopyan I, Teng WD (2011) Effects of bismuth oxide on the sinterability of hydroxyapatite. *Ceram Int* 37:599–606
7. Sanyal V, Raja CR (2016) Synthesis, characterization and in-vitro studies of strontium-zinc co-substituted fluorohydroxyapatite for biomedical applications. *J Non Cryst Solids* 81–87
8. Forero-Sossa PA, Olvera-Alvarez IU, Salazar-Martinez JD, Espinosa-Arbelaez DG, Segura-Giraldo B, Giraldo-Betancur AL (2021) Biogenic hydroxyapatite powders: effects of source and processing methodologies on physicochemical properties and bioactive response. *Mater Charact* 173:1–14
9. Ramesh S, Sara Lee KY, Tan CY (2018) A review on the hydrothermal ageing behaviour of Y-TZP ceramics. *Ceram Int* 44:20620–20634
10. Duraisamy N, Numan A, Ramesh K, Choi K-H, Ramesh S, Ramesh S (2015) Investigation on structural and electrochemical properties of binder free nanostructured nickel oxide thin film. *Mater Lett* 161:694–697
11. Bowen C, Ramesh S, Gill C, Lawson S (1998) Impedance spectroscopy of CuO-doped Y-TZP ceramics. *J Mater Sci* 33:5103–5110
12. Manladan SM, Yusof F, Ramesh S, Zhang Y, Luo Z, Ling Z (2017) Microstructure and mechanical properties of resistance spot welded in welding-brazing mode and resistance element welded magnesium alloy/austenitic stainless steel joints. *J Mater Process Technol* 250:45–54
13. Ramesh S, Zulkifli N, Tan CY, Wong YH, Tarlochan F, Ramesh S, Teng WD, Sopyan I, Bang LT, Sarhan AAD (2018) Comparison between microwave and conventional sintering on the properties and microstructural evolution of tetragonal zirconia. *Ceram Int* 44:8922–8927
14. Sampath Udeni Gunathilake TM, Ching YC, Chuah CH, Illias HA, Ching KY, Singh R, Nai-Shang L (2018) Influence of a nonionic surfactant on curcumin delivery of nanocellulose reinforced chitosan hydrogel. *Int J Biol Macromolecules* 118:1055–1064
15. Francis KA, Liew C-W, Ramesh S, Ramesh K, Ramesh S (2016) Ionic liquid enhanced magnesium-based polymer electrolytes for electrical double-layer capacitors. *Ionics* 22:919–925
16. Ramesh S, Amiriyani M, Meenaloshini S, Tolouei R, Hamdi M, Purbolaksono J, Teng WD (2011) Densification behaviour and properties of manganese oxide doped Y-TZP ceramics. *Ceram Int* 37:3583–3590

17. Azim Jais A, Muhammed Ali SA, Anwar M, Rao SM, Muchtar A, Wan Isahak WNR, Tan CY, Singh R, Brandon NP (2017) Enhanced ionic conductivity of scandia-ceria-stabilized-zirconia (10Sc1CeSZ) electrolyte synthesized by the microwave-assisted glycine nitrate process. *Ceram Int* 43:8119–8125
18. Cama G, Nkhwa S, Gharibi B, Lagazzo A, Cabella R, Carbone C, Dubruel P, Haugen H, Di Silvio L, Deb S (2017) The role of new zinc incorporated monetite cements on osteogenic differentiation of human mesenchymal stem cells. *Mater Sci Eng C* 78:485–494
19. Luo X, Barbieri D, Davison N, De Bruijn JD, Yuan H (2014) Zinc in calcium phosphate mediates bone induction: in vitro and in vivo model. *Acta Biomater* 10:477
20. Kamalanathan P, Ramesh S, Bang LT, Niakan A, Tan CY, Purbolaksono J, Hari Chandran Teng WD (2014) Synthesis and sintering of hydroxyapatite derived from eggshells as a calcium precursor. *Ceram Int* 40:16349–16359

Energy Cost Characteristics of a Micro-Wind Power System Based on Different Capacity Factor: A Case Study of Locations in Nigeria



Bashir Isyaku Kunya, Yusuf Alhassan, S. T. Auwal, Magaji Tambaya, D. Kurniawan, and S. Ramesh

Abstract A significant disadvantage of wind power systems (WPS) on electricity production is certainly their relatively high capital cost. However, a WPS may have lower levelized cost of energy (LCOE) than a fossil fuel source depending on site location and design of the power plant. LCOE from WPS depends on its capacity factor, which depends on the design specifications of a wind turbine model installed and the location's weather conditions. This work studied the cost characteristics of a micro-wind power system using different capacity factor based on locations with low average wind speed in Nigeria. Wind speed data was used to determine WPS's capacity factor for 16 locations in Nigeria. The levelized cost of energy of wind turbine system was obtained from a previous study on the cost of micro-wind turbines for a particular location and related to locations considered in this work. Based on the results obtained for the different locations, it was found that LCOE decreases non-linearly with increasing capacity factor of the WPS.

Keywords Wind power system · Wind turbine system · Capacity factor · Levelized cost of energy · Locations in Nigeria

1 Introduction

The rise in the concentration of greenhouse gases due to electricity generation involving fossil fuel combustion causes an increase in the Earth's surface temperature by trapping the heat radiated by the Earth [1]. Renewable energy source (RES)

B. I. Kunya (✉) · Y. Alhassan · S. T. Auwal · M. Tambaya
Department of Mechanical Engineering, Faculty of Engineering, Kano University of Science and Technology, P.M.B 3244, Wudil, Kano State, Nigeria
e-mail: kunyabashir@kustwudil.edu.ng

D. Kurniawan · S. Ramesh
Faculty of Engineering, Universiti Teknologi Brunei, Tungku Highway, Gadong 1410, Brunei Darussalam

S. Ramesh
Center of Advanced Manufacturing and Materials Processing, Department of Mechanical Engineering, Faculty of Engineering, University of Malaya, 50603 Kuala Lumpur, Malaysia

contribution to energy supply reduces not only environmental pollution but also the nation's dependence on fossil fuels thus, stabilizing the cost of electricity, supply distractions, and strengthening the security of national energy supply [2, 3].

There are certain disadvantages of RES in the production of electricity, such as dependence on weather conditions or low energy efficiency and low ability to produce electricity as they are not able to produce as large amounts of electricity as power plants using fossil fuels [4]. A significant disadvantage of RES on electricity production is their relatively high capital cost (CC). However, a RES may have a lower levelized cost of energy (LCOE) than a fossil fuel source depending on the site location and design of the (RES) power plant.

The LCOE by using WPS is not always the same in all locations around the globe, this is because weather conditions (wind velocity, etc.) in different locations may not be the same, and because LCOE depends also on capacity factor of WPS which depends on design specifications of a wind turbine model installed. A study analysis by Ajayi et al. [5] shows that wind electricity generation cost in South West locations in Nigeria can be as low as 0.02 €/kWh and as high as 5.03 €/kWh, depending on the turbine model employed. On the significance of wind turbine model/size on wind energy cost, Kabir et al. [6] compared three configurations of low power wind turbines (EN 5Kw, JA 20Kw, and NP 100Kw) to produce a nameplate power of 100 kW in the Halkirk region of Alberta, Canada applying LCA methodology at 10% internal rate of return (IRR), electricity price for NP is 0.21\$/kWh, whereas EN and JA prices are 65% and 16% higher respectively.

In recent years, wind turbines are becoming more efficient, which allows purchasing and installing wind turbines for homes and even sharing with someone or selling to utility company [7]. It is, therefore beneficial to know the cost characteristics of a micro-wind power system using a different capacity factor based on locations with low average wind speed like in Nigeria. This is what this study provides as the knowledge it contains could be very useful in decision-making by energy users and investors.

2 Materials and Methods

In this research work wind speed data is used in determining the capacity factor of WPS for 16 locations in Nigeria. And the levelized cost of energy of wind turbine system was obtained from a previous study on the cost of micro-wind turbines of a particular location and related to locations considered in this work. Nigerian wind speeds data for seventeen (17) years were used, and were obtained from the Nigeria Meteorological Agency.

2.1 Estimation of Capacity Factor of a WPS in a Location

In this project work, the assumption to determination of capacity factor was based on 5 kW rated Avatar™—v wind turbine system (A-WTS), the product of Avant Garde Innovations™, an international startup company established in India. The general specifications of the turbine system are: Rated power is 5 kW, 2.5 m/s Cut-in wind speed, 60 m/s survival wind speed, rotor diameter is 4.88 m, 25 kWh daily energy productions at 5.5 m/s, and its 3-bladed horizontal axil turbine system with a minimum of 20 years lifespan.

The daily kWh of the turbine at 5.5 m/s is 25 kWh, now for average one hour, the turbine generates 1.041 kW (that is, 25kWh/24 h). For this power, and considering the wind turbine specification, the performance coefficient (0.546) and the rated wind speed (9.3m/s) are determined using extractable wind power equation [8]:

$$P_o = \frac{1}{2} \rho A C_p V^3 \tag{1}$$

From the available wind speed data of a location and by considering the characteristics of the WPS, the output power,

$$P_o = \begin{cases} 0 & \text{for } V < 2.5 \\ 5000 \text{ Watt} & \text{for } V > 9.3 \\ \frac{1}{2} \rho A C_p V^3 = 6.254 V^3 \text{ Watt} & \text{for } 2.5 \leq V \leq 9.3 \end{cases} \tag{2}$$

A capacity factor of a wind turbine is average actual power output divided by its maximum power capability over a period of time [9], $C_f = \overline{P_o} / P_r$. Using Eq. (3),

$$C_f = \frac{1}{5000n} \sum_{i=1}^n (P_{oi}) \tag{3}$$

where $\sum_{i=1}^n (P_{oi}) = (P_{o1} + P_{o2} + P_{o3} + \dots + P_{on})$, the sum of actual power outputs, and n is the total number of wind speed data.

The annual energy production and the capacity factor of WPS can be determined by using statistical models such as Weibull probability distribution model, Rayleigh model, etc. and power characteristics of the wind turbine. The probability density function representing the Weibull distribution can be expressed by Eqs. 4 and 5 [9, 10].

$$f(v) = \frac{k}{c} \left(\frac{v}{c}\right)^{k-1} \exp\left[-\left(\frac{v}{c}\right)^k\right] \tag{4}$$

where k is the shape factor and c represent the scale factor.

$$F(v) = 1 - \exp\left[-\left(\frac{v}{c}\right)^k\right] \quad (5)$$

The annual energy production or output of a wind turbine in a particular location (AEP) is given by Eq. (6) [11].

$$AEP = F(v) \times P_o \times 8760 \text{ (kWh)} \quad (6)$$

2.2 Estimation of Levelized Cost of Energy

The LCOE measures the overall life cycle costs of a technology per unit of electricity produced and is given as [12]:

$$LCOE = \frac{\sum_t^T \frac{C_t + O_t + F_t + D_t}{(1+r)^t}}{\sum_t^T \frac{E_t}{(1+r)^t}} \quad (7)$$

where C is the capital cost; O is operations and maintenance (O&M) cost; F is fuel cost; D is the decommissioning cost; E is the amount of energy produced (kWh); r is the discount rate (%); and t is the year in which a cost occurs during the project lifetime T . No fuel is burned to generate power for a wind farm, so fuel cost is zero; however, indirect fuel use for transport is associated with many activities during the farm's life.

This work did not carry out life cycle cost study of WPS, but cost estimation based on the study by Ayodele et al. [13] was adopted and related to this work. Their work is on economic analysis of small-scale wind turbine for power generation in Johannesburg, South Africa. From their study based on 5 kW rated wind turbine at 20 m height for five years, and assumed discount rate of 12%, the average values of annual energy output, capacity factor, and levelized cost of energy (LCOE) are calculated as 4883 kWh, 0.108, and 0.75 \$/kWh respectively. Previously in this study, the same wind turbine rating and height was assumed for the determination of wind power system output and capacity factor in selected locations.

$$LCOE = \frac{\text{Levelized Annual energy cost, } LAEC}{\text{Annual energy production, } AEP} \quad (8)$$

$$LAEC = LCOE \times AEP = 0.75 \times 4883 = \$3,662.25$$

$$\text{Annual energy production} = \text{Rated annual energy production} \times C_f$$

$$AEP = AEP_R \times C_f = 4883 \text{ kWh}$$

$$AEP_R = \frac{4883}{C_f} = \frac{4883}{0.108} \quad (9)$$

For different location, and hence different capacity factor, AEP will be different:

$$AEP_R = \frac{AEP}{C_f} \quad (10)$$

Combining Eqs. 9 and 10, we get for the annual energy production,

$$AEP = \frac{4883}{0.108} C_f = 45213 C_f$$

Now the LCOE of WPS for any other location with different capacity factor,

$$LCOE = \frac{3662.25}{45213 C_f} = \frac{0.081}{C_f} \quad (\$/\text{kWh}) \quad (11)$$

3 Results and Discussion

The capacity factors of the WPS for 16 locations were determined and then estimated the LCOE by using Eq. 11. The results of the calculated capacity factor and LCOE are represented by bar charts as shown in Fig. 1. It can be seen clearly in the Fig. 1 that Abuja with lowest value of capacity factor (0.0101) has the highest LCOE (8.02 \$/kWh). The cost of wind energy generation is very high in this location. The LCOE keep on decreasing as the capacity factor increases in the x-axis positive direction. Jos has the lowest LCOE (0.298 \$/kWh) because WPS in this location has the best value of capacity factor (0.272), then followed by Kano (0.440 \$/kWh), Minna (0.714 \$/kWh), and Sokoto (0.777 \$/kWh) in the pecking order; their values of capacity factors indicate more potentiality of wind energy generation in the locations as the cost of energy is more affordable relative to other locations. The calculated values of capacity factors for Kano, Minna, and Sokoto are 0.184, 0.1135, and 0.777 respectively.

In order to know the real trend of how LCOE changes with WPS capacity factor, Fig. 2 shows a plot in which capacity factor is being varied evenly with 0.02 common difference starting from 0.02 to 0.3. The graph shows a smooth non-linear curve whereby LCOE decreases with the increasing capacity factor of WPS. This plot is important should someone need to know the LCOE for any other location with different capacity factor of a similar WPS (in terms of its specifications) used in this work.

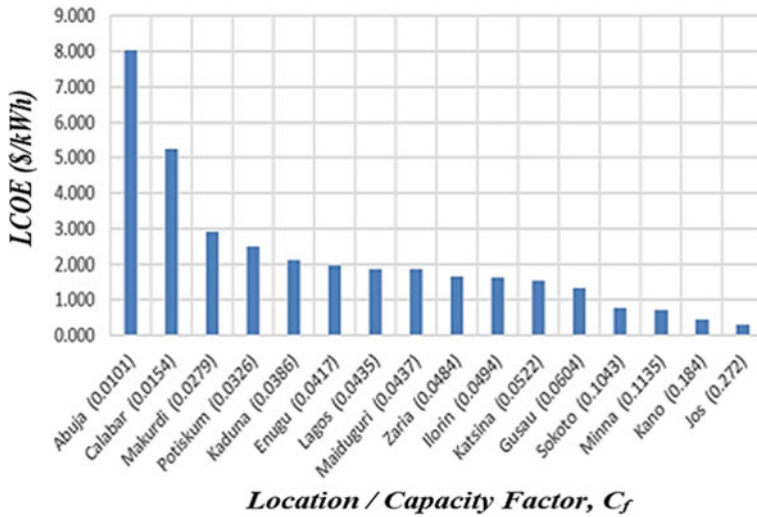
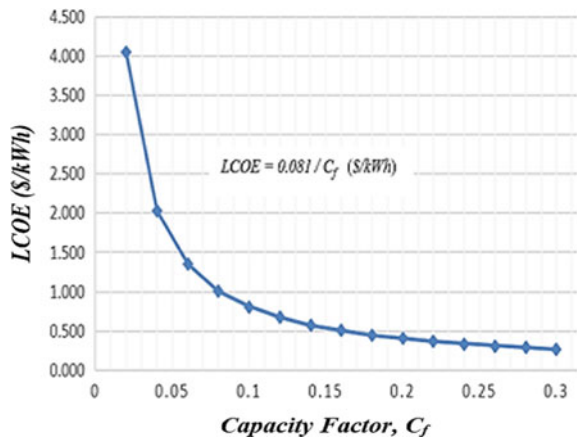


Fig. 1 LCOE of WPS for 16 locations in Nigeria

Fig. 2 LCOE Characteristics of a micro WPS with capacity factor



4 Conclusions

A study on energy cost characteristics of a micro-wind power system based on different capacity factors of 16 locations in Nigeria was carried out. The LCOE of a WPS were estimated for the selected locations:

- Abuja has the highest LCOE (8.02 \$/kWh) and lowest capacity factor (0.0101).
- Jos has the lowest LCOE (0.298 \$/kWh), then followed by Kano (0.440 \$/kWh), Minna (0.714 \$/kWh), and Sokoto (0.777 \$/kWh) in the pecking order; the cost of energy is more affordable relative to other locations.

- The calculated values of capacity factors for Jos, Kano, Minna, and Sokoto are 0.272, 0.184, 0.1135, and 0.777, respectively.
- The real trend of how LCOE changes with capacity factor of the WPS shows a non-linear curve whereby LCOE decreases with the increasing capacity factor.

References

1. Khan MA, Khan MZ, Zaman K, Naz L (2014) Global estimates of energy consumption and greenhouse gas emissions. *Renew Sustain Energy Rev* 29:336–344
2. Eastop TD, Mc Conkey A (1993) *Applied thermodynamics for engineering technologies*, 5th edn, Pearson
3. Ozturk I (2013) Energy dependency and energy security: the role of energy efficiency and renewable energy sources. *Pak Dev Rev*, 309–330
4. Maradin D (2021) Advantages and disadvantages of renewable energy sources utilization. *Int J Energy Econ Policy* 11(3):176
5. Ajayi OO, Fagbenle RO, Katende J, Ndambuki JM, Omole DO, Badejo AA (2014) Wind energy study and energy cost of wind electricity generation in Nigeria: past and recent results and a case study for South West Nigeria. *Energies* 7(12):8508–8534
6. Kabir MR, Rooke B, Dassanayake GM, Fleck BA (2012) Comparative life cycle energy, emission, and economic analysis of 100 kW nameplate wind power generation. *Renewable Energy* 37(1):133–141
7. Ribbing S, Xydis G (2021) Renewable energy at home: a look into purchasing a wind turbine for home use—the cost of blindly relying on one tool in decision making. *Clean Technol* 3(2):299–310
8. Rahimi S, Meratizaman M, Monadzadeh S, Amidpour M (2014) Techno-economic analysis of wind turbine–PEM (polymer electrolyte membrane) fuel cell hybrid system in standalone area. *Energy* 67:381–396
9. Adeyeye KA, Ijumba N, Colton JS (2021) A techno-economic model for wind energy costs analysis for low wind speed areas. *Processes* 9(8):1463
10. Gul M, Tai N, Huang W, Nadeem MH, Yu M (2019) Assessment of wind power potential and economic analysis at Hyderabad in Pakistan: powering to local communities using wind power. *Sustainability* 11(5):1391
11. Charrouf O, Betka A, Becherif M, Tabanjat A (2018) Techno-economic analysis of wind turbines in Algeria. *Int J Emerg Electr Power Syst* 19
12. Thomson C, Harrison G (2015) Life cycle costs and carbon emissions of wind power: executive summary. *ClimateXChange*
13. Ayodele T, Jimoh A., Munda, J., Agee, J., M’bongui, G.: Economic analysis of a small scale wind turbine for power generation in Johannesburg. In: *IEEE international conference on industrial technology (ICIT)*, pp 1728–1732

Parametric Study on Abrasive Wear of Reinforced Polytetrafluoroethylene Composites Using Taguchi Model



Musa Alhaji Ibrahim, Magaji Tambaya, Auwalu Gidado Yusuf, S. T. Auwal, D. Kurniawan, and S. Ramesh

Abstract Over the years reinforced polymer composites are extensively used in aircraft, automobile and structural industries owing to their high specific modulus and strength. However, the main issue is the method used to quantify the abrasive wear which often does not represent the true nature of the composite behaviour. This study presents optimization of parameters which affect the abrasive wear rate of reinforced polytetrafluoroethylene (PTFE) composites using Taguchi model. Friction and wear experiments were performed on a pin-on-disc arrangement as per ASTM G99 standard. A plan of experiment based on Taguchi design was used to obtain data in a controlled way. Load, grit size, distance and speed were considered as process parameters. Taguchi L_9 orthogonal array was chosen to find the optimum parameter settings. Analysis of variance (ANOVA) was applied to determine parameters that most significantly affect the abrasive wear rate of the reinforced PTFE composites. Confirmation test was conducted to validate the optimized conditions. Taguchi optimization model revealed different combinations of process parameters for desired coefficient of friction (COF) and specific wear rate (Ks). The study concluded that the load was the most significant parameter that controlled COF and Ks with a contribution of 82.13% and 81.54%, respectively.

Keywords Taguchi model · Coefficient of friction · Specific wear rate · Reinforced PTFE composites

M. A. Ibrahim (✉) · M. Tambaya · A. G. Yusuf · S. T. Auwal
Department of Mechanical Engineering, Faculty of Engineering, Kano University of Science and Technology, P.M.B 3244, Wudil, Kano State, Nigeria
e-mail: musaibrahim@kustwudil.edu.ng

D. Kurniawan · S. Ramesh
Faculty of Engineering, Universiti Teknologi Brunei, Tungku Highway, Gadong 1410, Brunei Darussalam

S. Ramesh
Center of Advanced Manufacturing and Material Processing, Department of Mechanical Engineering, Faculty of Engineering, University of Malaya, 50603 Kuala Lumpur, Malaysia

1 Introduction

Environmental and financial viability has pushed automotive and aerospace industries to use polymer matrix composites (PMCs) as alternatives to metallic materials due to their high specific strength and stiffness for abrasive applications [1]. Abrasive wear remains a big challenge to PMCs [2]. Abrasive wear resistant PMCs can be obtained by addition of suitable fillers into polymers [3–6]. Experimental studies of parametric optimization for abrasive wear performance of PMCs is costly and time consuming due to the several parameters involved. Thus, design of experiment (DOE) has been proposed as solution [7]. It is common in materials related studies to use DOE or any other suitable approach or best practice to narrow down the experimentation required to achieve the research objectives [8–15]. In particular, Taguchi method has been widely used for this purpose by considering the governing factors and levels required for the optimization of process parameters. For example, several researchers applied Taguchi model to optimize parameters controlling the abrasive performance of carbon-epoxy and polyphenylene sulfide/MoS₂/Al₂O₃ composites [16, 17], respectively. Similar works have been conducted by several other researchers [18–23] contributing to the parametric optimization of PMCs using Taguchi model. In this work, the Taguchi model was used to evaluate the abrasive wear performance of reinforced PTFE.

2 Materials and Methods

Materials used in this article are: 25 wt. % carbon, 25 wt. % glass and 40 wt. % bronze fibres coded as CF25, GF25 and BF40, respectively provided by Polymer Chemical Industry Ltd, Turkey in form of (100 × 100 × 6) mm plate. Samples of square size 25 × 25 mm² were cut using from the Computer Numerical Control (CNC) water jet cutting for the testing. Experiments were performed according to ASTM G99 on tribometer. SiC abrasives were glued to a rotating disc. Pins were bolted to a fixture and then put into arm of the tribometer. The weight before and after the tests was measured using a digital weighing balance with 10⁻³ g sensitiveness. The specific abrasive wear rate (K_s) was computed using Eq. 1:

$$K_s = \frac{W_L}{\rho LD} \quad (1)$$

where W_L weight loss (g), ρ is the density (gcm⁻³), L is load (N) and D is the sliding distance (m). Two replicates were performed and averaged for each sample. The coefficient of friction (COF) is read directly from the machine.

In the current study, parameters affecting the abrasive wear such as load (L, N), grit size (G, mesh), distance (D, m) and speed (S, ms⁻¹) were regarded as factors affecting the process. Codes and levels of the factors were shown in Table 1.

Table 1 Process variables and their levels

Symbol	Process variables	Level 1	Level 2	Level 3
S	Sliding speed, (ms ⁻¹)	0.10	0.12	0.15
D	Sliding distance, (m)	60	75	90
L	Load, (N)	5	8	10
G	Grit size (mesh)	220	320	1000

Table 2 Experimental results of L₉ (3⁴) orthogonal array design

Trials	L (N)	G (P)	D (m)	S (m/s)	COF	Ks (mm ³ /NM)	COF SNRs (dB)	Ks SNRs (dB)
1	5	220	60	0.1	0.18	0.0000867	14.8945	81.243
2	5	320	75	0.12	0.24	0.0000311	12.3958	90.136
3	5	1000	90	0.15	0.23	0.0000060	12.7654	104.442
4	8	220	75	0.15	0.01	0.0000423	40.0000	87.469
5	8	320	90	0.1	0.05	0.0000307	26.0206	90.243
6	8	1000	60	0.12	0.04	0.0000455	27.9588	86.839
7	10	220	90	0.12	0.19	0.0000011	15.9176	117.376
8	10	320	60	0.15	0.16	0.0000019	14.4249	115.363
9	10	1000	75	0.12	0.12	0.0000020	18.4164	113.843

Taguchi L₉ (3⁴) was chosen for this study and results obtained based on this design are converted into signal noise ratios (SNRs) by Eq. 2 and presented in Table 2.

$$SNRs = -\log_{10} \frac{1}{n} \left(\sum_{i=0}^n (y_i)^2 \right) \tag{2}$$

where n = is the number of observations and “y” is the observed data.

3 Results and Discussion

The effect of load, grit size, distance and speed on the COF and Ks of the PTFE reinforced composites are shown in Fig. 1a and Fig. 1b, respectively.

As observed in Fig. 1a COF indicated a decreasing and increasing trend as load increased. Decrease in COF between is linked to formation of tribolayer formed at the counterface and the viscoelastic temperature while increase in COF is due to tear of the tribolayer formed. Similarly, Ks decreased as load increased (Fig. 1b) and this linked to large contact area allowing particles coming in contact with the interface and sharing the stress as well as formation of transfer between samples and counterface.

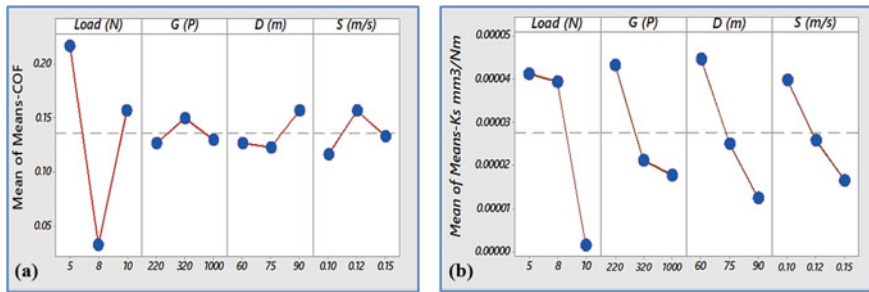


Fig. 1 Effect of process variables on **a** COF and **b** Ks

As for the influence of grit size, as shown in Fig. 1, increasing the grit size caused a decrease in both COF and Ks. The lower values in COF and Ks are related to smoothness of the SiC abrasive paper, the wear track becoming clogged with wear debris and transfer films thereby reducing efficacy SiC abrasives leading to lower wear.

In the case for sliding distance, the results as presented in Fig. 1 indicates that the COF increased with increase in distance. This is attributed to interaction with the counterface on the surface of the samples. However, Ks decreased when distance increased as depicted in Fig. 1b. This can be attributed to particles pull out or fracture of abrasive particles thereby depositing debris and forming transfer film between samples and counterface thus preventing samples from direct contact with the counterface.

The effect of speed on COF and Ks of PTFE reinforced composites shown in Fig. 1 shows that an increased in speed led to a decreased in both COF and Ks. As the speed increased and materials are oxidized, the counterface temperature also varies. This aids in a mechanically and rough mixed coating to be laid on the parts. This coating is impervious to removal and increases the wear surface of the materials. When the protection of the hard layer is heavily mixed and the surface of the counterface is less touched, COF and Ks are minimized. More so, with increase in speed the contact time between samples and counterface decreased leading to lower wear rate.

Based on mean response of SNRs analysis, it was found that optimum parameters for COF are L at 8 N, G at 220 mesh, D at 75 m and S at 0.15 ms^{-1} and is coded L2G1D2S3. Similarly, optimized conditions for Ks were L = 10 N, G = 1000 mesh, D = 90 m and S = 0.15 ms^{-1} and designated as L3G3D3S3.

ANOVA was performed to find the percentage contribution of each factor on COF and Ks. For COF it was found that L with contribution of 82.13% has the highest effect on COF followed by D with 9.06%, followed by S with 5.05% and finally G with 3.76%. With respect to Ks, it was found that L having a percentage contribution of 81.54% is the most influential parameter influencing Ks, then followed by D with 8.09%, followed by S with 7.29% and least significance G having 3.08%.

The final phase is to validate the improvement of quality characteristic using the optimal parameter settings according to Eq. (3).

Table 3 Confirmatory test results for COF and Ks

Response	Error	Experiment	Prediction
COF	$\gamma_{exp} - \gamma_{pre}$ 0.01	L2G1D2S3 0.02	L2G1D2S3 0.01
S/N ratio(dB)	1.10	40.00	38.90
Ks (mm ³ /Nm)	$\gamma_{exp} - \gamma_{pre}$ 2.1093E-07	L3G3D3S3 1.34787E-06	L3G3D3S3 1.1000E-06
S/N ratio (dB)	1.98	122.01	120.03

$$\varepsilon_{predicted} = \varepsilon_t + \sum_{i=1}^x (\varepsilon_o - \varepsilon_t) \tag{3}$$

where ε_t = total of SNRs, ε_o = mean noise ratio at optimum level and x number of input process variables.

According to the response table of SNRs for COF and Ks, the optimal parameter settings were found to be L2G1D2S3 and L3G3D3S3, respectively. Based on the predictions using Eq. (4), the predicted result of the SNRs for COF was computed to be 38.90 dB corresponding 0.01 in Table 2. Similarly, using optimal parameter settings for Ks, the estimated SNR was found to be 119.03 dB matching with 1.1000E-06 mm³/Nm which is the minimum Ks obtained from the experiment (Table 2). Table 3 shows results of the confirmatory test for COF and Ks. It can be deciphered from Table 3 that the error between the predicted and the experimental values are within reasonable limit of 1.10 dB for COF and 1.98 dB for Ks assuming 5% error limit.

4 Conclusions

The study found that the COF increased with increase in load and distance but decreased with increasing grit size and speed. It was revealed that Ks decreased when load, grit size, distance and speed increased. Optimization by Taguchi model revealed factor combination of L2G1D2S3 and L3G3D3S3 as the optimum parameter settings for desired COF and Ks, respectively. ANOVA results revealed that COF and Ks were most significantly influenced by load with a contribution of 82.13% and 81.54%, respectively. Confirmatory test revealed consistency between predicted and experimental results with values of COF and Ks lying close to the observed values having an error of 1.10 dB and 1.98 dB, respectively. The findings of this work would be of significant to researchers working in this area of composites particularly in reducing the amount of trial and error in selecting the test parameters to obtained the required COF and Ks.

References

1. Khedkar EI, Negulescu J, Meletis I (2002) Sliding wear behavior of PTFE composites. *Wear* 252:361–369
2. Schwartz S, Bahadur CJ (2001) The role of filler deformability, filler–polymer bonding, and counterface material on the tribological behavior of polyphenylene sulfide (PPS). *Wear* 251:1532–1540
3. Friedrich AK, Zhang K, Schlarb Z (2005) Effects of various fillers on the sliding wear of polymer composites. *Compos Sci Technol* 65:2329–2343
4. Kukureka YK, Hooke SN, Rao CJ, Liao M, Chen P (1999) The effect of fibre reinforcement on the friction and wear of polyamide 66 under dry rolling–sliding contact. *Tribol Int* 32:107–116
5. Ravi Kumar BN, Suresh B (2009) Effect of particulate fillers on mechanical and abrasive wear behaviour of polyamide 66/polypropylene nanocomposites. *Mater Des* 30:3852–3858
6. Yousif KJ, Nirmal BF, Wong U (2010) Three-body abrasion on wear and frictional performance of treated betelnut fibre reinforced epoxy (T-BFRE) composite. *Mater Des* 31:4514–4521
7. Montgomery CD (2001) Design and analysis of experiments, 5th ed. Wiley
8. Ramesh S, Sara Lee KY, Tan CY (2018) A review on the hydrothermal ageing behaviour of Y-TZP ceramics. *Ceram Int* 44:20620–20634
9. Duraisamy N, Numan A, Ramesh K, Choi K-H, Ramesh S, Ramesh S (2015) Investigation on structural and electrochemical properties of binder free nanostructured nickel oxide thin film. *Mater Lett* 161:694–697
10. Bowen C, Ramesh S, Gill C, Lawson S (1998) Impedance spectroscopy of CuO-doped Y-TZP ceramics. *J Mater Sci* 33:5103–5110
11. Manladan SM, Yusof F, Ramesh S, Zhang Y, Luo Z, Ling Z (2017) Microstructure and mechanical properties of resistance spot welded in welding-brazing mode and resistance element welded magnesium alloy/austenitic stainless steel joints. *J Mater Process Technol* 250:45–54
12. Ramesh S, Zulkifli N, Tan CY, Wong YH, Tarlochan F, Ramesh S, Teng WD, Sopyan I, Bang LT, Sarhan AAD (2018) Comparison between microwave and conventional sintering on the properties and microstructural evolution of tetragonal zirconia. *Ceram Int* 44:8922–8927
13. Sampath Udeni Gunathilake TM, Ching YC, Chuah CH, Illias HA, Ching KY, Singh R, Nai-Shang L (2018) Influence of a nonionic surfactant on curcumin delivery of nanocellulose reinforced chitosan hydrogel. *Int J Biol Macromol* 118:1055–1064
14. Francis KA, Liew C-W, Ramesh S, Ramesh K, Ramesh S (2016) Ionic liquid enhanced magnesium-based polymer electrolytes for electrical double-layer capacitors. *Ionics* 22:919–925
15. Ramesh S, Amiriyani M, Meenaloshini S, Tolouei R, Hamdi M, Purboloksono J, Teng WD (2011) Densification behaviour and properties of manganese oxide doped Y-TZP ceramics. *Ceram Int* 37:3583–3590
16. Ramesh B, Suresha BN (2014) Optimization of tribological parameters in abrasive wear mode of carbon-epoxy hybrid composites. *Mater Des* 59:38–49
17. Pogolian CBS (2005) Friction and wear studies using Taguchi method on polyphenylene sulfide filled with a complex mixture of MoS₂, Al₂O₃, and other compounds. *Wear* 258:1825
18. Sudarshan N, Varadarajan RK, Rajendra YS (2013) Investigation of the abrasive wear behavior of graphite filled carbon fabric reinforced epoxy composite-A Taguchi approach. *Int J Mech Eng Technol* 4:101–108
19. Basavarajappa JP, Arun S, Davim KV (2009) Effect of filler materials on dry sliding wear behavior of polymer matrix composites-A Taguchi approach. *J Miner Mater Charact Eng* 8:379–391
20. Sahin Y (2005) Optimization of testing parameters on the wear behaviour of metal matrix composites based on the Taguchi method. *Mater Sci Eng A* 408:1–8
21. Chauhan P, Kumara SR, Singh A, Kumar I (2010) Effect of fly ash content on friction and dry sliding wear behavior of glass fiber reinforced polymer composites-A Taguchi approach. *J Miner Mater Charact Eng* 9:365–387

22. Sudarshan RK (2013) Modelling and analysis of abrasive wear performance of glass epoxy composites using Taguchi approach. *Int J Miner Metall Mater* 3:19–28
23. Chauhan S, Thakur SR (2013) Effects of particle size, particle loading and sliding distance on the friction and wear properties of cenosphere particulate filled vinylester composites. *Mater Des* 51:398–408

Electric Vehicle Modeling: A Review



Ibraheem. S. M. Alzehawi, Waleed F. Faris , Fadly Jashi Darsivan,
and Mohammed Rafeeq

Abstract The emission of conventional vehicles nowadays contributes significantly to the escalating pollution issues. However, hybrid systems have more fuel economy than standard automobiles, and the end purpose is to have all-electric automobiles. Nowadays, hybrid electric vehicle systems can be located in various journal articles. However, there are few research papers to offer a detailed technical analysis of pure electric vehicles. The features and common types of energy sources and drive machine for Electric Vehicle is described. The current pure electric vehicle types are then illustrated. In addition, study comprehensively reviews and elaborated different approaches specifically using MATLAB-Simulink tool used for modeling and simulation of electric vehicle to increase performance metrics and build basis for experimental work. The review provides comprehensive understanding of electric vehicle and modelling techniques to address the challenges and issues of electric vehicle.

Keywords Pure electric vehicle · Modeling · MATLAB-Simulink

1 Introduction

The fear of the economic and environmental consequences of using carbon fuels has sped up the adoption of alternatives alternative energy sources. Due to the noticeable fast-growing population, technological advancements, urbanization, and expansion of cities, the automobile industry, which is one of the most significant users of fuels and the significant source of greenhouse gases, is rising exponentially, far faster than expected [1]. As a result, public mobility by automotive has been one of the industries

Ibraheem. S. M. Alzehawi (✉) · W. F. Faris · F. J. Darsivan
Mechanical Engineering Department, College of Engineering, International Islamic University,
53100 Gombak, Kuala Lumpur, Malaysia

M. Rafeeq
Mechatronics Engineering Department, College of Engineering, International Islamic University,
53100 Gombak, Kuala Lumpur, Malaysia

where R&D is much more significant, with the overall goal of reducing toxic emissions and car energy consumption. The suggested treatments usually consist of the following: complete battery electric cars (BEV), Fuel cell-powered electric vehicles (FCEV) are in which a fuel cell produces the power electricity to run an electrical motor on deck. HEVs combine the usage of internal combustion engines (I.C.E.), battery packs, and fuel cells to produce power electricity to run an electrical motor in various methods [2]. This study reviews the components of electric vehicles in detail, underlining the parameters influencing the performance of the electric vehicle. The study elaborated on the approaches used in the past to model and simulate the electric vehicle to increase performance metrics and highlighted the challenges ahead. This paper is organized with a section introducing electric vehicle modeling; Sect. 2 briefly highlights the electric vehicle types. Section 3 discusses electric vehicle power train components, Sect. 4 elaborates on modeling, and simulation in a MATLAB/Simulink environment.

2 Electric Vehicle Types

Electric vehicles are entirely run using electricity or with an internal combustion engine. The most basic type of electric vehicle simply uses a battery as its energy source. However, there are a few who use other energy sources. E.V.s can still be classified in the following ways [3]:

2.1 *Battery Electric Vehicle (BEV)*

BEVs are electric cars that depend exclusively on batteries for propulsion; they remove the standard internal combustion engine and should be recharged to use an alternate energy source. The current battery volume has a significant effect on the BEV's performance. A BEV can generally move 100–250 km on a full charge. High-end BEV designs are indeed accessible [4].

2.2 *Hybrid Electric Vehicle (HEV)*

HEVs have a hybrid powertrain that combines electric engine technology and internal combustion. Full HEVs might operate in both a normal and an electric power mode [5].

2.3 *Plug-In Hybrid Electric Vehicle (PHEV)*

To enhance the area of Hybrid vehicles, plug-in hybrids are created. A hybrid electric vehicle (PHEV) has an electric motor and a battery that can be charged from the grid. Once the car's batteries are low, an Engine can charge or replace it [4].

2.4 *Fuel Cell Electric Vehicle (FCEV)*

FCEVs are also known as fuel cell vehicles (FCV). Since the core of this selection for Fuel cells to conduct such action is hydrogen, they are frequently referred to as "hydrogen storage." FCVs transport hydrogen in special high-pressure tanks, and oxygen, which it obtains from the air from the atmosphere, is another component in the power-generating process [3].

3 **Electric Vehicle of Powertrain**

Electric cars provide an excellent option to popular combustion engine (I.C.) engine cars because they increase energy efficiency, easy maintenance, and pollution-free operation. The design of a complete electric vehicle requires developing a complete electric vehicle model.

3.1 *Batteries*

A battery is a mobile power source that typically consists of numerous electrochemical cells ability to convert chemical energy into electricity with good efficiency and no emissions into the atmosphere during use. Reactions occur throughout the bulk of the material in batteries. Three different types of batteries were used for electric vehicle [6].

Lead-acid batteries Lead-acid batteries are the most frequent battery types used in electric cars. The battery's positive and negative terminals are lead oxide and lead. The battery's terminals are soaked in a sulfuric acid solution. The negative terminal and the lead oxide's positive terminal react to sulfuric acid during the releasing operation [7].

The NiMH cell Due to its superior all-around performance and the greatest available combination of energy and energy density, thermal performance, and cycle life, nickel metal hydride batteries have dominated the automobile industry since the 1990s. They don't need servicing, have easy that are good for the environment. NiMH batteries only have a 1.35 V cell potential. [1].

Lithium-ion Battery The lithium-carbon combination is used as the negative electrode, the lithium transition metal oxide is used as the positive electrode, and the solution is an organic liquid or solid polymer. Lithium ions flow round-trip between the positive and negative electrodes during charging and discharging. The lithium-ion batteries have a greater voltage level, greater specific energy, and a greater energy density, they can be considered the highest specific energy of any battery [8].

3.2 *Motors in the Electric Vehicles*

Modern electrical motors vary more markedly than electric propulsion drives. E.V. drives must, in principle, provide strong torque and speed densities, high efficiency. Four different types of electric machines were used for Electric vehicle driving: the D.C., induction, switched reluctance (S.R.), and permanent magnet (PM) brushless motors [9, 10].

D.C. Motor For electric vehicles, D.C. drives were once generally accepted. The individually induced D.C., shunt D.C., series D.C., and PM DC kinds make up the entire group, which is established by mutual coupling between the field and armature windings or the usage of PM excitation.

Induction motors (I.M.) Squirrel cage induction motors have already been the most popular candidate because of their dependability, robustness, low maintenance, and ability to perform in harsh conditions. Of all A.C. rivals, induction motors have the most advanced technology [3].

Permanent Magnet Brushless DC Motor (BLDC) This motor's spin is composed of PM (most frequently NdFeB), and the stator receives an alternating current (A.C) provided from a direct current (D.C.) supplier via an inverter. Because the rotor has no windings, there is also no rotor copper waste, creating more efficiency than induction motors. This motor is lighter [3, 10].

Switched Reluctance Motor (S.R.M.) SRM drives are popular and are acknowledged as having a future in Electrical vehicles. These motor drives offer certain benefits including fault-tolerant torque-speed characteristics, simple and robust design, and more [11].

4 **Modeling of E.V. Components**

This can represent the E.V. with appropriate add-ons to represent other components in the power train, which are discussed in the following sections.

4.1 Longitudinal Vehicle Dynamic Model

A car's longitudinal movement could be modeled utilizing Newton's law, as shown in the diagram below:

$$F_{net} = m_{eff} a \quad (1)$$

where F_{net} Represents the vehicle's net force, and a the vehicle's acceleration. Also m_{eff} is also the vehicle's impactful load.

$$F_{net} = F_x - R_A - R_R \pm R_G \quad (2)$$

where F_x is the real traction force, aerodynamic drag resistance R_A , rolling resistance R_R and gradient resistance R_G , respectively [12].

4.2 Battery Model

P.E.V.s commonly use Li-ion batteries. Li-ion batteries is formed here as an example.

The battery discharged power P_b can be expressed as:

$$P_b = U_{oc} I_b^2 R_{int} \quad (3)$$

The state of charge (S.O.C.) of the battery namely SOC_{bat} , shows how much electric energy is still stored in the battery and can be defined as [15],

$$SOC_{bat} = SOC_0 - \frac{\int I_b dt}{C_n} \quad (4)$$

4.3 Motor Model

The electric vehicle employs a variety of electric motors for driving the vehicle wheels. The series D.C motor is selected and modelled for E.V. The equations related to the operation of the series D.C. motor representing the mathematical model are as follows: Electromotive force in the dynamic state [16]:

$$E_a = K_a \phi W_n \quad (5)$$

$$U_a E + R_a I_A + U_{ba} \quad (6)$$

5 Modeling of Electric Vehicle Using MATLAB/Simulink Environment

It is critical to get modeling or collection of simulations and structures in MATLAB Simulink because they can be utilized for vehicle development, sizing, and various estimates during the planning stage. O. Vatan, MATLAB/Simulink simulation of an electric vehicle [17]. Ahmet Onur Kiyaklı et al. built the dynamic model using MATLAB/Simulink of an electric vehicle. In this work cycle boosting the overall energy efficiency of E.V [14]. To determine the appropriate energy control technique and exact component size, as well as to reduce energy consumption, T.A.T. Mohd provides a simulation model of a full-electric vehicle utilizing the MATLAB-Simulink framework to investigate the flow of power while driving. Recovery on drive performance [13]. Burak URAZEL et al. modeled in the MATLAB/Simulink Electric drive vehicle (E.D.V.) and performed simulation UDDS (Urban Dynamometer Driving Schedule), NEDC (The New European Driving Cycle), and NREL is three separate cycles (National Renewable Energy Laboratory Class-3) [12].

6 Conclusion

Environmental problems, including pollution and global warming, have significantly impacted human life and production. For such purposes, high-efficiency P.E.V.s will now be the primary goal of vehicle development, so PEV.s are a step on the way trying to replace ICEVs. In this paper, the comprehensive review and components of energy vehicle and used in electric cars are outlined. Furthermore, the paper fully evaluates and elaborates on several modeling approaches and methodologies, particularly employing the Matlab-simulink tool used for modelling and simulation of electric vehicles in order to improve performance metrics and develop a foundation for research investigation. The paper includes a clear overview of electric vehicles as well as modelling strategies for addressing electric—vehicle problems and obstacles.

References

1. Sen C (2010) Performance analysis of batteries used in electric and hybrid electric vehicles
2. Campanari S, Manzolini G, Garcia de la Iglesia F (2009) Energy analysis of electric vehicles using batteries or fuel cells through well-to-wheel driving cycle simulations. *J Power Sources* 186(2):464–477
3. Un-Noor F et al (2017) A comprehensive study of key electric vehicle (EV) components, technologies, challenges, impacts and future direction of development. *Energies* 10(8):1217
4. Basu AK, Tatiya S, Bhattacharya S (2019) Overview of electric vehicles (EVs) and EV sensors. In: *Sensors for automotive and aerospace applications*. Springer, pp 107–122
5. Chellaswamy C, Ramesh R (2017) Future renewable energy option for recharging full electric vehicles. *Renew Sustain Energy Rev* 76:824–838

6. Dincer I, Hamut HS, Javani N (2017) Thermal management of electric vehicle battery systems. Wiley
7. Patel N et al (2021) Electric vehicles: modern technologies and trends. Springer
8. Lu JM, Wang XK (2014) Study on the lithium-ion batteries performance of electric vehicles. *Adv Mater Res* 986–987:1869–1872
9. Szántó A, Szíki GÁ (2020) Review of modern vehicle powertrains and their modelling and simulation in MATLAB/Simulink. *Int J Eng Manage Sci* 5(2):232–250
10. Chau K (2014) Pure electric vehicles. In: *Alternative fuels and advanced vehicle technologies for improved environmental performance*. Elsevier, pp 655–684
11. Eldho Aliasand A, Josh FT (2020) Selection of motor for an electric vehicle: a review. *Mater Today Proc* 24:1804–1815
12. URAZEL B, KESKİN K (2020) Electric drive vehicle model and simulation with MATLAB. *Iğdır Üniversitesi Fen Bilimleri Enstitüsü Dergisi* 10(4):2461–2473
13. Kula P, Sawicki J, Armand S, Castro T, Kruszyński P, Rochel A (2009) New possibilities of applications aluminium alloys in transport. *Arch Metall Mater* 54(4):1199–1205
14. Kiyakli AO, Solmaz H (2018) Modeling of an Electric Vehicle with MATLAB/Simulink. *Int J Automot Sci Technol* 2(4):9–15
15. Li Z, Khajepour A, Song J (2019) A comprehensive review of the key technologies for pure electric vehicles. *Energy* 182:824–839
16. Bitar Z, Al Jabi S, Khamis I (2014) Modeling and simulation of series DC motors in electric car. *Energy Procedia* 50:460–470
17. Vatan O (2011) Modelling and simulation of longitudinal dynamics of electric vehicles. İstanbul Technical University, Institute of Science and Technology

Wear and Corrosion of Ceramic Coated Metallic Surface in Presence of Biodiesel



Md Abdul Maleque , Masjuki Hassan , Safa Yusuf Cetin, Ihsan Efeoglu, and Md Mustafizur Rahman

Abstract The aim of this work is to study the wear and corrosion of TiC coated steel in the presence of biodiesel. The TiC coating was developed by replacement method on the alloy steel surface using liquid additive approach with the help of TIG torch machine. The wear test was performed using CSM pin-on-disc tribometer in presence of biodiesel. The corrosion test was done using Autolab potentiostat–galvanostat corrosion analyzer in presence of biodiesel as electrolytic solution followed by characterization of the tested materials. The wear exhibited better wear resistance for the coated material due to the formation of new microstructure. The Tafel plot exhibited lower corrosion current density (I_{corr}) for the coated material compared to uncoated substrate. However, both substrate and TiC-coated steel are susceptible to corrosion under a biodiesel environment.

Keywords Biodiesel · Wear · Corrosion · Alloy steel

1 Introduction

Biodiesel is constructed from hydrogen bonds with water, therefore, it is more hygroscopic than diesel that is composed of hydrocarbons. Besides, some of the properties of biodiesel accelerate oxidation of metallic materials. Other than that, combustion

M. A. Maleque (✉)

Department of Manufacturing and Materials Engineering, Kulliyah of Engineering, International Islamic University of Malaysia, Kuala Lumpur, Malaysia

e-mail: maleque@iium.edu.my

M. Hassan · S. Y. Cetin

Dept of Mechanical Engineering, International Islamic University Malaysia, Kuala Lumpur, Malaysia

I. Efeoglu

Faculty of Engineering, Ataturk University, Erzurum, Turkey

M. M. Rahman

Faculty of Mechanical Engineering, Universiti Malaysia Pahang, Pahang, Malaysia

process inside the engine will contribute to the corrosive wear of the engine component material. Corrosion caused by contact of metals in presence of biodiesel which reduces the life of component and deteriorates the fuel properties which in turn negatively affects engine performance [1]. The most well-known factor that causes corrosion is the oxidation effect induced by oxygen. Research shows that biodiesel's hygroscopic properties are 30 times greater than diesel [2]. However, biodiesel is more corrosive than diesel fuels [3]. Hence, the corrosive-wear behavior of biodiesel has received a great attention in recent years and has been a major focus because of the increasing prevalence in automotive engine in presence of biodiesel. Metals and alloys are in generally susceptible to corrosion in biodiesel due to the fact that biodiesel is more conductive compared to petroleum diesel. Biodiesel fuels absorb more water than conventional petroleum diesels. This condition is caused by biodiesel and the electronegativity of oxygen due to the presence of oxygen. For this reason, dissolved oxygen in biodiesel can cause corrosion [3, 4]. Wear between component materials in engine applications such as, piston, cylinder liner, crankshaft joints and valve system occurs during sliding of the mating surfaces. Oxidation of the moving motor component reacts with biodiesel, which facilitates wear [5]. Wear and corrosion behavior were studied and compared with a surface coating as explained in [6, 7] in absence of biodiesel.

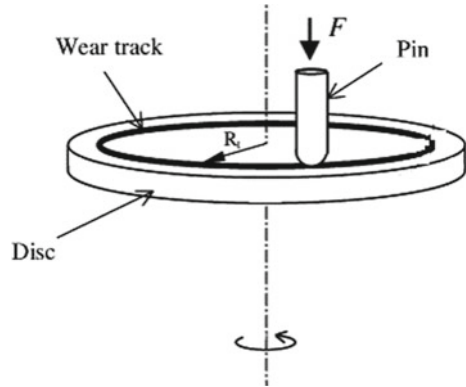
It is very important to investigate the wear and corrosion behavior of coated steel in contact with biodiesel, however, it is very hard to find this information in literature. Moreover, no work has been done on the interaction of corrosion and wear between coated material and biodiesel. Therefore, in the present work, the wear and corrosion behavior of alloy steel were performed under exposure of biodiesel.

2 Experimental Work

2.1 Wear Testing

In this work, 1 mg/mm² of 99.5% purity of TiC was used on a metallic alloy substrate. The TiC was mixed with polyvinyl acetate before preplacing on the metallic surface. The mixture was placed on the surface of the steel and then heated in the furnace at 80 °C for 1 h to remove the moisture. Miller tungsten inert gas machine (model: Telwin technology TIG 165) was used for coating after preplacing powder on the substrate surface. Inert gas, the argon, was used to shroud the arc from excessive oxidation at the rate of 20 l/min. The wear of material under *Jatropha curcas* biodiesel condition was assessed using CSM pin-on-disc tribo-tester with the duration of 1 h at ambient temperature as shown in Fig. 1. The test was conducted at three different loads such as 5 N, 7 N and 10 N load and four different rotation speeds (100 to 400 rpm with 100 rpm increment. The wear volume of disc material was calculated using Eq. 1 as cited in [7].

Fig. 1 Schematic diagram of pin-on-disk tribometer



$$\text{Disc volume loss} = 2\pi R \left[r^2 \sin^{-1}(d/2r) - (d/4)(4r^2 - d^2)^{1/2} \right] \quad (1)$$

where R , r , and d are the wear track's radius, the ball's diameter, and the wear track's width, respectively. The micrograph of the worn surfaces were investigated using SEM.

2.2 Corrosion Testing

The electrochemical corrosion test of both steel substrate and the coated material was carried out in order to assess the effect of coating on the corrosion behavior of the steel substrate under biodiesel. A method combining electrochemical experiment with computer controlled Autolab potentiostat–galvanostat (model: PGSTAT302) was utilized in this research to study the corrosion behavior. A standard electrochemical corrosion cell was used with three conventional electrodes. Pt rod of 3.5 cm² surface area was used as a counter electrode, Ag|AgCl saturated KCl was used as a reference electrode and finally the samples to be tested was used as a working electrode with a surface area of 1 cm². Before conducting the test, the sample was soaked in biodiesel for 30 min and linear polarization test was conducted over the range of -1.5 V to 1.5 V at a scanning rate of 10 mV/s. The i_{corr} and E_{corr} were obtained by fitting the experimental data and performing Tafel analysis using the electrochemical software (NOVA 1.8).

3 Result and Discussion

3.1 Wear Behavior in Biodiesel

The technical merit of biodiesel in automotive application is its improved performance behavior in comparison to convention diesel. This is mainly due to the the fatty acid ester of biodiesel can easily be absorbed on the metal surface after forming a monolayer film with hydrocarbon ends of the biodiesel which can inhibit the direct contact between the sliding asperities [8]. Presence of aliphatic fatty acids such as oleic and stearic acid with chemical formula of $C_nH_2 + nCOOH$ especially in the case of jatropha biodiesel can enhance the tribological behaviour of the metallic components upon sliding when exposed to biodiesel [9]. The stability of the film formation depends on process variables such as sliding speed, load, temperature, and the viscosity of the biodiesel. The influence of load on the wear of the tested samples at different sliding speeds are shown in Figs. 2 and 3.

The wear of both coated and uncoated materials exhibits linear correlation at all the applied conditions. This is attributed to the fact that increasing the load applied and the sliding speed reduces the stability of the boundary film due to the increases of the friction between contacts asperities which lead to the reduction of the lubrication behavior of the biodiesel. However, the coating shows higher wear resistance in comparison to the uncoated steel. This can be explained with the new microstructural

Fig. 2 Wear of uncoated material under biodiesel

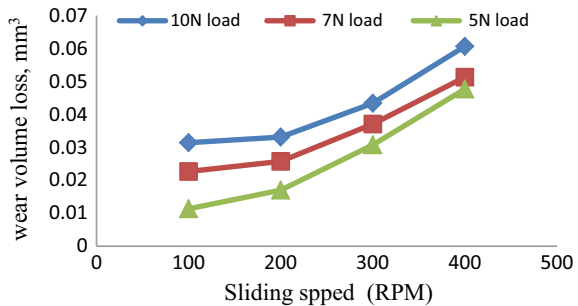
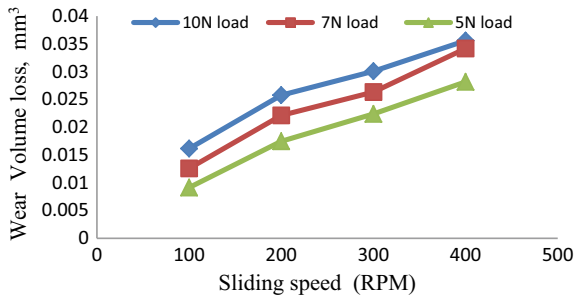


Fig. 3 Wear of coated material under biodiesel



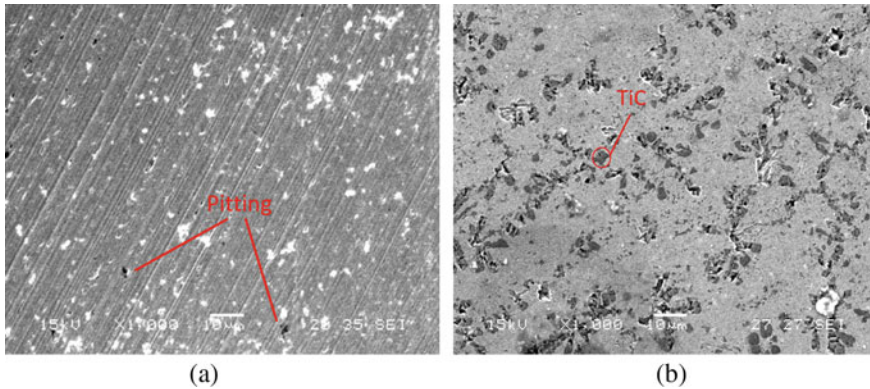


Fig. 4 SEM micrograph of the worn surfaces after exposure to biodiesel at fixed load of 10N and sliding speed of 400 rpm: **a** Uncoated material and **b** coated material

development in the morphology after re-solidified of the melt pool with new dendritic TiC formation on the surface of the coating. The high hardness of the TiC prevents penetration of the abrasive pin causing ploughing of the substrate.

In generally, the hard coated layer demonstrated lower wear rate (in terms of lower wear volume loss) compared to substrate material. The micrograph of the worn surfaces is shown in Fig. 4.

From Fig. 4 it can be clearly seen that the hard metallic coated surface has improved the wear resistance with the improvement of load carrying capacity. This in turn could reduce the contact between mating surfaces resulting lower abrasive particle on the surface from the counterpart material (mainly ball material). This also demonstrated that smooth worn surface generated after wear test on the coated material that strongly bonded to the steel substrate as shown in Fig. 4b. While uncoated surface (Fig. 4a) shows clear abrasive types of wear with some pitting mark as which can indicate corrosive type of wear under biodiesel condition and can consider a common wear mechanism for un-coated surface under biodiesel condition as also reported by [10]. Corrosion behavior in biodiesel. The main drawback of coating to be used in corrosion application is explained by the variation of corrosion potential between the substrate and the coating material that can supports formation of galvanic cell. Hence, increases the susceptibility of the material to corrosion. The same microstructure that helps increasing the wear resistance of the material can accelerate the failure of the material because of corrosion. Biodiesel unlike conventional diesel has high electrically conductive. While the corrosivity of the biodiesel is dependent on the concentration of the biodiesel especially when blended with conventional diesel fuel [11]. The Tafel curve for the coated steel and the substrate is shown in Fig. 5.

From the Tafel plot as shown in Fig. 5, it is clearly visible that incorporation of TiC for coating of the steel substrate increases the corrosion susceptibility under biodiesel environment. Table. 1 shows the output parameters such as E_{corr} and I_{corr}

Fig. 5 Tafel polarization curve of coated and un-coated material under biodiesel

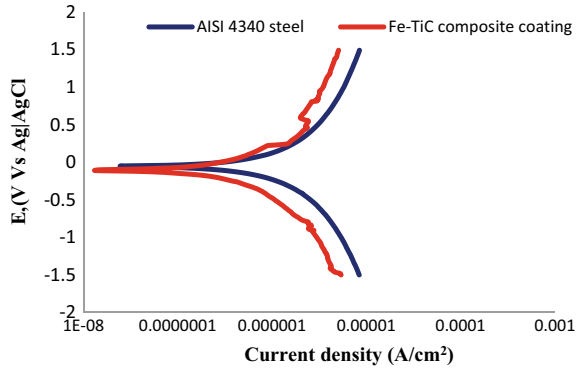


Table 1 E_{corr} and I_{corr} values of the steels under biodiesel derived from the polarization curves

Material	β_a (V/dec)	β_c (V/dec)	E_{corr} (V)	I_{corr} (A/cm ²)
Coated steel	0.87678	0.75624	- 0.106	3.68E - 07
Substrate steel	12.956	17.359	- 0.073	1.81E - 06

values extracted from the Tafel analysis by fitting the curve using a specialized Nova 1.8 software integrated with the corrosion analyzer.

The reason behind the reduction of the corrosion potential is attributed to the variation of the current conductivity between the steel substrate and the coating material (TiC) phase. TiC is considered electrochemically novel with electrical conductivity of $(2 \times 10^6 \Omega^{-1} m^{-1})$. Thus, reinforcing the steel with TiC can be a reason for generating a galvanic corrosion cell. However, the high impedance of TiC additionally to the impedance of the corrosion electrolyte aided in the reduction of the corrosion current density compared to substrate material to the same reason. This can be understood from the I_{corr} values that are tabulated in Table 1. Thus embedding TiC into the steel surface help reduction of the corrosion current density compared to substrate material under biodiesel.

4 Conclusion

Hard surface of AISI 4340 steel using a TIG torch melting approach was successfully developed after preplacing TiC particles on the steel substrate. The wear of the alloy steel exhibited better wear resistance for the coated surface due to the formation of new microstructure after coating reducing the wear volume of the steel by the factor of two. However, the incorporation of TiC for coating of the substrate increases the corrosion susceptibility in biodiesel environment after shifting it to

more active region. The corrosion behaviour of the coated material also demonstrated that corrosion current (I_{corr}) reduced compared to substrate material under biodiesel condition.

Acknowledgements The authors would like to acknowledge to the Malaysian Tribology Society (Project No.: MIG-0005-2021) and Ministry of Higher Education Malaysia of Malaysia (Project No.: FRGS/1/2021/TK0/UIAM/01/1) for funding this research.

References

1. Yeşilyurt MK, Öner İV, Yılmaz EÇ (2019) Biodiesel induced corrosion and degradation. *Pamukkale Univ J Eng Sci* 25(1):60–70
2. Nguyen XP, Vu HN (2019) Corrosion of The metal parts of diesel engines in biodiesel-based fuels. *Int J Renew Energy Dev* 8(2):119–132
3. Hoang AT, Tabatabaei M, Aghbashlo M (2020) A review of the effect of biodiesel on the corrosion behavior of metals/alloys in diesel engines. *Energy Sources, Part A Recovery, Utilization, and Environmental Effects* 42(23):2923–2943
4. Zuleta EC, Baena L, Rios LA, Calderón JA (2012) The oxidative stability of biodiesel and its impact on the deterioration of metallic and polymeric materials: a review. *J Braz Chem Soc* 23(12):2159–2175
5. Maleque A, Abdulmumin AA (2014) Tribocorrosion behaviour of biodiesel—a review. *Tribology Online* 9(1):10–20
6. Lepule ML, Obadele BA, Andrews A, Olubambi PA (2015) Corrosion and wear behaviour of ZrO₂ modified NiTi coatings on AISI 316 stainless steel. *Surf Coat Technol* 261:21–27
7. Wang XH, Song SL, Zou ZD, Qu SY (2006) Fabricating TiC particles reinforced Fe-based composite coatings produced by GTAW multi-layers melting process. *Mater Sci Eng A* 441(1–2):60–67
8. Lubis AMHS, Sudin MB, Ariwahjoedi B (2011) Investigation of worn surface characteristics of steel influenced by jatropha oil as lubricant and eco-friendly lubricant substituent. *J Appl Sci* 11:1797–1802
9. Sundus F, Masjuki HH, Fazal MA (2017) Analysis of tribological properties of palm biodiesel and oxidized biodiesel blends. *Tribology Transaction* 60(3):530–536
10. Maleque MA, Masjuki HH, Haseeb ASMA (2000) Effect of mechanical factors on tribological properties of palm oil methyl ester blended lubricant. *Wear* 239(1):117–125
11. Singh B, Korstad J, Sharma YC (2012) A critical review on corrosion of compression ignition (CI) engine parts by biodiesel and biodiesel blends and its inhibition. *Renew Sustain Energy Rev* 16(5):3401–3408

Linear Shrinkage of ZTA–TiO₂–Cr₂O₃ Ceramic Cutting Tool



Raqibah Najwa Mudzaffar, Ahmad Zahirani Ahmad Azhar,
Hanisah Manshor, Nik Akmar Rejab, and Afifah Mohd Ali

Abstract The linear shrinkage of the ZTA–TiO₂–Cr₂O₃ ceramic cutting tool was investigated in this work. In order to fabricate the tool, the process starts by wet mixing the raw materials and dried in the oven at 100 °C. The dried powder was crushed before being pressed into a round shape and sintered at 1600 °C with 1 h soaking time. The diameter of the cutting tool was measured before and after the sintering process to calculate the linear shrinkage. The result shows that the linear shrinkage of the ZTA–TiO₂–Cr₂O₃ ceramic cutting tool is 16.29%. This is due to the sintering process that affects the properties of the tool such as microstructure, fracture toughness, and Vickers hardness.

Keywords Linear shrinkage · Ceramic · Cutting tool

1 Introduction

Zirconia toughened alumina (ZTA) can be a great material for the cutting tool and can be expanded more for further improvement. The ZTA is known to be low in cost and ease the fabricating process [1]. Due to their advantageous mechanical properties, it is commonly recognized as a tool material with high hardness, high-temperature strength, and able to sustain the shape of cutting edge at higher temperatures [2]. In order to enhance ZTA's properties such as fracture toughness and hardness, additives are introduced into the ceramic compositions [3]. Researchers have made many efforts in their studies to develop the mechanical properties of the ZTA cutting tool [4]. In this study, titania (TiO₂) and chromia (Cr₂O₃) were used as additives. The significance of investigating linear shrinkage is to make sure the cutting tool fits on

R. N. Mudzaffar · A. Z. A. Azhar · H. Manshor · A. M. Ali (✉)

Department of Manufacturing and Materials Engineering, Kulliyyah of Engineering, International Islamic University Malaysia, 53100 Gombak, Kuala Lumpur, Malaysia
e-mail: afifahali@iium.edu.my

N. A. Rejab

School of Material and Mineral Resources Engineering, Universiti Sains Malaysia, Engineering Campus, 14300 Nibong Tebal, Pulau Pinang, Malaysia

the tool holder by measuring the shrinkage of the ZTA–TiO₂–Cr₂O₃ cutting tool. However, the study of linear shrinkage is still uncommonly reported. Thus, linear shrinkage was investigated in this work.

2 Methodology

In this research, alumina (Al₂O₃), yttria-stabilized zirconia (YSZ), titania (TiO₂), and chromia (Cr₂O₃) were used as the raw materials. Table 1 shows the list and characteristic features of the raw materials. The calculated weight of the raw materials in Table 2 was weighed accordingly by following the optimum percentage of the materials, studied by the previous researchers [2]. A ball mill was used to mix the powders for 24 h at 100 rpm and dried in the oven at 100 °C for 24 h before being crushed into powder by using agate mortar. The dried powder was manually pressed by using the hydraulic hand press at 100 MPa to produce a round shape sample. The samples were sintered at 1600 °C with a 1-h soaking time at a 5 °C/min sintering rate.

In order to study the linear shrinkage of the tools, a vernier caliper was used to measure the diameter of the tools before and after the sintering process as shown in Fig. 1. The linear shrinkage percentage was calculated by using Eq. (1).

$$\text{Linear shrinkage} = \frac{D_0 - D_1}{D_0} \times 100\% \quad (1)$$

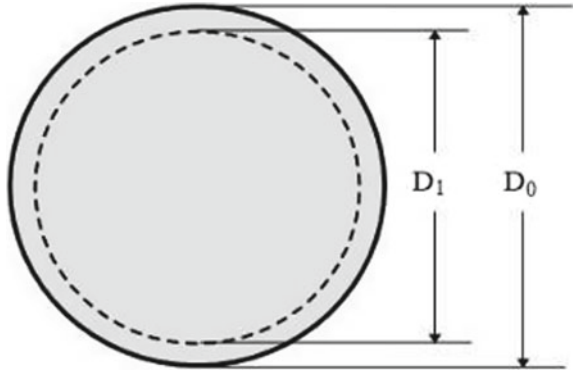
Table 1 List and characteristic features of the raw materials used to fabricate the ZTA–TiO₂–Cr₂O₃ cutting tool

Materials	Mean particle size (μm)	Purity (%)	Supplier
Alumina (Al ₂ O ₃)	1.0	99.8	Martinswerk, Germany
Yttria stabilized zirconia (YSZ)	0.1–2.0	94.5	Goodfellow, Cambridge Limited, USA
Titania (TiO ₂)	0.13	> 99.0	Sigma Aldrich
Chromia (Cr ₂ O ₃)	< 0.1	99.0	Sigma Aldrich

Table 2 Calculated weight of raw materials used to fabricate the ZTA–TiO₂–Cr₂O₃ cutting tool

Materials	Weight (%)	Weight (g)
Alumina (Al ₂ O ₃)	77.1	15.4269
Yttria stabilized zirconia (YSZ)	19.3	3.8567
Titania (TiO ₂)	3.0	0.5964
Chromia (Cr ₂ O ₃)	0.6	0.1200

Fig. 1 Diameter measured on the ZTA–TiO₂–Cr₂O₃ sample



where

- D₀ Diameter of ZTA–TiO₂–Cr₂O₃ sample before sintering
- D₁ Diameter of ZTA–TiO₂–Cr₂O₃ sample after sintering

3 Result and Discussion

The diameter of ZTA–TiO₂–Cr₂O₃ cutting tools before and after sintering is shown in Table 3. The calculated linear shrinkage percentage of the tool is 16.29%. The result of the linear shrinkage is acceptable since it is correlated to a study [3] that shows ZTA nano MgO (ZMN) and ZTA–MgO–CeO₂ (ZMC) ceramic cutting tools obtained a shrinkage percentage of 16.30% and 16.23% respectively.

The sintering process on the ceramic is the cause of the linear shrinkage of the ceramic itself. This is due to the atoms in the materials that can diffuse across the boundaries of the particles and fuse the particles to create one solid piece. The possibly affected properties are microstructure, fracture toughness, and Vickers hardness of the sample.

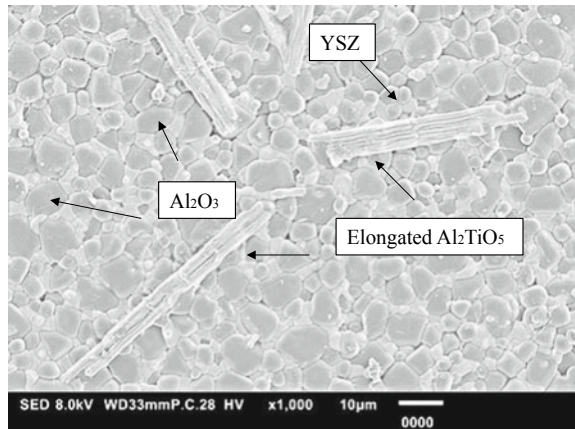
Figure 2 shows the microstructure of the ZTA–TiO₂–Cr₂O₃ cutting tool, where the YSZ and Al₂O₃ grains have no significant agglomeration and were well distributed within the sample. The elongated Al₂TiO₅ grains also can be observed due to the presence of TiO₂ [5]. The excess of TiO₂ produced the elongated Al₂TiO₅ grains and no longer be able to inhibit the grain growth of the Al₂O₃. The development of the elongated grains also could significantly affect the value of fracture toughness without diminishing the hardness value. It is proven when the fracture toughness and hardness of the ZTA–TiO₂–Cr₂O₃ ceramic cutting tool are 10.36 MPa.m^{1/2} and 1394.41 HV respectively, whereas the ZTA ceramic cutting tool exhibits 5.2 MPa.m^{1/2} of fracture toughness and 1438 HV of hardness value [6].

Additionally, the XRD analysis of the ZTA–TiO₂–Cr₂O₃ cutting tool is shown in Fig. 3, where the phases identified in the composite were Al₂O₃ or corundum, ZrO₂, and Al₂TiO₅. However, there were low peaks of TiO₂ and Cr₂O₃ detected,

Table 3 Diameter of ZTA–TiO₂–Cr₂O₃ cutting tools before and after sintering

No.	Diameter before sintering (mm)	Diameter after sintering (mm)
1	11.17	9.28
2	11.10	9.34
3	11.19	9.36
4	11.11	9.29
5	11.09	9.32
6	11.06	9.28
7	11.08	9.27
8	11.12	9.30
9	11.11	9.27
10	11.10	9.21
11	11.12	9.29
12	11.11	9.35
13	11.10	9.34
14	11.09	9.31
15	11.09	9.24
16	11.09	9.32
17	11.14	9.35
18	11.08	9.29
19	11.10	9.34
20	11.08	9.32
Avg.	11.11	9.30

Fig. 2 Microstructure of ZTA–TiO₂–Cr₂O₃ ceramic cutting tool



probably because of the low sensitivity of the XRD detection and the low content of TiO₂ and Cr₂O₃ in the sample, which are 3.0% and 0.6%, respectively. Therefore, an EDX analysis for the ZTA–TiO₂–Cr₂O₃ sample is done as shown in Fig. 4. The EDX weight ratios obtained are the quantity of O, Al, Zr, and Ti were 43.4%, 25.5%, 12.3%, and 1.8%, respectively. However, the Cr element was not detected via EDX due to the low weight percentage, which is 0.6%, and the low sensitivity of the machine. The C and Y elements were identified as voids. This is due to the condensation of the excess vacancies during the reactive diffusion between the elements [7].

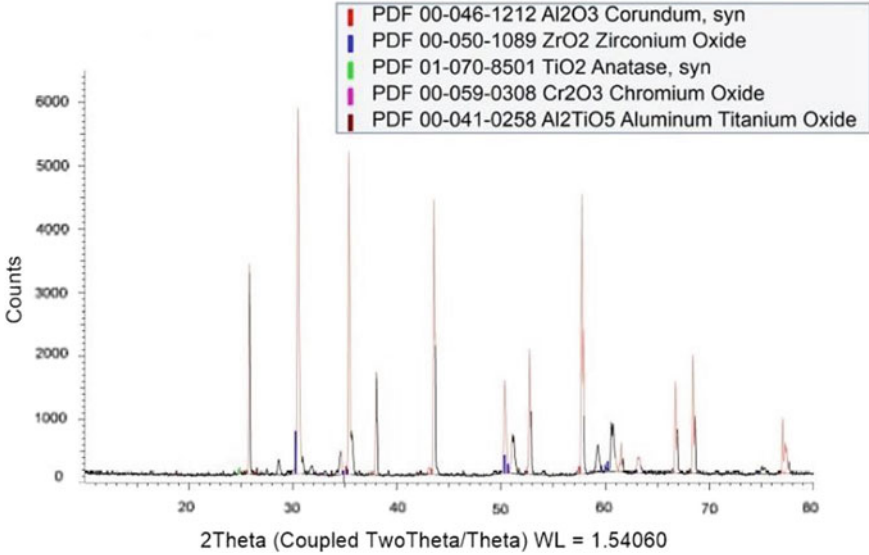


Fig. 3 XRD pattern for ZTA–TiO₂–Cr₂O₃ cutting tool

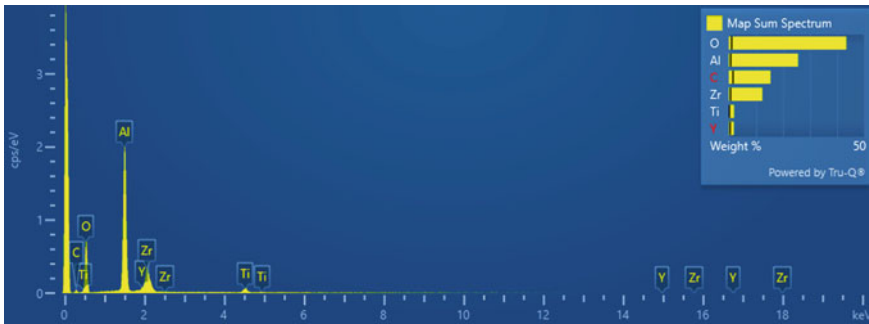


Fig. 4 EDX spectrum for ZTA–TiO₂–Cr₂O₃ sample

4 Conclusion

The linear shrinkage of the ZTA–TiO₂–Cr₂O₃ ceramic cutting tool is 16.29%. This is due to the sintering process that affects the properties of the tool such as microstructure, fracture toughness, and Vickers hardness.

Acknowledgements This work was funded by grant IIUM RMC Grant 2020—(RMCG20-031-0031). The authors also would like to acknowledge the International Islamic University Malaysia (IIUM) where this research has been conducted.

References

1. Varma BS, Kumar SS, Devi RS (2016) Behavior and wear mechanisms of ZTA based ceramic cutting tools on hardened steels. *Int J Res Eng Appl Sci* 6(4):8–14
2. Manshor H, Azhar AZA, Abd Rashid R, Sulaiman S, Abdullah EC, Ahmad ZA (2016) Effects of Cr₂O₃ addition on the phase, mechanical properties, and microstructure of zirconia-toughened alumina added with TiO₂ (ZTA–TiO₂) ceramic composite. *Int J Refract Metals Hard Mater* 61:40–45
3. Ali AM, Hamidon NE, Zaki NKM, Mokhtar S, Azhar AZA, Bahar R, Ahmad ZA (2018) The effect of cutting parameters on the performance of ZTA–MgO cutting tool. *IOP Conf Ser Mat Sci Eng* 290(1):012072
4. Rejab NA, Ahmad Azhar AZ, Ratnam MM, Ahmad ZA (2016) Role of MgO nanoparticles on zirconia-toughened alumina-5 wt-% CeO₂ ceramics mechanical properties. *Mat Sci Tech* 32(13):1316–1322
5. Manshor H, Aris SM, Azhar AZA, Abdullah EC, Ahmad ZA (2015) Effects of TiO₂ addition on the phase, mechanical properties, and microstructure of zirconia toughened alumina ceramic composite. *Cer Int* 41(3):3961–3967
6. Naga SM, Hassan AM, Awaad M (2015) Physical and mechanical properties of Ta₂O₅ doped zirconia-toughened alumina (ZTA) composites. *Cer Int* 41:62486255
7. Fukutomi H, Nakamura M, Suzuki T, Takagi SI, Kikuchi S (2000) Void formation by the reactive diffusion of titanium and aluminum foils. *Mat Trans JIM* 41(9):1244–1246

The Effect of LaB₆ Target Current on Mechanical and Tribological Properties LaB₆ Doped TiBCN Based Films Deposited by CFUBMS-HiPIMS



Nuriye Aksakalli , Ihsan Efeoglu , Berkay Gumus , and Evren Tan 

Abstract Improvements can be made to the surface properties of machine elements such as gears, bearings and shafts operating under different aggressive conditions such as high temperature, pressure, rotational speed. As surface wear properties, it is aimed to increase the performance and life of the machine elements by making the mechanical and tribological properties functional. In this study, CFUBMS-HiPIMS was used as an advanced PVD technology for the development of thin film coatings suitable for machine elements made of tool steel. LaB₆ doped TiBCN-based coatings were synthesized on 4140 base materials using a hybrid of pulsed dc and HiPIMS power supplies. Thus, coatings with dense microstructure and high adhesion were obtained. In coatings synthesized by Taguchi experimental design, Ti, Cr, TiB₂, LaB₆ targets and Ar, N₂, C₂H₂ gases were used by adding LaB₆ + TiB₂ on the Cr:CrN coating as a transition layer in TiBCN-based coatings. Optical Microscope, XRD, SEM were used to determine the characteristic microstructural properties of the coatings. Micro Hardness and Scratch testers were used to determine the mechanical properties, while tribological properties were determined with a pin-on-disc tribotest device under atmospheric conditions at room temperature. An increase in adhesion values (50N-88N-92N) and a decrease in microhardness values (12GPa-10GPa-9GPa) were observed with the increase of current applied (2A-2.5A-3A) to the LaB₆ target in TiBCN-based coatings.

Keywords TiBCN: LaB₆ · Microhardness · CFUBMS-HiPIMS

1 Introduction

Hexaborides of rare earth elements; As hard, wear and corrosion resistant coatings, it is interesting with its dark-purple-red color and chemical stability. LaB₆; It attracts

N. Aksakalli (✉) · I. Efeoglu
Faculty of Engineering, Atatürk University, Erzurum, Turkey
e-mail: nuriye.aksakalli12@ogr.atauni.edu.tr

B. Gumus · E. Tan
ASELSAN A.Ş., Ankara, Turkey

the attention of industry and researchers for strategic products with its features such as chemically stable, refractory, and high melting point (2170 °C) and long-term electron diffusion source. Despite its low spatter rate, it has high metallic conductivity properties [1]. It is seen that LaB₆-based film coatings are synthesized by different (Physical Vapor Deposition) PVD-based processes, and the relations between structure–property and process parameters are investigated in general terms. In the open literature, studies for the synthesis of LaB₆ thin films using HiPIMS (High Power Impulse Magnetron Sputtering) have been found to be quite limited. Advantages have been achieved. It has been noted that using LaB₆ as a target material will create a boron-rich plasma with different HiPIMS process variables, and the application of short pulses is beneficial in terms of discharge (process) stability. It has been observed that LaB₆ film synthesized by various sputtering techniques has improved adhesion and residual stresses and is extremely thin columnar with predominantly (100) oriented LaB₆ crystals. TiCN and TiBN coatings, on the other hand, are coatings with triple functional properties with amorphous matrix, which basically have high hardness, adhesion, and wear and corrosion resistance with the addition of various elements [2, 3]. In this study, TiBCN: LaB₆ multilayer coatings coated with optimized process parameters with Taguchi experimental design were synthesized on 4140 steel (6Gpa) and silicon using CFUBMS-HiPIMS, and its microstructural mechanical and tribological properties were investigated, and the effect of the current variable applied to the LaB₆ target was investigated. SEM, XRD, XPS were used to determine the microstructural properties of TiBCN-based coatings.

2 Experimental

TiBCN-based LaB₆ doped nanocomposite coatings were synthesized using HiPIMS (IONAUTICS-Hipster 6) with CFUBMS manufactured by Teer Coating Ltd. The microstructural, mechanical and tribological properties of thin film coatings synthesized on 4140 steel substrate and silicon wafer were investigated. Samples with a diameter of 35 mm steel substrate material were used. The surface roughness of the substrate material is approximately Ra = 1 μm. Cr, TiB₂ and LaB₆ targets as well as Ar, N₂ and C₂H₂ gases were used in the synthesis of TiBCN-based LaB₆ doped coatings and the formation of plasma. The magnetron arrangement of the targets is given in Fig. 1a. HiPIMS power supplies integrated into TiB₂ targets are positioned mutually. Pulsed-dc was applied to LaB₆ and Cr targets in the other two magnetrons. HiPIMS and Pulsed-dc power supplies were used as a hybrid in this process. The architecture of the coatings synthesized a Cr:CrN graded layer to increase adhesion, as seen in Fig. 1b. Also the Cr layer was grown for 10 min at the 3A Cr target current, the CrN was grown for an additional 10 min with 14 sccm N₂ flow. TiBCN-based LaB₆ doped nanocomposite coating layer was synthesized according to the determined parameters. Optimum experiment parameters were determined with Taguchi experiment design. EI Quanta FEG-450 SEM was used to determine the thickness and microstructural properties of thin film coatings. The crystal phase

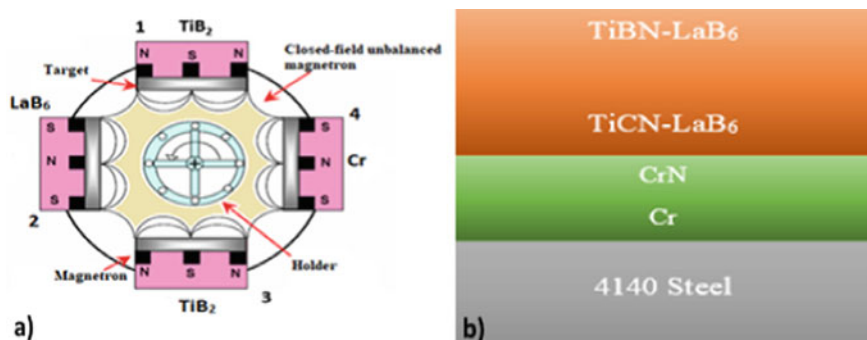


Fig. 1 **a** The Magnetron configuration of targets and **b** Architectural structure applied in the coating process

and densities were investigated by the Rigaku DMax-2200 system in the 10–90° scanning range with the XRD (Cu-K α : 1.5405 Å) radiation source also analyzing the chemical composition of the coatings by determining the binding energy (eV) of electrons with Specs-Flex XPS, the densities of the nitride phases were investigated. Buehler Micromet 2001 (Knoop indenter, 10gf load, 15 s) was used for the Microhardness value, which is one of the mechanical properties of TiBCN-based LaB₆ added coatings, while while Anton Parr (formerly CSM Instrument) Revetest tester (using 200 μ tip radius Rockwell-C diamond indenter with 100 N/min loading rate, and 10 mm/sec scratching speed) was used to characterize the adhesion at the base material-coating film interface. Tribological properties of the thin films were determined with Anton Parr (formerly CSM Instrument) tribotester (dead load: 1N, rotation speed: 10 cm/sec, pin: 100Cr6, Φ 1.5 mm) at room temperature and under normal atmosphere.

3 Results and Discussions

The thickness and microstructural characterization of TiBCN-based LaB₆-doped nanocomposite thin-film coatings synthesized using HiPIMS were analyzed using SEM, and dense and homogeneous structures of all coatings were observed in Fig. 2. The thicknesses of TiBCN: LaB₆ coatings were obtained as 0.696 μ m (R1), 0.705 μ m (R2) and 0.764 μ m (R3). This is due to the change in applied current. In order to improve the adhesion between the substrate and the coating film in thin-film coatings synthesized according to the determined experimental parameters, the synthesized Cr:CrN interlayer was obtained as approximately 200 nm.

As seen in the XRD graphs of TiBCN-based LaB₆ added coatings in Fig. 3, it is seen that TiB₂, TiN, LaB₆ (200), LaB₆(320), LaB₆ (321) phases have grown. In XRD graphics; While LaB₆ structure has a tendency towards amorphous growth in all coatings; In very small amounts, there are signs of crystallization in the

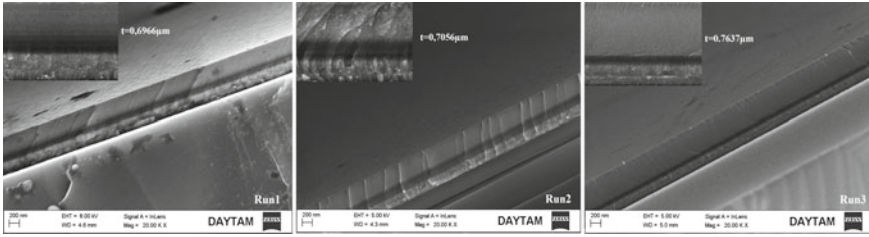
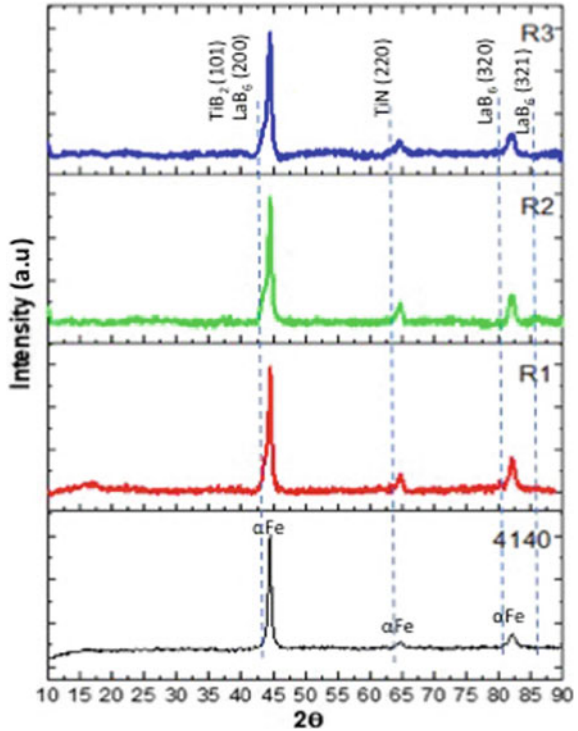


Fig. 2 SEM images of TiBCN: LaB₆ coatings

(200)/(220)/320)/(311)/(321) directions of LaB₆ [5–7] While the amperage value applied to R1 is 2A, the amperage value applied to R3 is 3A.

As seen in the N 1s, B 1s XPS graphs in Figs. 4 and 5 while TiN, B, BN phases are formed in all TiBN: LaB₆ coatings, the BN density in the R1 coating is the least in the R3 coating. The peaks of the N1s XPS plots at 398.1 eV and 397.86 eV corresponded to the BN and TiN phases, respectively. When B1s XPS graphs were examined, B and BN peaks were obtained at 186 eV and 190, 53 eV, respectively, as seen in the literature [6, 7]. The highest hardness value of TiBCN-based LaB₆ added coatings was 12GPa in R1 coating and the lowest hardness value was 9GPa in R3 coating.

Fig. 3 XRD graphics of TiBCN: LaB₆ coatings



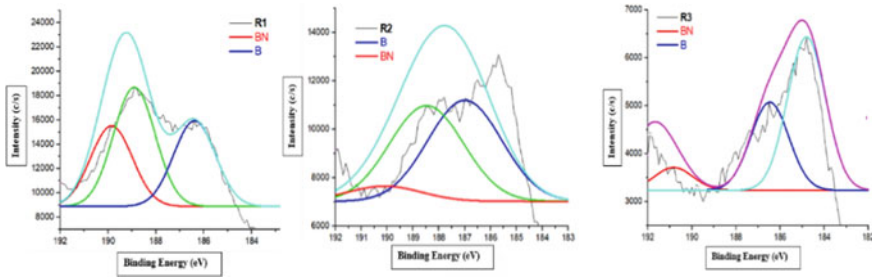


Fig. 4 XPS graphics of TiBCN: LaB₆ coatings for B 1 s

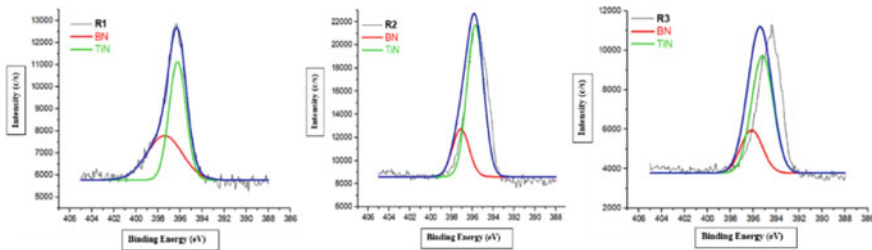


Fig. 5 XPS graphics of TiBCN: LaB₆ coatings for N 1 s

The critical load values and adhesion properties of the coatings were analyzed by the Scratch test and it was observed that the highest critical load value was 92N in the R3 coating, while the lowest critical load value was 50N in the R1 coating. While the lowest current was applied to R1, the highest current value was applied to R3. When the scratch profiles obtained by the Scratch test in Fig. 6 were examined under the microscope, no adhesive, chevron, edge damage, and spallation were observed in the coating. Considering the results of the studies on TiCN and TiBN coatings in the literature, it has been observed that the adhesion values of TiBCN-based coatings are high [4]. It was observed that the adhesion values were even higher when LaB₆ was added to the TiBCN-based coatings. To investigate the tribological properties of TiBCN: LaB₆ coatings, pin-on-disc wear test was performed under atmospheric conditions (45–55% RH) at room temperature (22 °C), and their friction coefficients were $\mu = 0.143$ (R1), $\mu = 0.366$ (R2) and $\mu = 0.511$ (R3). The increase in the applied current value causes an increase in LaB₆ in the structure, which affects the friction coefficient.

4 Conclusions

It was observed that an extremely dense microstructure was grown with the pulsed-dc parameters – 70 negative voltage applied to the base material, 3A applied to the Cr

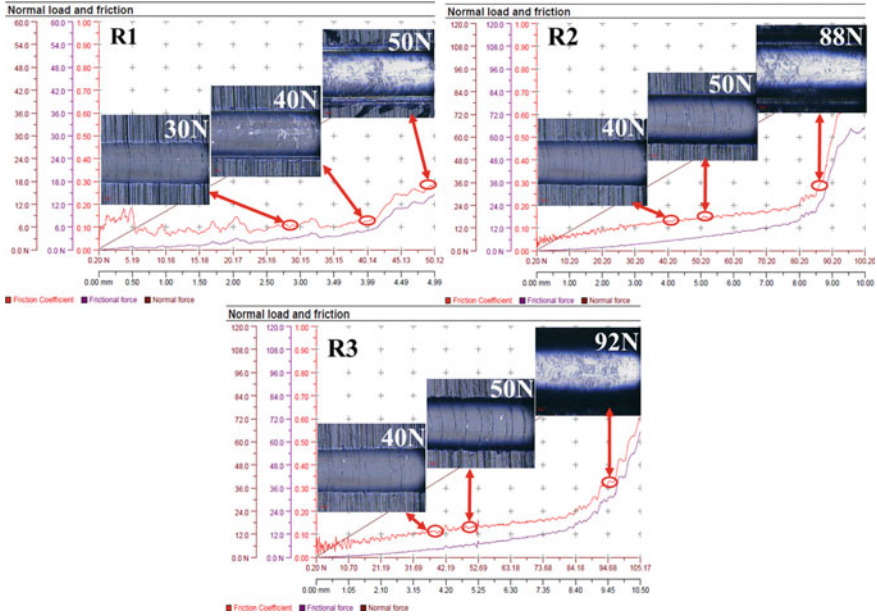


Fig. 6 Scratch test results of TiBCN: LaB6 coatings

target, and 7sccm (duty cycle: 30%) of the N₂ flux in the synthesis of the Cr:CrN graded layer in the coatings. In the next step, it was observed that the TiCN:TiBN nanocomposite structure, which was grown in a graded microstructure by adding LaB₆ using HiPIMS and Pulsed dc, was also grown intensively. In the TiBCN: LaB₆ coating process parameters, with the increase in the current applied to the LaB₆ target, the highest adhesion value was 92N (9.8GPa microhardness and 0.143 friction coefficient) and the lowest adhesion value was 50N (12GPa microhardness and 0.511 friction coefficient). The reason for this is that the amount of LaB₆ in the structure increases with the increase of current. The highest adhesion value was obtained at the highest LaB₆ target current (3A) and 4.5% duty cycle. In addition, an increase in the friction coefficients was observed with the increase of the applied current and voltage value. When the XRD and XPS graphs were examined, it was determined that the graphs were compatible with each other, and it was determined that TiN, B, BN, TiB₂, LaB₆ phases were formed in all coatings.

Acknowledgements This research is part of the project supported by ASELSAN A.Ş. under the Researcher Training Program for Industry (SAYP). The authors thank to ASELSAN A.Ş. for funding the project.

References

1. Craciun V, Cristea G, Lambers E, Trusca R, Fairchild S, Back T, Gruen G, Craciun D (2016) Characteristics of LaB₆ thin films grown by pulsed laser deposition. *J Vac Sci Technol A Vac, Surf Films* 34:051509
2. Han B, Neena D, Wang Z, Kondamareddy KK, Li N, Zuo W, Yan S, Liu C, Fu D (2017) Investigation of structure and mechanical properties of plasma vapor deposited nanocomposite tbn films. *Plasma Sci Technol* 19
3. Saoula N, Madaoui N, Tadjine R, Erasmus RM, Shrivastava S, Comins JD (2016) Influence of substrate bias on the structure and properties of tcn films deposited by radio-frequency magnetron sputtering. *Thin Solid Films* 616:521–529
4. Constantin L, Braic M, Dinu M, Balaceanu M, Braic V, Farcau C, Vladescu A (2016) Effects of zr, nb, or si addition on the microstructural, mechanical, and corrosion resistance of tcn hard coatings. *Mater Corros* 67:929–938
5. Onoprienko AA, Ivashchenko VI, Timofeeva II, Sineelnichenko AK, Butenko OA (2015) Characterization of Ti-BCN films deposited by dc magnetron sputtering of bicomponent Ti/B4C target. *J Superhard Mater* 37:14–20
6. Pruncu CI, Braic M, Dearn KD, Farcau C, Watson R, Constantin LR, Balaceanu M, Braic V, Vladescu A (2017) Corrosion and tribological performance of quasistoichiometric titanium containing carbo-nitride coatings. *Arab J Chem* 10:1015–1028
7. Liu Q, Cheng C, Du M, Wu Y, Ren C, Ding K, Song M, Huang C (2018) Porous hexagonal boron nitride sheets: effect of hydroxyl and secondary amino groups on photocatalytic hydrogen evolution. *ACS Appl Nano Mater* 1

Enhancing the Tool Life of Aluminium Oxide (Al_2O_3) Inserts Using Hybrid Microwave Energy in Dry Machining of High Strength Steel (KRUPP 6582)



Rakan Hatem Alawbali and Tasnim Firdaus Ariff 

Abstract Alumina (Al_2O_3) is a high-performance ceramic material with outstanding physical properties. Alumina is regarded as an extremely hard material with excellent wear resistance. However, tool wear remains a severe issue of dry machining resulting in a reduction in tool life, increased tool cost and a higher frequency of tool changing. Therefore, in this study, Hybrid Microwave (HMW) energy is employed to improve mechanical properties and extend tool life. Three different types of Alumina inserts were used. Al_2O_3 (HMW) was post-sintered with silicon carbide (SiC) as the susceptor, whereas Al_2O_3 (MW) was post-sintered with no susceptor. These two inserts were compared to the original sample Al_2O_3 (Untreated). The post-sintering processes lasted 20 min at 220 °C. Mechanical testing, such as density and hardness, was carried out. Dry machining was used to test the tool life and wear resistance of these Alumina inserts at three different cutting speeds (198, 250, and 310 m/min) at a feed rate of 0.2 mm/rev and a depth of cut of 0.2 mm. This study employed a high-strength steel workpiece (KRUPP 6582). When compared to Al_2O_3 (MW) and Al_2O_3 (untreated) inserts, the results showed that the density and hardness of Alumina inserts were increased using the HMW post-sintering procedure by 3.6% and 6.3% respectively. The tool life of Al_2O_3 (HMW) has increased by 28%, while for Al_2O_3 (MW), only 8.8%. HMW has demonstrated good performance in enhancing the mechanical properties and tool life of Al_2O_3 in dry machining of high strength steel (KRUPP 6582).

Keywords Hybrid microwave · Tool life · Al_2O_3 · SiC

1 Introduction

In today's industrial environment, achieving products with low manufacturing costs, high quality, and enhanced productivity is a challenge. One of the most significant aspects of the machining industry is selecting acceptable structural and mechanical

R. H. Alawbali · T. F. Ariff (✉)

Department of Manufacturing and Materials Engineering, Faculty of Engineering, International Islamic University Malaysia, Kuala Lumpur, Malaysia

e-mail: tasnim@iium.edu.my

features of cutting-tool inserts, which includes tool changing costs and time. The cost of machining operations is critical. One major challenge in machining industries is developing cutting tools with remarkable wear resistant properties and improved quality.

Aluminium Oxide (Al_2O_3) also known as alumina, is a hard material with exceptional wear resistance. It is well known for its favourable stiffness-to-weight ratio, low thermal expansion, good temperature stability and corrosion resistance. Nevertheless, a cutting tool insert still has great difficulty and imposes many challenges while functioning in dry cutting conditions. Dry machining of hardened steel which is a more sustainable option, would also result in higher tool wear rates, shorter tool life, and higher tool costs [1].

The microwave energy method for high-temperature processing of materials has a couple of advantages that have caught the attention of machining industries. It has better quality production, new materials and product, reduces processing costs, etc. In contrast to conventional methods, the microwave energy method can heat many essential materials rapidly, selectively, uniformly, less expensively and with much better control [2]. In current studies, ceramics are treated via hybrid microwave sintering (HMW) with the aid of susceptors. However, microwave and conventional heating characteristics are combined in HMW, resulting in a volumetric heating mechanism [3].

The discoveries of numerous new materials with functional and exciting properties using unconventional ideas and developments in material processing such as microwave energy have led to new technologies and ideas that are more capable, faster, economical, and environmentally friendly [4, 5]. HMW sintering generates TiC inserts with the highest density, hardness, and strength compared to conventional sintering and Hot Isostatic Pressing (HIP). Microwave ceramics processing can be used as an alternative to conventional sintering of ceramics. Rapid heating, more homogeneous microstructures, penetrating radiation, and higher densities are all advantages of microwave processing of ceramics [6].

Ceramic materials produced from microwave processing will have unique ceramic microstructures and features that conventional processing will not be able to achieve. Ceramic materials can be microwave processed for various technical and economic reasons. Improved physical and mechanical qualities, uniform and quick heating of ceramics, and increased energy efficiency are among the many advantages [7]. Microwave sintering entails energy conversion, whereas traditional sintering entails energy transfer. In microwave sintering, heat is generated internally within the material, whereas heat is received externally from external sources in conventional heating. Materials absorb microwave energy and transform electromagnetic energy into thermal energy within the sample volume during microwave heating and commonly known as volumetric heating [8]. This is microwave processing's inside-out heating, as opposed to conventional heating's outside-in heating [9].

Using original SiC rectangular plates positioned parallel to the electric field, Marinel et al. [10] constructed a completely automated 915 MHz single-mode cavity to sinter large alumina samples. They concluded that the largest surface of the SiC susceptor plates was the most suited geometry for uniform heating. The alumina

sample's grain size appeared to be slightly larger in the centre than on the outside. Furthermore, highly dense alumina with a density of $> 99.6\%$ and high hardness values ($\text{HV}1 \sim 20 \text{ GPa}$) was efficiently created.

The microstructure and densification of Al_2O_3 and 3Y-TZP were researched and compared across three distinct sintering cells comprising thermal insulators, a SiC susceptor, and a protective mullite tube in another study conducted by Khalile et al. [11]. Using a sintering cell comprising both mullite tube and SiC susceptor resulted in higher final densities, lower densification temperatures, and greater microstructure homogeneity. A putative susceptor effect of the mullite tube can explain this. For 3Y-TZP, which combines better with MW than Al_2O_3 , the impact of the sintering cell is less important. With the presence of SiC susceptor and without mullite tube, densification curves were also altered to higher temperatures during sintering.

SiC susceptors, particularly in solid form, have been the subject of extensive investigation in hybrid microwave sintering on ceramic materials. However, research on the effects of hybrid microwave radiation employing SiC powder as susceptors on machining performance is still in its early stages. As a result, this study examines and compares the mechanical properties of the alumina inserts such as their density and hardness, on tool life in dry machining of high strength steel (KRUPP 6582) after microwave (without susceptor) and hybrid microwave post-sintering process, using Silicon Carbide (SiC) powder as a susceptor.

2 Methodology

Microwave (MW) radiation was used to heat the triangular Al_2O_3 insert (Sandvik Coromant) without using a susceptor. These samples were heated to 220°C in a microwave oven (Panasonic NN-CD997S) for 20 min to apply the microwave post-sintering process. Meanwhile, 50 cm^3 of Silicon Carbide (SiC) powder (Alfa Aesar 300 mesh) was used for the hybrid microwave (HMW) post sintering method. The powder was weighed before being put in a crucible (250 ml). A 50 ml smaller crucible was used to place the insert with the SiC powder around it.

The mechanical properties of each sample, such as density and hardness, were then examined and compared to the untreated Al_2O_3 inserts. The density was measured using a Densimeter (MD-2005). The hardness values were obtained using the Rockwell Hardness Tester (660RLD/T). For all three samples, Al_2O_3 (untreated), Al_2O_3 (MW) and Al_2O_3 (HMW), the tool life and wear rates were determined through dry machining of high strength steel (KRUPP 6582) with a 100 mm diameter at cutting speeds of 198, 250, and 310 m/min. An optical microscope (Meiji Techno FU 1010) was used to measure tool wear, and graphs were applied to determine tool wear rates.

Fig. 1 Density comparison between Al_2O_3 inserts

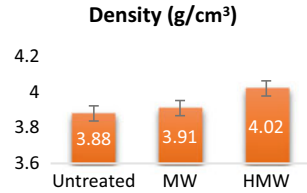
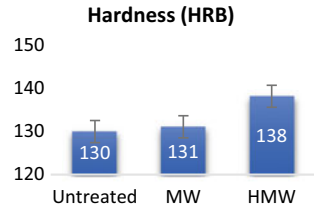


Fig. 2 Hardness comparison between Al_2O_3 inserts



3 Results and Discussion

3.1 Density

According to the density data in the bar chart shown in Fig. 1, the density increased after the MW and HMW post-sintering processes. The Al_2O_3 (untreated) insert has the lowest density (3.88 g/cm^3), whereas the Al_2O_3 (HMW) has the highest density (4.02 g/cm^3). The density of Al_2O_3 (MW) and Al_2O_3 (HMW) increased by 0.8% and 3.6% respectively when compared with Al_2O_3 (untreated).

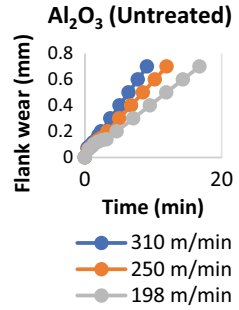
3.2 Hardness

The Al_2O_3 (HMW) insert, as seen in Fig. 2, has the highest hardness value, measuring 138 HRB, followed by the Al_2O_3 (MW) insert measuring 131 HRB, and the Al_2O_3 (untreated) insert, measuring 130 HRB. Rapid heating using SiC susceptors resulted in a 5.3% increase in hardness while sintering at the same temperature.

3.3 Tool Wear

The relationship between flank wear and cutting time is represented by the graphs in Figs. 3, 4, and 5. The graphs were extrapolated to determine the maximum flank wear value of 0.7 mm in order to determine the tool life. The Al_2O_3 (HMW) exhibits the least flank wear, as shown in the graphs, when dry machining high strength steel at

Fig. 3 Flank wear Al₂O₃ (Untreated)



three different cutting speeds of 198, 250, and 310 m/min. The Al₂O₃ insert displays a noticeably higher level of wear resistance following HMW treatment. The Al₂O₃ (MW) insert's wear resistance is a little bit higher than that of Al₂O₃ (untreated).

Fig. 4 Flank wear Al₂O₃ (MW)

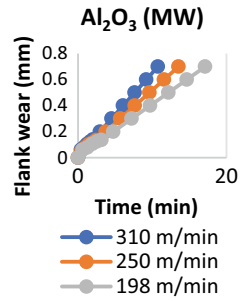
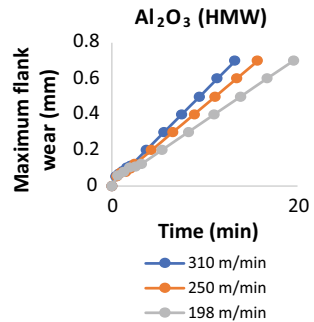


Fig. 5 Flank wear Al₂O₃ (HMW)



3.4 Tool Life

To achieve ideal machining productivity, there should be an optimum and desired cutting speed; when the cutting speed is high, the greater the output rate, the shorter the tool life. That is to say, the slower the cutting speed, the longer the tool life, but the lower the productivity. Taylor’s tool life equation (Eqs. 1–2) can be used to investigate the relationship between cutting speed and tool life [12].

$$VT^n = C \tag{1}$$

$$\log V + n\log T = \log C \tag{2}$$

where

- V Cutting speed (m/min)
- T Tool life (min)
- n slope
- C Machining constant.

The slope of the graph illustrating the linear relationship between logV and logT, shown in Fig. 6, can be used to determine the n values. The C values were estimated using Eq. 2 once the n values were determined, as shown in Table 1.

In dry machining at 198 m/min, the tool life of Al₂O₃ (HMW) and Al₂O₃ (MW) increased by 17.3% and 2.3% respectively, as compared to Al₂O₃ (Untreated). When the cutting speed was increased to 250 m/min, the tool life of Al₂O₃ (HMW) and

Fig. 6 Linear relation (log T and log V)

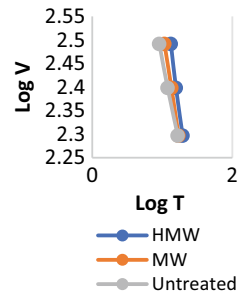


Table 1 Tool life of Al₂O₃

V (m/min)	Al ₂ O ₃ (Untreated)			Al ₂ O ₃ (MW)			Al ₂ O ₃ (HMW)		
	T(min)	n	C	T(min)	n	C	T(min)	n	C
198	16.7	0.73	1546	17.1	0.96	3027.4	19.6	1.15	6064
250	11.95	0.73	1529	13.55	0.96	3052.1	15.73	1.15	5945
310	9.7	0.73	1625.5	10.76	0.96	3032.6	13.3	1.15	6078

Al_2O_3 (MW) increased by 31.6% and 13.3% respectively. In comparison, when the cutting speed was increased to 310 m/min, the tool life of Al_2O_3 (HMW) increased by 37.1%, while Al_2O_3 (MW) tool life increased by 10.9%. When the cutting speed was raised, the tool life of Al_2O_3 inserts decreased. The C value, on the other hand, grew as the cutting speed increased.

3.5 Analysis of Results

Overall, 20 min of HMW post-sintering increased the density (3.6%) and hardness (6.3%) of the Al_2O_3 inserts. As a result, tool performance has improved in terms of tool wear reduction and hence tool life has increased (28%). Ionic induction, dipole relaxation, and photon-photon interaction can all be used to transport energy into materials without the use of an intermediate in the microwave energy process. Microwave energy alone is insufficient to heat the alumina effectively because alumina is a very poor microwave absorber [13]. This explains why there was no significant increase in the hardness for the Al_2O_3 (MW).

On the contrary, using SiC as a susceptor has rapidly increased the heating process because it comprises a particulate substrate that is considerably non-reflective of microwave radiation; SiC susceptors can absorb microwave energy effectively and efficiently. Then, each crystal lattice in the Al_2O_3 molecules rises at a constant amplitude of vibration, resulting in uniformly distributed heat throughout the ceramic body [8]. The overall improvement in Al_2O_3 inserts and their performance in dry machining of high strength steel is noticeable.

4 Conclusion

In comparison to MW, the HMW post-sintering technique using SiC susceptor has a significant influence in enhancing mechanical properties, wear resistance and the tool life of the Al_2O_3 tool inserts. Al_2O_3 (HMW) tool life has been enhanced by 28%, while Al_2O_3 (MW) tool life has increased by only 8.8%, which is seen in the dry machining of high strength steel (KRUPP 6582). SiC susceptor has the ability to rapidly heat the specimen volumetrically in a short duration of time effectively.






References

1. Goindi GS, Sarkar P (2017) Dry machining: a step towards sustainable machining—challenges and future directions. *J Clean Prod* 165:1557–1571
2. Sun J, Wang W, Yue Q (2016) Review on microwave-matter interaction fundamentals and efficient microwave-associated heating strategies. *Materials* 9(231):1–25

3. Karayannis VG (2016) Microwave sintering of ceramic materials. *IOP Conf Ser Mater Sci Eng* 161(1)
4. Yang G, Park SJ (2019) Conventional and microwave hydrothermal synthesis and application of functional materials: A review. *Materials* 12(7):1177
5. Tayier W, Janasekaran S, Tai VC (2022) Microwave hybrid heating (MHH) of Ni-based alloy powder on Ni and steel-based metals—a review on fundamentals and parameters. *Int J Lightweight Mater Manuf* 5(1):58–73
6. Ariff TF, Ibrahim HI, Roselley NS, Iqbal M, Hilmy I, Suryanto (2014) Enhancing tool life of silicon nitride inserts via hybrid microwave post sintering. *Aust J Basic Appl Sci* 8(15):80–85
7. Bekal A, Hebbale AM, Srinath MS (2018) Review on material processing through microwave energy. *IOP Conf Ser Mater Sci Eng* 376(1)
8. Ariff TF, Mohamed NMN, Binafif AA, Azhar AZ, Bahar R, Karim ANM, Amin AKM (2018) Improvements in the development of silicon nitride inserts using hybrid microwave energy for machining Inconel 718. *Int J Eng Res Technol* 7(10)
9. Ćurković L, Veseli R, Gabelica I, Žmak I, Ropuš I, Vukšić M (2021) A review of microwave-assisted sintering technique. *Transactions of FAMENA* 45(1):1–16
10. Marinel S, Manière C, Bilot A, Bilot C, Harnois C, Riquet G, Valdivieso F, Meunier C, Coureau C, Barthélemy F (2019) Microwave sintering of alumina at 915 MHz: modeling, process control, and microstructure distribution. *Materials* 12(16):2544
11. Khalile N, Petit C, Meunier C, Valdivieso F (2022) Hybrid microwave sintering of alumina and 3 mol% Y₂O₃-stabilized zirconia in a multimode cavity—influence of the sintering cell. *Ceram Int* 48(13):18143–18150
12. Kalpakjian S, Schmid SR (2019) *Manufacturing engineering and technology*. 8th edn. Pearson Prentice Hall, Singapore
13. Vukšić M, Ljubek M, Zmak I, Ćurković L (2020) Hybrid microwave sintering of alumina ceramics which contain waste alumina. *Nanomaterials Sci Eng* 2(4):154–161

A Comparative Study of Additively Manufactured Nickel Titanium (NiTi) Shape Memory Alloy (SMA)



Sivasanghari Karunakaran , Dayang Laila Abang Abdul Majid ,
Che Nor Aiza Jaafar , Muhammad Hussain Ismail ,
and Husam Yahya Imran 

Abstract Nickel titanium (NiTi) belongs to the class of Shape Memory Alloy (SMA) and has a memory capability to retain its original shape when subjected to stress or temperature changes. It undergoes solid to solid state phase transformations from an austenite to martensite phase which corresponds to the functional properties of pseudo elasticity (PE) and shape memory effects (SME). These indicate a strong coupling effect of NiTi in response to stress and temperature changes. These properties esteemed NiTi as an excellent candidate for many design applications in automotive, aerospace, robotic and biomedical industry. However, potential applications of NiTi are hindered by the conventional manufacturing methods that are limited to simple geometries. Therefore, advances in Additive Manufacturing (AM) techniques can simplify the process by fabricating NiTi parts with complex geometry and enhanced the mechanical aspects of NiTi. A review on additively manufactured NiTi is provided in this paper. This paper also reviews affecting parameters of additively manufactured NiTi. Besides that, a case study on NiTi fabrication through directed energy deposition (DED), selective laser melting (SLM) and electron beam melting (EBM) are briefly explained in this paper. The main aim of this paper is to provides a fundamental knowledge on additively manufactured NiTi and to give readers a better understanding on the perspectives of material properties.

Keywords Shape Memory Alloy (SMA) · Additive Manufacturing · Nickel Titanium (NiTi)

S. Karunakaran (✉) · D. L. A. A. Majid · C. N. A. Jaafar · H. Y. Imran
Faculty of Engineering, Universiti Putra Malaysia UPM, 43400 Serdang, Selangor Darul Ehsan, Malaysia

M. H. Ismail
Faculty of Mechanical Engineering, Universiti Teknologi MARA, 40450 Shah Alam, Selangor Darul Ehsan, Malaysia

1 Introduction

NiTi, also known as Nitinol, is most utilized used SMA in aerospace, automotive and medical industry due to its unique functional properties such as PE and SME [1] and has ability to deform its shape with load or temperature. Due to this reason, NiTi SMA face complications during machining in which thermal and stress issues arising throughout the manufacturing processes. Conventional manufacturing methods including casting, vacuum melting, grinding, machining and powder metallurgy attributes to poor mechanical properties, poor formability, high reactivity and difficulties in producing complex geometry parts [2]. To date, conventionally manufactured NiTi parts have been producing basic material forms such as sheets, bars, wire, ribbon and tubing [3].

However, with recent advancement in manufacturing technologies, AM techniques offers an ideal and viable solutions for simplifying the fabrication routes for complex geometry of NiTi parts while retaining SMA properties. AM methods upgrading the fabrications stages by directly producing near-net components in a single step. Yet research studies on the affecting parameters of additively manufactured NiTi parts is not extensive and to date, there is no definite parameters to produce a complete AM fabricated NiTi [4]. Therefore, extensive studies and research were conducted on the processing parameters, microstructure, material composition and mechanical properties to assist the development of additively manufactured NiTi.

Herein, this paper also presents a comparative case study on the properties of NiTi SMA alloy through three AM processes. This provides an insight into the affecting parameters for various AM techniques.

2 Additive Manufacturing and the Affecting Parameters for NiTi SMA

AM technology offers an ideal solution for processing NiTi parts as it has circumvented the difficulties resulted by the conventional PM methods. Fabrication of complex geometry parts of NiTi is possible with the integration of computer aided design (CAD) and computer aided manufacturing (CAM) in AM techniques [5] with higher dimensional accuracy in shorter time.

AM methods are divided in two types, powder-bed fusion and flow-based deposition. Powder-bed fusion AM methods includes Selective Laser Melting (SLM), Electron Beam Melting (EBM), Selective Laser Sintering (SLS), Direct Energy Deposition (DED) and Direct Metal Sintering (DMS) [5]. Flow-based deposition AM methods are Shaped Metal Deposition (SMD), Electron Freeform Fabrication (EFF), Laser Freeform Fabrication (LFF), Laser-based Rapid Manufacturing (LRM) and Laser Engineered Net Shaping (LENS) [5]. Powder-bed fusion uses fusion of powder material to build up layers of fabricated parts in a powder bed, whereas, flow-based deposition uses direct injection of beam into a fixed object by depositing

the powder layer by layer. To date, there are some researchers who have implemented AM techniques to fabricate NiTi parts for certain design applications.

In the last decades, several works employing LENS [6], SLM [7, 10], LRM [8] and DED [9] were reported as shown in Table 1. The reported studies utilized AM techniques in fabrication of NiTi parts thus, provides insight on how to modulate processing parameter to determine the target mechanical properties for different NiTi applications. Porous NiTi alloy which possess compression fatigue similar to metal foams for medical plants is fabricated using LENS. Besides that, SLM-fabricated NiTi alloy exhibit improved martensitic transformation temperature, damping property and tensile property. Compared to conventional methods, AM methods in research works such as LRM and DED are proven to exhibit good SME and thermo-mechanical property as well as facilitate thermal induced SME and PE thus control the phase transformation systematically.

The uniformity of material, mechanical properties, and the overall performance of NiTi alloys are dependent on the powder preparation, laser parameters and conditions in manufacturing chamber. These affecting parameters of AM techniques influences the microstructure characteristics, structural defects, printability, phase transformation temperatures, thermomechanical properties and functional properties of NiTi SMA. The first requirement in AM methods of NiTi is the powder preparation which is important in determining the desired functional properties; SME and PE for a specified design application. Ni-rich SMA exhibit pseudo elastic behaviour, whereas, Ti-rich SMA exhibit in shape memory effect with higher phase transformation temperature [11]. In AM techniques, pre-alloyed NiTi powder is preferred to

Table 1 Summary of current publication on AM techniques for processing NiTi

AM technology	Powder composition (%)	Particle size (µm)	Laser power	Application
LENS	Pre-alloyed Ni50Ti50	50–150	0.5 kW Nd: YAG laser	Biomedical
SLM	Ni55.92 Ti44.08	57 ± 1	100 kW fibre laser	Civil engineering, biomedical, structure engineering
LRM	Elementally blended Ni45Ti55 Ni50Ti50 Ni55Ti45	45–106 (Ni), 75–105 (Ti)	2 kW fibre laser	Automotive, aerospace, biomedical, robotics
DED	Elementally blended Ni47.9Ti52.1 Ni46.9Ti53.1	44–149	1 kW Yb fibre laser	Automotive, aerospace, robotics,
SLM	NiTi powders are Ni 55.92, Ni 12.66, O 0.067, C 0.008, N 0.0074 and Ti balance	15–53	500 W Ytterbium fiber laser	Aerospace and biomedicine

prevent intermetallic phases. In addition to powder preparation, the steps of making the powder including water atomization, gas atomization and mechanical attrition [12] to prevent contamination thus to ensure the functional properties of NiTi are not affected.

The second requirement in AM methods is the laser parameters. Defining optimum laser parameters is crucial to fabricate NiTi part with high level of density and low impurity level [12]. Optimization of laser parameters ensure the mechanical properties of NiTi is conserved and the determinization of NiTi parts for potential application is decided. Haberland et al. [13] in his investigation fabricated full dense NiTi parts with low impurity content by using high level of energy density (ED), one of the laser parameters. High ED increases the impurity pick-up during AM processing stages.

The third requirement is the conditions of manufacturing chamber; the region where the sample of NiTi alloy is fabricated which must be in inert atmosphere to ensure minimum oxidation and low level of impurity content in NiTi alloys [13]. Microstructural properties and functional properties of NiTi alloys are strongly affected by both the oxidation and impurity contents, thus inert atmosphere by including gas fillings of argon, nitrogen and hydrogen as well as the pre-heating of the substrate to minimize the residual stresses surrounding the NiTi samples will overcome the problems associated to the quality of NiTi alloys production through AM methods [13].

3 A Comparative Case Study on Fabrication of NiTi SMA Through DED, SLM and EBM

In this section, a comparative case study on fabrication on NiTi SMA through DED, SLM and EBM are discussed in terms of the affecting parameters of AM techniques. Table 2 summarized the affecting parameters associated with all the three different AM techniques. Wang C. et al. [14] has fabricated a full dense pre-alloyed NiTi SMA with good interlayer fusion by using DED. On the other hand, Zhang Q. et al. [15] has produced SLM-fabricated pre-alloyed NiTi SMA with excellent SME and superior tensile properties. The selective EBM fabricated NiTi by Zhou Q. et al. [16] exhibit excellent and stable PE as well as superior tensile properties for as-printed sample compared to pre-alloyed NiTi powder. All the methods above are using the laser to build up the layer to produce NiTi parts. The processing chamber are in inert atmosphere through gas atomization techniques for all the three AM methods thus prevent any contamination and maintained the chamber at low level of impurity content.

In DED, a solid NiTi SMA parts with good interlayer fusion is fabricated [14]. The fabricated NiTi SMA is homogeneous and exhibit distinct phase transformation with minor Ti_2Ni phases [14]. Presence of Ti_2Ni phases implies that there is depletion of Ni powder due to high temperature laser parameter which causes evaporation

Table 2 Affecting parameters associated with the AM techniques

Affecting parameters	AM techniques		
	DED	SLM	EBM
Particle size	Ni:20–63 μm Ti:45–105 μm	15–53 μm	45–150 μm
NiTi ratio	Ni50Ti50	Ni50.4Ti49.6	Ni51.4Ti48.6
Laser scanning speed	1000 mm/min	500 mm/s	1.2 × 10 ⁴ mm/s
Laser power	500 W and 1000 W	120 W	–
Hatch spacing	1.5 mm	80 μm	–
Layer thickness	1 mm	30 μm	150 μm
Hatch rotation	90°	67°	–
Beam current	–	–	38 mA

of Ni and different particle size [17]. On the other hand, SLM fabricated NiTi SMA shows presence of intermetallic phases with structural defects and inhomogeneous microstructure [15]. The intermetallic phases are due to the high ED rate and residual stress during SLM processing which proves that it exhibits good compression performances but poor tensile strain [15]. While as-printed NiTi by selective EBM exhibit excellent PE due to the presence of precipitates with dominant austenitic phase transformation. However, for elemental blended powder, SLM is unable to fabricate NiTi parts due to ignition mechanism of the NiTi powder mixture [15]. This happens during the preheating process which cause self-propagating combustion along the powder bed mixture thus producing porous NiTi parts [14–16].

In conclusion, AM technologies provides vast opportunity to fabricate NiTi SMA with tunable transformation temperature, functional and mechanical properties as well as geometrical variation. However, the influences of AM affecting parameters on the microstructure characteristics, structural defects, printability, phase transformation temperatures, thermomechanical properties as well as functional properties of NiTi SMA has not been extensively studied. This comparative study implies that optimum affecting parameters is crucial to determine the optimized fabrication process in accordance to the requirement of specific applications [12, 14]. However, other affecting parameters need to be considered simultaneously to improve the AM technique in production of quality high-demanded NiTi material [12]. The development of a universal algorithm to correlate the requirements of specific application with affecting parameters will be great to ensure the employments of AM technique in production NiTi SMA thus expand the possibilities in practical implementations.

4 Conclusion

A cluster of AM techniques which became alternative route to fabricate complex component of NiTi parts were reviewed. However, the affecting parameters associated to AM techniques need to be considered to produce a high quality NiTi components for practical implementations. Overall, this paper provides an insight into the utilization on AM techniques with regard to affecting parameters corresponding to the requirement of NiTi components in design applications.

Funding The authors would like to acknowledge the financial support from the Ministry of Higher Education under the Fundamental Research Grant Scheme with grant no. FRGS/1/2019/STG07/UPM/02/10.

References

1. Mitchell A, Lafont U, Hotońska M, Semprimoschnig C (2018) Additive manufacturing -A review of 4D printing and future applications. *Addit Manuf* 24:606–626
2. Elahinia MH, Hashemi M, Tabesh M, Bhaduri SB (2012) Manufacturing and processing of NiTi implants: a review. *Progress Mater Sci* 57:911
3. Dadbakhsh S, Speirs MV, Humbeek J, Kruth JP (2016) Laser additive manufacturing of bulk and porous shape-memory NiTi alloys: from processes to potential biomedical applications. *MRS Bull* 41:764
4. Speirs M, Wang X, Baelen SV, Ahadi A, Dadbakhsh S, Kruth JP, Humbeek JV (2016) On the transformation behavior of NiTi shape-memory alloy produced by SLM. *Shape Memory Superelasticity* 2(4):310–316
5. Parvazi S, Hashemi SM, Asgarinia F, Nematollahi M, Elahinia M (2020) Effective parameters on the final properties of NiTi-based alloys manufactured by powder metallurgy methods: a review. *Progress Mater Sci* 117
6. Bernard S, Balla VK, Bose S, Bandyopadhyay A (2012) Compression fatigue behavior of laser processed porous NiTi alloy. *J Mech Behav Biomed Mater* 13:62–68
7. de Wild M, Meier F, Bormann T, Howald CBC, Muller B (2014) Damping of selective-laser-melted NiTi for medical implants. *J Mater Eng Perform* 23:2614–2619
8. Shiva S, Palani IA, Mishra SK, Paul CP, Kukreja LM (2015) Investigations on the influence of composition in the development of Ni–Ti shape memory alloy using laser based additive manufacturing. *Opt Laser Technol* 69:44–51
9. Hamilton RF, Palmer TA, Bimber BA (2015) Spatial characterization of the thermal-induced phase transformation throughout as-deposited additive manufactured NiTi bulk builds. *Scripta Mater* 101:56–9
10. Shi G, Li L, Yu Z, Liu R, Sha P, Xu Z, Guo Y, Xi R, Liu J, Xin R, Chen L, Wang X, Zhang Z (2022) The interaction effect of process parameters on the phase transformation behavior and tensile properties in additive manufacturing of Ni-rich NiTi alloy. *J Manuf Process* 77:539–550
11. Bhaumik SK (2011) Nickel-titanium base shape memory alloys (SMAs): smart metallic materials. In: 6th symposium on national frontiers of engineering
12. Elahinia M, Moghaddam NS, Andani MT, Amerinatanzi A, Bimber BA, Hamilton RF (2016) Fabrication of NiTi through additive manufacturing: a review. *Progress Mater Sci* 83:630–663
13. Haberland C, Elahinia M, Walker JM, Meier H, Frenzel J (2014) On the development of high quality NiTi shape memory and pseudoelastic parts by additive manufacturing. *Smart Mater Struct* 23 (10)

14. Wang C, Tan XP, Du Z, Chandra S, Sun Z, Lim CWJ, Tor SB, Lim CS, Wong CH (2019) Additive manufacturing of NiTi shape memory alloys using pre-mixed powders. *J Mater Process Tech* 271:152–162
15. Zhang Q, Hao S, Liu Y, Xiong Z, Guo W, Yang Y, Ren Y, Cui L, Ren L, Zhang Z (2020) The microstructure of a selective laser melting (SLM)-fabricated NiTi shape memory alloy with superior tensile property and shape memory recoverability. *Appl Mater Today* 19
16. Zhou Q, Hayat MD, Chen G, Cai S, Qu X, Tang H, Cao P (2021) Selective electron beam melting of NiTi: Microstructure, phase transformation and mechanical properties. *Mater Sci Eng A* 744:290–298
17. Alagha AN, Hussain S, Zaki W (2021) Additive manufacturing of shape memory alloys: A review with emphasis on powder bed systems. *Mater Des* 204:109654

The Mechanical and Tribological Properties of LaB₆ Thin Films Deposited by Closed-Field Unbalanced Magnetron Sputtering



Gökhan Gülten , Mustafa Yeşilyurt , Banu Yaylalı , Yaşar Totik ,
and İhsan Efeoğlu 

Abstract Increasing the performance and life of cutting tools in machining applications provides an important advantage in terms of efficiency and economy. Many functional hard coatings have been developed to increase the surface quality, service life and performance of cutting tools used in machining. Being a member of the rare earth metal hexaborides family, Lanthanum added B-based coatings are the subject of intensive R&D studies to be used in industry and strategic applications due to their high hardness, wear and corrosion resistance, and thermionic properties. In this study, LaB₆ thin films were deposited on High-speed steel (AISI M2), Si and glass substrates by closed field unbalanced magnetron sputtering (CFUBMS) under different deposition pressure. The effects of deposition pressure on microstructure, mechanical and tribological properties were investigated. The characteristic properties and hardness of LaB₆ thin films were characterized by X-ray diffraction (XRD) and microhardness testing, respectively. The bond strength (adhesion) between the substrate and the film was analyzed by the scratch test. The tribological properties of LaB₆ films were determined with a pin-on-disk tribometer under atmospheric test conditions.

Keywords Magnetron sputtering · LaB₆ · Deposition pressure

1 Introduction

Increasing the life of high-speed steels used in cutting tools in surface engineering applications provides an important advantage in terms of productivity and economy. Many functional hard coatings have been developed to increase the surface quality, service life and performance of cutting tools used in machining [1]. The most widely used in these developed coatings are ultra-hard coatings with high wear and corrosion resistance based on nitrides and carbides of transition metals [2, 3]. However, these coatings deficient tribological properties restrict the enhance in usage areas. After

G. Gülten (✉) · M. Yeşilyurt · B. Yaylalı · Y. Totik · İ. Efeoğlu
Atatürk University, Erzurum 25240, Turkey
e-mail: gokhan.gulten@atauni.edu.tr

all, boride coatings continue to attract the attention of researchers due to their high hardness, high corrosion resistance, high tribological properties, high melting point and chemical stability [4].

Boron compounds (such as LaB_6 , CeB_6 , ScB_2 , YB_{12} and GdB_6) formed by rare earth metals (such as La, Ce, Sc, Y and Gd) are attractive materials for cathode applications due to their low work functions, good electrical conductivity, and high melting points [5]. Being a member of the rare earth metal hexaborides family, Lanthanum added B-based coatings are the subject of intensive R&D studies to be used in industry and strategic applications due to their high hardness, wear and corrosion resistance, and thermionic properties [4, 6, 7]. Among the techniques used in the literature to deposition LaB_6 thin films, the magnetron sputtering technique allows the structural, mechanical and tribological properties of the coating to be modify as desired, due to the easy control and variety of process parameters.

In this study, LaB_6 thin films were deposited on M2, Si and glass substrates by closed field unbalanced magnetron sputtering (CFUBMS) under different deposition pressure. The effects of deposition pressure on microstructure, mechanical and tribological properties were investigated. The characteristic properties and hardness of LaB_6 thin films were characterized by X-ray diffraction (XRD) and microhardness testing, respectively. The bond strength (adhesion) between the substrate and the film was analyzed by the scratch test. The tribological properties of LaB_6 films were determined with a pin-on-disk tribometer under atmospheric test conditions.

2 Experimental

LaB_6 thin films were deposited on M2, glass and Si substrates by closed-field unbalanced magnetron sputtering (CFUBMS) under different deposition pressure. Silicon and glass materials were used for microstructural analysis. The magnetron configuration of the targets and microstructure architecture given in Fig. 1 were used in the deposited of LaB_6 thin films.

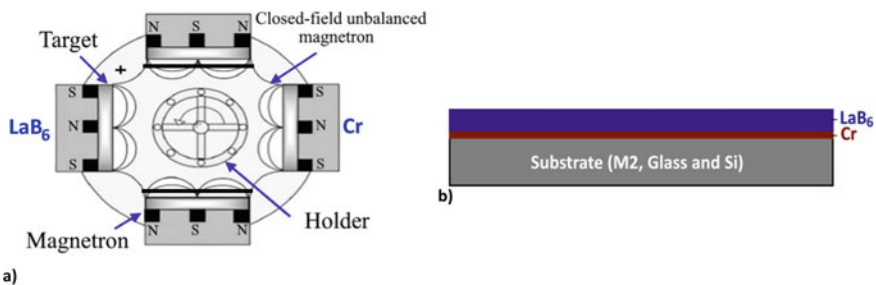


Fig. 1 a Magnetron sputtering system and b The architecture structure of LaB_6 films

Table 1 The deposition parameters of LaB₆ thin films

The variable parameters	R1	R2	R3
Deposition pressure (Pa)	0.27	0.33	0.40
<i>The constant parameters</i>			
Cr target current (A)		2	
LaB ₆ target current (A)		2	
Substrate bias (–V)		100	
Frequency (kHz)		150	
Duty time (μs)		2	
Ion cleaning time (min.)		30	
Cr inter layer deposition time (min)		5	
LaB ₆ top layer deposition time (min)		30	

To deposit LaB₆ thin film on the M2 steel, glass and silicon substrates, one Cr target and one LaB₆ target were used. Pulsed-dc power supply connected to Cr and LaB₆ targets. Argon gas was used for the formation of the plasma and sputtering of the targets. The substrates are fixed to a system that rotates around its axis in front of the targets. The distance between the substrates and the targets was set to 50 mm.

The deposition parameters used to deposit LaB₆ films are given in Table 1. It was aimed to investigate the structural, mechanical and tribological properties of LaB₆ thin films deposited under different deposition pressures.

The characteristic properties of LaB₆ thin films were examined by Rigaku DMax-2200 XRD (wavelength of $\lambda = 1.5405 \text{ \AA}$, 5–90° scan range). The mechanical properties of the LaB₆ thin films were carried out by Buehler Micromet 2001 microhardness tester (Knoop indenter, 10gf load, 15 s) and CSM Instruments scratch tester (100 N/min of progressive loading rate, 200 μ tip radius with Rockwell C diamond indenter). The tribological properties of LaB₆ thin films were performed by CSM tribotester under the 1 N load, 10 cm/s velocity, 6.25 mm diameter of Al₂O₃ counterpart.

3 Results and Discussions

According to the XRD peaks, three samples of LaB₆ thin films (R1, R2 and R3) at different deposition pressure (0.27, 0.33, and 0.40) have almost the same XRD patterns. The XRD patterns of the LaB₆ thin films deposited at different deposition pressure are shown in Fig. 2. When the XRD patterns were examined, (100), (110) LaB₆, α -Fe (110), α -Fe (200) and α -Fe (211) peaks clearly seen. As the deposition pressure increases from 0.27 Pa to 0.40 Pa, the LaB₆ (110) peak intensity increases. Considering these results, it is understood that LaB₆ thin films deposited by pulsed-dc magnetron sputtering have a primarily amorphous structure.

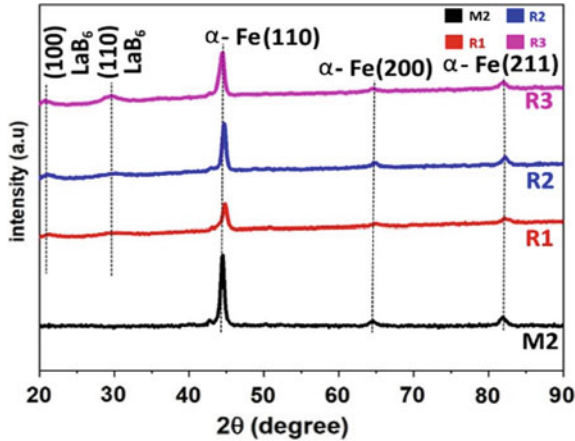


Fig. 2 XRD patterns of LaB₆ thin films

The hardness, critical load, and coefficient of friction values of LaB₆ thin films are given in Table 2. The highest film hardness was obtained in R1 where the lowest deposition pressure (0.27) was applied. A decrease in hardness was observed as the deposition pressure increased. A distinction must be made between crystalline and amorphous films so that hardness can be interpreted as depending on the deposition pressure. For coatings with crystalline structure, a significant decrease in film hardness is observed with increasing deposition pressures [7].

The adhesion (diffusion between the substrate and the film) between the film and the substrate is determined by the critical load, and the “critical load (Lc)” is defined as the load value at which the film is separated from the substrate. Scratch test was used to determine the adhesion of the LaB₆ thin films deposited on the M2 substrates (CSM Instruments Revetester test system was performed at 10 mm/min scratch speed and 100 N/min loading using Rockwell-C diamond tip). The critical load values of LaB₆ thin films are obtained as 60 N, 63 N, and 82 N for R1, R2 and R3, respectively. The critical load optical images of scratch scars at 20 N, 40 N and Lc value are shown in Fig. 3. According to the test results, the highest critical load value was obtained in the R3 film deposited under a deposition pressure of 0.40 Pa. According to scratch test results, spalling failures were observed in the R1 film at 20 N. Adhesive and spalling failures were observed at 40N. After 60 N, the spalling failures were enlarged, and it was observed that the film was separated from the substrate. The spalling failure

Table 2 The mechanical and tribological properties of LaB₆ thin films

	Hardness (GPa)	Critical load (N)	Coefficient of friction (CoF) (μ)
R1	35.5	60	0.419
R2	29.2	63	0.436
R3	24.4	82	0.482

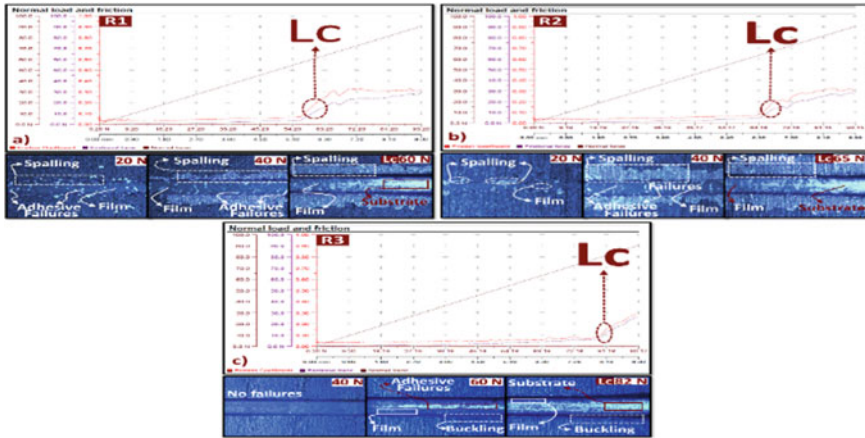


Fig. 3 The scratch test results for **a** R1, **b** R2, and **c** R3

occurs because of an increase in the compressive stress field in front of the moving stylus. When the scratch results of the R2 film are examined, the adhesion properties of the R1 film exhibited similar behavior, and the critical load value for the R2 film was determined as 65 N. The scratch results of the R3 film deposited under 0.40 Pa deposition pressure showed different behavior compared to R1 and R2 films. No failures were observed in the film up to a load value of 40N. At 60N, adhesive and buckling failures were observed due to the compressive stress in the film. After the load value of 82 N, the film began to separate from substrate [8]. There are limited studies on adhesion of LaB₆ thin films in the literature, and the adhesion values obtained in this study are quite promising when compared to the literature.

The friction coefficient values of LaB₆ thin films a pin-on-disc tribo-tester was performed. The coefficient of friction (CoF) and Laps graph of LaB₆ thin films is given Fig. 4. The coefficient of friction (CoF) is 0.419, 0.436, 0.482 for R1, R2 and R3 films, respectively. According to the test results, the coefficient of friction value decreases with increasing hardness value. It is due to the reduction of adhesive contact by decreasing the contact point at the interface as the surface hardness increases [9].

4 Conclusion

The LaB₆ thin films were deposited by pulsed-dc magnetron sputtering in different deposition pressure. The highest hardness for the LaB₆ thin films films were obtained as 35.5 GPa, in the lowest deposition pressure. According to XRD results, it is understood that LaB₆ thin films deposited by pulsed-dc magnetron sputtering have a primarily amorphous structure. The critical load values of LaB₆ films deposited on M2 steels using Cr interlayer are promising. The highest critical load value (82 N) was obtained in the R3 film, where the highest deposition pressure (0.40) was

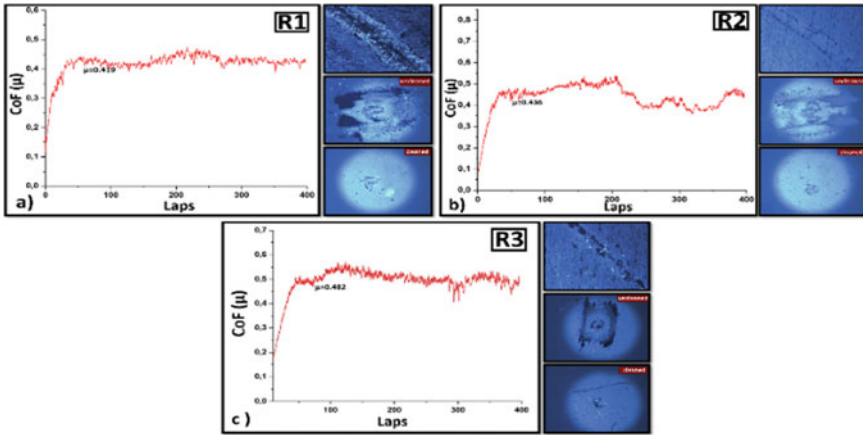


Fig. 4 The friction coefficient (CoF) to time graph and optic microscope image of the wear surface of LaB₆ thin film and counterpart (Al₂O₃) used in wear test for **a** R1, **b** R2, and **c** R3

applied. The lowest coefficient of friction value (0.419) obtained was found in the R1 film, where the lowest deposition pressure (0.27) was applied.

References

1. Libório MS, Praxedes GB, Lima LLF, Nascimento IG, Sousa RRM, Naeem M, Iqbal J (2020) Surface modification of M2 steel by combination of cathodic cage plasma deposition and magnetron sputtered MoS₂-TiN multilayer coatings. *Surf Coat Technol* 125327:384
2. Bobzin K, Brögelmann T, Kalscheuer C, Stahl K, Lohner T, Yilmaz M (2019) (Cr, Al, Mo) N and (Cr, Al, Mo) N hard coatings for tribological applications under minimum quantity lubrication. *Tribol Int* 105817:140
3. Ghailane A, Makha M, Larhlimi H, Alami J (2020) Design of hard coatings deposited by HiPIMS and dcMS. *Mater Lett* 128540:280
4. Jing XU, Min GH, Hu LJ, Zhao XH, Yu HS (2009) Dependence of characteristics of LaB₆ films on DC magnetron sputtering power. *Trans Nonferrous Metals Soc China* 19(4):952–955
5. Wang Y, Zhang GH, Chou KC (2022) Preparation of rare earth borides by reaction among rare earth oxides, boron carbide, and calcium. *J Aust Ceram Soc* 1–7
6. Zhao XH, Min GH, Xu J, Zhang L, Yu HS (2011) Effect of substrate bias voltage on the structure and mechanical properties of LaB₆ films. *METALLOFIZIKA I NOVEISHIE TEKHOLOGII* 33(3):375–382
7. Panich N, Wangyao P, Hannongbua S, Sricharoenchai P, Sun Y (2007) Effect of argon-nitrogen mixing gas during magnetron sputtering on titanium interlayer deposition with TiB₂ coatings on high speed. *Rev Adv Mater Sci* 16:80–87
8. Yıldız F, Alsaran A, Çelik A, Efeoğlu İ (2010) Multipass scratch test behaviour of TiAlN thin film deposited on 316L stainless steel and Ti6Al4V alloy with dc biased and pulsed magnetron sputtering. *Surf Eng* 26(8):578–583
9. Yi P, Peng L, Huang J (2016) Multilayered TiAlN films on Ti6Al4V alloy for biomedical applications by closed field unbalanced magnetron sputter ion plating process. *Mater Sci Eng, C* 59:669–676

Deposition of Nb Doped CrYN Thin Films: Investigation of Structural, Mechanical and Tribological Properties



Furkan Yuksel , Gokhan Gulten , Banu Yaylali , Yasar Totik ,
and Ihsan Efeoglu 

Abstract Hard coatings are generally applied to protect substrate surfaces from damage or deterioration. The development of hard protective coatings is increasingly encouraged, as machine elements used in the defense industry, automotive, aerospace, microelectronics and many other industrial applications require increasingly higher tribo-mechanical properties. Among these hard coatings such as CrN, CrYN and CrAlYN, which are deposited by closed-field unbalanced magnetron sputtering, which is one of the physical vapor depositions (PVD) techniques, are preferred because of their superior mechanical and thermal properties. In this study, Nb-added CrYN-based thin films were synthesized on 4140 (42CrMoS4), Si and glass substrates by closed-field unbalanced magnetron sputtering (CFUBMS) under different pressure, pulse frequency and pulse duty cycle. Scanning electron microscopy (SEM), X-ray diffraction (XRD) and Energy dispersive spectroscopy (EDS) were used to determine the structural features. The mechanical properties were analyzed with microhardness tester and scratch tester. Tribological properties were obtained by pin-on-disc method under atmospheric conditions at room temperature.

Keywords Magnetron sputtering · CrYNbN · 4140

1 Introduction

The importance of energy efficiency in industry is increasing day by day, especially in the aircraft and automotive sectors. It is necessary to improve the mechanical and tribological properties of machine parts, which play a key role in these areas, to prevent possible losses. Transition metal nitrides have been widely applied to improve the performance of the components. Transition metal nitrides have many advantages such as high hardness, wear resistance, chemical and thermal stability. By adding alloying elements to the structures of hard nitride coatings, it has been tried to increase the hardness, wear and oxidation resistance. As a third element,

F. Yuksel (✉) · G. Gulden · B. Yaylali · Y. Totik · I. Efeoglu
Atatürk University, Erzurum 25240, Turkey
e-mail: furkan.yuksel20@ogr.atauni.edu.tr

it was stated that the addition of an appropriate amount of Y had a positive effect on hardness and wear resistance [1]. Addition of 10.9% Nb increased the corrosion resistance of the Cr-Nb-N nanocomposite film [2].

In this study, a new composite coating was deposited by adding CrY interlayer and Nb-CrY(Nb)N, with the closed field unbalanced magnetron sputtering (CFUBMS) technique, which is a physical vapor deposition method. The effect of the formed thin film on the structural mechanical and tribological properties was investigated and discussed.

2 Material and Methods

CrYNbN film is deposited on AISI 4140 (42CrMo4), (30 mm diameter and 2 mm thickness) alloy steel, glass and silicon substrates. Before the deposition, the steel samples were respectively polished to Ra ~ 0.05 and ultrasonically cleaned with 400 600 800 1200 mesh grain SiC abrasives and Al2O3. The films were deposited with the CFUBMS instrument manufactured by Teer Coating Ltd. The architecture of the system and composite structure is given in Fig. 1.

A CrY and an Nb target for CrYN film formation and nitrogen gas for the formation of the Nitride phase were also used. The substrates were cleaned with argon gas for 30 min to remove possible impurities and to obtain a homogeneous film. A CrY interlayer was placed between the substrate and the film for high adhesion. CrYNbN film was deposited with 3A target current for CrY targets and 2A target current for Nb target, 6 sscm nitrogen flow, (-) 100 V bias voltage and 0.25–0.35 Pa pressure. The coating parameters are given in Table 1. FEI Quanta FEG-450 SEM-EDAX was

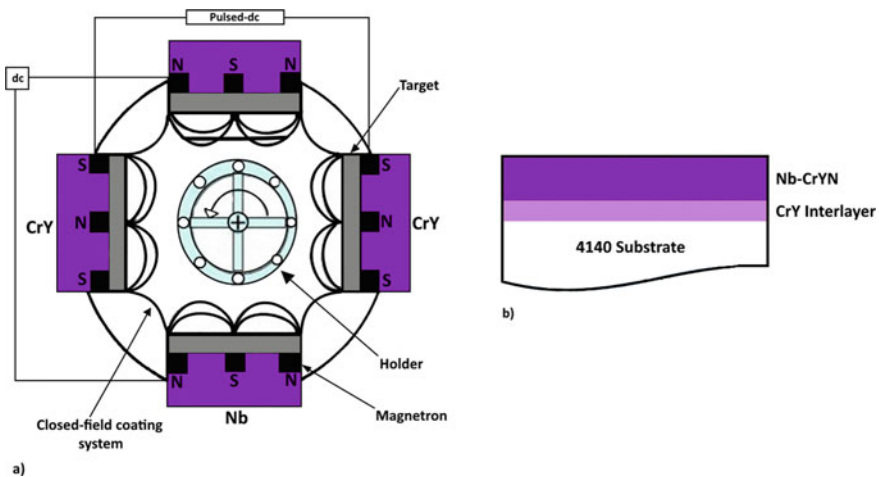


Fig. 1 a The magnetron configuration of the targets, b The architecture of CrYNbN based graded composite structure

Table 1 The deposition parameters of CrYNbN

The variable parameters	R1	R2	R3	R4
Deposition pressure (Pa)	0.25	0.35	0.35	0.25
Pulse frequency (kHz)	150	150	100	100
Duty time (μ s)	2.5	2	2.5	2
<i>The constant parameters</i>				
CrY target current (A)		3		
Nb target current (A)		2		
Nitrogen flow (sccm)		6		
Ion cleaning time (min.)		10		
Substrate bias (V)		100		
CrYNbN top layer deposition time (min)		90		

used to achieve information about the film thickness and microstructure, and Rigaku DMax-2200 XRD (wavelength of $\lambda = 1.5405 \text{ \AA}$, $5\text{--}90^\circ$ scan range) was also used to get information about structural features. Microhardness measurements of the base material and CrYNbN thin films grown on it were made with a Buehler Micromet 2001 microhardness tester (Knoop indenter, 10gf load, 15 s). Adhesion tests were performed with scratch tests using CSM Instruments scratch tester (100 N/min of progressive loading rate, 200 μ type radius with Rockwell C diamond indenter). CSM tribotester (under the 1 N load, 10 cm/s velocity, 6.25 mm diameter of Al₂O₃ counterpart.) was used to determine the tribological properties of the coated samples. The tests were done at room temperature. To obtain the friction coefficient and wear rate of the coatings numerically, the traces on the coating were used under computer control.

3 Result and Discussion

Thickness and microstructure analyzes of the films were made with Sem. Cross-sectional images of CrYNbN films are given in Fig. 2. When SEM images are examined, it is seen that the films do not have large cracks and distortions. It is seen that all samples have columnar crystal morphology and there are no big differences between them. The reason for this is thought to be the constant nitrogen current and bias voltage. The thicknesses of CrYNbN films vary between 0.686 and 1.391 μ m. With 1.391 μ m, the highest thickness belongs to the sample stored under R2 conditions, and the lowest thickness belongs to the sample stored under R3 conditions.

According to the EDS results, the % atomic amounts of Cr, Y, Nb and N are shown in Table 2. It was observed that the Y content increased depending on the CrY target current and low operating pressure. Y addition has a positive effect on the hardness

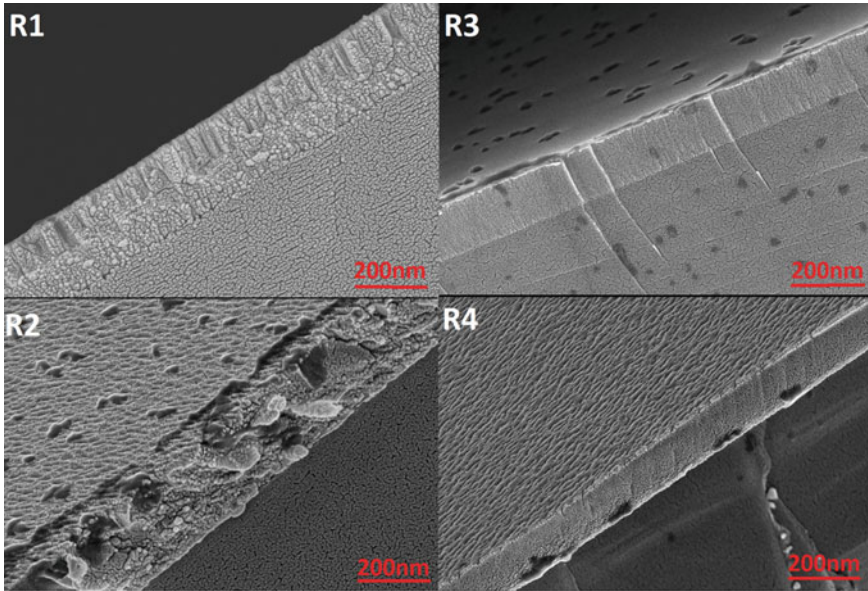


Fig. 2 The cross-sectional SEM images for CrYNbN

and adhesion of CrN coatings. The hardness values are 21.6 GPa, 14.42 GPa, 15.56 GPa, 12.43 GPa for R1, R2, R3, R4, samples, respectively.

The XRD spectra of the coatings deposited on the AISI 4140 base material are given in Fig. 3. According to the Xrd peaks, the most prominent reflection belongs to Cr [3].

Scratch test was performed to determine the adhesion properties of CrYNbN films. The critical load values of the films deposited under different conditions are between 27 and 60 N. The lowest critical load 27 N belongs to the sample deposited under R1 conditions with the highest hardness (21.16 GPa). The highest critical load 60 N, the lowest hardness (12.436 GPa) belongs to the sample deposited in R4 conditions. The critical load values obtained from the scratch tests for R1, R2, R3, R4 are given in Fig. 4.

Adhesive failures, tensile cracking, spalling and buckling cracking were observed in the scratches obtained from the adhesion tests. The critical load (L_c) values of the

Table 2 The EDS results of CrYNbN films

Film No.	R1	R2	R3	R4
Cr (%at)	29.74	61.37	73.67	90.5
Y (%at)	0.61	0.87	0.84	0.24
Nb (%at)	6.17	13.1	16.02	9.26
N (%at)	63.49	24.66	9.47	0

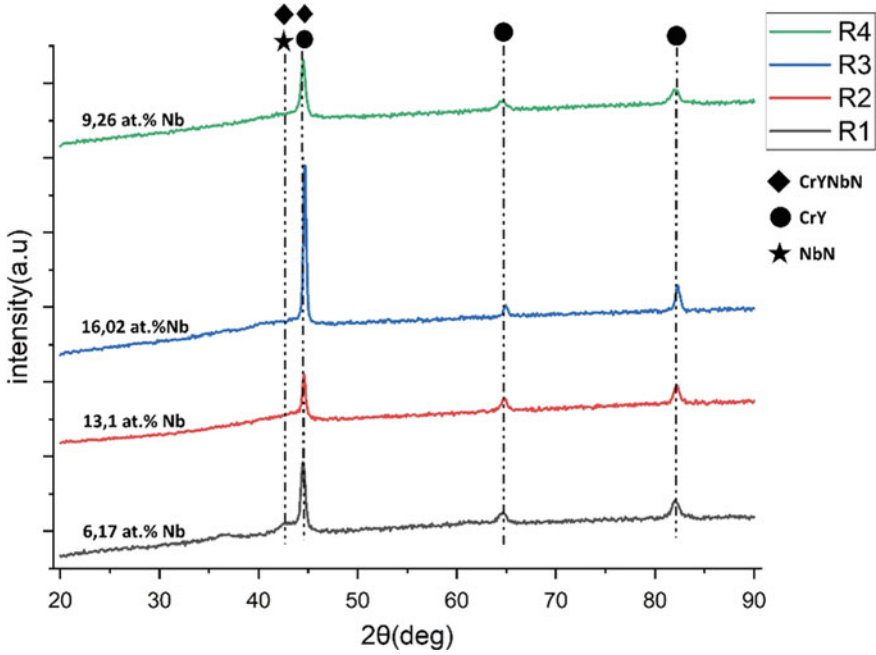


Fig. 3 XRD graphs

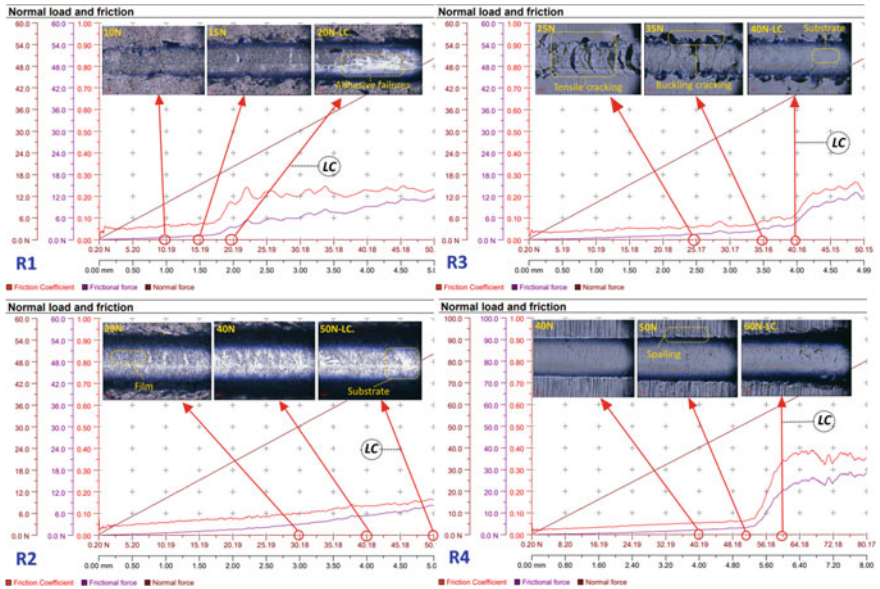


Fig. 4 The critical load values obtained from the scratch test for R1, R2, R3, R4

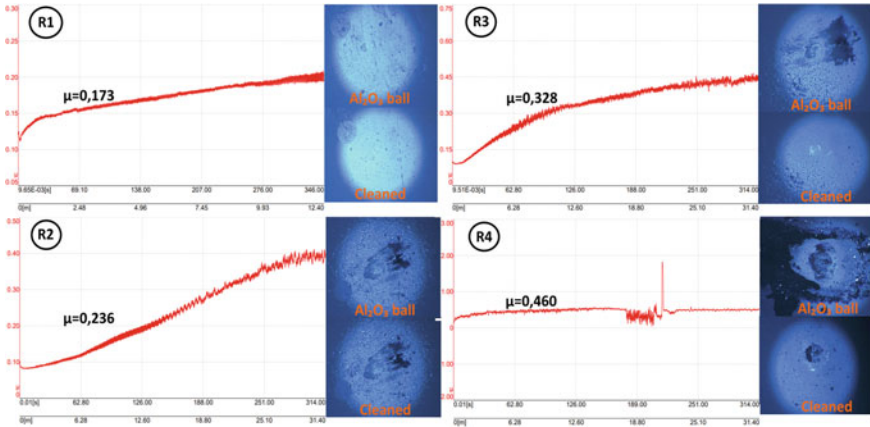


Fig. 5 Friction graphs and wear images of CrYNbN coatings

coatings mainly depend on the hardness of the coatings, while the hardness depends on the working pressure and the nitrogen content of the coatings [3].

Pin-on disc wear test was performed to obtain the tribological properties of CrYNbN films. Friction coefficients (CoF) of R1, R2, R3, R4 samples were obtained under atmospheric conditions. Due to atmospheric conditions, oxide layers form on the film surfaces [4]. Therefore, the wear values are lower. The friction coefficients range from 0.173 to 0.46. The highest coefficient of friction is in the film obtained under R4 conditions. The friction coefficients and the optical microscope images of the Al_2O_3 wear marks on the ball are shown in Fig. 5.

4 Conclusion

In summary, CrYN films containing 6.17–16.02% Nb were coated on 4140 Alloy steel. All coatings produced under different conditions showed a dense and columnar microstructure. The hardness of Nb-doped coatings is more promising than the CrN coatings in the literature. It was observed that the hardness decreased with the increase of Nb content. According to the Xrd results, the coatings showed similar peaks in all conditions. According to scratch tests, the highest critical loading was obtained as 60 N under R4 conditions. It is thought that this value changes depending on the nitrogen flow. The coefficients of friction (CoF) of the samples under atmospheric conditions were obtained. According to the friction coefficients, it has been seen that CrYNbN thin film coatings have a positive effect on the tribological behavior of AISI 4140 steel compared to uncoated. CrYNbN films are thought to have a positive effect on machine parts used in aggressive environments.

References

1. Wu Z, Qi Z, Zhu F, Liu B, Wang Z (2013) Influences of Y addition on mechanical properties and oxidation. *Phys Procedia* 50:150–155
2. Wang D, Fu Y, Hu M, Jiang D, Gao X, Wang Q, Weng L (2018) Effect of Nb content on the microstructure and corrosion resistance of the sputtered Cr-Nb-N coatings. *J Alloy Compd* 740:510–518
3. Myandoab MT (2016) CrAlYN/CrY Çok Tabakalı Kompozit İnce Film Sentezlenmesi: Yapısal-Mekanik-Tribolojik ve Termal Özelliklerinin Araştırılması. Doktora Tezi, Makine Mühendisliği Anabilim Dalı, Erzurum
4. Efeoğlu I, Totk Y, Keleş A, Gülten G, Ersoy K, Durkaya G (2019) The adhesion and tribological properties of c-BN films deposited by high power impulse magnetron sputtering. *Ceram Int* 45:3000–3006
5. Cunha L, Andritschky M, Pischow K, Wang Z (1999) Microstructure of CrN coatings produced by PVD techniques. *Thin Solid Films* 355–356:465–471
6. Hovsepian P, Reinhard C, Ehiasarian A (2006) CrAlYN/CrN superlattice coatings deposited by the combined high power impulse magnetron sputtering/unbalanced magnetron sputtering technique. *Surf Coat Technol* 4105–4110

Annealing Effect on Nb Additive CrYN Thin Films Deposited by Magnetron Sputtering



Banu Yaylalı , Gökhan Gülten , Mustafa Yeşilyurt , Furkan Yüksel ,
M. Alperen Polat , and İhsan Efeoğlu 

Abstract Thermal barrier coatings (TBC) are widely used to protect the structural components of gas/steam turbines in the energy and aerospace industries against aggressive operating conditions (environmental conditions such as high temperature, high pressure and oxidation/corrosion etc.). These coatings help prolong the life of components, reduce costs and ensure safe component operation. With the developing technology, the need for barrier coatings is constantly increasing. In this study, Nb additive CrYN film was coated on 4140 steel using the CFUBMS (Closed Field Unbalanced Magnetic Field Sputtering) technique. The specimens coated with Nb additive CrYN thin films were annealed at 400, 500, 600, 700 and 800 °C. Then, the structural and mechanical properties of the films were investigated. Microhardness and adhesion test were used to determine mechanical properties. Structural features were observed in X-ray diffraction (XRD). The critical load values of Nb additive CrYN thin films were analyzed by scratch tester.

Keywords CrYNbN · TBC · Annealing

1 Introduction

Barrier coatings are applied to many machine system elements that are exposed to aggressive/hard working conditions to prevent corrosion, oxidation and wear at high temperatures. These coatings are widely used to protect the structural components of gas/steam turbines in the energy and aerospace industries against harsh operating conditions (environmental conditions such as high temperature, high pressure and oxidation/corrosion etc.) [1]. TBCs are expected to withstand high temperature, high pressure, temperature differences, wear, complex stress conditions and corrosion [1]. With the increase in technological developments, gas/steam turbines and aircraft/jet engines are expected to operate in supercritical conditions and with minimum losses from high temperature components [2, 3]. In recent studies, it has been reported that

B. Yaylalı (✉) · G. Gülten · M. Yeşilyurt · F. Yüksel · M. A. Polat · İ. Efeoğlu
Atatürk University, Erzurum 25240, Turkey
e-mail: banu.yaylali@atauni.edu.tr

nitride-based hard thin coatings (average coating thickness of $\sim 100\text{--}400\ \mu\text{m}$ for Thermal Barrier coatings vs. $\sim 2\text{--}3\ \mu\text{m}$ and/or less for nitride-based coatings) can be used as barrier coatings [4, 5]. A number of studies show that chromium nitride, chromium yttrium nitride and chromium aluminum yttrium nitride coatings may be suitable for high temperature and high pressure applications [2, 6, 7]. CrN coatings; They have fine-grained structure and low internal stress. These coatings; They have very good properties in terms of tribological properties, corrosion resistance and fracture toughness [8]. In this study, films with superior properties were synthesized by adding Y and Nb to CrN films. With the addition of yttrium, an increase in oxidation resistance, thermal stability and mechanical properties is observed in the films [9–12]. It has been reported that corrosion resistance will increase and mechanical properties will improve with the addition of Nb [5]. CrYNbN films synthesized on 4140 steel by physical vapor deposition (PVD) method were subjected to annealing at 400, 500, 600, 700 and 800 °C, and then their mechanical and structural properties were investigated.

2 Materials and Methods

In this study, 4140 steel was preferred as the substrate to examine the mechanical and tribological properties of the synthesized CrYNbN films. Silicon and glass materials were used to examine the microstructural analyzes of the grown films. In order to be used in this study, 7 pieces of 4140 steel with a diameter of 30 mm and a thickness of 5 mm were prepared according to the sample preparation methods. CrYNbN coatings were synthesized on the base materials using Pulsed-dc and Dc power supplies. The coating process was carried out with a Closed Field Unbalanced Magnetic Field Sputtering System (CFUBMS) manufactured by Teer Coating Limited. 1 Nb and 2 CrY targets were used in the process (Fig. 1a). CrY interlayer was coated to increase the adhesion between the film and the substrate.

The architecture of the synthesized microstructure is available in Fig. 1b. Taguchi experimental design was used to determine the experimental parameters. The experimental parameters used to synthesize CrYNbN films are given in Table 1. To investigate the effect of temperature on the coated films, the samples were annealed at five different temperatures (400, 500, 600, 700 and 800 °C) for one hour in a heat treatment furnace under laboratory conditions (humidity = 50–55). An optical microscope was used to examine the surface topography of the substrate after polishing. X-ray diffractometry was used to examine the structural properties of the coatings, and a micro-hardness device was used to determine their hardness. In order to determine the adhesion of CrYNbN films coated on 4140 steel substrates at the interface between the coating and the substrate, scratch tests were performed on the Revetester test device manufactured by CSM Instruments. Wear tests were carried out at room temperature and under normal atmosphere using CSM high temperature tribo-test device.

Table 1 Taguchi experiment plan for parameters and levels used for growth of CrYNbN films

The variable parameters	R1
Deposition pressure (Pa)	0.25
Nitrogen flow (sccm)	6
Substrate bias (-V)	50
<i>The constant parameters</i>	
CrY target current (A)	2
Nb target current (A)	2
Frequency (kHz)	350
Duty cycles (%)	30
Ion cleaning time (min.)	30
CrY interlayer deposition time (min.)	10
CrYNbN top layer deposition time (min.)	90

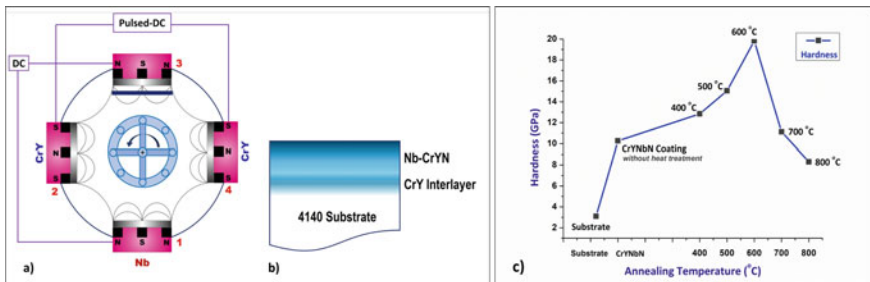


Fig. 1 a) Schematic representation of the CFUBMS system to be used, b) architecture of the micro-structure to be created, c) variation in hardness of CrYNbN coatings annealed at different temperatures

3 Results and Discussion

X-ray diffractometry was used to detect the phases in the structure before and after annealing and to reveal how these phases changed. Between 20° and 90° scans were made. The XRD spectra of the coatings grown on 4140 materials are given in Fig. 2. As can be seen in Fig. 2, XRD reflections showed the same peaks at different intensities. Peaks representing NbN around 40° and CrYNbN/CrY around 45° are seen in unannealed and annealed thin films. In addition to these, there is a peak representing CrYNbN/CrY around 52° and 75°. CrY peaks around 36° were found in the coatings at 600, 700 and 800 °C [13].

The hardness changes of the 4140 substrates, the unannealed CrYNbN coating and the coatings at different temperatures are shown in Fig. 1c. As can be seen in Fig. 1c, the CrYNbN coating layer increased its hardness value approximately 4 times (from 3.1 GPa to 10.26 GPa). It is known that with the addition of Nb to nitride-based coatings, solid solution formation will increase, a finer grained, dense and columnar

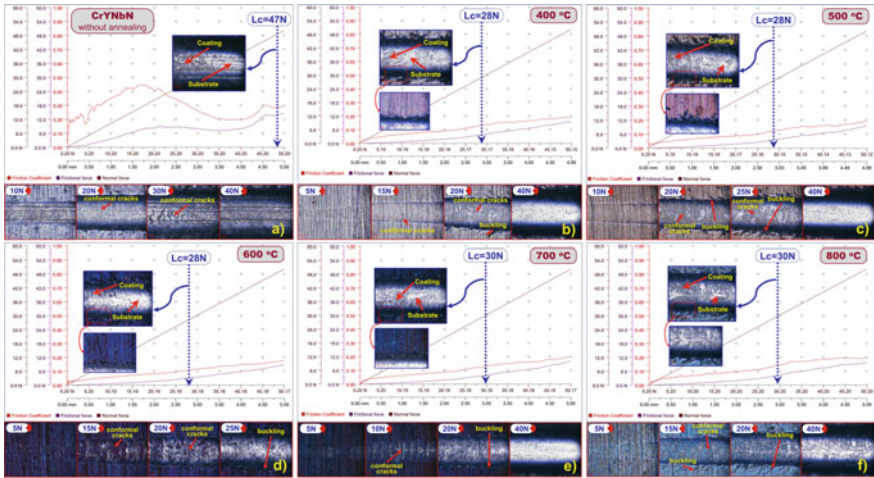


Fig. 3 Scratch (adhesion) test results of unannealed (a) and annealed CrYNbN coatings (b, c, d, e, f)

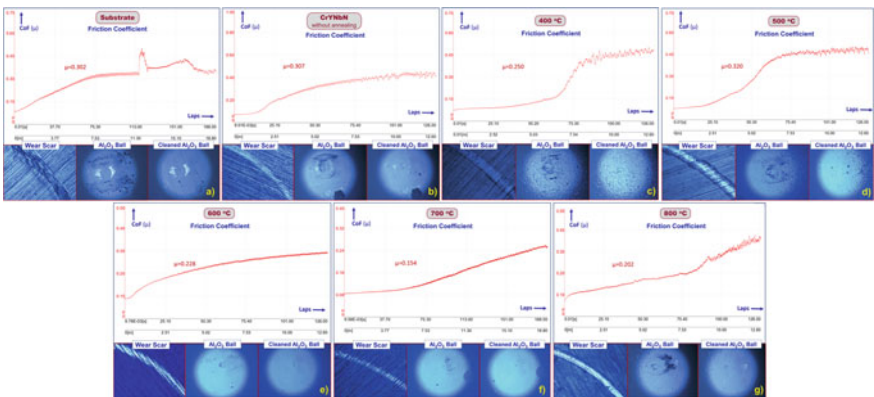


Fig. 4 Coefficient of friction graphs and wear images of substrate (a), unannealed (b) and annealed CrYNbN (c, d, e, f and g) coatings

4 Conclusion

The effect of annealing at different temperatures on the properties of CrYNbN film deposited on 4140 steel specimens was investigated. According to the X-ray diffractometry analysis, the peaks representing NbN around 40°, CrYNbN/CrY around 45°, and CrYNbN/CrY around 52°, and 75° were determined in unannealed and annealed thin films. In addition, CrY peaks around 36° were observed in the coatings at 600, 700, and 800 °C. The results from the hardness tests showed that the CrYNbN coating layer increased the hardness value by about 4 times (from 3.1 GPa to 10.26 GPa).

Especially after 600 °C, a remarkable change in hardness occurred. When the friction coefficient graphs are examined, it is seen that the friction coefficient decreases when yttrium is added to the CrN films at high temperatures. By examining the critical load value of L_c with the scratch test method, conformal cracks were observed in the scratch marks as a result of decreased adhesion strength with annealing and residual stresses increasing with temperature. It was understood that the images of the samples and abrasive balls evaluated together with the friction coefficients also confirmed this assessment. Promising results have been obtained regarding the use of annealed CrYNbN thin films as thermal barrier coatings.

References

1. Xu H, Guo H (2011) Thermal barrier coatings. Woodhead Publishing Limited, Cambridge
2. Agüero A, Juez-Lorenzo M, Hovsepian PEh, Ehiasarian AP, Purandare YP (2018) Long-term behaviour of Nb and Cr nitrides nanostructured coatings under steam at 650 °C. Mechanistic considerations. *J Alloys Compd* 739:549–558
3. Hovsepian PE, Ehiasarian AP, Purandare YP, Mayr P, Abstoss KG, Feijoo MM, Schulz W, Kranzmann A, Lasanta MI, Trujillo JP (2018) Novel HIPIMS deposited nanostructured CrN/NbN coatings for environmental protection of steam turbine components. *J Alloys Compd* 746:583–593
4. Braun R, Lange A, Hovsepian PEh, Ehiasarian AP, Tietema R, Leyens C (2011) Oxidation behaviour of TiAlYN/CrN and CrAlYN/CrN nanoscale multilayer coatings with Al₂O₃ topcoat deposited on γ -TiAl alloys. *Mater High Temp* 28(4):324–335
5. Wu ZT, Qi ZB, Zhang DF, Wei BB, Wang ZC (2016) Evaluating the influence of adding Nb on microstructure, hardness and oxidation resistance of CrN coating. *Surf Coat Technol* 289:45–51
6. Hovsepian PE, Ehiasarian AP, Purandare, YP, Biswas B, Perez FJ, Lasanta MI, Miguel MT, Illiana A, Juez-Lorenzo M, Muelas R, Agüero A (2016) Performance of HIPIMS deposited CrN/NbN nanostructured coatings exposed to 650 °C in pure steam environment. *Mater Chem Phys* 179:110–119
7. Liu S, Yang Y, Ng FL, Ji R, Zeng XT (2017) Oxidation behaviour of CrAlYN coatings at elevated temperatures. *Surf Coat Technol* 320:357–361
8. Wua ZT, Qi ZB, Zhu FP, Liu B, Wang ZC (2012) Influences of Y addition on mechanical properties and oxidation resistance of CrN coating. *Phys Procedia* 50:150–155
9. Liua S, Ongb BD, Guoa J, Liu E, Zenga X (2019) Wear performance of Y-doped nanolayered CrN/AlN coatings. *Surf Coat Technol* 367:349–357
10. Hovsepian PE, Reinhard C, Ehiasarian AP (2006) CrAlYN/CrN superlattice coatings deposited by the combined high power impulse magnetron sputtering/unbalanced magnetron sputtering technique. *Surf Coat Technol* 201:4105–4110
11. Walker JC, Rossa IM, Reinhardb C, Rainfortha WM, Hovsepian PE (2009) High temperature tribological performance of CrAlYN/CrN nanoscale multilayer coatings deposited on γ -TiAl. *Wear* 267:965–975
12. Qi ZB, Wu ZT, Wang ZC (2014) Improved hardness and oxidation resistance for CrAlN hard coatings with Y addition by magnetron co-sputtering. *Surf Coat Technol* 259:146–151
13. Biswas B (2017) Growth defects in CrN/NbN coatings deposited by HIPIMS/UBM technique. Sheffield Hallam University. Phd Thesis

14. Zhou J, Hu C, Chen L (2021) Structure, mechanical properties and thermal stability of CrAlNbN/TiN multilayers. *Vacuum* 188:110–182
15. Burnett PJ, Rickerby DS (1987) The relationship between hardness and scratch adhesion. *Thin Solid Films* 154:403–416
16. Pang X, Gao K, Luo F, Yang H, Qiao L, Wang Y, Volinsky AA (2008) Annealing effects on microstructure and mechanical properties of chromium oxide coatings. *Thin Solid Films* 516:4685–4689

Structural, Optical, and Photocatalytic Performance of ZnO Particles Synthesized via Direct Heating Technique for Rhodamine B Removal



Chee Meng Koe , Swee-Yong Pung , and Sumiyah Sabar 

Abstract A cost- and time-effective DH technique has been developed to synthesize ZnO particles. In this work, a 50 W electrical power was used to heat up the precursor solution. Particles were formed and precipitated at the bottom of beaker after 10 min. This was attributed to the rapid and direct transfer of heat energy from heating coil into the precursor solution. The XRD analysis indicates that these particles were 91.5% of ZnO and 8.5% of Zn(OH)₂. The particles have irregular size, with medium of 151 nm. The EDX analysis shows that the particles consisted of Zn and O elements. After 240 min of ultraviolet irradiation, the ZnO particles degraded 68.8% of RhB. This work presents a viable and cost-efficient alternative for the synthesis of ZnO particles and its application as photocatalyst.

Keywords Zinc Oxide (ZnO) · Photocatalyst · Ultraviolet · Direct heating

1 Introduction

Zinc oxide (ZnO) is a direct, n-type semiconductor with broad bandgap of 3.37 eV and large excitation binding energy (60 meV) at room temperature [1]. Because of these unique properties, it is a potential candidate for fabrication of opto-electronic devices such as field effect transistors, light emitting diodes, solar cells, and field emitters. ZnO particles have shown to be a prominent photocatalyst candidate because it is cost friendly, non-toxic, and more efficient in the absorption of solar spectrum.

A variety of processes have been established to synthesize ZnO particles, including sol-gel, microwave, hydrothermal, precipitation vapour deposition techniques [2]. Nevertheless, these techniques typically demand extended synthesis duration (> 6 h) and high temperatures (100 °C-1000 °C), frequently losing energy from the heat

C. M. Koe · S.-Y. Pung (✉)

School of Materials and Mineral Resources Engineering Campus, Universiti Sains Malaysia,
14300 Nibong Tebal, Pulau Pinang, Malaysia
e-mail: sypung@usm.my

S. Sabar

School of Distance Education, Universiti Sains Malaysia, 11800 Minden, Pulau Pinang, Malaysia

source to the environment. A longer duration was needed to heat up the chemical solution before chemical reactions and nucleation of ZnO occurred. In short, a viable synthesis technique is needed for the mass production of ZnO particles.

In this work, a rapid and cost-effective direct heating (DH) technique was developed to produce ZnO particles. The DH technique has been used to produce TiO₂ particles [3] and MnO₂ particles [4]. The DH technique presents a feasible alternative synthesis technique, i.e., by passing electricity through the coil, directly transmitting heat into the precursor solution, thus minimizing the dissipation of heat into the environment. Hence, the production of ZnO particles is possible with low power consumption (50 W). Formation and precipitation of ZnO particles was observed. Nevertheless, the particles were collected after 2 h of synthesis in order to have sufficient amount of materials for various characterization.

2 Experimental

The synthesis of ZnO particles by DH technique was initiated by preparing the precursor solution of zinc nitrate hexahydrate (Sigma-Aldrich, Germany) and hexamethylenetetramine (Merck, Germany) in distilled water (1:1) to obtain a 0.1 M solution. Next, the heating coil was submerged in the precursor solution. Both ends of the heating coil were connected to an electrical power supply (Guangfa electrical, Zhejiang China). The applied electrical power during the synthesis of ZnO particles was 50 W. The particles were cleaned with ethanol and distilled water after being heated continuously for 2 h. The particles were then dried for 8 h at 100 °C.

In the photocatalytic study, 0.1 g of ZnO particles was dispersed into a beaker filled with 100 ml of 5 mM Rhodamine B (RhB) solution. The mixture was stirred in the dark for 30 min under ambient conditions to achieve an adsorption–desorption equilibrium. Photocatalytic activity was initiated by placing the solution in a chamber with an ultraviolet light source (17 W, 254 nm, Philips). The distance between the UV lamp and the solution was 9 cm. A 2.5 mL aliquot was drawn from the beaker at every 30 min up to 240 min. A UV–Visible spectrometer was used to determine the concentration of the obtained aliquots. The intrinsic absorbance of RhB dye (553 nm) was used to calculate the degradation efficiency of RhB using Eq. (1). By plotting graph $\ln(C_t/C_0)$ vs t using Eq. (2), the rate constant could be determined.

$$\text{Photo degradation Efficiency(PE)\%} = \frac{C_0 - C_t}{C_0} \times 100\% \quad (1)$$

$$\ln(C_t/C_0) = -kt \quad (2)$$

where C_0 and C_t are the absorbance of RhB aqueous solution at $t = 0$ min (after 30 min of adsorption–desorption) and t min of reaction, respectively.

Scavenger tests were performed with 1 mM solution each of isopropanol (IPA), potassium iodide (KI) and p-benzoquinone (BQ) as scavengers for hydroxyl radical

($\bullet\text{OH}$), hole (h^+) and superoxide radical ($\bullet\text{O}_2^-$) respectively [3]. The photocatalytic studies with scavengers were carried out using identical test conditions as those described above. If a specific scavenger greatly reduced the RhB dye removal efficiency of ZnO particles, this would indicate that it was the primary reactive species.

Scanning electron microscope (FEI Quanta 650 FEG SEM/EDX) was used to examine the surface morphology of the particles. X-ray diffraction (XRD) analysis was performed to determine the crystal structures using Bruker D2 Phaser automated X-ray diffractometer system (Cu-K_α radiation, 0.15406 nm) at 30 kV and 10 mA at ambient temperature. The XRD spectra were analyzed using the Rietveld Refinement method and X-pert High Score software. With a sample size of 170 pieces, the average diameter of the particles was determined using Image J software (National Institute of Health, USA). UV–Visible spectroscopy (Varian Cary 50) was used to determine the photocatalytic behavior of ZnO particles.

3 Results and Discussion

3.1 Structural and Optical Properties of ZnO Particles

Figure 1a shows the XRD diffraction pattern of particles synthesized using DH technique. The XRD result shows the existence of wurtzite ZnO (91.5%, zincite) and orthorhombic $\text{Zn}(\text{OH})_2$ (8.5%, ϵ -zinc hydroxide). The presence of $\text{Zn}(\text{OH})_2$ was due to the unreacted precursor solution. The $\text{Zn}(\text{OH})_2$ could precipitate from solution when the pH range was between 6 and 9 [5]. As shown in Fig. 1b, the ZnO particles have irregular shape and highly agglomerated. The particle size distribution is positively skewed as seen in Fig. 1c. The median of ZnO particles was 151 nm, with interquartile range from 115 to 252 nm. The EDX analysis in Fig. 1d shows that the particles contained Zn and O elements, verifying that the particles were ZnO. The C was originated from the carbon adhesive tapes, whereas Pt was come from Pt conductive coating that pre-deposited on the surface of ZnO particles.

3.2 Photocatalytic Performance of ZnO Particles Under Ultraviolet Irradiation and Scavenger Test

Figure 2a shows the absorbance of degraded RhB solution by ZnO particles. As displayed in Fig. 2b, ZnO particles produced by DH technique recorded 68.8% of PE after 4 h under UV irradiation. Figure 2c shows that the PE of RhB by ZnO particles followed a pseudo first order kinetic with a reaction rate constant of 0.005 min^{-1} , as seen by the linear fits. The linear findings implied that the PE of the ZnO photocatalyst was influenced by the amount of RhB dye present. The severe agglomerated ZnO

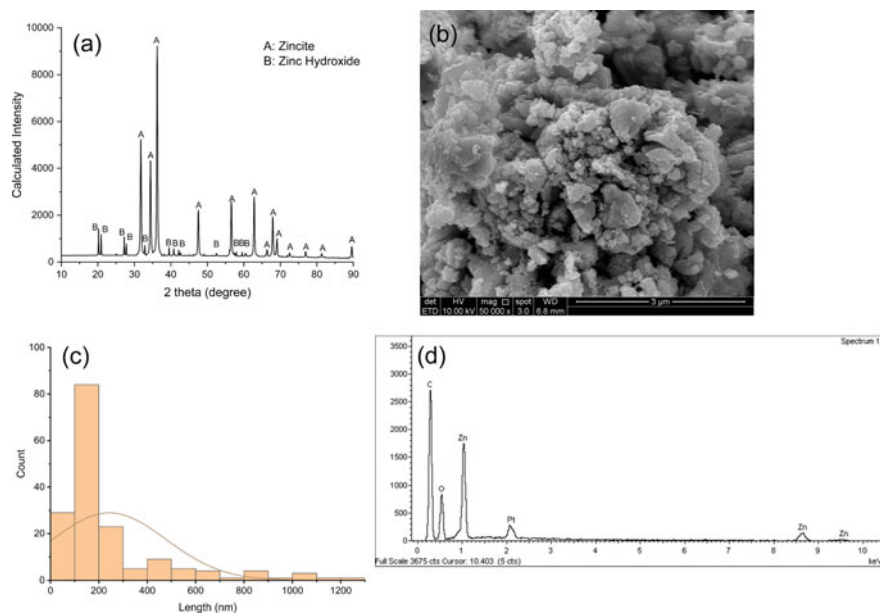


Fig. 1 a XRD diffraction patterns, b SEM image, c particle size distribution and d EDX analysis of ZnO particles synthesized by DH technique

particles, resulted in reduction of total surface area for adsorption of RhB dye, could be the cause of deteriorating its photocatalytic performance.

The intrinsic characterization absorbance peak of RhB (553 nm) degraded by ZnO particles experienced blue shifted as shown in Fig. 2d. This indicates that the RhB dye was removed through degradation by ZnO particles. After 240 min of UV irradiation, the highest absorbance peak of RhB degraded by ZnO particles decayed from 553 to 550 nm, suggesting that deethylation process occurred [6].

As shown in Fig. 3, the PE of RhB dye was greatly reduced from 68.76% to 39.80% in the presence of IPA, The PE of RhB dye was reduced to 30.99% in the presence of KI. The PE of RhB dye was suppressed to 30.31% in the presence of BQ. This result suggests that $\bullet\text{OH}$, h^+ and $\bullet\text{O}_2$ free radicals were the dominant species responsible for the degradation of RhB molecules.

4 Conclusions

DH technique was developed for the synthesis of ZnO particles. The XRD analysis revealed that the particles composed mainly of ZnO. The particles have irregular shape with medium of 115 nm. The EDX analysis verified that the particles were ZnO. These ZnO particles demonstrated its photocatalytic capability, achieving 68.8% PE

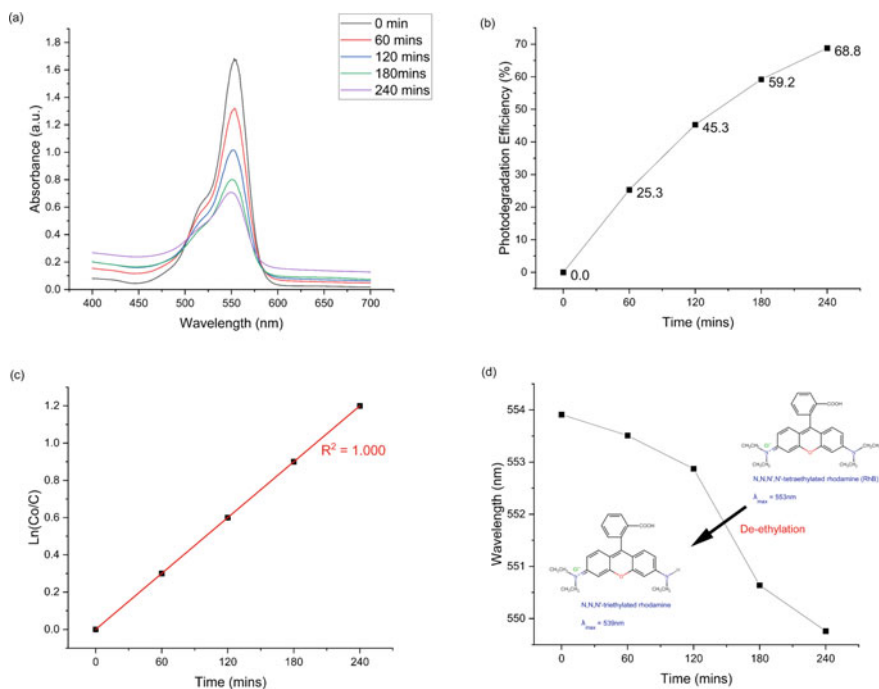
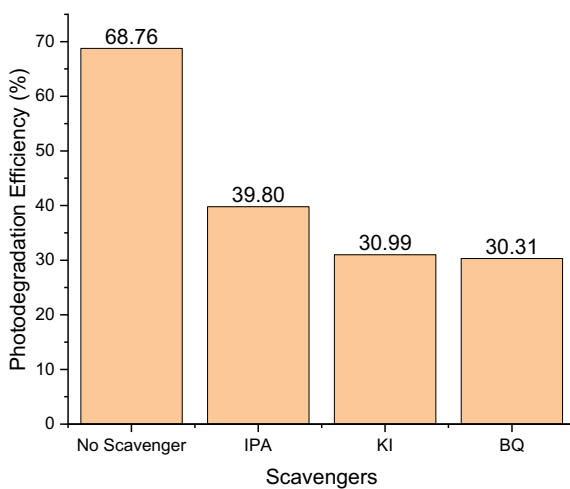


Fig. 2 a Absorption spectra, b photodegradation efficiency, c kinetic plot, and d maximum absorbance peak of RhB degraded by ZnO particles

Fig. 3 Effect of scavengers on the removal efficiency of RhB



after 240 min of UV light irradiation. The scavenger tests showed that all the $\bullet\text{OH}$ free radicals, h^+ and $\bullet\text{O}_2^-$ free radicals were equally important in degradation of the RhB solution. The current work presents a captivating setup, providing easy control over synthesis conditions and scaling potential while being affordable and simple.

Acknowledgements The authors gratefully acknowledge the financial support of Ministry of Higher Education, Malaysia for providing the research funding under Fundamental Research Grant Scheme (FRGS) (FRGS/1/2020/TK0/USM/02/27) to conduct this project.

References

1. Manoj V, Karthika M, Kumar VSRP, Boomadevi S, Jeyadheepan K, Karn RK, Balaguru RJB, Pandiyan SK (2014) Synthesis of ZnO nanoparticles using carboxymethyl cellulose hydrogel. *Asian J Appl Sci* 7(8):798–803
2. Kołodziejczak-Radzimska A, Jesionowski T (2014) Zinc oxide—from synthesis to application: a review. *Materials* 7(4):2833–2881
3. Sin-Ling C, Qian-Yee S, Swee-Yong P, Mohsen A (2021) Polycrystalline TiO_2 particles synthesized via one-step rapid heating method as electrons transfer intermediate for Rhodamine B removal. *Mater Chem Phys* 257:123784
4. Swee-Yong P (2021) Synthesis of MnO_2 Particles via One Step Localized Heating Method as Catalyst for Dye Degradation. *Malays Catalys Int J* 1:1–11
5. Strano V, Urso RG, Scuderi M, Iwu KO, Simone F, Ciliberto E, Spinella C, Mirabella S (2014) Double role of HMTA in ZnO nanorods grown by chemical bath deposition. *J Phys Chem C* 118(48):28189–28195
6. Xing Y, Que W, Liu X, Javed HA, He Z, He Y, Zhou T (2014) $\text{Bi}_2\text{Sn}_2\text{O}_7\text{-TiO}_2$ nanocomposites for enhancing visible light photocatalytic activity. *RSC Adv* 4(91):49900–49907

Synthesis and Characterization of Ta/TaN Coatings with CFUBMS-HiPIMS Technology



Muhammed Alperen Polat , Gökhan Gülten , Yaşar Totik ,
Md. Abdul Maleque , Haji Hassan Masjuki , Safa Yusuf Çetin,
and İhsan Efeoglu

Abstract The aim of this work is to study the mechanical and tribological behavior of Ta/TaN coated 52,100 tool steel. Ta/TaN thin film have been deposited by CFUBMS-HiPIMS method. In the early 2000s, it started to show itself in R&D studies with the technological developments in electronic power designs for HiPIMS technology. Today, HiPIMS has been integrated and successfully used as a hybrid in magnetic field sputtering systems for R&D purposes and industrial scale. HiPIMS technology provides a stable and uniform discharge plasma formation with high current density, ensuring that the growth of the high-density coating and the adhesion bond at the interface is strong. The development of graded Ta/TaN coating structures to optimize adhesion and wear behavior are crucial in high adhesion and lower wear levels when depositing very hard brittle coatings. Ta/TaN films have excellent friction and wear properties. For this reason, it is predicted that it will be effective in increasing efficiency and performance for many industrial applications, especially in biodiesel injectors. Studies on the mechanical and tribological characteristics of the TaN system in comparison to other transition metals, however, are few since it has a hard protective layer. This work looked into the mechanical and tribological characteristics of thin Ta/TaN thin films. The maximum hardness (28.069 GPa) was obtained for the film deposited at 9 sccm N₂ amount. The highest critical load value is achieved as 45 N. The lowest coefficient of friction value (0.419) obtained was found in the R1 film, where the lowest deposition pressure (0.27) was applied.

Keywords Ta/TaN · Adhesion · Tribological properties

M. A. Polat (✉) · G. Gülten · Y. Totik · İ. Efeoglu
Department of Mechanical Engineering, Atatürk University, Erzurum 25240, Turkey
e-mail: muhamedalperen.polat11@ogr.atauni.edu.tr

Md. A. Maleque
Department of Manufacturing and Materials Engineering, Kulliyah of Engineering, International Islamic University of Malaysia, Kuala Lumpur, Malaysia

H. H. Masjuki · S. Y. Çetin
Department of Mechanical Engineering, International Islamic University Malaysia, Kuala Lumpur, Malaysia

1 Introduction

Transitions metal nitride hard coatings are widely used in industry to improve the performance and life of machine elements due to their excellent properties in hardness, adhesion strength, and wear and corrosion resistance [1]. Efforts have made to develop and improve the tribological and mechanical properties of machine elements operating under harsh conditions. For this reason, great attention has been paid to multi-layer coatings of single-crystalline or polycrystalline materials [2]. When the studies carried out, it was found that multi-layer coatings have superior mechanical and tribological properties and good adhesion of the matrix film interface when compared to single-layer coatings. Tantalum metal is one of the metals with a very high melting point. Like other transition metals, it can form stable nitride compounds. Especially Ta doped thin film coatings have various application areas in industry due to their high corrosion resistance against various chemical environments and high melting temperature [3]. However, as a hard protective coating, TaN coating has been rarely reported due to the lack of ductility and complexity of the Ta-N system. TaN tribologically has a high melting point (3380 °C) and high hardness (1450 HV) [2]. The use of metal/metal-nitride multilayer films is an effective way to solve the brittleness problem of TaN films, and Ta/TaN multilayer coatings are expected to have higher toughness than TaN coatings [4].

In this study, Ta/TaN multilayer thin films deposited on 52,100 substrates by High-Power Impulse Magnetron Sputtering (HiPIMS) system. The characterization of Ta/TaN films were investigated by X-ray Diffraction (XRD). The mechanical properties of Ta/TaN films were determined by microhardness and scratch tester. The tribological properties of Ta/TaN films were carried out with pin-on-disk tribometer under the atmospheric conditions.

2 Experimental

Ta/TaN multilayer thin films deposited on 52,100, glass and silicon substrates by High-Power Impulse Magnetron Sputtering (IONAUTICS—Hipster 6) with CFUBMS system patented by Teer Coating Ltd. The deposition parameters are given in Table 1. The CFUBMS-HiPIMS system used in the synthesis of the Ta/TaN coatings and the microstructure architecture created are given in Fig. 1.

Firstly, the substrates (52,100) were polished with mesh SiC abrasives (240, 400, 600, 800 and 1200), respectively, from coarse-grained abrasive to fine-grained abrasive. Secondly, all substrates were cleaned with acetone + ethyl alcohol in an ultrasonic bath and dried. Finally, all substrates etched in 5% Nital solution. The etched samples were placed in the system and the ion cleaning process was started. During the ion cleaning process, the substrate voltage was set to -800 V, and the process was carried out for 30 min. The substrates to be coated are fixed in front of a Ta

Table 1 The deposition parameters of Ta/TaN thin films

The variable parameters	R1	R2	R3
N ₂ amount (sccm)	5	7	9
Ar amount (sccm)	20	20	20
<i>The constant parameters</i>			
Ta target voltage (V)		600	
Frequency (Hz)		500	
Duty time (μs)		90	
Ion cleaning time (min.)		30	
Deposition time (min.)		80	

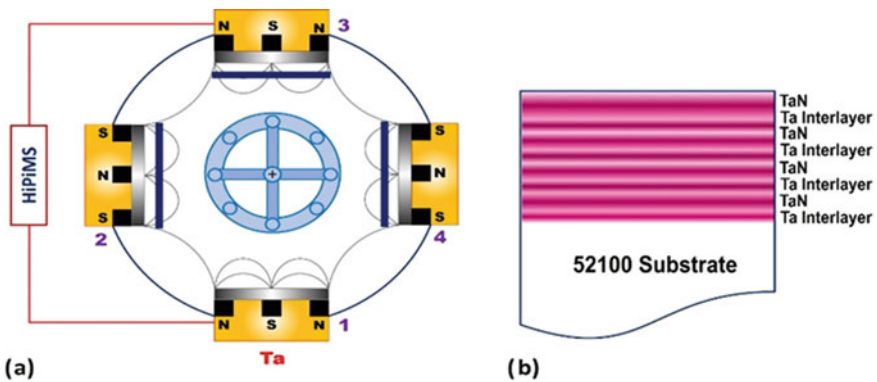


Fig. 1 The CFUBMS system and architecture structure of Ta/TaN films

target. HIPIMS voltage set as 600 V during the deposition process. Working pressure is set as 2×10^{-3} torr. In order to synthesis the architecture given in Fig. 1b, Ta layer synthesized for 5 min and then TaN layer was synthesized for 15 min by giving nitrogen to the chamber. This step was repeated 4 times.

To determine the characteristic properties of Ta/TaN thin films Rigaku DMax-2200 XRD (wavelength of $\lambda = 1.5405 \text{ \AA}$, $20\text{--}80^\circ$ scan range) were used. The mechanical properties of the Ta/TaN thin films were performed by Buehler Micromet 2001 micro-hardness tester (Knoop indenter, 10gf load, and 15 s) and CSM Instruments scratch tester (100 N/min of progressive loading rate, 200μ tip radius with Rockwell C diamond indenter). CSM tribotester system were used to determine the coefficient of friction values of Ta/TaN thin films under 1 N load, 10 cm/s velocity and 6.25 mm diameter of Al_2O_3 counterpart.

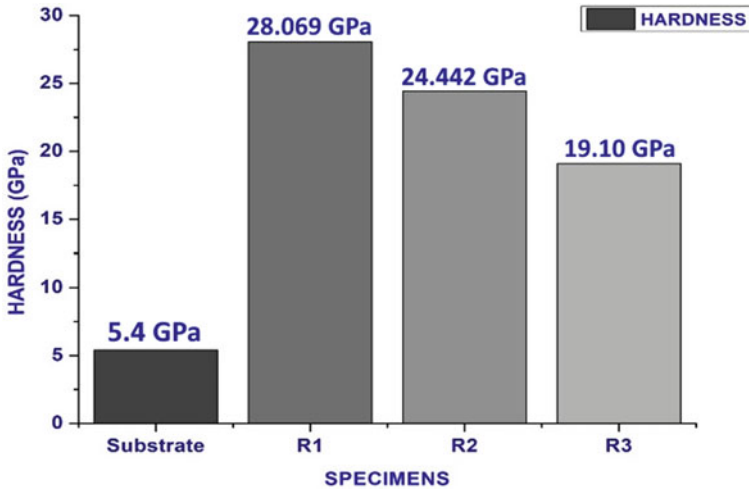


Fig. 2 The hardness value of AISI 52,100, R1, R2 and R3 films

3 Results and Discussions

Ta/TaN thin films have been deposited on 52,100 steel, glass and silicon substrates by CFUBMS-HiPIMS hybrid system under the different N_2 amount (5, 7 and 9 sccm). The hardness value of Ta/TaN thin films were obtained as 28.069, 24.442 and 19.10 GPa for R1, R2, and R3 films, respectively (Fig. 2). All the films are much harder than the uncoated 52,100 substrate (5.4 GPa). The maximum hardness (28.069 GPa) was obtained for the film deposited at 9 sccm N_2 amount (N_2/Ar : 5/20). It is known that the hardness values of the film increase up to 45% N_2 amount depending on the change of grain size, stoichiometry, and phases of the film [5]. XRD patterns of Ta/TaN thin films deposited on AISI 52,100 steel at different N_2 amounts by HiPIMS are given Fig. 3. When the XRD patterns were examined δ -TaN (111), α -Ta (110) and δ -TaN (222) peaks clearly seen. As the N_2 amount increases from 5 to 9 sccm, the α -Ta (110) peak intensity increases.

In this work, the adhesion properties (critical load values) of Ta/TaN thin film were analyzed by CSM Instruments scratch tester. Scratch test results for R1, R2 and R3 are shown in Fig. 4. The highest critical load value is achieved as 45 N. While the highest hardness was obtained in R1 coatings synthesized at 5 sccm nitrogen amount (N_2/Ar : 5/20), the lowest adhesion was obtained. In addition, chipping failures due to the compressive stress started to appear on the coating after a load value of 10N. When the load value of 19 N was reached, adhesive failures were observed, and the coating started to separate from the substrates. On the other hand, R2 and R3 films, unlike R1, did not exhibit any edge failures up to the critical load values. Additionally, conformal cracks started to be seen in R2 and R3 films after 30 N load values [6]. Friction-wear tests of Ta-TaN coated samples and AISI 52,100 base material were carried out. Friction coefficient graphics and sample wear scars-abrasive ball images

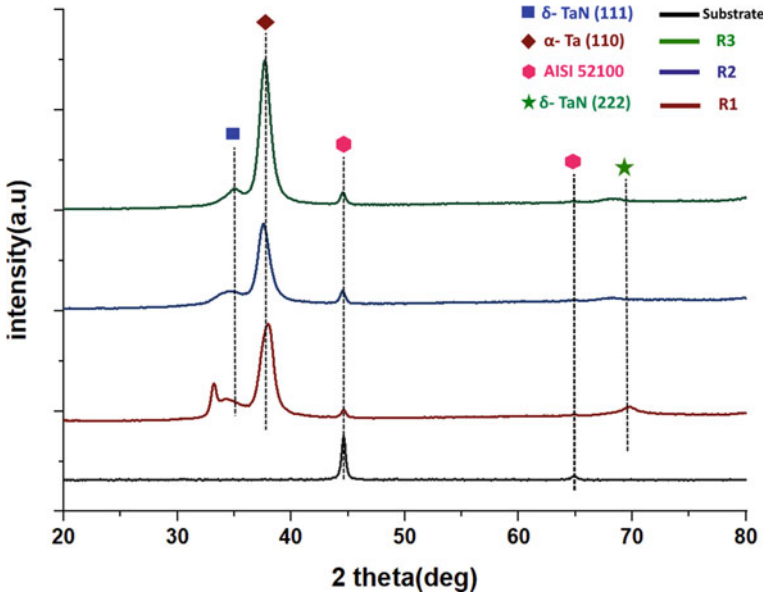


Fig. 3 XRD graphs of AISI 52,100, R1, R2, and R3 films

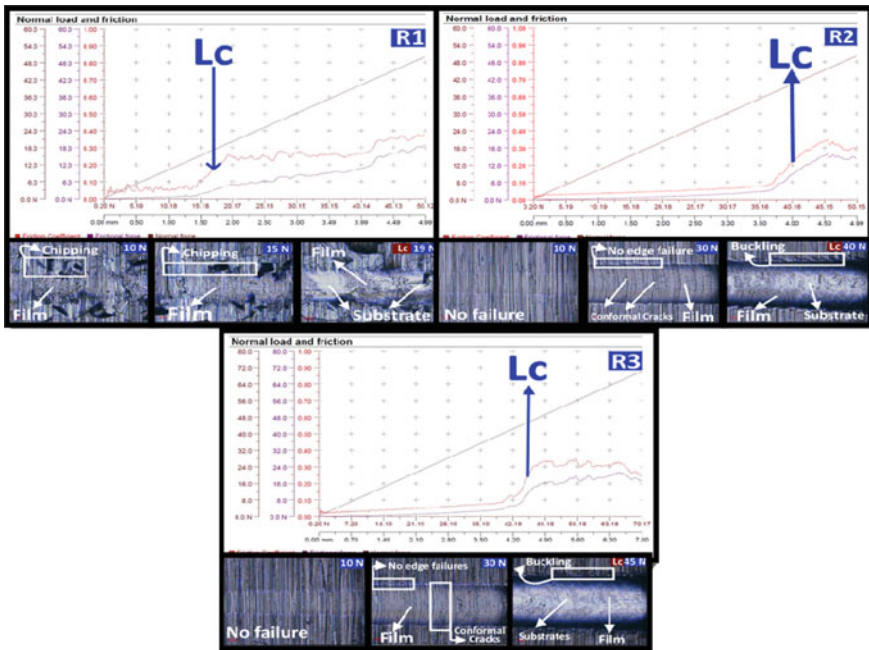


Fig. 4 The scratch test results of Ta/TaN thin films for R1, R2 and R3

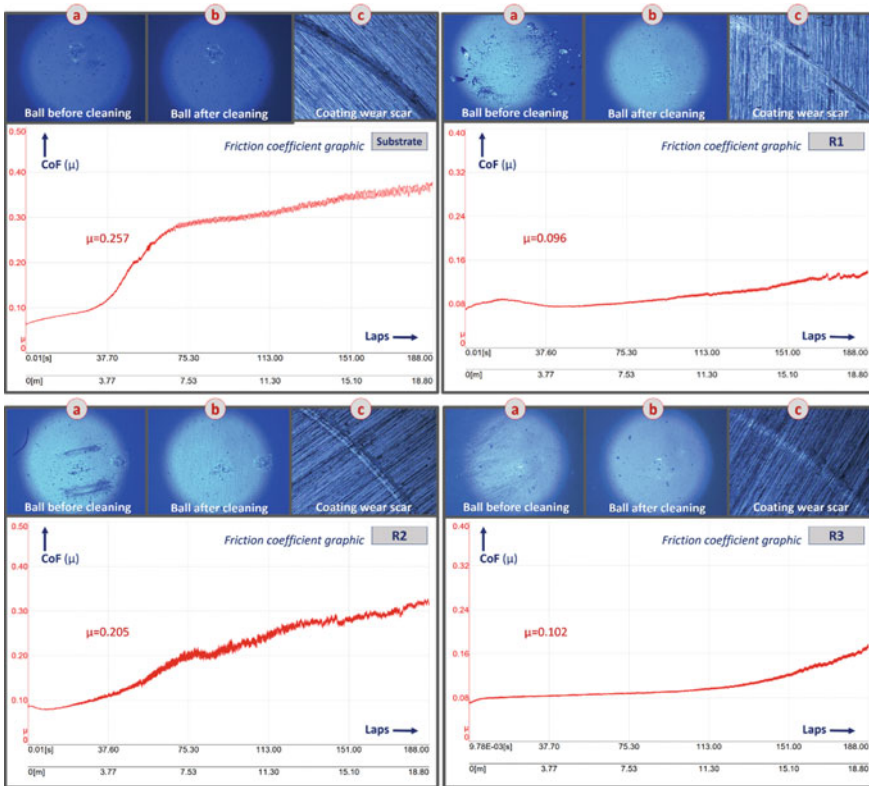


Fig. 5 The coefficient of friction (CoF) values, wear scar of Al₂O₃ counterpart, substrate, and film surfaces for R1, R2 and R3

are given in Fig. 5. As can be seen from the figure, the friction coefficient of the substrate is greater than that of all coating films (R1, R2 and R3).

Considering the friction coefficients of the R1 and R3 samples, the coating film significantly reduces the friction coefficient (approximately a twofold decrease). By examining the wear scar images of the samples in Fig. 5, the decrease effects in the friction coefficient can also be seen from the wear traces. This decrease in the coefficient of friction in the films relative to the base material is closely related to the Ta-TaN multilayer coating structure. While the Ta-TaN multilayer structure contributes to the wear resistance of the base material, the friction coefficient decreases as the 3-element abrasive wear will occur late. Considering the hardness and coefficient of friction values, the coefficient of friction value decreases with increasing hardness value due to the decreasing the contact area [7].

4 Conclusion

The Ta/TaN thin films were deposited by high power impulse magnetron sputtering in various deposition pressure N_2 amounts (5, 7, and 9 sccm). The maximum hardness (28.069 GPa) was obtained for the film deposited at 5 sccm N_2 amount (N_2/Ar : 5/20).

When the XRD patterns were examined δ -TaN (111), α -Ta (110) and δ -TaN (222) peaks clearly seen. As the N_2 amount increases from 5 to 9 sccm, the α -Ta (110) peak intensity increases. The maximum adhesion value (82 N) was achieved in the R3 film, where the highest N_2 amount was used. The lowest coefficient of friction value (0.419) obtained was found in the R1 film, where the lowest deposition pressure (0.27) was applied.

Acknowledgements The authors would like to acknowledge to the Atatürk University, Turkey and International Islamic University Malaysia that made this study possible.

References

1. Aditya A, Krishna V, Subrahmanyam A, Deepak GB (2006) Pulsed DC magnetron sputtered tantalum nitride hard coatings for tribological applications. *Surf Coat Technol* 201(7):4401–4405
2. Ma G, Lin G, Gong S, Liu X, Sun G, Wu H (2013) Mechanical and corrosive characteristics of Ta/TaN multilayer coatings. *Vacuum* 89:244–248
3. Yang LY, Zhang DH, Li CY, Foo PD (2004) Comparative study of Ta, TaN and Ta/TaN bi-layer barriers for Cu-ultra low-k porous polymer integration. *Thin Solid Films* 462:176–181
4. Fréty N, Bernard F, Nazon J, Sarradin J, Tedenac JC (2006) Copper diffusion into silicon substrates through TaN and Ta/TaN multilayer barriers. *J Phase Equilib Diffus* 27(6):590–597
5. Burnett PJ, Rickerby DS (1987) The relationship between hardness and scratch adhesion. *Thin Solid Films* 154(1–2):403–416
6. Yıldız F, Alsaran A, Çelik A, Efeoğlu İ (2013) Multipass scratch test behaviour of TiAlN thin film deposited on 316L stainless steel and Ti6Al4V alloy with dc biased and pulsed magnetron sputtering. *Surf Eng* 26(8):578–583. Ma G, et al. Mechanical and corrosive characteristics of Ta/TaN multilayer coatings. *Vacuum* 89:244–248
7. Yi P, Peng L, Huang J (2016) Multilayered TiAlN films on Ti6Al4V alloy for biomedical applications by closed field unbalanced magnetron sputter ion plating process. *Mater Sci Eng, C* 59:669–676

Enablers and Barriers of Lean Manufacturing Implementation in Indonesian Manufacturing Companies



Herry Agung Prabowo, Erry Yulian Triblas Adesta, Farida, and Avicenna

Abstract Various previous studies stated that the success rate of implementing the Lean Manufacturing (LM) strategy varies greatly depending on the readiness of the organization, the readiness of individual employees, and also the work environment/work culture that has existed so far. Previous research was also mostly carried out in developed countries that had long implemented this Lean strategy, but very limited was done in developing countries like Indonesia. This study aims to complement and enrich the results of research on the implementation of Lean in developing countries, especially Indonesia. A survey method distributed 100 questionnaires, with 32% of them eligible for further processing. Using the Cochran test method, four enablers were found to significantly affect the success of Lean implementation, namely: top management commitment and support, high employee involvement, synergic cooperation of production and maintenance, and integration of LM with other programs. The accompanying results also revealed that there were five barriers believed to significantly influence the successful implementation of Lean.

Keywords Lean manufacturing · Enablers and barriers · Cochran test

1 Introduction

Lean manufacturing (LM) is an organized effort to improve production efficiency and is typically carried out by companies to prevent budget and production waste. Today, LM is a very important part of many large companies which executions

H. A. Prabowo · Farida

Department of Industrial Engineering, Mercu Buana University, Jln. Meruya Selatan Raya, Kembangan Jakarta Barat 11650, Indonesia

E. Y. T. Adesta (✉)

Department of Occupational Safety and Health, Indo Global Mandiri University, Jln. Jend. Sudirman No.62, Palembang, Sumatera Selatan 30129, Indonesia
e-mail: eadesta@uigm.ac.id

Avicenna

Department of Manufacturing and Materials Engineering, Kulliyah of Engineering, International Islamic University Malaysia, Jln. Gombak, 53100 Kuala Lumpur, Malaysia

may vary, whether systemic or systematic, in identifying and eliminating all types of production wastes and activities. Several successful implementations [1–4] and failed attempts [2, 4, 5] have been reported from notably developed countries but not from the developing ones; hence, the execution of the current research in Indonesia.

A previous study in the Iran manufacturing industry revealed that there were at least five significant practices for LM, including processes and equipment, supplier relationships, planning and control, customer relations, and human resources [6]. In a parallel study with an analytical hierarchy process (AHP), such practices may include Kaizen, TPM, and 5S [7]. In a similar manner, the current study evaluated various enablers and barriers which might affect the accomplishment of LM implementation in Indonesia's manufacturing industry. There were six LM enablers being evaluated, including: (1) top management commitment, (2) employee involvement and training, (3) dedicated suppliers, (4) synergic cooperation of production and maintenance, (5) LM integration with other programs (TPM, Six Sigma, TQM), and (6) supported infrastructure and information and communications technology (ICT), [8–10]. Simultaneously, eight barriers were also evaluated, including: (1) high rejection rate, (2) high setup and lead times, (3) high inventory level, (4) lack of top management commitment, (5) lack of employee involvement and training, (6) low overall equipment effectiveness (OEE), (7) lack of infrastructure and ICT, and (8) lack of dedicated suppliers [10, 11].

2 Methodology

This research employed a survey method to collect data from various industries located at several industrial centers in Indonesia. All enlisted enablers and barriers were broken down into sixteen questions that were embedded in a questionnaire. Considering that the number of medium and large industries in Indonesia as of 2019 was 24,529 companies, and with an assumption that 5% of them have implemented LM, then the hypothetical total population of the survey was 1,227 companies. The ideal number of samples to be taken should be 5% (63 companies) out of the total population. However, due to time and cost limitations, samples were drawn only from 12 companies out of 3 industrial estates in Greater Jakarta (Jabodetabek). Questionnaires were distributed to a total of 100 respondents, with an allocation of 8–10 participants per company whose positions were in the middle or upper managerial level. A total of 32 returned questionnaires were then found to be suitable for further process and analysis.

Table 1 Percentage of respondents agreeing with the suggested LM enablers

Tested LM enablers	In agreement (%)
Top management support and involvement	92.64
Employee training and education	88.23
Dedicated suppliers	64.70
Synergic cooperation of production and maintenance	83.82
LM integration with other programs	83.82
Supported infrastructure and ICT	66.18

3 Results

3.1 The Enablers of LM Implementation

The respondents of the study were asked whether each of the enablers included in the questionnaire was capable of affecting the success rate of LM implementation by answering “Yes” or “No”. The results are presented in Table 1.

The evaluation to measure the significance of each enabler using the Cochran test, with a critical limit of 11.070 (Chi-Square value of Qtable for $\alpha = 5\%$ and $k = 6$ or $df = 5$), resulted in the removal of two least-agreed enablers, i.e., ‘dedicated suppliers’ and ‘supported infrastructure and ICT’. Therefore, only four remaining factors were considered to be significant in affecting the success rate of the LM implementation.

3.2 The Barriers to LM Implementation

In a similar manner, various responses were recorded on the inhibiting factors (barriers) that might affect the implementation of LM (Table 2). Four factors were seen to have an in-agreement percentage greater than 70%, where the ‘lack of management commitment and support’ was observed as the most substantial barrier, while at the opposite end, the ‘lack of dedicated suppliers’ was observed to be the least notable barrier with a value of 57.69%.

Similar to the enablers, a Cochran test was also conducted to evaluate which factors significantly and genuinely acted as barriers to the LM implementation. Based on the critical value of 14.067 ($\alpha = 0.05$, $k = 8$, or $df = 7$), three least-agreed barriers were then removed, i.e., the ‘high level of inventory’, ‘lack of dedicated suppliers’, and ‘lack of infrastructure and ICT’.

Table 2 Percentage of respondents agreeing with the suggested LM barriers

Tested LM barriers	In agreement (%)
Lack of management commitment and support	92.30
Lack of employee involvement and training	84.62
Low overall equipment effectiveness (OEE)	79.15
High rejection rates	71.15
High setup and lead times	69.23
High level of inventory	65.38
Lack of dedicated suppliers	57.69
Lack of infrastructure and ICT	65.38

4 Discussion

4.1 LM Enablers

Surveyed industrial practitioners agreed that there are four important enablers that can be considered significant factors in the implementation of LM in Indonesia, including: (1) top management support and involvement, (2) high employee involvement and training, (3) synergic cooperation of production and maintenance and, (4) integration with other programs. Each with the respondent's selection rate of 92.64%, 88.23%, 83.82% and 83.82%, respectively.

The 'top management support and involvement' became the most preferred and was considered to be the most important in determining the success of Lean implementation. The enabler is very much needed for the implementation of any new program and policy in which top management should lay down rules and regulations for the effective implementation of an LM program. It is broadly accepted that every change in business and work needs commitment and leadership, especially from top management [12, 13], considering its critical position, functions, and responsibilities to lead a change. Since LM implementation affects an organizational structure, workers' attitudes, values, and above all, cultural change (individual and organizational) [12, 14], it is almost impossible to carry out the process without commitment, support, and involvement from this supreme administrative.

Employee involvement followed in the second position of highly important enabler. The rationale behind this was mostly because without the involvement of the employee, thoroughly and continually, any planned for changes may suffer from failure. Top management of the organization usually motivates its employees through awards, financial incentives, or empowerment to ensure the success of the LM program. The management for 'synergic cooperation of production and maintenance' was surprisingly entailed as the thirdly prioritized enabler since LM implementation, without any doubt, requires cooperation from the external units for maintenance.

Any production optimization program would be rendered to be unsuccessful if the machines often malfunctioned.

The last priority was given to the 'integration with other program' enabler. Nonetheless, it has to be underlined that LM (through TPM) acts as the cornerstone for many Lean initiatives. Ahuja and Khamba [15] showed this through their pyramid blocks, exhibiting the relationship between LM, TPM, and other philosophies such as TQM, JIT, and Six Sigma.

4.2 LM Barriers

In a simultaneous result, only five LM barriers were deemed to be significant in the current study, including: (1) the lack of top management commitment (92.30%), (2) lack of employee involvement (84.62%), (3) low OEE (79.15%), (4) high rejection rate (71.15%), and (5) high setup (69.23%).

The 'top management lack of commitment' was the main concern for companies with a Lean implementation program. The lack of top management commitment could come from various reasons, such as the lack of experience and training, reluctance to change, and hesitation to start the improvement program. With an antagonistic effect as opposed to the first enabler, the absence of management support leads to the premature failure of an LM program. Similar to their counterpart enablers, 'employee involvement' was also an integral and important part of the LM implementation strategy. The concept involved participation from all departments, including engineering, operations, and maintenance. Insufficient employee involvement leads to undetected and uncorrected equipment problems, and on top of that, failure in modifications and improvements.

The remaining three barriers of 'low OEE, high rejection rate, and high setup time' can be treated as an integrated component and discussed simultaneously. The OEE value is a multiplication of availability rate (Ar), performance rate (Pr), and quality rate (Qr) [15–17]. The availability rate is significantly affected by the breakdown and setup rates, Pr is affected by the speed losses and minor idling, and Qr is dependent on the rejection and reworking rates. The 'high rejection rate' and 'setup time' is inversely related to Qr and Ar , thus lowering the rates of both factors [18–20]. Furthermore, the decline of Ar and Qr would end up in the decline of OEE value, too.

5 Conclusions

Two main findings can be derived from the results of the current study. First of all, industrial practitioners believed that four factors could facilitate the implementation of LM in the industries, including the 'top management support and involvement, high employee involvement and training, synergic cooperation of production and

maintenance, and dan the integration of LM with other programs. On the other hand, there were five noticeable inhibitors for the LM implementation, including the lack of management commitment and support, lack of employee involvement and training, low OEE, high rejection rate, high setup time, and high lead time. Since all enablers and barriers were rated by various manufacturing companies that have been working in an LM program, any stakeholders who have an interest in implementing LM in their organizations can focus their resources on the sorted factors mentioned in the results for a higher prospect of implementation.

References

1. Bortolotti T, Boscari S, Danese P (2015) Successful lean implementation: organizational culture and soft lean practices. *Int J Prod Econ* 160:182–201
2. Worley JM, Doolen TL (2015) Organizational structure, employee problem solving, and lean implementation. *Int J Lean Six Sigma* 6(1):39–58
3. Mostafa S, Dumrak J, Soltan H (2013) A framework for lean manufacturing implementation. *Prod Manuf Res* 1(1):44–64
4. Scherrer-Rathje M, Boyle TA, Deflorin P (2009) Lean, take two! Reflections from the second attempt at Lean implementation. *Bus Horiz* 52(1):79–88
5. Secchi R, Camuffo A (2019) Lean implementation failures: the role of organizational ambidexterity. *Int J Prod Econ* 210:145–154
6. Zahraee SM (2016) A survey on Lean manufacturing implementation in a selected manufacturing industry in Iran. *Int J Lean Six Sigma* 7(2):136–148
7. Thanki S, Govindan K, Thakkar J (2016) An investigation on lean-green implementation practices in Indian SMEs using analytical hierarchy process (AHP) approach. *J Clean Prod* 135:284–298
8. Marodin GA, Saurin TA (2013) Implementing lean production systems: research areas and opportunities for future studies. *Int J Prod Res* 51(22):6663–6680
9. Naslund D (2013) Lean and six sigma—critical success factors revisited. *Int J Qual Serv Sci* 5(1):86–100
10. Netland TH (2015) Critical success factors for implementing lean production: the effect of contingencies. *Int J Prod Res* 54(8):2433–2448
11. Upadhye N, Deshmukh SG, Garg S (2016) Lean manufacturing system implementation barriers: an interpretive structural modelling approach. *Int J Lean Enterp Res* 2(1):46–65
12. Attri R, Grover S, Dev N, Kumar D (2013) An ISM approach for modelling the enablers in the implementation of Total Productive Maintenance (TPM). *Int J Syst Assur Eng Manage* 4(4)
13. Tsang AHC, Chan PK (2000) TPM implementation in China: a case study. *Int J Qual Reliab Manage* 17(2):144–157
14. Park KS, Han SW (2001) Total productive maintenance: impact on competitiveness and a framework for successful implementation. *Hum Factors Ergon Manuf* 11(4):321–338
15. Ahuja IPS, Khamba JS (2008) Total productive maintenance: literature review and directions. *Int J Qual Reliab Manage* 25(7):709–756
16. Dutta S, Dutta AK (2016) A review on the experimental study of overall equipment effectiveness of various machines and its improvement strategies through TPM implementation. *Int J Eng Trends Technol* 36(5):224–232
17. Adesta EYT, Prabowo HA (2018) Total Productive Maintenance (TPM) implementation based on Lean manufacturing tools in Indonesian manufacturing industries. *Int J Eng Technol* 7(3):156–159

18. Sukma DI, Prabowo AH, Setiawan I, Kurnia H, Fahturizal IM (2022) Implementation of total productive maintenance to improve overall equipment effectiveness of linear accelerator synergy platform cancer therapy. *Int J Eng* 35(7):1246–1256
19. Herry AP, Farida F, Lutfia NI (2018) Performance analysis of TPM implementation through overall equipment effectiveness (OEE) and six big losses. *IOP Conf Ser Mater Sci Eng* 453:012061
20. Purba HH, Wijayanto E, Aristiara N (2018) Analysis of Overall Equipment Effectiveness (OEE) with total productive maintenance method on jig cutting: a case study in manufacturing industry. *J Sci Eng Res* 5(7):397–406

Study on the Challenges of Implementing Industry 4.0 in UAE Using Analytical Hierarchy Process AHP Method



Muataz Al Hazza, Hamdah Al Dahmani, Fatmah Alyammahi,
and Amel Al Naqbi

Abstract Intelligent manufacturing, or the fourth industrial revolution, can significantly reduce the environmental impacts of products and processes by reducing resource consumption such as energy, water, and other resources. However, many challenges may face the implementation of Industry 4.0. The current study tries to prioritize these challenges using sequential steps. A structured literature review was conducted to identify the main challenges, and then a questionnaire specially designed to use the AHP method was distributed to the relevant industrial experts. Three iterations of revising the AHP results have been done to get a consistency ratio of less than 10%. The results show that the main challenges were the cost of infrastructure followed by cybersecurity.

Keywords Industry 4.0 · AHP method · Challenges

1 Introduction

The integration between the new advanced technologies and artificial intelligence led to what is known as Industry 4.0 (I4.0), or the fourth industrial revolution. I4.0 was first mentioned at the Hanover Fair in 2011. Integrating the current manufacturing systems with the new technologies is challenging. One of the challenges is how to monitor manufacturing processes from virtually anywhere. Quality control personnel can set up smartphones that connect to the cloud with minimal investment [1].

On the other hand, they are detecting the errors immediately by using machine learning algorithms, rather than at later stages when the cost of repairs is higher and considered an advantage. According to Süzen [2], low-price technologies are more likely to be adopted. However, employees must be trained to use these technologies and digitalized processes, which costs money and time. Cyber security is another challenge in which cyber security controls and protects the system, devices, data, and network programs from cyber-attacks [3].

M. Al Hazza (✉) · H. Al Dahmani · F. Alyammahi · A. Al Naqbi
Mechanical and Industrial Engineering, American University of Ras Al Khaimah, Ras Al
Khaimah, United Arab Emirates
e-mail: muataz.alhazza@aurak.ac.ae

Prause [4] highlights that the workforce must hold fundamental processes and interdependencies. However, developing employee skills is required. Another challenge is protecting data's accessibility, integrity, and privacy as one of the top responsibilities for cyber security. According to Rane et al. [5], a cyber-attack is any behavior that impairs cyber security supply. Organizations' challenges in implementing industry technologies include cybercrime threats, rapid technological changes, and global corruption [6]. Culot et al. [7] explained that large data sets pose a legal danger to businesses that process and store personal information. If a vast data set covers any personal data, privacy and data protection principles will apply to the company. A problem will arise when big data transmits to know-how or other sensitive information, such as constructions, structures, or production technologies. In industry, lack of skills is a big gap that affects the industries productivity, quality, and cost. According to Müller et al. [8], Industry 4.0 is oppressed by different difficulties and takes place in a fast-paced competitive atmosphere. It reshapes industry borders, establishes new industries, and puts current industrialized firms up against the new competition. Lack of skills is also a big challenge in industries because if employees don't have proper skills, they don't understand how to do their jobs and do not understand the organization's goals. The degree to which technological innovation may be easily combined with existing infrastructure and processes is referred to as compatibility [9].

Ziebermayr [10] claimed that many threats related to cyber-attacks like loss of data integrity. They also claim that in Industry 4.0, risk will be more predominant. Because of, among other things, the availability of real-time data, the risk management method must also vary. This demands the adaption of currently available devices and tools. The presence of an open index of solutions to the danger of legal risks is made conceivable using modern technology. The following are some illustrations of legal risks that may arise because of Industry 4.0, including violation of intellectual property, employee's rights violations, property destructions, misuse of personal data, a gap in the contract, and loss of control of the machine, and personal injuries. The challenges and difficulties that the manufacturers may face when implementing I4.0 will be discussed in this article. This study uses a literature-based analysis to discuss the risks and challenges of industry 4.0 from different aspects. Environmental problems, numerous climate changes, and global warming result from a lack of environmental care in development and manipulation, all of which have an impact on human health.

2 Research Methodology

The research methodology is designed based on three sequential steps: comprehensive literature review, data gathering using a unique design questionnaire, and AHP implementation. A comprehensive literature review was conducted through reviewing 20 different research papers [2–8, 10–22]. The possible challenges were listed in Table 1.

Table 1 List of possible challenges

Challenges			
Cybersecurity	Lack of technology	Cost	Awareness
Safety	Lack of skills	Knowledge	Legal
New manufacturing process	Lack of top management commitment	Intellectual property	Lack of standards
Quality	Data management	Resource resistance	Infrastructure

Table 2 Top six challenges

Challenges	Times referred	Code
Cost	14	C1
Cybersecurity	12	C2
Data management	12	C3
Lack of skills or unqualified labor	9	C4
Knowledge	9	C5
Infrastructure	9	C6

After analyzing and filtering the literature review results, it was found that six different challenges were the most repeated as shown in Table 2.

Secondly, the data was gathered using a questionnaire designed specifically to be used in the AHP method. The questionnaire is scored using the Saaty scale, which ranges from 1 to 9, to determine whether two factors are equally essential, or one is more important than the other, as shown in Table 3.

The questionnaire was distributed to experts. Respondents were asked to compare factors together. A dropdown menu was provided for them to select the appropriate values.

Table 3 Pairwise scale [23]

Importance scale	Definition of importance scale
1	Equally important preferred
2	Equally to moderately important preferred
3	Moderately important preferred
4	Moderately to strongly important preferred
5	Strongly important preferred
6	Strongly to very strongly preferred
7	Very strongly important preferred
8	Very strongly to extremely important preferred
9	Extremely important preferred

3 Results

The results were analyzed. However, the results did not show consistency due to many reasons such as, people may not understand the way of questions and what is the Saaty scale. Therefore, the need to reevaluate and revise the questionnaire was needed. In the first iteration, the average answers were taken to proceed with the AHP method matrix, while in the second iteration. Table 4 concludes the results of the first evaluation, where CI is the consistency index and CR is the consistency ratio.

In the second iteration, the evaluation was done by comparing the number of answers that choose the first option (with a star) with the second option (without a star). The Saaty scale was used to end up with an evaluation. The results for both are concluded in Table 5. As the consistency ratio in the first and second iteration was not acceptable, in the third iteration, the judgment was done after looking in the previous research and articles on the same topic; as the below matrix shows, the possible challenges such as infrastructure was merged with the cost because they have a direct relationship together.

As the consistency ratio in the first and second iterations was not acceptable, in the third iteration, the judgment was done after looking at the previous research and articles on the same topic and merging some of the challenges together to avoid any confusion. Therefore, the challenges were reduced to be four as shown in Table 6.

Table 4 First evaluation (pairwise matrix and AHP calculation)

Pairwise matrix							Calculation	
	C1	C2	C3	C4	C5	C6		
C1	1	7	6	6	7	8	λ_{Max}	8.510
C2		1	7	7	7	6	CI	0.502
C3			1	6	7	7	CR	0.405
C4				1	7	7	Result	Not acceptable
C5					1	7		
C6						1	Decision	Reevaluate

Table 5 Second evaluation (pairwise matrix and AHP calculation)

Pairwise matrix							Calculation	
	C1	C2	C3	C4	C5	C6		
C1	1	2	2	1	1	1	λ_{Max}	9.200
C2		1	3	3	6	4	CI	0.640
C3			1	4	3	1	CR	0.516
C4				1	5	2	Result	Not acceptable
C5					1	3		
C6						1	Decision	Reevaluate

Table 6 Challenges

Challenges	Code
Cost and infrastructure	C1
Cybersecurity	C2
Lack of skills or unqualified labor	C3
Data management	C4

Table 7 Third evaluation (pairwise matrix and AHP calculation)

Pairwise matrix					Calculation	
	C1	C2	C3	C4		
C1	1	2	5	6	CI	0.043
C2		1	4	6	CR	5%
C3			1	4	Result	Consistency is less than 10%
C4				1	Decision	Accept

Table 8 Priorities for the four challenging factors

Cost and infrastructure	Cybersecurity	Lack of skills	Data management
0.495	0.331	0.116	0.058

As the matrix below shows, the possible challenges, such as infrastructure, were merged with the cost because they have a direct relationship. Table 7 shows the calculation after the 3rd evaluation.

The results show a consistency ratio of less than 5%, so the result was accepted. Table 8 shows that the main factor is the cost and infrastructure with about 50%, followed by cybersecurity with 33%.

4 Conclusion

This study sought to understand how Industry 4.0 is a need even though it is associated with many challenges. However, analyzing and identifying the main challenges can reduce that risk. The analyses showed that the main challenges are the cost of infrastructure and the cybersecurity issue. In this study, the AHP method was used as one of the most effective methods in prioritizing the different factors. However, to have excellent and accurate results, one needs clear and accurate data. Industry 4.0 is the future of all types of business; therefore, more study is needed to overcome the risk and the challenges in implementation.

References

1. Gentner S (2016) Industry 4.0: reality, future or just science fiction? How to convince today's management to invest in tomorrow's future! Successful strategies for industry 4.0 and manufacturing IT. *CHIMIA Int J Chem* 70(9):628–633
2. Süzen AA (2020) A risk-assessment of cyber attacks and defense strategies in industry 4.0 ecosystem. *Int J Comput Netw Inf Secur* 12(1)
3. Moeuf A, Lamouri S, Pellerin R, Tamayo-Giraldo S, Tobon-Valencia E, Eburdy R (2020) Identification of critical success factors, risks and opportunities of Industry 4.0 in SMEs. *Int J Production Res* 58(5):1384–1400
4. Prause M (2019) Challenges of industry 4.0 technology adoption for SMEs: the case of Japan. *Sustainability* 11(20):5807
5. Rane SB, Potdar PR, Rane S (2019) Development of project risk management framework based on Industry 4.0 technologies. *Benchmarking Int J*
6. Vrchota J, Řehoř P, Maříková M, Pech M (2020) Critical success factors of the project management in relation to industry 4.0 for sustainability of projects. *Sustainability* 13(1):281
7. Culot G, Fattori F, Podrecca M, Sartor M (2019) Addressing industry 4.0 cybersecurity challenges. *IEEE Eng Manag Rev* 47(3):79–86
8. Müller JM, Kiel D, Voigt K-I (2018) What drives the implementation of Industry 4.0? The role of opportunities and challenges in the context of sustainability. *Sustainability* 10(1):247
9. Gould-Williams J (2003) The importance of HR practices and workplace trust in achieving superior performance: a study of public-sector organizations. *Int J Hum Resour Manag* 14(1):28–54
10. Ziebermayr T (2021) Protecting intellectual property rights of industrial software. *Proc Comput Sci* 180:862–866
11. Tupa J, Simota J, Steiner F (2017) Aspects of risk management implementation for Industry 4.0. *Proc Manuf* 11:1223–1230
12. Sepasgozar SM (2020) Digital technology utilisation decisions for facilitating the implementation of Industry 4.0 technologies. *Construction Innovation*
13. Badri A, Boudreau-Trudel B, Souissi AS (2018) Occupational health and safety in the industry 4.0 era: a cause for major concern? *Safety Sci* 109:403–411
14. Habrat D (2020) Legal challenges of digitalization and automation in the context of Industry 4.0. *Proc Manuf* 51:938–942
15. Sony M, Naik SS (2019) Ten lessons for managers while implementing Industry 4.0. *IEEE Eng Manag Rev* 47(2):45–52
16. Ras E, Wild F, Stahl C, Baudet A (2017) Bridging the skills gap of workers in Industry 4.0 by human performance augmentation tools: challenges and roadmap. In: *Proceedings of the 10th international conference on Pervasive technologies related to assistive environments*, pp 428–432
17. Bonilla SH, Silva HR, Terra da Silva M, Franco Gonçalves R, Sacomano JB (2018) Industry 4.0 and sustainability implications: a scenario-based analysis of the impacts and challenges. *Sustainability* 10(10):3740
18. Moktadir MA, Ali SM, Kusi-Sarpong S, Shaikh MAA (2018) Assessing challenges for implementing Industry 4.0: implications for process safety and environmental protection. *Process Safety Environ Protection* 117:730–741
19. Vuksanović Herceg I, Kuč V, Mijušković VM, Herceg T (2020) Challenges and driving forces for industry 4.0 implementation. *Sustainability* 12(10):4208
20. Autenrieth P, Lörcher C, Pfeiffer C, Winkens T, Martin L (2018) Current significance of it-infrastructure enabling industry 4.0 in large companies. In: *2018 IEEE international conference on engineering, technology, and innovation (ICE/ITMC)*. IEEE, pp 1–8
21. Najdawi A (2020) Assessing AI readiness across organizations: the case of UAE. In: *2020 11th international conference on computing, communication and networking technologies (ICCCNT)*. IEEE, pp 1–5

22. Alaref EA, Khan SA (2021) Industry 4.0 and its technologies: a systematic literature review. In: 2021 IEEE international conference on industrial engineering and engineering management (IEEM). IEEE, pp 1004–1009
23. Saaty T (1980) The analytic hierarchy process (AHP) for decision making. Kobe, Japan, pp 1–69

Surface Treatment of Polyethylene Terephthalate Substrate by Sodium Hydroxide



Najwa Ibrahim  and Mariatti Jaafar 

Abstract The popularity of polyethylene terephthalate (PET) as a polymer substrate for flexible electronics has lately increased. The interaction between conductive inks and substrates is crucial. The high surface tension and poor surface wettability provide challenges when using conductive ink on PET substrates. To increase its adherence and compatibility with conductive inks, surface treatment is required. This paper describes how the PET substrate is hydrolyzed using sodium hydroxide (NaOH) to cause surface erosion. The treatment was carried out by adjusting the NaOH concentration and hydrolysis duration. The findings supported the increase in wettability after treatment as the water contact angle decreased from 78.60° (untreated PET substrate) to 39.90° (maximum). Fourier transform infrared spectroscopy identified an O–H group in the PET as a change in surface chemistry. Additionally, the hydrolysis in a 10 M NaOH solution showed the best improvement in wettability.

Keywords Flexible electronic · PET substrate · Chemical treatment · Advanced materials

1 Introduction

PET substrates have been used wide range in various flexible electronic applications due to their high flexibility, lightweight, and excellent durability. The conventional electronic display model currently consists of expensive and brittle glass materials [1–3]. In order to replace traditional glass in a variety of electronic display applications, such as touch screens and flexible large area displays, multiple studies have created a more flexible and resilient polymer substrate. Radio-frequency identification (RFID) tags, printed circuit boards (PCB), and electronic packaging are examples of flexible electronics that use PET substrate.

Substrates made of polymers are dense, multi-part systems. The surface energy, surface treatment functionality, and crystallinity change of a substrate are all closely

N. Ibrahim · M. Jaafar (✉)

School of Materials and Mineral Resources Engineering, Engineering Campus, Universiti Sains Malaysia, 14300 Nibong Tebal, Penang, Malaysia
e-mail: mariatti@usm.my

related to its ability to adhere inks, coatings, or adhesives. The adhesion of printing inks is affected by polymer substrate surfaces that are impermeable and chemically inert. Most low surface energy polymer substrate are hydrophobic and have poor wettability because they lack polar groups on their surfaces [4]. However, because to their hydrophobicity, PET substrates need to have their surfaces treated in order to add O–H groups to improve adhesion and compatibility. The wettability and adherence of conductive ink on PET surfaces are made possible by adding this O–H group by hydrolysis [5].

PET has been reported to have had hydrophilic surfaces treated utilising a variety of techniques, including ultraviolet waves [6], layer-by-layer deposition [7], plasma treatment [8], and hydrolysis by NaOH [9, 10]. Hydrolysis treatment was found to be more cost-effective and less equipment needed. It was discovered that hydrolysis treatment was less expensive and required less equipment. As a result, in this work, NaOH is used to perform hydrolysis on the PET substrate utilizing different soaking periods and concentrations in accordance with the theory of a surface erosion process. Fourier-transform infrared spectroscopy was used to examine the alteration of the chemical link.

In contrast, erosion upon O–H bonding resulted in changes in the thickness of the PET substrate, therefore the contact angle was recorded to evaluate the improvement in wettability. To determine the optimum conditions for enhanced wettability treatment PET, this study also investigated thickness variations.

2 Materials and Methods

2.1 Materials

PET substrates were used as received. Ethanol, hydrochloric acid (HCl), and (NaOH) were purchased from Merck and used as received.

2.2 Methods

PET surface treatment

To eliminate contaminants, PET substrates were submerged in a 1:1 mixture of ethanol and water for 10 min. Then, NaOH solution was added to the clean PET substrates at varying concentrations of 5 and 10 M at 60 °C. There were five alternative soaking times: 20, 60, 120, 180 and 240 min. The unreacted NaOH was removed from the PET substrate by washing it with 1 M HCl after the soaking period. To create the NaOH hydrolyzed PET substrate, the substrate was washed in ethanol and water and dried at 60 °C.

Characterization

The PET thickness changes were measured using a Mitutoyo 547-401 Thickness gauge before and after treatment. The morphology of the obtained PET was examined using an Olympus optical microscope. The contact angle was used to investigate the wettability of the modified PET. These water droplets were then photographed and used to calculate contact angles with the Ossila Contact Angle Goniometer. Attenuated total reflection-Fourier transform infrared spectroscopy (ATR-FTIR) was used on a Perkin Elmer to investigate the chemical structure of treatment PET scanned at 4000–400 cm^{-1} .

3 Results and Discussion

3.1 The Thickness Change of PET Substrate After Treatment

The ester group of the PET substrate reacts with the NaOH concentration due to hydrolysis-induced surface erosion. On the polymer chain, this reaction led to the production of O–H and carboxyl groups. Consequently, the polymer chain eruption can result in a weight loss due to the creation of detachable oligomeric components at the molecular level, reducing the PET substrate thickness [10]. Table 1 shows the thickness changes of PET substrate at varied NaOH concentrations. The increasing hydrolysis time and NaOH concentrations significantly affected the thickness of the PET substrate. Generally, the most erosion surface loss was observed using 10 M NaOH, reaching up to 90% thickness changes after 240 min of treatment. The surface erosion may due to the degradation of carboxyl group and addition of O–H group.

Table 1 The thickness of treatment PET substrate at a varied NaOH concentration and time

Soaking time (min)	The thickness of 5 M NaOH (mm)	The thickness of 10 M NaOH (mm)
Untreated	0.120	0.120
20	0.114	0.102
60	0.089	0.085
120	0.063	0.050
180	0.048	0.027
240	0.025	0.012

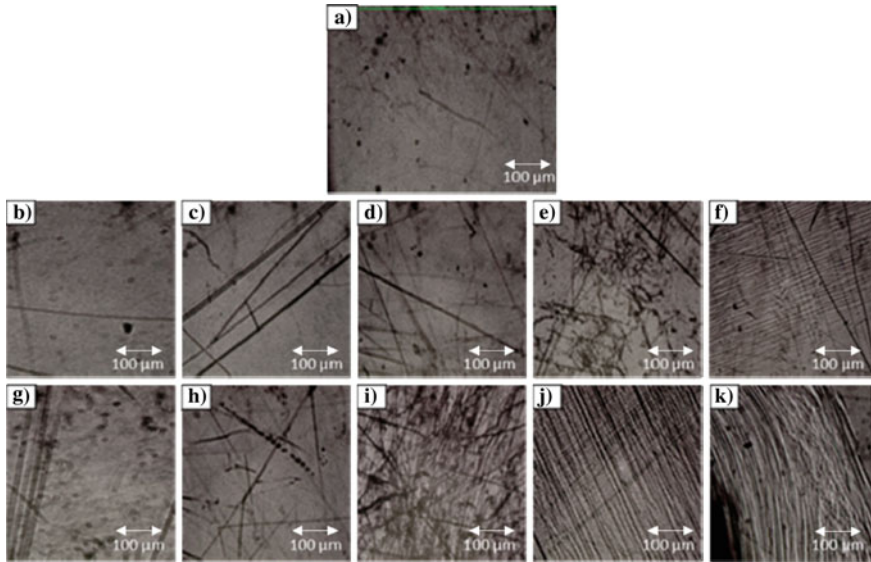


Fig. 1 Optical microscopy image of modified PET substrates as a function of hydrolysis time at varied NaOH compositions at scale magnification of 10×10 , $100 \mu\text{m}$. **a** Untreated PET, treated PET with 5 M NaOH at; **b** 20 min, **c** 60 min, **d** 120 min, **e** 180 min, **f** 240 min, treated PET with 10 M of NaOH at; **g** 20 min, **h** 60 min, **i** 120 min, **j** 180 min, **k** 240 min

3.2 The Morphology of PET

Figure 1 presents the hydrolyzed morphology of a PET substrate soaked in 5 M and 10 M NaOH for varying amounts of time. Figure 1a shows a relatively smooth surface for untreated PET. As hydrolysis was introduced, the PET surface layer's erosion and destruction increased as treatment times and NaOH concentrations increased. The morphology of PET substrate treated with 5 M NaOH increases soaking time, shown in Fig. 1b–f. In comparison, Fig. 1g–k is the morphology of PET substrate hydrolyzed with 10 M NaOH. Obviously seen in Fig. 1e, f, i–k the surface erosion of PET substrate. The surface erosion supposedly could increase the compatibility and adhesion of conductive ink to the substrate. This phenomenon will be discussed in detail in Sect. 3.3. Adina et al. [11] reported a similar result, which analyzed the degradation of more than 98% of PET by alkaline hydrolysis.

3.3 Wettability of PET

Table 2 shows the contact angle of untreated and treated PET substrate upon NaOH treatment at various times and NaOH concentrations. It is clear that increasing the soaking time influences the surface wettability. The contact angle decreased from

78.6° to 51.3° and 39.7° for hydrolysis at 240 min. Furthermore, increased NaOH concentration also affected the surface wettability and thus adhesion of conductive ink on treatment PET. Wettability is defined when the contact angle is less than 90°. In contrast, a contact angle greater than 90° suggests hydrophobicity [4]. The wettability and adherence of conductive ink dropped on untreated PET, 5 M 240 min PET, and 10 M 240 min PET are depicted in Fig. 2a–c. In Fig. 2a, b, the ink does not completely cover the PET surfaces. In contrast, in Fig. 2c, as time passed and the concentration of NaOH increased to 10 M, surface wettability changes causing the conductive ink to completely cover the PET substrate.

Figure 3 displays the FTIR spectra of untreated PET and PET treated with varying amounts of NaOH. The spectra reveal that the primary bonds present in PET are C=O at 1716 cm^{-1} , ethyl C–H (2970 cm^{-1}), ester C–O at 1250 cm^{-1} and 1182–1177 cm^{-1} , C=C, and phenyl ring (3055 and 1578 cm^{-1}). At wavenumbers 1250 cm^{-1} and 1182–1177 cm^{-1} , the C–O bond is attached to the carboxylate group. Upon examination with NaOH, the FTIR spectra of treated PET differed significantly from those of untreated PET. On PET treated with 10 M NaOH and 5 M NaOH, the broad peak of O–H groups appears at 3476 and 3434 cm^{-1} , respectively. Furthermore, the intensity and shift of the strong C=O peak at 1716 cm^{-1} of untreated PET reduced with 10 M NaOH and 5 M NaOH, indicating that these bonds were degraded by NaOH.

Table 2 The contact angle of PET substrate hydrolyzed at different NaOH concentrations and time

Treatment time (min)	NaOH concentration	
	5 M	10 M
Untreated	78.6°	78.6°
20	64.9°	60.7°
60	59.2°	56.0°
120	56.1°	55.1°
180	54.8°	46.2°
240	51.3°	39.7°

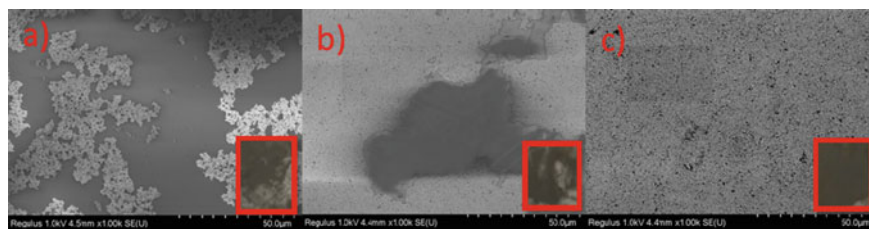
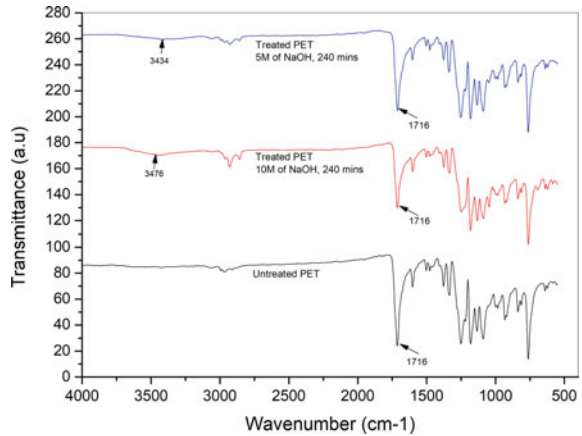


Fig. 2 Wettability of conductive ink on **a** untreated PET, treated PET with **b** 5 M of NaOH at 240 min, **c** 10 M of NaOH at 240 min. Inset image is a quality of printing conductive ink on PET substrate

Fig. 3 FTIR of the untreated and treated PET substrate



4 Conclusion

By comparing the attributes of PET substrates before and after treatment, the influence of soaking times and NaOH concentrations on the thickness changes, wettability, and adherence of conductive ink on PET substrates was explored in depth. Using the NaOH treatment erosion method, it was possible to successfully treat the surface of PET substrates to increase wettability with a considerable effect on surface morphology. The FTIR study revealed the introduction of new O–H surface chain bonds in PET.

Acknowledgement We are very grateful to the Ministry of Higher Education Malaysia for awarding us a Fundamental Research Grant Scheme (FRGS/1/2021/TK0/USM/01/4) and Universiti Sains Malaysia for making this study possible.

References

1. Yang W, Wang C, Arrighi V (2018) Silver oxalate ink with low sintering temperature and good electrical property. *J Electron Mater* 47(5):2824–2835
2. Rivadeneyra A, Loghin F, Falco A (2018) Technological integration. In: *Printed electronics, in flexible electronics*. IntechOpen
3. Wu W (2019) Stretchable electronics: functional materials, fabrication strategies and applications. *Sci Technol Adv Mater* 20(1):187–224
4. Aydemir C, Altay BN, Aykol M (2021) Surface analysis of polymer films for wettability and ink adhesion. *Color Res Appl* 46(2):489–499
5. Wieszczycka K et al (2021) Surface functionalization—The way for advanced applications of smart materials. *Coord Chem Rev* 436:213846
6. Liu XD et al (2013) UV-assisted surface modification of PET fiber for adhesion improvement. *Appl Surf Sci* 264:61–69
7. Xiao S et al (2017) Layer-by-layer assembly of polyelectrolyte multilayer onto PET fabric for highly tunable dyeing with water soluble dyestuffs. *Polymers* 9(12):735

8. Vesel A et al (2020) Evolution of the surface wettability of PET polymer upon treatment with an atmospheric-pressure plasma jet. *Polymers* 12(1):87
9. Donelli I et al (2010) Surface structure and properties of poly-(ethylene terephthalate) hydrolyzed by alkali and cutinase. *Polym Degrad Stab* 95(9):1542–1550
10. Prorokova N et al (2014) Chemical method of fibrous materials surface activation on the basis of polyethylene terephthalate (PET). *Ch&ChT* 8(3):293–302
11. Adina C et al (2017) Alkaline hydrolysis of polyethylene terephthalate under microwave irradiation. *Rev Roum Chim* 62:531–538

Enhancement of Fenton Process Using High Entropy Alloy Powder as Catalyst



Nur Hudawiyah Abu Hassan, Mohammed Saedi Jami,
Farah Diana Mohd Daud, Nur Ayuni Jamal, and Norhuda Hidayah Nordin

Abstract The Fenton process is one of the chemical oxidation degradation processes widely used in wastewater management due to being environmentally safe. The Fenton process is a reaction in which iron-catalyzed hydrogen peroxide to generate hydroxyl radical. Even though the Fenton process can degrade the azo dye solution, there are still substantial limitations, such as high sludge production and limited catalytic activity. This study focus on improving the azo dye degradation process in the Fenton process. Thus, a novel alloy material known as High Entropy Alloy (HEA) powder has been proposed for use as a catalytic material in the Fenton process. Mechanical alloying method was used to produce HEA powder, which is expected to considerably improve its efficiency in the degradation of azo dyes. The result shows the presence of HEA as catalyst improves the Fenton reaction by providing additional actives sites. This research contributed to the development of an appealing, low-cost, and efficient approach for HEA functional applications in wastewater management.

Keywords Azo dye · Catalyst · Degradation · Fenton process · High entropy alloy (HEA)

1 Introduction

Dyes are colored substances that chemically bond to the substrate to which are being applied. There are two main functional groups of dyes, chromophores and auxo-chromes. Chromophores are responsible for the color of the dyes where its functional group characteristic is a delocalized system with conjugated double bonds which are normally electron-withdrawing groups such as $-C = C-$, $-C = N-$, $-C = O-$, $-N = N-$, $-N = O-$ and $-N O_2$ groups while auxo-chromes responsible for the intensity of

N. H. A. Hassan · F. D. M. Daud · N. A. Jamal · N. H. Nordin (✉)
Department of Manufacturing and Materials Engineering, International Islamic University
Malaysia, Jalan Gombak, 53100 Kuala Lumpur, Malaysia
e-mail: norhudahidayah@iium.edu.my

M. S. Jami
Department of Biotechnology Engineering, Kulliyah of Engineering, International Islamic
University Malaysia, Gombak, Malaysia

© The Author(s), under exclusive license to Springer Nature Singapore Pte Ltd. 2023
Md. A. Maleque et al. (eds.), *Proceeding of 5th International Conference on Advances in
Manufacturing and Materials Engineering*, Lecture Notes in Mechanical Engineering,
https://doi.org/10.1007/978-981-19-9509-5_41

the color and its functional groups are electron donating substituent such as $-\text{NH}_2$, NR_2 , $-\text{COOH}$, $-\text{SO}_3\text{H}$ and $-\text{OH}$ [1]. According to the Ecological and Toxicological Association of the Dyestuffs Manufacturing Industry (ETAD), basic dye and diazo direct dyes have the highest toxicity among 4000 dyes tested. The properties of azo dyes are high-intensity color, medium–high color fastness properties, cheapness and insoluble in water. Cheap is the main reason why azo dyes are widely used in the textile industry. On one hand, azo dyes are insoluble in water, causing water pollution that can harm humans and the environment due to their toxicity and carcinogenicity.

Azo dyes must be degraded from wastewater properly. Hence, various methods have been proposed to treat textile dye effluents economically and efficiently. The methods are categorized into three groups consisting of physical, biological, and chemical and chemical oxidation treatment processes. The application of these approaches depends on the type of wastewater treated and the cost-effectiveness of treatments. Due to the absence of toxicity of the reagents, the Fenton technique is reported to be an excellent technology for the degradation of a wide range of hazardous and organic pollutants, making it environmentally safe [2].

In order to accelerate the breakdown of azo dyes in the Fenton process, a catalyst is required. Then, based on the conventional treatment, several types of catalysts such as iron activated carbon [3], ferrite bismuth [4], two electron catalyst [5] and zero valent metal [6] were discovered, studied, and experimented with. Nonetheless, catalysis is sluggish and time-consuming. As a result, it's critical to design a new catalytic material that can speed up the breakdown of azo dye without forming any secondary products that require additional processing.

A combination of five or more elemental concentrations between 5 and 35% is designated as a high entropy alloy (HEA). All elements are concentrated in HEAs, and there are no identifiable basis elements [7]. Because of their highly complicated atomic structure and severely distorted crystal structure, HEAs have been touted as viable catalysts. As a result of these factors, HEAs have a greater ability to tune adsorption characteristics and have higher potential energy, resulting in the production of more catalytic active sites. High entropy alloys (HEAs) are proposed as catalytic materials to improve Fenton's process performance. The catalytic mechanism or characteristics of HEA in degrading azo dye have not been extensively researched, with only a few papers published in the literature.

2 Materials and Method

The mechanical alloying process was started using a Fritsch Pulverisette P-5 planetary ball mill. A powder combination of iron (Fe), cobalt (Co), nickel (Ni), aluminum (Al), boron (B), and silicon (Si) were placed in the grinding bowl. The experiment was repeated for varied milling durations (5H, 30H, 70H, 100H and 160H) and different boron compositions. In this work, three parameters were used, FeCoNiAlBSi (B = 0.00); FeCoNiAlBSi (B = 0.02); FeCoNiAlBSi (B = 0.04); namely HEA-1, HEA-2 and HEA-3 respectively.

In the Fenton process, ferrous (II) sulfate heptahydrate salt, $\text{FeSO}_4 \cdot \text{H}_2\text{SO}_4$ and hydrogen peroxide, H_2O_2 were normally used as Fenton's reagent. Solution of the wastewater was prepared by adding the methyl orange as dyes and water into a 500 ml glass beaker. The research involves manipulating Fenton reagent parameters such as the amount of hydrogen peroxide, H_2O_2 and the ferrous sulfate heptahydrate, FeSO_4 , to find the optimum Fenton reagent for the Fenton process. The solution was then stirred and its pH was adjusted with the diluted sulphuric acid/sodium hydroxide. Because the influence of temperature is another parameter to consider, the methyl orange solution was kept at room temperature. After determining the optimum parameter of Fenton reagent, 0.01 g of HEA powder and Fenton reagents (H_2O_2 and FeSO_4) were combined in a methyl orange solution. The degrading efficiency for each variable was calculated and recorded for each run. Azo degradation efficiency in the Fenton process can be estimated by using this formula, $D(\%) = \frac{C_0 - C_t}{C_0}$ where C_0 and C_t correspond to the initial dye concentration and the concentration of dye at the reaction time, t respectively.

3 Result and Discussion

3.1 Characterizations of HEA Powder

XRD patterns of HEA powders at various milling periods are shown in Fig. 1. For the unmilled sample at 0H, several peaks corresponding to each element can be detected, indicating polycrystalline mixes of the element powders where diffusion has yet to occur. Peaks corresponding to B, Si, Co, Ni, and Al start to disappear after 5 h of milling due to element diffusion into the iron matrix during the milling process [8]. The reduction in crystallite size and lattice strain is also responsible for the decrease in peak height. Due to the progressive elimination of the BCC phase, the creation of the FCC phase began to occur at 15H. The lattice expansion caused by elemental diffusion of B, Si, Co, Ni and Al, which led to the production of FCC and BCC/B2 after 30H, is determined by the Fe peaks at 0H shifting toward smaller angles. Only two simple phases exist when the milling duration surpasses 70H. Meanwhile, the introduction of B into HEA-3 resulted in the formation of the intermetallic iron boride (Fe_2B) as a result of the interaction between Fe and B in HEA-3, as shown in Fig. 2. However, the Fe_2B phases did not appear in the HEA-2 crystal structure due to the low weight percentage of B in the HEA-2 powder. Thus, after 160 h of milling, three phases are discovered in HEA-1 and HEA-2: FCC, BCC, and BCC/B2, whereas three phases are identified in HEA-3: FCC, BCC/B2 and Fe_2B . The particle size of HEA powder was observed to increase from 0.960 μm at 5H to 1.167 μm at 30H milling times, as shown in Fig. 3 and tabulated in Table 1. The fact that milled powders at high intensity milling is proof of this, and research on particle disruption homogeneously is currently underway.

Fig. 1 XRD patterns of HEA powder at different milling time

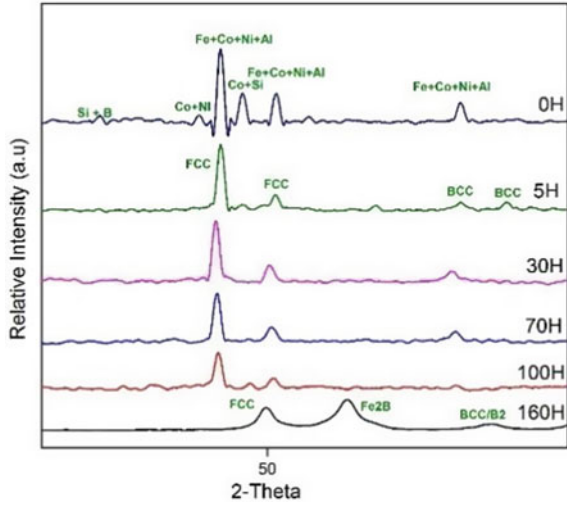
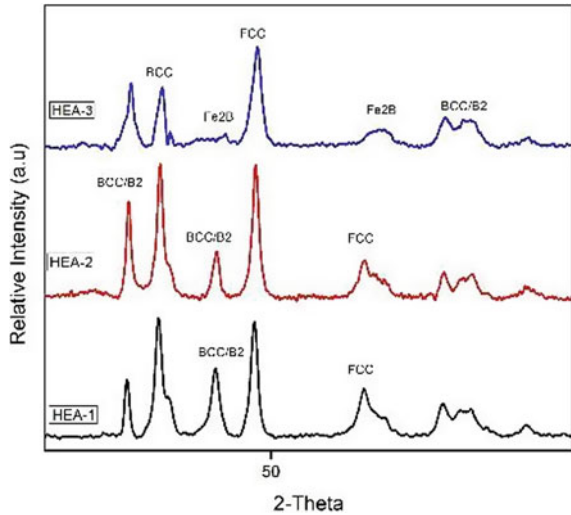


Fig. 2 XRD patterns of HEA powder with different composition of B



Fenton process is strongly influenced by two reagents which are ferrous (II) sulphate, FeSO_4 and hydrogen peroxide, H_2O_2 . The reaction between these two reagents produces ferric ions and hydroxyl radicals. Hydroxyl radical plays an important role in Fenton reagent to attack the molecule of methyl orange dye and degrades the amine bond which helps the decolorization dye in the solution which can be seen in the Fig. 4. Both the iron (II) ion (Fe^{2+}) and H_2O_2 react to form HO, but they also act as HO scavengers. The rate of HO production and scavenging should be influenced by the $[\text{Fe}^{2+}]/[\text{H}_2\text{O}_2]$ ratio. As a result, it is critical to employ the optimum $[\text{Fe}^{2+}]/[\text{H}_2\text{O}_2]$ ratio possible. The constant concentration 50 mM of methyl orange, MO was

Fig. 3 Graph of particle size of HEA powder over milling time

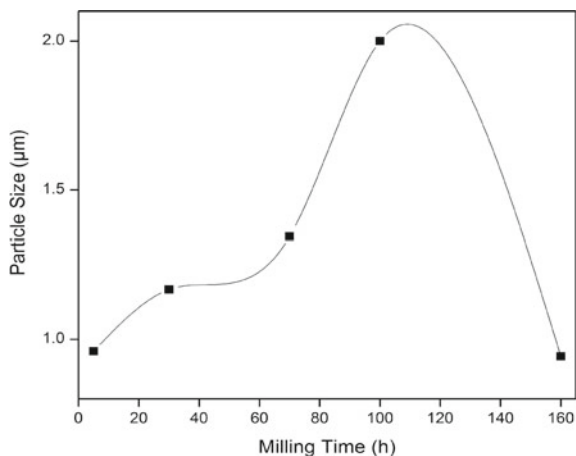


Table 1 Particle size of HEA powder over milling time

5	0.960
30	1.167
70	1.344
100	2.000
160	0.943

investigated at varied FeSO_4 and H_2O_2 concentrations to generate molar ratios of 1:5–3:5 to get the ideal starting concentration ratio of $[\text{Fe}^{2+}]/[\text{H}_2\text{O}_2]$ on the removal of MO. The optimal molar ratio was found to be 1:10. The findings almost matched with what was published in the literature on Fenton treatment for the degradation of azo dyes, which found that an iron-to-hydrogen peroxide ratio of 1:17 was the most efficient condition [9].

Fig. 4 Azo dye degradation efficiency with different ratio of Fenton reagent within two hours of Fenton reaction

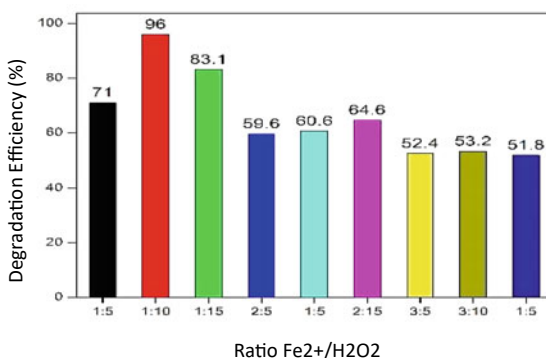


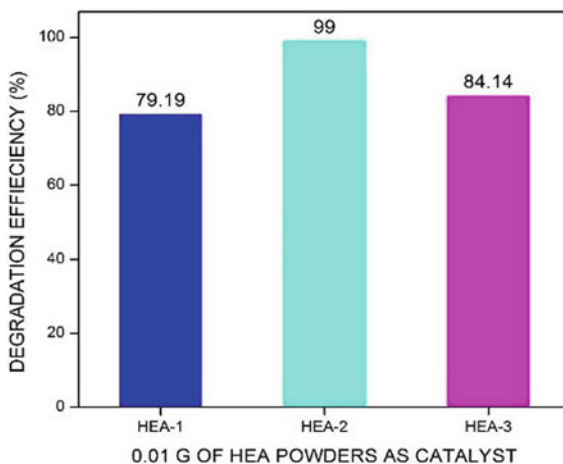
Table 2 Azo dye degradation in Fenton process with different particle size of HEA powder milling time

Manipulated		Responding
Milling time (hours)	Particle size (μm)	Degradation efficiency (%)
5	0.960	93.84
70	1.344	92.87
160	0.943	99.00

3.2 HEA as Catalyst in Fenton Process

Particle size and homogenous dispersion of HEA powder are the biggest influence in the degradation efficiency of azo dye in the Fenton process, as shown in Table 2. Figure 5 shows that the degradation efficiency of azo dye in the Fenton process is 99% when the particle size of HEA powder catalyst is 0.943 μm . This shows that, as the milling time increases, the particle size decreases and increases the surface area of HEA where it exhibits a more active site for HEA powder. Figure 5 depicts that HEA-2 and HEA-3 with the presence of B have higher degradation efficiency which was 99% and 84.14% respectively, compared to HEA-1 which 79.19% within two hours of Fenton reaction. Ramirez et al. [10] suggested that the presence of B in alloy increases acidic sites that may be associated with condensation reactions between close B-O-H groups and also with Al-OH groups, which may occur with increasing boron composition. However, excessive acidic sites may depict the reaction of the Fenton process [11].

Fig. 5 Azo dye degradation efficiency with different HEA powders



4 Conclusion

The development of HEA powder by the planetary ball milling process was achieved. Three phases of crystal structure which are FCC, BCC and BCC/B2 were present in HEA-1, HEA-2 and HEA-3 with the addition of intermetallic boride, Fe₂B indicate the presence of B. The reduction of particle sizes during the milling process will exhibit high surface area and more active catalytic sites of HEA. The optimum ratio of Fe²⁺/H₂O₂ was found to give the best result for the decolorization of MO in the Fenton process. Fenton reagents with a Fe²⁺/H₂O₂ molar ratio of 10:1 have the best degradation efficiency (96%). Furthermore, the presence of B in HEA improves the Fenton reaction by attracting additional acid sites where MO degradation efficiency with HEA-1 and HEA-2 as catalysts are 77.19% and 99%, respectively.

Acknowledgements Financial support from Malaysian of Higher Education (MoHE) grant no. (FRGS/1/2019/TK05/UIAM/03/3).

References

1. Gordon PF, Gregory P (2012) Organic chemistry in colour. Springer Science & Business Media. Springer Berlin, Heidelberg
2. Nidheesh PV, Gandhimathi R (2012) Trends in electro-Fenton process for water and wastewater treatment: an overview. *Desalination* 299:1–5
3. Muhammad AB, Mash AL (2020) Application of central composite design to the photo Fenton degradation of methyl orange azo dye using Fe-activated carbon catalyst. *Int J Innov Sci Research Technol* 5(8):479–485
4. Severo DC, Dotto E, Luiz G, Siara S, Nunes S, Isaac LE (2020) Improved catalytic activity of EDTA modified BiFeO₃ powders for remarkable degradation of procion red by heterogeneous Photon-Fenton process. *J Environ Chem* 103853
5. Matyszczyk G, Sędkowska A, Kuś S (2019) Comparative degradation of metanil yellow in the electro-Fenton process with different catalysts: a simplified kinetic model study. *Dyes and Pigments* 108076
6. Matyszczyk G, Krzyczkowska K, Fidler A (2020) A novel, two electron catalysts for the electro-Fenton process. *J Water Process Eng* 36:101242
7. Miracle DB (2019) High entropy alloys as a bold step forward in alloy development. *Nat Commun* 10(1):1805
8. Murali M, Babu K, Krishna B, Vallimanalan A (2016) Synthesis and characterization of AlCoCrCuFeZn_x high-entropy alloy by mechanical alloying. *Progress in Natural Sci: Mater Int* 26(4):380–384
9. Zhang MH, Dong H, Zhao L, Wang DX, Meng D (2019) A review on Fenton process for organic wastewater treatment based on optimization perspective. *Sci Total Environ* 670:110–121
10. Jorge R, Perla C, Luis C, Rogelio C, Marco C, Jose MP, Antonio LA (1995) Effect of boron addition on the activity and selectivity of hydrotreating CoMo/A₁₂O₃ catalysts. *Appl Catal A* 132:317–334
11. Abdur-Rahim A, Giwa A, Isah A, Bello A, Abdullahi BO, Olugbenga SB, Tawfik AS (2020) Kinetic and thermodynamic studies of Fenton oxidative decolorization of methylene blue. *Heliyon* 6(8):e04454

Analysis of the Adjusting Bolts System's Contribution to Levelling Error of the Heated Bed in FDM 3D Printer



Rudi Kurniawan Arief , Nor Aiman Sukindar , Irfan Hilmy ,
and Erry Yulian T. Adesta 

Abstract The 3D printer as one of the key technologies in the industrial revolution 4.0 has developed rapidly to improve manufacturing efficiency. Various printing machines and methods have been invented and the Fused Deposition Modelling (FDM) 3D printer is one of them. It works by depositing melted polymer materials layer by layer to form a product. Difficulties in setting up the level of the heated bed are one of the difficulties faced by the users. Tiny bolts that are used as the levelness adjuster of the heated bed's platform contribute to the error of the levelness setup. This research analyzes how difficult is the leveling setup process and how the adjusting bolt might involve in leveling error of the heated bed. This research examines three leveling methods to adjust the levelness of a heated bed. Each method was performed three times then the results were checked using the Coordinate Measurement Machine (CMM). The experiment shows all leveling methods obtained a levelness deviation that is higher than the maximum allowance. The mathematical equation also explained that the adjusting bolts system may cause levelness difficulties.

Keywords FDM 3D printer · Heated bed · Surface levelness · Rapid prototyping

1 Introduction

3D printing technology as one of the key technologies in the industrial revolution 4.0 has developed rapidly [1] to improve manufacturing efficiency [2]. The FDM 3D

R. K. Arief (✉)

Muhammadiyah University of Sumatera Barat, Padang, Indonesia
e-mail: rudikarief@umsb.ac.id

N. A. Sukindar · E. Y. T. Adesta
International Islamic University Malaysia, Gombak, Malaysia

I. Hilmy
Higher Colleges of Technology, Fujairah, United Arab Emirates

E. Y. T. Adesta
University Indo Global Mandiri, Palembang, Indonesia

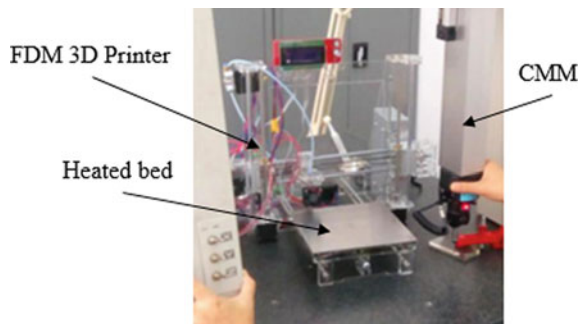
printing process has become the cheapest one that makes it possible for everyone to purchase [3]. Problems existed behind so much exposure about the creation made by desktop FDM 3D printers. Plenty of problems still take place during the operation of the FDM 3D printer and one of them was the leveling of the heated bed. Failure caused by the lack of bed levelness [4] and human error is relatively high during the FDM 3D printing process [5]. Most FDM 3D printers are equipped with small bolts as bed levelness adjusters, this condition might contribute to the error during the bed levelling, therefore a new system is needed [6]. This research will analyze how the adjusting bolt is involved in leveling error of the heated bed.

2 Experiment Methods

This research was performed using a low-cost Desktop FDM 3D printer machine. The experiments examine three leveling methods to adjust the levelness of the heated bed. Each method was performed three times then the results were checked using the Coordinate Measurement Machine (CMM) as shown in Fig. 1.

A common leveling method for FDM 3D printers is manual adjustment by using plain paper which is widely used among printer users. This method highly depends on the operator's sense during the setup. Secondly, a spirit level tool that is widely used to detect the level surface condition was also observed. Lastly, a dial indicator tool was also used in this experiment. The experiment result was measured using CMM to evaluate the levelness of the heated beds by measuring the levelness deviation that occurs. The result should be less than 80% [7]. The maximum deviation for a standard 0.4 mm nozzle hole should be 0.3 mm.

Fig. 1 Levelness examination using CMM



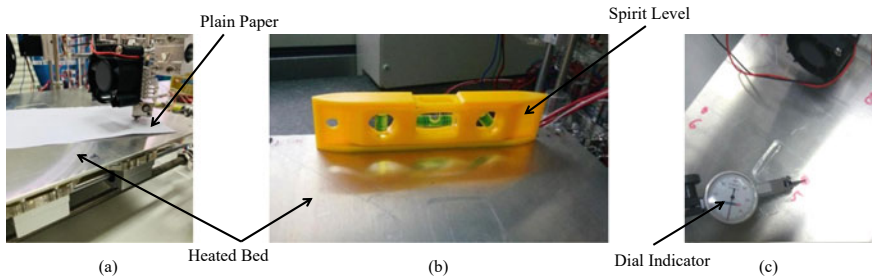


Fig. 2 a Levelling method using plain paper, b using spirit level tool, c using a dial indicator

2.1 Manual Adjustment Method

A plain 70 gsm white paper was used to adjust the gap between the nozzle and the heated bed's platform as a gap adjuster as shown in Fig. 2a. First, the nozzle position was set to home all position (0,0,0), then moved upward for 10 mm (0,0,10). The setting position decided was 10 mm from each side of the bed, therefore the position for the first corner should be; 10,10,10. Next, put the plain paper below the extrusion head then moved the extrusion head down for 10 mm (10,10,0) or used the home Z menu. Pulled the paper to check the gap, it should be easy to pull with light friction sensed while the adjuster bolts are adjusted.

2.2 Spirit Level Method

Another common tool to examine the surface levelness is a spirit level as shown in Fig. 2b. A feeler gauge is compulsory for this method where the hard materials could use to adjust the gap between the heated bed and nozzle. Firstly, set the extrusion head to home all position (0,0,0), then moved upward for 10 mm (0,0,10) then moved to the center of the bed (100,100,10). The feeler gauge was placed under the nozzle and then moved downward for 10 mm (10,10,0).

2.3 Dial Indicator Gauge Method

The dial gauge indicator is used as a quality control tool to precisely check the levelness of a surface as shown in Fig. 2c. A dial gauge with 0.01 mm of accuracy was used to level and a feeler gauge to adjust the gap. Firstly, the nozzle was set to home all position (0,0,0), then moved upward for 10 mm (0,0,10), then moved to the center of the bed (100,100,10). The feeler gauge was then placed below the nozzle then select the Home Z menu. The dial indicator gauge dragged around on the edge

side of the heated bed while adjusting the adjuster screw. A good and leveled surface was indicated by a stand-still needle although the dial was moving around.

2.4 Bolts Adjustment Error

Another source of failure is the unprecise screwing of the small adjusting bolts. The M3 adjusting bolt works by converting the rotation movement into linear movement [8]. Different stop positions on each bolt could result in bed height differences that lead to unlevel conditions. The movement's distance can be checked using the thread's lead angle (β) equation as follows:

$$\beta = \arctan((1 - P)/(d2 \cdot \Pi)) \quad (1)$$

Thread arch length equation is used to calculate the length of travel:

$$L = \theta(\Pi/180) \cdot r \quad (2)$$

Height of translation calculated using trigonometry equation:

$$h = \tan \beta \cdot L \quad (3)$$

where

β = Lead angle

P = Pitch

d = Nominal diameter of the thread

L = Length of travel

h = Height of translation or movement.

The equations explain that the adjusting bolt moves upward or downward if the adjusting nut is rotated. Errors in rotating the adjusting nut in opposite direction could double the distance and create a huge unlevel surface gap in the heated bed platform.

3 Results and Discussion

3.1 Result of Experiment Using Manual Levelling Method

In this method, the nozzle gap is adjusted by using plain paper to create levelness of the bed surface. The adjusting bolt is adjusted to press the paper until it feels not too loose and not too tightly pressed. This method highly depends on the sense and

Table 1 Leveling deviation using manual setup method

Checkpoint	Height deviation from datum		
	1st	2nd	3rd
1	0.4870	1.7480	1.3623
2	0.8807	0.6437	1.1636
3	0.6584	1.6827	1.5701
4	1.3553	0.7104	1.4152

Table 2 Leveling deviation using spirit level setup method

Checkpoint	Height deviation from datum		
	1st	2nd	3rd
1	-2.6259	-2.7187	0.8672
2	0.1205	0.0269	0.5673
3	-2.9059	-2.7397	1.0317
4	-1.9331	-1.7907	0.6067

experience of the operator. Table 1 shows the result of the total average deviation obtained is 0.793 mm exceeding the maximum nozzle distance which is 0.3 mm [7], where one corner of the bed printer is lower or higher by 0.793 mm than the others, this condition may cause difficulties of the filament to stick to the bed. The results are still above the maximum allowance even though this setup was performed by an experienced user and this shows the difficulties of this task. This also explained the inaccurate of this method and requires to be developed further.

3.2 Result of Experiment Using Sprit Level Gauge

The second experiment was using a spirit level, one of the easiest tools for evelling, to maintain the levelness of a flat surface. The experiment resulted in a total average deviation obtained is 2.0858 mm which exceeds the maximum nozzle distance which is 0.3 mm as shown in Table 2. A high deviation of the levelness could cause the worst printing result. This method should produce better levelness but this experiment has shown a contrary result, this may be caused by the adjusting system which could easily cause a human error during adjusting the bed.

3.3 Result of Experiment Using Dial Indicator Gauge

Dial indicator gauge is one of the precision levelness inspection tools to perform quality inspection and this tool is expected to evince better leveling setup results. As a result of the data shown in Table 3, the total average deviation obtained is

Table 3 Leveling deviation using dial indicator setup method

Checkpoint	Height deviation from datum		
	1st	2nd	3rd
1	0.8503	0.2616	0.8715
2	0.4858	-1.9196	0.5702
3	1.4752	0.3947	1.0330
4	0.5981	0.0519	0.6112

1.2555 mm which exceeds the maximum nozzle distance which is 0.3 mm. This method may not be applicable to be used by the FDM 3D printer user since this tool is relatively expensive and special skill is required. Theoretically, this method should produce better levelness conditions but this experiment has shown a contrary result, this may be caused by the adjusting system that could easily cause a human error during adjusting the bed, therefore the chance for human error during the bolt adjustment should be analyzed.

3.4 Bolts Adjustment Error

To set the heated bed levelness by screwing the adjusting nut is one of the trickiest works to perform. The height shall adjust by rotating the nut, and this relies on the operator's feelings. Too much or too less rotating degrees may cause different translation movements resulting differences in the heated bed platform's height.

The theoretical calculation result of adjusting bolt movement found that:

$$\beta = 3.38^\circ$$

$$L = 0.026 \text{ mm}$$

$$h = 0.0015 \text{ mm}$$

This result explains that the adjusting bolt will move by 0.0015 mm for each 1° of rotation. A full 360° of adjusting nut rotation will lift the heated bed platform by 0.54 mm, this could create a bigger gap than the maximum allowance and produce a bad product, therefore the operator should perform this setup carefully. This experiment shows the tendency of the bolt and screw system to be the cause of difficulties experienced in leveling setup and might be the cause of failure of the leveling methods above.

4 Conclusion

The results obtained from the experiments by using three manual methods show the difficulties to obtain accurate and better levelness conditions of the heated bed. Out of the three leveling methods, the manual method provides the best result, however, it is still over the maximum allowance of 0.3 mm. Theoretical analysis using the mathematical formula to adjust the bolt's translation movements also indicated the difficulties in leveling the heated bed using the bolts system. The equation indicated the occurrence of a large gap deviation if the setup was performed carelessly by an inexperienced operator. These experiments confirmed the difficulties of obtaining a good levelness condition using the current bolt adjuster system. Even though further analysis and observation shall be conducted, this research provides the ground for further development of new adjustment tools to replace the bolts system.

References

1. Shahrubudin N, Lee TC, Ramlan R (2019) An overview on 3D printing technology: technological, materials, and applications. *Proc Manuf* 35:1286–1296
2. Perez M, Carou D, Rubio EM, Teti R (2020) Current advances in additive manufacturing. In: 13th CIRP conference on intelligent computation in manufacturing engineering, pp 439–444
3. Rasiya G, Shukla A, Saran K (2021) Additive manufacturing-a review. In: *Materials today: proceedings, India*, vol 47(19), pp 6896–6901
4. Arief RK, Adesta EYT, Hilmy I (2019) Hardware improvement of FDM 3D printer : issue of bed leveling failures. *Int J Technol Explor Eng* 8(4):603–614
5. Song R, Telenko C (2016) Material waste of commercial FDM printers under realistic conditions. In: *Proceedings 27th annual international solid freeform fabrication symposium*, pp 1217–1229
6. Arief RK, Adesta EYT, Hannaf RAA, Hilmy I (2020) A design consideration of heated bed's rapid levelling tool based on von mises stress using FEA simulation. In: *2020 advances in science and engineering technology international conferences (ASET), IEEE, Dubai*, pp 1–5
7. Griffey J (2017) 3-D printers for libraries. American Library Association, Chicago
8. Budynas RG, Nisbet JK (2020) *Shigley's mechanical engineering design*, 11th edn. McGraw-Hill, New York

Failure Mechanism on Ti-6Al-4V Material Processed Using Selective Laser Melting (SLM)



**Sukri Mubarak, Poppy Puspitasari, Andoko Andoko,
Abdul Munir Hidayat Syah Lubis, Avita Ayu Permanasari,
and Muhammad IIman Hakimi Chua Abdullah**

Abstract Titanium alloy has been massively used in automotive and aerospace fields, such as Ti-6Al-4V titanium alloy. Further, the emergence of metallic additive manufacturing (AM) technology has been a breakthrough in the workpiece formation, such as selective laser melting (SLM). Besides, additive manufacturing is capable of producing complex metal components with high performance and speed that have fulfilled the mechanical requirements and light structure. A further study on the use of Ti-6Al-4V titanium powder is required, specifically on its mechanical properties and material failure mechanism due to the selective laser melting (SLM) process. The mechanical properties of Ti-6Al-4V titanium alloy rely highly on the phase of its composer, grain morphology, and characteristic length scale, as well as grain orientation (texture). Also, the heat treatment post SLM process also affects the strength of material produced through SLM using titanium alloy. In specific cases, the microstructure study has to be carried out since, in the biomedical implementation, such as in bone-implant on the joining area and wrist, fractures tend to occur. The fracture caused by the imperfect formation process during the melting of Ti-6Al-4V titanium powder or parameter of selective laser melting can be dangerous. This study reviews the failure mechanism of Ti-6Al-4V titanium using selective laser melting.

S. Mubarak · P. Puspitasari (✉) · A. Andoko · A. A. Permanasari
Mechanical and Industrial Engineering Department, Universitas Negeri Malang, Malang,
Indonesia
e-mail: poppy@um.ac.id

P. Puspitasari · A. A. Permanasari
Center of Advanced Materials for Renewable Energy, Universitas Negeri Malang, Malang,
Indonesia

A. M. H. S. Lubis
Mechanical Engineering Department, Universitas Muhammadiyah Surakarta, Surakarta,
Indonesia

M. I. H. C. Abdullah
Centre for Advanced Research On Energy, Universiti Teknikal Malaysia Melaka, Melaka,
Malaysia

Fakulti Teknologi Kejuruteraan Mekanikal Dan Pembuatan, Universiti Teknikal Malaysia Melaka,
Melaka, Malaysia

Keywords Failure mechanism · Ti-6Al-4V · Selective laser melting

1 Background

Selective Laser Melting (SLM) is a 3D printing process or additive manufacturing (AM) designed to melt and merge metal powder using a high-density laser. This SLM technique is also popular as direct selective laser sintering. This technique has been confirmed to produce parts that are almost net-shaped. Within the SLM process, the printing area is filled with nitrogen or argon gas to avoid oxidized metal. The layer thickness or high ranges from 20 to 100 μm , with lower layer high resulting in more excellent obtained resolution. The primary material for SLM is metal powder, in which the powder with greater particle size produces poor resolution, while powder with smaller particle size tends to agglomerate induced by the Van der Waals force.

The powder materials of SLM have varying characteristics depending on their main material, as well as the absorbing factor of the laser beam in examining the laser intensity for the SLM. The powder material's properties carry substantial effects on the SLM results [1].

In a study of the ratio of strength toward excellent weight corrosion resistance², the titanium alloy is found to be capable of being applied in light and strong structures, such as in aerospace and biomedical fields. In most structural titanium alloys, there are two phases, namely, the α phase at a low temperature and the β phase at a high temperature. The $\alpha + \beta$ titanium alloy may have different morphology (such as fully flat, fully crystalline, or a combination of both) depending on the thermal processing. However, the fully flat structure is generally preferable due to its resistance to fracture and fatigue crack. A fracture is a forced fracture that divides material into two parts. Brittle and ductile. Therefore, an investigation of Ti-6Al-4V titanium alloy processed using selective laser melting (SLM) is essential, primarily to discover its mechanical and failure mechanism.

2 Review

The strength ratio between excellent strength, weight, and corrosion resistance results in stimulating titanium alloy for powerful and light components, primarily in aerospace and biomedical application. Particularly, titanium alloy consists of two phases, namely the α phase at a low temperature and the β phase at a high temperature. The $\alpha + \beta$ titanium has diverse morphology (such as fully flat, fully crystalline, or a combination of both) relying on thermal processing. However, the entirely flat structures are generally preferable for their high fracture and fatigue crack resistance.

The ductility value of Ti-6Al-4V material in SLM ranges between 1.7 and 11.9%. For the mechanical properties, that range has an excellent distribution. Besides, during the SLM process, microheterogeneity may also emerge. With SLM's speedy

solidification and cooling rate, the β phase at a high temperature of Ti-6Al-4V transforms into α' martensite. Due to the high cooling rate and density, deficiencies, such as dislocation, commonly occur in the printed structure. Also, the printed layer experiences numerous heating cycles with peak shedding temperature, while the later layer is stored and will modify the microstructure of each layer afterward. The epitaxial growth of the previous layer on the consecutive lasering results in β columnar.

Previous research by Moridi et al. showcases that a tensile test and microstructure analysis was carried out on the SLM with Ti-6Al-4V material, showing that the printed parts have a micro hierarchical structure consisting of primary, secondary, and tertiary α' martensite. This hierarchical structure is formed by the heat cycles during the SLM coating process. After tensile deformation, strain localization within primary α' martensite produces ductile microscopic and microvoid coalescence formation, as well as macroscopic brittle fracture. Aside from localization in primary α' , the surface of grain boundary formed at this high ratio indicates the interfacial plasticity's contribution to the overall material deformation. The brittle fracture occurs in SLM using Ti-6Al-4V material originating from (i) martensite phase and (ii) general defects in the print structure. The first phase can be resolved by in situ decomposition, from the fragile α' phase into the stronger $\alpha + \beta$ phase [2].

In addition, Yang et al. investigated the ductile fractures of Ti-6Al-4V alloy processed using additives manufacturers—Selective laser melting (SLM). Titanium alloys are widely used in the automotive and aerospace fields, such as the Ti-6Al-4V. Titanium alloys are highly recommended in structural and biomedical applications due to their excellent biocompatibility, corrosion resistance, and comprehensive mechanical properties. The examination of the fracture and damage behavior on Ti-6Al-4V alloys with SLM fabrication was carried out by constructing specimens, with variances of SLM direction manufacture angle (0° , 45° , 90°) and heat treatment of annealing and solution-aging. The observed variables consist of tensile, compressive, and torsional [3].

Figure 1 illustrates the apparent microstructure of specimens with different build angles after the annealing heat treatment. As presented in the figure below, the grain size and phase composition show no significant differences, as marked by the interlocking woven structure. In the annealing treatment condition (two hours at 800°C), the structure of acicular α' martensite in the untreated specimen begins to unravel and transform into two-phase α and β grain structure due to the lower temperature than the phase transition temperature, in which the α phase (the bright area in the picture) presents as fine needles, while β phase (the dark area in the picture) are distributed between them [4].

Figure 2 shows the microstructure of SLM fabricated Ti-6Al-4V alloy after the aging heat treatment for different manufacturing directions. All of those structures are similar as characterized by the triple mixed structure, consisting of a secondary flat α phase, transformed β phase, and equiaxed primer α phase.

In the solution processing, the Ti-6Al-4V alloy is heated at 920°C (below the transformation temperature of the β phase), stimulating the decomposition of the original acicular α martensite and forming the $\alpha + \beta$ equilibrium phase structure. In the air-cooling process, the secondary α phase is nucleated on the β phase boundary

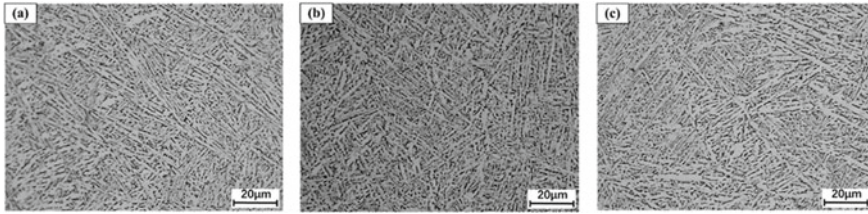


Fig. 1 Optical micrograph showing the microstructure of Ti-6Al-4V alloy fabricated using SLM with different manufacturing directions: **a** 0°; **b** 45°; **c** 90°. (The bright zone represents a phase, while the dark zone represents a phase)

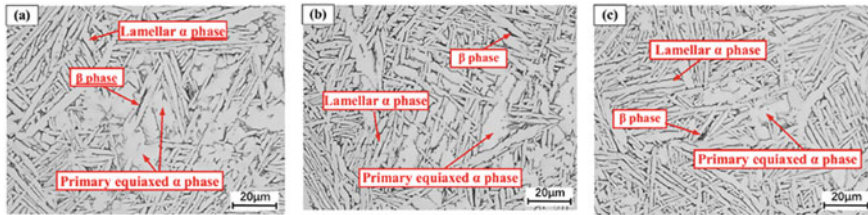


Fig. 2 Optical micrograph showing the microstructure of the SLM fabricated Ti-6Al-4V alloy after solution aging heat treatment with different manufacturing directions: **a** 0°; **b** 45°; **c** 90°

and continues to grow in the matrix. But the partial primary phase remains caused by the excellent temperature drop gradient. Lastly, during the aging process at 540 °C for 4 h, the α primary grain's wide and length continue to decrease and cause grain globalization phenomena. Meanwhile, during the longer aging period, the secondary α phase experiences an increase in fraction volume and becomes lamellae [5].

The morphology of the smooth round rod (SRB) and notched round bar (NRB) specimens is presented in Fig. 3. The typical ductile fracture mode is called 'cupcone' fracture surface, consisting of a central fibrous zone and an outer shear lip zone. The absence of radial zone shows excellent ductility from Ti-6Al-4V alloy fabricated using SLM. The rough surface of the fibrous zone and some big pits are apparently observed [6].

The fracture surface of the fine and crooked shear lip zone is at around an angle of 45° toward the tension direction. Generally, in the specimen experiencing axial tensile loading, the fracture begins in the minimum center area with the highest stress triaxiality and propagates outward, producing a circular fibrous zone. Then, the fractures in the front area approach the free surface, and a stress state transition from plane strain to plane stress occurs in the remaining thin skin sections, leading to the formation of a shear lip zone by the shear effect [7].

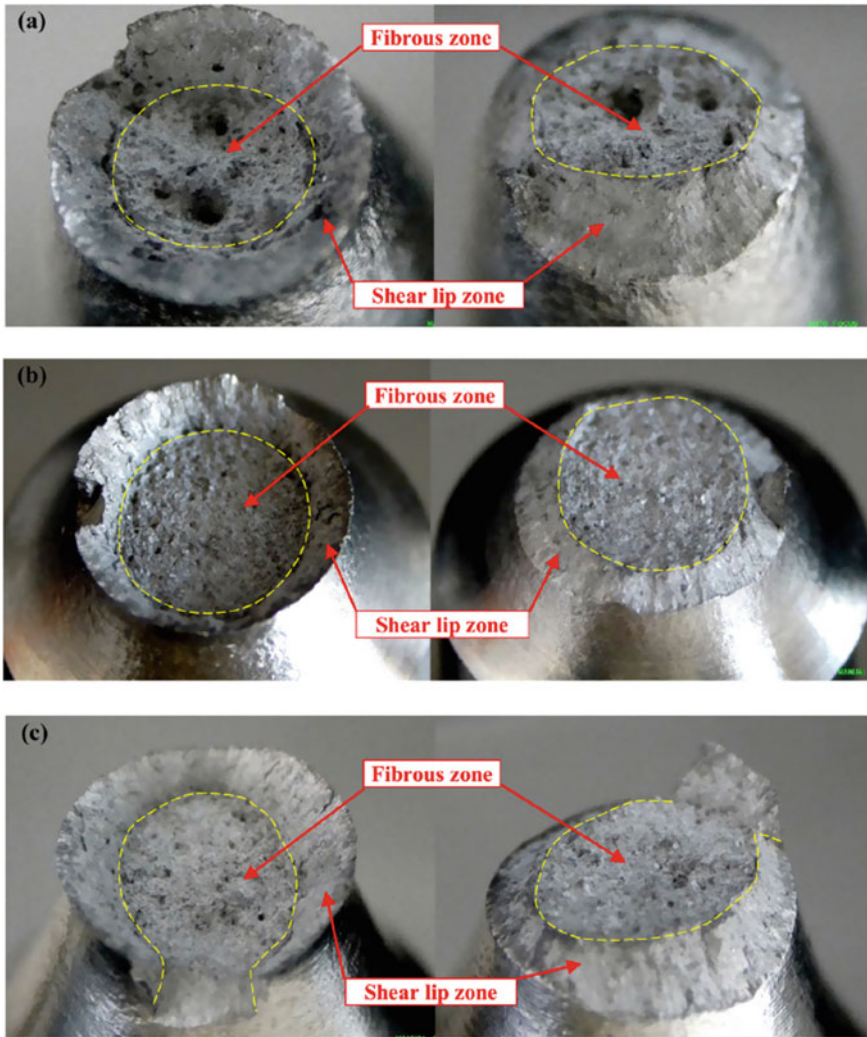


Fig. 3 The macroscopic fracture surface of SRB and NRB specimen: **a** SRB; **b** NRB-R3; **c** NRB-R12

3 Conclusion

We investigate the deformation response and failure mechanism of melted SLM Ti-6Al-4V using tensile test and post-mortem fracture analysis. According to our analysis, numerous conclusions are drawn.

1. The SLM result is in the hierarchical microstructure based on the martensite transformation order.

2. After tensile deformation, the strain is primarily localized in the primary α' . The central localization occurs in primary α' , with the central axis oriented at around 45° , in connection to the loading direction.
3. The surface topography evolution during the deformation reveals the role of interfacial plasticity on the entire printed Ti-6Al-4V deformation
4. The strain localization produces cavities in the primary α' . The growth of cavities and coalescence results are in the final fracture of the material. The local decay is very ductile, but it results in brittle fracture. The apparent embrittlement is also observed in the fracture surface, consisting of dimple-like and cleavage features.
5. Macroscopic and microscopic fractographic analysis show typical ductile fracture mode from the SLM fabricated Ti-6Al-4V, while the fracture mechanism in different stress situations is also clarified.

References

1. Yap CY et al (2015) Review of selective laser melting: materials and applications. *Appl Phys Rev* 2(4):041101
2. Moridi A et al. (2019) Deformation and failure mechanisms of Ti-6Al-4V as built by selective laser melting. *Mater Sci Eng A* 768:0–25
3. Yang X et al (2021) An investigation of ductile fracture behavior of Ti6Al4V alloy fabricated by selective laser melting. *J Alloys Compd* 890:161926
4. Song B, Dong S, Zhang B, Liao H, Coddet C (2012) Effects of processing parameters on microstructure and mechanical property of selective laser melted Ti6Al4V. *Mater Des* 35:120–125
5. Nouari M, Makich H (2014) On the physics of machining titanium alloys: Interactions between cutting parameters, microstructure and tool wear. *Metals (Basel)* 4:335–358
6. Tarzimoghdam Z, Sandlöbes S, Pradeep KG, Raabe D (2015) Microstructure design and mechanical properties in a near- α Ti-4Mo alloy. *Acta Mater* 97:291–304
7. Rafi HK, Starr TL, Stucker BE (2013) A comparison of the tensile, fatigue, and fracture behavior of Ti-6Al-4V and 15–5 PH stainless steel parts made by selective laser melting. *Int J Adv Manuf Technol* 69:1299–1309

Lean Manufacturing and Six Sigma Principles Implementation in the Industry: Case Study



Muataz Hazza Al Hazza, Syahir Zahari, Islam Bourini,
Md Yusof Bin Ismail, Mohammad Yeakub Ali, and Erry Y. T. Adesta

Abstract Meeting customer satisfaction is significant for manufacturers to support their company's competitiveness. Different lean tools can enhance manufacturing firm's capability in the severe competence market. However, integrating lean practices with the six-sigma approach will increase productivity and reduce waste. This research aims to improve the Process Cycle Efficiency (PCE) of the pre-stressed spun concrete pole production at a Private Company. The define-measure-analyze-improve-control (DMAIC) methodology and value stream map (VSM) were used to minimize waste and improve the process. The results show that the highest waste was in work in progress (WIP) inventory. The analysis showed that the manufacturer's push system is not proper for the specific product under investigation. One of the significant outputs of the research is by suggesting using a pull system. Finally, using the Lean Six Sigma approach by DMAIC methodology positively impacts the pole's PCE. The results show a significant improvement when using the lean six sigma approach.

Keywords Lean manufacturing · Six sigma · VSM

M. H. Al Hazza (✉)

Mechanical and Industrial Engineering, American University of Ras Al Khaimah, Ras Al Khaimah, United Arab Emirates
e-mail: muataz.alhazza@aurak.ac.ae

S. Zahari · M. Y. B. Ismail

Department of Manufacturing and Materials Engineering, Faculty of Engineering, International Islamic University Malaysia, P.O. Box 10, 50728 Kuala Lumpur, Malaysia

I. Bourini

Dubai Business School, University of Dubai, Dubai, United Arab Emirates

M. Y. Ali

Mechanical Engineering Programme Area, Faculty of Engineering, Universiti Teknologi Brunei, Tungku Highway, Gadong 1410, Brunei Darussalam

E. Y. T. Adesta

Planning and Cooperation, Universitas Indo Global Mandiri, Palembang, Indonesia

1 Introduction

Inadequate design and inappropriate handling of equipment may increase bottleneck risk, longer production time, and higher total production cost [1]. Continuous process efficiency improvement becomes necessary for companies to survive in the market. Many researchers have discussed the concepts of lean, and Six Sigma has mainly added to the concepts of just-in-time (JIT) and total quality management (TQM) [2]. However, Lean and Six Sigma are two different concepts with the same objective. Both aim to minimize waste and reduce resources with maintaining the output [3]. Lean professionals believe that waste comes from unnecessary activities and does not add value but only adds cost. On the other side, six sigma professionals claim that waste is coming from the variation related to the process. However, both concepts aim to achieve less waste with minimums variation. So, there are focusing on the statistical approach in analyzing and improving the process. Recently, most companies and organizations have merged both concepts to maximize the output of implementing the techniques of lean and six Sigma techniques. Six Sigma is a concept that was originated by Motorola in the USA in the late 1980s [4]. During that time, competition in the electronics industry was very aggressive with expanding the market size. Therefore, all companies were trying to increase their market shares to survive. The six-sigma concept can define in many ways.

Munro et al. [5] said that the definition of Six Sigma could differ in four opinions: philosophy, set of tools, methodology, and metrics. From a philosophical perspective, six Sigma is a process that can be defined, measured, analyzed, improved, and controlled (DMAIC). The tools included all qualitative and quantitative tools, such as control charts, failure mode, effect analyses, and process mapping. The metrics are focused on achieving only 3.4 parts per million defects. However, the possibility of attaining 3.4 defects per million opportunities is challenging. The chance is relatively narrow because the process is rarely at the center, according to the Six Sigma philosophy. It can be a "shift" to the left or right from the nominal value [6].

Schroeder et al. [7] stressed that Six Sigma is a strategic process for improving new product and service inventions based on statistical and scientific methods. Six Sigma can be defined to be either in statistics or business terms. Statistically, Six Sigma refers to 3.4 Defects Per Million Opportunities (DPMO). In business terms, it refers to the profit improvement, waste elimination, cost reduction, and improvement of the overall operations for the customer requirements [8]. Six Sigma is a statistical method to reduce variations, defects, and waste from the products, processes, and transactions [9]. Many researchers in both industry and services tried to implement six sigma principles. Motwani et al. [10] studied a success story for implementing a six-sigma methodology to examine the factors that facilitated the success of six-sigma quality efforts at the Dow Chemicals Company. Prasanna and Vinodh [11] stated that Six Sigma required a cultural change to gain a company a competitive advantage for ensuring the customer's fullest satisfaction and profitability. Further, it required cooperation from leadership commitment, availability of the skilled workforce, sufficient

money flow, and training infrastructure. In this research, the integration of lean principles presented in the Value stream map with the six-sigma methodology to detect the waste sources in the manufacturing system.

2 Research Methodology

Collecting accurate data is the most crucial step in implementing lean six Sigma. To identify related problems by firstly considering current process mapping. The value stream map (VSM) has been implemented as one of the most effective visualization tools. All the related and vital information has collected during the visit to the case study company. The company produces varied sizes of pre-stressed spun concrete poles: 7.5, 9 and 10 m. The data was collected using observation and interviewing the production and administration team. In addition, the direct measurement for each process was conducted by the researchers—the collected data is summarized in Fig. 1.

2.1 Measure Phase

In this phase, some crucial metrics such as takt time and current Process Cycle Efficiency (PCE) have been calculated before improvement. Table 1 shows the necessary data to calculate takt time and current PCE. The table shows Working hours, hours per shift, break minutes per shift, shift per day, days per week, monthly demand, packaging, customer shipment, and supplier shipment.

The PCE for the current process to produce concrete pole is 0.25% that there is still a chance of improvement that can be made by identifying the problems through looking at the inventory part. The PCE can increase significantly by reducing the inventory used between the processes. In this case, critical inventory or inventory that invests the most to the lead time will focus. Those inventories will identify in the next stage which is analyses phase.

2.2 Analyze Phase

To identify the most critical inventories, the researchers create a Pareto diagram based on the information in Table 2 as shown in Fig. 2. The figure shows that the most critical activities that the researchers should focus on are activities: I, A and M. these activities become the most critical inventories that affect more than 80% of the total lead time. Once the inventories have known, it is time to make some improvements to inventory I, A, and M to make sure that the PCE can significantly increase.

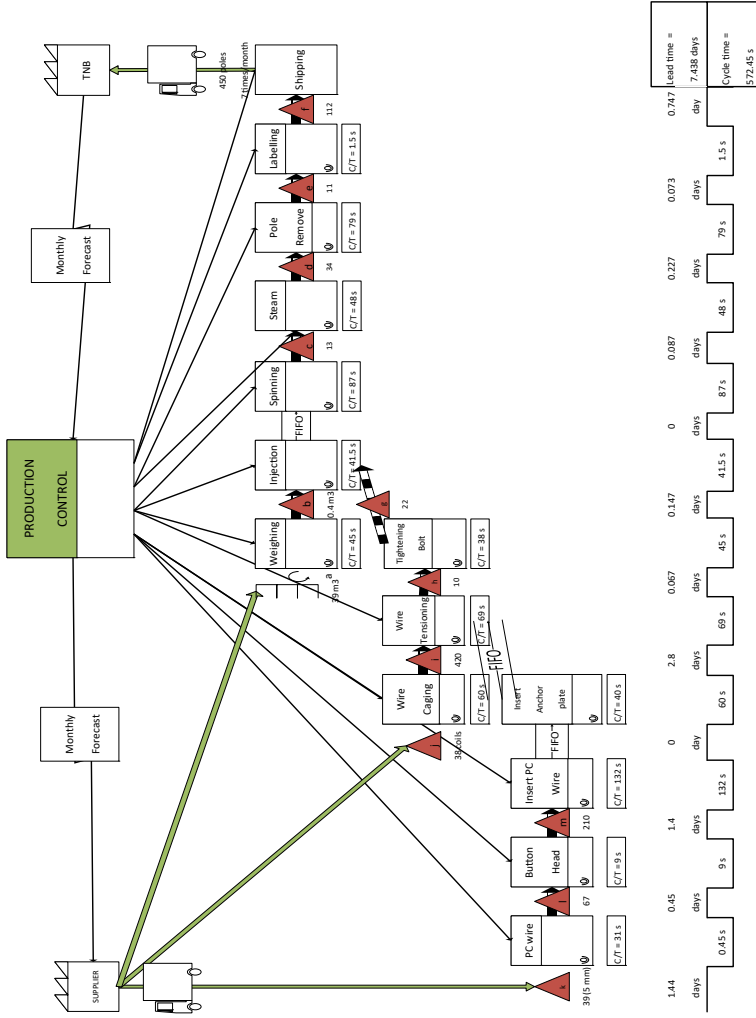
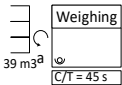
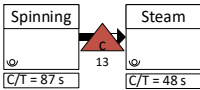
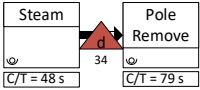
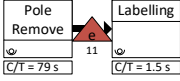
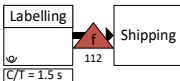
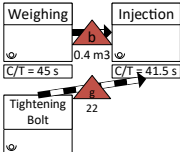
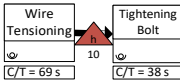


Fig. 1 Current State Value Stream Map of the manufacturing process

Table 1 Data needed to calculate Takt time and current PCE

Description	Detail	Description	Detail
Working hours	8am to 5 pm	Days per week	5 production days, 1 day machines inspection/maintenance
Hours per shift	9 h	Monthly demand	3000 units
Break (min per shift)	1 h (stop production), twice 15 min (mini break)	Supplier shipment	Once/3 days
Shift per day	1	Customer shipment	based on client (assumption: 7 times/month) (Truck)

Table 2 Time taken to hold the parts in the inventory

Process between inventory	Inventory	Time taken (Days)	Cumulative
	A	1.44	1.44
	C	0.087	1.527
	D	0.227	1.754
	E	0.073	1.827
	F	0.747	2.574
	G	0.147	2.721
	H	0.067	2.788

(continued)

Table 2 (continued)

Process between inventory	Inventory	Time taken (Days)	Cumulative
	I	2.8	5.588
	L	0.45	6.038
	M	1.4	7.438
Total waiting time = 7.438 days			

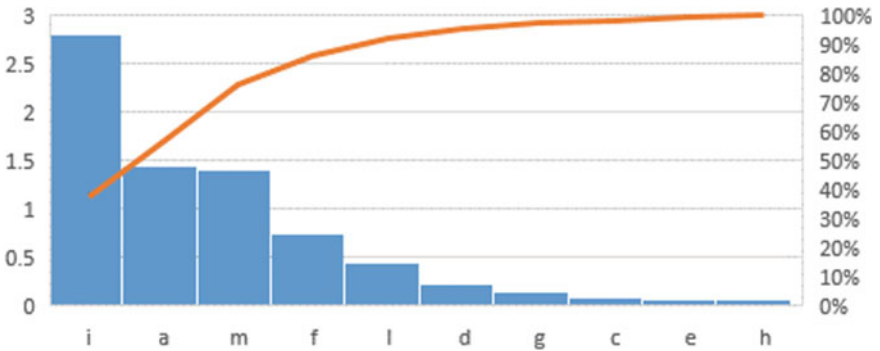


Fig. 2 Pareto diagram to identify the inventories that investing 80% of the total lead time

2.3 Improvement Phase

In this phase, the researchers propose to the company to change the inventory system. Karim and Arif-Uz-Zaman [12] said that pull system could apply to the inventory for many proposes such as Continuous Flow, One-piece flow, Sequential Flow, First-In-First-Out (FIFO), and Replenishment Flow for Supermarket. After analyzing the production line type, it found that the best is using a FIFO lane. This type of pull system can implement inventory (I) because of the long distance between two processes: Wire Caging process and Wire Tensioning Process. To utilize a FIFO lane the size or limit must be calculated:

Total Inventory time

$$= (1.15 + 0.45 + 1.15 + 0.32 + 0.067 + 0.147 + 0.087 + 0.227 + 0.073 + 0.747) \\ \times 8.5 \text{ production hours} \times 60 \text{ mins} \times 60 \text{ sec} = 135190.8 \text{ sec}$$

Total production lead time = 135190.8 sec + 572.45 sec = 35763.25 sec

$$\text{Future PCE} = \frac{572.45}{135763.25} \times 100\% = 0.42\%$$

The future state of VSM created as shown in Fig. 3.

3 Conclusion

In this paper, the integration of Lean Six Sigma has been implemented using a real case study in one of the industrial companies. The improvement of the Process Cycle Efficiency (PCE) of the pre-stressed spun concrete pole was conducted. The most challenging step is collecting accurate data through different tools: observation, interviewing the production team, and finally, using the spot measurements, Value stream map where is used as a valuable tool to present and preview the manufacturing process. The study results have been tabulated in Table 3 to summarize the improvement that has been made.

The improvements supposedly should not stop at this point. Many recommendations have given the company a continuous improvement system, such as using the Kaizen system. Finally, these recommendations show that it is general but without changing the organization's culture, without sharing the knowledge practices, and without a motivation system. All other efforts will end up failing.

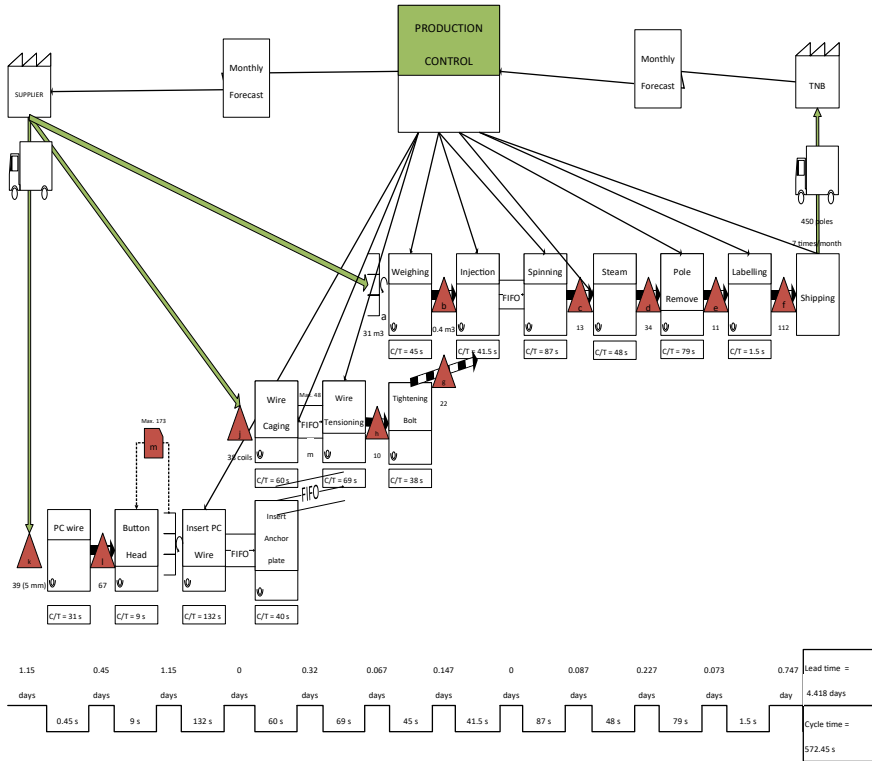


Fig. 3 Future state value stream map of manufacturing process

Table 3 Results DMAIC methodology to the real-life case study

Metric	Current state	Future state	Improvement (%)
Production lead time	224 848.8 s	135 190.8 s	39.9%
Cycle time	572.45 s	572.45 s	0%
Process cycle efficiency (PCE) (%)	0.25	0.42	68
No. of process	13	13	0%

References

1. Bourini IF, Al Hazza MHF, Taha AH (2018) Investigation of effect of machine layout on productivity and utilization level: what if simulation approach. *Int J Eng Mater Manuf* 3(1):32–40
2. Näslund D (2008) Lean, six sigma and lean sigma: fads or real process improvement methods. *Bus Process Manag J* 14(3):269–287

3. Andersson R, Eriksson H, Torstensson H (2006) Similarities and differences between TQM, six sigma and lean. *TQM Mag* 18(3):282–296
4. Nonthaleerak P, Hendry LC (2006) Six sigma: literature review and key future research areas. *Int J Six Sigma and Compet Adv* 2(2):105–161
5. Munro RA, Ramu G, Zrymiak DJ (2015) *The certified six sigma green belt handbook*. ASQ Quality Press 48(12):77
6. Besterfield DH (2013) In: *Quality improvement*. Pearson Ninth Edition
7. Schroeder RG, Linderman K, Liedtke C, Choo AS (2008) Six sigma: definition and underlying theory. *J Oper Manag* 26(4):536–554
8. Antony J, Banuelas R (2002) Key ingredients for the effective implementation of six sigma program. *Meas Bus Excell* 6(4):20–27
9. Montgomery DC, Woodall WH (2008) An overview of six sigma. *Int Stat Rev* 76(3):329–346
10. Motwani J, Kumar A, Antony J (2004) A business process change framework for examining the implementation of six sigma: a case study of Dow chemicals. *TQM Mag* 16(4):273–283
11. Prasanna M, Vinodh S (2013) Lean Six Sigma in SMEs: an exploration through literature review. *J Eng Design and Technol* 11(3):224–250
12. Karim A, Arif-Uz-Zaman K (2013) A methodology for effective implementation of lean strategies and its performance evaluation in manufacturing organizations. *Bus Process Manag J* 19(1):169–196

Study of Burrs in Milling of Marine Grade AISI 316 Stainless Steel with Minimum Quantity Lubrication



Muhammad Haziq Bin Haji Awang Jaafar, Mohammad Yeakub Ali, Maziri Bin Morsidi, S. Ramesh, Erry Yulian T. Adesta, and Seri Rahayu Ya'akub

Abstract Due to the excellent properties of AISI 316, the demand for creating a product built with this material is also growing, such as in the oil and gas sector for floating oil rigs and refinery piping. Conventionally, milling AISI 316 utilizes cutting fluids to reduce high-temperature generation linked to higher cutting speed, feed rate, and depth of cut. However, cutting fluids can impose several problems to the environment, health, and cost of production. The purpose of this study is to perform quantitative experimental research on the effectiveness of minimal quantity lubrication in milling AISI 316. This experiment used spindle speeds of 500, 1000, and 1500 rpm, feed rates of 360, 660, and 860 mm/min, depths of cut of 0.1, 0.2 and 0.4 mm, and flow rates of 100 and 200 ml/h for minimum quantity lubrication (MQL). The formation of burr height is considered the investigation's response. The burr height was measured using a surface profilometer, and the optimum condition for achieving the lowest burr height were 500 rpm, 360 mm/min, 0.1 mm, and flood conditions for spindle speed, feed rate, depth of cut, and flow rate, respectively, with a value of 43.429 μm .

Keywords Milling · Minimum quantity lubrication · Taguchi orthogonal array

1 Introduction

Marine-grade AISI 316 stainless steel contains elements including molybdenum and nickel, producing excellent properties such as corrosion resistance, high toughness, and weldability. Due to their excellent properties, there are many applications of AISI 316 stainless steel in various industries, including the pharmaceutical industry and the oil and gas industry. A comparative investigation of the corrosion behavior of AISI 316 stainless steel and pure Titanium in a sulfuric acid solution done by Wang

M. H. B. H. A. Jaafar · M. Y. Ali (✉) · M. B. Morsidi · S. Ramesh · S. R. Ya'akub
Universiti Teknologi Brunei, Tungku Highway, Gadong BE1410, Brunei Darussalam
e-mail: yeakub.ali@utb.edu.bn

E. Y. T. Adesta
Universitas Indo Global Mandiri, Jl. Jendral Sudirman, Palembang 30129, Indonesia

et al. [1] is one example of the excellent corrosion resistance qualities of AISI 316 stainless steel.

There are three main parameters in milling: cutting speed, feed rate, and depth of cut. Identifying the outcome of the machining process (e.g., minimal burr height) is a critical factor in selecting the condition of the parameters. The present studies in [2] and [3] show that varying the parameters changed the outcome burr heights. Other aspects that influence the machining output include the product's material, the geometrical shape of the cutting tool, and the lubrication/coolant system.

MQL employs less cutting fluid during milling to alleviate this issue. MQL's rapid evaporation rate allows for faster workpiece cooling. Using less cutting fluid saves money on lubrication [4]. Yuan et al. [5] utilized MQL in their experimental investigation using several types of vegetable oil-based lubricants.

During machining, excess materials may not be removed entirely from the surface. The most common is the formation of burr. This is due to the effect of plastic deformation of the material, which often forms at the edge of the workpiece adjacent to the machined area. Burrs on a workpiece can reduce the fit and ease of assembly, damage dimensional accuracy and surface finish, increase production costs and time, risk worker and consumer safety, cause electrical short circuits, reduce cutting performance and tool life, and deteriorate aesthetics [6].

One way to prevent the undesirable effect of burr formation is by effectively designing the process parameters. This can be achieved by employing Taguchi's technique. The technique utilizes the design of the orthogonal array in the experiment to analyze the entire parameter space with a minimum number of experiments only. In addition, Taguchi also recommended analyzing the response using the signal-to-noise ratio derived from the quadratic loss function [7]. Hassan et al. [8] used the Taguchi approach to determine the ideal surface roughness for glass fiber reinforced plastic (GFRP) milling. This method identified the best spindle speed and feed rate to improve surface roughness by 90.3%. Machining or micromachining with environmentally friendly MQL and significant improvement in surface quality were reported by many researchers [9–11].

In this study, milling parameters, including spindle speed, feed rate, depth of cut, and flow rate of MQL, are considered during the milling of AISI 316 stainless steel. Burr height is formed as a result of the response. The goal of using Taguchi's technique is to identify the minimal parameters that result in the smallest burr height.

2 Materials and Methods

2.1 Workpieces and Milling Parameters

A square plate of AISI 316 stainless steel of $100 \times 100 \times 10$ mm dimension is used in this investigation. Five experiments were conducted on each side of the plate.

Table 1 The orthogonal array positioning of the milling parameters

No	Coded values				Real values			
	A	B	C	D	n [rpm]	f [mm/min]	A _p [mm]	Q [mL/h]
1	1	1	1	1	500	360	0.1	1000
2	1	2	2	2	500	660	0.2	2000
3	1	3	3	3	500	860	0.4	Flood
4	2	1	2	3	1000	360	0.2	Flood
5	2	2	3	1	1000	660	0.4	1000
6	2	3	1	2	1000	860	0.1	2000
7	3	1	3	2	1500	360	0.4	2000
8	3	2	1	3	1500	660	0.1	Flood
9	3	3	2	1	1500	860	0.2	1000

Table 1 depicts the milling parameters sequence according to Taguchi's orthogonal array design, generated using Minitab 18 software.

2.2 Milling and Measurement of Burr Height

Slot milling was performed on the workpiece according to the conditions set in Table 1. The cutting tool material selected for the investigation was the high-speed steel with a diameter of 5 mm, and the selected cutting fluid was the ACCU-LUBE LB-3000, a vegetable oil-based cutting fluid supplied under an external MQL system.

The MarSurf GD 25 burr height measurement came last. The maximum profile peak height was used to calculate burr height ($R_{p_{max}}$). $R_{p_{max}}$ was calculated mechanically. The stylus was passed through both edges of the slot in each trial, and three measurements (front, middle, and back) were taken to calculate the average burr height.

3 Results and Discussion

3.1 Recorded Data for Burr Height

The average burr height is shown in Table 2. At 500 rpm, 360 mm/min, 0.1 depth of cut, and 1000 mL/h, the lowest burr height of 43.43 μm was achieved. At 1500 rpm, 860 mm/min, 0.2 mm depth of cut, and 1000 mL/h flow rate, the maximum burr of 213.7 μm height was measured. According to this study, the lowest level of each parameter results in the lowest burr height. 500 rpm spindle speed, 360 $\mu\text{m}/\text{min}$

Table 2 Experimental parameters and measured mean burr height

No	n [rpm]	f [$\mu\text{m}/\text{min}$]	A_p [mm]	Q [mL/h]	Mean burr height [μm]
1	500	360	0.1	1000	43.429
2	500	660	0.2	2000	169.929
3	500	860	0.4	Flood	161.032
4	1000	360	0.2	Flood	113.389
5	1000	660	0.4	1000	204.129
6	1000	860	0.1	2000	71.511
7	1500	360	0.4	2000	187.897
8	1500	660	0.1	Flood	81.525
9	1500	860	0.2	1000	213.737

feed rate, 0.1 mm depth of cut, and flood flow rate offer the minimum burr height 43.43 μm .

3.2 Signal-to-Noise Ratio Analysis

As the objective is to achieve minimum burr height, the criteria selected from Taguchi's quality characteristic is the smaller-the-better. This criterion is used to calculate the signal-to-noise ratio for each experiment. In principle, parameters with the highest signal-to-noise ratio show the best quality with the least variation (optimal value). The governing equation is shown in Eq. (1) where y_i is the data obtained from experiments and n represents the number of experiments conducted.

$$\eta = -10 \log \left[\frac{1}{n} \sum_{i=1}^n y_i^2 \right] \quad (1)$$

Table 3 represents the mean response table resulting from the smaller-the-better criteria calculation. According to Table 3, the depth of cut ranked first, depicting that it plays a significant role in influencing the burr height. On the contrary, the flow rate ranked last. Figure 1 is the graph of signal-to-noise ratio for burr height. According to Table 3, the optimal conditions to obtain minimum burr height are 500 rpm spindle speed, 360 $\mu\text{m}/\text{min}$ feed rate, 0.1 mm depth of cut and flood cooling.

3.3 Analysis of Variance (ANOVA)

By assessing the relative value of the milling parameters concerning burr height, ANOVA was used to discover the best combination of milling variables. The Minitab

Table 3 Mean response table for burr height

Parameter	Mean S/N ratio [dB]			Delta	Rank
	Level 1	Level 2	Level 3		
<i>n</i>	-40.50*	-41.46	-43.43	2.93	3
<i>f</i>	-39.78*	-43.01	-42.61	3.23	2
<i>A_p</i>	-36.02*	-44.10	-45.27	9.25	1
<i>Q</i>	-41.85	-42.39	-41.15*	1.24	4

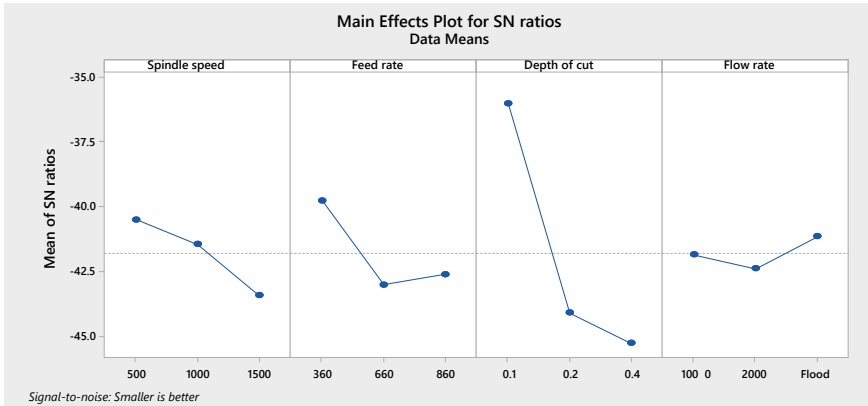


Fig. 1 S/N graph for burr height

18 software was used to conduct the analysis, with a 95% confidence level. The percentage contribution was determined by dividing the parameter’s sum of squares by the overall sum of squares. From Table 4, the highest contribution was from the depth of cut with 81.6%, followed by feed rate (10.0%), spindle speed (7.20%), and flow rate (1.24%). A similar trend can be observed in the response table of signal-to-noise ratio in Table 3.

Table 4 ANOVA for burr height

Source	DF	Seq SS	Adj SS	Adj MS	% Contribution
<i>n</i>	2	13.430	13.430	6.7150	7.20
<i>f</i>	2	18.648	18.648	9.3240	10.0
<i>A_p</i>	2	152.121	152.121	76.0603	81.6
<i>Q</i>	2	2.314	2.314	1.1569	1.24
Total	8	186.512	–	–	–

4 Conclusion

In this research marine grade AISI 316 stainless steel plates were machined using various combination of milling parameters. All the experiments were designed based on Taguchi method to minimize the burr heights. The depth of cut was found to be the most influential for producing burrs of different heights and shapes. The optimal milling conditions to obtain minimum burr height of 43.43 μm are found to be 500 rpm spindle speed, 360 $\mu\text{m}/\text{min}$ feed rate, 0.1 mm depth of cut and flood cooling conditions.

References

1. Wang Z, Hu H, Zheng Y (2018) Synergistic effects of fluoride and chloride on general corrosion behavior of AISI 316 stainless steel and pure titanium in H_2SO_4 solutions. *Corros Sci* 130:203–217
2. Adeniji D, Schoop J, Gunawardena S, Hanson C, Jahan M (2020) Characterization and modeling of surface roughness and burr formation in slot milling of polycarbonate. *J Manuf Mater Process* 4(2):59
3. Hajiahmadi S (2019) Burr size investigation in micro milling of stainless steel 316L. *Int J Lightweight Mater Manuf* 2(4):296–304
4. Sen B, Mia M, Krolczyk GM, Mandal UK, Mondal SP (2021) Eco-friendly cutting fluids in minimum quantity lubrication assisted machining: a review on the perception of sustainable manufacturing. *Int J Precision Eng Manuf-Green Technol* 8:249–280
5. Yuan S, Hou X, Wang L, Chen B (2018) Experimental investigation on the compatibility of nanoparticles with vegetable oils for nanofluid minimum quantity lubrication machining. *Tribol Lett* 66:106
6. Chern GL (2006) Experimental observation and analysis of burr formation mechanisms in face milling of aluminum alloys. *Int J Mach Tools Manuf* 46:1517–1525
7. Kilickap E (2010) Modeling and optimization of burr height in drilling of Al-7075 using Taguchi method and response surface methodology. *Int J Adv Manuf Technol* 49:911–923
8. Hassan SMFBS, Shafei SB, Rashid RBA (2020) Optimization of machining parameters in milling process for high speed machining using Taguchi method for best surface roughness. In: IOP conference series: materials science and engineering, vol 864. pp 012110
9. Mohamad NB, Bahar R (2016) Minimum quantity lubrication (MQL) and its effect on tool wear during miniature drilling : an experimental study. *Int J Eng Mater Manuf* 1(2):65–70
10. Patil A, Raval J, Bangma T, Edinbarough I, Tai B, Stephenseon D, Suleiman O, Hung WN (2020) Characterization and performance of minimum quantity lubricants in through-tool drilling. *Int J Eng Mater Manuf* 5(4):98–115
11. Hossain S, Abedin MZ (2021) Effect of minimum quantity lubrication system for improving surface roughness in turning operation. *Int J Eng Mater Manuf* 6(1):50–59

Friction Welding of Similar and Dissimilar Materials: Analysis of Tensile Strength



Ak. Md. Asyraf Aditya, Mohammad Yeakub Ali, S. Ramesh, Ahmad Shamil Abd Rahman, and Muataz Al Hazza

Abstract Friction welding is a solid-state process where two similar or dissimilar materials are joined due to mechanical friction and lateral force. Friction welding such as friction force, friction duration, and upset force play significant role differently for different materials and eventually determine the weld strength. Finding optimal parameters is of main concern for many researchers in the field. The purpose of this research is to determine the most effective process parameters and to establish empirical relationships among them. Experiments were conducted to join three pairs of materials namely stainless steel-stainless steel, mild steel-mild steel, and stainless steel- mild steel. Then tensile strength was measured for all friction welded pairs. These experimental studies showed that rotational speeds are the most important parameter and mild steel-mild steel friction welding is having highest tensile strength of 343 MPa compared to other samples. In addition, use of lathe machine for the purpose of friction welding is found to be effective for laboratory based experimental studies.

Keywords Friction welding · Mild steel · Stainless steel · Tensile strength

1 Introduction

Friction welding is a type of joining process that uses no external heat to generate effective weld connections between two components with chemical compositions that are either equivalent or different [1]. One of the friction components is usually stationary while the other is spinning in most circumstances. To make a weld, external pressure is applied to a solid state. The workpieces to be bonded rotate relative to one another in friction welding. By warming the materials at the contact points, this

Ak. Md. A. Aditya · M. Y. Ali (✉) · S. Ramesh · A. S. A. Rahman
Mechanical Engineering Programme Area, Universiti Teknologi Brunei, Tungku Highway,
Gadong BE1410, Brunei Darussalam
e-mail: yeakub.ali@utb.edu.bn

M. Al Hazza
Mechanical and Industrial Engineering Department, American University of Ras Al Khaimah,
PO Box 10021, Ras Al Khaimah, UAE

© The Author(s), under exclusive license to Springer Nature Singapore Pte Ltd. 2023
Md. A. Maleque et al. (eds.), *Proceeding of 5th International Conference on Advances in Manufacturing and Materials Engineering*, Lecture Notes in Mechanical Engineering,
https://doi.org/10.1007/978-981-19-9509-5_46

343

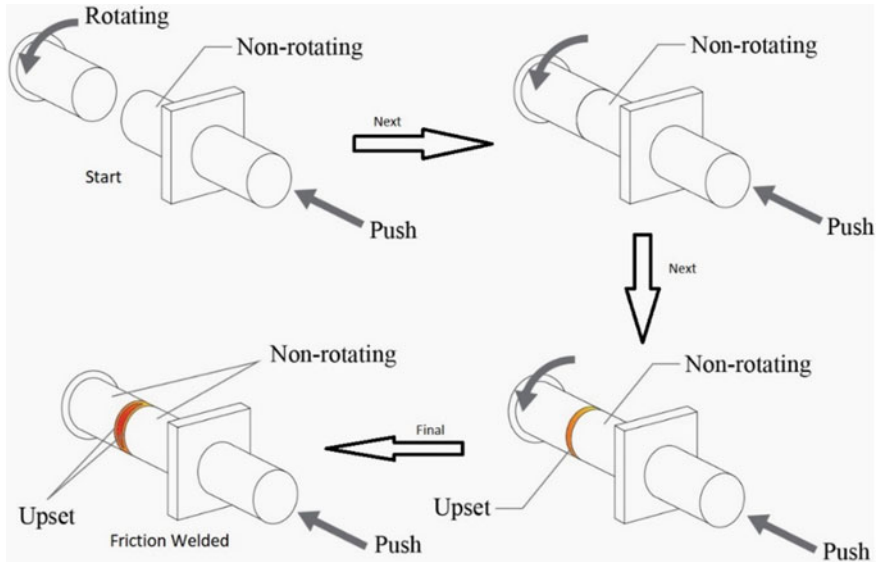


Fig. 1 Friction welding working principle

process generates friction. Up to the end of the welding cycle, a high-pressure force is employed. Metal bars and tubes with diameters more than 100 mm can be joined by friction welding (such as steel and aluminium) [2]. Figure 1 shows how the friction welding theory is put into practice.

Even though there are several varieties of friction welding, they all operate on a similar, if not identical, premise. The first step is to place one workpiece in a rotor-driven chuck while the other remains motionless. The rotor enables high-speed rotation of the linked workpiece [3]. The stationary workpiece is pressed into contact with the revolving workpiece by a pressure force. When two workpieces meet, a large amount of friction is formed, which creates a lot of heat on the surfaces in contact, softening the two materials (plasticizing) [4]. After the materials have reached a plasticized condition, the static piece is subjected to increased forging pressure, causing the two components to join. After the components have fused together and the interface has begun to cool, the rotor will stop, and the materials have resolidified [5]. The forging pressure is maintained for a few seconds before being released, thereby completing the weld. Figure 2 depicts the setup for the friction welding principle stated earlier.

Dissimilar welding is a welding process for combining materials of differing alloys. A welder must evaluate several factors before deciding on the best welding process and equipment for combining two dissimilar materials. Even if dissimilar metals include alloys of the same metal, the properties of these metals are determined by their composition [6]. A welder must consider a variety of issues while developing a welding project with dissimilar metals, including physical and chemical qualities. The four different types of friction welding are inertia friction welding, direct drive

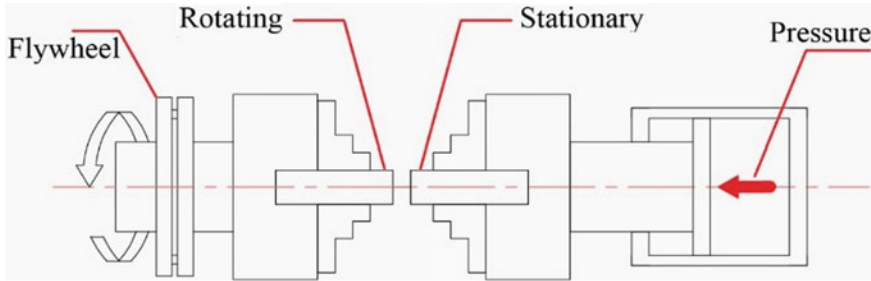


Fig. 2 Setup for friction welding experiment

friction welding, linear friction welding, friction stir welding, orbital friction welding [7]. The objectives of these projects are:

1. To optimize process parameters and to develop empirical relationships of friction welding parameters.
2. To carry out a comparative study for pair of similar and dissimilar materials.
3. To find the effects of friction welding input parameters such as friction force, friction time and upset force role on the tensile strength of the weld.

2 Friction Welding of Similar and Dissimilar Materials

Friction-welding between AISI 304 and AA6082 aluminium alloys has been investigated [8]. For the AISI 304, step cut bars with a length of 100 mm, an exterior diameter of 18 mm, and an inner extruded part diameter of 14 mm were used. For the AA 6082, step cut bars with a length of 100 mm, an outside diameter of 17 mm, and an inner extruded part diameter of 15 mm were used. During this experiment, the spinning speed, upset time, and upset pressure were held constant, while friction time and friction pressure were adjusted. The exterior piece was found to be properly bonded, but not the centre. This is because the temperature in the outer zone was higher than in the inner zone during the friction stage. When the friction time and friction pressure were increased, the strength of the friction-welded joints increased [9]. As an example, friction pressure 104 MPa, friction time 5 s, forging pressure 210 MPa, forging time 6 s, and rotational speed 1400 rpm are found to be appropriate for welding (Table 1).

3 Materials and Methods

A conventional lathe machine used is used to friction fuse a pair of similar or dissimilar steels, two metals together. The setup is completed by mounting one specimen to the chuck and the second work item to the drill chuck. In this position, the chuck is

Table 1 Results of the tensile strength

Trials	Friction pressure (MPa)	Friction time (s)	Upset pressure (MPa)	Upset time (s)	Tensile strength
1	65	3	210	6	136.43
2	104	5	210	6	188.40
3	156	7	210	6	149.60

spun while the other work piece on the drill chuck stays stationary [9]. The two independent components to be welded are placed in the drill chuck and the lathe chuck, both of which are attached to the lathe machine. The work piece spins in tandem with the chuck, which rotates at varying revolutions per minute. The work piece in the drill chuck is pressed against the fast-revolving work piece. The temperature rises as a result of the friction. As the temperature rises, a red-hot zone develops, as seen in Fig. 3. Reverse braking is used at this point to achieve a flawless weld. If there is no efficient braking system, no proper weld can be formed.

All the samples are being tested at various rpms to check if the chosen materials can be friction welded and if the alternative method of friction welding works. An experiment was conducted using various combinations of materials to see if the combinations were successful. After evaluating reported scientific articles, it has been determined that only three combinations are suitable for this experiment: stainless-stainless, mild-mild, and mild-stainless. This simple experimental set up based on lathe machine is very useful for student learning towards quality education for engineering accreditation [13].

**Fig. 3** Red-hot zone as the melting point reached while rotating

4 Results and Discussions

Only few combinations of elements with high melting points that were observed to be effective for friction welding. Figure 4 shows two stainless steel rods that were successfully friction welded at 1400 rpm. This experiment took 47.13 s to complete, as stated in Table 2 in the outcome discussions. This is one of several instances of workpieces that have been friction welded successfully at various spindle speeds. The workpieces from the other two combinations that have been successfully welded together are shown in Figs. 5 and 6. The length of time it takes for the two specimens to be welded together from the moment their surfaces come into contact is known as friction time. Table 2 displays the friction time for all material combinations at various speeds.

Table 2 demonstrates that the faster the rotations rotate, the shorter the friction time. Furthermore, among the other combinations, mild steel and mild steel is the combination that takes the longest to friction. Because mild steel has a slightly greater melting point than stainless steel, this is the case. As a result, friction welding a stainless–stainless combination will take less time.

Stress–strain relationships for various welded combinations are presented in Figs. 7, 8 and 9. In terms of the strain and stress diagram, as the rotational speed rises, the tensile strength increases as well. This applies to all combinations of materials, not just one. For a spindle speed of 2000 rpm, the mild–mild combination has the maximum tensile strength, with up to 340 MPa tensile stress and 160,000% tensile strain before breaking point. The tensile strength in Table 3 were obtained using Eq. (1) from the data given during the tensile test of all the specimens.

$$\text{Tensile strength} = \frac{\text{Force required to break}}{\text{Cross section area}} \quad (1)$$



Fig. 4 Successfully friction welded stainless–stainless specimen

Table 2 Friction time for every material combination in different rpm

Speed (RPM)	Friction time (s)		
	Stainless–Stainless	Stainless–Mild	Mild–Mild
725	199.84	205.14	212.66
1050	62.20	68.73	75.32
1400	47.13	59.50	67.09
2000	38.48	43.14	58.89



Fig. 5 Successfully friction welded of mild-mild specimen



Fig. 6 Successfully friction welded of mild-stainless steel specimen

Fig. 7 Stress-strain for mild-stainless

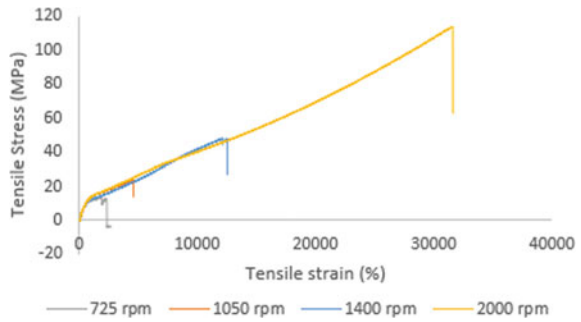
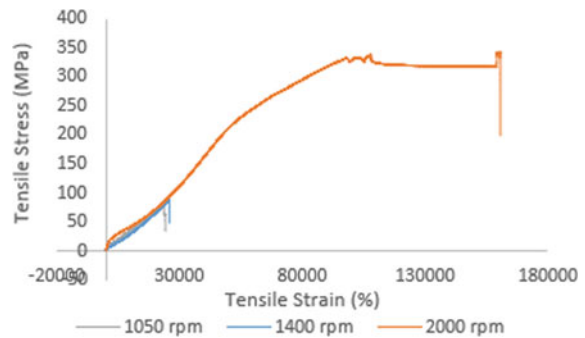


Fig. 8 Stress-strain for mild-mild



5 Conclusions

In this research similar and dissimilar materials are friction welded using lathe machine based experimental setup. The welded joints were investigated based on

Fig. 9 Stress–strain graph for stainless–stainless

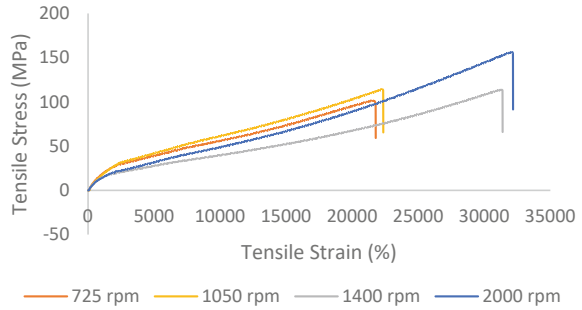


Table 3 Tensile strength for every specimen tested in different speed

Tensile strength (MPa)			
Speed (RPM)	MS-SS	MS–MS	SS-SS
725	14.15	–	101.68
1050	23.87	80.46	114.06
1400	47.75	87.54	114.06
2000	114.06	343.07	156.50

tensile strength. This research showed that rotational speeds are the most important parameter impacting tensile strength. Rotational speed was found to be proportional to tensile strength up to the maximum speed 2000 rpm used in this research. When compared to other materials, mild steel–mild steel friction welding has the highest tensile strength 343 MPa. Use of lathe machine for the purpose of friction welding is found to be effective only for laboratory based experimental studies.

References

- Sathiya P, Aravindan S, Haq AN, Paneerselvam K (2009) Optimization of friction welding parameters using evolutionary computational techniques. *J Mater Process Technol* 209(5):2576–2584
- Dey AK (2022) What is friction welding? Principle and types of friction welding–what is piping, *Whatispiping.com*, <https://whatispiping.com/friction-welding>. Last Accessed 20 May 2022
- Akiyama T, Honda T, Nakanishi Y (2016) Friction welding of lightweight motor shafts for electric vehicles. In: 5th international conference renewable energy applications, vol 5. pp 259–264
- Ramesh P, Subramaniyan M, Eswaran P (2019) Review on friction welding of similar/dissimilar metals. *J Phys Conf Ser* 1362(1):012032
- Hattingh DG, Wielligh LV, Thomas W, James MN (2019) Friction processing as an alternative joining technology for the nuclear industry. *J S Afr Inst Min Metall* 115(10):903–912
- Chaudhari R, Loharkar PK, Ingle A (2020) Applications and challenges of arc welding methods in dissimilar metal joining. In: IOP conference series: material science engineering, vol 810, pp 012006

7. Friction Welding (2022). <https://www.mech4study.com/2017/04/friction-welding-principle-working-types-application-advantages-and-disadvantages.html>. Last Accessed 31 May 2022
8. Rn S, Surendran S (2012) Friction welding to join dissimilar metals. *Int J Emerg Technol Adv Eng* 2(7):200–210
9. Lohan A (2013) Friction welding on lathe machine with special fixture. 2(3):258–261
10. Mohamad HA, Islam S, Khandoker N, Mazid AMM (2021) Shear and hardness properties study of AA-6061 aluminium alloy lap-joints produced by friction stir spot welding process using H13 tool steel. *Int J Eng Mater Manuf* 6(3):187–194
11. Kothari M, Hung WN (2018) suppressing aluminum carbide in welding aluminum silicon carbide composite. *Int J Eng Mater Manuf* 3(1):41–54
12. Ahmed YM, Lafta HD, Rahman AAA, Salih BT (2020) Experimental study of the performance of base metal and welding line of the household LPG cylinder manufactured in Kurdistan region. *Int J Eng Mater Manuf* 4(3):116–123
13. Ali MY, Ya'akub SR, Singh R (2021) Quality assurance in engineering education: accreditation and its global influence. In: *Proceedings 11th annual international conference on industrial engineering and operations management*, Singapore, pp 7503–7510

Performance of Graphite Based Nanofluid in MQL Grinding of Mild Steel



M. R. Hasmizuan Rais, Mohammad Yeakub Ali, S. Ramesh, Seri Rahayu Ya'akub, and Zunaidi Ibrahim

Abstract Grinding of any metallic materials are usually done under flood cooling using cutting fluid. However, excessive use of cutting fluid is not environmentally friendly. Researchers in the field are always looking for efficient as well as environmentally friendly grinding process for sustainable development. Minimum quantity lubrication with nanofluid is found to be one of the ways out. The main objective of this research is to identify the competitive effectiveness of MQL grinding over dry and flood cooling grinding. Graphite nanoparticles created from 2B pencil leads were mixed with ACCU-LUBE LB-3000 cutting fluid to prepare the nanofluid. Taguchi L9 Orthogonal Array was used to design the experiments. There were total of nine experiments, where three experiments were conducted under each of dry, flood-cooling and MQL with graphite-oil-based nanofluid conditions. Surface roughness and signal-to-noise ratios were analyzed. It was found that the condition during grinding is the largest contributor to surface roughness, contributing 54.82% of total, while depth of cut contributes 42.43% to the grinding process. Furthermore, grinding with MQL with graphite-oil-based nanofluid gives the lowest surface roughness value. After analyzing the S/N ratio and ANOVA, the optimum grinding condition is found to be MQL with graphite-oil-based nanofluid and 40 μm depth of cut.

Keywords Grinding · MQL · Nanofluid · Surface Roughness

1 Introduction

Grinding is a finishing procedure that is universally utilized when accuracy, fine surface finishes, and close dimensional tolerances are required. Cooling and lubrication are vital in producing superior surface finishes while minimizing the negative impacts on the grinding wheel and workpieces. This also minimizes the likelihood of a grinding wheel crack because of thermal distortion, unacceptable residual tensile stress, and unfavorable phase change [1, 2]. Minimum Quantity Lubrication (MQL)

M. R. H. Rais · M. Y. Ali (✉) · S. Ramesh · S. R. Ya'akub · Z. Ibrahim
Mechanical Engineering Programme Area, Faculty of Engineering, Universiti Teknologi Brunei,
Tungku Highway, Gadong BE1410, Brunei Darussalam
e-mail: yeakub.ali@utb.edu.bn

has been widely employed in the machining industry due to its long-term lubrication usage while also preserving the condition of the cutting tools and workpiece [3]. To provide high-pressure air, the MQL system employs a compressor. The fluid chamber is connected to a small-diameter flexible tube. This tube is intended to pass via a roller flow controller, which permits a very small amount of fluid to flow at high pressure and velocity. The pressure created by compressed air entering the entrance port causes the fluid to flow continuously and steadily to the mixing chamber via the controller. The air and cutting fluid were then mixed in the mixing chamber, resulting in a high-velocity mixture of cutting fluid and air infringing on the tool-work piece interface via the nozzle [4, 5]. Nanofluids are prepared by dispersing nanometer-sized materials in base fluids to increase its influence the heat transfer and pressure drop performance potentials. It also can be defined as heat transfer fluids with improved heat transfer properties such as thermal conductivity, viscosity, thermal diffusivity, and heat transfer coefficients by the addition of nanoparticles [6]. Many types of nanoparticles, such as metallic nanoparticles and metallic oxide, have been studied in recent years. Nanofluids have been prepared using two different approaches. One-step approach is the first technique that manufactured utilizing mechanical, biological, chemical, and chemical processes in the one-step technique [7]. The second approach for creating nanofluid is a two-step process. In general, this method consists of two procedures. The first step is to create a nanomaterial, normally a dry powder. Secondly dispersing nanoparticles in a base liquid like water, ethanol, or ethylene glycol through direct mixing. Some procedures, such as the addition of dispersant or sonication, are typically performed to improve the stability of [8]. Cutting fluids contribute to the production of fine surface roughness by reducing friction and heat generation. As a result, nanofluids can be used to substitute cutting fluids in order to increase product quality and reduce surface roughness. Multi wall carbon nanotube (MWCNT) nanoparticles, according to Sharma et al. [9], act as a layer that reduces heat generation. Nanofluids also help improve surface roughness quality by decreasing coefficient friction, which leads to a decrease in cutting temperature and grinding forces [10–13]. When oil-based fluids are used for base fluids, the surface roughness and thermal conductivity is reduced more than when water-based fluids are utilized [14–17]. Aside from that, oil-based fluids such as sunflower oil and rice bran oil are found to be environmentally safe and cost effective due to their biodegradability [14]. Machining or micromachining with environmentally friendly MQL and significant improvement in surface quality were reported by many researchers [18–20].

2 Methodology

Mild steel workpiece of 170 mm long and 25 mm diameter was ground under dry, flood cooling with nanofluid and MQL with same nano fluid. Lead pencils of 2B P7700 grade was used to produce nanoparticles [21] which were mixed with ACCU-LUBE LB-3000 base cutting fluid for the preparation of nanofluid. The mixing

Table 1 Outlines of the experiment

Run	Condition	Depth of cut (μm)
1	Dry	40
2	Dry	60
3	Dry	80
4	Flood-Cooling	40
5	Flood-Cooling	60
6	Flood-Cooling	80
7	MQL with graphite-oil-based-nanofluid	40
8	MQL with graphite-oil-based-nanofluid	60
9	MQL with graphite-oil-based-nanofluid	80

process was enhanced with magnetic stirrer and whole process took approximately 40 min.

During the grinding process, two parameters were used which are depth of cut with values of 40, 60 and 80 μm , and grinding conditions with dry, flood-cooling, and MQL with graphite oil-based nanofluid. Throughout the experiment, the grinding wheel speed, feed rate, and spindle head speed remain constant at 112 rpm, 0.05 mm/rev, and 56 rpm, respectively. Based on the parameters set and organized using Taguchi Orthogonal L9 Array, nine grinding experiments were done as shown in Table 1. The experiments were performed while grinding in dry conditions with depths of cut of 40, 60 and 80 μm . The same set of depths of cut was utilized for grinding under flood-cooling and MQL with graphite-oil-based nanofluid.

3 Results and Discussion

3.1 Surface Roughness R_a Values

The R_a surface roughness of the ground surface was measured using Marsurf GD25 (Mahr, Germany) and listed as shown in Table 2. Referring to Table 1, the smallest R_a is 0.1645 μm when grinding during MQL with graphite-oil-based nanofluid with the depth of cut of 40 μm . The highest R_a is 1.2349 μm when grinding under dry conditions with a depth of cut of 80 μm . Based on the results shown in Table 2, using MQL with nanofluid produces better surface roughness compared to dry and flood-cooling. The nanofluid in this case, graphite-oil-based nanofluid help mitigates the heat produced from the sample and the grinding wheel during the grinding operation. The results obtained are similar as other researchers where surface roughness is significantly low when grinding using MQL with nanofluid [11, 12, 14]. However,

Table 2 Surface roughness Ra values from grinding operation

Run	Condition	Depth of cut (μm)	R_a (μm)
1	Dry	40	0.4470
2	Dry	60	0.7349
3	Dry	80	1.2439
4	Flood-cooling	40	0.3868
5	Flood-cooling	60	0.6799
6	Flood-cooling	80	0.7096
7	MQL with graphite-oil-based nanofluid	40	0.1645
8	MQL with graphite-oil-based nanofluid	60	0.3772
9	MQL with graphite-oil-based nanofluid	80	0.3790

grinding under dry conditions lead to the highest surface roughness. The reason for this may be due to poor heat dissipation during the grinding operation. This eventually leads to increase in cutting temperature and causes abrasive grains to accumulate on the sample.

3.2 *S/N Ratio and Mean S/N Ratio*

The experiment was performed using the Taguchi method. Hence, it has been possible to reach more comprehensive results with fewer experiments. The ‘less is more’ principle is applied. The term “signal” and “noise” indicate desirable and undesirable values. The *S/N* ratio is calculated using the formula [22].

$$SN = -10 \times \log \left[\frac{1}{n} \sum_i^n y_i^2 \right] \quad (1)$$

where *n* is the number of experiments and *y* represents the calculated characteristics.

Smaller *R_a* values indicate a better surface quality. Thus, a smaller-the-better quality characteristic is implemented. Minitab 18 software is used to determine the *S/N* ratio. As shown in Table 3, the highest *S/N* ratio is 15.6767 dB, that is when grinding with the depth of cut of 40 μm under MQL with graphite-oil-based nanofluid. While the lowest *S/N* ratio is -1.8597 dB for depth of cut of 80 μm under dry conditions. The optimum condition is when the grinding using MQL with graphite-oil-based nanofluid and the depth of cut is 40 μm . This is indicated through the highest *S/N* ratio.

The mean response values for *S/N* ratio were calculated by grouping the mean responses for each parameter for each factor level for each column in the OA, then the total value was taken as an average. Minitab 18 software then simulated the given data and produce mean results for each parameter on each level. The condition

Table 3 S/N ratio for grinding operation

Run	Condition	Depth of cut (μm)	S/N ratio (dB)
1	Dry	40	6.9938
2	Dry	60	2.6754
3	Dry	80	-1.8957
4	Flood-Cooling	40	8.2503
5	Flood-Cooling	60	3.3511
6	Flood-Cooling	80	2.9797
7	MQL with graphite-oil-based nanofluid	40	15.6767
8	MQL with graphite-oil-based nanofluid	60	8.6845
9	MQL with graphite-oil-based nanofluid	80	8.4272

during grinding operation affects the surface roughness value, Ra the most with the mean S/N ratio of 10.896 dB compared to the depth of cut, 10.307 dB. From the investigation, it was observed that the optimum grinding operation was found to be MQL with graphite-oil-based nanofluid and depth of cut 40 μm . These combinations mentioned provided the best surface roughness.

4 Analysis of Variance (ANOVA) for Taguchi Method

Minitab 18 software was used to obtain the analysis of variance for surface roughness. Table 4 shows the result of the analysis of variance for surface roughness (Ra) for the Taguchi method for grinding operation. The condition during grinding operation is the parameter that affects the surface roughness the most, with a percentage of 54.82% compared to the depth of cut, where the percentage contributed is 41.34%.

Table 4 Analysis of variance (ANOVA) for surface roughness (Ra) for Taguchi method for grinding operation

Parameters	DOF	F-value	p-value	Sum of squares	% Contribution
Condition	2	28.55	0.004287	110.551	54.82
Depth of cut	2	21.53	0.007225	83.376	41.34
Residual	4	-	-	7.746	3.84
Total	8	-	-	201.673	100

4.1 Confirmation Test

The predicted S/N ratio using the optimal level of the precision grinding parameters can be calculated using the equation [23].

$$\text{Predicted } \frac{S}{N} \text{ ratio} = \varepsilon_m + \sum_{i=1}^n (\varepsilon_o - \varepsilon_m) \quad (2)$$

Here ε_m is the total mean S/N ratio, ε_o is the mean S/N ratio at an optimal level and n is the number of parameters. The S/N ratio can then be converted into Ra using the Eq. 1, finding y through the S/N ratio obtained. The optimum conditions to achieve optimum surface roughness is when grinding using MQL with graphite-oil-based nanofluid with the depth of cut of 40 μm . The predicted S/N ratio of 15.087 dB is then transformed to Ra using Eq. 1 to Ra of 0.158 μm . From Table 2, the value of Ra under optimum level is 0.165. This means that there is a difference of 3.77%.

5 Conclusions

According to the overall findings of the experiment, the condition during grinding influences surface roughness the most, accounting for 54.82% of the total contribution from the grinding process, followed by the depth of cut, contributing for 41.34%. It has been found that grinding with a low depth of cut and using MQL with a graphite-oil-based nanofluid would help produce a low surface roughness. The ideal condition was discovered during MQL using graphite-oil based nanofluid at a depth of cut of 40 μm . Overall, by comparing the three conditions during grinding with the optimum depth of cut, grinding with MQL with graphite-oil-based nanofluid has provided the better and more smooth surface roughness.

References

1. Jamishidi H, Budak E (2018) Grinding temperature modelling based on time dependent heat source. Proc CIRP 77:299–302
2. Rifat M, Rahman MH, Das D (2017) A review on application of nanofluid MQL in machining. In: AIP conference proceedings, vol 1919. pp 020015
3. Zamiruddin N, Rosli N (2020) Application of minimum quantity lubrication for various machining process. J Modern Manuf Syst Technol 4:40–47
4. Shen B, Shih AJ, Tung SC (2008) Application of nanofluid in minimum quantity lubrication grinding. J Tribol Trans 51:730–737
5. Kananatahn J, Samykano M, Sudhakar K, Subramaniam SR, Selvani SK, Kumar NM, Keng NW, Kadirgama K, Hamzah WAW, Harun WSW (2018) Nanofluid as coolant for grinding process: an overview. In: IOP conference series materials science engineering, vol 342. pp 012078

6. Esarte J, Riehl RR, Mancin S, Blanco JM, Aresti M, Estella J (2021) Nanofluids as advanced cooling technology. In: Success stories. heat transfer-design, experimentation and applications, Intech Open, London
7. Kong L, Sun J, Bao Y (2017) Preparation, characterization and tribological mechanism of nanofluids. *RSC Adv* 7:12599–12609
8. Saifei W, Rahman MM, Yusoff AR, Radin MR (2020) Preparation, stability and wettability of nanofluid. *J Mech Eng Sci* 14(3):7244–7257
9. Sharma P, Sidhu BS, Sharma J (2015) Investigation of effects of nanofluids on turning of AISI D2 steel using minimum quantity lubrication. *J Cleaner Prod* 108:72–79
10. Khrisna PV (2019) Effectiveness of vegetable oil based nanofluids in machining of steel. *J Multidisciplinary Stud* 2(1):49–57
11. Kulkarni HB, Nadakatti MM, Kulkarni SC, Kulkarni RM (2020) Investigation on effect of nanofluid based minimum quantity lubrication technique for surface milling of A17075–T6 aerospace alloy. *Mater Today: Proc* 27:251–256
12. Mahadi MA, Choudhury IA, Azuddin M, Nukman Y (2017) Use of boric acid power aided vegetable oil lubricant in turning AISI 431 steel. *Proc Eng* 184:128–136
13. Vasu V, Kumar KM (2011) Analysis of nanofluids as cutting fluids in grinding EN-31 steel. *Nano-Micro Lett* 3:209–214
14. Virdi RL, Chatha SS, Singh H (2020) Performance evaluation of Inconel 718 under vegetable oils based nanofluids using minimum quantity lubrication grinding. *Mater Today: Proc* 33:1538–1545
15. Diabb J, Rodríguez CA, Mamidi N, Sandoval JA, Taha-Tijjerina J, Martínez-Romero OO, Elías-Zúñiga A (2017) Study of lubrication and wear in single point incremental sheet forming (SPIF) process using vegetable oil nanolubricants. *Wear* 376:777–785
16. Sofiah GN, Samykan M, Pandey AK, Kadirgama K, Sharma K, Saidur R (2021) Immense impact from small particles: Review on stability and thermophysical properties of nanofluids. *Sustain Energy Technol Assess* 48:1011635
17. Minh DT, The LT, Bao NT (2017) Performance of Al_2O_3 nanofluids in minimum quantity lubrication in hard milling of 60Si₂Mn steel using cemented carbide tools. *Adv Mech Eng* 9:1–9
18. Mohamad NB, Bahar R (2016) Minimum quantity lubrication (MQL) and its effect on tool wear during miniature drilling: an experimental study. *Int J Eng Mater Manuf* 1(2):65–70
19. Patil A, Raval J, Bangma T, Edinbarough I, Tai B, Stephenseon D, Suleiman O, Hung WN (2020) Characterization and performance of minimum quantity lubricants in through-tool drilling. *Int J Eng Mater Manuf* 5(4):98–115
20. Hossain S, Abedin MZ (2021) Effect of minimum quantity lubrication system for improving surface roughness in turning operation. *Int J Eng Mater Manuf* 6(1):50–59
21. Liao CA, Kwan YK, Chang TC, Fuh YK (2018) Ball-milled recycled lead-graphite in machining of steel. *J Polym* 10(7):799
22. Gupta MK, Sood PK, Sharma VS (2016) Machining parameters optimization of titanium alloy using response surface methodology and particle swarm optimization under minimum quantity lubrication. *J Mater Manuf Process* 31:1671–1682
23. Sivaiah P, Chakradhar D (2019) Modelling and optimization of sustainable manufacturing process in machining of 17–4 PH stainless steel. *Measurement* 134:142–152

Study of Surface Integrity in Turning Ti-Alloy Using Optimal Depth of Cut



Dinesh Reddy Nallagangula, Abdul Md Mazid, Neamul Khandoker, and Mohammad Yeakub Ali

Abstract Surface integrity is one of the most relevant parameters used for evaluating the quality of machined surfaces for any industrial application. Significant surface defect can cause dangerous failure of machine element or at least reduce the service life significantly. Although, titanium alloy is a promising material for producing aircraft structural and engine components for high reliability, it is difficult to machine as well as difficult to achieve desired surface quality. Each of the turning parameters such as cutting speed, feed rate, depth of cut affects the machined surface quality with different level of contribution. The main objective of this research is to investigate the influence of depth of cut on surface finish keeping other parameters constant. Slots on Ti-alloy shaft were turned with varying depth of cut to generate surfaces with different surface roughness. Taylor-Hobson roughness measuring device was used to measure the surface roughness. The results of optimum surface roughness value are found to be $0.40\ \mu\text{m}$ for depth of cut $0.50\ \text{mm}$ for constant cutting speed and feed rate $81.05\ \text{m/min}$ and $0.055\ \text{mm/rev}$ respectively.

Keywords Ti-Alloy machining · Depth of cut · Surface roughness · Surface integrity

1 Introduction

One of the most widely used metal cutting process is lathe turning where material properties, turning parameters, tool wear interacts in a complex way and eventually

D. R. Nallagangula · A. M. Mazid (✉) · N. Khandoker
School of Engineering and Technology, Central Queensland University, Rockhampton,
QLD 4702, Australia
e-mail: a.mazid@cqu.edu.au

M. Y. Ali
Mechanical Engineering Programme Area, Faculty of Engineering, Universiti Teknologi Brunei,
Tungku Highway, Gadong 1410, Brunei Darussalam

affect the surface integrity. In this paper the turning of titanium alloy has been investigated to achieve high surface integrity. Titanium alloys are used in various industrial applications specially in aviation, aerospace and automotive industries because of its high strength-to-weight ratio, high corrosion resistance and high strength at higher application temperature. However, titanium alloy (Ti-6Al-4V) is a “difficult to cut” material due to low thermal conductivity and high chemical reactivity causing temperature rise specially on cutting tool and workpiece interaction zone [1]. As such optimizing cutting parameters for better surface integrity remains as a challenge for researchers and practitioners in academia and industries. Lathe turning parameters has been optimized for different grade of titanium alloy by analyzing various methods such as surface roughness [1, 2], vibration signal [3], lubrication method [4], cutting tool temperature [5]. In addition, stress that remains in a body which is stationary at equilibrium condition after removal of external load is “residual stress” [6]. This stress involves numerous sub-surface and superficial characteristics inclusive of plastic deformation, metallurgical changes, crack formation and surface roughness. Residual stress is induced on the microstructure layers due to mismatching in the thermal expansion coefficient of the deposited layers (non-uniform), plastic deformation, interstitial impurities and deposition process as shown in the Fig. 1.

For the residual stress assessment in Ti-alloy, the most important thing is the machining process since residual stress is evident in the machining process. The machining can be performed using the lathe machining. For the cutting speed optimization, with different speed and machining fluid-applied, turning operation is shown with measurement of the surface stress at each step.

Afterwards, the plot of these average surface roughness helps to visualize the surface roughness variation. Likewise, feed rate optimization helps to determine surface quality. Another study [7] illustrated that the stress evident in the solid

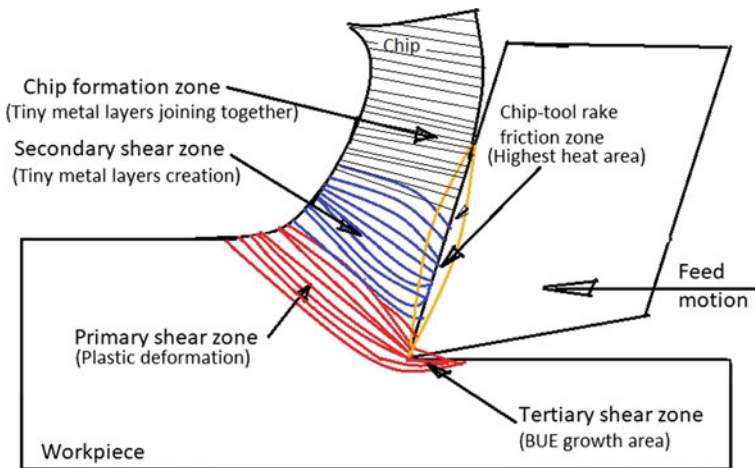


Fig. 1 Machining process (2D model)

body that exists remaining when external loading is removed from the workpiece is known as residual stress. This residual stress has a different effect on the machining phenomenon such as deformation, static strength, dynamic strength, chemical resistance and magnetism. The residual stress that is obtained from the hard turning and the grinding is different such as for the fresh tool wear hook-shaped residual stress is evident for the hard turning. In contrast, grinding produces a significant amount of residual surface stress only. Similarly, tool wear is a critical issue as turning using the worn tools, a considerable amount of tensile/compressive stress has been generated. The project focus on the research for the economic and sustainable manufacturing for Ti-alloy to obtain better surface integrity by optimizing the depth of cut. The specific objectives are:

- To perform machining for Ti-alloy to find optimal machining parameters with the help of uncoated carbide tools.
- To determine the optimum depth of cut that provides good surface roughness as well as increase the life of the cutting tool.
- To study about residual stress how it impacts on Ti-alloy during the machining process.
- To provide procedure for manufacturing industries to make the Ti-alloy based material.

The resources required for the project are (i) lathe machine, (ii) cutting tools, (iii) surtronic 3 + (iv) microscope to know the surface integrity.

2 Literature Review

Machining is a process of thermomechanical procedure during removal of tiny material extracted from the surface in the form of chips as a result of plastic deformation [8]. This phenomenon of deformation occurs in three different shear zones, clearly viewable in the Fig. 1.

- Primary shear zone—In this zone plastic deformation of bulk will occur as in the top layer of workpiece from Fig. 1
- Secondary shear zone—will occur at the interface of chip or tool (shown in the surface between tool and workpiece)
- Tertiary shear zone—at workpiece interface or tool interface.

The plastic deformation is transformed into heat mostly during machining. Because of the actions of mechanical loads created by chip and thermal loads raising from friction, deformation of plastic in the shear zone cause deformation of the workpiece surface.

Heavy plastic deformations occur due to thermomechanical loading beneath the machined surface. When the tool is discovered, stress relaxation occurs as workpiece gets cooled to surrounding air temperature in the absence of the external loads. Residual stress develops because of large incompatibilities occurs between

the machined surface and underlying layers. Machining induced residual stress is allocated to 3 main streams which are mechanical loads, thermal loads, and phase transformation.

During the machining process, thermal and mechanical sources are in evident. Based on the deformation extent and rise in temperature, phase transformations may generate contributing to residual stress formation. Therefore, constant interactions happen between metallurgical, thermal and mechanical impacts. So, it is difficult to correlate residual stress occurrence to a single source [8].

Another study [9] on the titanium machinability revealed that the hard to cut material titanium has low research in the field of advanced machining tools such as PCD and BCBN. The titanium operation for machinability the use of CBN and PCD causes the tool to wear faster [10].

Machinability of the titanium alloys performed using the lathe machine under microscopic view illustrates that the alpha alloy contains higher aluminium [11]. The beta alloy has a higher amount of V. From the observation it is seen that adiabatic shear banding is present in the chips formed during machining process inherent due to high amount of localization and deformation of the shears in small layers resulting in the thermo-mechanical instability resulting fracture and tear of the chips [12].

The experimental process [13], showed that the sub-surface deformation can be reduced with the help of the twinning process at the time of both the dry and the lubricating stage. Similarly, for the better distribution of the heat to elaborate the tool life, the increase in the feed resulting in long contact tool length is essential [10, 14, 15].

3 Methodology

Ti-alloy cylindrical bar of 600 mm long and 60 mm diameter was used for step turning with varying depth cut using uncoated carbide tools. The surface roughness is measured in all the steps with a roughness measuring device “surtronic roughness” (Taylor-Hobson, USA). By keeping cutting speed and feed rate constant and optimizing the depth of cut a better surface finish is sought.

The depth of cut ranges from 0.2 to 1.7 mm where feed rate and cutting speed constant were kept constant at 0.07 mm/rev and 95 m/min respectively. Significant tool wear may occur during some time when the depth of cut increases above the maximum setpoint (1.7 mm) sparking can occur when a tool gets damaged. Surface roughness can be measured using surface roughness measuring device and then the specimen is inspected with a microscope to know the surface integrity such as, plastic deformation, cracks and the factors that influence machining operation in the Table 1.

Table 1 Factors influencing machining operation

Parameter	Influence and interaction
Speed, cutting fluids, cut depth	Power, force, temperature, chip, tool life, surface finish
Tool angle	Chip flow direction, tool wear resistance
Build up edge chip	Poor surface finish
Temperature rise	Tool life influence
Machinability	Surface finish, chip produced
Tool wear	Dimensional accuracy, surface finish influences

4 Results and Discussion

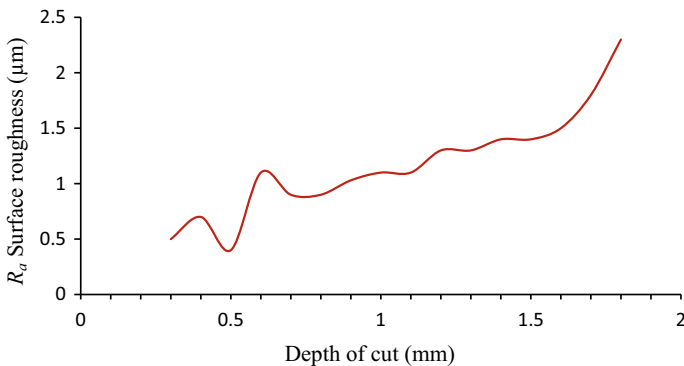
Table 2 describes the machining process for depth of cut (d) from 0.3 to 1.8 mm by increasing 0.1 mm for every step up to 1.8 mm, Now the sixteen different depths of cut are followed to obtain the optimum surface roughness value by keeping feed rate (f) and cutting speed (v) at constant 0.055 mm/rev 81.05 m/min respectively. The graph in Fig. 2 describes the machining process for depth of cut optimization. The graph is plotted between depth of cut (mm) to surface roughness (μm). The optimum surface roughness value is obtained in between 0.3 and 0.5 mm. The surface roughness value is found to be 0.4 μm for 0.5 mm depth of cut. As the depth of cut increases the surface roughness value also increases.

5 Conclusions

Based on experimental analysis of turning Ti-alloy using uncoated carbide tool, the optimum depth of cut for lower surface roughness has been identified. In this experimental research the feed rate 0.055 mm/rev and cutting speed 81.05 m/min are kept constant. The optimum surface roughness value is found to be 0.4 μm is obtained when the depth of cut is at 0.5 mm. However, this traditional machining of titanium alloy has to be benchmarked with non-traditional such as electro discharge machining of titanium alloy [16].

Table 2 Surface roughness variation in respect of depth of cut

No	d (mm)	R _{a1} (μm)	R _{a2} (μm)	R _{a3} (μm)	Average) R _a μm
1	0.3	0.5	0.5	0.5	0.5
2	0.4	0.9	0.7	0.5	0.7
3	0.5	0.3	0.5	0.5	0.4
4	0.6	1.3	1.1	1.1	1.1
5	0.7	0.9	0.9	0.9	0.9
6	0.8	0.9	0.9	1.1	0.9
7	0.9	1.1	1.1	0.9	1.03
8	1.0	1.1	1.3	0.9	1.1
9	1.1	1.1	1.1	1.1	1.1
10	1.2	1.3	1.3	1.5	1.3
11	1.3	1.3	1.5	1.3	1.3
12	1.4	1.5	1.5	1.3	1.4
13	1.5	1.3	1.5	1.5	1.4
14	1.6	1.3	1.5	1.5	1.5
15	1.7	1.8	1.8	1.8	1.8
16	1.8	2.1	2.3	2.5	2.3

**Fig. 2** Relationship of surface roughness and depth of cut


References

1. Umasekar VG, Gopal M, Rahul K, Saikiran S, Mowli GVS (2017) Investigation of surface roughness in finish turning of titanium alloy Ti-6Al-4V. *ARPN J Eng App Sci* 12(17):5029–5034
2. Akkuş H, Yaka H (2021) Optimization of cutting parameters in turning of titanium alloy (Grade 5) by analysing surface roughness, tool wear and energy consumption. *Experim Techniques* 1–12
3. Rodrigues, A.P., Pai, P.S.: D’Mello, G. Surface roughness evaluation in high-speed turning of Ti-6Al-4V using vibration signals. *Indian Journal of Advances in Chemical Science* S1,

- 160–164 (2016).
4. Revankar GD, Shetty R, Rao SS, Gaitonde VN (2014) Analysis of surface roughness and hardness in titanium alloy machining with polycrystalline diamond tool under different lubricating modes. *Mater Res* 17(4):1010–1022
 5. Vinayagamorthy R, Xavier MA (2014) Investigations on the machinability of titanium alloy during precision turning. *Middle-East J Sci Res* 22(12):1782–1787
 6. Withers PJ, Bhadeshia HKDH (2001) Residual stress. Part 2—Nature and origins. *Mater Sci Technol* 17(4):366–375
 7. Guo YB, Li W, Jawahir IS (2009) Surface integrity characterization and prediction in machining of hardened and difficult-to-machine alloys: a state-of-art research review and analysis. *Mach Sci Technol* 13(4):437–470
 8. Kalpakjian S, Steven RS (2013) *Manufacturing engineering and technology*, Pearson
 9. Ulutan D, Ozel T (2011) Machining induced surface integrity in titanium and nickel alloys: a review. *Int J Mach Tools Manuf* 51(3):250–280
 10. Dargusch MS, Zhang M-X, Palanisamy S, Buddery AJM, St John DH (2008) Subsurface deformation after dry machining of grade 2 titanium. *Adv Eng Mater* 10(1–2):85–88
 11. Hasan MS, Mazid AM, Clegg R (2016) The basics of satellites in machining perspective. *Int J Eng Mater Manuf* 1(2):35–50
 12. Ahsan KB, Mazid AM, Pang GKH (2016) Morphological investigation of Ti-6Al-4V chips produced by conventional turning. *Int J Mach Mach Mater* 18(1/2):138–154
 13. Choudhury SK, Rao IVK (1999) Optimization of cutting parameters for maximizing tool life. *Int J Mach Tools Manuf* 39(2):343–353
 14. Hazza M, Najwa NA (2016) Optimization of cutting parameters to minimize tooling cost in high speed turning of SS304 using coated carbide tool using genetic algorithm method. *Int J Eng Mater Manuf* 1(1):11–15
 15. Ogedengbe TS, Abdulkareem S, Aweda JO (2018) Effect of coolant temperature on surface finish during turning of titanium alloy Ti6Al4V. *Int J Eng Mater Manuf* 3(4):237–244
 16. Ali MY, Atiqah N (2011) Erniyati: Silicon carbide powder mixed micro electro discharge milling of titanium alloy. *Int J Mech Mater Eng* 6(2):338–342

Tribology Properties of Titanium Alloy (Ti-6Al-4V) at Various Temperature on α/β Solution Treatment and Aging Condition



Poppy Puspitasari , Muhammad Raffli Putra Wardana, Diki Dwi Pramono, Abdul Munir Lubis, Avita Ayu Permanasari, Muhammad Iman Hakimi Chua Abdullah, and Puput Risdanareni

Abstract Titanium Ti-6Al-4V has outstanding mechanical and chemical properties including high strength ratio, light weight, high melting point, and good corrosion resistance. However, this titanium alloy also has disadvantages, namely low hardness, high coefficient of friction, and poor wear resistance. One way to improve the properties of material is by heat treatment. Titanium Ti-6Al-4 V in this study was heat-treated at a temperature of 900 °C for 1 h and the aging process was carried out with temperature variations of 550, 650 and 750 °C each time temperature was 8 h. The tests carried out in this study included tests of wear resistance, surface roughness and microstructure of titanium Ti-6Al-4V. The analysis revealed that the test results for the wear resistance test using the ogoshi method have decreased to 8.5628×10^{-5} mm³/kg m, while for the surface roughness test there has been a significant increase of 0.15 m, and for microstructure analysis, the results showed that the grain size changed smaller as the aging temperature increased.

Keywords Wear resistance · Surface roughness · Ti-6Al-4 V · Ogoshi method

P. Puspitasari (✉) · M. R. P. Wardana · D. D. Pramono · A. A. Permanasari
Mechanical and Industrial Engineering Department, Universitas Negeri Malang, Malang, Indonesia
e-mail: poppy@um.ac.id

P. Puspitasari · A. A. Permanasari
Center of Advanced Materials for Renewable Energy, Universitas Negeri Malang, Malang, Indonesia

A. M. Lubis
Mechanical Engineering Department, Universitas Muhammadiyah Surakarta, Surakarta, Indonesia

M. I. H. C. Abdullah
Centre for Advanced Research On Energy, Universiti Teknikal Malaysia Melaka, Melaka, Malaysia

Fakulti Teknologi Kejuruteraan Mekanikal Dan Pembuatan, Universiti Teknikal Malaysia Melaka, Melaka, Malaysia

P. Risdanareni
Civil Engineering and Planning Department, Universitas Negeri Malang, Malang, Indonesia

1 Introduction

Recent development in technology has attracted research studies in the field of new materials which are much needed to support industrial progress [1]. An example of a material that is needed by industry today is metal. Metal is a material that is quite a lot and has various properties and uses, each according to needs [2].

One of the widely used metal by industry is titanium Ti-6Al-4V. Titanium Ti-6Al-4V is a titanium alloy that has been widely used as an implant material, because it has lower stiffness properties than Co-Cr alloys and stainless steels [3] and has high strength, light weight, high melting point, and corrosion resistance [4], which makes titanium Ti-6Al-4V widely used in several industries in the world other than for implants. For examples are the used of Ti-6Al-4V for aerospace, energy generation and petrochemical industries [5]. This titanium alloy also has weaknesses that are considered sufficient for use in industry, namely having poor wear resistance properties, high coefficient of friction, and low hardness [6]. Therefore, it is necessary to carry out research to improve mechanical properties of titanium alloy (Ti-6Al-4 V) by heat treatment method that consists of solution treatment and aging.

2 Methods

The base material used in this research is titanium Ti-6Al-4V. The titanium Ti-6Al-4V are heat treatment using electric vacuum furnace at a temperature of 900 °C with a holding time of 1 h and then followed by a cooling process with cooling media, namely water. After the specimens were heat treated, the next step was to age the specimens at different temperatures, namely 550, 650 and 750 °C, with a holding time of 8 h at each different temperature and then continued with cooling using air. All specimen were testing using wear resistance Rieken Ogshi Universal Wear Type OAT-U tool which refers to the ogoshi method, surface roughness test using the Mitutoyo Surftest SJ-301, microstructure testing observed using an optical microscope (NIKON Type 59,520) with a magnification of 650X.

3 Results and Discussion

3.1 *Wear Resistance*

The results of the wear rate data for titanium Ti-6Al-4V were obtained from the wear resistance testing process. The number of specimens used in this test is three specimens for each treatment variation between non-aging specimens and aging specimens. Each specimen was taken 3 test points. In Fig. 1 it can be seen that the results of the wear test have decreased significantly when given the aging treatment.

The average wear rate decreased from $1.75 \times 10^{-4} \text{ mm}^3/\text{kg m}$ on non-aging Ti-6Al-4V titanium to $8.5628 \times 10^{-5} \text{ mm}^3/\text{kg m}$ on aging Ti-6Al-4V titanium. From the figure it can also be seen that with the aging treatment process, the value of the wear rate on titanium Ti-6Al-4V decreased. Based on the results of the research, the wear resistance of titanium Ti-6Al-4V which was treated with heat treatment and aging decreased. The value of the wear rate decreased even more after the specimen was treated with aging. The greatest decrease in wear rate was found in the Ti-6Al-4V specimen which was treated with aging at a temperature of 650 °C. The average wear rate decreased from $1.75 \times 10^{-4} \text{ mm}^3/\text{kg m}$ to $8.5628 \times 10^{-5} \text{ mm}^3/\text{kg m}$. The results of increasing and decreasing a wear rate can be influenced by several factors, including the difference in the treatment that occurs in the test specimen and also the difference in the cooling method used. The treated specimens can produce a lower wear rate value than the untreated specimens [1-2]. Ganesh et al. [2] in their research, they found a significant decrease in the use of cooling media after the specimen was heat treated at a temperature of 950 °C for a holding time of 1 h and aging at a temperature of 550 °C for a holding time of 3 h, then cooled using the medium. water and air cooling. This is caused by the high value of hardness in the quenched specimen with the formation of a martensitic structure due to the heat treatment process followed by cooling using water and the aging process and caused by the slow cooling system of the specimen.

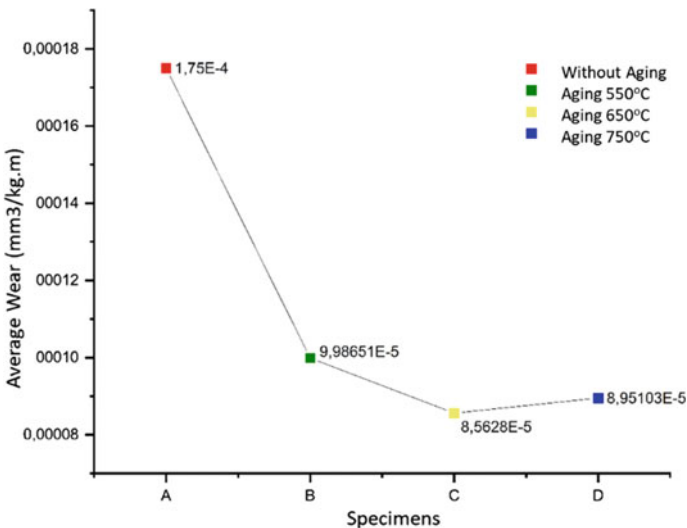


Fig. 1 The average wear of titanium Ti-6Al-4V after being heat treated and aging at temperatures of 550, 650 and 750 °C

3.2 Surface Roughness

The results of surface roughness test is shown in Fig. 2, in this test are in the form of average surface roughness data taken from processing the test data at 3 points on the surface of the test specimen. The results of the surface roughness test of titanium Ti-6Al-4 V experienced very extreme differences at different levels of aging temperature variations with specimens without aging. The lowest average surface roughness value was found in specimens without aging with an average value of $0.077 \mu\text{m}$, then an increase of $0.1 \mu\text{m}$ was obtained from specimens using aging at a temperature of $550 \text{ }^\circ\text{C}$. In other specimens using the same aging temperature at $650 \text{ }^\circ\text{C}$, there was a significant decrease with an average value of $0.073 \mu\text{m}$, but the specimen with an aging temperature of $750 \text{ }^\circ\text{C}$ had the highest average surface roughness value than the other specimens, which was equal to $0.15 \mu\text{m}$. This happens because the factor of heat treatment can improve the quality of a material, and heat treatment can also reduce the effect of surface roughness. Heat treated materials can make a significant difference in terms of surface roughness tests compared to non-heat treated specimens. The temperature difference factor also plays an important role in the heat treatment process. Because the greater the heat treatment temperature, the more the hardness of the material increases which will also be related to the results of the surface roughness [3–4].

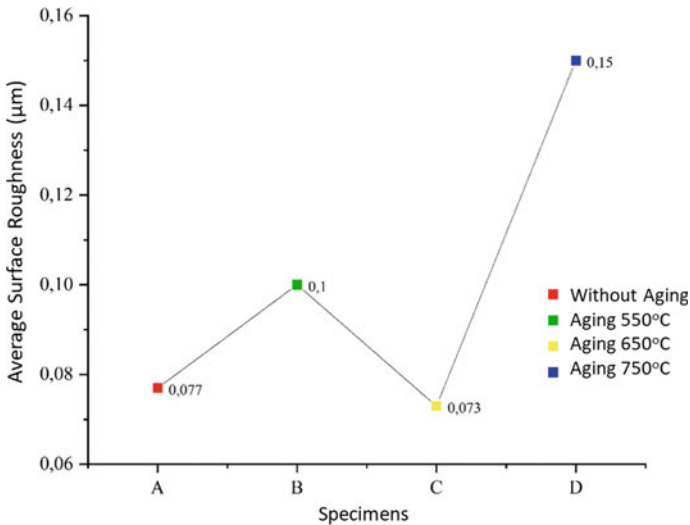


Fig. 2 The average surface roughness of titanium Ti-6Al-4V after being heat treated and aging at temperatures of 550, 650 and $750 \text{ }^\circ\text{C}$

3.3 Microstructure

Result the microstructure testing of titanium Ti-6Al-4V can be shown in Fig. 3, it can be seen the microstructure of the titanium Ti-6Al-4V specimen. In the figure, there are dark dots/lines indicating the phase β and in other areas that have a lighter color indicate the phase α [5]. Then in Fig. 3a shows that the phase β is more dominant than the phase α . While Fig. 3 b, d both experiencing a more balanced phase change between the phase α and the phase β compared to the raw-material specimen. This can occur due to material defects or problems with cooling [5]. For the specimens in Fig. 3c and e a phase change occurs again, in which the phase structure of the two specimens is more dominant in the phase β and the specimen undergoes a change in grain size. which is getting smaller. The smallest grain size was obtained in specimens that used aging and the larger size was obtained by raw specimens or specimens that were not given any treatment, this is because the solution treatment can control the stability of the matrix and the grain size of a material, where the higher the solution treatment temperature, the larger the grain size. The effect of grain size resulting from this treated specimen makes it difficult for dislocations to occur so that it can increase the hardness value, and high hardness will result in a decrease in strength [6].

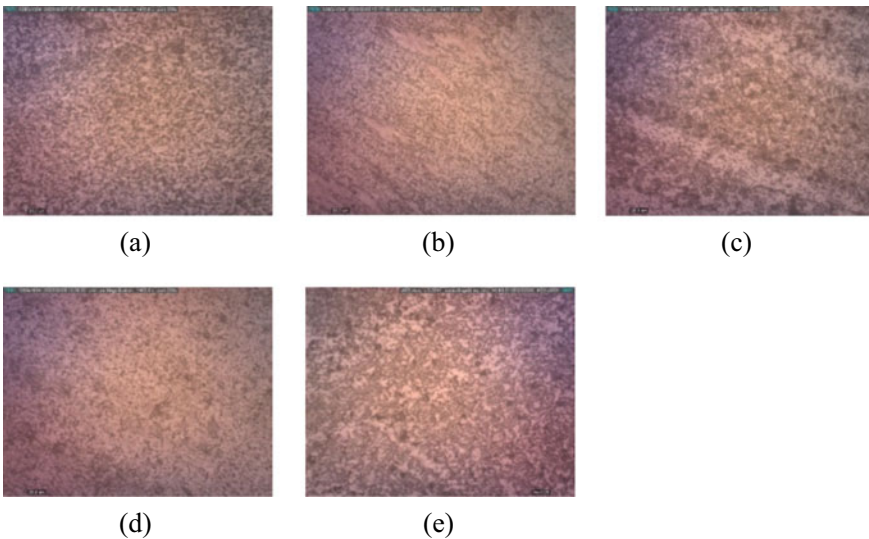


Fig. 3 Microstructure of titanium Ti-6Al-4V **a** raw material, **b** non-aging specimens, **c** aging specimens at 550 °C, **d** aging specimens at 650 °C, and **e** aging specimens at 750 °C

4 Conclusion

Ti-6Al-4V titanium specimens without aging treatment experienced the highest wear rate of $1.75 \times 10^{-4} \text{ mm}^3/\text{kg m}$, and the lowest wear rate was obtained on Ti-6Al-4V specimens using the process aging is $85628 \times 10^{-5} \text{ mm}^3/\text{kg m}$ with a temperature of $650 \text{ }^\circ\text{C}$. This is due to the difference in temperature obtained during the aging process, and the difference in material roughness which can affect the wear rate value. The highest surface roughness value occurs in specimens using aging $750 \text{ }^\circ\text{C}$. The grain size of the aging specimen has a smaller size than the grain size of the raw material, therefore, the hardness value is higher.






Acknowledgements Authors would like to thank Universitas Negeri Malang for Hibah Kerjasama Internasional 2022 with contract number 19.5.1254/UN32.20.1/LT/2022 for PP.

References

1. Youssef SS, Ibrahim KM, Abdel-Karem M (2013) Effect of heat treatment process on tribological behavior of Ti-6Al-4V alloy. *Int J Mech Eng Robot Res* 2:385–394
2. Ganesh BKC, Ramaniah N, Rao PVC (2012) Effect of heat treatment on dry sliding wear of titanium- aluminum-vanadium (Ti-6Al-4V) implant alloy. 4:67–74. <https://doi.org/10.5897/JMER11.090>
3. Li Z, Liu C, Wang B, Wang Z, Yang F, Gao C, Liu H, Qin Y, Wang J (2018) Heat treatment effect on the mechanical properties, roughness and bone ingrowth capacity of 3D printing porous titanium alloy. 8:12471–12483. <https://doi.org/10.1039/c7ra13313h>
4. Kahraman F, Sagbas A (2010) An investigation of the effect of heat treatment on surface roughness in machining by using statistical analysis. *Iran J Sci Technol* 34:591–595
5. Galarraga H, Warren RJ, Lados DA, Dehoff RR, Kirka MM, Nandwana P (2017) Effects of heat treatments on microstructure and properties of Ti-6Al-4V ELI alloy fabricated by electron beam melting (EBM). 1:1–24
6. Ramadhan TS (2019) Analisis variasi temperatur solution treatment terhadap perubahan struktur mikro, kekerasan dan ketahanan korosi paduan Ti-6al-7nb untuk aplikasi implan gigi. Universitas Islam Negeri Syarif Hidayatullah Jakarta

Experimental and Thermal Modeling of Beeswax-Filled Extruder via Solidwork for Batik Printing



Sharifah Imihezri Syed Shaharuddin ,
Sharifah Nur Balqis Syed Azman , Norhashimah Shaffiar ,
M. K. Nor Khairusshima , and Nor Aiman Sukindar 

Abstract The advances made in printing technology have recently been adapted for batik wax printing processes. The thermal system of the batik printer's extruder is critical as non-uniform beeswax's temperature distribution leads to inconsistent deposition of wax lines, clogging at the extruder's nozzle, and wax spillage. Therefore, this study aims to validate the thermal model for the beeswax-filled extruder and obtain a description of the thermal distribution of the beeswax in the extrusion chamber at various heat inputs. A 3D model of the newly designed batik wax extruder was constructed in SolidWorks. Subsequently, the Thermal Analysis SolidWorks was used to assign the 3D model with appropriate material properties, boundary conditions, and mesh to simulate the thermal model. Comparative analysis between actual and simulated temperature showed almost similar readings with differences of less than 4%, indicating a significant thermal model. Further simulations of the beeswax in the extruder chamber at a heat input of 70, 77 and 85 °C revealed a temperature drop of less than 2 °C. The results of the simulations indicated that heat was nearly uniformly distributed along the length of the extrusion chamber. Thus, it is anticipated that the possibility of intermittent wax spillage and clogging is remote for the batik printer. The satisfactory heating response indicates that the in-house designed extruder system can be used for the direct deposition of continuous wax lines for batik printing applications.

Keywords Batik printer · Extruder · Thermal simulation

1 Introduction

Beeswax is produced naturally by worker bees of the genus *Apis* and is comprised of multi-component material with at least 284 different compounds [1]. Beeswax structure mainly consists of long-chain alcohols and esters of fatty acids [2]. Beeswax

S. I. S. Shaharuddin (✉) · S. N. B. S. Azman · N. Shaffiar · M. K. N. Khairusshima · N. A. Sukindar

Department of Manufacturing and Materials Engineering, Kuliyyah of Engineering, International Islamic University Malaysia, 53100 Kuala Lumpur, Malaysia
e-mail: shaimihezri@iium.edu.my

behaves as a phase change material (PCM) which means that it can absorb and accumulate heat before releasing a high amount of thermal energy as it transitions into a phase change [3]. Studies have also investigated beeswax's potential applications as low-temperature heat energy storage to resolve energy issues [4, 5]. Other than for advanced technological applications, this organic substance has been used traditionally for decades to create traditional batik motifs that derive from local floras such as '*pucuk rebung*' or bamboo shoot and geometrical designs such as spiral.

The batik production in Malaysia involves the use of various blends of resist materials to control the spreading of dye on the textile. Over the years, there have been innumerable advancements made toward the traditional batik process using automated batik printers [6, 7]. A recent survey study by Asri et al. [8] reveals that the extruder, which functions to deposit wax on the textile is the most critical component for an automatic batik printer.

In batik processing, the thermal regulation of the wax in the extruder is highly critical to ensure that a continuous and consistent wax line can be deposited. Overheating and unstable temperature control of the wax leads to uneven wax deposition, frequent clogging at the extruder tip, and spillage on the fabric. However, very few studies have studied the relationship between the beeswax's melt processing temperature and extrusion system. The current work presents validation and description of the thermal distribution of beeswax in the extrusion chamber that was heated using a ceramic heater at various processing temperatures.

2 Methodology

2.1 Actual Temperature Measurements

Figure 1a shows the main components of the extruder system which include an extruder die, ceramic heater, and ceramic heater element. Figure 1b shows the location of the five temperature points on the extruder body including the beeswax (point 5). Each temperature point was measured using LINI-T digital thermocouple at a heat input of 77 °C.

2.2 3D Modelling and Thermal Simulation

The actual extruder components were modeled in SolidWorks (2021) and the thermal simulations were performed via Thermal Analysis SolidWorks (2021). Each component was assigned with appropriate material properties, boundary conditions, and meshing components. The material attributes of each component in the 3D model are enumerated in Table 1. The material properties of beeswax were obtained from Sinaringati et al. [4].

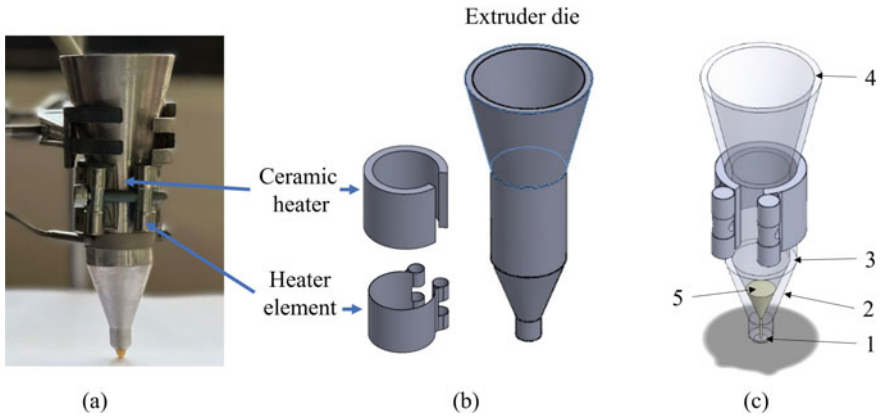


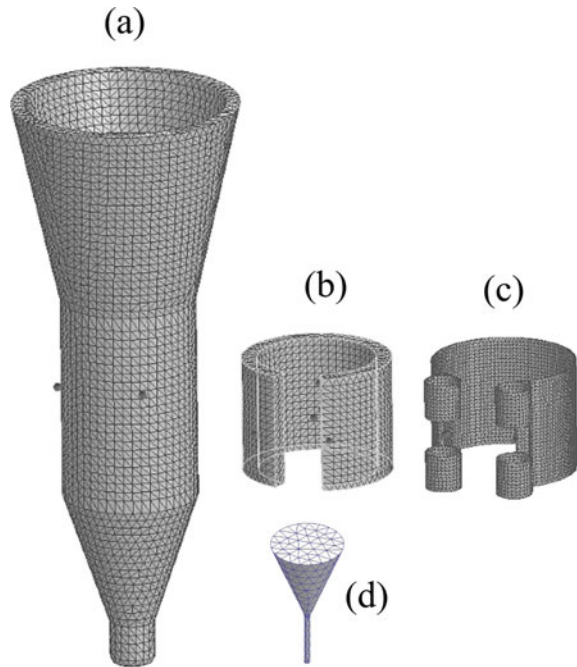
Fig. 1 a Actual extruder design b chematics of the main components of the extruder drawn using Solidwork and c Location of measured temperature points

Table 1 Material attributes assigned for the extruder unit and beeswax for the thermal simulation

Extruder component	Material	Thermal conductivity [W/m·K]	Density [kg·m ⁻³]	Specific heat [J/kg·k]
Extruder die	Aluminum 1060 alloy	200	2700	900
Heater element	Plain carbon steel	43	7800	440
Ceramic heater	Ceramic porcelain	1.4949	2300	878
	Beeswax	0.41	970	476

The thermal model shown in Fig. 1c was defined with a face in contact between the heater element, the ceramic and the extruder die. The heat then spreads throughout the extruder unit and air by conduction and convection. Convection coefficient (as air losses) of $7.5 \text{ Wm}^{-2} \text{ k}^{-1}$ (free convection) and the surrounding temperature of 303 K was used for the simulation. The thermal model was evaluated at a heat input of 70, 77 and 85 °C. Each component was designated with a 3D linear hexahedral element that was varied based on the thickness and size of each component as shown in Fig. 2. Thin parts, such as the ceramic heater and heater element, were given fine mesh density to ensure successful continuous meshing of the model.

Fig. 2 Assigned meshing density for **a** extruder die (total elements: 33,740) **b** ceramic heater (total elements: 11,724) **c** heater element (total elements: 26,334), and **d** beeswax (total elements: 686)



3 Results and Discussion

The actual aluminum extruder used in this study was fabricated using a lathe machine and has a nozzle with an outlet diameter of 1 mm to emulate the nozzle diameter of *tjanting*. Batik *tjanting* is a pen-like tool traditionally used to create wax lines on the fabric. Table 2 shows the actual temperature readings taken at five different locations along the length of the beeswax-filled extruder. In this study, the heater ceramic was set at 77 °C. The actual temperature readings showed that there was a temperature gradient within 3 °C along the length of the extruder die. Figure 3 shows the thermal simulation of the beeswax-filled extruder due to a similar heater temperature of 77 °C. A comparison between actual and simulated temperature readings indicated a temperature discrepancy of less than 4% at each point. The temperature difference obtained in this study was attributed to the discrepancy in heat convection in the actual environment [9]. Other studies using Solidwork have also shown temperature discrepancy of 3–6% [10] and less than 4% [11]. Thus, it is concluded that the thermal model for the extruder is significant due to the small difference between actual and simulated temperature readings.

The thermal simulation was also performed at a heat input of 70 and 85 °C. Figure 4a shows the resultant temperature distribution of beeswax at various points along the length of the extruder's chamber. The analysis showed that there was a small temperature drop of less than 2 °C. The simulation results indicate that the heat from the heater is almost uniformly distributed in the beeswax in the extrusion chamber

Table 2 The actual and simulated temperature readings at five different temperature points

Point	Actual temperature (°C)	Final simulation temperature (°C)	Final temperature difference (%)
1	72.5	75.3	3.71
2	74.1	76.1	2.70
3	74.8	75.7	1.20
4	74.8	75.5	0.94
5	78.4	75.4	3.83

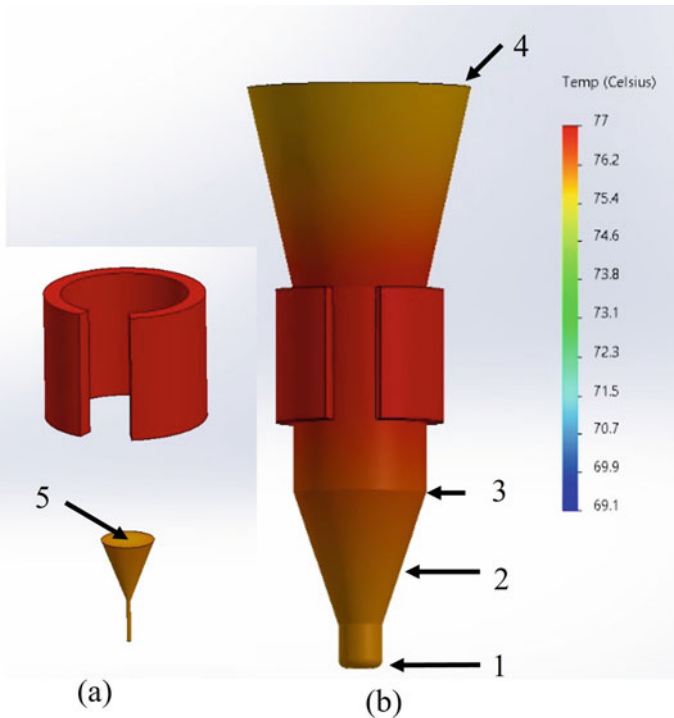


Fig. 3 The simulated thermal distribution at **a** point 5 and **b** point 1–4 of the extruder based on heater temperature of 77 °C

and the possibility of clogging the outlet is low. Figure 4b shows the successful extrusion of beeswax on cotton fabric with good linewidth consistency and no wax spillage.

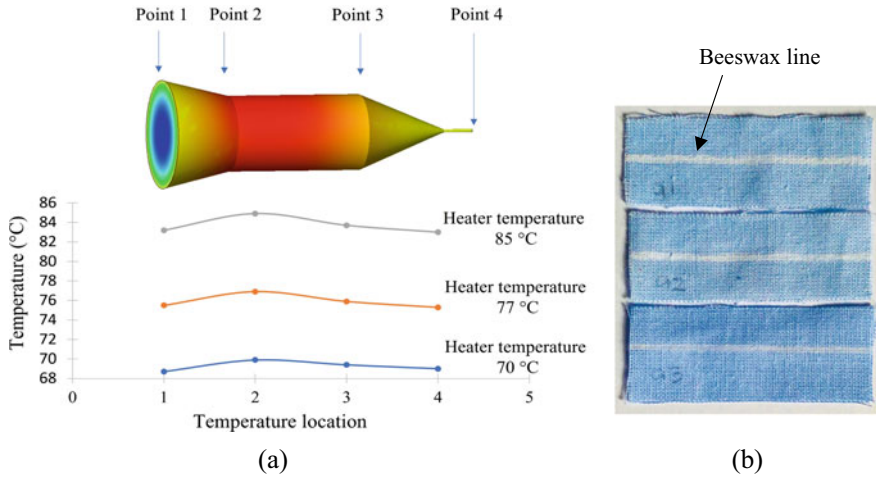


Fig. 4 **a** Thermal distribution of beeswax in the extrusion chamber at various heater temperatures **b** Extrusion of beeswax on cotton fabric using the extruder system

4 Conclusion

The batik printer's extruder design and system play a significant role to ensure the wax in its chamber is uniformly heated and has the capacity to render consistent and quality wax lines. In this study, a thermal model for the beeswax-filled extruder was successfully established with a temperature discrepancy of less than 4%. It was also noted that the actual temperature distributions vary within 3 °C along the length of the extruder. Further thermal simulations of the beeswax in the extrusion chamber at 70 and 85 °C showed low temperature drops of less than 2 °C. The simulation result suggests that heat from the heater is almost uniformly distributed in the extrusion chamber and the possibility of clogging the outlet is low.

Acknowledgements This work was fully supported by International Islamic University Malaysia and funded by the Ministry of Higher Education Malaysia (FRGS/1/2018/TK03/UIAM/02/3). The authors would like to express their deepest gratitude for the support from all co-researchers.

References

1. Morgan J, Townley S, Kemble G, Smith R (2002) Measurement of physical and mechanical properties of beeswax. *Mater Sci Technol* 18:463–467
2. Putra N, Prawiro E, Amin M (2016) Thermal properties of beeswax/CuO nano phase-change material used for thermal energy storage. *Int J Technol* 7:244–253
3. Dzindziora A, Cieřlik J, Wojciechowski J (2021) Phase change materials and their use for energy accumulation. In: 34th scientific conference, problems of working machines development, vol 01006. EDP Sciences, Les Ulis

4. Sinaringati S, Putra N, Amin M, Afriyanti F (2016) The utilization of paraffin and Beeswax as heat energy storage in infant incubator. *ARNP J Eng Appl Sci* 11:800–804
5. Dinker A, Agarwal M, Agarwal GD (2017) Experimental study on thermal performance of beeswax as thermal storage material. In: *Materials today: proceedings*, vol 4(9). Elsevier Ltd, Amsterdam, pp 10529–10533
6. Hitchcock M, Nuryanti W (2016) *Building on batik: the globalization of a craft community*, 1st edn. Routledge, Oxfordshire
7. Elamvazuthi L, Morris AS (1997) Automating batik colouring process: a proposal. *J Ind Technol* 6:15–23
8. Asri NAM, Hamid AMA, Shaffiar N, Sukindar NA, Shahrudin SIS, Hassan FS (2022) Application of house of quality in the conceptual design of batik wax extruder and printer. *IJUM Eng J* 23:310–328
9. Vargas RS, Gonda V, Ruiz LC (2018) Thermal analysis and control for heating of an extrusion die. *Banki Közlemények* 1:63–66
10. Shahrudin SIS, Shah TNATB, Khairusshima MKN (2017) Thermal modelling and analysis of batik canting design. *Proc Eng* 184:326–333
11. Asri NAM, Yahaya HNM, Shahrudin SIS, Shaffiar N (2021) Experimental and thermal modeling of batik wax extruder via Solidwork. In: *1st international conference on manufacturing engineering technology 2021*, AIP Publication, Maryland, pp 1–9

Electrical Resistance of Fabric Immersed with PEDOT:PSS Doped Ag NPs and DMSO Solution



Nur'Aishah Ahmad Shahrim , Zuraida Ahmad ,
Wan Nur' Alia Nadhirah Wan Solah, Amelia Wong Azman ,
Norshahida Sarifuddin , and Yose Fachmi Buys

Abstract Electronic textiles based on conductive polymers like poly (3,4-ethylene dioxythiophene): poly (styrene sulfonate) (PEDOT:PSS) produced by immersion technique has been employed. PEDOT:PSS alone, however exhibits high resistance. In this work, the effect of adding silver nanoparticles (Ag NPs) and dimethyl sulfoxide (DMSO) in PEDOT:PSS on electrical resistance together with its mechanism and mechanical properties are investigated. The PEDOT:PSS/DMSO/Ag NPs colloids solutions were prepared and cotton fabric substrate was immersed in the solution at different durations: 3, 5, and 7 h. The adhesiveness of the liquid on the fabric is improved by adding waterborne polyurethane (PU). The electrical resistance of the immersed fabrics was measured by two-probe resistance meter and it was observed that the value decreased from 42.3 to 35.7 Ω when immersing at 3–5 h. Immersing fabric in doped PEDOT:PSS with addition of PU increasing elongation at break at 6%, but reducing the electrical resistance and wettability behavior. These findings offer potential application of the e-textiles as flexible electrode.

Keywords PEDOT:PSS · Silver nanoparticles · Immersion · Electrical resistance

1 Introduction

Conductive polymers like poly (3,4-ethylene dioxythiophene): poly (styrene sulfonate) (PEDOT:PSS) are ideal to be integrated with textile materials through

N. Ahmad Shahrim (✉) · Z. Ahmad · W. N. A. N. W. Solah · N. Sarifuddin
Department of Manufacturing and Materials Engineering, International Islamic University
Malaysia, 53100 Kuala Lumpur, Malaysia
e-mail: nuraishah.shahrim@live.iium.edu.my

A. W. Azman
Department of Electrical and Computer Engineering, International Islamic University Malaysia,
53100 Kuala Lumpur, Malaysia

Y. F. Buys
Department of Mechanical Engineering, Faculty of Industrial Technology, Universitas Pertamina,
12220 Jakarta, Indonesia

different processes owing to their low electrical resistance [1]. Liquid immersion of fabric in PEDOT:PSS doped polar organic solvent like dimethyl sulfoxide (DMSO) lower the electrical resistance by a factor of 10 due to the Coulombic interaction between PEDOT⁺ and PSS⁻ by the screening effect [2, 3]. Adding PEDOT:PSS/DMSO with metal nanoparticles like silver (Ag NPs) is expected to improve the electrical performance and rarely reported [4]. Immersion time duration and fabric materials are also influenced the electrical resistance of the doped PEDOT:PSS. Meanwhile, waterborne polyurethane (PU) coating offers good mechanical properties of the fabric that can be used as stretchable electrode in biomedical application because PU is adhesive, highly elastic, and easy to apply on textile substrates [5]. Therefore, this work aimed to investigate the effect of immersion of fabric in PEDOT:PSS doped Ag NPs and DMSO solution on the electrical resistance, flexibility, and wetting properties.

2 Experimental

2.1 Sample Preparation

Ag NPs colloidal solutions with 5000 parts per million (ppm) concentration (99.99% pure silver, average particles diameter of 10–50 nm, 5000 ppm, Silver-Sol®, Nanosilver Manufacturing Sdn. Bhd., Malaysia) were prepared according to our previous work [6]. The Ag NPs were subjected to evaporation at 100 °C to remove excess water by 60%. Then, 1.5 v/v% Ag NPs was dropped into PEDOT:PSS (0.5 wt.%: 0.8 wt.%) containing 1.3 wt.% dispersion in H₂O (1 S cm⁻¹) (conductive grade, Sigma Aldrich, Malaysia) dispersion in the ultrasonic bath and left agitated for 20 min at room temperature to minimize the nanoparticles agglomeration. After that, the solution was prepared by magnetically stirring with and 5 v/v% DMSO (C₂H₆OS, 99%, molarity of 78.13 g mol⁻¹), at 300 rpm for 20 min. Then, the woven cotton fabric with a GSM of 180 supplied by the local manufacturer (Malaysia) was immersed in the PEDOT:PSS/Ag NPs/DMSO composite dispersion by gently stirring for 5 min and left for various time: 3, 5, and 7 h at room temperature. The immersion was performed only once. Further work on adding 0.5 v/v% PU grade U4101 (39–41% solid content, Alberdingk Boley) in the dispersion using an optimum immersion duration was carried out with the same steps. Finally, the samples were dried at 90 °C for 30 min followed by curing at 130 °C for 5 min using an oven to obtain the conductive fabric. Table 1 lists the materials' abbreviation of the samples.

Table 1 Materials' abbreviation of samples

Samples	Material's abbreviation	Composition (v/v%)				Immersion time (h)
		PEDOT:PSS	Ag NPs	DMSO	PU	
Untreated fabric	UTF					
PP/AgNP/DMSO_3h	TF1	1	1.5	5		3
PP/AgNP/DMSO_5h	TF2	1	1.5	5		5
PP/AgNP/DMSO_7h	TF3	1	1.5	5		7
PP/AgNP/DMSO/PU_5h	TF4	1	1.5	5	0.5	5

2.2 Characterization and Testing

The functional groups existed in the samples were determined using a Fourier Transformed Infrared (FTIR) spectrophotometer (Bruker INVENIO-S, United States) within the range from 4000 to 600 cm^{-1} with resolution of 4 cm^{-1} . Scanning Electron Microscope (SEM) images of samples were taken by JEOL SEM (JSM-IT100 InTouchScope™, Japan). The samples were cut and sputter-coated with palladium prior observation using SEM. Surface resistance measurements of samples were measured using a Prostat Resistance Meter (PRS-801, USA). A SHIMADZU universal tensile machine was used to investigate the tensile strength and elongation properties on doped PEDOT:PSS-based fabric according to ASTM D5035-95 [7]. The testing was done on a 10 mm broad sample that was carefully hammered in the wale direction using a homemade spacer equipped with sharp blades. Contact angle measurement (OCA20 instrument; Dataphysics, Germany) was used to measure the surface contact angle of PEDOT:PSS doped Ag NPs. Images of the droplet were taken to measure the contact angle from different parts of the sample and an average contact angle was calculated for each sample.

3 Results and Discussion

3.1 FTIR Analysis

The analysis of FTIR spectra shows the hydrogen bond interaction between PEDOT:PSS, Ag NPs, DMSO, PU, and the fibers of cotton fabric in Fig. 1. The characteristic peaks that were attributed to O–H bond stretching are shifted and the intensity decreased indicating the doped PEDOT:PSS has occupied the surface hydroxyl (OH) groups of the cotton fabric. C = O bond at 1710 cm^{-1} shows prominent peak due to the addition of DMSO that has altered PEDOT:PSS chains by forming hydrogen bond with PSS and carbonyl group. The vibration at 1112 cm^{-1} is

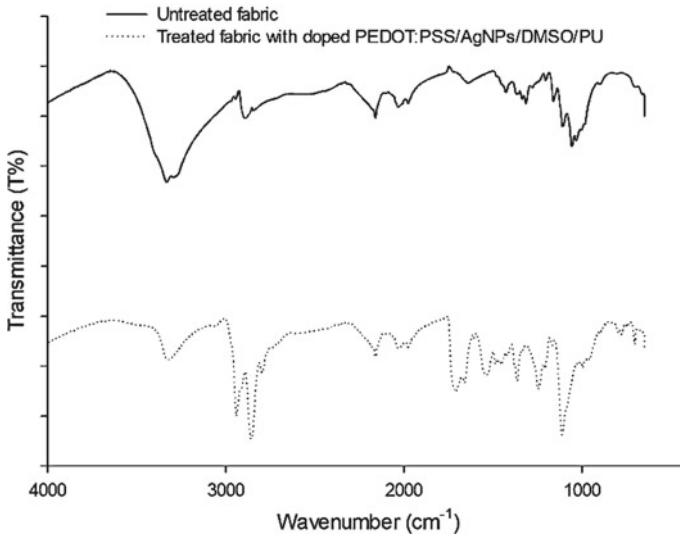


Fig. 1 FTIR spectra of untreated and treated cotton fabric with doped PEDOT:PSS

due to the C–O–C bond stretch in the ethylenedioxy group. The presence of the functional groups of the composite formulation corresponds to the successful introduction of conductive enhancers to the PEDOT:PSS dispersion by immersion method.

3.2 Morphology

Figure 2a exhibits the rough surface of untreated cotton fabric with fibers wrapping each other. Immersing the fabric in pristine PEDOT:PSS resulting more even and smooth appearance reflecting to the covered PEDOT:PSS (Fig. 2b). The smooth surface morphology of PEDOT:PSS/Ag NPs/DMSO/PU-based cotton fabric indicates that the fibers have been coated and the gaps between them have been filled. As a result, the fabric surface was covered with a continuous thin film of PU (Fig. 2c) [8].

3.3 Electrical Resistance

The surface resistance of the treated fabric with doped PEDOT:PSS was lowered by many orders of magnitudes from $50.3 \times 10^8 \Omega$ as listed in Table 2. It was found that the resistance of PEDOT:PSS doped Ag NPs and DMSO is the lowest when immersed for 5 h, followed by 3 h and 7 h with a value of 35.7Ω , 42.3Ω and 47.7Ω respectively. The decrease in resistance is due to the homogeneous dispersion of

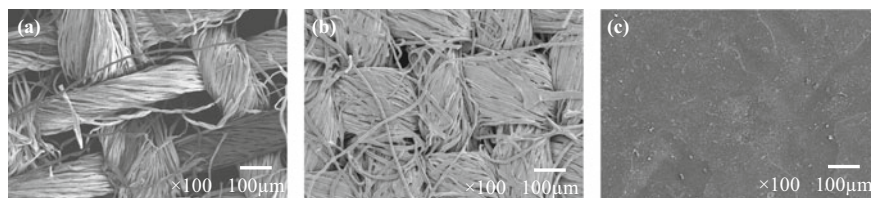


Fig. 2 SEM images of cotton fabric: **a** untreated, treated by immersion with **b** PEDOT:PSS/Ag NPs/DMSO, and **c** PEDOT:PSS/Ag NPs/DMSO/PU

Table 2 Surface resistance of cotton fabric treated with doped PEDOT:PSS

Samples	Electrical resistance (Ω)
UTF	$5.03\text{E}+09 \pm 4.26\text{E}+08$
TF1	$4.23\text{E}+01 \pm 4.41\text{E}+00$
TF2	$3.57\text{E}+01 \pm 2.03\text{E}+00$
TF3	$4.77\text{E}+01 \pm 4.18\text{E}+00$
TF4	$2.30\text{E}+05 \pm 6.00\text{E}+04$

doped PEDOT:PSS in the yarn and fiber pores [5]. Using an optimum time of 5 h of immersion, the composite formulation was added with PU, and it was observed that the resistance is slightly increases by a factor of 1000 probably due to the fact that PU provides greater strength and toughness of the substrate [9]. The obtained resistance are lower than the one reported by Azman et al. [3] because of the presence of metal nanoparticles and organic solvent that allow charges to flow through the cellulosic fiber. Different fabric material and structure used in this work is woven cotton, while the one reported used knitted polyamide/lycra [5]. The trend of lower resistance after immersion of fabric with the conductive polymer solution are in agreement with the findings reported [3–5].

The mechanism for the lower resistance of the immersed fabric in PEDOT:PSS doped Ag NPs and DMSO at 5 h can be related to the chemical structure shown in Fig. 3. The removal of insulating PSS chains around PEDOT chains by DMSO [10], creating interaction between Ag^+ and PSS^- and establishing a bridge between the isolating PSS chains and the conductive PEDOT chains [11]. The structure is rearranged because of the reducing Coulombic interaction between PEDOT and PSS with incorporation of Ag NPs and DMSO.

3.4 Tensile Properties

Treated cotton fabric with PEDOT:PSS/AgNP/DMSO significantly decreases tensile strength by 53% compared to untreated fabric (Fig. 4a) because of the damaged cellulosic fiber due to hydrolyzed in an acidic environment [8]. Adding PU to the

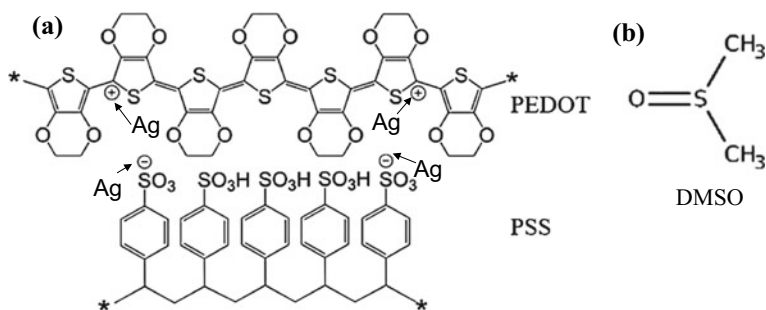


Fig. 3 Chemical structure of **a** PEDOT:PSS/Ag NPs, and **b** DMSO

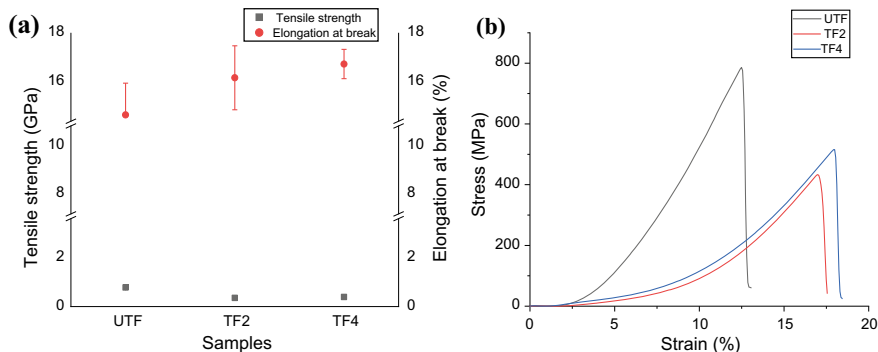


Fig. 4 Tensile properties of untreated and treated cotton fabric by immersion of doped PEDOT:PSS **a** tensile strength and elongation at break, and **b** stress–strain curve

doped PEDOT:PSS slightly increases tensile strength by 8% because its penetration keeps the yarns holding together from fracture [9]. Stress–strain curve plotted in Fig. 4b supports the increasing flexibility of the treated fabric from 14 to 17%. This is due to the polymer chain structure of PU consist of soft and hard segments that provide high elongation and good stiffness, respectively [8].

3.5 Wettability

Wettability behavior of samples are shown in Fig. 5. The comparison between contact angles before and after immersion indicates increased in hydrophobicity due to the increasing contact angle at 26%. This effect can be related to the hydrophilic PSS being partially removed when the fabric is immersed in PEDOT:PSS mixed with Ag NPs, DMSO and PU. The decrease in hydrophilicity of the samples also attributed to the change in the polarity of the carbonyl group discussed in the FTIR analysis.

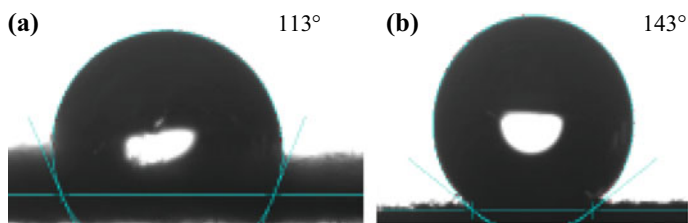


Fig. 5 Water contact angle measurement of treated fabric with **a** PEDOT:PSS, and **b** doped PEDOT:PSS (TF3)

4 Conclusion

Immersion of fabric with PEDOT:PSS doped Ag NPs and DMSO lower the electrical resistance compared to the untreated fabric at 5 h. The smooth surface of treated fabric supports the findings with the hydrogen bonding existence in FTIR spectra. Adding PU in the treated fabric improve the flexibility. The wetting behavior of the treated fabric indicates its hydrophilicity. Altogether, immersing cotton fabric with doped PEDOT:PSS in this study offers potential use for electrode in bioelectronic applications because of its low electrical resistance.

Acknowledgements This work was supported by Ministry of Education (MOE) through Fundamental Research Grant Scheme (FRGS/1/2018/TK05/UIAM/02/2).

References

1. Tadesse MG, Loghin C, Chen Y, Wang L, Catalin D, Nierstrasz V (2017) Effect of liquid immersion of PEDOT:PSS-coated polyester fabric on surface resistance and wettability. *Smart Mater Struct* 26(6)
2. Azmy U, Ahmad Z, Ahmad Shahrim N, Azman AW, Fajingbesi FE (2020) Effects of silver nanoparticles concentration on resistivity of PEDOT:PSS thin conductive films. *TEST Eng Manage* 83(5–6):1008–1013
3. Azman AW et al (2018) An analysis of a flexible dry surface electrodes. *Indones J Electr Eng Comput Sci* 10(1):74–83
4. Shahrim NA, Ahmad Z, Azman AW, Buys YF, Sarifuddin N (2021) Mechanisms for doped PEDOT:PSS electrical conductivity improvement. *Mater Adv* 2:7118–7138
5. Tadesse MG, Mengistie DA, Chen Y, Wang L, Loghin C, Nierstrasz V (2019) Electrically conductive highly elastic polyamide/lycra fabric treated with PEDOT:PSS and polyurethane. *J Mater Sci* 54(13):9591–9602
6. Tokarska M (2019) Characterization of electro-conductive textile materials by its biaxial anisotropy coefficient and resistivity. *J Mater Sci Mater Electron* 30(4):4093–4103
7. Standard test method for breaking force and elongation of textile fabrics (strip method) (2019) <https://www.astm.org/d5035-95.html>. Accessed 28 Apr 28 2022
8. Gunesoglu S, Cerci E, Topalbekiroglu M (2017) The improved breathability of polyurethane coated cotton fabric via micro-cracking. *J Text Inst* 108(10):1815–1821

9. Bhuiyan MAR, Wang L, Shanks RA, Ding J (2019) Polyurethane–superabsorbent polymer-coated cotton fabric for thermophysiological wear comfort. *J Mater Sci* 54(12):9267–9281
10. Chou TR, Chen SH, Te Chiang Y, Lin YT, Chao CY (2015) Highly conductive PEDOT:PSS film by post-treatment with dimethyl sulfoxide for ITO-Free liquid crystal display. *J Mater Chem C* 3: 3760–3766
11. Xiong Z, Dong C, Cai H, Liu C, and Zhang X (2013) Composite inks of poly(3,4-ethylenedioxythiophene)/poly(styrenesulfonate)/ silver nanoparticles and electric/optical properties of inkjet-printed thin films. *Mater Chem Phys* 141(1): 416–422

An Experimental Study on the Tensile Strength of Friction Stir Welded AA5052 Aluminum Alloy



Ky-Thanh Ho , Ba-Hoi Nguyen, Ngoc-Tuan La, Thai-Son Le, and Van-Thong Pham

Abstract This paper presents new experimental study on the tensile strength of friction stir welded (FSW) joining similar aluminum AA5052 sheet alloys, which alloy is widely used in ship building, aerospace and automotive industries. The experiments were designed and were implemented. In the investigation range, the results showed that the mean value of ultimate tensile strength reaches maximum at rotation speed of 1000 rpm and feed rate of 150 mm/min. The results also shows that the quadratic quantity $s * s$ has the largest contribution on the tensile strength of joining samples. The experimental results would be useful for further research on the design and operation of FSW processing.

Keywords FSW—Friction Stir Weld · AA5052 aluminum alloy · Tensile strength

1 Introduction

Nowadays many industrial applications, steel is readily replaced by non-ferrous alloy, in most cases aluminum alloys are used. Some of these materials allow for a significant reduction of weight because they combine mechanical strength comparable with structural steel and low weight [1]. However, the joining of aluminum alloys can sometimes cause serious problem, such as weld cracking, porosity, heat-affected zone (HAZ) degradation [2, 3]. Friction stir welding offers many significant benefits for welding of aluminum alloy. Invented and patented by The Welding Institute, United Kingdom in 1991, friction stir welding (FSW) is one of the solid state welding processes in which the materials do not melt for the joining. Some studies showed that FSW allows both low and high melting point metals, such as aluminum, lead, magnesium, steel, titanium, zirconium, copper those are continuously welded with a non-consumable rotating tool, mechanically traversed through the work materials

K.-T. Ho (✉)

Faculty of Mechanical Engineering, Thai Nguyen University of Technology, Nguyen, Vietnam
e-mail: hkyhthanh@tmut.edu.vn

B.-H. Nguyen · N.-T. La · T.-S. Le · V.-T. Pham

Faculty of Mechanical Engineering, Vinh University of Technology Education, Vinh, Vietnam

[4, 5]. During FSW processing, friction heat is generated between the material of the work-pieces and the wear resistant welding tool shoulder and pin [5]. So FSW can locally eliminate casting defects and refine microstructures; by that way this process maintains and improves strength and ductility, increases resistance to corrosion and fatigue, enhances formability and improves other properties of the joining metals [1].

Usually, the quality joining of FSW is evaluated through ultimate tensile strength [6–8], microstructure [5, 8, 9], hardness of material [5, 7]. There are many technological parameters that affect the quality joining of FSW, such as: tool rotation speed, feed rate or welding speed, geometry of tool. The objective of this work is to investigate the effect of rotational speed s and feed rate f on the tensile strength of the friction stir welded AA5052 aluminum sheet alloy.

2 Experimental Set-Up

2.1 Material and Experimental Implementation

In this study, AA5052 aluminum sheet alloy was used. Chemical composition this alloy is shown in Table 1 and mechanical properties are depicted in Table 2. This is one of the types of deformed aluminum alloys and is non-heat-treatable. Due to its high strength and hardness [9], AA5052 aluminum alloy is commonly used for inner body and trim panels in the automotive industry [10]; vehicle components, ships, and vessels [11]. Samples were cut to size of $L \times B \times H$ (in mm), as $200 \times 100 \times 5$.

A CNC vertical milling center Vcenter-85, as shown in Fig. 1a, was selected as experimental machine. Figure 1b shows a photograph of the experimental diagram

Table 1 The elemental composition of AA5052 aluminum alloy

Chemical element	Mg	Si	Fe	Cu	Cr	Zn	Mn	Al
Weight content (%)	2.20–2.80	0.25 Max	0.40 Max	0.10 Max	0.15–0.35	0.10 Max	0.10 Max	Remaining

Table 2 Mechanical properties of AA5052 aluminum alloy

Property	Notation	Unit	Value
Young modulus	E	GPa	70
Yield strength	σ	MPa	190
Ultimate tensile strength	σ_u	MPa	210
Brinell hardness		HB	60

for FSW process. In the Fig. 1b, the FSW tool (2) was attached on the head of vertical milling center (1). The work piece (7) was held on the mold (4), both were clamped by vertical clamp (3) and horizontal clamp (5) on table (6) of machine tool. During the FSW process, table (6) will perform a reciprocating motion in the y direction to perform the full length of the weld. Meanwhile, the FSW tool (2) moved vertically and rotated by head of machine tool (1) to create depth of penetration and perform FSW process.

The processing tool is a stirrer (as depicted in Fig. 2a), with the shape of a cone and right thread, shoulder diameter $\varnothing 15$, shoulder concave angle 5° , stirrer length 4.8 mm. The stirring tool is made of 40X steel. The detailed design parameters of the stirring tool are shown in Fig. 2b.

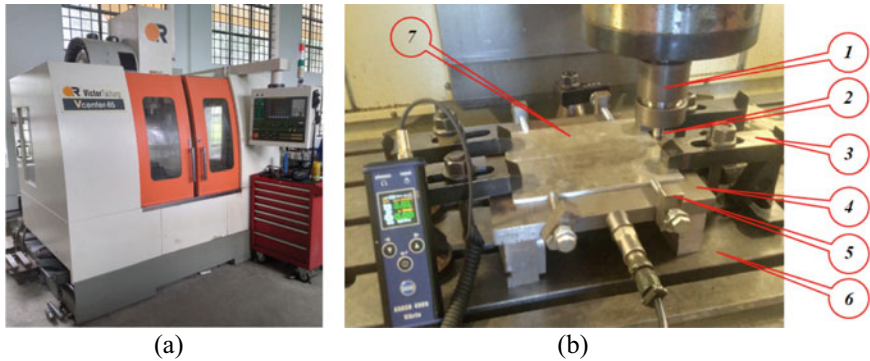


Fig. 1 Photos of vertical milling center Vcenter-85 (a) and the experimental diagram (b); 1—head of vertical milling center; 2—FSW tool; 3—vertical clamp; 4—mold; 5—horizontal clamp; 6—table of machine tool; 7—workpiece

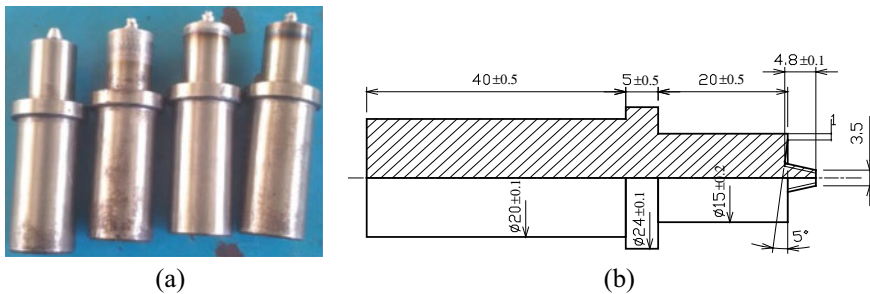


Fig. 2 A photo (a) and detailed design parameters (b) of the FSW tool

Table 3 Input parameters and their levels

Parameters, notation	Units	Levels		
		Level 1	Level 2	Level 3
Rotational speed, s	rpm	800	1000	1200
Welding speed, f	mm/min	100	150	200

Table 4 L9 array of orthogonal

Experiment number	Rotational speed, s (rpm)	Welding speed, f (mm/min)
1	800	100
2	800	150
3	800	200
4	1000	100
5	1000	150
6	1000	200
7	1200	100
8	1200	150
9	1200	200

2.2 Experimental FSW Design

In order to examine the influences of FSW parameters on the tensile strength of joining, Minitab 18 Software (Minitab Inc., USA) was used to build experimental procedure. The FSW parameters chosen for studying on the welding strength was rotational speed s (rpm), welding speed of FSW process f (mm/min), both with three levels (see Table 3). Meanwhile, the depth of penetration t (mm) was kept constant in all experiments, as 0.15 mm. The L9 orthogonal array was selected using design of experiments, as shown in Table 4.

2.3 Designing Sample for Experimental Tensile Test

After FSW processing, welded quality is checked by ultrasonic flaw detector OLYPULSEPOCH 600. Then work pieces were cut to form the sample tensile test. Figure 3a depicts the detailed specifications and Fig. 3b shows one of the experimental samples of tensile test. Welding strength of the samples was examined by universal tensile testing machine.

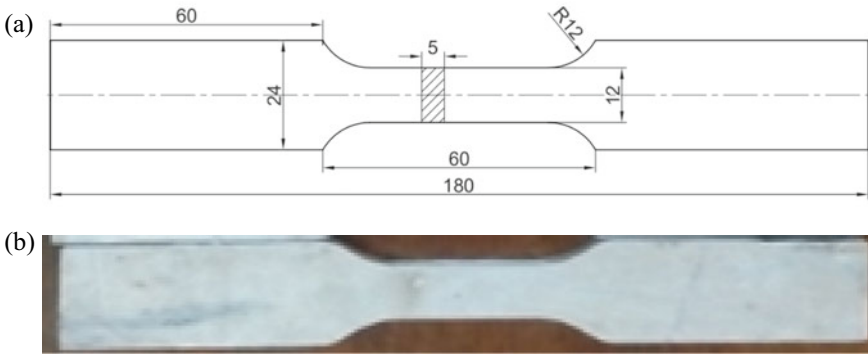


Fig. 3 Detailed specifications (a) and photo of experimental tensile test samples (b)

3 Results and Discussion

Table 5 depicts the experimental results of ultimate tensile strength. Where, σ_i ($i = 1-3$) is the ultimate tensile strength of the FSW corresponding to the first, second and third tensile tests; σ_m is mean ultimate tensile strength of three tests. Table 6 depicts analysis of variance (ANOVA) of means of tensile strength. Figure 4 shows surface and contour plot of σ_m versus rotation speed s and feed rate f , using Minitab 18 Software.

From Table 6, it can be concluded that the process is in control from the F test for the 95% confidence level on each parameter. Table 6 also shows that the quadratic quantity $s * s$ has the largest contribution on the tensile strength of joining samples. Meanwhile, the interaction between the two parameters $s * f$ is insignificant.

The results from Fig. 4 shows that the tensile strength of the FSW joining reached its maximum value, upper 172 MPa, in the region around $s = 1000$ rpm and $f = 150$ mm/min, average values of tool rotation speed and feed rate. The mean of maximum value of tensile strength is about 81.9% comparing with ultimate strength

Table 5 Experimental results of ultimate tensile strength

Std. order	Run order	s	f	σ_1	σ_2	σ_3	σ_m
3	1	800	200	159.3	158.7	158.3	158.7
4	2	1200	200	159.4	158.4	157.6	158.4
2	3	1200	100	153.4	155.3	155.9	154.9
8	4	1000	200	168.5	167.9	167.3	167.9
9	5	1000	150	170.5	171.2	172.4	171.4
5	6	800	150	167.8	168.2	170.2	168.7
1	7	800	100	155.3	156.0	155.6	155.6
6	8	1200	150	161.4	163.3	164.2	162.9
7	9	1000	100	169.8	168.4	168.9	169.0

Table 6 Analysis of Variance (ANOVA) of means of tensile strength

Source	DF	Adj. SS	Adj. MS	F-value	P-value
Model	5	291.511	58.302	5.54	0.095
Linear	2	12.748	6.374	0.61	0.601
<i>s</i>	1	7.707	7.707	0.73	0.455
<i>f</i>	1	5.042	5.042	0.48	0.538
Square	2	278.723	139.361	13.25	0.032
<i>s</i> * <i>s</i>	1	183.042	183.042	17.40	0.025
<i>f</i> * <i>f</i>	1	95.681	95.681	9.10	0.057
2-Way interaction	1	0.040	0.040	0.00	0.955
<i>s</i> * <i>f</i>	1	0.040	0.040	0.00	0.955
Error	3	31.551	10.517		
Total	8	323.062			

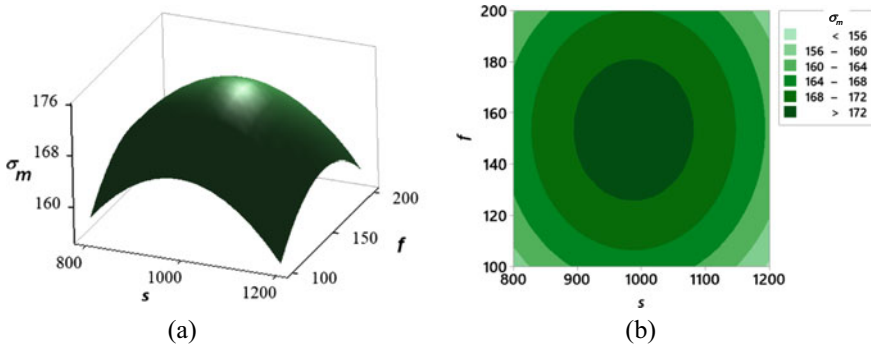


Fig. 4 Surface plot (a) and contour plot (b) of σ_m versus *s* and *f*

of original alloy (see Table 2). This can be explained by the consistence of *s* and *f* so that the temperature at the weld is large enough to minimize defects in the joint. Meanwhile, the lower or higher of both *s* and *f* give tensile strength values much lower than the maximum value, about lower than 156 MPa. The lower tensile strength of the joining compared with the tensile strength of the original aluminum alloy can be explained by a number of reasons such as: (1) the appearance of pores in the weld; (2) the transfer of heat from the welding zone to the adjacent areas.

4 Conclusion

The results showed that ultimate tensile strength of the joining depended on both rotation speed *s* and feed rate *f*. In the investigation range, the mean value of ultimate

tensile strength reaches maximum at rotation speed $s = 1000$ rpm and feed rate $f = 150$ mm/min. The results also shows that the quadratic quantity $s * s$ has the largest contribution on the tensile strength of joining samples. The experimental results would be useful for further research on the design and operation of FSW processing.

References

1. Singh G, Singh K, Singh J (2011) Effect of axial force on mechanical and metallurgical properties of friction stir welded AA6082 joints. *Adv Mat Res* 383–390:3356–3360
2. El-Batahy AM, Terad B, Omar A (2013) Effect of friction stir welding parameters on properties of AA6061 aluminum alloy butt welded joints. In: *Proceedings of the 1st international joint symposium on joining and welding.* Woodhead Publishing, pp 33–40
3. Çam G, İpekoğlu G (2016) Recent developments in joining of aluminum alloys. *Int J Adv Manuf Technol* 91:1851–1866
4. Hattingh DG et al (2015) Friction processing as an alternative joining technology for the nuclear industry. *J South Afr Inst Min Metall* 115:903–912
5. Joseph B et al (2015) Investigations on the effect of tool geometries on friction stir welded 5052 H32 aluminium alloy. *Appl Mech Mater* 766–767:712–720
6. Hariharan V et al (2021) Experimental investigation of friction stir welding on aluminium AA6063. *Mater Today: Proc* 47:6830–6834
7. Krishna GG, Reddy PR, Hussain MM (2014) Hardness and tensile behavior of friction stir welded aluminum AA6351 alloy. *J Mech Eng* 44:23–26
8. Pedapati SR et al (2020) Effect of process parameters on mechanical properties of AA5052 joints using underwater friction stir welding. *J Mech Eng Sci* 14:6259–6271
9. Paramaguru D, Pedapati SR, Awang M (2018) Microstructural analysis on underwater friction stir welded 5052 aluminium alloy. *AIP Conf Proc* 2035(1):050005
10. Jeon C-S et al (2012) Material properties of friction stir spot welded joints of dissimilar aluminum alloys. *Trans Nonferrous Met Soc China* 22:s605–s613
11. Tiwan I, Kusmono MN (2021) Microstructure and mechanical properties of friction stir spot welded AA5052-H112 aluminum alloy. *Heliyon* 7(2):e06009

Palladium/Lathanum Cobaltite Catalyst Polymer Exchange Membrane Fuel Cell for Electric Vehicle



Ataur Rahman, Sany Ihsan, and Ali Momoud

Abstract An 100% battery-electric vehicle has a limited travel distance about 150–200 km and a battery life of about 5–6 years. A FC hybrid car has been demonstrated for the mileage about 500 km with a single full charge battery and 2 L of hydrogen. Currently available fuel cell materials (Platinum, Pt) appear to be adequate with a high-cost entry point, easily poisoned, fermented (forming alcohol), and gives off carbon monoxide (CO). The aim of this study is to develop a palladium (Pd)/lathanum cobaltite (LaCoO_3) catalyst polymer proton-exchange-membrane (PEM) FC for the cost reduction, prevents FC poisoning, fermentation and energy efficient. Furthermore, palladium a large volumetric quantity of H_2 absorption at room temperature and forms palladium hydride (PdH_x) could be an attraction for the FC technology development. Two-layers of Pd/LaCoO₃ catalyst will be fused as a catalyst by gas-diffusion technique for the FC'S anode and cathode. The polymer electrolyte membrane (PEM) will be fused together with the Pd/LaCoO₃ catalyst for FC model. It is expected that Pd/La/CoO₃_PEM FC stack will improve efficiency of FC about 40% and generate open-circuit-voltage 0.9 V and closed-circuit-current 1A.

Keywords Pd/LaCoO₃ Catalyst electrode · Fuel cell · High efficient energy source

1 Introduction

The global trends toward the introduction of next-generation vehicles, such as battery-powered electric vehicles and hydrogen fuel cell electric vehicles, will be beneficial in reducing fossil-fuel dependency, which is more important in the current crisis of rising fossil-fuel prices due to the Ukraine war than combating climate change. However, the problems associated with the 100% battery-electric vehicle, which has a limited travel distance about 150–200 km and a battery life of about 5–6 years [1–3]. Furthermore, the charging time for a battery electric car is 5–6 h. In addition, dumping damaged batteries can result in landfill fires that might burn for years

A. Rahman (✉) · S. Ihsan · A. Momoud
Department of Mechanical Engineering, Kulliyah of Engineering, International Islamic University Malaysia, 53100 Kuala Lumpur, Malaysia
e-mail: arat@iium.edu.my

© The Author(s), under exclusive license to Springer Nature Singapore Pte Ltd. 2023
Md. A. Maleque et al. (eds.), *Proceeding of 5th International Conference on Advances in Manufacturing and Materials Engineering*, Lecture Notes in Mechanical Engineering, https://doi.org/10.1007/978-981-19-9509-5_53

397

underground. As a result, harmful substances are released into the air, groundwater, and environment, increasing the risk of human exposure (Battery University, 2019). Many studies show that the hydrogen fuel cell and lithium battery hybrid power is the best option for an electric vehicle, which could allow the vehicle to cover the traveling distance of 400–500 km with a full charge battery and an FC with a 5 kg of hydrogen tank. The FC hybrid power system for the electric vehicle will span about 15 years. Thus, the new FC technology will contribute to the world's reach a 20% renewable energy target by 2025 and reduction of CO₂ emission per capita of the nation.

Hydrogen fuel cell vehicles (FCVs) have recently emerged as a zero tailpipe-emission alternative to the battery electric vehicle (EV). Like battery vehicles, FCVs produce no tailpipe emissions (other than water vapor) and also have the potential to be near-zero-emission on a full fuel-cycle basis when coupled with renewable energy sources. As the lightest element in existence, hydrogen has several intrinsic characteristics that make it an attractive transportation energy carrier. It has a high energy density by weight, and it can be produced in large quantities from a diverse array of primary energy sources [4]. Furthermore, in contrast to battery recharging, hydrogen can be refueled at speeds comparable to gasoline. These advantages have generated considerable interest in FCVs among governments and the automotive industry. Since that initial deployment, demonstration projects involving hydrogen fuel cell buses began to expand rapidly [5]. These deployments offered multiple opportunities to evaluate passenger response and perception of FC technology. This included hydrogen bus deployments in Luxembourg, Berlin, Perth, and London, which offered an opportunity to explore consumer response on a broader scale.

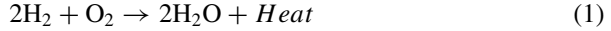
Common types of hydrogen FCs are: Polymer Electrolyte Fuel Cells (PEFCs), Direct Methanol Fuel Cells (DMFCs), and Phosphoric Acid Fuel Cells (PAFCs). Chemical reactions of fuel cells in power generation are highly dependent on the use of platinum (Pt) catalysts [5, 6]. Platinum, a noble metal catalyst, increases the cost of fuel cells, which is a major obstacle to the availability of fuel cells worldwide. In addition, platinum used as an anode material is easily poisoned, fermented (forming alcohol), and gives off carbon monoxide (CO) due to the lower activity of the oxygen reduction reaction (ORR) [6, 7]. Thus the hydrogen fuel cell efficiency shows an average of 30%.

This study presents a palladium (Pd)/ lathanum cobaltite (LaCoO₃)_PEM FC for electric vehicles that has the characteristics of increasing oxygen reduction reaction rate (ORR), preventing catalyst poisoning, reducing CO emission, and reducing the FC costs without interrupting the FC efficiency which can be supported by the authors research output [8]. In addition, Pd/LaCoO₃_PEM FC has the noble property of absorbing large volumes of hydrogen at room temperature and pressure and subsequently forms palladium hydride (PdH_x). While the high photon energy of 60 Co (average energy = 1.25 meV) and cooling system will make the Pd/LaCoO₃_PEM FC more energy efficient, longer life and reduce operational cost [9].

2 Methodology

2.1 Mathematical Model

The FC's electrical activity is focused on the transformation of chemical energy contained in reactants to electrical energy. The amount of energy released as a result of the reaction is:



The available energy of a chemical reaction that can be used to do work is called Gibb's free energy (ΔG). Changes in Gibbs free energy can also be expressed this form:

$$\Delta G = G_{\text{Products}} - G_{\text{Reactants}} \tag{2}$$

$$G = H - TS \tag{3}$$

where, G is the Gibbs free energy in J, S entropy J/K, H enthalpy ($\Delta H = mc_p\Delta T$, m is mass, g, c_p specific heat, J/g* $^{\circ}\text{C}$), and T temperature $^{\circ}\text{C}$, J (At ambient conditions (Pressure 1 bar), water boils at 100°C and the specific enthalpy of water is 418 kJ/Kg, and T temperature K. The enthalpy of water at 100°C is 40.7 kJ/mol and entropy 109.1 J/(mol*K) (entropy, $\Delta S = \frac{\Delta T}{T}$).

$$\text{Entropy of hydrogen, } S_{1\text{bar}} = 130.68 \text{ J/mol} * \text{K}$$

By considering the independent activity (a) of hydrogen (H_2), oxygen ($\text{O}^{1/2}$) and water (H_2O), The changes of Gibbs free energy per mole can be estimated as:

$$\Delta G = \Delta G^0 - RT \ln \left[\frac{\alpha_{\text{H}_2} \alpha_{\text{O}_2}^{\frac{1}{2}}}{\alpha_{\text{H}_2\text{O}}} \right] \text{ with } \alpha = \frac{P_i}{P_0} \tag{4}$$

where, G° is the Gibbs free energy reference values 8.6 kJ/mol at 289 K and 1 atm, R gas constant ($R = 8.3145 \text{ J}_{\text{SC}}/\text{mol} * \text{K}$), a is the activity, P_i partial pressure in Pa, P_0 standard pressure Pa ($p_0 = 1 \text{ atm} = 101.3 \text{ kPa}$), a_{H_2} , a_{O_2} , and $a_{\text{H}_2\text{O}}$ are the activity of H_2 , O_2 , and H_2O respectively.

$$E_{\text{Nerrnst}} = E^0 - \frac{RT}{nF} \ln \left[\frac{\alpha_{\text{H}_2} \alpha_{\text{O}_2}^{\frac{1}{2}}}{\alpha_{\text{H}_2\text{O}}} \right] \text{ with } E^0 = E_0^0 - (T - T_0) \left(\frac{\Delta S^0}{nF} \right) \tag{5}$$

where, n is the number of electrons moving ($n = 2$), F is the Faraday's constant (96,485 C/mol), E_0^0 is the Nernst reference potential, V , S° is the entropy reference (known values) J/K, E_0^0 reference potential of FC (1.22 V) at steady state condition V , and T_0 temperature at room temperature ($T_0 = 298.15$ K).

Nernst Voltage,

$$E_n = \begin{cases} E^0 + (T - 298) \frac{-44.43}{nF} + \frac{RT}{nF} \ln(P_{H_2O} P_{O_2}^{1/2}) & \text{when } T \leq 100^\circ\text{C} \\ 1.229 + (T - 298) \frac{-44.43}{nF} + \frac{RT}{nF} \ln(P_{H_2O} P_{O_2}^{1/2}) & \text{when } T > 100^\circ\text{C} \end{cases} \quad (6)$$

where, P_{H_2O} and P_{O_2} are the partial pressure of water vapor inside the stack (atm), w percentage of water vapor in the oxidant (%).

2.1.1 Overvoltage Activation

The instantaneous current density of the FC can be estimated using the following equation:

$$\eta_{act} = -\frac{RT}{\alpha n F} \ln \left[\frac{J}{J_0} \right] \quad \text{with} \quad J = J_0 \left[e^{\frac{-\alpha n F \eta}{RT}} - e^{\frac{(1-\alpha) n F \eta}{RT}} \right] \quad (7)$$

where, j_{sc} is density of current [A/cm²], j_0 is exchange current density A/cm² at no load, η overvoltage [V], and α a transfer coefficient.

2.1.2 Overvoltage Resistive

$$\eta_{ohm} = -J_0 \left[e^{\frac{-\alpha n F \eta}{RT}} - e^{\frac{(1-\alpha) n F \eta}{RT}} \right] R_a \quad (8)$$

where, η_{ohm} is the overvoltage resistive, V, R_0 specific resistance per area, ohm/cm²,

2.1.3 Overvoltage Concentration

$$\eta_{con} = -\frac{RT}{nF} \ln \left(1 - \frac{J}{J_0} \right) \quad (9)$$

The total FC voltage can be estimated as,

$$V_{cell} = E_{ernst} + \eta_{act} + \eta_{con} + \eta_{ohm} \quad (10)$$

Mass flow rate of hydrogen required to get the 70 A current with 100 cells can be estimated with considering the heating affect of hydrogen/min as:

$$N_{cell} = \frac{nF * \dot{m}_{h_2o}}{\Delta f H^0(H_2O_{gas}) * \eta_{nom}}, \quad \text{Hydrogen conversion efficiency}$$

$$\eta_{nom} = 55\% \tag{11}$$

where, $\Delta f H^0 (H_2O(gas))$ is the change of enthalpy of water gas = $241.83 \times 10^3 \text{ J/mol}$

3 Result and Discussion

The simulation studies has been conducted with considering the simulation parameters as shown in Fig. 1 and the Pd/Co₂O. PEM FC with considering the simulation parameters as shown in Table 1.

3.1 Pd/La/Co₂O₃ FC STACK

Fuel cell STACK modeling have not doe yet. But it will be made using the Pd/LaCoO₃_PEM electrodes (both anode and cathode). The cells interconnection will be made by a “separator” or “bipolar plate”. This will make connections all over a cathode of one cell and an anode of the next cell (hence “bipolar”). The bipolar plate will serve as a means of feeding oxygen to the cathode and hydrogen gas to the anode. This distribution of the reactant gases over the electrodes will be made using a ‘serpentine pattern flow channel’ formed into the surface of the plates. The

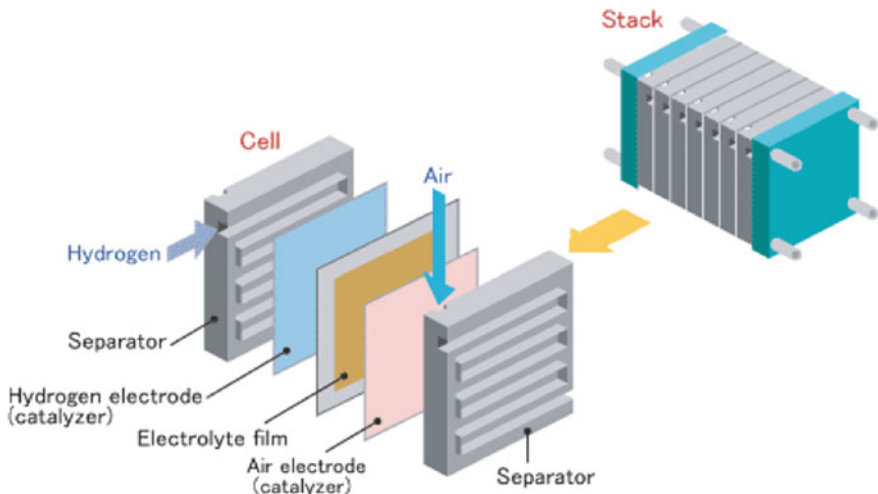


Fig. 1 Pd/LaCo₃ stack model

Table 1 Simulation parameters

Fuel cell	PEMFC—8.0 kW–120 Vdc
Voltage	V_0A(120), V_70A(100)
Normal operating point	
Number of cells	65
Stack efficiency (%)	55
Operating temperature (°C)	50 < T < 65 °C
Normal supply pressure: H ₂ _1.5 bar and O ₂ _1 bar	
Normal composition (%): H ₂ _99.99, O ₂ _21, H ₂ O_1	
Voltage overshoot @ peak O ₂ utilization (V): 100 V	
Peak O ₂ utilization (%): 80	

Pd/LaCoO₃ catalyst will be used as a hydrogen electrode catalyzer and air electrode (oxygen) catalyzer for both anode and cathode. The surface area of the catalyzer will be in contact with the reactants. Both reactant gases (hydrogen and oxygen) will be supplied under pressure into the flow channels of the plate. The collection of cells in series is known as a 'STACK'. Once the Pd/LaCoO₃ nanocomposite electrodes and the simulated characteristics are satisfied in terms of open-circuit voltage (V_{oc}) in the range of 700–900 mV per cell and short circuit current density (J_{sc}) in the range of 1300 to 1400 mA/cm², the FC model will be designed developed using the Pd/Co catalyst, an electrolyte film and a bipolar plate as shown in Fig. 1.

Figure 2 shows the IoT-based control system which will be developed from this study for testing the Pd/LaCoO₃ catalyst electrode PEM FC steady-state power generation. The model is equipped with a hydrogen flow sensor, oxygen flow sensor, motor rpm sensor, and controller. The flow sensor of the sensor will indicate the hydrogen tank pressure and the oxygen flow sensor will detect the flow of oxygen to the FC. While the motor sensor will detect the level of FC power generation. If it will indicate the lower than the steady power generation (not reported), then the pressure valve of the hydrogen will be open more than the pre-setting while the oxygen pump speed will be increased to increase the oxygen flow. The hydrogen flow sensor also sends the signal to the dashboard to show how long the hydrogen tank able to power the motor to propel/operate the system.

Figure 3 shows that a maximum mass flow rate of hydrogen 0.12 g/s at a tank opening of 85% is effective in producing a maximum current of 76 A and a temperature of 65 °C. With a temperature of 65 °C, a hydrogen flow of more than 0.12 g/s at tank valve opening of more than 85% causes a greater thermal effect, which tends to degrade PEM effectiveness and hydrogen generation due to a decrease in FC efficiency.

Figure 4 illustrates that despite raising the valve opening and allowing additional hydrogen, the FC is unable to produce higher current levels. This is primarily related to the problem of thermal affect. However, if an FC thermal management system is used, it can be effective.

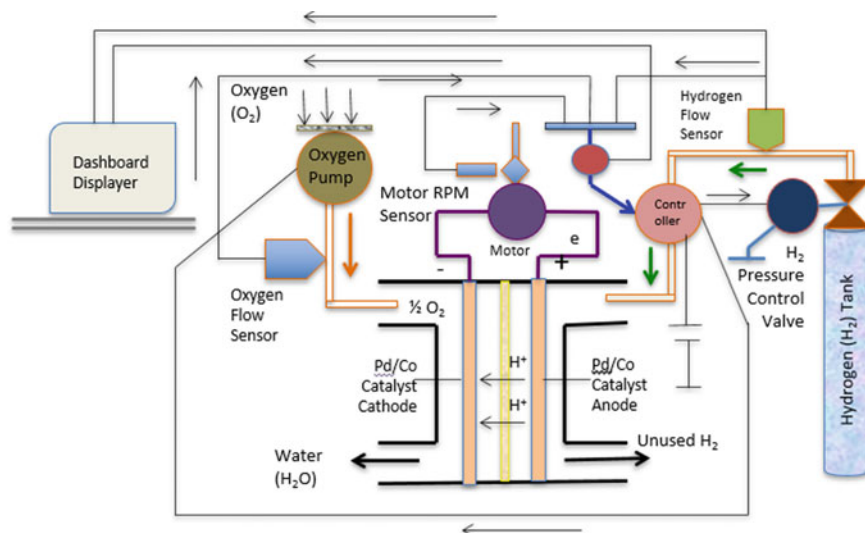


Fig. 2 IoT-based model to control the hydrogen flow

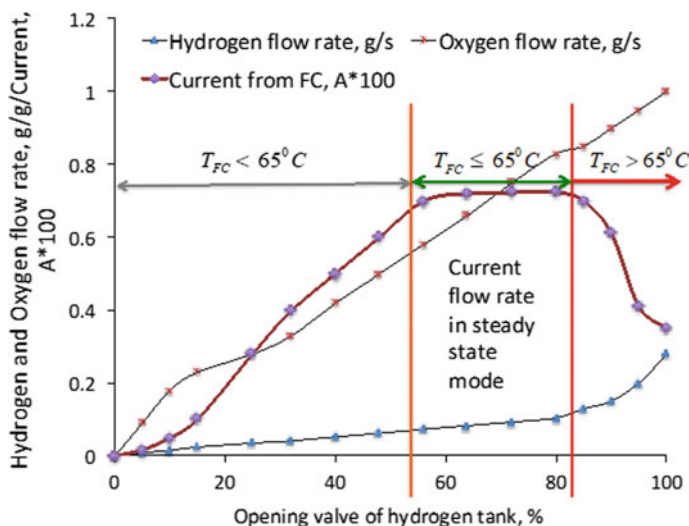


Fig. 3 Simulated performance of Pd/LaCoO₃

3.2 Performance Investigation of Pd/LaCoO₃ Catalyst PEM FC

The laboratory-scale Pd/LaCoO₃ catalyst fuel cell will be tested using a 100 ml hydrogen tank and 12-V DC motor. Performance investigation of palladium/cobalt

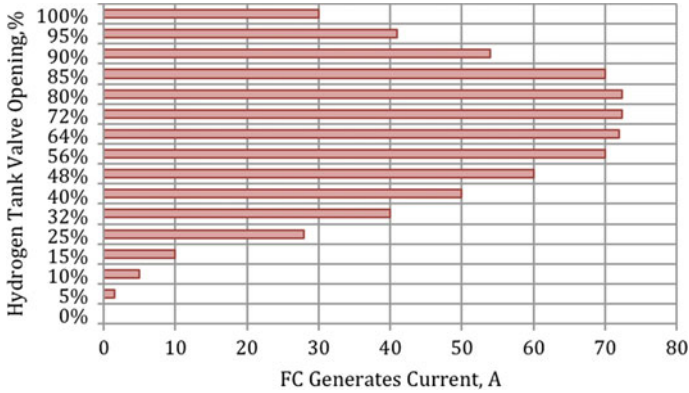


Fig. 4 Current generation by the Pd/LaCoO₃

catalyst electrode polymer proton exchange membrane fuel cell will be made in the laboratory in terms of open-circuit voltage, current density, hydrogen conversion efficiency, and carbon mono-oxide emission. In addition, the Pd/LaCoO₃_PEM FC hydrogen enrichment test will be conducted at room temperature without a hydrogen tank connected. This will be conducted by connecting the Pd/LaCoO₃ FC anode and cathode to an external electrical circuit with an IoT-based control model as shown in Fig. 5. Voltage generation will indicate hydrogen enrichment in the Pd/LaCoO₃ FC at room temperature and atmospheric pressure.

To power the EV, a Pd/LaCoO₃ catalyst PEM FC model will be developed, with 100 cells connected in series and parallel. It is expected the model will be able to power the EV for 200 km using about 1.8 kg (considering mass flow rate of hydrogen, 0.12 g/s based on Fig. 3 and opening the hydrogen tank valve about 80%) of hydrogen.

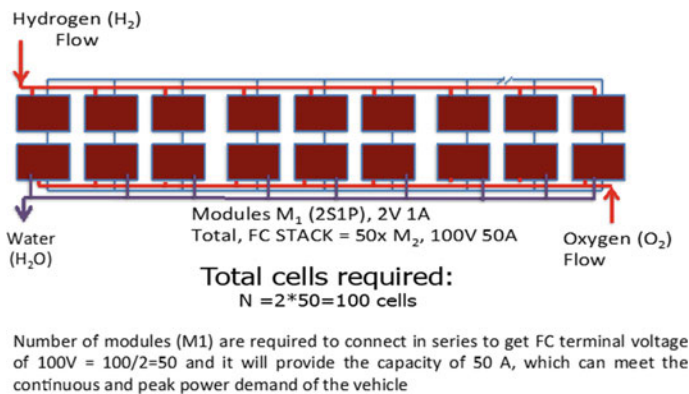


Fig. 5 Model of Pd/LaCoO₃ STACK for EV

4 Conclusion

The Pd/LaCoO₃ catalyst PEM FC mitigates the effects of climate change, reduces costs, increases ORR, and prevents FC poisoning, making the FC zero emission and preventing the fermentation towards alcohol formation. The Pd/LaCoO₃ electrode enriched hydrogen storage at room temperature and pressure, making the FC energy efficient. It is expected that Pd/LaCoO₃_PEM FC stack will improve efficiency of FC about 40% and generate open-circuit-voltage 0.9 V and closed-circuit-current 1 A.


Acknowledgements The authors are grateful to the International Islamic University Malaysia for the approval of the Flagship Project 2 entitled “Electric Coaster Innovation- Zero carbon ultrafast DC charging station for EV”.

References

1. Amritanshu S, Atul S (2016) Energy system analysis of the fuel cell buses operated in the project: clean urban transport for Europe. *Energy* 33(5):689–711
2. Rahman A, Rahman M, Sany II, Ahmad FI (2018) Power optimization of electric coaster. *Int J Electr Hybrid Veh Indersci Publ* 10(2):272–278
3. Singh S, Jain S, Tiwari AK (2015) Hydrogen: a sustainable fuel for future of the transport sector. *Renew Sustain Energy Rev* 51:207–214
4. Oscar LJ, Rhian S, Scott K (2019) Content analysis of interviews with hydrogen fuel cell vehicle drivers in Los Angeles. *J Transp Res Board* 2673(9)
5. Coutanceau C, Baranton S (2016) Electrochemical conversion of alcohols for hydrogen production: a short overview. *Wiley Interdiscip Rev Energy Environ* 5:388–400
6. Sasidharan S, Gopinathan MA, Takanori T, Takeo Y (2018) Cobalt-modified palladium bimetallic catalyst: a multifunctional electrocatalyst with enhanced efficiency and stability toward the oxidation of ethanol and formate in alkaline medium. *ACS Appl Energy Mater* 1(8):4140–4149
7. Manabe K (2015) Palladium catalysts for cross-coupling reaction. *Catalyst* 5(1):38–39
8. Brian D, Adams, Aicheng C (2011) The role of palladium in a hydrogen economy. *Materialstoday Sci Direct* 14(6):282–289
9. Rahman A, Hawlader MNA, Khalid H (2015) Two phase fuzzy controlled evaporative thermal management system for EVs/HEVs. *Int J Autom Technol* 28(4):297–304

Review on Fused Deposition Modelling Extruder Types with Their Specialities in Filament Extrusion Process



Muhammad Afif Md Azhar, Nor Aiman Sukindar , Mohd Hanafi Ani, Hazleen Bt Anuar, Shafie Bin Kamaruddin, Sharifah Imihezri Syed Shaharuddin, Mohd Yusry Mustafa, Erry Yulian Tribblas Adesta, Rudi Kurniawan Arief, and Mohd Hafis Sulaiman

Abstract 3D printing is one of the growing technologies in the entry era of the industrial revolution 4.0. Fused Deposition Modelling (FDM), one of the 3D printing methods, has advantages in the manufacturing process where various product shapes can be made. One of the advantages of FDM lies in the extruder used. Various types of extruders can be used and installed on FDM machines. Findings from a review of five types of extruders found that some models have the ability to extrude specific types of material. Each extruder has advantages and specializations, which can affect the printing result. Therefore, this paper reviews the types of extruders for FDM and their capabilities so that the selection of the type of extruder to be used can be made accurately.

Keywords FDM 3D printer · FDM extruder · Additive manufacturing · Rapid prototyping

1 Introduction

3D printing is a cutting-edge technology that allows users to turn a computer model into a tangible thing. It was first called rapid prototyping in 1980 since the goal of the technique was to make prototypes faster and cheaply. Additive process methods are used to create prototypes or 3D-printed objects. An object is made in an additive process by putting down consecutive layers of material until the product is complete, which is why this method is also known as additive manufacturing (AM) [1].

One of the most popular AM processes is fused deposition modelling (FDM). In general, FDM works by extruding a pre-formulated thermoplastic filament through a heated print head onto a heated bed, layer by layer, slowly producing a 3D item. This

M. A. M. Azhar · N. A. Sukindar (✉) · M. H. Ani · H. B. Anuar · S. B. Kamaruddin · S. I. S. Shaharuddin · M. Y. Mustafa · E. Y. T. Adesta · R. K. Arief · M. H. Sulaiman
Manufacturing and Materials Engineering Department, International Islamic University Malaysia, 53100 Gombak, Malaysia
e-mail: noraimanuskindar@gmail.com

extrusion method is straightforward and repeatable, and it may be used with practically any material that can be forced through a die and hardens rapidly. Polylactic acid (PLA) and acrylonitrile butadiene styrene (ABS) are the most commonly utilized thermoplastic polymers [2]. There has been a growth in the number of filament types with various qualities in recent years. Nanocomposites, metal composites, ceramics, and biopolymers are among the new and unique materials utilized in FDM [3–5].

The filament extruder is the mainstay in the operation of FDM machines. A filament extruder works by feeding a continuous solid strand of material into an extrusion head, which heats and extrudes the polymer quickly. The unheated part of the polymer strand is employed against the heated section to propel the polymer out through the die, similar to how a piston works [6]. The material is then laid down and built into layers to form a 3D item throughout the printing process. The 3D printer will not be able to generate geometrically or mechanically accurate pieces if the extruder fails [7].

As a result, numerous academics have spent a lot of time and effort trying to improve extruder designs and quantify their performance [8]. Therefore, this paper reviews the types of an extruder that can be used on FDM machines as well as their capabilities in the extrusion process. This review is expected to facilitate the right selection in choosing the appropriate extruder to ensure the quality print results as expected.

2 General Description of FDM Extruder Types

This section covers matters related to the types of extruders that can be used on FDM machines. There are various types of extruders that are often used and developed, such as a direct extruder, Bowden extruder, bi-extruder, pellet extruder and component embedded extruder. Each type of extruder has its mechanism and characteristics to facilitate the printing process.

Generally, a motor-gear feeder assembly is used to feed the filament from a material spool to the print head in FDM. A melt chamber, a heater block, a temperature sensor, and a nozzle make up the print head. To keep the melt chamber at the desired temperature, the heater block and temperature sensor are synced with a temperature controller. The feed filament is melted in the melt chamber and subsequently extruded via the nozzle aperture [1]. A schematic diagram of a typical FDM system is shown in Fig. 1. Meanwhile, Table 1 explains the general description of different types of FDM extruders.

3 Specific Features of Each Type of Extruder

Each type of extrusion described in the previous chapter has its role in the extrusion process. Starting with the direct extruder type, due to the extruder assembly position

Fig. 1 Schematic of a common FDM system [9]

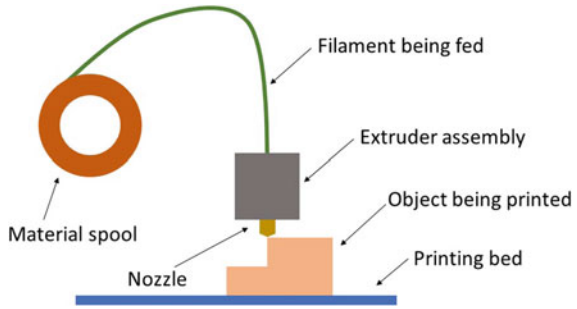


Table 1 General description of different extruder types

Extruder type	Schematic diagram	Properties
Direct extruder	See Fig. 2	The extruder is positioned on the printhead in a direct drive method where it is directly coupled to the hot end and are part of the print head, which at the same time pushing the filament directly into the hot end [8]
Bowden extruder	See Fig. 3	Bowden extruder is not connected to the hot end. The filament input to the liquefier is located quite far away from the extruder motor. A teflon tube is then used to feed the filament to the hot end [11]
Bi-extruder	See Fig. 4	The bi-extruder hot-end was created to print two thermoplastic materials simultaneously. It has two thermoplastic filament guide ways, a melt chamber divided into two parts, and a nozzle [13]
Pellet extruder	See Fig. 5	Pellet extruders work in the same way as filament extruders, but instead of filament, they use pellets. The screw facilitates pellet transfer from the inlet to the nozzle opening [15]
Component embedded extruder	See Fig. 6	In this extruder, there are two entries: one for raw plastic filament and the other for carbon fibre roving. The carbon fibre roving passes through the hot block in a short stainless steel conduit that keeps the fibre from coming into touch with the molten plastic until it reaches the nozzle [17]

Fig. 2 Direct extruder [10]

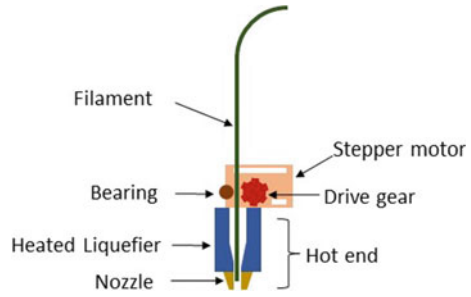


Fig. 3 Bowden extruder [10]

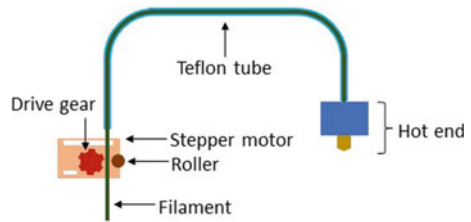
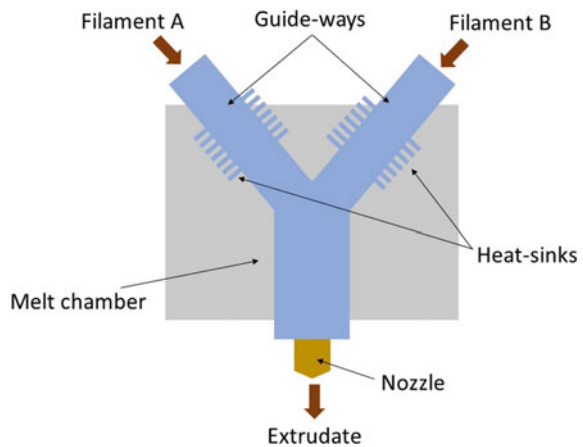
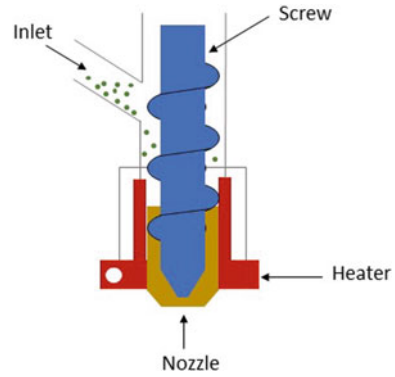
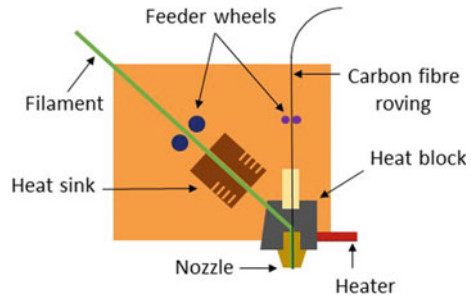


Fig. 4 Bi-extruder [12]



immediately above the hot end, there is less slack of filament between the extruder and the hot end, resulting in faster retraction, a smaller motor used, and better filament handling. These advantages facilitate various types of materials to be printed, including flexible and abrasive filaments and can reduce stringing problems [18].

As for the Bowden extruder, there is less weight on the print carriage since the extruder has been removed from the print head. A 3D printer with a Bowden extruder can also print faster, more accurately, and precisely since the print head is lighter. Because the print head can travel at higher speeds, this can result in either higher

Fig. 5 Pellet extruder [14]**Fig. 6** Component embedded extruder [16]

quality or faster prints. Bowden extruders are also smaller and less space-consuming than direct extruders [19].

Afterwards, the bi-extruder's features may be observed in its split construction, which allows easy access to internal channels, and its modular design, which includes a separate mixing chamber, inlet feed-guides, and nozzle, allowing for future adjustments and optimization. The bond strength of the polymer interface within and between filaments can be considerably improved by mixing two polymers right adjacent to the nozzle orifice. This intermixing characteristic can further improve the inter-layer bond strength of printed items by ensuring that at least some regions of the bonding contact are between the same material [20].

Next, the working mechanism of the pellet extruder shows an advantage over the filament extruder in that it lowers the cost of printing because PLA pellets are less expensive than PLA filaments. Furthermore, since it has large nozzle sizes and a heat zone nozzle, users can print a wide choice of materials using a pellet extruder, increasing the speed of prints and the recyclability of the 3D printing process. Commercial pellet extruders have a small nozzle and a light body, making them compatible with a wide range of 3D printers [21].

Lastly, a component embedded extruder is different from other types of extruders in that they were created with the goal of printing continuous fibre-reinforced thermoplastics (CFRT). The result of CFRT printing using a mechanism from this type

of extruder successfully produces a quality print where the mechanical properties are even better than ordinary thermoplastics. In terms of machine assembly, it can be used with existing FDM 3D printers, eliminating the need to construct a new chassis. As a result, the FDM printer can generate high-performance composite parts for a variety of applications, such as robotics and the automobile industry [22].

4 Conclusions

All types of extruders that have been reviewed in previous chapters have specific functions and capabilities, each of which has its own advantages in producing quality prints. Determining which extruder is better than the other will depend on the user. There are several things to consider in choosing a suitable extruder. Among them are the types of filaments to be used, the physical characteristics of the printing product, the mechanical properties of the printed part and the speed of the printing process. By recognizing and understanding the type of result desired, the selection for the type of extruder can be made, and good quality printing results can be obtained.

Acknowledgements The authors express their appreciation for the Tin Grant under the Tin Industry (Research and Development) Board of Malaysia under project number TBRG21-001-0001 and Research Management Centre, International Islamic University Malaysia under project number RMCG20-033-0033.






References

1. Lipson H, Kurman M (2013) *Fabricated*. Wiley, Indianapolis
2. Hunt E, Zhang C, Anzalone N, Pearce J (2015) Polymer recycling codes for distributed manufacturing with 3-D printers. *Resour Conserv Recycl* 97:24–30. <https://doi.org/10.1016/j.resconrec.2015.02.004>
3. Dul S, Fambri L, Pegoretti A (2016) Fused deposition modelling with ABS–graphene nanocomposites. *Compos Part A Appl Sci Manuf* 85:181–191. <https://doi.org/10.1016/j.compositesa.2016.03.013>
4. Salea A, Prathumwan R, Junpha J, Subannajui K (2017) Metal oxide semiconductor 3D printing: preparation of copper(ii) oxide by fused deposition modelling for multi-functional semiconducting applications. *J Mater Chem C Mater* 5:4614–4620. <https://doi.org/10.1039/c7tc00990a>
5. Brooks B, Arif K, Dirven S, Potgieter J (2016) Robot-assisted 3D printing of biopolymer thin shells. *Int J Adv Manuf Technol* 89:957–968. <https://doi.org/10.1007/s00170-016-9134-y>
6. Turner B, Gold S (2015) A review of melt extrusion additive manufacturing processes: II. Materials, dimensional accuracy, and surface roughness. *Rapid Prototyp J* 21:250–261. <https://doi.org/10.1108/rpj-02-2013-0017>
7. Durgun I, Ertan R (2014) Experimental investigation of FDM process for improvement of mechanical properties and production cost. *Rapid Prototyp J* 20:228–235. <https://doi.org/10.1108/rpj-10-2012-0091>
8. Tlegenov Y, Wong Y, Hong G (2017) A dynamic model for nozzle clog monitoring in fused deposition modelling. *Rapid Prototyp J* 23:391–400. <https://doi.org/10.1108/rpj-04-2016-0054>

9. Kun K (2016) Reconstruction and development of a 3D printer using FDM technology. *Procedia Eng* 149:203–211. <https://doi.org/10.1016/j.proeng.2016.06.657>
10. Advantages and disadvantages of direct and Bowden extrusion. Fargo 3D Printing. <https://www.fargo3dprinting.com/advantages-disadvantages-direct-bowden-extrusion/>.
11. Hullette T. All3DP. <https://all3dp.com/2/direct-vs-bowden-extruder-technology-shootout/#:~:text=In%20a%20direct%20drive%20system,to%20reach%20the%20hot%20end>
12. Khondoker M, Asad A, Sameoto D (2018) Printing with mechanically interlocked extrudates using a custom bi-extruder for fused deposition modelling. *Rapid Prototyp J* 24:921–934. <https://doi.org/10.1108/rpj-03-2017-0046>
13. Khondoker M, Sameoto D. Design and characterization of a bi-material co-extruder for fused deposition modeling. In: ASME international mechanical engineering congress and exposition, phoenix, 11–17 Nov 2016
14. Shaik Y, Schuster J, Shaik A (2021) A scientific review on various pellet extruders used in 3D printing FDM processes. *OALib*. 08:1–19. <https://doi.org/10.4236/oalib.1107698>
15. Valkenaers H, Vogeler F, Ferraris E. A novel approach to additive manufacturing: screw extrusion 3D-printing. In: Proceedings of the 10th international conference on multi-material micro manufacture, San Sebastián, 8–10 Oct 2013
16. Heidari-Rarani M, Rafiee-Afarani M, Zahedi A (2019) Mechanical characterization of FDM 3D printing of continuous carbon fiber reinforced PLA composites. *Compos B Eng* 175:107147. <https://doi.org/10.1016/j.compositesb.2019.107147>
17. Li N, Li Y, Liu S (2016) Rapid prototyping of continuous carbon fiber reinforced polylactic acid composites by 3D printing. *J Mater Process Technol* 238:218–225. <https://doi.org/10.1016/j.jmatprotec.2016.07.025>
18. Daramwar V, Kadam S (2020) Design and development of multi-material extrusion in FDM 3D printers. *Int J Adv Res Sci Eng Technol* 7:2395–2456
19. Günaydın K, Türkmen H, Ferraris E. Common FDM 3D printing defects. In: International congress on 3D printing (additive manufacturing) technologies and digital industry (2018)
20. Rap R. 3-way quick-fit extruder and colour blending nozzle. <https://richrap.blogspot.com/2012/08/3-way-quick-fit-extruder-and-colour.html>
21. Whyman S, Arif K, Potgieter J (2018) Design and development of an extrusion system for 3D printing biopolymer pellets. *Int J Adv Manuf Technol* 96:3417–3428. <https://doi.org/10.1007/s00170-018-1843-y>
22. Naranjo-Lozada J, Ahuett-Garza H, Orta-Castañón P, Verbeeten W, Sáiz-González D (2019) Tensile properties and failure behavior of chopped and continuous carbon fiber composites produced by additive manufacturing. *Addit Manuf* 26:227–241 <https://doi.org/10.1016/j.addma.2018.12.020>

Extrusion Temperature and Viscosity of Various Soy Wax/Beeswax Blends



Sharifah Imihezri Syed Shaharuddin , Nur Amalina Mustafa ,
Norhashimah Shaffiar , M. K. Nor Khairusshima ,
and Nor Aiman Sukindar 

Abstract Recent technological advancement has led to the development of automated batik printers based on the melt extrusion process as an alternative method for the batik *tjanting* or hand-drawn process. The study aimed to measure the throughput of an in-house design extruder and verify the range of extrusion temperature for soy wax/beeswax composition. In addition, the viscosity of the waxes was also evaluated in the extrusion temperature region. The study revealed that the throughput of the waxes at peak melt temperature was in the range of 0.00916–0.00883 g/s. Results also showed that the throughputs were increased at higher extrusion temperatures corresponding to the low viscosity of the waxes. Further additions of beeswax resulted in a decreased throughput attributed to the highly viscous nature of beeswax. The viscosity for direct deposition or extrusion of soy wax/beeswax blends for batik printing application was measured to be in the region of 0.010 and 0.025 Pa s. Further viscosity analysis estimated that soy wax has the highest tendency to change rapidly with temperature. Thus, the temperature of soy wax needs to be precisely controlled to maintain a consistent viscosity during extrusion. The result of this study contributes toward establishing alternative resist materials and their processing temperatures to ensure quality batik patterns are produced using the batik printer.

Keywords Batik printer · Extruder · Wax

1 Introduction

The batik production in Malaysia and Indonesia has been facing numerous challenges due to the ever-changing landscape in local culture and community and social values. The development of human capital to support the growth of the batik industry is critical as the process involves in creating batik textile is very much labor-intensive and requires skilled artisans. In recent years, the number of batik workers has dwindled, and it has been harder to attract workforce from the younger generation in this

S. I. S. Shaharuddin (✉) · N. A. Mustafa · N. Shaffiar · M. K. N. Khairusshima · N. A. Sukindar
Department of Manufacturing and Materials Engineering, Kuliyyah of Engineering, International
Islamic University Malaysia, 53100 Kuala Lumpur, Malaysia
e-mail: shaimihezri@iiu.edu.my

© The Author(s), under exclusive license to Springer Nature Singapore Pte Ltd. 2023
Md. A. Maleque et al. (eds.), *Proceeding of 5th International Conference on Advances in
Manufacturing and Materials Engineering*, Lecture Notes in Mechanical Engineering,
https://doi.org/10.1007/978-981-19-9509-5_55

415

heritage industry [1–4]. Therefore, there is a need to engage in alternative methods to produce batik textiles such as computer-aided batik printers that have been adapted with wax extrusion-based printings.

The Indonesian batik artisans use batik waxes that are composed of various ingredients, namely paraffin, beeswax, residue of pine-gum distillation, cat's-eye resin, micro wax, recycled wax, and animal fat [5]. In comparison, the batik artisans in Malaysia use waxes that are mainly made from different compositional ratios of beeswax, paraffin, microcrystalline wax, dammar, rosin and vegetable oil [6]. Recently, there have been growing environmental concerns about the use petrol-based waxes such as paraffin and microcrystalline wax as they are non-biodegradable. Thus, studies on alternative resist materials made from renewable and sustainable resources are necessary.

Soy wax has been given attention as a biodegradable and renewal candidate for paraffin [7]. In this study, beeswax was added to improve the lack of adhesiveness of soy wax. Incorrect viscosity/temperature used during extrusion may result in under or over extrusion issues, thermal degradation, wax clogging, and poor batik textile quality. Therefore, in this study, the throughput of an in-house designed extruder and the range of extrusion temperature for soy wax/beeswax composition were verified. In addition, the viscosity properties were also evaluated in the melt extrusion region of these soy wax/beeswax blends.

2 Methodology

2.1 Throughput Measurement

The quantities of beeswax (Global Sdn Bhd, Malaysia) and soy wax (Jargeous Sdn Bhd, Malaysia) were weighed according to the wt% ratios shown in Table 1. Each component was melted in a pan in the order of decreasing melting temperature as follows; beeswax (melting point = 70 °C), and finally soy wax (melting point = 55 °C). The prepared batik wax blends were then left to solidify for 48 h before being re-melted for ensuing tests.

The throughput for the in-house design extruder was measured at the peak melting temperature (T_{peak}) and end melting temperature (T_{end}) enumerated in Table 1. The wax was collected for 3 min as it flowed out of the extruder's nozzle. The throughput was then calculated based on the ratio of collected wax mass (g) over extrusion time (3 min). The experiments were repeated twice for each wax blend at these two temperatures to obtain the average throughput readings.

Table 1 Sample codes and wt% for the soy wax/beeswax blends

Sample code	Soy wax (wt%)	Beeswax (wt%)	Temperature (°C)	
			T _{peak}	T _{end}
Neat soy wax	100	–	57	63
Soy80bees20	80	20	60	64
Soy60bees40	60	40	64	68
Soy40bees60	40	60	65	69
Soy20bees80	20	80	67	71
Neat beeswax	–	100	72	78

2.2 Viscosity Measurement

Three compositions were selected for the rheological test which was neat soy wax, soy60bees40, and neat beeswax. The viscosity of each sample was measured using the rotational rheometer (Rheolab QC, Austria) at various temperature points within the melting region of the waxes. The melting points for the sample were set between 58 and 65 °C for neat soy wax, 65–75 °C for soy60bees40, and lastly from 73 to 85 °C for neat beeswax. For the test, 20 ml of the wax blend was placed into a concentric cylinder. A cylinder spindle was used for this experiment at a constant speed of 100 s⁻¹. The Peltier temperature device was used to heat the samples.

3 Results and Discussion

3.1 Extruder's Throughput at Various Melt Temperatures

Figure 1 compares the average throughput for each wax composition at T_{peak} and T_{end}. It was observed that the extruder's throughput for the waxes at T_{end} was significantly higher in the range of 42–57% compared to T_{peak}. The higher throughput at T_{end} was attributed to the low viscosity of the waxes at a higher temperature which increases the mass flow rate of the waxes. It was also observed that there were no clogging issues at the extruder's nozzle during the extrusion process. Thus, this work verifies that these waxes can be successfully extruded within the studied temperature range. In traditional batik production, the author observed that using incorrect melt temperature of batik waxes leads to several consequences such as frequent wax splurge on the textile and poor wax penetration into the fibers of the fabric which leads to uncontrolled dye dispersion.

The extruder's throughput measured at a fixed temperature of 80 °C is shown in Fig. 2. The additions of beeswax from 20 wt% to 40 wt% gave an almost similar throughput of 0.021 g/s. Further increments of beeswax (wt%) resulted in throughput reduction during the extrusion process. The decreasing throughput was attributed

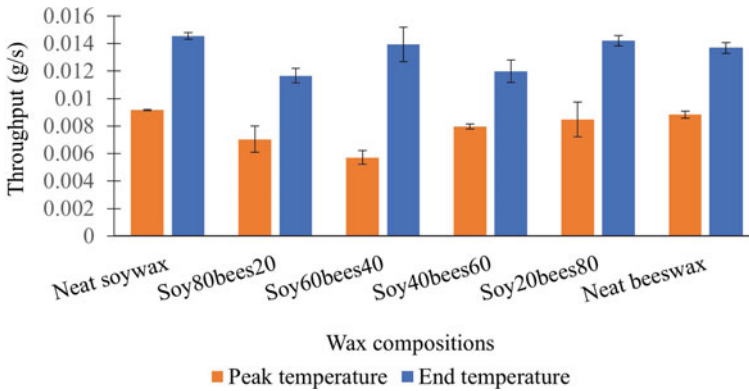


Fig. 1 Throughput at peak melting temperature T_{peak} and end melting temperature T_{end}

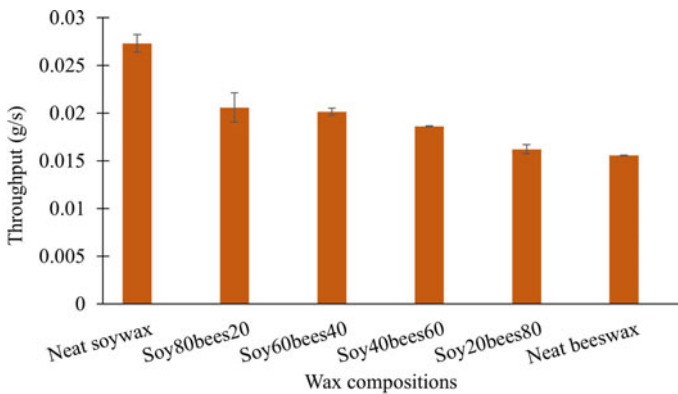


Fig. 2 Extrusion throughput at a fixed temperature of 80 °C

to the highly viscous nature of beeswax as it consists of long esters mixed with some hydrocarbon chains [8]. The hydrocarbon lipid in particular contributes to the viscoelastic properties of beeswax [9]. Prior studies have shown that the additions of beeswax resulted in emulsion with an increase in viscosity [10] and improved stability [11].

3.2 The Viscosity of Waxes at the Melt Temperature Region

Viscosity analysis was conducted only for the following compositions: soy wax, soy60bees40, and neat beeswax. The soy60bees40 composition was selected as it represents the mid-range throughput at fix temperature of 80 °C (refer to Fig. 2). Figure 3 shows the viscosity-temperature relationship for the waxes. It is deduced

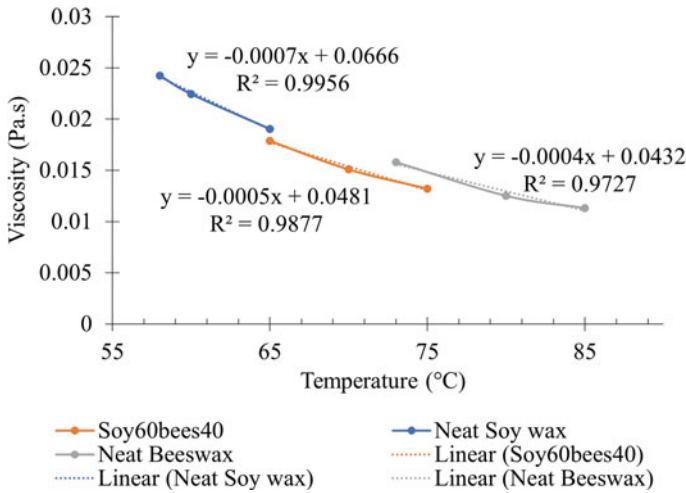


Fig. 3 Corresponding viscosity at the melting temperature region for soy-based waxes and beeswax

that the viscosity for direct deposition or extrusion of soy wax/beeswax blends is in the region of 0.010 and 0.025 Pa s. The measured viscosity of the neat beeswax at 0.013 Pa s was slightly higher than the reported value of approximately 0.09 Pa s at 80 °C [8] attributed to the different grades of beeswax used. Neat beeswax’s low viscosity profile requires a higher extrusion temperature than other soy wax/beeswax blends which explains the low throughput obtained at 80 °C. To compare how viscosity changes with temperature, each curve was fitted with a linear trendline. Each linear trendline obtained R² value approaching 1, therefore, the slope value can be used as an estimated index that represents the change in viscosity with temperature in the melt region. It was apparent from the fitted trendline that rapid viscosity changes with temperature in the melt region occurred for soy wax compared to other waxes. This implies that the temperature of soy wax needs to be precisely controlled to maintain consistent viscosity during the direct deposition or extrusion process.

4 Conclusion

In the present study, the throughput and viscosity of various soy wax/beeswax blends for batik wax printing were evaluated. The throughput of the waxes increased in the range of 42% to 57% at a higher temperature. Additions of beeswax into the blends at fixed temperature resulted in decreasing throughput by 41% due to the highly viscous nature of beeswax. The extrusion temperatures used corresponded to the waxes’ viscosity in the region of 0.011 and 0.024 Pa s. Wax extruded at the right viscosity helps the batik artisan to avoid issues related to clogging at the nozzle and improves the print quality and production time. The result of this project provides

alternative sustainable soy wax-based compositions and their range of extrusion temperatures for batik printing applications.

Acknowledgements This work was fully supported by International Islamic University Malaysia and funded by the Ministry of Higher Education Malaysia (FRGS/1/2018/TK03/UIAM/02/3). The authors would like to express their deepest gratitude for the support from all co-researchers.

References

1. Akhir NHM, Ismail NW, Said R, Kaliappan SR (2015) *Islamic perspectives relating to business, arts, culture and communication*. Springer, Singapore (2015)
2. Dwinugroho TB, Kumarajati DYH, Kurniawanti Hapsari YT (2019) Design and implementation of CNC (computer numerical control) based automatic stamp batik machine program with automatic gripper using Mach 3. *J Phys: Conf Ser* 1254
3. Khalili SSM. Social media lifeline for block batik. *The News Straits Times Online*. <https://api.nst.com.my/lifestyle/bots/2018/06/383745/social-media-lifeline-block-batik>. Last accessed 09 Aug 2022
4. Vatvani C. Prints, patterns and preservation: how Indonesia's batik artisans draw a younger generation. Channel News Asia Publication: International Edition. <https://www.channelnewsasia.com/news/asia/indonesia-batik-drawing-younger-generation-national-fabric-11434190>. Last accessed 14 Feb 2019
5. Malik A, Rahmillah FI, Atmaja BD, Ihsan BF (2018) The effect of microwax composition on the staining quality of Klowong batik wax. *MATEC Web Conf* 154:01118
6. Shaharuddin SIS, Shamsuddin MS, Drahman MH, Hasan Z, Asri NAM, Nordin AA (2021) A review on the Malaysian and Indonesian batik production, challenges, and innovations in the 21st Century. *SAGE Open* 11:1–19
7. Rezaei K, Wang T, Johnson LA (2002) Hydrogenated vegetable oils as candle wax. *J Am Oil Chem Soc* 79:1241–1247
8. Bucio A, Moreno-tovar R, Bucio L, Espinosa-dávila J, Anguebes-franceschi F (2021) Characterization of beeswax, candelilla wax and paraffin wax for coating cheeses. *Coatings* 11:1–18
9. Hu W, Yu X (2014) Thermal and mechanical properties of bio-based PCMs encapsulated with nanofibrous structure. *Renew Energy* 62:454–458
10. Chen M, Abdullah, Wang W, Xiao J (2022) Regulation effects of beeswax in the intermediate oil phase on the stability, oral sensation and flavor release properties of pickering double emulsions. *Foods* 11
11. Shi Y, Zhang M, Bhandari B (2021) Effect of addition of beeswax based oleogel on 3D printing of potato starch-protein system. *Food Struct* 27:100176

Investigation Study on Risk Management Practices in Adding Value to the New Product Development



Muataz Hazza Al Hazza, Nasuha Bt Mohd Nasir, Islam Bourini,
Zubaidah M. Hazza, Atiah Abdullah Sidek, and Mohammad Yeakub Ali

Abstract Over the years, companies have found new ways to generate profits based on innovation, both internationally and locally. Innovation has recently become the organization's primary resource or competence to adapt to the change in the environment and thus continue to compete in the harsh climate. To maintain their competitive advantage and survive in such an environment, companies should not rely solely on a single product, new capabilities and new products must be developed continuously. It can be a complicated process with a high risk of creating a new product. In addition to the need to develop new products, the risk associated with the innovation process is also related to new product failure, with estimation rates of 33–60% or higher. However, the research shows that risk management is one of the relevant factors for NPD success. This research aims to investigate a risk management system's success and risk factors that led to effective risk management systems and brought success to new product development. Success and risk factors are evaluated to achieve the research objective, and research surveys are designed based on the literature review. Next, confirmatory Factor Analysis (CFA) is completed to validate the factors, where items with low factor loading are eliminated. Then, the result is used to measure the highest variance percentage to determine each factor's most significant element. Thus, this research provides insights that help people take advantage of reducing risk in new product development.

Keywords Risk management · New product management · Challenges

M. H. Al Hazza (✉)

Mechanical and Industrial Engineering, American University of Ras Al Khaimah, Ras Al Khaimah, United Arab Emirates
e-mail: muataz.alhazza@aurak.ac.ae

N. B. M. Nasir · Z. M. Hazza · A. A. Sidek

Department of Manufacturing and Materials Engineering, Faculty of Engineering International Islamic University Malaysia, PO Box 10, 50728 Kuala Lumpur, Malaysia

I. Bourini

Dubai Business School, University of Dubai, Dubai, United Arab Emirates

M. Y. Ali

Mechanical Engineering Programme Area, Faculty of Engineering, Universiti Teknologi Brunei, Tungku Highway, Gadong Bandar Seri Begawan BE1410, Brunei Darussalam

1 Introduction

The market customer preference nowadays is favorably dynamic and varies exceptionally quickly. Thus, developing new products becomes a crucial problem and not an option for any business to stay in this severe competitive market [1]. Under these circumstances, the manufacturers become under tremendous pressure to continuously develop new products by reducing the existing product's cost, adding new features to the current developments, or innovating new products. Therefore, constantly introducing new products is not an option for companies to stay in this dynamic market. However, the high failure rate associated with the new products is due to their nature of high uncertainty. Without sufficient market knowledge, research and feasibility study will increase the ratio of failures [2]. Hill et al. [3] claim that the failure of new product introductions is high because of uncertainty, low commercialization, poor positioning strategy, slow cycle time, and technological myopia. Page [4] said product innovation does not always lead to company success. Out of 10 ideas, only three will be developed, 1.3 will be launched, and only one will make any profit. A global analysis of 360 industrial companies establishing 576 new industrial products showed an overall success rate of 60% [5]. However, the development of new products is a complex and challenging task due to the high uncertainty associated with the new product's development process [1]. Therefore, reducing the uncertainties related to NPD will increase the opportunities and mitigate the threats. In other words, risk management is to identify hazards, plan to reduce their harmful effect, identify opportunities, and try to take advantage of its positive impact. The risk management process identifies analyses and plans for future actions to manage these possible uncertainties. The goal of risk management as the process that aim to maximize the opportunities by adding value to the product and minimizing the threats that may happen in NDP. Risk management is essential for all types of businesses to survive and grow in the industry. One of the sectors that usually suffers from NDP failure is the small and medium-sized enterprises (SMEs) due to their limitations and constraints on money. The industries can overcome the failure and survive in this competitive environment by implementing efficient and effective risk management. Despite gaining attention and frequently discussing, there is still a lack of standardized tools and techniques for assessing the risk [6]. The new product development becomes critical and challenging, especially for SMEs. NPD aims to maximize fit with customer requirements, minimize product development cycle time, and reduce the developing cost [7]. The risk factor in the development process can be classified as Technical Risk, Market Risk, Commercial Risk, and Organizational Risk. Early discovery of risk can prevent huge losses, which is preferable to treating casualties when unpreventable [8]. Risk management should be implemented to increase the success rate of the NPD project. A study suggested that the success factor for new product development is effective strategies to reduce the risk [9].

2 Research Methodology

Sequential steps were followed to achieve the objective of the research. A structured questionnaire of six sections was developed: demographic, implementing risk management in the organization, Critical success factors for effective risk management, Risk factors encountered by a new product, and Tools and techniques used to assess risk in the organization. Different methods of analysis were conducted: Reliability Analysis, Correlation Analysis (Pearson Correlation), Confirmatory Factor Analysis (CFA), and Principal Component Analysis (PCA).

3 Results and Discussion

The results show that the NDP success factors can be categorized into five main categories: Commitment to top management, Communication, Culture, Organization, and Training. Other results that focus on the risk show that the risk can be categorised into five main parts: market, organizational, resources, and technological risks. Table 1 concludes the normality analysis of the success factors.

All skewness values are from -2 to 2 which means the good weight and all items are normally distributed except for communication. The value for skewness is beyond the range. However, the skewness is within the acceptable range of -7 to 7 . For estimation analysis, the items give a robust measurement model above 0.7 . Thus, no item is eliminated. The success factor shows a substantial value where all levels of acceptance are satisfied. The measurement of the success factor is all validated. No item is removed because it offers a high value of cut-off and regression weights (Table 2).

The kurtosis values for A1 to A5 are between -1 and 1 , which indicate these variables are normal. However, A3 has a kurtosis value of 2.246 , which indicates that this item is not normally distributed. In organization risk values, the highest skewness value is B3 which has a value of -1.013 . All other items have kurtosis values and skewness in the range of -1 to 1 , indicating that these items are normally distributed. The kurtosis values for resources risk range from -1 to 1 for C1 to C5; therefore, this variable is in the normal distribution range. The highest value of kurtosis for technological risk is D2, which has a value of 1.042 . While the lowest value of skewness is D4, which has a value of -0.617 . All the kurtosis values are

Table 1 Normality of success factors

Success factor		Commitment top management	Communication	Culture	Organization	Training
Normality analysis	Skewness	-1.396	-2.01	-1.3	-1.468	-1.468
	Kurtosis	1.405	4.156	1.224	1.88	1.88

Table 2 Normality and estimation assessment

Risk factors	Item	Normality assessment		Estimation assessment	
		Skewness	Kurtosis	Regression weight analysis	Regression weight analysis after item is removed
Market risk	A1	-0.396	-0.359	0.854	Removed
	A2	0.236	-0.207	0.685	0.287 (Correlate with A3)
	A3	0.958	2.246	0.733	0.481 (Correlate with A2)
	A4	0.564	0.423	0.291	0.784
	A5	0.288	0.333	0.328	0.850
Organizational risk	B1	0.116	-0.778	0.532	Removed
	B2	0.233	-0.232	0.503	0.459
	B3	0.061	-1.013	0.717	0.545
	B4	0.420	0.013	0.565	0.488
	B5	0.245	0.428	0.403	0.676
Resources risk	C1	-0.081	-0.942	0.369	Removed
	C2	0.050	-0.785	0.070	0.033
	C3	0.289	-0.403	0.651	0.687
	C4	-0.504	0.833	0.896	0.842
	C5	-0.119	-0.232	0.508	0.672
Technical risk	D1	0.586	-0.589	0.501	Removed
	D2	0.188	1.042	0.578	0.439
	D3	0.353	0.007	0.550	0.431
	D4	0.106	-0.617	0.779	0.786
	D5	0.018	0.833	0.751	0.855

within the normal distribution range (-2 to 2). Therefore, it can be concluded that this variable is in the normal distribution.

Market Risk factor has weak measurement model. Therefore, the component suggested by SPSS AMOS is removed from the model: “New entrants threaten the company’s competitive position (A1)” with the loading of 0.854. Even though it has a good regression weight, however, the model fit index shows a poor result. Thus the item is eliminated. Besides, unexpected market changes threaten the company’s competitive position (A2), and The company’s processes do not consistently meet or exceed customer expectations (A3) are correlated to get the best result of the measurement model. The same steps are applied through the Organizational Risk where the item 1, Management fraud adversely affects the company’s reputation or exposes the company to financial loss (B1), is removed from the model. Next, it is also practiced to Resources Risk where item 1 with the loading of 0.369 is eliminated

Table 3 Cut-off value of risk factor

Risk factors		Index				
		CMIN/df ≤ 3	CFI ≥ 0.90	SRMR	RMSEA	Pclose
Market risk	Before	3.448	0.849	0.140	0.291	0.04
	After	–	1.000	0.033	0	0.400
Organizational risk	Before	4.862	0.441	0.223	0.365	0
	After	0.642	1.000	0.074	0	0.040
Resources risk	Before	1.327	0.922	0.132	0.106	0.289
	After	0.113	1.000	0.025	0	0.900
Technological risk	Before	2.117	0.840	0.119	0.196	0.079
	After	0.242	1.000	0.006	0	0.843

from the model. Besides, the Technological Risk also has been eliminated in item 1: dramatic shifts or adjustments in emerging technology are not capitalized upon due to the company’s reliance on the current paradigm (D1) (Table 3).

All factors need to be improved by deleting some items or correlates the items based on suggested covariance. In Market Risk, it can be seen that CFI increases from 0.849 to 1.000 after deleting the items that contribute to low factor loading. Besides, items 2 and 3 in Market Risk are correlated depending on suggested covariance between 2 error items. From all 20 items for 4 important risk factors of product development, 1 element are eliminated from each risk (Table 4).

From the results, the four risk factors give an eigenvalue of more than one except for Technological Risk, which is 0.321. The highest eigenvalue is the Market Risk factor which is 13.727. The extraction value for all variables is more significant than 0.50. The maximum value obtained by the product may not be able to out-market the competition in the market in Market Risk, and experience members attain the lowest in Technological Risk. Factors that do not explain much variance might not be worth it. In other words, it has less importance. Market Risk explains a plan for successfully reducing risk, identifying the most important risk that needs to be analyzed. This factor demonstrates 42.915% of the total variance of success criteria. The product may not be able to out-market the competition in the current market has the highest commonality indicating the critical components in Market Risk. Second, the Organizational Risk describes a variance of 26.949% after Market Risk. The highest was given by B5, which is “there is lack of employee competency in fulfilling tasks related risk management system” item in Organizational Risk, which is 0.900. There is a lack of teams to handle and operate the risk management system in the organizations due to the lack of training, knowledge, and skills. Next, ineffective communication channels result in messages inconsistent with authorized responsibilities. They do not effectively convey information as intended, giving the third-highest elements followed by employees resisting changes to the existing system in the organization. Next, Resources Risk explains 17.821% of the total variance, with the most essential item being organizational slack, unused resources within or available in organizations

Table 4 Principle component analysis

Success factors	Item	Extraction (Commuality)	Eigenvalue	Variance (%)
Market risk	A1	0.834	13.727	42.915
	A2	0.786		
	A3	0.764		
	A4	0.907		
	A5	0.937		
Organizational risk	B1	0.869	4.488	26.949
	B2	0.874		
	B3	0.866		
	B4	0.712		
	B5	0.900		
Resources risk	C1	0.857	1.45	17.821
	C2	0.862		
	C3	0.743		
	C4	0.781		
	C5	0.858		
Technological risk	D1	0.599	0.321	12.315
	D2	0.659		
	D3	0.836		
	D4	0.722		
	D5	0.777		

that can turn into material waste, 0.862. It is followed by a project that cannot secure a skilled technician within the scheduled time frame, failure to manage outsourced, or not performing in a manner consistent with the company's strategies, objectives, or regulatory requirements. Finally, Technological Risk has the lowest total variance, which is 12.315%. The last item of technology risk is essential since people need time to adjust to the technology change.

4 Conclusions

The literature review identified the top four risk factors: market, organizational, resources, and technological risk. Next, the measurement model of success factors is analyzed and validated using Confirmatory Factor Analysis (CFA) in SPSS AMOS. This method eliminates the elements in the risk factors with low factor loading to improve the cut-off value. Finally, the third objective is achieved by calculating the percentage of variance extracted from Principal Component Analysis (PCA). The highest variance percentage shows the most critical factors that have to be focused







on by the organizational owner. Above all, the highest percentage is given by the Market Risk factor, 42.915%.

References

1. AlHazza MH, Bourini IF, Zubaidah MH, Selamat NB (2019) Success factor in new product development for start-up companies using fuzzy logic approach. In: 2019 International conference on electrical and computing technologies and applications (ICECTA). IEEE, pp 1–5
2. Kim Y-H, Park S-W, Sawng Y-W (2016) Improving new product development (NPD) process by analyzing failure cases. *Asia Pac J Innov Entrepreneurship* 10(1):134–150
3. Hill CW, Jones GR, Schilling MA (2014) *Strategic management: theory: an integrated approach*. Cengage Learning
4. Page AL (1991) New product development practices survey: performance and best practices. In: PDMA's 15th annual conference
5. Stevens GA, Burley J (2003) Piloting the rocket of radical innovation. *Res Technol Manag* 46(2):16–25
6. Thäuser J, De Visser M, Ehrenhard ML (2017) Risk management of new product development. a manual for SMEs
7. Schilling MA, Hill CWL (1998) Managing the new product development process: strategic imperatives. *Acad Manag Perspect* 12(3):67–81
8. Ahmed A, Kayis B, Amornsawadwatana S (2007) A review of techniques for risk management in projects. *Benchmark Int J* 14(1):22–36
9. Porananond D, Thawesaengskulthai N (2014) Risk management for new product development projects in food industry. *J Eng Proj Prod Manage* 4(2):99–113

A Comparison of the Thermal Conductivity of 3D Printed ABS and ABS/Graphite at Various Infill Patterns and Densities



Ahmad Amri Nordin , Siti Nazehah Mohd Sofian ,
Sharifah Imihezri Syed Shaharuddin , Norhashimah Shaffiar ,
Abd Malek Abdul Hamid , and Nor Aiman Sukindar 

Abstract Fused Deposition Modelling (FDM) using acrylonitrile butadiene styrene (ABS) filament is commonly used in additive manufacturing processes as it is cost effective and fast. ABS has inherently poor thermal conductivities, thus conductive fillers such as graphite and carbon black have been added to improve the polymer's thermal conductivity. This study aims to compare the thermal conductivities of neat ABS and ABS/graphite at two infill patterns which are cubic-subdivision and triangular at various infill densities of 50, 75 and 100%. The thermal conductivities of the samples were measured using the linear heat conduction technique in accordance with ASTM C518. The results revealed that the presence of graphite had slightly improved the lack of thermal conductivity of neat ABS. ABS/graphite with triangular infill pattern provided better thermal conductivity with increased infill density compared to cubic subdivision. The increased infill density from 50 to 100% for both infill patterns affected the thermal conductivity due to the increased formation of interconnecting structures and reduced air gap. These results shall influence the printing material and parameter selection for thermoelectric application.

Keywords FDM · Thermal conductivity · ABS · ABS/Graphite

1 Introduction

Additive manufacturing (AM) is one of the most promising manufacturing technologies which offers significant advantages over subtractive manufacturing processes. This 3D printing approach offers geometrical flexibility that leads to increased design freedom which reduces manufacturing limitations [1]. FDM printed parts are mostly used in making prototypes and functional models for medical and automotive applications [2, 3]. Parts printed via FDM mainly rely on the infill patterns and infill densities structures to improve their mechanical properties. Parts printed via FDM

A. A. Nordin (✉) · S. N. M. Sofian · S. I. S. Shaharuddin · N. Shaffiar · A. M. A. Hamid · N. A. Sukindar
International Islamic University Malaysia, 53100 Gombak, Malaysia
e-mail: ahmadamri.nordin@gmail.com

mainly rely on the infill densities and patterns to improve their mechanical properties. Studies have shown that the strength performance improved with increased infill densities above 50% for cubic subdivision and triangular infill patterns [4, 5].

Acrylonitrile butadiene styrene (ABS), is an engineering thermoplastic that has been widely used in many industries such as electrical, electronic, or automotive [6]. ABS is polymerized from acrylonitrile and styrene monomers in the presence of polybutadiene. ABS has major advantages compared to other engineering materials as it is cheaper and more durable [7]. Al-Ghamdi [8], reported that the usage of ABS in FDM is time efficient which minimizes energy consumption. The poor thermal conductivity of ABS has led to various studies on the use of additive fillers to attain greater material functionalities in terms of thermal, electrical, magnetic and optical properties [9]. Conductive particles such as graphite and zinc oxide have thermal conductivity of 2.4W/mK [10] and 0.3508 W/mK [11] respectively. Incorporation of these conductive fillers into ABS resulted with improved thermal conductivity, rigidity and strength of printed parts [9].

Despite the potential applications of conductive ABS, it is noted that studies which compare the thermal conductivity of 3D printed neat ABS and conductive ABS/graphite at various infill patterns and densities have been limited in literature. Therefore, it is the purpose of this study to characterize and compare the temperature distribution and thermal conductivities of FDM printed neat ABS and ABS/graphite at two infill patterns which are cubic-subdivision and triangular at various infill densities of 50, 75 and 100%.

2 Methodology

2.1 Sample Preparation

The neat ABS and ABS/graphite samples were purchased from Triventor Solution Malaysia. The estimated ratio for ABS/graphite used in this study was 75:25 [10]. Cylindrical samples with radius of 25 mm and height of 30 mm in accordance with ASTM C518 were fabricated using FDM Prusa Mini+ (Prusa, Rep. Czech). The infill patterns used were cubic-subdivision infill pattern and triangular infill pattern while the infill density used were 50, 75 and 100%. Figure 1 shows the infill patterns at various infill densities using the Prusaslicer. In this study, 12 samples at various infill patterns and densities were fabricated for the test at printing temperature of 220 °C and printing speed of 40 mm/s.

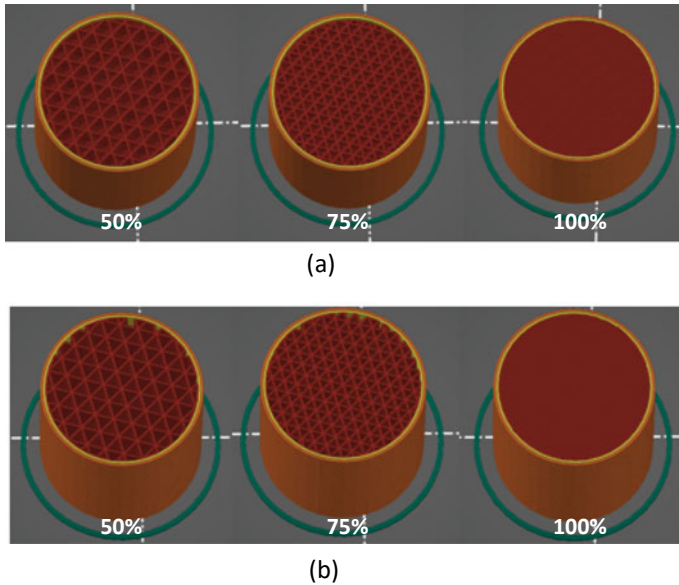


Fig. 1 Infill patterns **a** cubic subdivision and **b** triangular at various infill densities using the Prusaslicer

2.2 Thermal Conductivity Measurements

The thermal conductivities of neat ABS and ABS/graphite were evaluated using linear heat conduction in accordance with the ASTM C518 standards. A constant power source of 10 W was used for the linear heat conduction experiment. The temperatures at various points (T_1 – T_8) shown in Fig. 2 were taken after 20 min at the input temperature of 60 °C. The thermal conductivity (k) for each sample was calculated using Eq. 1.

$$k = \frac{Q \Delta x}{A \Delta T} \tag{1}$$

where Δx = probe distance at two different points, ΔT = temperature differences in the specimen taken at T_4 and T_5 , A = area of the contact surface (m^2) and Q = power usage (W).

3 Result and Discussion

Figures 3 and 4 show the temperature distribution of the neat ABS and ABS/graphite at various infill patterns and densities. In general, the temperature decreased as the

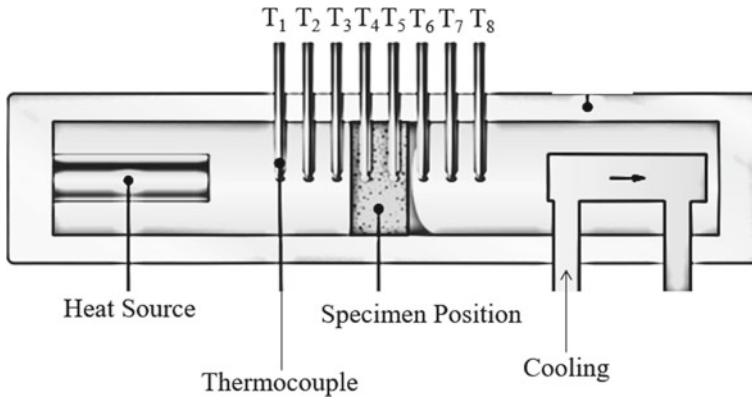


Fig. 2 Schematics of linear heat conduction experiment. Amended based on Yildirim Beyazıt Universitesi [12]

heat flows from thermocouple 1 to thermocouple 8, regardless of the types of infill densities and patterns. As ABS is an excellent thermal insulator, therefore, there was a great temperature drop from T_3 ($60\text{ }^\circ\text{C}$) to T_5 ($20\text{ }^\circ\text{C}$) as shown in Fig. 3a, b. For insulator materials, the heat is mostly being transported by phonons and energy quanta of atomic lattice vibrations. ABS is chemically composed of twisted random orientation with weak intermolecular coupling of Van der Waals forces, thus making the number of phonons to become smaller and deter the transport of heat [13]. Additions of graphite into neat ABS for triangular infill pattern and cubic-subdivision infill pattern as shown in Figs. 3b and 4b showed a gradual drop of temperature from 62 to $25\text{ }^\circ\text{C}$ and 61 to $21\text{ }^\circ\text{C}$ respectively compared to neat ABS.

Figure 5 shows the measured thermal conductivities for ABS and ABS/graphite. Incorporating graphite estimated at 25 wt% [9] into neat ABS showed only slight average improvement of 1.5 and 0.67% for cubic subdivision and triangular infill pattern respectively. The thermal conductivity of ABS/graphite for cubic-subdivision infill pattern showed slight improvement by 0.69% at 100% infill density. Whereas

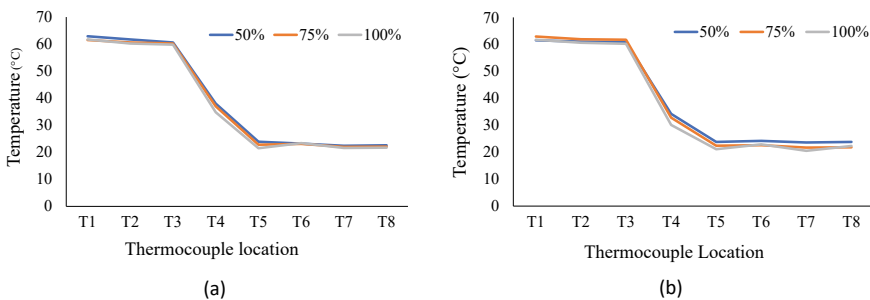


Fig. 3 Measured temperature of the **a** neat ABS and **b** ABS/graphite with cubic subdivision infill pattern at various infill densities

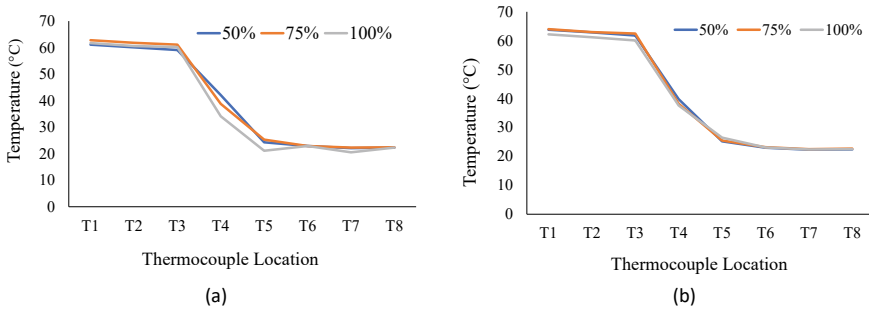


Fig. 4 Measured temperature of the **a** neat ABS and **b** ABS/graphite at triangular infill pattern at various infill pattern

the thermal conductivity of triangular pattern improved by 0.67% from 50 to 75% infill density and by 0.76% from 75 to 100% infill density. It is concluded that the cubic subdivision infill pattern has less pronounced impact on thermal conductivity compared to triangular infill pattern at similar infill density.

As the infill density was increased, the ABS/graphite with cubic subdivision and triangular infill pattern showed an average improvement of 1.5% and 0.67% respectively. The thermal conductivity for cubic subdivision and triangular correlates to the formation of its internal structure. Figure 6 shows the actual cross sections of the neat ABS and ABS/graphite at various infill patterns and densities used in this study. It can be observed that the increase in infill density of the samples was directly proportional to the interconnecting structures and inversely proportional to air gap. The presence of dense interconnecting structures for ABS/graphite allows heat to be conductively transferred, resulting with increased in the thermal conductivity of the samples [14]. A study done by Sonsalla et al. [15] concluded similar trend of thermal conductivity for 3D printed neat ABS that, increasing the infill density had a proportional effect with thermal conductivity.

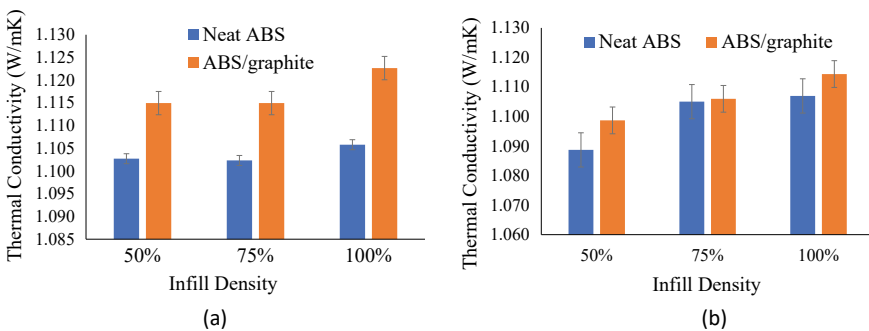


Fig. 5 Thermal conductivity of 3D printed neat ABS and ABS/graphite at various infill density for **a** cubic subdivision and **b** triangular infill pattern

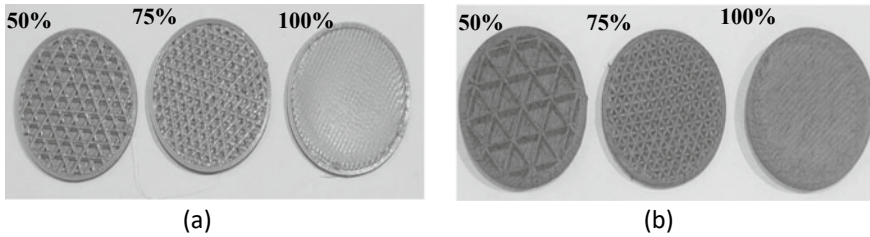


Fig. 6 Cross section of 3D samples printed with **a** cubic subdivision infill pattern at various infill densities **b** triangular infill pattern at various infill densities

4 Conclusion

In this study, the thermal conductivity of neat ABS and ABS/graphite was being compared at cubic subdivision and triangular infill patterns at various infill density. The presence of graphite had only slightly improved the lack of thermal conductivity of neat ABS. It was concluded that the cubic subdivision infill pattern had less pronounced impact on thermal conductivity compared to triangular infill pattern at similar infill density. It was observed from the graphs that incorporating graphite into ABS gave only slight improvement of 1.5 and 0.67% for cubic subdivision and triangular infill pattern respectively. The increase of infill density from 50 to 100% for both cubic subdivision and triangular infill pattern correlates to the interconnecting structures and air gap.

Acknowledgements This work was fully supported by International Islamic University Malaysia and funded by the Ministry of Higher Education Malaysia (FRGS/1/2018/TK03/UIAM/02/3). The authors would like to express their deepest gratitude for the support from all co-researchers.

References

1. Bikas H, Lianos AK, Stavropoulos P (2019) A design framework for additive manufacturing. *Int J Adv Manuf Technol* 103:3769–3783
2. Ngo TD, Kashani A, Imbalzano G, Nguyen KTQ, Hui D (2018) Additive manufacturing (3D printing): a review of materials, methods, applications and challenges. *Compos Part B Eng* 143:172–196
3. Chen H, Yang X, Chen L, Wang Y, Sun Y (2016) Application of FDM three-dimensional printing technology in the digital manufacture of custom edentulous mandible trays. *Sci Rep* 6:1–6
4. Chicos L-A, Pop MA, Zaharia S-M, Lancea C, Buican GR, Pascariu IS, Stamate V-M (2022) Infill density influence on mechanical and thermal properties of short carbon fiber-reinforced polyamide composites manufactured by FFF process. *Materials (Basel)* 15:3706
5. Pandzic A, Hodzic D, Milovanovic A (2019) Effect of infill type and density on tensile properties of PLA material for FDM process. In: Annual DAAAM proceedings of international DAAAM symposium, vol 30, pp 545–554

6. Sy D (2015) Material and application report 2015 acrylonitrile butadiene styrene (ABS) and 3D printer, vol 2
7. Letcher T, Rankouhi B, Javadpour S (2015) Experimental study of mechanical properties of additively manufactured abs plastic as a function of layer parameters. In: ASME's international mechanical engineering congress & exposition proceedings, vol 2A-2015
8. Al-Ghamdi KA (2019) Sustainable FDM additive manufacturing of ABS components with emphasis on energy minimized and time efficient lightweight construction. *Int J Light Mater Manuf* 2:338–345
9. Cholleti ER, Gibson I (2018) ABS nano composite materials in additive manufacturing. *IOP Conf Ser Mater Sci Eng* 455
10. Singh R, Sandhu GS, Penna R, Farina I (2017) Investigations for thermal and electrical conductivity of ABS-graphene blended prototypes. *Materials (Basel)* 10
11. Aw YY, Yeoh CK, Idris MA, Amali HK, Aqzna SS, Teh PL (2017) A study of tensile and thermal properties of 3D printed conductive ABS-ZnO composite. *AIP Conf Proc* 1835:1–6
12. Yildirim Beyazit Universitesi (2010) Experiment: heat conduction. Yildirim Beyazit Universitesi, pp 1–12
13. Chen H, Ginzburg VV, Yang J, Yang Y, Liu W, Huang Y, Du L, Chen B (2016) Thermal conductivity of polymer-based composites: fundamentals and applications. *Prog Polym Sci* 59:41–85
14. Acquah SFA, Leonhardt BE, Nowotarski MS, Magi JM, Chambliss KA, Venzel TES, Delekar SD, Al-Hariri LA (2016) Carbon nanotubes and graphene as additives in 3D printing. Carbon nanotubes-current progress of their polymer composites. <https://doi.org/10.5772/63419>
15. Sonsalla T, Moore AL, Meng WJ, Radadia AD, Weiss L (2018) 3-D printer settings effects on the thermal conductivity of acrylonitrile butadiene styrene (ABS). *Polym Test* 70:389–395

Optimizing Tensile Strength of PLA-Lignin Bio-composites Using Machine Learning Approaches



Mohd Romainor Manshor, Amjad Fakhri Kamarulzaman, Hazleen Anuar, Siti Fauziah Toha, Fathilah Ali, Nor Aiman Sukindar, Jonghwan Suhr, and Nursyam Dzuha Haris

Abstract It is imperative to accurately estimate the final performance of composite parts during the initial design phase of the manufacturing process. In generating sustainable bio composites with superior mechanical properties such as tensile strength, the combination of fillers and plasticizers, as well as their concentration in the mixture, are always deemed crucial. In order to reduce the number of experimental runs and their associated costs and timescales, statistical optimization of the core design elements has become increasingly important. The filler and plasticizer concentrations of extruded bio composites were adjusted in this study utilizing both statistical (analysis of variance (ANOVA) and response surface methodology (RSM)) and machine learning (Multilayer Perceptron (MLP)) approaches. Initial ANOVA results indicated that lignin, epoxidized palm oil (EPO), and their respective combinations were the most influential factors in enhancing the durability of lignin/poly(lactic acid) (PLA) bio composites. In this work, RSM and MLP were used to model and predict the data in order to maximize the various solutions and establish the nonlinear relationship between the concentration of lignin and EPO.

M. R. Manshor (✉) · H. Anuar · N. A. Sukindar · N. D. Haris
Department of Manufacturing and Materials Engineering, Kulliyah of Engineering, International Islamic University Malaysia, Jalan Gombak, 53100 Kuala Lumpur, Malaysia
e-mail: romainor@gmail.com

A. F. Kamarulzaman · S. F. Toha
Department of Mechatronics Engineering, Kulliyah of Engineering, International Islamic University Malaysia, Jalan Gombak, 53100 Kuala Lumpur, Malaysia

F. Ali
Department of Biotechnology Engineering, Kulliyah of Engineering, International Islamic University Malaysia, Jalan Gombak, 53100 Kuala Lumpur, Malaysia

J. Suhr
Department of Polymer Science and Engineering, Sungkyunkwan University, Seobu-ro, Jangan-gu, Suwon-si 206616419, Gyeonggi-do, Korea

M. R. Manshor
Food Sciences and Technology Research Center, Malaysian Agricultural Research and Development Institute, 43400 Serdang, Selangor, Malaysia

Keywords Multilayer Perceptron (MLP) · Machine learning · Analysis of Variance (ANOVA) · Response Surface Methodology (RSM) · Lignin bio composites

1 Introduction

Recently, scientists and engineers have made several efforts to develop eco-friendly materials that degrade without affecting the environment. Biopolymer is one of the materials used to manufacture eco-friendly materials for the environment. Throughout the years, PLA has been utilized in the packaging of food products. It is likewise a crystalline polymer with a glass transition temperature between 60 and 65 °C. PLA is a great biodegradable material for processing a wide range of resins into a variety of products. Lignin and epoxidized palm oil (EPO) is another alternative material that can be used to produce natural polymers without affecting the environment [1]. Moreover, behind cellulose, lignin is the second most prevalent polymer substance. As an additive, it is used in composite materials and bio-based products.

According to the intended properties of the biomaterials and prospective applications for them, the fillers and plasticizers utilized, as well as the concentration, vary substantially (s) [2]. It takes a lot of trial and error to get these settings just right. It's feasible to reduce the number of experiments and the amount of time it takes to conduct them, though, by utilizing statistical analysis and computer approaches. Multivariate statistical analyses have grown increasingly common in recent years, allowing researchers to identify the optimal combination of design factors and their interactions [3]. To conduct multivariate investigations, researchers can use a range of approaches, ranging from the basic factorial design to the more complex response surface method (RSM). Polymer bio composites were typically fabricated using RSM to optimize the fabrication method, to analyze the influence of various process factors on the technique under discussion, and to quantify the effect of various parameters on the properties of polymer bio composites [4]. A linear link between causes and responses cannot be established through RSM. In fact, the RSM approach can't handle a nonlinear relationship with a complicated situation. Since these models can develop and calculate nonlinear relationships [5] using the current experimental data, artificial intelligence and machine learning have gained a lot of attention when modeling experimental data [6]. As far as the authors are aware, there has not been a comprehensive and systematic approach using statistical and machine learning techniques to study the mechanical characteristics of PLA/lignin bio composites. In order to improve the tensile properties of lignin/PLA bio composites, this article used ANOVA, RSM, and MLP to discover the optimal blending that works best together.

2 Methodology

2.1 Materials

OPEFB, a fiber obtained from a local plantation, was employed in this work. It was obtained from Budi Oil Enterprise Sdn. Bhd., Telok Gong, Port Klang, Selangor, Malaysia, which has a density of 0.886 g/mL and an oxirane oxygen concentration of 2.84. NatureWorks Co. Ltd. provided the PLA 2003D pellets needed for this experiment. Sigma Aldrich supplied the sodium hydroxide (NaOH) pellets used in the alkaline extraction method, while Merck Millipore provided the phosphoric acid (H_3PO_4). Lignin powder used in the research was fractionated from OPEFB fibers utilizing a chemical technique (alkaline extraction).

2.2 Preparation of PLA/Lignin Bio Composites

PLA/lignin bio composites were produced using a twin screw extruder (Brabender Lab Station) in accordance with RSM's recommendations of 50 rpm speed and 160–180 °C mixing temperature. Next, hot and cold press process (14 mm × 14 mm × 1 mm spacer mold with temperature 160 °C for upper and lower platens, compression pressure of 1 kpsi) (LP50 LABTECH Engineering Company) was used to compress the blends into sheets. For specimen testing, the sheets were cut according to ASTM D638 specifications.

2.3 Characterization—Tensile Test

A universal testing machine (UTM), Shimadzu Autograph AGS-X series, with a crosshead speed of 2.5 mm/min and a 5 kN load cell was used to evaluate the produced PLA/lignin bio-composite. The composites' tensile strength was measured at room temperature (25 ± 2 °C) and relative humidity (50%–5%) using a set of five 25-mm-gauge filament samples for each filament composition.

2.4 Optimization

The experimental design included two parameters (lignin concentration and EPO), three center points, and five replicates. RSM and Multilayer Perceptron (MLP) were used to model the variables.

Response Surface Methodology (RSM)

The manufacture preparation of Lignin/ PLA/lignin bio composites was accomplished by various of conducted at different mixing and blending techniques, which needed a total of that required 13 sets of experiments, as recommended suggested by RSM (Design Expert software 7.1.5).

Multilayer Perceptron (MLP)

Multilayer Perceptron (MLP) has been chosen for developing a machine learning model since MLP models can be utilized for regression with more input. Adam optimization model and mean square error (MSE) loss function has been used to improve the machine learning predicted output. MSE is derived from Euclidean distance, are based on the relations below:

$$MSE = \frac{1}{n} \sum_{i=1}^n (Y_i - \hat{Y}_i)^2 \quad (1)$$

n = number of data points, Y_i = observed value and \hat{Y}_i = predicted values

3 Result and Discussion

3.1 Analysis of Variance (ANOVA)

The comparison between experimental and predicted values of tensile strength of PLA/lignin bio composites is tabulated in Table 1. Model fitting in RSM/CCRD yielded these anticipated values.

The total interaction between Lignin (A) and EPO (B) that affects the tensile strength of PLA/lignin bio composites can be presented mathematically as follows:

$$\begin{aligned} \text{Tensile strength (MPa)} = & 13.10 + 3.33\text{Lignin} + 4.97\text{EPO} \\ & + 0.06\text{Lignin*EPO} \end{aligned} \quad (2)$$

In Eq. (2), the positive value of the coefficient remarks synergistic effects while negative value denotes antagonistic effects for each variable. R^2 coefficient value for this model is 0.9050, signifying 90.50% of the total variations in the optimization are greatly influenced by the independent variables. Statistically, models with $R^2 >$

Table 1 The mean mechanical properties of the developed lignin/PLA bi composites

No.	Lignin loading (%)	EPO loading (%)	Tensile strength (MPa)		
			Experimental	RSM prediction	MLP prediction
1	6.50	3.00	31.61	31.42	26.71
2	6.50	3.00	30.99	31.42	26.71
3	10.00	5.00	24.44	25.82	27.33
4	11.45	3.00	20.39	20.66	23.57
5	6.50	3.00	31.85	31.42	26.71
6	6.50	3.00	32.11	31.42	26.71
7	6.50	0.17	20.64	22.3	22.69
8	10.00	1.00	21.21	19.68	21.65
9	1.55	3.00	27.76	26.7	29.85
10	3.00	1.00	31.32	24.73	30.37
11	6.50	5.83	32.35	29.9	30.72
12	6.50	3.00	32.54	31.42	26.71
13	3.00	5.00	27.01	29.32	31.77

0.5 indicate high correlation values among variables [7]. The Predicted R^2 of 0.4197 is not as close to the Adjusted R^2 of 0.8371 as one might normally expect; because of the difference is more than 0.2. Moreover, as the majority of points pass over the straight line illustrated in Fig. 1 normality plots, the models avoid the normality issue. The Model F-value of 13.33 implies the model is significant. Even though some of the regression coefficients found in RSM were not high enough, P-values less than 0.05 indicate model terms are significant.

3.2 Modelling with Multilayer Perceptron (MLP)

After numerous tunings of the MLP model, the neural network architecture for the MLP model was decided that the three hidden layers would have 8, 5, and 3 nodes, respectively, because the anticipated results were reasonable for the specified layers and nodes. The model's output is the material's tensile strength, while the three inputs are represented by the percentages of PLA, EPO, and lignin. In comparison to the previous generation, the MSE value has somewhat improved, indicating that the outcome is still within the acceptable range for machine learning prediction [8]. Figure 2 depicts the graph of the MSE's value during the period.

After adding the learning rate, the validation loss for the model is significantly reduced, with training and validation loss values of 10.52 and 22.64, respectively. This demonstrates that the training and validation are well-aligned, and the model seems to perform better than expected, which is useful for comparing actual and predicted results.

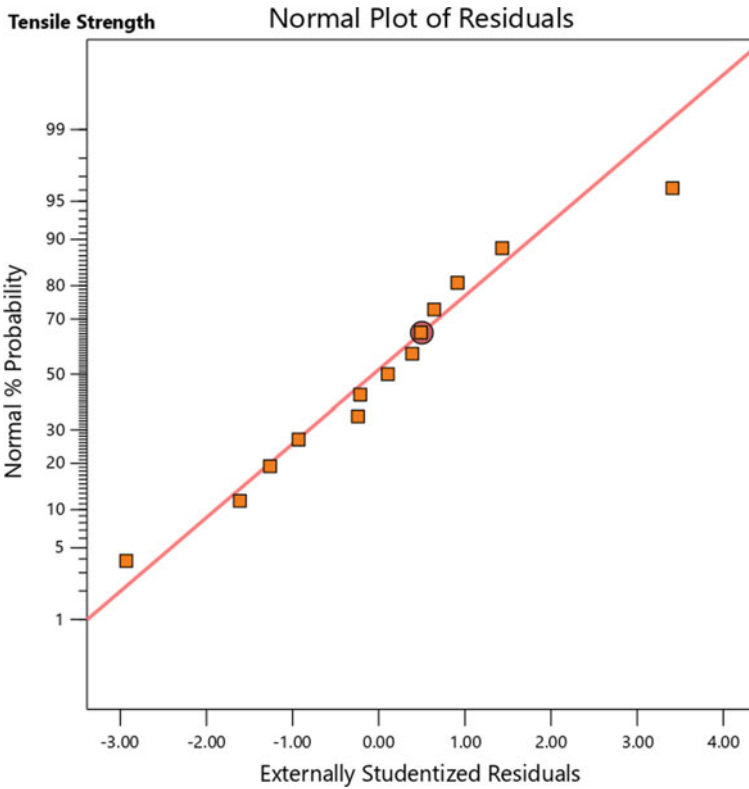


Fig. 1 Normality and residual plots obtained from RSM

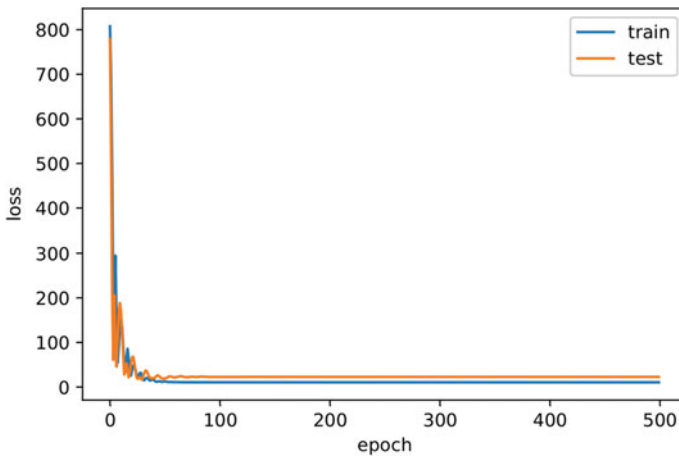


Fig. 2 Training and validation loss

In the meantime, the MLP projected R^2 for tensile strength of lignin/PLA bio composites was found to be 0.60, indicating that the constructed network is competent for producing the optimal predicted outputs with minimal errors [9].

4 Conclusion

Both RSM (statistical approach) and MLP (algorithm for machine learning) are effective methods for determining the relationship between dependent and independent variables. By fitting the experimental data, these models were both able to predict the outcomes. To determine the efficacy of a model, the difference between experimental and predicted values (i.e., errors) is utilized. The R^2 values predicted by RSM were 42.97 percent, whereas the R^2 values predicted by the MLP model were greater than 60 percent.

As a conclusion, thermomechanical properties of bio composites play an important role in their performance depending on the application of interest. On a trial-and-error basis, a wide range of substances (i.e., fillers, plasticizers etc.) is typically added into the polymer matrix to improve the mechanical durability of the bio composites. Nonetheless, this trial-and-error process is time-consuming, costly, and occasionally unreliable. Yet, statistical and machine learning approaches can be utilized to reduce the time and costs associated with extensive experimentation.

References

1. Abd Rahman NA, Anuar H, Mohd. Nordin, N, Mohd Asri SEA, Ali F, Jonghwan S (2021) Mechanical and thermal properties of polylactic acid filled lignin powder biocomposite filaments with epoxidized palm oil for sustainable 3D printing application. *Perintis eJournal* 11(1):23–39
2. Bernhard JC, Vunjak-Novakovic G (2016) Should we use cells, biomaterials, or tissue engineering for cartilage regeneration? *Stem Cell Res Ther* 7:56
3. Zare Y, Garmabi H, Sharif F (2011) Optimization of mechanical properties of PP/Nanoclay/CaCO₃ ternary nanocomposite using response surface methodology. *J Appl Polym Sci* 122:3188–3200
4. Montgomery D Wiley (2017) *Design and analysis of experiments*, 8th edn. Douglas C. Montgomery, Wiley
5. Goodfellow I, Bengio Y, Courville A (2016) *Deep learning*. MIT Press, Cambridge, MA, USA
6. Farahnakian M, Razfar MR, Moghri M, Asadnia M (2011) The selection of milling parameters by the PSO-based neural network modeling method. *Int J Adv Manuf Technol* 57:49–60
7. Wan Busu WN, Chen RS, Shahdan D, Mohd Yusof MJ, Saad MJ, Ahmad S (2021) Statistical optimization using response surface methodology for enhanced tensile strength of polyethylene/graphene nanocomposites. *Int J Integr Eng* 13(6):109–117
8. Liu X, Tian S, Tao F, Du H, Yu W (2020) How machine learning can help the design and analysis of composite materials and structures? [arXiv:2010.09438](https://arxiv.org/abs/2010.09438)
9. Mairpady A, Mourad A-HI, Mozumder MS (2021) Statistical and machine learning-driven optimization of mechanical properties in designing durable HDPE nanobiocomposites. *Polymers*

Detection Method of *Kelulut* Honey Adulteration



Nurul Zafiqha Jefferi, Adibah Amir, and Hadi Purwanto

Abstract The high demand for honey and its expensive market price have lured adulterated honey into the honey industry. Advancements in technology today made it very difficult for consumers to distinguish between pure and adulterated honey. The texture, scent and taste of adulterated honey can be created to be very similar to pure honey to disguise its identity. In this study, a user-friendly detection method has been developed to identify adulterated *kelulut* honey. Four types of adulterants at varied percentages have been mixed with pure *kelulut* honey (PKH). The adulterants are 25% syrup, 50% syrup, 25% vinegar and 50% vinegar, all samples were compared against an original sample that contains 100% PKH. The results have shown that the adulterated samples can be identified by comparing their wavelength values with the original sample using an infrared detection method. The outcome of this study will benefit the consumers to protect their healthcare and well-being from the hazardous effects of consuming adulterated *kelulut* honey because it can affect people's health of every age, race, gender, and income level.

Keywords Adulterated *Kelulut* honey · Consumers healthcare · Infrared detection method

1 Introduction

Pure honey is a natural and raw food that can be consumed as a sweetener and provide medicinal benefits due to its therapeutic impact on human health [1]. The growing health concerns in the wake of the COVID-19 pandemic have driven the demand in the honey sector as honey is a well-known source of numerous nutritional ingredients including vitamins, minerals, and antioxidants. Due to its antibacterial, antiviral, and anti-fungal properties, the product is receiving appreciation and wider acceptance as an effective medicine to treat acute cough and throat infection observed in corona-infected patients [2]. Furthermore, honey also has been cited as an anti-cancer agent

N. Z. Jefferi · A. Amir (✉) · H. Purwanto
Department Manufacturing and Materials Engineering, Kulliyah of Engineering, International Islamic University Malaysia, Kuala Lumpur, Malaysia
e-mail: adibah@live.iium.edu.my

and treatment for eczema, lip sores, sterile and infected wounds, genital lesions, burns, surgery scars and athlete's foot [1]. High demand for nutritious food products is a prominent factor driving the market, as people are increasingly becoming more aware of the benefits of living a healthy lifestyle. The global honey market size was valued at USD 8.58 billion in 2021 and is expected to expand at a compound annual growth rate (CAGR) of 5.2% from 2022 to 2030 [2]. Alas, food adulteration is a major global setback that occurs in the honey industry as well in other food commodities. Adulteration could harm the economic growth in the respective industry and pose hazardous health issues for consumers. An adulteration is an act of intentionally decreasing the quality of food either by adding or swapping low-quality materials or eliminating various important integrants. When cheaper and low-grade elements are added to an original product that threatens the consumer's health, it is considered and declared "adulterated" [1]. Adulterated honey is much cheaper and easier to produce compared to pure honey. Identification of adulterated honey is challenging particularly for consumers because the advancement of technology made ways for doctored adulterated honey to become more sophisticated, resembling similar characteristics to pure honey. Long-term study on lab rats had reported that apparent effects of adulterated honey consumption showed weight increase, abnormal renal and hepatic function parameters, increased circulating triglycerides, cholesterol and glucose level and augmented fat deposition [3]. Therefore, detection of adulteration in food is an essential requirement for ensuring the safety of foods people consume. Although sophisticated lab techniques are accurate, precise, and reliable, they are costly and time-consuming. It is essential to develop reliable "quick screening tests" that a common person can perform at the level of a household to have a broad picture of the status of adulteration in his food in case of doubt [4].

In this study, an approach using infrared wavelength as the detection method of adulteration in pure *kelulut* honey was explored. The purpose of developing this detection method is to provide an alternative to the consumers for quick and easy screening to detect adulterated *kelulut* honey from the products that they purchased in the market.

2 Development of Device

Kelulut honey is a complex substance which contains several hundred compounds belonging to various chemical groups. Besides, the composition of the *kelulut* honey can be different depending on the species, location, storage method, and harvesting period. For example, the unprocessed harvested *kelulut* honey or improper storage method will result in increased moisture content. Furthermore, different characteristics need to be measured with different types of devices. To measure the authenticity of honey, it must comply with the standard requirement of each country. The important characteristics are moisture content, total sugar content, total acidity, ash content, hydroxymethylfurfural (HMF) content, pH value and the presence of plant phenolics. All of these characteristics must be within the range of the standard requirement of

each country [5]. This study developed a self-test kit to detect adulteration in pure *kelulut* honey (PKH) that has been mixed with adulterants. *Kelulut* honey is a tropical honey produced by the Meliponini tribe from the Apidae bee family.

There have been many established detection methods for honey adulteration as summarized by Fakhlaei et al. [1] but it requires expensive high-tech equipment and must be performed in the laboratory by competent personnel. There are a few types of existing test kits in the market such as the quinolone honey rapid test kit which is used to detect the presence of quinolone in honey [6]. Another example is the sulfonamide residue rapid test which is used to detect the presence of sulfonamide in honey [7]. The potential design for this study is infrared (IR) spectroscopy which is usually used to detect adulterants in food, this method was adapted and adopted from Buda et al. [8] who developed a portable non-invasive blood glucose monitoring device using IR detection method. This study developed a self-test detection kit using an infrared detection circuit consisting of a transmitter and receiver to read the wavelength value of the *kelulut* honey sample. The wavelength value will be displayed on the liquid crystal display (LCD) keypad shield. The developed kit can be used to detect the difference in wavelength value based on the different concentrations of a liquid between the original sample of PKH with the adulterated *kelulut* honey.

3 Materials and Method

Figure 1 presents the flowchart of how the detection method works in the detection kit. An original sample of 100% PKH was placed inside a cuvette to enable the first infrared detection circuit to read the wavelength value of a PKH. The second infrared detection circuit was used to detect the wavelength of another sample placed in another cuvette, that was mixed with adulterants. Both samples are placed in the self-test detection kit and the user can proceed to choose the original sample to get the reading for PKH, and then the user can choose sample 1 to get the reading for *kelulut* honey mixed with adulterant. Finally, the user can choose “compare” to identify if sample 1 has been adulterated or not. The result will be shown on the display screen within 3 seconds.

Figure 2 is the assembled self-test detection kit that has been developed for laboratory testing to identify its capability to detect adulterated *kelulut* honey. While Fig. 3 showed step by step the working flow of the detection kit.

Table 1 is the description of the varied adulterated samples prepared to test the capability of the self-test kit in detecting adulterated *kelulut* honey. There were five types of samples, the first type of sample is the original sample, which contains 100% PKH from species *Geniotrigona Thoracica*. The other four types of samples are a mixture of PKH with different adulterants in different ratios. All samples of PKH were collected from a *kelulut* farm at the International Islamic University Malaysia campus, Kuala Lumpur.

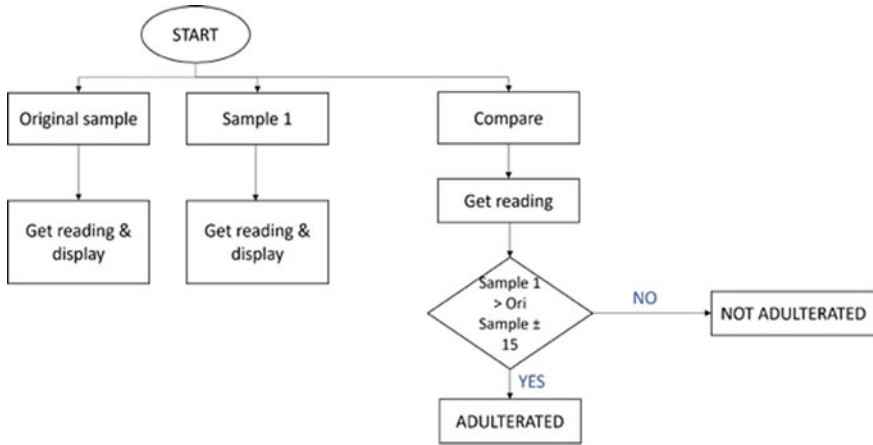


Fig. 1 Flowchart of how the detection kit works to detect *kelulut* honey adulteration

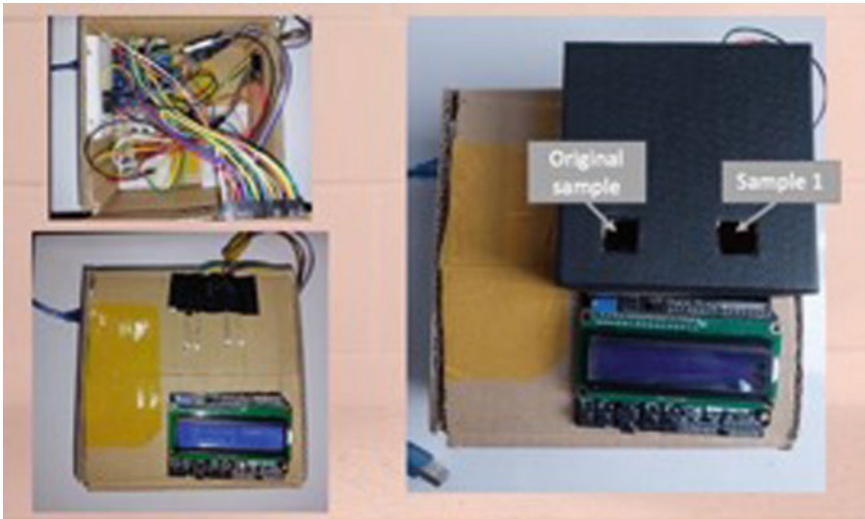


Fig. 2 Self-test detection kit for laboratory testing to detect *kelulut* honey adulteration

4 Results and Discussions

Results obtained from Test No. 1 exhibited the lowest differences, only 2 nm, thus the result displayed on the LCD screen is “Not Adulterated”. Test No. 3 exhibited the highest differences, that is 44 nm when 50% PKH was mixed with 50% vinegar. Whereas when 50% PKH was mixed with 50% syrup and 25% syrup, the differences in wavelength value are 27 and 20 nm. 50% PKH mixed with 25% vinegar gives a



Fig. 3 Step by step the working flow of the self-test detection kit to detect adulterated *kelulut* honey

Table 1 Samples prepared for detection of adulterated *kelulut* honey

Sample label	Sample description
Original	100% pure <i>kelulut</i> honey (PKH)
1	50% PKH mixed with 50% sugar
2	50% PKH mixed with 50% vinegar
3	75% PKH mixed with 25% sugar
4	75% PKH mixed with 25% vinegar

difference of 19 nm. All the tests number 2, 3, 4 and 5 produced result “Adulterated” (Table 2).

5 Conclusion

The outcome from this study showed promising potential for the self-test detection kit to be made available for consumers to carry out quick and easy screening to detect *kelulut* honey adulteration. More detailed work needs to be conducted to improve the prototype design and a greater number of tests need to be conducted using various mixtures of adulterants at various ratios. It is hoped a user-friendly self-test detection kit with high accuracy and fast result could be introduced to the consumers market at affordable price.

Table 2 Comparing authenticity of 100% PKH with different adulterants at different ratios

Test No.	Original sample	Comparison sample	Reading for original sample (nm)	Reading for comparison sample (nm)	Difference (nm)	Result displayed
1	100% PKH	100% PKH	135	133	2	Not adulterated
2	100% PKH	50% PKH + 50% syrup	139	166	27	Adulterated
3	100% PKH	50% PKH + 50% vinegar	128	172	44	Adulterated
4	100% PKH	75% PKH + 25% syrup	137	157	20	Adulterated
5	100% PKH	75% PKH + 25% vinegar	136	155	19	Adulterated





Acknowledgements The authors are thankful to the International Islamic University Malaysia for providing the resources and facilities to conduct this study.

References

1. Fakhlaei R, Selamat J, Khatib A, Abdull Razis AF, Sukor R, Ahmad S, Babadi AA (2020) The toxic impact of honey adulteration: a review. *Foods* 9(11):1538
2. Honey market size, industry report, 2022–2030. <https://www.grandviewresearch.com/industry-analysis/honey-market#:~:text=The%20global%20honey%20market%20size%20was%20estimated%20at%20USD%208.58,USD%2013.57%20billion%20by%202030>. Last accessed 18 June 2022
3. Samat S, Enchang FK, Abd. Razak A, Hussein FN, Wan Ismail WI (2018) Adulterated honey consumption can induce obesity, increase blood glucose level and demonstrate toxicity effects. *Sains Malaysiana* 47(2):353–365
4. Dudeja P, Gupta RK, Minhas AS (2016) *Food safety in the 21st century: public health perspective*, 1st edn. Academic Press
5. Puścion-Jakubik A, Borawska MH, Socha K (2020) Modern methods for assessing the quality of bee honey and botanical origin identification. *Foods* 9(8):1–21
6. Quinolone honey rapid test kit. https://www.alibaba.com/product-detail/Quinolone-honey-rapid-test_62333520253.html?spm=a2700.common-compass.0.0.58b0tEIftElf5m. Last accessed 18 June 2022
7. Honey antibiotics test kit sulfonamides rapid test. https://www.alibaba.com/product-detail/Honey-Antibiotics-Test-Kit-SulfonamidesRapid_60461191268.html?spm=a2700.galleryoffer-list.normal_offer.d_title.7e631bd1ZQvpNs. Last accessed 18 June 2022
8. Buda RA, Addi MM (2014) A portable non-invasive blood glucose monitoring device. In: *IEEE conference on biomedical engineering and sciences*. IEEE, Miri pp 964–969
9. Azmi MFI, Jamaludin D, Abd. Aziz S, Yusof YA, Mustafah AM (2021) Adulterated stingless bee honey identification using VIS-NIR spectroscopy technique. *Food Res* 5(Suppl 1) 85–93

Investigation of the Wear Behavior of Forging Tool by Ball on Disc and Impact Sliding Tribometer



Yaşar Sert , Tevfik Küçükömeroğlu , Hüccet Kahramanzade ,
and İhsan Efeoğlu 

Abstract DIN 1.2714 steel is frequently used as a die material in forging applications. The dies used in the forging process are exposed to both impact and sliding effect during the manufacturing. Therefore, the wear tests of such tools will be possible with a setup that can reflect the process with quantitatively identical resemblance on a laboratory scale. Accordingly, the differences in terms of wear mechanism between the impact sliding wear test setup designed by our team and the conventional ball disc wear setup were evaluated. Moreover, DIN 1.2714 steels are coated with an innovative (TiCrNb-hBN) PVD layer using a high impulse closed field unbalanced magnetron sputtering method to improve their wear performance. Structural investigations of coatings were evaluated using Scanning electron microscope. It was observed that the coatings grown on the surface in granular and columnar structure. Hardness and adhesion strength values were determined by microhardness and scratch tests, respectively. Hardness value of the steel has been increased by approximately 90% owing to TiCrNb-hBN layer. In the wear tests of the specimens under different principles, distinctly different wear mechanisms occurred. While plastic deformation, flaking and groove mechanisms were dominant in impact sliding wear, adhesive and abrasive wear showed itself in ball on disc. It has been demonstrated that the impact sliding wear assembly can better reflect the forging process.

Keywords Forging · PVD · Impact sliding · Ball on disc

1 Introduction

Forging is one of the most common manufacturing methods used in industrial applications. In the forging process, the most important factor affecting the production cost is the forging dies [1]. Wear is the most common problem that limits the service

Y. Sert (✉) · T. Küçükömeroğlu · H. Kahramanzade
Karadeniz Technical University, Trabzon, Turkey
e-mail: yasarsert@ktu.edu.tr

İ. Efeoğlu
Atatürk University, Erzurum, Turkey

life of forging dies [2]. Various surface treatments are applied in order to minimize these wear problems [3, 4]. Among these processes, physical vapor deposition technique come to the fore effectively [5]. Compounds formed from transition metal nitrides between coating layers appear as successful applications. Titanium Nitride (TiN) layer is among the first produced PVD coatings [6]. In the following periods, TiCrN coatings were produced by adding Cr to TiN coatings in order to improve the coating hardness and oxidation resistance [7]. The Nb transition element is used to improve the thermal stability of the coating layer at high temperatures [8]. On the other hand, hexagonal boron nitride (h-BN) structure offers unique properties to the friction and wear performance of the coating layer with its self-lubricating feature. Therefore, it is predicted that the TiCrNb-hBN layer produced within the scope of the study will improve the usage performance of the forging dies. The wear tests used to determine the wear performance of a material should be carried out by considering the working principle of the relevant material in the field of use. Tests should also be carried out in forging dies, taking into account the interaction between the work piece and the die. For this purpose, both the traditional ball on disc and the impact sliding wear test setup designed by our team were compared, and the differences between the setups and their suitability for the forging process were evaluated.

2 Material Method

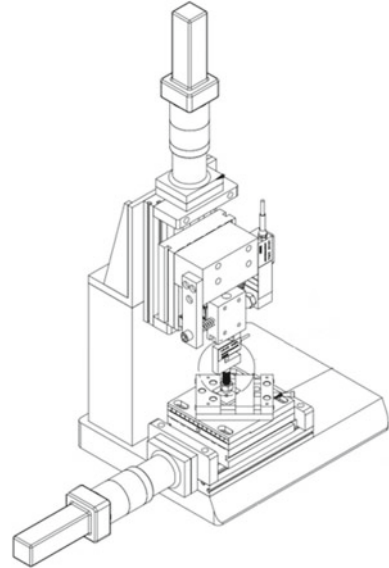
In this study, DIN 1.2714 forging tool steels were prepared in $25 \times 25 \times 4 \text{ mm}^3$ dimensions by machining. In the first stage, the prepared steels were subjected to the heat treatment procedure to obtain $500 \pm 10 \text{ HV}$. The steel specimens, which were hardened and tempered by the applied heat treatments, were subjected to metallographic surface preparation process to remove the traces that occurred during the machining process on their surfaces before the coating processes. After these processes, the topographic examinations of the specimens were carried out with an optical profilometer. As a result of the examination, the surface roughness values of the specimens were determined as $0.05 \text{ }\mu\text{m}$.

Before the deposition process, ion cleaning was carried out for 30 min to clean the possible contamination of the 1.2714 specimens used as the base material. The ion cleaning process was performed using an argon noble gas atmosphere in the vacuum chamber. After the ion cleaning process, the Cr interlayer was deposited on the surface for 10 min to increase the adhesion and oxidation resistance between the coating layer and the base material. The working layer was deposited on the substrate surface as CrN for 10 min, TiCrNbN for 20 min, and TiCrNb-hBN for 30 min. The design of the coating is given in Table 1.

The microstructure and coatings' thickness was determined using the scanning electron microscope (SEM) examination. The mechanical properties of the coatings were investigated using microhardness and scratch tests, respectively. The wear performances of the TiCrNb-hBN layer were determined using at room temperature using a ball-on-disc based and uniquely designed impact sliding wear test setup

Table 1 The design of coating layer

TiCrNb-hBN
TiCrNbN
CrN
Cr
1.2714

Fig. 1 The schematic of impact sliding wear test setup

shown in Fig. 1. The wear mechanisms were characterized as a result of SEM examinations of the worn surfaces, and the differences in two different mechanisms were revealed.

3 Results and Discussion

3.1 Microstructural Analysis

The cross-section and surface of the TiCrNb-hBN coating layer is shown in Fig. 2. When looking at the cross-sectional view (Fig. 2a), it is observed that the layer grows to the substrate surface in the columnar structure and there is no structural defect between the columns. In addition, the thickness of the coating layer was determined as 1.037 μm . On the surface image (Fig. 2b), it is seen that a dense and granular structure is formed. This dense structure is attributed to the high energy of the atoms sputtered from the target materials in the high power density PVD method. The

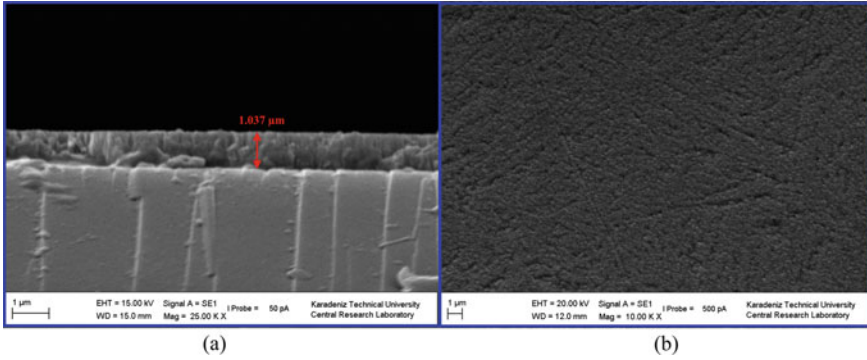


Fig. 2 The Cross-section and surface of TiCrNb-hBN coating

mobility of high-energy atoms during deposition on the substrate surface is higher, thus a dense coating layer is obtained.

3.2 Hardness and Adhesion Strength Properties

The micro hardness values of the specimens are seen in Fig. 3. In Fig. 3 presents that the hardness of the coating is superior than the 1.2714 tool steel. This finding indicates that the TiCrNb-hBN layer have higher resistance of plastic deformation than the substrate. The reason for this statement is attributed to the dense microstructure of the coating, as mentioned before. Due to the high power density PVD system, as the ion density level in the plasma increases, substrate surface is bombarded with more ions and a dense and tightly structure is obtained. The graph and optical microscope images obtained after the scratch test of the coating are given in Fig. 4. According to the relevant figure, the adhesion strength of the coating layer was determined as 65 N. In the optical microscope images, it is observed that the first damage to the coating layer occurs at about 30N (L_{c1}). The presence of micro cracks was detected in this region. There is a smooth break in the section called L_{c2} where the coating is completely separated from the surface. This is also seen from the color changes (orange to blue) in the optical profilometer images in Fig. 4. In addition, the toughness of scratch (the resistance of crack propagation) was obtained as 1050 N^2 using Eq. 1.

$$CPRs = L_{c1}(L_{c2} - L_{c1}) \quad (1)$$

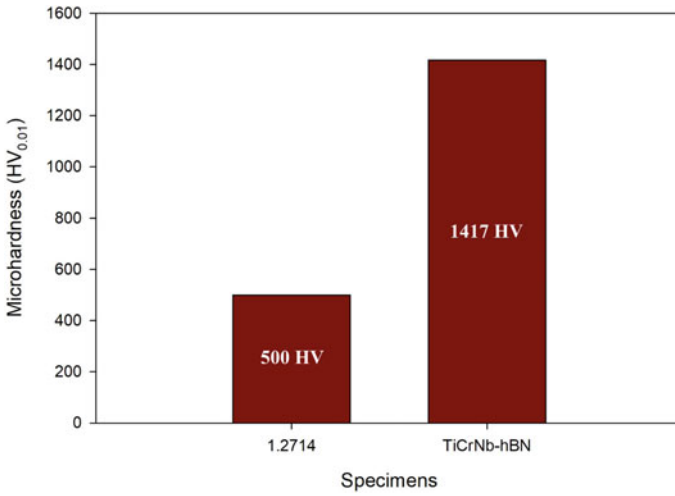


Fig. 3 Hardness values of specimens

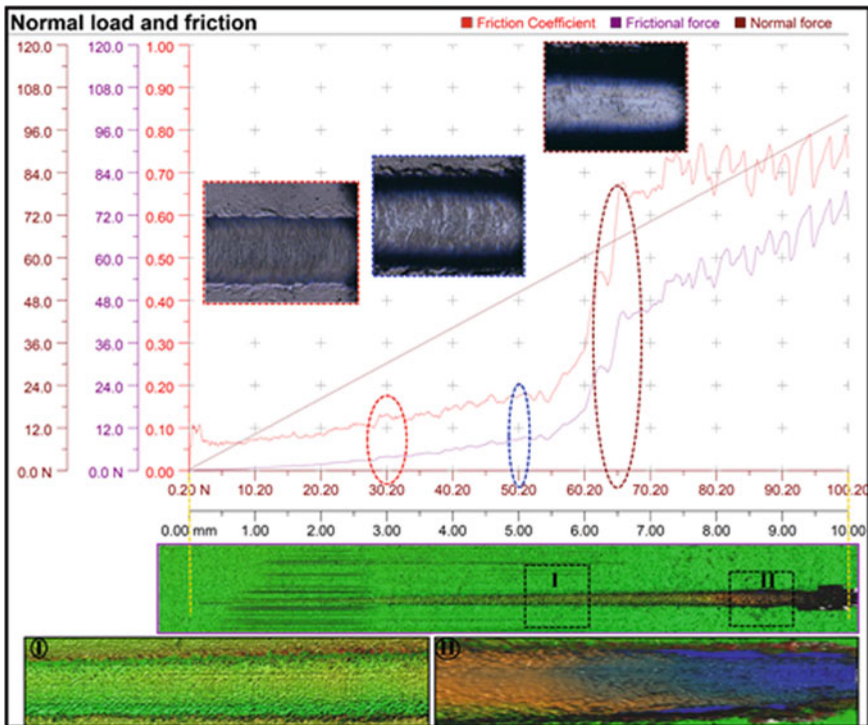


Fig. 4 The scratch graph of TiCrNb-hBN coating

3.3 Wear Properties

The friction coefficient (CoF) graphs obtained as a result of the ball on disc wear tests of the specimens are given in Fig. 5. As can be seen from the figure, a significant decrease has occurred in the CoF of the substrate due to the TiCrNb-hBN layer. A sudden increase in the graph observed in the running-in section of the wear test. A very stable graph was obtained in the coating layer after the sudden increase in this section, which is also called the adaptation phase of the mating surfaces. From this steady state, it was determined that the coating layer remained protective until the end of the wear test and did not separate from the surface. Optical profilometer images of the worn surfaces of the specimens are given in Fig. 6. It has been observed that the Al_2O_3 counter body used in the ball disc wear test could not create an obvious wear mark on the coating layer, just only crushed the roughness of the surface. Therefore, the wear mark is quite superficial. There is a distinct wear mark on the substrate, which is shown in red in the detail view. The wear rates calculated by performing the optical profilometer analysis were obtained as $1.54\text{E}-04$ and $1.12\text{E}-05$ for the substrate and the coating layer, respectively.

The optical profilometer images obtained after the impact sliding wear test of the specimens is given in Fig. 7. As can be seen in the figure, the wear surface is examined in three different sections as impact, sliding and final contact region. In both samples, it was determined that the wear depth in the impact region was higher as expected. Then, in the second region, it was observed that the wear particles that were broken off in the first region were carried along with the counter body. Therefore, it is particularly evident in Fig. 7a that the roughness is higher in this section. Wear particles carried in the sliding region caused accumulations in the final contact area.

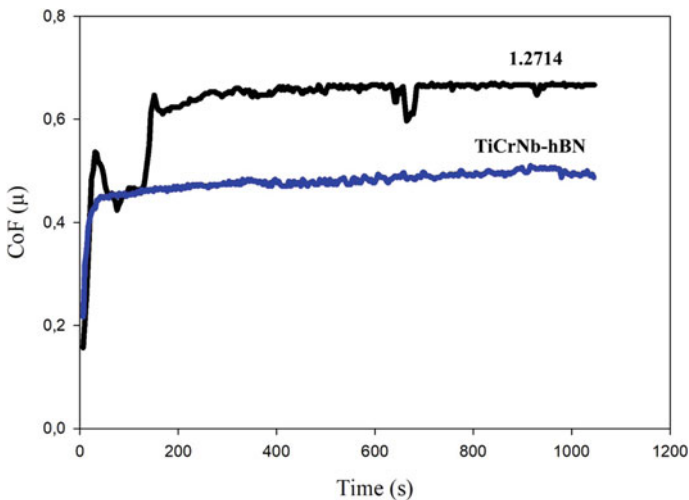


Fig. 5 CoF graph of specimens

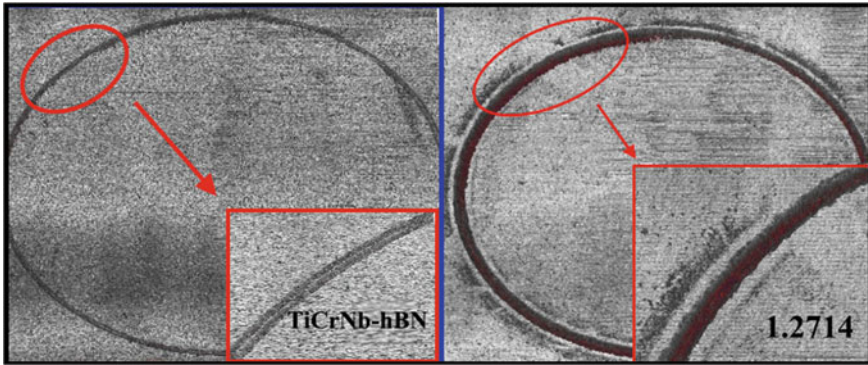


Fig. 6 Optic profilometer images of worn surfaces

It is seen that the said accumulation is more severe in the substrate. This indicates the difference in plastic deformation strength between the specimens. The increased hardness owing to the TiCrNb-hBN coating also contributed to the impact sliding behavior of the coating.

SEM images of the wear surfaces obtained as a result of the wear tests of the specimens are given in Fig. 8. According to the Fig. 8a, the dominant wear mechanism in the substrate is adhesive wear. With the frictional heat, micro-weld joints were formed between mating surfaces. In the course of the experiment, the broken microweld connections caused irregularities on the wear surface. The entrapment of the broken particles (wear debris) between the friction surfaces resulted in third-body wear. The wear surface of the TiCrNb-hBN coated sample is smooth compared to the base material. It is observed that oxide particles are collected at the trace edges. In addition, the capillary scratches caused by abrasive wear have occurred along the wear track.

As can be seen from the SEM images Fig. 8b, it is understood that the wear damages on the specimens started with the fatigue microcracks formed in the wear path due to the impact effect. It is seen that the wear mechanisms in the samples are

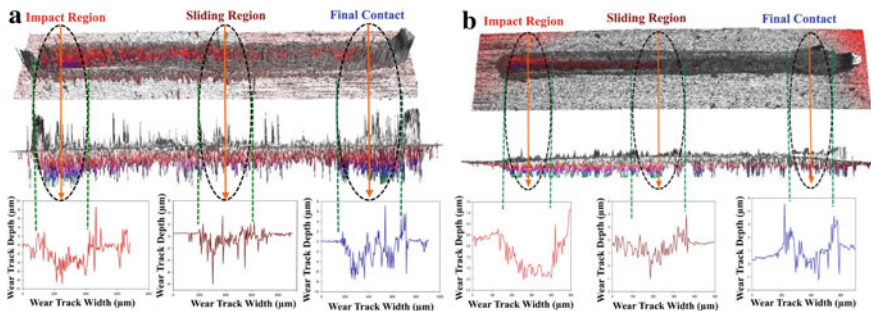


Fig. 7 Optical profilometer images of specimens. a 1.2714, b TiCrNb-hBN coating

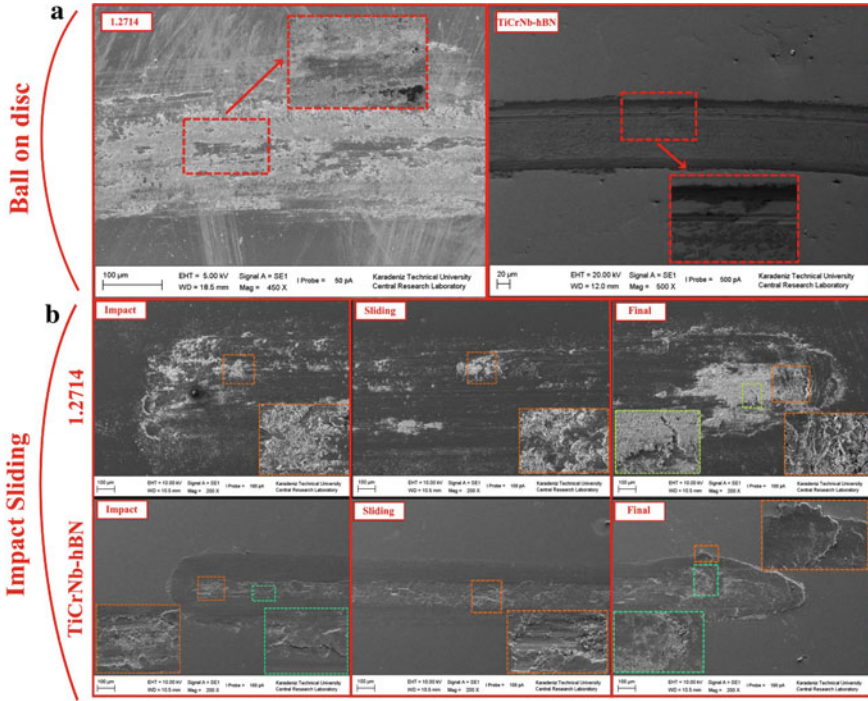


Fig. 8 SEM images of wear surface. a Ball on disc, b impact sliding

concentrated towards the center of the wear track (sliding region). When looking at the SEM image of the wear path of the substrate, severe plastic deformation damage is observed especially in the impact region. In the final contact region, the particles that broke off from the impact region are transported between the counter surface and the sample in the sliding region, creating deep grooves, chipping and scratches. On the other hand, a relatively smooth wear surface is encountered in the coating layer, as in the ball-on-disc. In the impact region, deep cavities are formed with plastic deformation on the surface due to the loading effect. In the sliding and final contact area, the substrate is damaged due to the removal of the coating from the surface.

4 Conclusions

In this study, the surface, hardness, adhesion strength and wear properties of uniquely designed TiCrNb-hBN coatings produced to improve the wear performance of forging dies were investigated. The wear properties of the samples were determined using with the traditional ball disc and the original designed impact sliding test setup,

which is predicted to have a higher ability to reflect the working principle of forging dies. The results obtained are below.

The TiCrNb-hBN coating layer was grown on the DIN 1.2714 steel in a columnar structure without any structural defects. The thickness of the coating was obtained as 1.037 μm . The hardness of substrate material (500 HV_{0.01}) was enhanced to 1414 HV_{0.01} owing to the TiCrNb-hBN coating. The adhesion strength (L_{c2}) of layer was determined as 65 N. Besides, the crack propagation strength was calculated as 1050 N². In the wear tests carried out in the ball on disc test setup, the TiCrNb-hBN coating layer reduced the friction coefficient of the substrate. The fluctuating friction coefficient graph has become stable due to the coating layer. However, the improvement in wear rates is quite evident. The wear mark on the coated sample is superficial. The wear performance of the coating layer is also remarkable in the tests conducted using impact sliding wear test setup. The use of the impact sliding test setup has provided more realistic findings in investigating the wear performance of forging dies.

Acknowledgements This research is partially supported by TUBITAK (Scientific and Technical Research Council of Turkey) Grant No: 5190089. Also supported by Karadeniz Technical University. Grant No: FDK-2019-8487.

References

1. Anderson M, McGuire K, Zante R, Ion W, Rosochowski A, Brooks W (2013) Identifying the dominant failure mode in the hot extrusion tooling used to forge nickel based superalloy. *J Mater Process Technol* 213:111–119
2. Tercelj M, Panjan P, Urankar I, Fajfar P, Turk R (2006) A newly designed laboratory hot forging test for evaluation of coated tool wear resistance. *Surf Coat Technol* 200(11):3594–3604
3. Hacısalihoğlu I, Kaya G, Ergüder OT, Mandev E, Manay E, Yıldız F (2021) Tribological and thermal properties of plasma nitrided Ti₄₅Nb alloy. *Surfaces Interfaces* 22:100893
4. Fernandez-Valdes D, Meneses A, Lopez- A, Ocampo A (2021) Sliding wear analysis in borided AISI 316L steels. *Mater Lett* 285:129138
5. Sert Y, Ghahramanzadeh H, Küçükömeroğlu T (2022) Tribological properties of in-situ PVD TiAlN, TiSiN, and TiAlN/TiSiN coatings under ambient air and vacuum environment. *J Mater Des Appl* 236:1777–1792
6. Xie W, Zhao Y, Liao B, Wang S, Zhang S (2022) Comparative tribological behavior of TiN monolayer and Ti/TiN multilayers on AZ31 magnesium alloys. *Surf Coat Technol* 441:128590
7. Thampi VV, Bedavid A, Subramanian B (2016) Nanostructured TiCrN thin films by pulsed magnetron sputtering for cutting tool applications. *Ceram Int* 42(8):9940–9948
8. Cicek H, Baran O, Keles A, Totik Y, Efeoglu I (2017) A comparative study of fatigue properties of TiVN and TiNbN thin films deposited on different substrates. *Surf Coat Technol* 332:296–303

Towards Whole Day Thermoelectric Energy Scavenging from Solar Using Carbon Based Photothermal Nanofluid



Penzi Panguot, Abdah Nadhirah Khamis, Mohd Aszwan Jimal,
Nur Natasha Erna Herman, Lily Yong,
and Megat Muhammad Ikhsan Megat Hasnan

Abstract Direct energy harvesting using thermoelectric energy conversion of large amounts of low-grade thermal energy into electricity is a promising sustainable green technology. Solar thermal energy systems, specifically solar hot water household heating or storage systems, are commonly considered to be the most cost-effective alternatives to fossil fuel hot water heating systems. However, many hybrid systems found in the literature are still unable to generate electricity efficiently at night, when family users consume the most. This research demonstrates electrical energy scavenging from solar heat by using a thermoelectric generator that is driven by water-based carbon nanofluid as heat storage. Furthermore, a sensible heat storage medium is tested using nanofluids such as water, graphite, graphene oxide and carbon nanotubes. This study shows successful proof of concept of carbon nanotube as the best light-absorbing carbon material that has been tested and is capable of powering up a 2 Mohm light device during the night and sustaining it for a minimum of 4 h using 1 L volume of nanofluid without emitting any greenhouse gases.

Keywords Thermoelectric · Carbon based nanofluid · Energy scavenging · Solar · Photothermal

1 Introduction

Energy shortages have plagued islands and remote coastal communities like Sabah for decades [1]. Electricity provision is seen as one of the pillars of a country's socioeconomic prosperity and a crucial tool for lifting people out of poverty, particularly in rural areas. Almost 0.8 million Malaysians do not have access to power. Submarine cables or fossil-fuel-based generation facilities give their energy, which has massive carbon footprints, limited fuel mix diversification, and probable supply disruptions [2]. Solar and thermally produced electricity as a fuel substitute, as well as the sustainable utilisation of global energy resources, are two of the most promising

P. Panguot · A. N. Khamis · M. A. Jimal · N. N. E. Herman · L. Yong · M. M. I. M. Hasnan (✉)
Faculty of Engineering, Universiti Malaysia Sabah, Jalan UMS, Kota Kinabalu, 88400 Sabah,
Malaysia
e-mail: megatikhsan@ums.edu.my

© The Author(s), under exclusive license to Springer Nature Singapore Pte Ltd. 2023
Md. A. Maleque et al. (eds.), *Proceeding of 5th International Conference on Advances in Manufacturing and Materials Engineering*, Lecture Notes in Mechanical Engineering,
https://doi.org/10.1007/978-981-19-9509-5_61

461

renewable energy technologies [3]. Photovoltaic technology converts solar energy into electricity, whereas thermoelectric technology converts heat energy into electricity. However, both require light and heat respectively to function and neither has a built-in single device energy storage unit. Solar panel efficiency is limited by thermal and it cannot operate without light [4].

An alternative to solar panels is a thermoelectric power generator, which may directly convert heat energy into electrical energy via the thermoelectric effect. It can employ waste heat in a variety of applications, including running electronic gadgets, automobiles, indoor buildings, and even the human body [5]. A thermoelectric system with a high capacity thermal storage element enables a simple system to immediately tap heat, store it for an extended period of time, and convert it to energy all day. Solar hot water systems with thermoelectric generators (TEGs) have recently been combined and are considered sustainable solutions [6]. The Seebeck effect is used by TEG devices to convert heat energy into electrical energy [7]. The Seebeck effect S_e is governed as Eq. (1) below where V is electrical potential and T is temperature.

$$S_e = \frac{V_{Hot} - V_{Cold}}{T_{Hot} - T_{Cold}} \quad (1)$$

The TEG generates electricity by creating a temperature difference between its two surfaces. Thermal storage materials such as phase change material (PCM) and molten salt are limited in their application for thermal energy storage due to their low thermal conductivity, poor solar-thermal conversion efficiency, and poor shape stability [8]. The direct insertion of high-thermal-conductivity elements such as carbon materials [9, 10], metal foam [11], and nanoparticles [11] has previously been used to improve the thermal conductivity of phase transition materials. These methods work well for organic phase transition thermal storage materials at low temperatures but are challenging to implement at high temperatures.

This research will create an all-day energy harvesting lab-scale solar-thermal-electric power system based on a thermoelectric generator and carbon-based nanofluid photothermal heat storage. The goal of solar photothermal conversion is to turn sunlight into heat through system collection and absorption. In terms of the photothermal effect, the infrared band of the solar spectrum, which limits the solar panels' performance due to overheating can be utilised as an abundance green heat source to power up TEG. The light-absorbing materials must be used to absorb the sun's rays, resulting in photothermal conversion. When light strikes the light-absorbing material, photon energy interacts with the crystal lattice, causing the vibration to strengthen and the temperature to rise. The material must absorb a wide range of light spectrums to improve light-to-heat conversion.

In this study, carbon-based nanoparticles are utilised to generate a higher heat flux desirable for better TEG power generation from solar radiation by producing a high temperature on the TEG's hot side surface. Carbon-based materials have a high capacity for sunlight absorption across the whole solar spectrum due to their conjugated structure. The photothermal conversion process of π -bonded carbon-based materials can be illustrated in Fig. 1. The sensible nanofluid heat storage

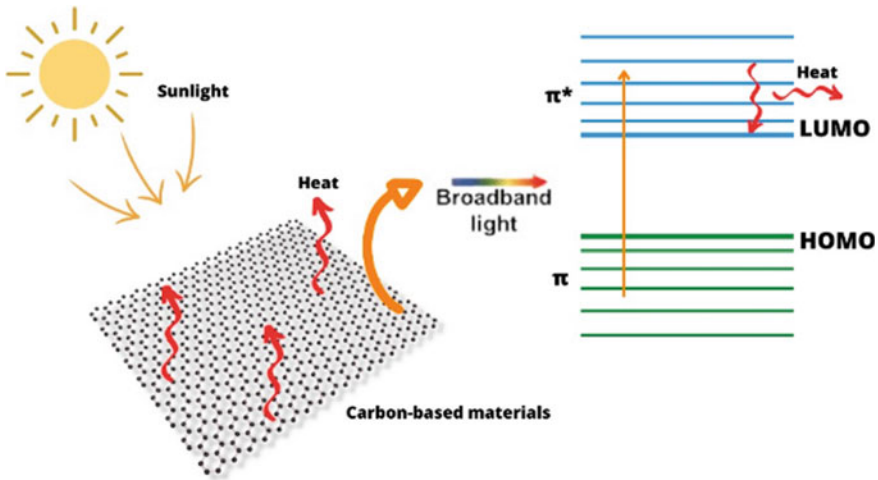


Fig. 1 Mechanism of photothermal conversion process of π -bonded carbon-based materials

mediums, graphite, carbon nanotubes, and graphene are tested in this study in terms of photothermal effect. The thermal energy is stored from solar light during the day. The suggested method is unique in that the heat stored as hot photothermal nanofluid is employed for TEG to provide a high-temperature source throughout the night. It is then kept as a thermal nanofluid to be used in numerous applications such as in a model house to light up LED arrays. The fundamental findings from this project will be well suited to harvesting energy from Malaysia's environmental conditions which have a high UV to IR band of the solar spectrum and allow application in countries of similar geographical conditions.

2 Methodology

2.1 Materials

The details of the material and tool used for this study are as shown in Table 1.

2.2 System Design and Working Principle

The solar-thermal-electric power generation flow diagram is illustrated in Fig. 2. Copper heat pipes will be employed for heat transfer. To reduce the effect of air micro gap that increases the thermal resistance between TEG and copper heat pipes, between TEG and the water tank (hot chamber), thermal paste is placed between

Table 1 Details of material and tool

Materials	Details
Photothermal material	Graphene oxide, graphite, carbon nanotube
Thermal paste	Thermal conductivity of 8 W/mK
TEG module	Bismuth Telluride, 40 mm × 40 mm × 4 mm, internal resistance of 1.90 Ω
Fresnel lens	Focal length of 10 mm
Thermometer	precision: ± 0.1 (0–200)
Solvent	1 L distilled water

them. During daytime, solar radiation (light) is allowed to illuminate nanofluid through an optical window, focusing the light on a nanofluid for photothermal charging. Once the minimum temperature to operate the TEG is achieved, the hot nanofluid is transferred to the thermoelectric subsystem. The temperature difference between the hot nanofluid and the cold water will power the TEG, which will then illuminate the LED. Three types of photothermal nanofluid is prepared to be tested as photothermal storage to power up TEG. 0.1% of the total water weight of graphene graphite and carbon nanotube is used to be dispersed in water as photothermal nanofluid.

During the night, due to the photothermal tank volume being larger than the size of the thermoelectric subsystem tank, the remaining nanofluid that is still warm during the day is poured into the thermoelectric subsystem tank to replace the daytime nanofluid. As a result, the heat flow in the system will be continuously generated to power up the TEG during nighttime.

3 Results and Discussion

Figure 3a shows the absorption obtained from four different types of materials such as carbon nanotube, water, graphite, and graphene oxide that prepared. As shown in the Fig. 3a, b, the carbon nanotube produced maximum absorption intensity and maximum temperature rise compared to water, graphite, and graphene oxide when illuminate with solar light.

The corresponding open circuit voltage to the applied temperature difference was recorded for CNT. The photo thermal effect was driven by solar energy conversion and thermal energy storage. Figure 4a shows the open-circuit voltage of the module corresponding to the applied temperature difference across the hot and cold ends. The linear fits to the data are used to determine the average Seebeck coefficient of the TEGs. The Seebeck of the system found to be 135 mV/°C. Figure 4b shows the increment of power density at 2 Mohm load resistor. By the rule of thumb, the power density of the system can be scaled up by increase the TEG module and surface area to meet the practical user requirement. For this lab scale study, the minimum

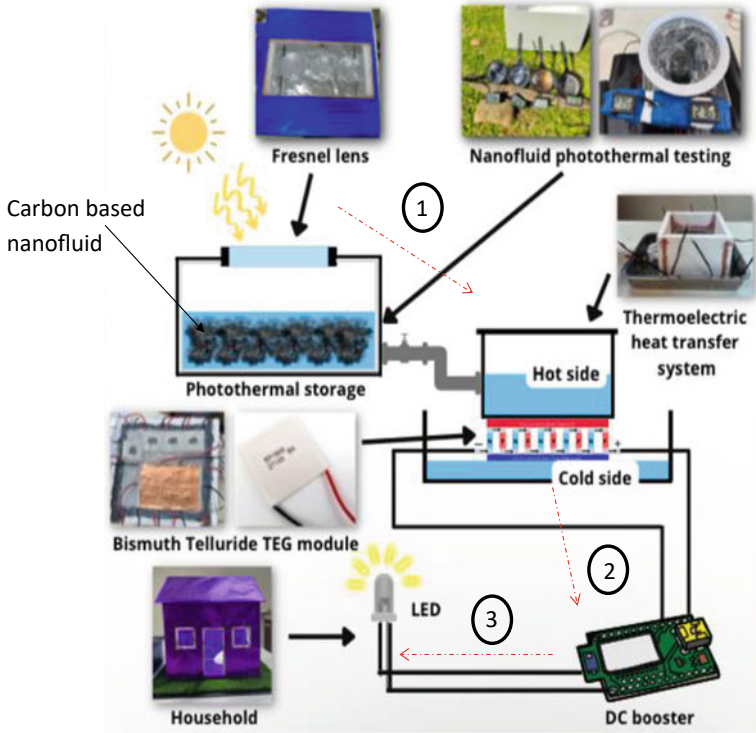


Fig. 2 Schematic process of the photo-thermoelectric storage and power generator

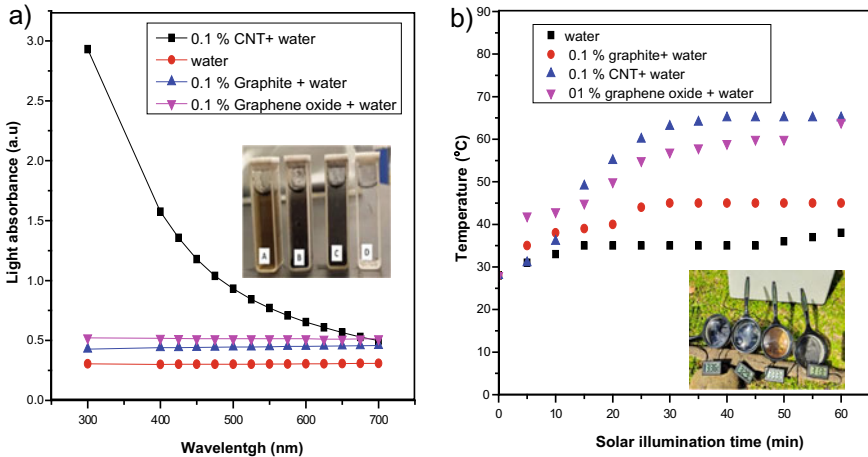


Fig. 3 Measured of **a** absorbance and **b** temperature rise of various photothermal carbon nanofluid materials

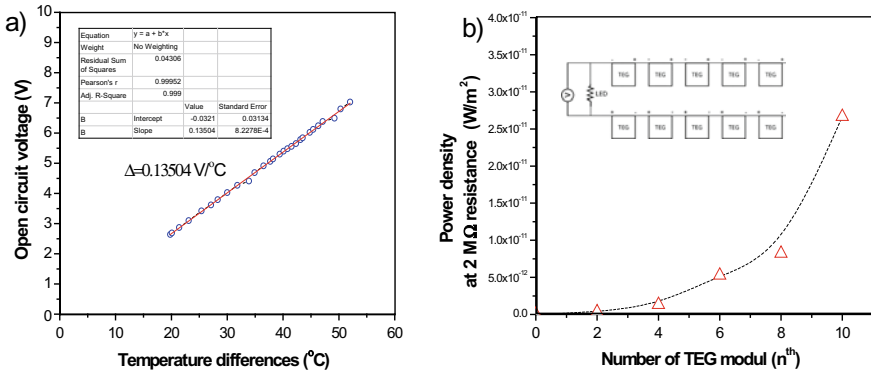


Fig. 4 a Open circuit voltage generation and b power generation versus number of TEG module at 2MΩ resistance

TEG module needs to power 2.1 Mohm LED found was 8 modules and the ability of the system to maintain the power generation at least 4 h to light up the 2 Mohm LED just using 1 L photothermal nanofluid. According to the Seebeck effect, higher temperature difference yields larger potential and vice versa [6]. As time progresses, the power start to decrease since the temperature difference continuously become lower. It is necessary to make the temperature decrease much more slowly using more thermal insulation or to make the temperature difference constant so that, the power of LED much higher.

4 Conclusions

In summary, a whole-day energy-scavenging power system based on the TEG and water-based heat storage was successfully tested experimentally. The experiment demonstrated that the designed system can generate power using stored heat both during the day and at night using photothermal nanofluid. The best photothermal nanofluid found was carbon nanotube, followed by graphene oxide, graphite and water. The application of this alternative green technology in converting waste-heat energy into electrical power can be implemented in rural areas that are outside of the electrical grid. Therefore, this study has successfully shown proof of concept for sustainable green energy that can impact on society, particularly in rural and remote areas.

Acknowledgements This project is funded by Ministry of Higher Education Malaysia under Fundamental Research Grant Scheme (FRGS), with a reference number of FRGS/1/2022/TK08/UMS/02/17. We acknowledged Mr. Hazwan Horace, Lab Assistant of the High Voltage Lab and members of High Voltage Power Energy Research (HiPER) club, Faculty of Engineering, Universiti Malaysia Sabah for support.

References

1. Koh S, Lim Y (2010) Meeting energy demand in a developing economy without damaging the environment—a case study in Sabah, Malaysia, from technical, environmental and economic perspectives. *Energy Policy* 38(8):4719–4728
2. Roques R, Newbery D, Nuttall W (2008) Fuel mix diversification incentives in liberalized electricity markets: a mean-variance portfolio theory approach. *Energy Economics* 30(4):1831–1849
3. Crabtree G, Lewis N (2008) Solar energy conversion. *Phys Today* 60(3):37–42
4. Good C, Andresen I, Hestnes N (2015) Solar energy for net zero energy buildings—a comparison between solar thermal, PV and photovoltaic–thermal (PV/T) systems. *Solar Energy* 122:986–996
5. Little A, Garimella S (2011) Comparative assessment of alternative cycles for waste heat recovery and upgrade. *Energy* 36(7):4492–4504
6. He W, Zhang G, Zhang X, Ji J, Li G, Zhao X (2015) Recent development and application of thermoelectric generator and cooler. *Appl Energy* 143:1–25
7. Uchida K et al (2008) Observation of the spin Seebeck effect. *Nature* 455(7214):778–781
8. Eanest Jebasingh B, Valan Arasu A (2020) A detailed review on heat transfer rate, supercooling, thermal stability and reliability of nanoparticle dispersed organic phase change material for low-temperature applications. *Mater Today Energy* 16:100408
9. Berber S, Kwon Y, Tománek D (2006) Unusually high thermal conductivity of carbon nanotubes. *Phys Rev Lett* 84(20):4613–4616
10. Chen Y, Ting T (2002) Ultra high thermal conductivity polymer composites. *Carbon* 40(3):359–362
11. Yu X, Tao T, He Y, Lv Z (2022) Temperature control performance of high thermal conductivity metal foam/paraffin composite phase change material. An experimental study. *J Energy Storage* 46:103930

Diffusion, Seebeck and Conductivity of Spin Crossover Complexes Towards Thermoelectric Power Generation



Megat Muhammad Ikhsan Megat Hasnan, Chai Chang Yii, Nur Aqilah Mohamad, Ahmad Razani Haron, Pungut Ibrahim, Herwansyah Lago, Ismail Saad, and Hazlihan Haris

Abstract Development of Seebeck generation from heat requires understanding of the behavior of electrochemical properties as a function of temperature. This study performs cyclic voltammetry of octahedral iron, manganese, and cobalt spin-crossover materials to relate the electrochemical properties of the spin-crossover complex with the Seebeck performance. The diffusion coefficient, which is determined by cyclic voltammetry, determines the magnitude and sign of the Seebeck coefficient. From the results, the higher Seebeck iron complex in 3-Methoxypropionitrile solvent compared to the iron complex in Dimethyl sulfoxide solvent, is due to its high diffusion ratio, high total diffusion and high conductivity. Thus, this study shows that, the selectivity of transition metal type for spin crossover material and solvent affects Seebeck coefficient significantly by the diffusion that is extracted from cyclic voltammetry analysis.

Keywords Spin-crossover · Redox electrolyte · Seebeck · Thermoelectrochemical cell

1 Introduction

The ability of solid-state materials to convert a temperature gradient into energy is referred to as thermoelectric (TE) technology. This TE behaviour is also found in thermoelectric chemical cells (TEC), which consist of two inert electrodes and an active redox material [1–5]. The active redox materials are dissolved in a solvent or ionic liquid. The temperature difference (T) between the hot and cold electrodes induces an imbalance in the redox processes, resulting in an electromotive force (V). The electrochemical Seebeck effect is based on the difference in redox reaction entropy between the hot and cold sides of the electrode. The reaction entropy during a redox reaction is proportional to the ratio of the ΔV between the electrodes and

M. M. I. Megat Hasnan (✉) · C. C. Yii · N. A. Mohamad · A. R. Haron · P. Ibrahim · H. Lago · I. Saad · H. Haris
Faculty of Engineering, Universiti Malaysia Sabah, Jalan UMS, Kota Kinabalu, 88400 Sabah, Malaysia
e-mail: megatikhsan@ums.edu.my

the ΔT , as indicated in Eq. (1) [6–8].

$$S_e = \frac{\Delta V}{\Delta T} = \frac{\Delta S_{reaction}}{nF} \quad (1)$$

where n is the number of electron involves in the redox reaction and F is Faraday constant. Based on Born's model [7], is as expressed in Eq. (2).

$$\Delta S_{reaction} = \frac{-e^2 N}{2\epsilon T} \left(\frac{d \ln \epsilon}{d \ln T} \right) \left(\frac{z_{ox}^2}{r_{ox}} - \frac{z_{red}^2}{r_{red}} \right) \quad (2)$$

where ϵ is the dielectric constant Z_{ox} and Z_{red} are the valence charges of the oxidant and reductant, respectively. R_{ox} and r_{red} are the corresponding radius, e is the electronic charge, and N is the Avogadro's constant. The ability to change the electronic spin state of charge carriers using temperature rather than a magnetic field makes spin crossover (SCO) material as appealing as TEC material. SCO complexes have previously been explored as materials for TEC applications [7–12], with considerably large S_e (2 mVK^{-1}) values reported, making them interesting TEC candidates. The $\text{Co}^{II/III}(\text{bpy})_3(\text{NTf}_2)_{2/3}$ is an example of SCO material with a high S_e range of $1.4\text{--}2.19 \text{ mVK}^{-1}$ [12].

The key to boosting the Seebeck coefficient is to increase the entropy reaction, which can be done by increasing the difference in molecular radius and valence charges between the oxidised and reduced species at hot side and cold side [13]. It is especially fascinating to apply this to SCO materials because changes in their HS and LS states are associated with a considerable shift in their molecular structure [7–13]. The temperature drives the spin-state transition in this situation. This works is using cyclic voltammetry to assess the diffusion characteristics of the SCO material relationship with the magnitude and sign of the Seebeck generation. Thus, this work will provide on understanding the TEC parameters of SCO complexes using electrochemical analysis for the future rational design of SCO molecular structure for TEC application.

2 Methodology

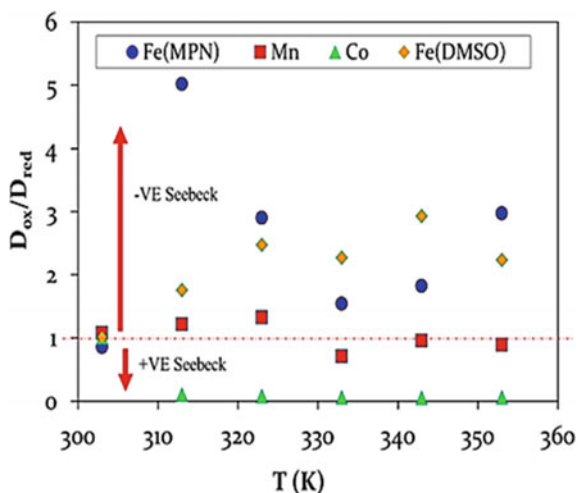
In this study, the electrochemical properties of the octahedral structure containing transition metal (Fe, Mn, and Co) as the base metal centre with ligands of intermediate field strengths using N-donor ligands is investigated [7–13] using the previous synthesis method [13]. The Fe complex was dissolved in DMSO and MPN solvents due to the solubility in both solvent, whilst Mn and Co was dissolved in DMSO, respectively. Cyclic voltammetry (CV) was measured as a function of temperature from 300–355 K, using Pt (length 1 cm and diameter 0.1 mm) as the working, counter and reference electrode at low scan rate 5 mVs^{-1} . From the CV, redox potential and limitation current peak was determined for the diffusion ratio and electrode formal

potential calculations using Randles-Sevcik and Nernst equation. The half-cell can be extracted from cyclic voltammetry that can be related to the simplified Nernst equations [12]. Thus, the half-cell potential depends on the (i) diffusion rate ratio ($D_{\text{ox}}/D_{\text{red}}$), which is calculated from limitation current peak) and (ii) E_f , the total electrode formal potential, calculated from the average redox potential. The D_{ox} and D_{red} are Diffusion coefficients of oxidation and reduction process respectively, calculated by using Randles–Sevcik theorem[12]. The Seebeck coefficients for the complexes were measured for three cycles using the two-beaker experiment setup [12], where T_{cold} is 305 K and T_{hot} is 300–350 K. A thermocouple type K was used to validate the temperature for each measurement. The ionic conductivity is measured using electrochemical impedance spectroscopy using 10 mV of AC voltage at sweep frequency of 1 m-1 MHz.

3 Results and Discussion

The mass transport behaviour of charge carriers due to thermodynamic equilibrium (steady-state) in TEC can be described using diffusion coefficient analysis. Fe(II) in MPN had higher total diffusion than the other complexes. It is inferred that the magnitude of total diffusion contributes to the magnitude of the Seebeck coefficient. The diffuse layers with nonzero net charge near the working electrode can be summarised as a diffusion ratio as shown in Fig. 1. The diffusion ratio is the ratio of total oxidation activity to total reduction activity of charge carriers at both hot and cool electrodes. The Seebeck sign of the complexes is inferred to have relationship with the diffusion ratio trend, where the Seebeck sign is inferred to be positive for diffusion ratios greater than one and negative for diffusion ratios less than one.

Fig. 1 Diffusion ratio extraction from CV scan rate 5 mVs^{-1} versus temperature



The complexes' Seebeck coefficient that shown in Fig. 2 was determined using the non-isothermal two-beaker experiment, during three cycles with $T_{\text{cold}} = 305$ K and $T_{\text{hot}} = 305\text{--}400$ K. The Seebeck sign of the complexes has shown good correlation with the previous diffusion ratio trend, where the Seebeck sign is found to be positive for diffusion ratios greater than one and negative for diffusion ratios less than one. There is positive sign for Co and a negative sign for Fe and Mn, respectively. Interestingly, there was a crossover in the Seebeck gradient for Mn from negative to positive across the temperature range. The diffusion ratio of Mn was greater than one only between 300 and 320 K and was less than one after 320 K. Because of the substantial molecular distortion of paramagnetic Mn(II) complexes caused by the Jahn–Teller distortion, the reduction process of the Mn(III) complex to Mn(II) was assumed to be more difficult at high temperatures. In DMSO solvent, the Seebeck coefficient for Mn was $-0.60.01$ mVK $^{-1}$ at $T = 0\text{--}25$ K and $+0.40.01$ mVK $^{-1}$ at $T = 25$ K. Whilst, the Seebeck coefficient for the Co complex was $+0.30.01$ mVK $^{-1}$ at $T = 0\text{--}50$ K, where the diffusion ratio became less than unity after applying heat, indicating the difficulties in oxidising the paramagnetic Co(II) complex's extremely deformed structure. Due to unequal electron occupancy in the d-orbital, the Co(II) complex experienced substantial octahedral distortion when switching from LS to HS and vice versa. Furthermore, an increase in the Seebeck coefficient for the Fe complex demonstrates that its solubility in a polar MPN solvent generated a greater Seebeck coefficient (-0.960 ± 01 mVK $^{-1}$) compared to the Fe in DMSO ($S_e = -0.50 \pm 01$ mVK $^{-1}$). The high Seebeck magnitude found of Fe in MPN compared to the other exhibited good correlation with the magnitudes of total diffusion. The oxidation process dominated the diffusion ratio of Fe(II) in MPN and DMSO, as shown in Fig. 1, since the diffusion ratio was more than unity, as expected for a diamagnetic Fe(II) complex. Fe(II) exhibits a distinct diffusion ratio trend in MPN when contrasted to the more linear Fe(II) diffusion ratio in DMSO. Thus, the electrochemical parameter extracted from CV was shown to be a critical parameter in elucidating the Seebeck sign and magnitude in order to design and develop new remarkable performance of the SCO TEC material. The optimisation of the Seebeck of the SCO complex will be further investigated in future in terms of optimum molar concentration, complex ligand length and ionic conductivity through CV analysis.

Diffusion activity of the metal complex as a function of temperature is a major contribution to the ionic conductivity of the complexes. Highest ionic conductivity of Fe(II) in MPN due to the high diffusion ratio and total diffusion magnitude compared to the others has been proven based on ionic conductivity measurement. Figure 3 shows that Fe in MPN has a higher ionic conductivity, by three orders of magnitude compared to the other samples. The complexes demonstrated nonlinear characteristics of ionic conductivity as a function of temperature due to changes in its spin state when stimulated by heat. The high conformational stability of the LS Fe complex in MPN is the key factor that leads to the high ionic conductivity for Fe in MPN. The ionic conductivity of Co shown a step profile that inferred due to the change of LS to HS state at the transition temperature of 320 K. Interestingly, for the Mn complex, the crossover of the ionic conductivity was found after the transition temperature (320 K) due to the change from LS to HS state. The lower energy of the d-orbital

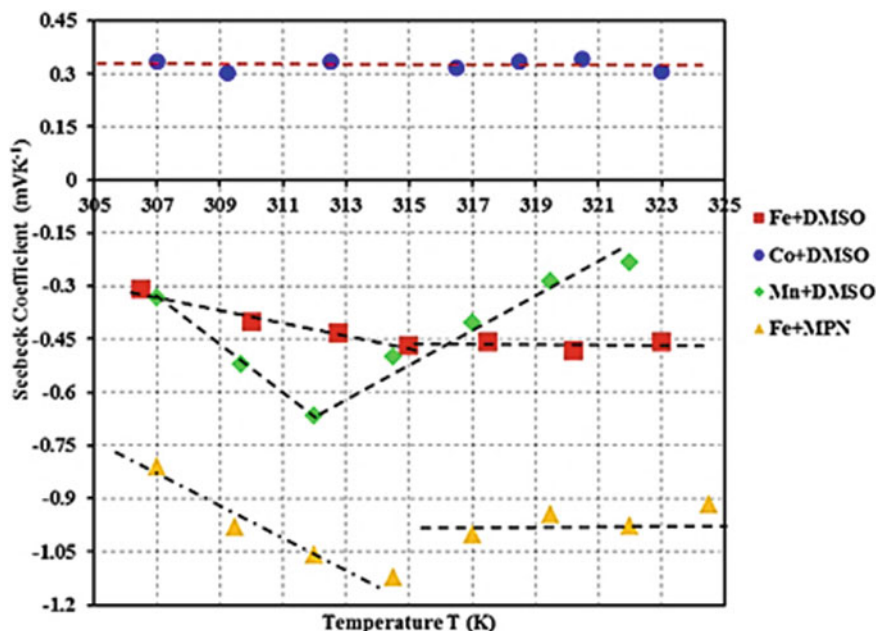


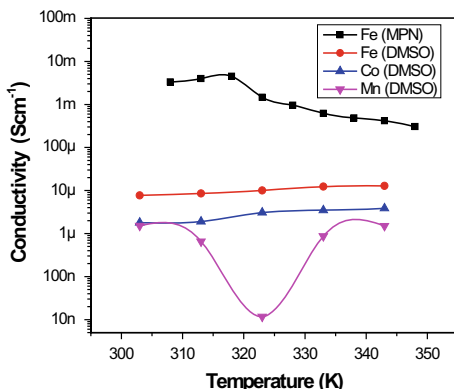
Fig. 2 Seebeck for Fe(II) in MPN Fe(II) in DMSO Mn(II)in DMSO and Co(II) in DMSO respectively

for the HS Mn complex compared to the higher energy of the LS Mn complex, led to the drastic increasing of ionic conductivity of the distorted Mn complex at higher temperature. We inferred that the best selection complex for TEC in this study was Fe in MPN which has both high Seebeck and ionic conductivity. The optimisation of the Seebeck of the SCO complex will be further investigated in future in terms of optimum molar concentration, complex ligand length and ionic conductivity through CV analysis.

4 Conclusions

From the temperature-dependent examination of the SCO electrochemical characteristics, Fe in MPN solvent was found to have a high diffusion ratio and activity, as demonstrated by cyclic voltammetry. In this case, diffusion shows a strong correlation with the Seebeck coefficient and ionic conductivity. The Sign of the Seebeck can also be predicted from the ratio of diffusion of oxidation over diffusion of reduction by using cyclic voltammetry. Based on electrochemical investigation, this work demonstrated the uniqueness of spin SCO as a redox electrolyte for the generation of nonlinear Seebeck from temperature differences. From the understanding of this work, the optimisation of the Seebeck of the SCO complex can be done in the

Fig. 3 Ionic conductivity for Fe(II) in MPN Fe(II) in DMSO Mn(II) in DMSO and Co(II) in DMSO respectively



future by finding the optimum molarity using diffusion analysis in order to obtain the optimum power density for energy harvesting.

Acknowledgements This project is funded by Ministry of Higher Education Malaysia under Fundamental Research Grant Scheme (FRGS), with a reference number of FRGS/1/2022/TK08/UMS/02/17. We acknowledged Mr. Hazwan Horace, Lab Assistant of the High Voltage Lab and members of High Voltage Power Energy Research (HiPER), Faculty of Engineering, Universiti Malaysia Sabah for support.

References

1. Abraham TJ, MacFarlane DR, Pringle JM (2011) Seebeck coefficients in ionic liquids—prospects for thermo-electrochemical cells. *Chem Commun* 47(22):6260–6262
2. Chang WB, Evans CM, Popere BC, Russ BM, Liu J, Newman J, Segalman RA (2016) Harvesting waste heat in unipolar ion conducting polymers. *ACS Macro Lett* 5(1):94–98
3. Lee SW, Yang Y, Lee HW, Ghasemi H, Kraemer D, Chen G, Cui Y (2014) An electrochemical system for efficiently harvesting low-grade heat energy. *Nat Commun* 5(1):1–6
4. Quickenden TI, Mua Y (1995) A review of power generation in aqueous thermogalvanic cells. *J Electrochem Soc* 142(11):3985
5. Abraham TJ, MacFarlane DR, Baughman RH, Jin L, Li N, Pringle JM (2013) Towards ionic liquid-based thermoelectrochemical cells for the harvesting of thermal energy. *Electrochim Acta* 113:87–93
6. Hasnan MMIM, Said SM, Sabri MFM, Hussin SAM, Abdullah N, Ibrahim NMJN, Shah NM (2019) Optimised thermally driven molecular stability of an SCO metal complex for TEC Seebeck generation enhancement. *RSC Adv* 9(19):10626–10634
7. Hupp JT, Weaver MJ (1984) Solvent, ligand, and ionic charge effects on reaction entropies for simple transition-metal redox couples. *Inorg Chem* 23(22):3639–3644
8. Kang TJ, Fang S, Kozlov ME, Haines CS, Li N, Kim YH, Baughman RH (2012) Electrical power from nanotube and graphene electrochemical thermal energy harvesters. *Adv Func Mater* 22(3):477–489
9. Abraham TJ, MacFarlane DR, Pringle JM (2013) High Seebeck coefficient redox ionic liquid electrolytes for thermal energy harvesting. *Energy Environ Sci* 6(9):2639–2645

10. Megat Hasnan MMI, Mohd Noor IS, Nayan N, Ahmad MK, Mohd Said S, Mohd Sabri MF, Mohd Zin R (2021) Enhancement of spin Seebeck effect of reverse spin crossover Fe (II) micellar charge transport using PMMA polymer electrolyte. *Appl Organomet Chem* 35(8):e6268
11. Hayami S, Komatsu Y, Shimizu T, Kamihata H, Lee YH (2011) Spin-crossover in cobalt (II) compounds containing terpyridine and its derivatives. *Coord Chem Rev* 255(17–18):1981–1990
12. Koerver R, MacFarlane DR, Pringle JM (2015) Evaluation of electrochemical methods for determination of the Seebeck coefficient of redox electrolytes. *Electrochimica Acta* 184:186–192
13. Hasnan MM, Abdullah N, Said SM, Salleh MM, Hussin SM, Shah NM (2018) Thermo-electrochemical generation capabilities of octahedral spin crossover complexes of Mn (II), Fe (II) and Co (II) with N-donor ligands and benzoate counter ion. *Electrochim Acta* 261:330–339

In Situ Measurement and Remediation of Condensation Issue in Sarawak General Hospital Molecular Lab During COVID 19



Muhammad Syukri Imran Abdullah, Azhaili Baharun,
Abdul Malik Zainal Abidin, Noor Muhammad Abd Rahman,
and Nyuk Yen Chin

Abstract Sarawak General Hospital Molecular laboratory suffers significant condensation issues particularly above its ceiling due to combination of design and construction shortfall. Overcooling of laboratory and inappropriate selection of insulation were found to be the major contributing factor. The solution was to introduce 50 mm Expanded Polystyrene (EPS) layer as a thermal barrier within the ceiling layers. Two units of dehumidifier with a total capacity of 70L/day were installed at attic level to control humidity to 60%. The corrective measures have been able to reduce the condensation risk greatly by increasing the difference between air dew point and surface temperature of ceiling by 6.7 °C. In general, the rectification work selected was able to minimize the laboratory downtime using a sustainable, environmental and budget friendly material.

Keywords Condensation · Mold · Insulation · Thermal image · Moisture content

1 Introduction

Condensation in building is a complex issue that could contribute to sick building that requires multidisciplinary investigation and environmental monitoring. Extended dampness and periodic condensation can also corrode critical structural fasteners inside walls, floors and roofs of building leading to structural risk [1]. Building condensation issue requires correct approach to determine its root cause and finding

M. S. I. Abdullah (✉)

Engineering Faculty, University Malaysia Sarawak, 94300 Kota Samarahan, Malaysia
e-mail: amsimran@unimas.my

A. Baharun

Faculty of Built Environment, University Malaysia Sarawak, 94300 Kota Samarahan, Malaysia

A. M. Zainal Abidin · N. M. A. Rahman

Engineering Services Division, Ministry of Health Malaysia, 62590 Putrajaya, Malaysia

N. Y. Chin

Engineering Section, State Health Department Sarawak, 93050 Kuching, Malaysia

Table 1 List of relevant documented works on condensation assessment, remediation and use of expanded polystyrene

	Author	Main highlights of paper
1	Almeida and Barreira [2]	Methods of in situ measurement
2	Singh, Yu and Kim [3]	Key area and document that should be included in the building assessment
3	Lee and Yeo [4]	Adoption of IoT application such as real time sensors
4	Less et al. [5]	Important points to be considered in building with sealed and insulated attics
5	Harriman [1]	4 methods of quantitative test to identify excessive moisture accumulation
6	Galvin [6]	Removing moisture using dehumidifier in a suburban UK home
7	Cornish et al. [7]	Use of dehumidifiers as remedial measure for occupied dwelling
8	Alam et al. [8]	Performance of Expanded polystyrene (EPS) as building external wall insulation layer
9	Saadatian, Freire and Simões [9]	Life cycle assessment of EPS as building insulation material
10	Tingley et al. [10]	EPS low environmental impact
11	Li et al. [11]	Energy consumption and carbon emission in the material production phase of EPS
12	Barnaure et al. [12]	Advantages of EPS, XPS and mineral wool as building insulation
13	Caglar and Beskirli [13]	EPS inhibits heat bridge, prevents condensation and moisture build up
14	Ramli et al. [14]	How EPS satisfies building insulation requirement and fire safety

the right solution. Table 1 provides list of documented works on condensation assessment and remediation which are relevant in this paper to guide the best solution for similar problem in Sarawak General Hospital (SGH) new PCR lab building.

2 Problem Statement

The new SGH molecular lab ceiling structure had collapsed due to ceiling condensation, improper thermal insulation system and very low indoor room temperature. This paper describes the remediation work taken to ensure safety and minimum downtime.

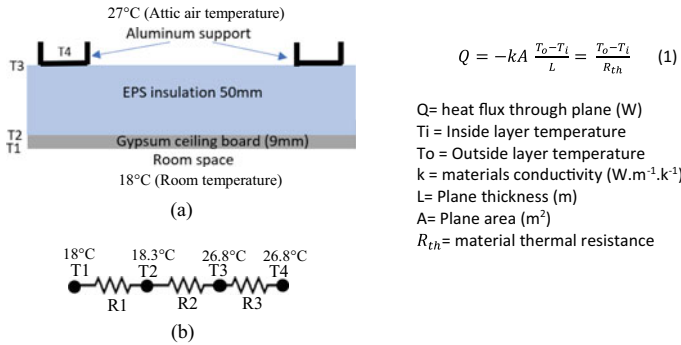


Fig. 1 Cross section of new ceiling assembly and corresponding thermal circuit

3 Methodology

A site investigation was carried out to identify the cause which have led to the development of condensation and eventually the collapse of ceiling structure. For this purpose, several tools and monitoring instrument were used such as pocket thermal imager, material moisture meter, surface, and air temperature datalogger as well as relative humidity dataloggers. The choice of remedial work is governed by time and budget constraint and the need to reduce laboratory downtime as it is critically required to operate during COVID 19 pandemic surge. 50 mm Expanded Polystyrene (EPS) was proposed as insulation layer in the new gypsum ceiling assembly as it is readily available in the market at low cost. Portable dehumidifiers were also used to control the attic air relative humidity (RH) to 55%. A condensation risk assessment was carried out on the new ceiling assembly as shown in Fig. 1a. Point T1 to T4 represents the change of temperature across the ceiling material layers. The conduction heat transfer formula were used to calculate the temperature gradient between layers of material [15].

Temperature gradient across ceiling material layers for a range of room temperature and attic air temperature combination were calculated. Analysis indicates that surface temperature at T3 and T4 are less sensitive to the cold indoor temperature with the use of EPS insulation over the gypsum ceiling board.

4 Results and Discussion

4.1 Site Assessment Result

Background check of the new lab building reveals that there have been complaints about water dripping off the ceiling from the laboratory staff a few months after it was built. Observation also revealed that water has been accumulating on the U-shaped



Fig. 2 Incident of ceiling cave in due to heavy condensation build up above ceiling

metal support of the ceiling due to condensation of humid air in the attic as shown in Fig. 2a. The lab indoor air temperature was found to be at 16 °C have led to the over cooling of ceiling board and its metal support. The topside surface temperature of ceiling and metal support was lower than the dew point temperature of the attic air at time of measurement. The attic area RH was nearly 100% particularly at night-time since the attic was leaky and not sealed entirely. The ceiling finally collapsed as shown in Fig. 2b.

Thermal camera scanning also confirms the cold surface condition of the ceiling topside ranging between 16 °C and 21 °C. The original rockwool insulation layer which was placed loosely above the ceiling have failed to prevent the condensation. Furthermore, rockwool is a breathable material which allow air vapor to pass through it [16]. Material moisture check also revealed high level of water content up to 48% that exceeded the recommended limit of 15%.

4.2 Remediation Work and Monitoring

Remediation work took about 7 working days to complete. Primary solution includes the installation of EPS on top of ceiling and deploying two units of portable compact dehumidifier with combine moisture removal capacity of 72L/day. Both the dehumidifiers are located above the ceiling to control the attic RH to 60% which led to a significantly lower air dewpoint of about 18.9 °C. Apart from that some minor modifications were made to the ceiling air conditioning air diffuser to divert cold air away from the adjacent ceiling surface. Figure 3 shows post treatment attic area air humidity of about 60%.

The measured surface temperature on top of the new ceiling was 23.5 °C or 4.6 °C higher than the attic air dew point. This differential value increased up to 6.7 °C with the installation of dehumidifier inside the attic area. It was also observed that the room temperature drops by 1.5 °C from 24.1 °C to 22.6 °C with the presence of dehumidifier. This is most probably due to the drying effect of the dehumidifier in the attic which partly absorbed latent load from the room. Figure 4a and b shows the ceiling surface temperature before and after the modification of air diffuser. Figure 4c

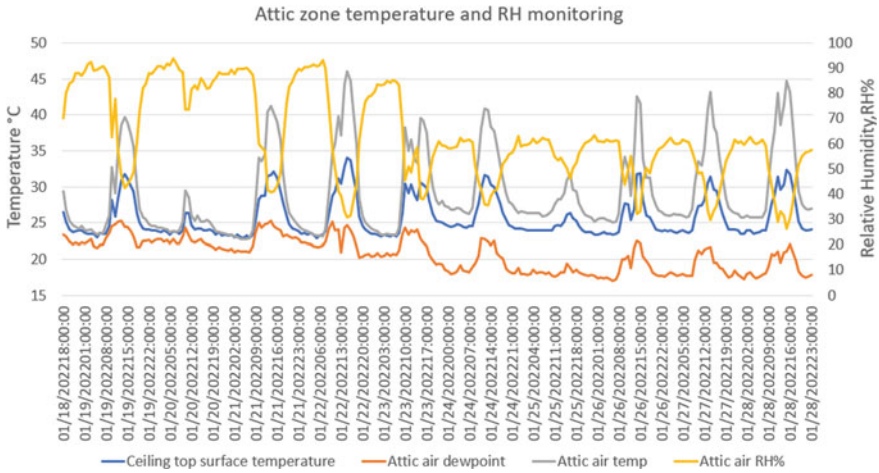


Fig. 3 Attic zone temperature and RH condition

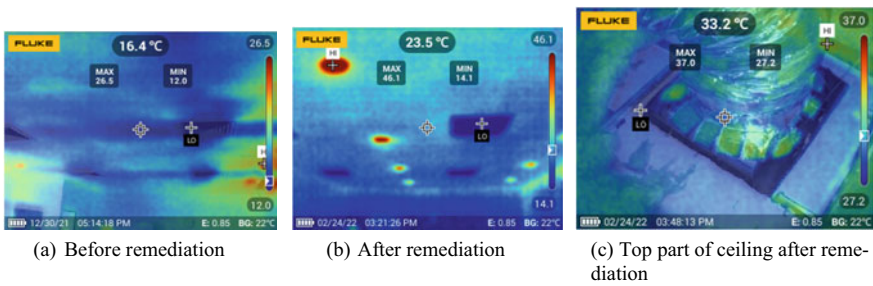


Fig. 4 Ceiling surface temperature before and after modification of AC air diffuser

shows thermal image on top of the ceiling assembly reveals that there were no cold spot present anymore that would cause condensation risk.

5 Conclusion

In general, the risk of condensation on top of the ceiling surfaces is very low because there were no cool surfaces for attic air moisture to form dew or water droplets. Application of EPS insulation and compact portable dehumidifier provided quick corrective option to eliminate the risk of condensation. The remediation work was carried out using most sustainable and fastest possible method to minimize laboratory downtime, hospital service interruption and reduced future risk. The method also considered time, budget and resources constraint faced by the building owner and the project team.

Acknowledgements We would like to thank Sarawak General Hospital, Engineering Services Division of Sarawak State Health Department and Engineering Services Division of Ministry of Health Malaysia for their contribution and support to this study.

References

1. Harriman L (2020) Damp buildings, human health and ventilation design. *ASHRAE Journal*
2. Almeida RMSF, Barreira E (2017) Condensation and mold risk evaluation in a gymnasium: In situ measurements and numerical simulation. *J Perform Constructed Facility* 31(5):4017049
3. Singh J, Yu CWF, Kim JT (2010) Building pathology, investigation of sick buildings toxic moulds. *Indoor Built Environ* 19(1):40–47
4. Lee JH, Yeo MS (2020) Condensation control to cope with occupancy activity and effectively mitigate condensation in unheated spaces by real-time sensor control strategy. *Sustainability* 12(10):4033
5. Less B, Walker I, Slack J, Rainer L, Levinson R (2022) Sealed and insulated attic hygro-thermal performance in New California homes using vapor and air permeable insulation field study and simulation
6. Galvin R (2010) Solving mold and condensation problems: a dehumidifier trial in a suburban house in Britain. *Energy Build* 42(11):2118–2123
7. Cornish JP, Sanders C, Garrett J (1988) Remedies for condensation and mould. UK National symposium-combating condensation, Sheffield City Polytechnic, Sheffield
8. Alam M, Singh H, Suresh S, Redpath DAG (2017) Energy and economic analysis of vacuum insulation panels (Vips) used in non-domestic buildings. *Appl Energy* 188:1–8
9. Saadatian SS, Freire F, Simões N (2016) Comparative life-cycle analysis of insulation materials in a dwelling, addressing alternative heating systems and life spans. *EPS* 40:0–1
10. Tingley DD, Hathway A, Davison B (2015) An environmental impact comparison of external wall insulation types. *Build Environ* 85:182–189
11. Li Y, Gong XZ, Wang ZH, Li H, Fan MM (2016) External insulation design impacts on the energy consumption and greenhouse gas emission of building. *Mater Sci Forum* 847:381–390. *Trans Tech Publ*
12. Barnaure M, Ghita AM, Iftode MC (2017) Life cycle assessment of thermal insulation solutions for buildings. *Int Multidiscip Sci GeoConference SGEM* 17:683–689
13. Caglar H, Beskirli M (2014) Investigation of thermal insulation materials technical specifications and cost analysts. *Energy Educ Sci Technol Part B: Soc Educ Stud* 6(2):213–222
14. Ramli Sulong NH, Mustapa SAS, Abdul Rashid MK (2019) Application of expanded polystyrene (EPS) in buildings and constructions: a review. *J Appl Polym Sci* 136(20):47529
15. *Thermodynamics Ht. Doe Fundamentals Handbook*. Published online (1992)
16. Itewi M (2011) Green building construction thermal isolation materials (Rockwool). *Am J Environ Sci* 7(2):161–165

Cement-Based with Partial Replacement of Nano-Silica for Improvement in Compressive Strength



Mudrikah Sofia Mahmud, Aina Fadzleen Aadnan, Farah Diana Mohd Daud, Norshahida Sarifuddin, Hafizah Hanim Mohd Zaki, Norhuda Hidayah Nordin, and Nur Farahiyah Mohammad

Abstract This study aims to utilize nano-silica in cement paste to improve the strength of hardened cement-based materials, and to determine the most significant percentage of addition based on improvement in compressive strength as well as to relate it with formation of hydration products. Nano-silica used had been synthesized from rice husk ash (RHA) by precipitation method. The synthesized powder consists of ~ 99% amorphous silica particles in the size range of 74 nm to 93 nm. Nano-silica had partially replaced some amount of cement in percentage of 0%, 1%, 3% and 5%. At each curing duration of 7 and 28 days, the hardened cement-based samples were collected and characterized through compression test and XRD analysis. Significant increments were observed in compressive strength of cement-based materials upon the addition of nano-silica. This study found that addition of 3% nano-silica resulted in the highest improvement in compressive strength compared to the other samples with and without addition of nano-silica throughout the curing duration. Addition beyond this value resulted in the significant decrement in compressive strength at all curing duration. Meanwhile, XRD analysis indicates the presence of hydration products such as $\text{Ca}(\text{OH})_2$ and C-S-H at different intensities. Upon addition of nano-silica, the decrement in peak intensity of $\text{Ca}(\text{OH})_2$ and increment in peak intensity of C-S-H were obvious which maximised at 28 days of curing. This indicates the presence of nano-silica promotes hydration reaction and produce more hydration products which responsible to a significant improvement in compressive strength of cement-based samples at all curing duration.

Keywords Cement-based sample · Nano-silica · Compressive strength

M. S. Mahmud · A. F. Aadnan · F. D. M. Daud (✉) · N. Sarifuddin · H. H. M. Zaki · N. H. Nordin
Department of Manufacturing and Materials Engineering, Kulliyyah of Engineering, International Islamic University Malaysia, P.O. Box 10, 50728 Kuala Lumpur, Malaysia
e-mail: farah_diana@iium.edu.my

N. F. Mohammad
Faculty of Electronics Engineering Technology, Universiti Malaysia Perlis, Pauh Putra, 02600 Arau, Perlis, Malaysia

1 Introduction

Throughout the years, there are many efforts that have been done to increase the mechanical strength of cement-based material, and one of them is by partially replaced some amount of cement with additive which is known as supplementary cementitious materials (SCMs). This SCMs commonly possess cementitious properties when there is a presence of water in which it will react with cement and cement hydration product which lead to the formation of more hydration product such as calcium hydroxide ($\text{Ca}(\text{OH})_2$) and calcium silicate hydrate (C–S–H). C–S–H is responsible for mechanical strength of hardened cement-based material, in which with formation of more hydration products the significant improvement in cement-based materials' performance could be expected [1–4].

Utilization of nano-size additive materials had attracted interests due to its contribution in significant enhancement in performance of cement-based sample. It has been known, reduction in material's particles size down to less than 100 nm would provide higher reactivity during reaction due to its higher surface area. Thus, improvement in performance could be expected. Among the wide variety of available additive materials in nano-size, nano-silica is one of the preferred materials to be used as an additive material to partially replace cement. It has been reported that, benefitting from the nano-size and amorphous structure, nano-silica provide higher reactivity in reaction and provide filler effect which has led to the acceleration of cement hydration due to high pozzolanic reactivity [1, 3–5]. This pozzolanic reaction altered the morphology characteristic of cement-based materials due to production of more C–S–H species which increase the density of the cement samples and hence, increased the mechanical property [1, 2, 6, 7]. Besides, secondary hydration reaction of nano-silica with cement hydration product of $\text{Ca}(\text{OH})_2$ also could occur generating secondary C–S–H which led to the significant increment of C–S–H species in the cement-based material [1]. However, this increment varied with the amount of nano-silica added, and some led to the decrement in properties.

Thus, the main objective of this study is to determine the effect of addition of different percentage of nano-silica on the compressive strength of cement-based samples. Cement-based samples with addition of 0%, 1%, 3% and 5% of nano-silica were prepared and the most significant percentage of addition was determined which resulted in the highest mechanical strength throughout the curing duration. Nano-silica used in this study has been synthesized from RHA through precipitation method.

2 Materials and Method

2.1 Materials

The main materials to prepare the cement-based samples are nano-silica, ordinary Portland cement (OPC) and water. Nano-silica used in this study was synthesized from RHA through precipitation method. The synthesized powder consists of ~ 99% amorphous silica particles in the size range of 74 nm to 93 nm. Meanwhile, the OPC brand YTL Cement was purchased from local supplier and water used in sample preparation was local tap water.

2.2 Preparation of Cement-Based Samples

Cement-based samples were prepared according to Table 1.

To determine the effect of addition of nano-silica in cement-based material, water to cement ratio (0.4) was kept constant in this study. For preparation of a reference sample, water was added into cement, and mixed using the mortar mixer at low speed (140 rpm) for 30 s then change to high speed (285 rpm) for 1 min. For preparation of cement-based samples with inclusion of nano-silica, firstly, nano-silica powder was mixed dry with the cement powder at low speed. After 1 min of dry mixed, water was added into the mixture. The mixture paste was mixed at low speed for 30 s, then mixed again at high speed for another 1 min to ensure that all the materials were blending well.

Next, the paste was poured into the cube-shape mould. The samples were prepared according to ASTM C109 using a 50 mm × 50 mm × 50 mm cube sample. The moulded cement paste was left for 24 h to let it set completely. Then, after demoulding, all the cement-based samples were fully immersed in water for curing process up to 28 days. The samples were characterized according to curing duration of 7 and 28 days.

Table 1 Composition of the cement-based samples prepared in this study

Sample	Cement (%)	Nano-silica (%)
Reference	100	0
NS1	99	1
NS3	97	3
NS5	95	5

2.3 Characterization

The prepared cement-based samples had been characterized through following characterization method. Mechanical strength of the prepared cement-based samples was tested by using compression testing machine brand Kensains by Kensains Sdn Bhd. The phase structure developed in the cement-based sample had been analysed through X-Ray Diffraction (XRD) D2 Phaser by Bruker. The diffraction data were set down with 2θ range from 10° to 60° and 0.075 s/step scanning rate.

3 Result and Discussion

3.1 Compressive Strength

The compressive strength results of the cement-based samples of curing duration 7 and 28 days were shown in Fig. 1. Based on the result obtained, addition of nano-silica up to 3% improved the compressive strength of cement-based sample as compared to the reference sample at 7 and 28 days of curing process. At 7 days of curing, the improvement was at about 65% and 70% with replacement of 1% and 3% of nano-silica compared to the reference sample or sample without addition of nano-silica. Meanwhile, at 28 days of curing, the compressive strength improved in 22% and 30% with replacement of 1% and 3% of nano-silica.

However, replacement of 5% nano-silica had resulted in decrement of compressive strength compared to the compressive strength value of reference sample and samples with addition of 1% and 3% of nano-silica at all curing duration. This decrement could be explained by the presence of excessive nano-silica particles that have high

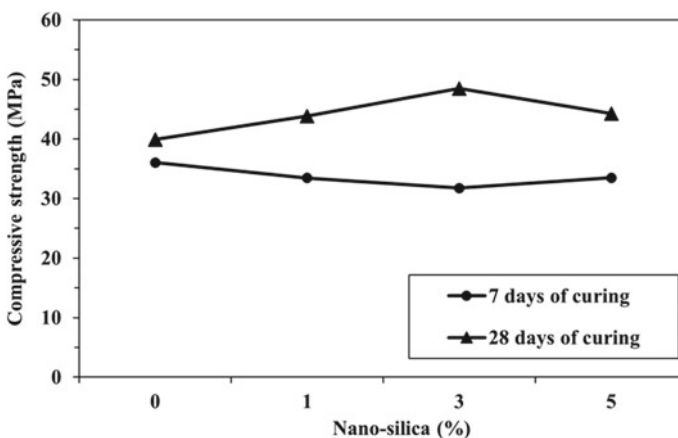


Fig. 1 Compressive strength of the cement-based samples for 7 and 28 days of curing

tendency to agglomerate which do not contribute to the strength improvement. The presence of too much nano-silica would hinder the performance of nano-particles due to several factors, and one of them is the risk of high agglomeration. Partially replaced nano-silica in optimum amount is recommended to obtain significant improvement in properties since addition of higher percentage could lead to the agglomeration of nanoparticles and thus, do not conform to a higher improvement [5, 7, 8].

According to this observation, it could be concluded that the most significant replacement of cement with nano-silica is 3% due to the higher percentage of improvement in compressive strength for all curing duration. Besides, replacement of 5% nano-silica resulted in decrement of compressive strength.

3.2 X-ray Diffraction (XRD) Analysis

Figure 2 shows the XRD pattern of the cement-based samples with different percentage of nano-silica replacement at 7 and 28 days of curing process.

All the pattern obtained display the presence of the common hydration products in cement-based material which are calcium hydroxide ($\text{Ca}(\text{OH})_2$), belite or dicalcium silicate (C_2S) and calcium silicate hydrate (C-S-H) in all samples, however with different intensity. As indicated in the patterns, the peaks that belong to $\text{Ca}(\text{OH})_2$ decreased in intensity, especially peaks at about 18.07° and 34.17° . This decrement is observed upon partial replacement of nano-silica in cement-based sample at all curing duration. Meanwhile, the intensity of the peaks at about 29.66° increased significantly which indicates the presence of more C-S-H upon addition of nano-silica at all curing duration.

Increment of C-S-H species could be related with the reaction between $\text{Ca}(\text{OH})_2$ and nano-silica. Since this reaction consumed $\text{Ca}(\text{OH})_2$ crystal, the decrement of $\text{Ca}(\text{OH})_2$ crystal in the system was indicated by the decrement of peak intensity of $\text{Ca}(\text{OH})_2$. Meanwhile, production of more C-S-H was indicated by the significant increment in peak intensity of C-S-H in XRD pattern obtained. The presence of this aggressive pozzolanic reaction upon addition of nano-silica in cement-based materials had been reported in previous studies [5, 7, 9].

This XRD analysis proved production of more C-S-H in cement-based system would contribute to a significant enhancement in mechanical strength of cement-based sample. This explained the improvement in compressive strength of cement-based samples, at all curing durations.

4 Conclusion

This study proved that the partial replacement of 3% nano-silica in cement paste resulted in significant improvement in compressive strength of hardened cement-based samples of 7 and 28 days curing durations. Addition of nano-sizes silica

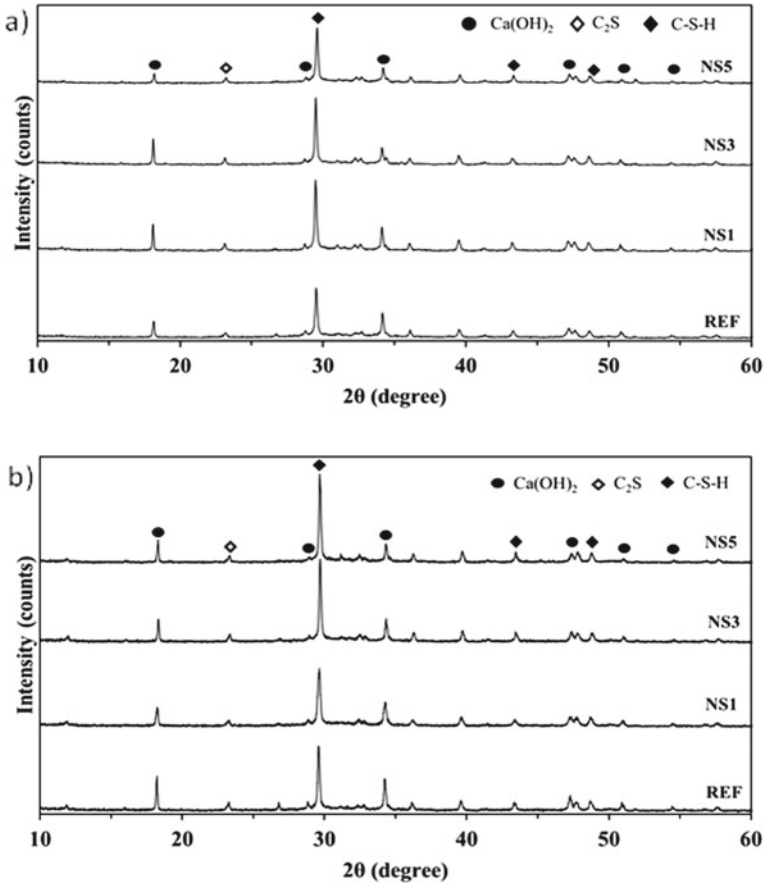


Fig. 2 XRD patterns of the cement-based samples at **a** 7 days and **b** 28 days of curing

in cement-based materials promotes aggressive pozzolanic reaction which exhibit reaction between nano-silica and Ca(OH)₂. This reaction consumed Ca(OH)₂ and lead to the formation of more hydration product such as C-S-H which provide the strengthening effect and responsible for the improvement in compressive strength of cement-based materials.

Acknowledgements This research was supported by Ministry of Higher Education (MoHE) Malaysia through the Fundamental Research Grant Scheme (FRGS/1/2019/TK05/UIAM/03/1).

References

1. Meng T, Ying K, Yang X, Hong Y (2021) Comparative study on mechanisms for improving mechanical properties and microstructure of cement paste modified by different types of nanomaterials. *Nanotechnol Rev* 10(1):370–384
2. Li G, Liu Q, Niu M, Cao L, Nan B, Shi C (2020) Characteristic of silica nanoparticles on mechanical performance and microstructure of sulphoaluminate cement/ordinary Portland cement binary blends. *Constr Build Mater* 242:118158
3. Xiao H, Zhang F, Liu R, Zhang R, Liu Z, Liu H (2019) Effects of pozzolanic and non-pozzolanic nanomaterials on cement-based materials. *Constr Build Mater* 213:1–9
4. Sharkawi AM, Abd-Elaty MA, Khalifa OH (2018) Synergistic influence of micro-nano silica mixture on durability performance of cementitious materials. *Constr Build Mater* 164:579–588
5. Montgomery J, Abu-Lebdeh TM, Hamoush SA, Picornell M (2016) Effect of nano silica on the compressive strength of harden cement paste at different stages of hydration. *Am J Eng Appl Sci* 9(1):166–177
6. Zhang L, Ma N, Wang Y, Han B, Cui X, Yu X, Ou J (2016) Study on the reinforcing mechanisms of nano silica to cement-based materials with theoretical calculation and experimental evidence. *J Compos Mater* 50(29):4135–4146
7. Wang L, Zheng D, Zhang S, Cui H, Li D (2016) Effect of Nano-SiO₂ on the hydration and microstructure of Portland cement. *Nanomaterials* 6(12):1–15
8. Garg R, Garg R, Bansal M, Aggarwal Y (2021) Experimental study on strength and microstructure of mortar in presence of micro and nano-silica. *Mater Today Proc* 43(2):769–777
9. Ramezaniapour AA, Mortezaei M, Mirvalad S (2021) Synergic effect of nano-silica and natural pozzolans on transport and mechanical properties of blended cement mortars. *J Build Eng* 44:102667

Effect of Oxygen Gas Exposure on T91 Alloy at High Temperature Oxidation of Steam Reformer



Muhammad Rafiq Haikal Rosdin, Ahmad Abdul Mun'im Ismail, Abd Malek Abdul Hamid, Hadi Purwanto, Suhaimi Illias, Syed Noh Syed Abu Bakar, and Mohd Hanafi Ani

Abstract Steam-Methane Reforming (SMR) is one of the most economical ways to produce hydrogen from natural gas. Steam reforming industry is hugely relied on using supercritical power plant where the working temperature of the plant must exceed 600 °C. Along with the high operating temperature, the situation promotes the acceleration of high temperature oxidation. This will cause fouling and spalling of oxide scales at the boiler tube. Eventually, fouling will reduce heat transfer between the tube and steam generated, causing a higher temperature is needed to produce steam. Until now, the only approach used by the industry is to manually replace the corroded boiler tube. Other than that, many studies have been conducted on the behavior of boiler tubes at temperatures exceeding 800 °C. However, to our knowledge, no study has been done to investigate the air electrolyte substrate interfacial electrochemical reaction at high temperature. This project was carried out to investigate the corrosion potential of T91 boiler tube at 650 °C for 2 h, 8 h, and 12 h, measure the current density (I_{corr}) by calculating corrosion potential (E_{corr}) value using Tafel Extrapolation and determine the oxidation potential of oxygen gas at 650 °. The oxide layer thickness at exposed temperature was determined to measure the oxidation kinetics. The study concludes that there was an increase of 8.49% in current conductivity between the blank experiment and T91 alloy oxidation potential test. The oxidation process was following the parabolic rate law which manifest that the corrosion is controlled by ionic diffusivity in the oxide layer. The oxide layer formed on the sample has an average thickness of 54.10 μm and this value can be used to calculate the oxidation kinetics of the sample using parabolic rate constant, K_p , resulting with the value of $6.78 \times 10^{-14} \text{ m}^2/\text{s}$.

M. R. H. Rosdin · A. A. M. Ismail · A. M. A. Hamid · H. Purwanto · S. N. S. A. Bakar · M. H. Ani (✉)

Department of Manufacturing and Materials Engineering, Kulliyah of Engineering, International Islamic University Malaysia, 53100 Gombak Selangor, Malaysia
e-mail: mhanafi@iium.edu.my

S. Illias

Faculty of Mechanical Engineering Technology, Universiti Malaysia Perlis, 02600 Arau Perlis, Malaysia

Keywords High temperature corrosion · Cathodic protection · T91 Alloy · Steam reformer

1 Introduction

Hydrogen is a simplest element on earth. It usually combined with other chemical elements such as water, carbon dioxide and fossil fuels. Due to that, hydrogen needed to be extracted from its chemical elements. Hydrogen can be extracted from virtually all energy supplies, either renewable or non-renewable. In recent years, hydrogen demand has been increased throughout the world as it provides as an alternative for cleaner, greener energy. As reported by U.S Energy Information Administration [1] there is an increase for global demand of hydrogen from 1975 to 2018.

According to Khan et al. [2], 48% of worldwide hydrogen is produced from steam-methane reforming (SMR) with efficiency of 85% [3, 4]. SMR is process that chemically synthesis methane obtained from natural gas to produce syngas (hydrogen and carbon monoxide). Technically, methane is reacted with steam at high temperature (500–900 °C) and pressure around 30 atm in presence of nickel as catalyst. To produce pure hydrogen gas via SMR, the process consists of three main processes: reforming of natural gas to syngas, Water–Gas Shift (WGS) and pressure-swing absorption [5]. Superheated steam plays a significant role in both SMR and WGS process. The main combustion fuel to generate steam in SMR is by using waste heat recovery steam generator. Water will flow in T91 alloy boiler tube mostly consisting of iron-chromium (Fe–Cr) mixture and heated via convection up to 650 °C with steam pressure 3–25 bar by which at this stage, water is in superheated steam condition [6].

The main product of the combustion from natural gas are mainly carbon dioxide, water vapor, excess oxygen as well as small amount of soot, carbon monoxide, nitrogen oxides and sulphur dioxide which also known as flue gas. As the flue gas temperature is very high, it can promote corrosion to the boiler tube, resulting in fouling and spalling of oxide scales at the tube. Other than that, Poquillon and Monceau [7] revealed that overheating of the tube can be caused by spalling of oxide scale due to a combination of a weak metal-oxide interface and mechanical strains created by differing thermal expansion coefficients between alloy and oxide. A study conducted by Ahmad et al. [8] also confirms the presence of numerous creep cavities which will eventually forms micro and macro cracks because of overheating of the tube.

Corrosion is a serious issue in most industries as it is the main causes of energy and material loss, accounting for 20% of global energy use and the average of gross national product (GNP) is lost each year due to corrosion-related issues is 4.2% [9]. Therefore, this paper will focus on the study of Impressed Current Cathodic Protection (ICCP) as an alternative solution to overcome by determining the current conductivity of oxygen gas at 650 °C, compute oxidation kinetics of T91 Alloy by measuring the thickness of oxide layer formed and employing Wagner's theory,

identify E_{corr} and I_{corr} at different timeframes and calculate activation polarization for anodic and cathodic branch using Tafel equation.

2 Materials and Method

A sample of T91 boiler tube is chosen in this project. The sample was prepared by cutting it into 10.4 mm × 6.6 mm × 4.2 mm. Then, the sample is grinded using four abrasive papers with different grades: P800, P1000, P1500 and P2000. After that, the grinded sample is polished using a polishing machine with particles grade of 0.3 μm to obtain smooth surface. Alumina fine polishing suspension is used to reduce surface distortion and producing an excellent polishing result. Etching is done using nital solution. Sample's weight can be measured using electronic balance.

Platinum wire with length of 1 m is used as anode and cathode and reference electrodes. T91 Alloy will be spot welded on the working electrode. These wires are attached inside the ceramic tube with tips sticks out. The ceramic tube will be placed inside a glass tube with tips on the other side sticks out to the isothermal zone. Thermocouple is placed at the isothermal zone. Heat is supplied by the furnace and oxygen gas is provided. Oxidation potential measurement experiment was conducted 2 h, 8 h, and 12 h at 650 °C. Final characterization is carried out onto the sample to verify either the sample corrodes or not by measuring the changes in weight and presence of oxide layer using Scanning Electron Microscopy (SEM) (Fig. 1).

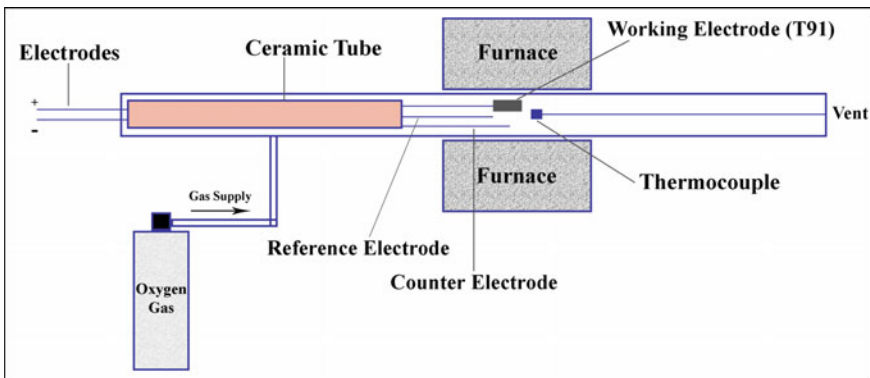


Fig. 1 Schematic diagram for oxidation potential measurement setup

3 Result and Discussion

3.1 Blank Experiment

Figure 2 shows current versus voltage graph obtained from running the blank experiment. The experiment is done for a timeframe of 400 s. Oxygen gas is let to flow at rate of $5.53 \times 10^{-6} \text{ m}^3/\text{s}$. Referring to the graph, the blue line on the graph indicates the movement of current values from -4 V to 4 V while the red line refers to the movement of current values from 4 V to -4 V . The pattern of the movement between those two lines are opposite to each other except on the blue line from 1 to 2 V and red line from 0 to 1 V.

When the voltage is applied, oxygen gas started to decompose to become oxygen ions. These ions started to move from one electrode toward the other. As the opposing electrodes becomes saturated with oxygen ions, this creates a non-equilibrium condition on the other electrodes. Hence, electrons started to move from the saturated electrode towards the other electrode to counteract the issue. The process is repeated until the voltage is not supplied anymore. Brownian motion may happen at the blue line as the voltage is applied between 1 and 2 V as well as on the red line between 0 to 1 V. This causes a slight alteration on the pattern of the graph. Overall, the result obtained from blank experiment confirmed that oxygen gas decomposed into oxygen ions and current conductivity of oxygen gas is vigorous when at temperature of $650 \text{ }^\circ\text{C}$.

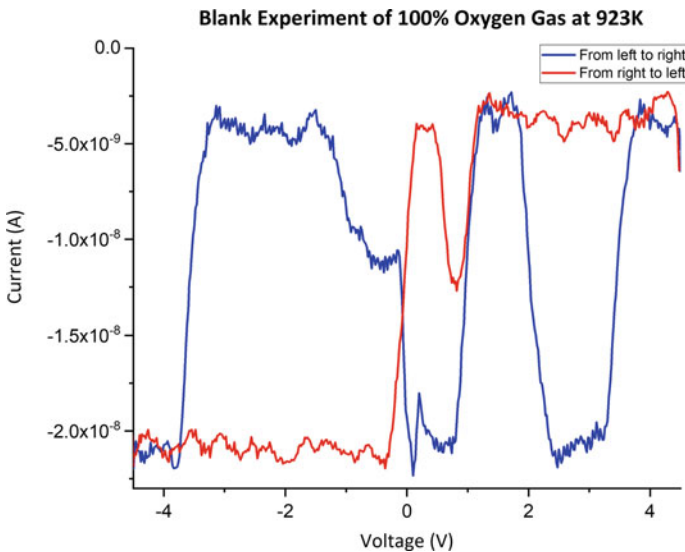


Fig. 2 Blank experiment result after exposed at $650 \text{ }^\circ\text{C}$ on 100% oxygen gas exposure

3.2 Sample Mass

Table 1 shows the weight of the sample and its weight difference according to the time exposed. From the weight difference, the sample’s weight gain can be calculated and Fig. 3 shows the graphical representation from the Table 1. The result shows a parabolic law when polynomial fit is applied on it. This confirms that metal ions from the metal substrate migrate toward the oxide gas interface, where they react with oxygen, or oxygen ions diffuse through the oxide layer to enter the metal/oxide interface and react with the metal. As time goes by, the oxide scale continues to grow, and the ions will take longer time to reach the metal/oxide interface. This makes the weight gain of the sample to increase slightly.

The graph shows a slight increase of weight gain on the 120th minute of exposure to oxygen. This is because oxide layer start to grow on the surface of the sample. Oxygen ions will have to travel throughout the oxide layers to reach metal interface which is then slows down the growth of oxide layer on the sample. However, on the 480th minute of exposure, it shows a drastic increase in weight gained of the sample.

Table 1 Weight difference and weight gain of the sample at different timeframe

Time (min)	Initial weight (g)	Final weight (g)	Weight difference (g)	Surface area (cm ²)	Weight gain (g/cm ²)
0	1.5873	1.5873	0	2.4482	0
120	1.5873	1.5891	0.0026	2.4510	1.061×10^{-3}
480	1.5891	1.5922	0.0031	2.4530	12.64×10^{-4}
720	1.5904	1.5928	0.0024	2.4567	9.769×10^{-4}

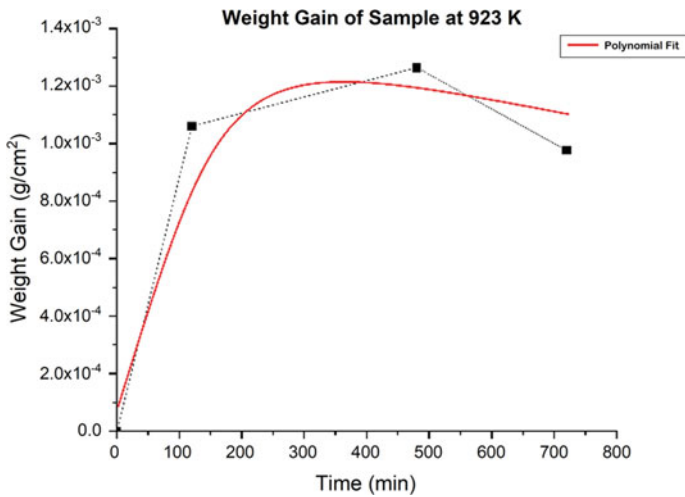


Fig. 3 Graphical representation of sample’s weight gain

At this time, the oxide scale started to crack and lost its protective properties, causing a catastrophic reaction between oxygen ion and metal interface. This causes the oxide scale to grow rapidly and hence, increasing the weight of the sample.

3.3 SEM Analysis

The morphology of the sample reveals that oxide layer which appears as dark grey in color has successfully formed on the surface of the sample. On the interface between metal and the oxide layer, it shows an uneven terrain. This is due to the polishing grade used during polishing process which is 0.3 microns.

The formation of voids within the magnetite scale is due to the ionic flux. Based on a study done by Ueda et al. [10], they stated that the partial pressure of oxygen affects the void formation in the oxide layer. The higher the oxygen partial pressure, the higher the oxygen chemical potential and hence, a greater number of voids formed. Even though the partial pressure of this experiment is high (1.01×10^5 Pa), hematite formation is favored. Figure 4 shows only few voids appear on the oxide scale. This is due to the phase of the oxide layer which consists of thick hematite as the picture is taken on the surface of the sample.

Apart from that, Taniguchi [11] stated that the oxide formed in the initial stage are not thermodynamically stable. During oxidation process, the amount of Fe in the alloy started to decrease to form wustite, magnetite and hematite. The new oxide formation can develop stresses and soon, it will form microcracks. This allows oxygen to penetrate the oxide layer using this microcracks as a pathway to form a new oxide layer. Compressive stress can later be developed due to this matter, causing pores to be form.

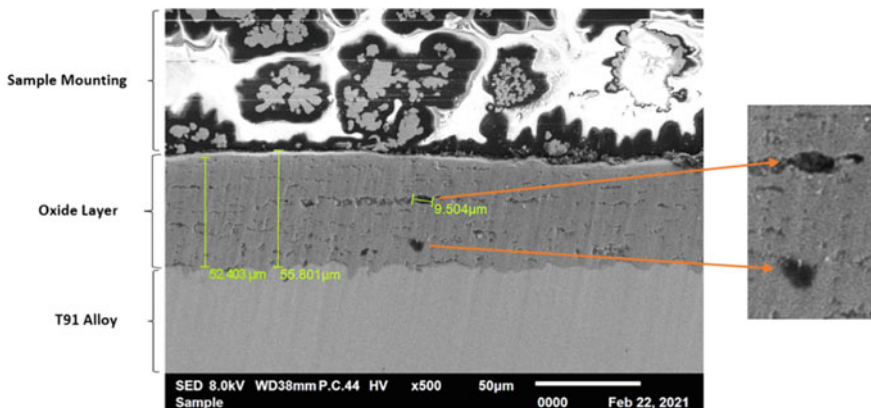


Fig. 4 SEM results for the sample after exposed to 12 h with enlarged void

Proven in Sect. 3.2, the weight gain follows the parabolic law of oxidation. Hence, the oxidation kinetics can be calculated using the average thickness of oxide layer formed. Basically, the growth of oxide layer follows the following equation:

$$x^2 = K_p t \quad (1)$$

From the average value of thickness of oxide layer obtained from SEM, the value for K_p is $6.78 \times 10^{-14} \text{ m}^2/\text{s}$ which is in good agreement with K_p value obtained in Ueda's research ($1.3 \times 10^{-15} \text{ m}^2/\text{s}$) [10].

Wagner [12] also has proposed a theoretical expression for the oxidation kinetics:

$$x^2 = \frac{2N_O^{(S)} D_O}{vN_{Cr}} t \quad (2)$$

Note that the value of D_O is different for every type of oxide layers. Nevertheless, this experiment uses the apparent value of D_O . It is understood that K_p is proportional to the oxygen permeability, $N_O^{(S)} D_O$ [13]. By relating equation both equations, the value for $N_O^{(S)} D_O$ after 12 h of exposure is $4.57 \times 10^{-15} \text{ m}^2/\text{s}$.

3.4 Oxidation Potential Measurement at 650 °C

Based on Fig. 5, all the results follow the Tafel plot except for 12 h. Hence, it is impossible to calculate E_{corr} and I_{corr} for 12 h' result. Table 2 shows the values obtained for 2 h and 8 h.

Tafel slope for 2 h shows a very clear shift to the left. One of the reasons for this anomaly is due to passivation. It is generally recognized that the passivity of alloy in such conditions is due to the formation of a chromium-rich oxide layer which provides a diffusion barrier and reduces the corrosion rate [14]. As passivity occur, the polarization will shift away from a free corroding potential (open circuit potential). Hence, it is confirmed that cathodic polarization has occur in the system because the potential has shifted in the negative direction. Most of the studies stated that cathodic polarization only occurs in aqueous environment [15]. However, the results from the test shows that in dry condition, cathodic polarization can occur. On top of that, the weight gain of the sample after exposed for 2 h (Refer Fig. 4) also shows the least value. This verify that corrosion rate has been reduced, causing the Tafel slope to shift.

Current conductivity plot at 12 h does not exhibit Tafel slope pattern. Instead, the reading shows a slight concave pattern facing downward. This is because the reaction follows the parabolic law whereas time increases, the oxidation rate of scale formation will decrease. As the scale grows, diffusing species such as metal ions and oxygen ions take longer to reach the oxide/gas contact or the metal/oxide interface [16].

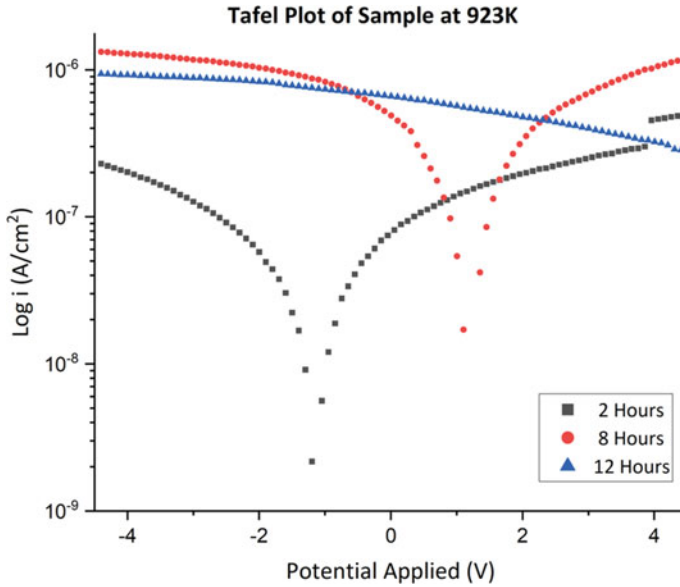


Fig. 5 Tafel plot obtained for different timeframe

Table 2 Correspond values calculated from Tafel plot

Time (min)	E _{corr} (V)	I _{corr}
120	- 1.142	6.39 × 10 ⁻⁸
480	1.241	3.711 × 10 ⁻⁷

4 Conclusion

The conductivity of oxygen gas during high temperature oxidation of T91 Alloy has been measured using Tafel plot. It was compared with blank experiment and the result shows that the current value of oxidation potential measurement was 2 magnitudes higher compared to blank experiment. This shows that oxygen is a very good conductor and act effectively as an electrolyte in high temperature environment. The SEM image reveals the formation of oxide layer and oxide layer thickness also shows that it follows the parabolic law with estimated apparent oxygen permeability of 4.57 × 10⁻¹⁵ m²/s. The parabolic rate constant was also determined as 6.78 × 10⁻¹⁴ m²/s which is in good agreement with value reported by Ueda. It is understood that T91 alloy has corroded when it is exposed to oxygen gas at supercritical temperature.

Acknowledgements This research was supported by Ministry of Higher Education, Malaysia and International Islamic University Malaysia with Grant Number FRGS/1/2019/TK03/UIAM/02/5.

References

1. EIA, "The Future of Hydrogen (2019). <https://www.iea.org/data-and-statistics/charts/global-demand-for-pure-hydrogen-1975-2018>
2. Khan Z, Yusup S, Ahmad M, Vui Soon C, Uemura Y, Sabil K (2010) Review on hydrogen production technologies in Malaysia. *Int J Eng Technol* 10(2):111
3. Kumar R, Kumar A, Pal A (2020) An overview of conventional and non-conventional hydrogen production methods. *Mater Today Proc* 46:5353–5359
4. Subraveti SG, Roussanaly S, Anantharaman R, Riboldi L, Rajendran A (2021) Techno-economic assessment of optimised vacuum swing adsorption for post-combustion CO₂ capture from steam-methane reformer flue gas. *Sep Purif Technol* 256
5. Al-Megeren H, Xiao T (2012) Natural gas dual reforming catalyst and process. *Adv Nat Gas Technol*
6. "Hydrogen Production: Natural Gas Reforming," U.S Department of Energy (2021). <https://www.energy.gov/eere/fuelcells/hydrogen-production-natural-gas-reforming>. Accessed 21/11/8
7. Poquillon D, Monceau D (2003) Application of a simple statistical spalling model for the analysis of high-temperature, cyclic-oxidation kinetics data. *Oxid Met* 59(3–4):409–431
8. Ahmad J, Purbolaksono J, Beng LC, Ahmad A (2010) Failure evaluation on a high-strength alloy SA213-T91 super heater tube of a power generation. *Proc Inst Mech Eng Part E J Process Mech Eng* 224(4):269–273
9. Vazirinasab E, Jafari R, Momen G (2018) Application of superhydrophobic coatings as a corrosion barrier: A review. *Surf Coat Technol* 341(November 2017):40–56
10. Ueda M, Kawamura K, Maruyama T (2006) Void formation in magnetite scale formed on iron at 823 K -elucidation by chemical potential distribution, vol 523, pp 37–44
11. Taniguchi S (1985) Stresses developed during the oxidation alloys
12. Wagner C (1959) Reaktionstypen bei der Oxydation von Legierungen, pp 772–782
13. Hanafi M, Ani B, Kodama T, Ueda M (2009) The effect of water vapor on high temperature oxidation of Fe–Cr Alloys at 1073 K (11)
14. Galtayries, Paristech C, Marcus P, Paristech C, Foucault M, Combrade P (2007) Kinetics of passivation of a nickel-base alloy in high temperature water (3)
15. CorrosionClinic, "Polarization and its effect on corrosion," corrosionclinic.com (2008). https://www.corrosionclinic.com/corrosion_A-Z/polarization.htm. Accessed 21/3/4
16. Khanna S (2018) "High-temperature oxidation. In: Handbook of environmental degradation of materials, 3rd edn. Elsevier Inc., pp 117–132

Effect of Zn Content on Biodegradable Mg Alloy Synthesized via Mechanical Alloying for Biomedical Application



Emee Marina Salleh and Zuhailawati Hussain

Abstract The aim of this work was to study the effect of zinc content on biodegradable binary magnesium-zinc (Mg-Zn) alloy synthesized using mechanical alloying. A powder mixture of Mg with the different content of Zn (3, 5, 10 and 15 wt%) was mechanically milled at constant rotational speed of 250 rpm for 5 h. At low Zn content up to 5 wt%, the Mg-Zn alloy mainly consisted of α -Mg matrix. However, with higher addition of Zn from 10 wt% and further, the intensities of α -Mg peaks decreased and secondary phase of γ -MgZn was identified as the solid solubility limit of Zn in Mg was only 6.2 wt% at 340 °C. The sintered density and microhardness of the alloy increased as a function of Zn content due to its higher elemental density, thus restraining the growth of crystal grains and refine the crystal grains of Mg.

Keywords Biodegradable alloy · Magnesium · Zinc · Mechanical alloying · Microhardness

1 Introduction

Magnesium (Mg) alloys are of special attention in the context of structural lightweight applications in the transport and aerospace industries and for temporary implants in clinical because of their biocompatibility and biodegradability [1]. Mg alloys have attracted considerable attention for biomaterial applications due to its density of 1.74 g/cm³ that is comparable to natural bone (1.8–2.1 g/cm³) and elastic modulus of 45 GPa which is closed to that of human bone (30–57 GPa) [2, 3]. These resembled properties are beneficial in order to minimize the failure of biomaterials due to stress shielding during implantation. However, the rapid corrosion rate of Mg especially in body surroundings containing chloride ions (Cl⁻) limits its performance [4].

E. M. Salleh (✉)

Department of Mineral and Geoscience Malaysia, Mineral Research Centre, Jalan Sultan Azlan Shah, 31400 Ipoh, Perak, Malaysia
e-mail: emeemarina@jmg.gov.my

E. M. Salleh · Z. Hussain

Structural Materials Niche Area, School of Materials and Mineral Resources Engineering, Universiti Sains Malaysia, Engineering Campus, 14300 Nibong Tebal, Penang, Malaysia

Alloying with potential element is anticipated to improve the corrosion resistance of Mg and simultaneously may increase its mechanical properties as well. Incorporating Zn into Mg may improve both tensile strength and the corrosion resistance [3]. Therefore, it is a contributing approach to develop Mg-Zn alloy with temporarily good corrosion resistance in biomedical applications. Moreover, Zn is an inexpensive alloying element with a potential of accelerating the metabolism of cells and bone healing [2, 4]. Thus, in this study, Mg-Zn was produced by mechanical alloying (MA) since it is an effective route to produce metallic alloys with fine microstructure. MA i.e., the high-energy ball milling enables high energy impact on the charged powder by collision between the grinding media and powder particles, which causes severe plastic deformation, repeated fracturing and cold welding of the particles leading to nanocrystalline materials formation [5, 6]. In this present study, density and microhardness were investigated in order to ensure the alloys produced have ranges close to that of human bones.

2 Research Methodology

A mixture of elemental magnesium powder (99.00% pure) and zinc powder (99.70% pure) of different Zn content (3, 5, 10, 15 wt%) was mechanically milled at room temperature using a high-energy Fritsch Pulveristte P-5 planetary mill under argon atmosphere. 20 mm-diameter stainless steel balls were used during mechanical milling. 3% n-heptane was added to the powder mixture prior to the milling process to prevent excessive cold welding of the elemental alloy powders. Then, the milled powders were uniaxially cold pressed under 400 MPa for 2 min at room temperature to produce 10-mm diameter of green Mg-Zn alloy pellets and sintered at 300 °C under argon flow at 5 °C/min for both heating and cooling rate for an hour in order to form solid bodies. Qualitative X-ray diffraction (XRD) analysis with angular scanning range $20^\circ \leq 2\theta \leq 90^\circ$ was conducted to identify the presence of element and phases. The data attained using D8 Advance, Bruker AXS. Phase identification of stripping its $K\alpha_2$ component is represented in form of diffractogram of intensity versus 2θ . Crystallite size and internal strain was determined by the Williamson-Hall method. Density of the sintered composite was measured by pycnometer density equipment according to Archimedes' principle. The samples were immersed in tap water which was placed on Precisa electronic analytical balance with four decimals accuracy. Microhardness test using LECO tester was carried out by placing samples with the 100 mm² surface area under a diamond indenter. The test was performed under 500 gf of indentation load with 10 s of dwell time. Ten readings were taken from the same samples.

3 Research Findings

3.1 Phase Analysis of Mg–Zn Alloy

Figure 1 shows the XRD pattern of sintered Mg–Zn alloy for various percentages of Zn incorporation. At low weight percentage (wt%) of Zn up to 5 wt%, the alloy mainly consisted of α -Mg matrix. According to binary Mg–Zn system, solubility limit of Zn in Mg phase is 6.2 wt% at eutectic temperature (340 °C), nevertheless it is very diminutive at room temperature [7]. Therefore, at this composition, approximately the added Zn element was completely solid solved into Mg to form α -Mg. However, when Zn was added from 10 wt% and further, the intensities of α -Mg peaks decreased which was resulted from the formation of secondary phase. The explanation was attributable to the residual Mg depleted crystalline phase transformed to non-congruently melting γ -MgZn phase at a temperature of 300 °C [8]. At this Zn content, γ -MgZn started to form collectively with α -Mg phase. The intensity of the γ -MgZn increased in respect to Zn addition. It can be implicit since added amount was exceeding the solubility limit of Zn in Mg leading to the formation of γ -MgZn and gradually increased as a function of its incorporation. In addition, by increasing in Zn content, the presented peaks of α -Mg slightly shifted to a lower diffraction angles due to the refinement of the Mg crystallite. The refinement of the grain size during mechanical alloying increased the number of grain boundaries. The numerous interfaces provided higher density of short-circuiting diffusion paths [5].

The formation of γ -MgZn phase was in agreement with the reported binary phase diagram of Mg-Zn system [3, 8] where incorporating Zn above its solubility limit (6.2 wt%) induced the formation of secondary γ -MgZn phase due to eutectic reaction. In

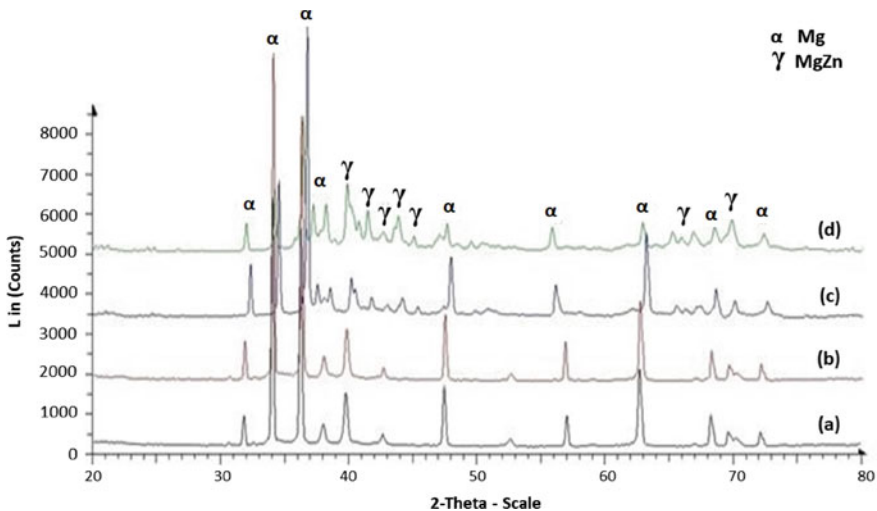


Fig. 1 XRD pattern of sintered Mg–Zn alloy for different Zn content a 3, b 5, c 10 and d 15 wt%

addition, by increasing in Zn content, the presented peaks of α -Mg slightly shifted to a lower diffraction angles and broadened due to the refinement of the Mg crystallite. The refinement of the Mg crystallite size increased the number of grain boundaries. In addition, the peak relocation was also resulted from the shrinkage of host lattice as the smaller atomic size of Zn (134 pm) substituted the position Mg (157 pm) atom.

3.2 Crystallite Size and Internal Strain of Mg–Zn Alloy

As exhibited in Fig. 2, crystallite size of Mg continuously reduced as the Zn content increased. This scenario might be explained by the increasing rate of dissolution of Zn particles leading to an increase in transformation of Mg to α -Mg phase in the Mg matrix, which in turn resulted in an increase of lattice strain. During mechanical alloying process, the powder particles were also subjected to high energy collisions causing a severe plastic deformation and occurrence of stress yields which associated with multiplication of the linear dislocations and refinement of the Mg grains [2]. In contrast, the crystallite size of the non-congruently melting γ -MgZn phase, calculated from the most intense peak of γ -MgZn, was about 137 nm for 10 wt% of Zn and increased to 152 nm for 15 wt% at the temperature of its formation. This phenomenon suggested that the grain growth of this phase occurred rapidly and was considerably stable only in the bulk state due to high interfacial energy (high angle grain boundary) typically exhibited by non-congruently melting phase [6]. However, the grain growth of γ -MgZn phase was not effectively distracted the refinement of Mg crystallites. This situation considerably facilitated the enhancement of internal strain in the Mg up to certain Zn incorporation [5].

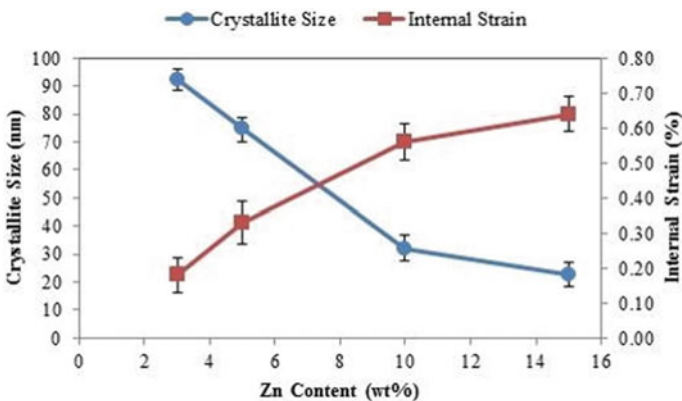


Fig. 2 Crystallite size and internal strain of sintered Mg–Zn alloy with different Zn contents

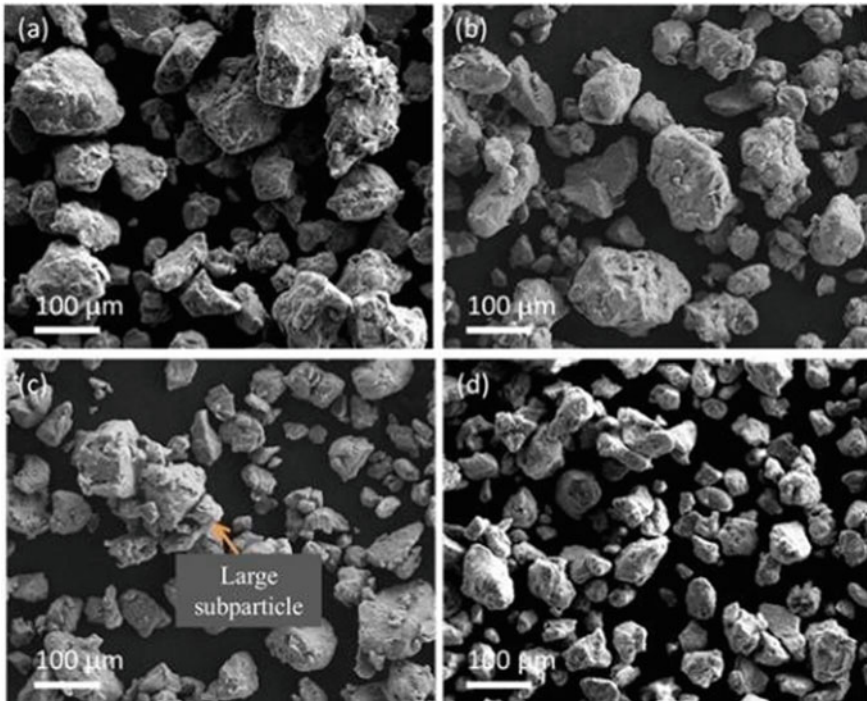


Fig. 3 FESEM images of as-milled Mg-Zn powder with **a** 3 wt%, **b** 5 wt%, **c** 10 wt% and **d** 15 wt% of Zn

3.3 Morphological Evaluation of Mg–Zn Alloy

Figure 3 illustrates the morphology of the as milled Mg-Zn powder with addition of different Zn contents. As observed, there was no flattening of the particles in all mechanically alloyed powders. Micrographically, the alloy incorporated with 3 to 5 wt% Zn consisted of large agglomerates. This scenario indicated that in low addition of alloying element, cold welding was predominant over powder fracturing [3]. At this condition, the morphology of the particles was irregular shape, arising from the ductile characteristic of the starting Mg and Zn powders.

3.4 Density and Microhardness of Mg–Zn Alloy

Figure 4 displays the density of sintered Mg–Zn alloys as a function of Zn incorporation. The sintered density proportionally increased in a respect to Zn addition

as elemental Zn has inherently higher density than Mg element. Therefore, as high-density Zn was added, the density of the fabricated Mg–Zn alloy was also considerably high regardless of its particle size as well as the densification of the alloy powder. In general, the addition of second harder particle to a pure soft metal enables an improvement in the mechanical properties of metallic materials as a result of inherent properties of hard particle itself and finer final grain size obtained during high energy milling [7]. The distribution of microhardness and XRD suggested that increasing Zn content resulted in higher formation of α -Mg phase in the matrix. The dispersion of Zn particles in the Zn matrix acted as strengthening phase and hindered the movement of dislocation when plastic deformation occurred [2]. This phenomenon is known as solid solution strengthening. The formation of α -Mg solid solution consequently improved the microhardness of the Mg–Zn alloy. The Zn particles might restrain the growth of crystal grains and refine the crystal grains of Mg. On the whole, as the Zn content was increased, secondary γ -MgZn phase which was due to exceeding its solubility of Zn in the Mg matrix. Theoretically, the formation of secondary phase continued to refine the particles therefore the microhardness of the bulk alloy increased since finer particles contributed to the decreasing in the localized stress concentration of the alloy [8]. However, from the current finding, there was only a slight increment of hardness at higher Zn content (10 to 15 wt%) which was in correlation with a slight reduction of Mg crystallite size. At this condition, the presence of γ -MgZn had not effectively improved the microhardness of Mg–Zn alloy. Both strengthening effects of Zn incorporation and crystallite refinement of Mg improved the microhardness of binary Mg–Zn alloy. Nonetheless, the formation of γ -MgZn phase at high Zn content (10 to 15 wt%) was not significantly affected the increasing in microhardness of Mg–Zn alloy.

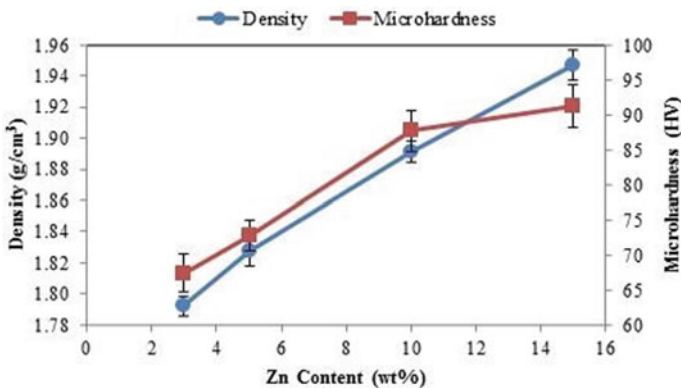


Fig. 4 Density and microhardness of Mg–Zn alloy with different Zn contents

4 Conclusion

Biodegradable Mg-Zn alloys at various Zn content (3, 5, 10 and 15 wt%) were successfully prepared following mechanical alloying procedure. At low Zn content up to 5 wt%, the alloy mainly consisted of α -Mg matrix. However, when Zn was added from 10 wt% and further, the intensities of α -Mg peaks decreased secondary phase of γ -MgZn was detected as the solid solubility limit of Zn in Mg is only 6.2 wt% at 340 °C. The sintered density and microhardness of the alloy proportionally increased in respect to Zn content as elemental Zn has inherently higher density than Mg element and Zn particles might restrain the growth of crystal grains and refine the crystal grains of Mg. The mechanical improvement of the produced Mg-Zn alloys occurred in a mode of solid solution strengthening.

Acknowledgements This work was supported by the Universiti Sains Malaysia RU-PRGS [Grant No. 8046026] and Universiti Sains Malaysia FRGS [Grant No. 6071304]. The authors would like to thank Mineral Research Centre, Department of Mineral and Geoscience Malaysia, Ministry of Energy and Mineral Resources for the technical supports.

References

1. Li W, Guan S, Chen J, Hu J, Chen S, Wang L, Zhu S (2011) Preparation and in vitro degradation of the composite coating with high adhesion strength on biodegradable Mg-Zn-Ca alloy. *Mater Charact* 62:1158–1165
2. Bahman H, Abdollah A (2014) Microstructure, mechanical properties, corrosion behavior and cytotoxicity of Mg-Zn-Al-Ca alloys as biodegradable materials. *J Alloy Compd* 607:1–10
3. Bakhsheshi-Rad HR, Idris MH, Abdul-Kadir MR, Ourdjini A, Medraj M, Daroonparvar M, Hamzah E (2014) Mechanical and bio-corrosion properties of quaternary Mg-Ca-Mn-Zn alloys compared with binary Mg-Ca alloys. *Mater Des* 53:283–292
4. Jing L, Li C, Xue Z, Shao G (2020) Enhancing biocompatibility and corrosion resistance of biodegradable Mg-Zn-Y-Nd alloy by preparing PDA/HA coating for potential application of cardiovascular biomaterials. *Mater Sci Eng, C* 109:110607
5. Fei X, Shang L, Dongdi Y, Jichang X, Pol MR, Zhou X, Ming L, Ulrike R (2022) Recent progress in Mg-based alloys as a novel bioabsorbable biomaterials for orthopedic applications. *J Magnes Alloys* 10:1428–1456
6. Gu X, Zheng Y, Cheng Y, Zhong S, Xi T (2009) In vitro corrosion and biocompatibility of binary magnesium alloys. *Biomaterials* 30:484–498
7. Salleh EM, Ramakrishnan S, Hussain Z (2016) Synthesis of biodegradable Mg-Zn alloy by mechanical alloying: effect of milling time. *Procedia Chemistry* 19:525–530
8. Zhou BC, Shang SL, Wang Y, Liu ZK (2016) Diffusion coefficients of alloying elements in dilute Mg alloys: a comprehensive first-principles study. *Acta Mater* 103:573–586

Effect of Pore Forming Agent on Phase Transformation Behavior of Porous NiTi Shape Memory Alloy



Hafizah Hanim Mohd Zaki, Nur Amanina Abd Kadir, Nur Ayuni Jamal, M. Abd. Maleque, Farah Diana Mohd Daud, Norshahida Sarifuddin, and Jamaluddin Abdullah

Abstract Porous NiTi shape memory alloy is of special interest for bioimplant materials due to its attractive features of NiTi dense structure such as low stiffness, high strength and excellent shape memory and pseudoelastic behavior. This porous NiTi can be produced via powder metallurgy technique using pore forming agent. The pore forming agent is used to create temporary pores that are occupied during sintering where the final sintered sample depends on the composition ratio of the pore forming agent. Porosity of up to 30–50% is predicted to be achieved which is similar to cancellous bone. However, there are queries whether the porous NiTi alloy produced may hinder the phase transformation behavior which is an indicator for shape memory behavior. Therefore, in this research, the effect of composition of pore forming agent such as calcium hydride, CaH₂, on porosity level and how it correlates with phase transformation behavior of porous NiTi alloy were investigated. It shows that by increasing the percentage of CaH₂ to 15 wt%, the porosity level of sintered sample can reach up to 42%. For phase transformation, there are martensitic transformation peaks observed for samples at a composition of ≤ 3 wt% of CaH₂ with enthalpy value of ~ 4.9 J/g. Increasing the percentage of CaH₂ to ≥ 6 wt%, the transformation enthalpy (ΔH) values drop significantly as the samples exhibit no martensitic transformation. This associated with the pores structure and undesirable phase that co-exist with NiTi formation, thus hindered the transformation enthalpy for porous NiTi.

Keywords Pore forming agent · Porous · Shape memory alloy · Phase transformation

H. H. Mohd Zaki (✉) · N. A. Abd Kadir · N. A. Jamal · M. Abd. Maleque · F. D. Mohd Daud · N. Sarifuddin

Department of Manufacturing and Materials Engineering, Kulliyyah of Engineering, International Islamic University Malaysia, Jalan Gombak, 53100 Selangor, Malaysia
e-mail: hafizahhanim@iium.edu.my

J. Abdullah

School of Mechanical Engineering, Universiti Sains Malaysia, 14300 Nibong Tebal, Pulau Pinang, Malaysia

1 Introduction

Shape memory alloy (SMA) is metallic alloy that can revert to its original size or shape after being loaded. Among all SMAs available, NiTi alloy is commonly used in engineering and biomedical applications because of their excellent properties, such as shape memory effect (SME), pseudoelasticity (SE), resistance to corrosion, and biocompatibility which render this alloy operationally suitable for bracket, implantation, and regeneration of hard tissues [1–3].

Porous NiTi alloy has recently received a lot of interest for its possible use as implant materials due to its low stiffness to minimize stress shielding effect and high strength to prevent deformation and fracture [4]. In addition, this alloy exhibits SME which is a unique property that allows a material to recover to its original shape after deformed (plastic deformation) upon heating [5, 6]. As a result, it may facilitate the insertion of the implant when implanted in the body and receive minimally invasive surgery. On the other hand, SE is a material's capability to fully recovered after being deformed by large mechanical stress, resulting in good mechanical stability inside the host tissue. Many researchers have noticed that both SME and SE contribute to the large recovery strain that results in the material resisting large cyclic deformation without leaving residual strain [7]. Since bone is the main cell that supports our body so mainly all stress will be transferred to it. Thus, porous NiTi alloy is a suitable candidate for bone implant and has the potential to withhold all the stresses. Besides, porous structures that are well distributed will help the transportation of body fluid resulting in a more natural and reliable body [3].

Porous NiTi alloy can be produced via powder metallurgy technique by adding CaH₂ as pore forming agent [8]. This pore forming agent is used due to its good pore elimination as it will create temporary pores that are occupied during compaction and will be eliminated during sintering process [9, 10]. Thus, the final sintered bodies depend on the composition percentage of this pore formation agent. It is predicted that porosity of up to 30–50% can be achieved which is similar to cancellous bone [11]. However, there is a challenge to produce porous NiTi with good transformation behavior. Therefore, in this study, the effect of CaH₂ composition on porosity level and phase formation and how it correlates with phase transformation behavior were investigated.

2 Methodology

High purity Ni with 99.9% and TiH₂ with 97.5% purity were used as powder precursors whereas CaH₂ (purity = 95%) was used as pore forming agent. The particle sizes of the Ni and TiH₂ powders are 10–30 μm and 1–3 μm, respectively. The powders precursor with equiatomic composition were then mixed with CaH₂ homogeneously at various percentages of 0.25 wt% to 15 wt% using tumble milling. The sample was then cold-compacted and sintered at constant temperature of 900 °C for 3 h.

The sintering was done in flowing argon using a tube furnace at a heating rate of 10 °C/minute. The porosity of a sintered sample was measured using a densitometer. Then, the samples were characterized using Scanning Electron Microscope, SEM (JEOL JSM-6300F) equipped with Energy Dispersive Spectroscopy, EDS and X-Ray Diffraction, XRD (Bruker) for microstructural analysis and phase identification, respectively. Meanwhile, the phase transformation behavior was analyzed using Differential Scanning Calorimeter, DSC (Mettler Toledo) where the magnitude of this enthalpy change was measured. The value of the enthalpy change is an indicator of the martensitic transformation which is a vital necessity for shape memory effect behavior.

3 Results and Discussion

3.1 Porosity Measurement

Figure 1 shows the graph of density and porosity vs composition of pore forming agent for the samples sintered at 900 °C for 3 h. According to the graph, the density of the sintered sample decreases as the composition of CaH₂ increases. This is due to the increase in the formation of pores in the sample. By adding 15 wt% of CaH₂, the porosity level of sample sintered can reach up to 42%. This indicates that the used of pore forming agent is able to produce a sintered sample with high porosity.

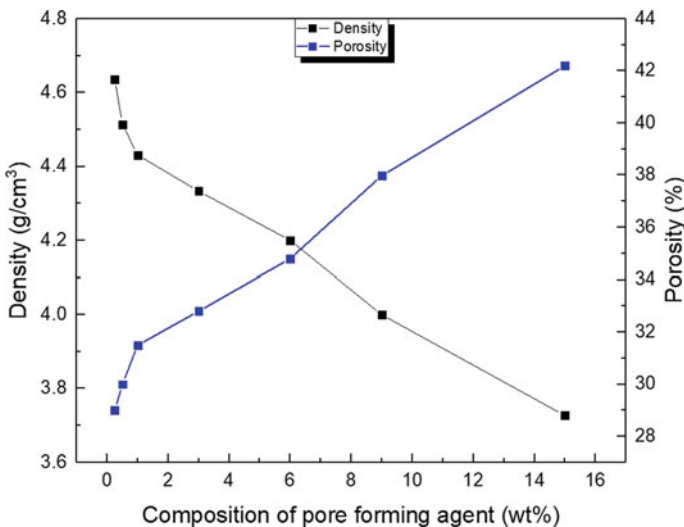


Fig. 1 Density and porosity (in percentage) for sample after sintering with various percentages of pore forming agent

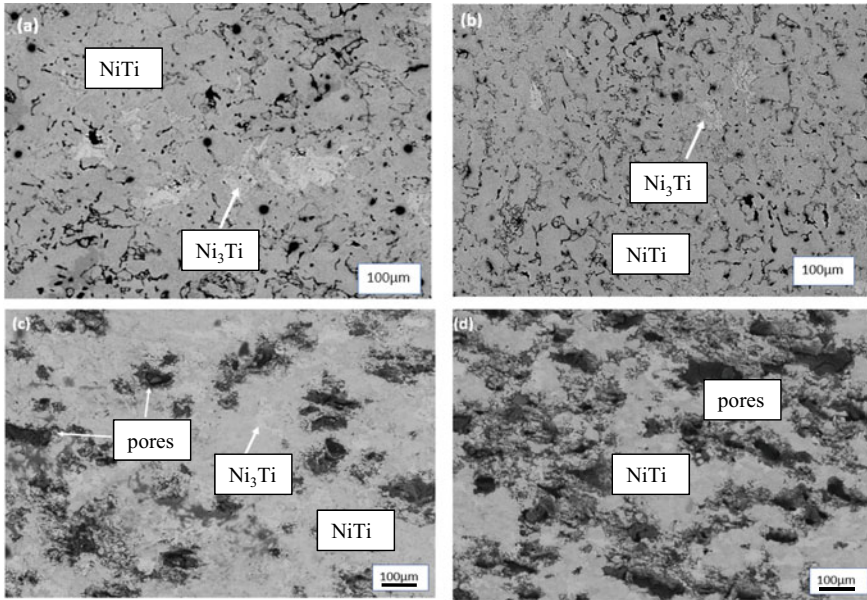


Fig. 2 SEM images of sintered porous NiTi alloy with various percentages of CaH_2 **a** 0.25 wt%, **b** 0.5 wt%, **c** 6.0 wt% and **d** 15.0 wt%

3.2 Morphology and Phase Identification

Pore morphology of sintered samples with different percentages of CaH_2 are shown in Fig. 2a–d. Increasing the percentage of CaH_2 , it shows significant differences in pore size and distribution. The pore structures are small, irregularly scattered and rarely interconnected for samples < 0.5 wt%, whereas the pore structures for samples with ≥ 6 wt% have irregular shape and are partly interconnected. This shows that higher wt% of CaH_2 will have a tendency to create more interconnected pores. Interconnected pores are very important for the transportation of body fluid and the bone healing process [12].

For phase identification, the major phase is NiTi. However, there are other phases such as NiTi_2 , and Ni_3Ti and Ni-rich phase that mutually formed with NiTi during phase formation as shown in Fig. 3.

3.3 Phase Transformation

Figures 4 and 5 shows the DSC curve and graph of enthalpy change (ΔH) for samples sintered with various percentage of CaH_2 , respectively. For DSC curve, there are several peaks observed for reference and samples with ≤ 3 wt% of pore

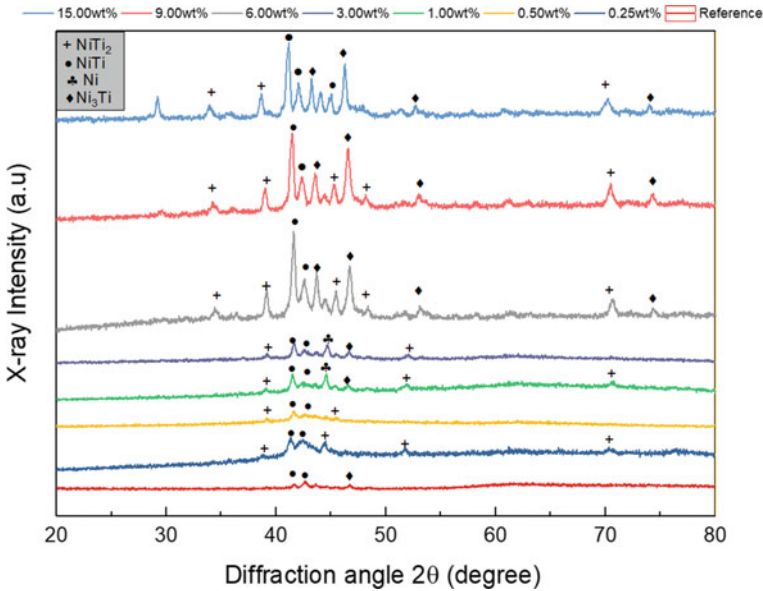


Fig. 3 XRD pattern of reference and sintered porous NiTi alloy samples with various percentage of CaH₂

forming agent, indicating the occurrence of phase transformation from martensite to austenite upon heating. However, the transformation enthalpy (ΔH) values are low in average (~ 4.9 J/g) and drop significantly for samples $> 3\text{wt}\%$ of CaH₂. Increasing the percentage of pore forming agent to ≥ 6 wt%, the samples exhibit no martensitic transformation. This is due to the formation of pores which widen the transformation hysteresis. Moreover, the formation of multiple phases also may have correlation with transformation behavior in which the undesired phases such as NiTi₂, Ni₃Ti and Ni-rich do not participate in B2 \rightarrow B19' phase transformation, thus exhibit no martensitic transformation [13].

4 Conclusion

Pore forming agent of CaH₂ was successfully used to create porous structure in NiTi alloy where it led to higher porosity level up to 42%. However, the porous NiTi sample with higher porosity level exhibits no martensitic transformation peaks. This is associated with the pore structure which widen the transformation hysteresis and the formation of undesirable phases that formed together with NiTi phases, thus hindering the transformation enthalpy for porous NiTi.

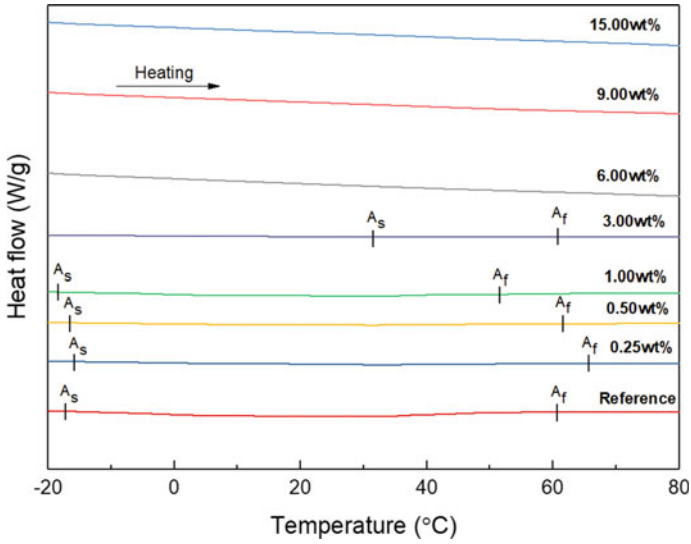


Fig. 4 DSC curve of reference and sintered samples with various percentage of CaH₂ upon heating from - 20 °C to 80 °C

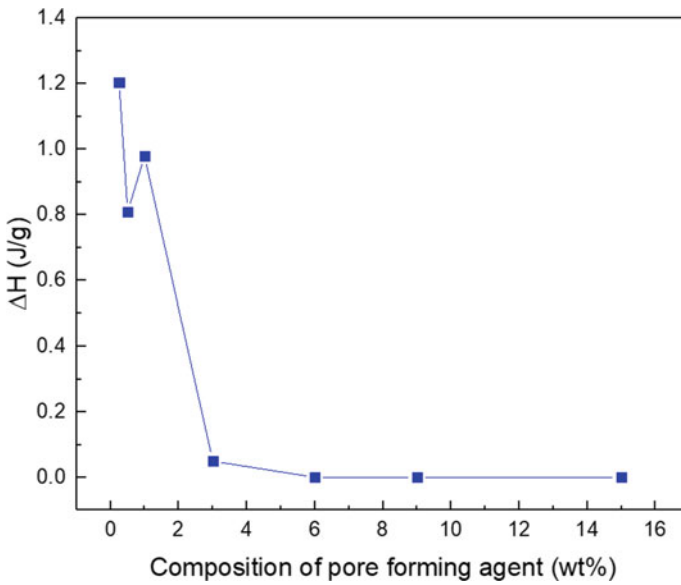


Fig. 5 ΔH versus various percentage of CaH₂ for sample after sintering

Acknowledgements The authors acknowledge the research funding received from Ministry of Higher Education via the FRGS-RACER scheme (RACER/1/2019/TK05/UIAM//1)

References

1. Kaya M, Çakmak Ö (2016) Shape memory behavior of porous NiTi alloy. *Metall Mater Trans A* 47(4):1499–1503
2. Elahinia M, Shayesteh Moghaddam N, Taheri Andani M, Amerinatanzi A, Bimber BA, Hamilton RF (2016) Fabrication of NiTi through additive manufacturing: a review. *Prog Mater Sci* 83:630–663
3. Dawood NM, Abid Ali ARK, Atiyah AA (2019) Fabrication of porous NiTi shape memory alloy objects by powder metallurgy for biomedical applications. *IOP Conf Ser Mater Sci Eng* 518(3):032056
4. Greiner C, Oppenheimer SM, Dunand DC (2005) High strength, low stiffness, porous NiTi with superelastic properties. *Acta Biomater* 1:705–716
5. Naresh C, Bose PS, Rao CS (2016) Shape memory alloys: a state of art review. *IOP Conf Ser Mater Sci Eng* 149:012054
6. Kaya M, Çakmak Ö, Gülenç B, Atlı KC (2017) Thermomechanical cyclic stability of porous NiTi shape memory alloy. *Mater Res Bull* 95:243–247
7. Parvizi S, Hashemi SM, Asgarinia F, Nematollahi M, Elahinia M (2021) Effective parameters on the final properties of Niti-based alloys manufactured by powder metallurgy methods: a review. *Prog Mater Sci* 117:100739
8. Kadir NA, Zaki HHM, Abdullah J, Daud FDM, Sariffudin N (2022) Porous NiTi shape memory alloy fabricated via powder metallurgy technique using pore forming agent. *Key Eng Mater* 908:119–124
9. Lai T, Xu JL, Xiao QF, Tong YX, Huang J, Zhang JP, Luo JM, Liu Y (2021) Preparation and characterization of porous NiTi alloys synthesized by microwave sintering using Mg space holder. *Trans Nonferrous Met Soc China* 31:485–498
10. Fang ZZ (2010) *Sintering of advanced materials: Fundamentals and processes*. Woodhead Publishing, Oxford, England
11. Ma X, Wang H, Xie H, Qu J, Chen X, Chen F, Song Q, Yin H (2019) Engineering the porosity and superelastic behaviors of NiTi alloys prepared by an electro-assisted powder metallurgical route in molten salts. *J Alloy Compd* 794:455–464
12. Abbasi N, Hamlet S, Love RM, Nguyen NT (2020) Porous scaffolds for bone regeneration. *J Sci Adv Mater Devices* 5(1):1–9
13. Zaki HHM, Abdullah J (2016) The role of CaH₂ in preventing oxidation for the production of single-phase NiTi alloy in solid state. *J Alloy Compd* 655:364–371

Nano-Structured Zinc Oxide/Silicon Dioxide Thermoelectric Generator: A Waste Heat Harvesting Technology



Ataur Rahman, Yusuf Abdi, Kyaw Myo Aung, and Sany Ihsan

Abstract Internal Combustion Engine in Hybrid powered transportation system is combating issues such as rising power costs, pollution, and global warming. The exhaust of internal combustion engines wastes a significant amount of fuel energy. Many academics are attempting to develop the waste energy harvesting-based power generator in order to reduce the negative effects. However, they have achieved only 5–7% of waste energy harvesting. The goal of this work is to describe a semiconductive thermoelectric generator (STEG) that uses a semi-conductive zinc oxide (ZnO)/silicon di-oxide (SiO₂) composite to achieve a waste energy harvesting efficiency of 10–15%. The samples for the STEG models have been developed using ZnO blended epoxy resin and hardener for n-type and SiO₂ blended epoxy resin and hardener pasted on CF for p-type. STEG models have made by sandwiching dielectric film by p-type and n-type SC. Each of the final samples has a 100 mm² surface area. The STEG samples were examined in the electronic lab using Keithley Parametric Analyzer software to determine the best composition based on the performance of electric conductivity (σ), short circuit current density (J_{sc}), open circuit voltage (V_{oc}), zT merits, seeback coefficient (α) and conversion efficiency (η_{con}). The samples were tested with applying heat externally at 150 °C. The best results were obtained for the sample of 30 wt.% of ZnO and 70% of SiO₂ as σ of $5.4 \times 10^{-8} \text{ m}^{-1} \Omega^{-1}$, V_{oc} of 525 mV, J_{sc} of $14 \times 10^{-9} \text{ A/m}^2$ and η_{con} of 15%.

Keywords Semi-conductive thermoelectric generator · Waste heat energy harvesting · Current density · Synthesising and characterization

1 Introduction

TEGs are solid-state devices without moving parts, thus operating quietly, holding a long service life [1, 2]. Various Authors developed p-type nanostructured (Bi, Sb)₂Te₃ bulk materials with an average $ZT \sim 1.4$ between 300 and 450 K, p-type

A. Rahman (✉) · Y. Abdi · K. M. Aung · S. Ihsan
Kulliyah of Engineering, International Islamic University Malaysia, Kuala Lumpur, Malaysia
e-mail: arat@iium.edu.my

K-doped PbTe_{0.7}Si_{0.3} bulk materials $ZT \sim 1.56$ at 550 K and 2.2 at 800 K, and silicon germanium alloys (Si₈₀Ge₂₀) with $ZT \sim 1.84$ at 1073 K, respectively [4, 5]. Thermoelectric generators (TEG) offer several distinct advantages over other technologies of waste heat harvesting [3, 6, 7]. The main disadvantage of the TEG is the efficiency of its conversion being relatively very low, usually about 5% [8–10]. Thus, it has become the main reason for the limitation of their use in the production of electricity for specialized areas with extensive fields of application, where reliability is the main factor, other than cost. At the exhaust pipes, in internal combustion engine cars, the exhaust gas temperature is too high in the range of 500–2700 K [11, 12]. The conductivity of ZnO in the lower temperature range is due to the ionization of zinc atom pairs, whose ionization energy is 2×10^{-2} V or less. The author Liang has used the ‘Hall Effect’ measurements and reported that the free electron density about 10^{15} cm^{-3} incurred at room temperature [12]. At 800 °C the conductivity of this type begins to reach saturation. The thermal coefficient of ZnO are given in the range of $4.31 \times 10^{-6} \text{ Wm}^{-1}$ and $2.49 \times 10^{-6} \text{ Wm}^{-1}\text{K}^{-1}$ at 300 K [13]. SiO₂ has a high dielectric strength and a relatively wide band gap, making it an excellent insulator of electron transfer through its surface. It has high temperature stability of up to 1600 °C, making it a useful material for process and device integration [4]. The energy band gap of ZnO is 3.44 eV at low temperatures and 3.37 eV at room temperature [14]. The energy band gap of SiO₂ grown on p-type and n-type silicon, the activation energies of conduction in the temperature range 500–176 °C were found to be 1.65 and 2.10 eV, respectively [5]. The objective of this research is to develop a SiO₂ (p-type)/ZnO (n-type) dielectric thermo-electric generator to harvest the waste heat energy into electric energy with a conversion efficiency about 10–15%. This developed technology has been made based on the waste heat energy of ICE about 70% harvest and convert into electric energy.

2 Methodology

3 ZnO-ER Film for STEG n-type

The samples of Zinc Oxide and Epoxy Resin (ZnO-ER) thin film for n-type semiconductor and SiO₂-ER film for p-type semiconductor were prepared using the solution casting process. To achieve a good homogenous solution and good interaction between the ER matrix and nano-filler particles, ZnO was added to an ethanol–water solvent mixture in a proportion of 70/30% (volume/volume). The ZnO/solvent mixture was held under constant stirring for 2 h before being sonicated to disseminate the filler particles equally. At 80 °C, the ER was progressively added to the dispersion under vigorously stirring and it was sonicated for 30 min. The slurry was casted onto a clean and dry glass cup at 30 °C to make a ZnO-ER film. To remove residual solvent, the resultant film composite was left at room temperature for 3 h before being dried in a vacuum oven at 50 °C for 3 h. In addition, the thin film was

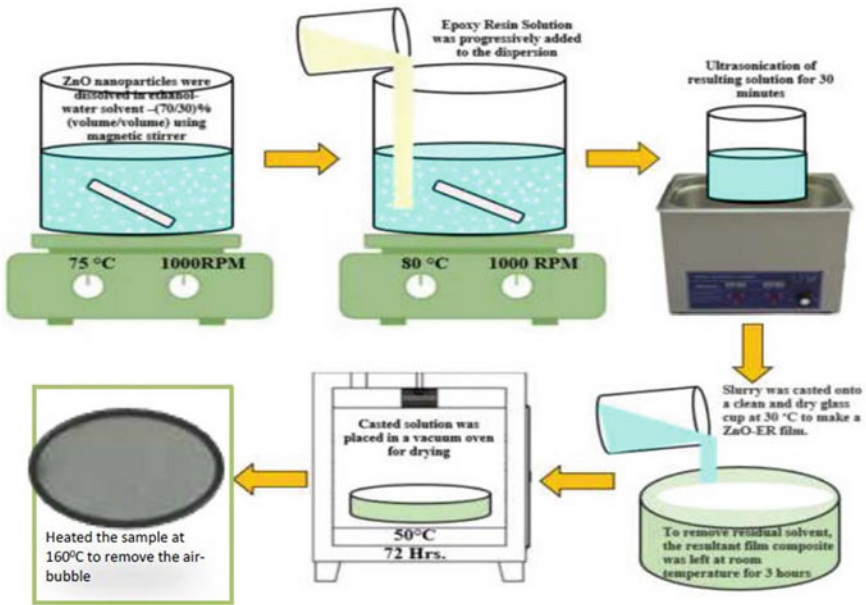


Fig. 1 Schematic of the synthesised ZnO-ER samples

heated to 120–160 °C to confirm that the bubble was gone before cooling to ambient temperature as shown in Fig. 1. A total of 15 samples has been made for the STEG with a thin film of ZnO-ER with varying the wt.% ZnO and mass of ER and film of SiO₂-ER with varying the wt.% of SiO₂ and ER mass. There are five different forms of STEG samples have been made with varying the weight percentage (wt.%) of ZnO (n-type) and SiO₂ (p-type) and epoxy. The thickness of the sample films was measured with a micrometre and found to be between 3 and 7 mm.

4 Characterisation of the STEG

A laboratory-based STEG has been developed with ZnO/SiO₂ composite. The characterization of the ZnO-ER and CuO-ER has been characterized using Scanning Electron Microscope (SEM) for the Morphological analysis of the ZnO-ER Nanocomposite, Fourier Transform Infrared Spectroscopy (FTIR) for the observation of the presence of functional groups present in ZnO-ER Nanocomposite, X-ray diffraction (XRD) for the examination of the diffraction pattern of the ZnO-ER Nanocomposite, UV–visible Spectrophotometer (UV–Vis) to find out the absorption and band gap of ZnO-ER Nano-composite. Figure 2 shows the morphological structure of the ZnO/ER. Nano-composite structure has been made with SEM to characterize the morphological structure for the detection of high energy electrons emitted from the

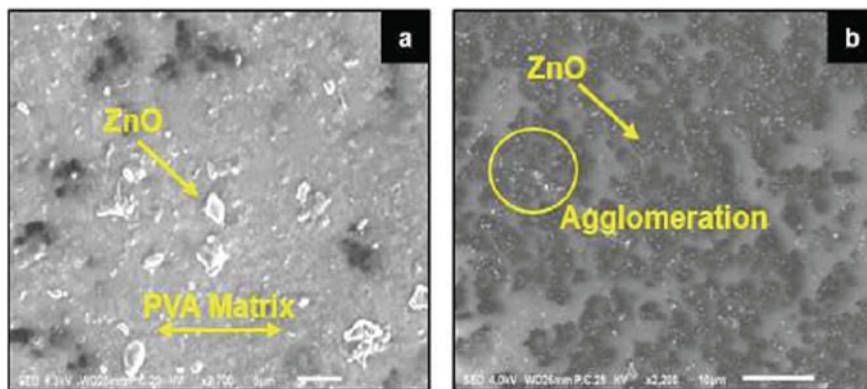


Fig. 2 Image of SEM of the ZnO filler ER FILM

surface. The SEM image shows the ZnO layer structure favourable to form the heat pathways due to its interstitial atom vacancy. However, it contains several small particles with an average size of less than 14 nm when dispersed in the ER. The aggregate shape of the FF causes a non-linear electron flow, which leads to a decrease in energy generation. Spectrometer spectroscopy of the synthesized ERZnO membranes was performed to identify the functional groups, present in the membranes and to analyse the interaction between cross-linked ER and ZnO Nano-particles. The FTIR spectra were caused by the transmittance mode.

All spectra were recorded and analyzed. The X-ray diffraction (XRD) pattern of ZnO 30 wt.%/ER (25 g) sample displays a relatively high peak of $2\theta = 35.96^\circ$. However, typically the 2θ value is 19.8° . Diffraction peaks for the ER and the regular ZnO wurtzite (JCPDS 36–1451). Using the Debye Scherrer formula, the crystallite size of ER/ZnO Nano-composite films was measured and found to be in the 14.19–14.28 nm range and the average particle size (D) is about 14.23 nm. Ultra-violet—Visible Spectrophotometer (UV–Vis) was carried out to test the samples of ZnO/ER Nano-composite in order to find the energy band-gap. The effect of zinc oxide nanoparticles on ER matrix was obtained using the energy band gap.

5 Result and Discussion

The laboratory scale STEG has been developed by sandwiched the dielectric thin film using the ZnO-ER n-type semiconductor and SiO_2 -ER p-type semiconductor. Electrical conductivity of SiO_2 /ER-Dielectric-ZnO/ER was measured with Fluke 27 Digital Multimeter and conductivity probe TetraCon 925, Digital multimeter was used to measure the open circuit voltage (VOC). To stabilize temperature water bath was used. Values of electrical conductivity were calculated as average from 10 measurements during 5 min. The measurements of electrical conductivity were

conducted with 1.0% uncertainty of measurement. The STEG module has been developed using the optimum sample, ZnO of 30 wt.% for n-type and SiO₂ of 70 wt.% for p-type contents ER 25 g and hardener of 25 g, based on the laboratory characterization results and experimental results. The STAG module has been developed in different thickness 3 mm (1), 5 mm (2), 7 mm (3) and 9 mm (4) and equal length of 50 mm. Each of the samples was tested with 100 °C temperature to measure its electric conductivity. ZnO 30 wt.% and ER 25 g has been identified as a best sample from the samples characterization using the SEM, XRD, FTIR, UV-Vis. Hardener content of 40 g has a substantially greater impact on the samples' electric conductivity than hardener content of 20 g. It indicates that the higher contents of epoxy resin and hardener cause the higher resistivity and lower current density due to the higher insulating properties to transfer even the exchange of photon within the surface of n-type and p-type semiconductor of the STEG. The heat energy conversion efficiency is higher at heating time with constant temperature of 100 °C than any TEG efficiency reported in the literature. This efficiency could be maintained if the coolant can be used.

A thermoelectric device is made up of a sequence of primitive thermoelectric units, which are made up of a pair of p and n materials in their most basic form as shown in Fig. 3. If a prototype thermoelectric module is built by connecting 24 n-type (ZnO) and p-type (CuO) connected in series for a module and 23 modules connected in parallel. The thermal energy recovered is estimated that the STEG will yield 170.0 Ws. A prototype of a cylindrical thermoelectric module has been made using both n- type ZnO and p-type SiO₂ based on the synthesised, characterisation and experimental studies. The composition of SiO₂ (70%) and ZnO (30%) STEG is the best composition for TEG model based on its conductivity, open circuit voltage (VOC), short circuit current (J_{SC}), and power conversion efficiency (η_c). The prototype device had a maximum zT merit of 3.55 at a temperature of 150 °C and a heat conversion efficiency of 21.31 percentage without cooling for 20 s. This STEG has the potential to convert waste heat into electric energy by roughly 21% in 20 s of operation time at room temperature. If the coolant is implanted with the STEG, it may work similarly throughout its operation. By using a sodium chloride solution with a boiling point of 1413 °C as the aqueous dielectric of the STEG sandwiched by ZnO/ER (n-type) and SiO₂/ER (p-type), the STEG's performance can be enhanced by up to 30%.

6 Conclusion

A prototype of a cylindrical thermoelectric module has been made using both n-type ZnO and p-type SiO₂ based on the synthesised, characterisation and experimental studies. The composition of SiO₂ (70%) and ZnO (30%) STEG is the best composition for TEG model based on its conductivity, open circuit voltage (VOC), short circuit current (J_{SC}), and power conversion efficiency (η_c). The prototype device

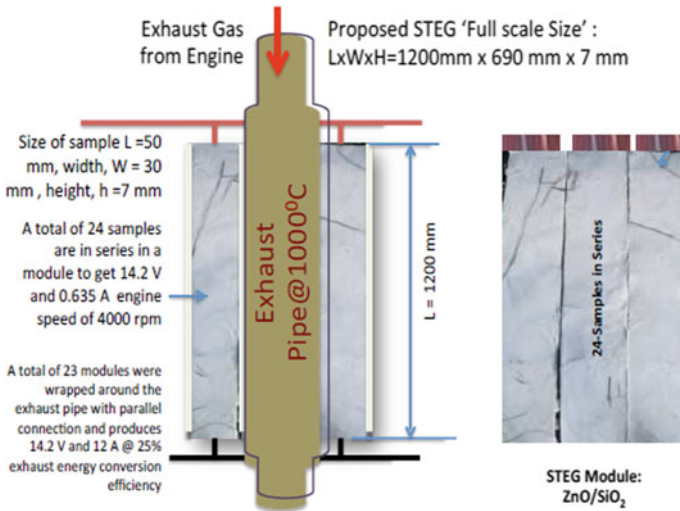


Fig. 3 Infographic of full scale STEG for engine

had a maximum zT merit of 3.55 at a temperature of 150 °C and a heat conversion efficiency of 21.31% without cooling for 20 s. This STEG has the potential to convert waste heat into electric energy by roughly 21% in 20 s of operation time at room temperature. If the coolant is implanted with the STEG, it may work similarly throughout its operation. By using a sodium chloride solution with a boiling point of 1413 °C as the aqueous dielectric of the STEG sandwiched by ZnO/ER (n-type) and SiO₂/ER (p-type), the STEG's performance can be enhanced by up to 30%.

References

1. Snyder GJ (2008) Small thermoelectric generators. *Electrochem Soc Interface* 17:54
2. Mohamed HE, Dhafer AD, Faizul MS, Suhana MS, Masjuki HH, Bashir AB, Mahazani M (2014) A review on thermoelectric renewable energy: principle parameters that affect their performance. *Renew Sustain Energy Rev* 30:337–355
3. Riffat SB, Ma X (2003) Thermoelectrics: a review of present and potential applications. *Appl Therm Eng* 23:913–935
4. Basu R, Bhattacharya S, Bhatt R, Roy M, Ahmad S, Singh A, Gupta SK (2014) Improved thermoelectric performance of hot pressed nanostructured n-type SiGe bulk alloys. *J Mater Chem A* 2(19):6922–6930
5. Roberto S, Lars S, Michael PD (2017) Electrical conductivity of SiO₂ at extreme conditions and planetary dynamos. *Proc Natl Acad Sci of the USA* 114(34):9009–9013
6. Minnich AJ, Dresselhaus MS, Ren ZFG, Chen G (2009) Bulk nanostructured thermo- electric materials: current research and future prospects. *Energy Environ Sci*
7. Goupil C, Seifert W, Zabrocki K, Müller EGJ, Snyder GJ (2011) Thermodynamics of thermoelectric phenomena and applications. *Entropy*

8. Omer SA, Infield DG (2000) Design and thermal analysis of two stage solar concentrator for combined heat and thermoelectric power generation. *Energy Convers Manage* 41:737–756
9. Yadav A, Pipe KP, Shtein M (2008) Fiber-based flexible thermoelectric power generator. *J Power Sources* 175:909–913
10. Ataur R, Abdul RF, Hawlader MNA, Rashid M (2013) Nonlinear modeling and simulation of waste energy harvesting system for hybrid engine: fuzzy logic approach. *J Renew Sustain Energy* 5(3):1–13
11. Ataur R, Fadhialh R, Afroz R, Hawlader MNA, Mohiuddin AKM (2015) Power generation from the waste of IC engine. *J Renew Sustain Energy Rev, Elsevier Publisher* 51:382–395
12. Liang S, Zheng D, Standley DM, Guo H, Zhang C (2013) A novel function prediction approach using protein overlap networks. *BMC Syst Biol* 7:61
13. Nam WH, Lim YS, Choi SM, Seo WS, Lee JY (2012) High-temperature charge transport and thermoelectric properties of a degenerately Al-doped ZnO nanocomposite. *J Mater Chem* 22:14633–14638
14. Champier D (2016) Thermoelectric generators: a review of present and future applications. *Springer Proceedings in Energy; Springer Science and Business Media LLC: Cham, Switzerland*, pp 203–212

Mechanical and Structural Properties of Epoxy Bio-Composite Using Fish Bones as Bio-Filler



Azriena Nathasa Zakaria and Tasnim Firdaus Ariff 

Abstract This research investigates the mechanical and structural properties of epoxy bio-composites made from recycled bio-waste (fish bones). Epoxy bio-composites are made by embedding fish bone particles into epoxy with weight percentage compositions of 0 wt.% (E), 2 wt.% (E2FB), 8 wt.% (E8FB), and 12 wt.% (E12FB). The fish bone was washed and dried overnight at 70 °C in the oven. Fish bones were crushed and ground into small particles less than 250 μm in size using the grinder. Hardness, density, tensile, and flexural strength were tested mechanically in this study, while surface morphology was investigated structurally using a Scanning Electron Microscope (SEM). The epoxy bio-composite was measured against a 0 wt. % fish bone in epoxy (E). E2FB has the highest hardness strength (140.04 HV), followed by E12FB (138.62 HV) and E8FB (132.33 HV), whereas E2FB has the lowest density (1.14 g/cm³); density increases as the weight percentage of fish bone increased. Regarding tensile and flexural strength, E2FB takes the lead, obtaining the highest in both tests (2.03 MPa and 42.55 MPa) compared to E8FB and E12FB. According to the experimental results, using 2 wt. % of fish bones as a bio-filler in epoxy improves the mechanical and structural qualities of the epoxy biocomposite. The images produced from the Scanning Electron Microscope show that the distribution of the fish bone appeared to have sunk uniformly at the base of the samples.

Keywords Epoxy · Epoxy bio-composite · Fish bones · Bio-filler

1 Introduction

There are two types of waste which are biodegradable and non-biodegradable. The biodegradable wastes can decompose in soils throughout time, while the non-biodegradable wastes cannot decompose themselves. However, bio-waste products

A. N. Zakaria · T. F. Ariff (✉)

Department of Manufacturing and Materials Engineering, Faculty of Engineering, International Islamic University Malaysia, Kuala Lumpur, Malaysia

e-mail: tasnim@iium.edu.my

are one of the types of waste that can be reused, such as eggshells, rice husks, sea urchins, coconut shells, peanut shells, Phoenix Pusilla plants and fish bones.

According to Vijay et al. [1], composite materials (based on matrix) are divided into three parts: ceramic matrix, organic matrix and metal matrix. Bio-composites are divided into natural fibre and matrix and synthetic matrix. Polymer matrix composites with reinforced filler are used to improve the strength of the mechanical properties. When a matrix (epoxy) is combined with natural fibres, it will become a composite material called a bio-composite. Jagdev et al. [2] said that when epoxy resin composite is reinforced with non-biodegradable waste (glass polymer), the mechanical properties of the epoxy resin are increased.

A study by Tserpes et al. [3] explained that epoxy bio-composite was brilliant in its ageing role and had a comparable water absorbability as water absorption induces a slight decrease in its interlaminar shear strength as to the reduction of carbon-fibre reinforced plastics. Another study by Wan et al. [4] found that the compatibility between silane functionalized rapheme oxide and the epoxy matrix can be enhanced with silane functionalization containing epoxy ended group. They also stated that combining those materials will boost the thermal stability, tensile and flexural properties, storage modulus, fracture toughness and glass transition temperature.

The study by Azman et al. [5] found that chicken eggshell particles (ESPs) produced a better feature than CaCO_3 as they were more environmentally friendly inexpensive fillers. The benefits of eggshells are that they can be reused as fertilizer, skin care and decorative items [6]. Carbon-aramid reinforced epoxy is the most common hybrid composite made as they increase the strength of the materials and are reasonable in price [7]. Furthermore, in an observation-based study by Prakash and Viswanathan [8], the finding showed that sea urchin spike filler and kenaf also could be used as biofiller. They aim to use eco-friendly materials to have an excellent mechanical property and thermal stability of composites.

Epoxy composites made from fishbones, which are hydroxyapatite-based waste materials, exhibit increased mechanical characteristics with higher Tg values and are appropriate for semi-structural applications [9]. According to Singh et al. [10], adding fishbone as a nanofiller to a jute/carbon composite increases its tensile strength. Since fish bones are a biodegradable waste product, they will benefit the environment and the circular economy. Due to lower production costs for the composites reinforced with bio-fillers, less trash will be dumped at landfills, and the circular economy will flourish. Keychains, phone cases, and home décor are a few examples of the products made from epoxies that have societal advantages.

Fig. 1 Dried fish bones

2 Experimental Procedure

2.1 Materials

First, the project started with procuring fish bones from household waste, epoxy resin, hardener, dog bone and rectangular moulds. The epoxy resin and hardener are purchased from the local supplier. The fish bones are washed several times to remove any residue left on the bones. Then, they are dried in a forced-air convection oven PROTECH (FAC-100) at 70 °C overnight to remove the moisture. Figure 1 shows the dried fish bones that have been left dried in the convection oven.

Next, the fish bones are crushed and ground in the grinder AIRMAC (MDY-200) for up to 5 min to become a fine particle. Then, the particles are sieved using a metal sieve to get a particle size less than 250 μm . The fish bone particles and epoxy resin are mixed with the hardener and poured into dog bone and rectangular moulds. Before the mixtures are poured into the mould, silicon spray is applied on the surface to ease the samples pullout after dried.

2.2 Preparation of Epoxy Bio-Composites

Three paper cups containing a ratio of 2:1 of epoxy and hardener are prepared to be mixed with a different weight percentage of fish bone particles. The hardener and epoxy are mixed in one direction for three minutes using a wooden stick. Next, fish bone particles are added according to the name tag of the formulation shown in Table 1. Figure 2 shows the samples for each formulation.

Table 1 Name tags and formulation of epoxy with fish bone particles

Samples	Epoxy resin (wt.%)	Fish bone particles wt.%)
E	100	0
E2FB	98	2
E8FB	92	8
E12FB	88	12

Fig. 2 Fish bone epoxy bio-composite samples



2.3 Mechanical Testing

The mechanical testing in this research included hardness, density, tensile and flexural strength. This testing aims to determine the suitable percentage of fish bone particles to get the highest strength in mechanical testing. For the hardness test, Vickers machine HV-1 (HUATEC, Beijing) with a diamond tip was used to determine the hardness of the composites. Based on ASTM E384, the load range used for this test is 500 gf.

Next, the density of the sample is tested using densimeter machine. It can measure an accurate density for solid and liquid samples. Furthermore, the density of the samples also is calculated by Eq. 1:

$$\rho_c = m_c / V_c \quad (1)$$

The dog-bone and rectangular samples are used to test the tensile and flexural strength of the composite. SHIMADZU Universal Testing Machine (UTM) with ASTM D638-04 and ASTM D790-97 is used to perform the test. The maximum load is 5kN with crosshead speeds of 5 mm/min and 10 mm/min each.

2.4 Microstructural Observation

All the samples are coated to create a conductive layer and improve the imaging of the samples using the coating machine (SC-7620). The microstructure of the composites samples is examined using Scanning Electron Microscope (SEM) JSM IT-100 (JEOL, Japan). It is operated with a magnification of 30 times and an accelerated voltage of 20 kV to visualize fractured tensile samples. Images from the magnification are taken for further analysis.

3 Results and Discussion

3.1 Mechanical Properties

Table 2 summarizes the mechanical test results of the epoxy bio-composite in this project. The E sample act as the epoxy bio-composite benchmark to compare each sample's strength. E2FB has the highest mechanical strength, followed by E12FB and E8FB. The results show that as the weight percentage of the fish bones increases, the composite's hardness is decreased. E2FB has a similar hardness to epoxy alone (E), which is only 0.55% different in hardness strength. However, at 8 wt. % fish bones, the hardness value is the lowest (132.33 HV) as it is 5.51% lower compared to E2FB.

The density values of the epoxy bio-composites are measured in two ways: using a densimeter (experimental value) and a theoretical value. As the percentage of fish bones is increased from 0 to 12 wt.%, the density of the samples increases from 1.14 to 1.18 g/cm³. This is because when the mass of the composite is increased, the volume of the composite increases and the density of the composite will be increased too.

Epoxy resin alone (E) is more brittle than epoxy bio composite, whereas E2FB needs 0.19 MPa more to get the same strength as the epoxy alone. From this case, the condition of the sample is looked up as the E2FB has some bubble in the middle of the sample. The bubble affected the tensile strength reading when the sample broke

Table 2 Mechanical test results

Sample	Hardness (HV)	Density (g cm ⁻³)	Tensile (MPa)	Flexural (MPa)
E	140.81	1.14	2.22	2.72
E2FB	140.04	1.14	2.03	42.55
E8FB	132.33	1.16	1.36	12.31
E12FB	138.62	1.18	1.62	27.15

where the bubble was located when conducting the experiment. E8FB has the lowest tensile strength, 33% lower than E2FB.

E2FB has shown to have the highest flexural strength, which is 42.55 MPa. Meanwhile, the E8FB composition gave the lowest flexural strength (12.31 MPa) compared to the 2 and 12 wt.% fish bones. Adding 2 wt.% of fish bone has enhanced the mechanical properties where it has the highest hardness, tensile strength and flexural strength with low density and light weight has been achieved. E8FB has shown to have the lowest values for tensile strength and flexural strength. This can be due to poor adhesion of filler matrix and agglomeration of fish bones. The stress concentration points and poor interfacial interaction between filler and the matrix reduce the tensile and flexural strength. Thus, the more weight percentage of fish bones added, the more brittle the samples become and decreased the mechanical strength of the bio-composites.

3.2 *Surface Morphology Analysis*

The structural properties test of the samples is taken after the tensile strength test. The SEM images of the samples, in Fig. 3 show that the distribution of the fish bones have sunk to the bottom of the sample even though they were mixed well before pouring into the mould. In Fig. 3a, the epoxy surface shows a plain image because 0 wt.% fish bone was added to the sample. The sample is just a mixture of epoxy with hardener (2:1). However, with the addition of fish bone particles, as shown in Fig. 3b–d, the fish bone particles are uniformly distributed at the base of the sample when it dried. The more fish bone particles added, the more visible it is in the images.

4 Conclusion

E2FB has the highest hardness (140.04 HV), the highest tensile strength (2.03 MPa) and the highest flexural strength (42.55 MPa). On the other hand, the density of the epoxy bio-composite is marginally increased when the weight percentage of the fish bone is increased, resulting in E12FB having the highest density (1.18 g/cm³). Nevertheless, E2FB is only 3% lower than E12FB. With the increasing weight percentage of fish bones reinforced with epoxy, the samples become more brittle, decreasing the mechanical strength. The images produced by Scanning Electron Microscope show that the fish bone particles were homogeneously distributed at the base of the sample.

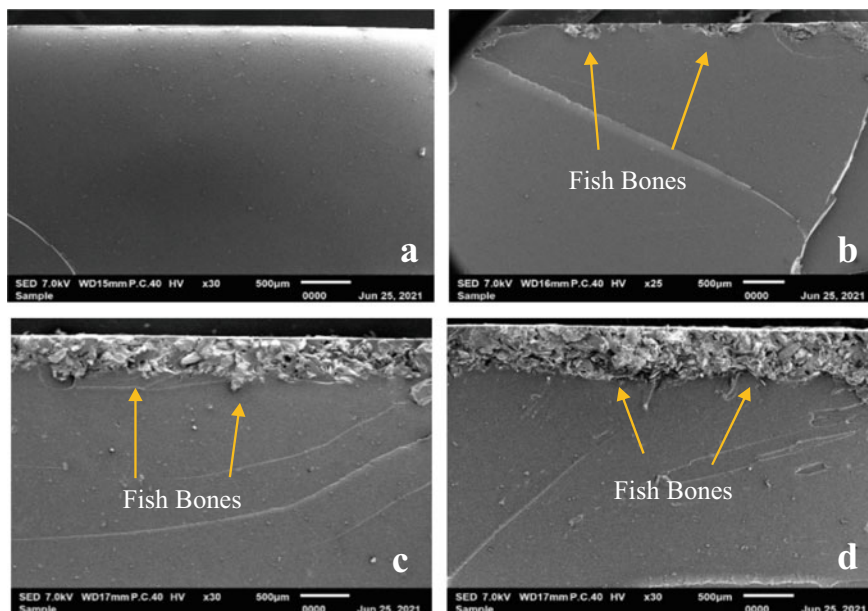


Fig. 3 SEM images of different samples: **a** E, **b** E2FB, **c** E8FB, **d** E12FB

References

1. Vijay N, Rajkumara V, Bhattacharjee P (2016) Assessment of composite waste disposal in aerospace industries. *Procedia Environ Sci* 35:563–570
2. Jagdev A, Prava Jena B, Bijeta Nayak B, Satapathy S (2018) Preparation and characterization of mechanical properties of epoxy resin composites reinforced with non-biodegradable wastes. *Mater Today Proc* 5(9):19723–19727
3. Tserpes K, Tzatzadakis V, Katsiropoulos C (2019) Effect of hygrothermal ageing on the interlaminar shear strength of carbon fiber-reinforced rosin-based epoxy bio-composites. *Compos Struct* 226
4. Wan Y-J, Gong L-X, Tang L-C, Wu L-B, Jiang JX (2014) Mechanical properties of epoxy composites filled with silane-functionalized graphene oxide. *Compos Part A: Appl Sci Manuf* 64:79–89
5. Azman NAN, Islam MR, Parimalam M, Rashidi NM, Mupit M (2020) Mechanical, structural, thermal and morphological properties of epoxy composites filled with chicken eggshell and inorganic CaCO₃ particles. *Polym Bull* 77(2):805–821
6. Joann P (2021) 15 Reasons why you need to stop throwing away your eggshells. <https://www.tasteofhome.com/collection/eggshell-uses>. Accessed 2021/3/20
7. Pincheira G, Canales C, Medina C, Fernández E, Flores P (2018) Influence of aramid fibers on the mechanical behavior of a hybrid carbon–aramid–reinforced epoxy composite. In: *Proc Inst Mech Eng, Part L: J Mater Des Appl* 232(1):58–66
8. Prakash VA, Viswanthan R (2019) Fabrication and characterization of echinoidea spike particles and kenaf natural fibre-reinforced Azadirachta-Indica blended epoxy multi-hybrid bio composite. *Compos A Appl Sci Manuf* 118:317–326

9. Hani F, Firouzi A, Islam MR, Sumdani MG (2020) Mechanical and thermal properties of fishbone-based epoxy composites: the effects of thermal treatment. *Polymer Compos* 42(3)
10. Singh H, Batra NK, Dikshit I (2021) Development of new hybrid jute/carbon/fishbone reinforced polymer composite. *Mater Today Proc* 38(1):29–33

Characterization of New Biofluid Lubrication Formulation Using Castor Oil with Hyaluronic Acid Additive for Artificial Joints



Amira Atikah Suhairi , M. Mazwan Mahat ,
and Nurul Nadiah Mohd Kamaldin 

Abstract This study focused on the properties of biofluid, a new formulation proposed to generate synthetic synovial fluid using Castor Oil, and three various compositions of Hyaluronic acid (HA) which are 0 ml, 5 ml, and 10 ml as the addition for total knee replacement (TKR) utilising the Pin-on-Disc approach. This research led to the use of vegetable oils as bio-fluid lubrication, which may imitate the characteristics of synovial fluid with friction coefficients as low as 0.03 while being safe for the human body. Thus, the frictional force, friction coefficient, and wear rates indicated by the sample at the same pace of activity, 6 kg, and speed of 60 rpm, were investigated in this study. The study used 316L stain- less steel as the pin and Polylactis Acid (PLA) as the disc to duplicate the notion of stress and compression on artificial joints. The friction coefficient in this investigation is 0.023, and the average frictional force is 1.574N. The average wear is 0.005303 mm. This experimental study's key contribution is that it demonstrates how castor oil may be treated with HA to function as a lubricant for artificial joints and how modern medicine can use it to treat synovial fluid-related issues.

Keywords Synthetic synovial · Castor Oil · Artificial joints

1 Introduction

The mobility of the knee joint needs an adequate lubrication mechanism and synovial fluid is the usual lubricant in the human body to perform this purpose [1]. Knee joint replacement implants require a capsule to keep the artificial lubricant in place between the joints, reducing friction and wear and avoiding debris migration [2]. Dr. John Charnley, the investor in whole hip joint prostheses, acknowledged that synovial fluid behavior as a lubricant had very low frictional qualities at any joints [3]. In comparison to the substantial gap in knowledge of the fundamental of lubrication process in artificial joints, it was scarcely behavior lubricant can determine film forms

A. A. Suhairi · M. Mazwan Mahat (✉) · N. N. M. Kamaldin
School of Mechanical Engineering, College of Engineering, Universiti Teknologi MARA, 40450
Shah Alam, Selangor, Malaysia
e-mail: mazwan@uitm.edu.my

and wear rates on the joints [4]. The investigation of artificial lubrication and wear processes by synovial fluids is a crucial problem in tribological research, but it is also a significant barrier to achieving optimal articular prosthetic lubrication [5]. Over the years, research on lubrication for artificial joints has grown in order to identify the ideal alternative for synovial fluid that is both inexpensive and ecologically friendly while being compatible with the human body.

Environmentally friendly bio lubricant fluids have drawn a lot of interest during the past several decades [6]. Non-biodegradable mineral oils had a significant negative impact on the environment, which increased public awareness of the problem. Vegetable oils and other renewable resources were consequently suggested as a solution [7]. Vegetable oils have a larger potential for use as lubricants since they produced less wear scars than mineral oils [8]. Around 350 oil-bearing plants, including Jatropha, Karanja, Neem, Soybean, and Castor, have the potential to be sources of bio-lubricants, according to a few studies [9]. Castor oil has the best tribological capabilities, according to a study on the tribological characteristics of lubricants based on sunflower, soybean, and castor oil [10]. Castor oil has the potential to be used as a green lubricant, and the application has been well detailed [11]. It is made up of methyl esters, which give it great viscosity, a low pour point, and good lubricity [12].

Synovial fluids (SFs) are bio tribological fluids that are essential for optimal lubrication of synovial joints [5, 13]. Synovial fluid (SF) is a plasma dialysate that contains compounds generated by joint tissues, including significant levels of hyaluronic acid [14]. Synovial joints enable animals and humans to move freely while avoiding friction and wear [15]. The Newtonian behavior at low shear rates, with a noticeable drop in viscosity as shear rate increases, and the tendency of the polymer chains to entangle at low concentration, displaying viscoelastic behavior, make HA a natural biopolymer ideal for replenishing joint fluids [16].

2 Methodology

2.1 Disc Preparation

3D printing was used to create samples of Poly Lactic Acid (PLA) discs with thickness of 4 mm and diameter of 74 mm. The disc models require 100% infill density and a line pattern, however it takes 20 layers of filament to print a perfect disc shape. The visible printed lines on the 3D printing PLA disc might cause additional friction during testing. To reduce the proportion of additional friction, the discs were smoothed using tetra-hydrofuran (THF) alcohol.

2.2 Pin Preparation

316L stainless steel with diameter of 8 mm was used in this investigation from long stainless-steel rod was shortened in length using a hand grinder to 33 mm. As a work-around, an abrasive cutter was used to lower the pin's size into 25 mm as water travels with the blade rotation as a coolant, the abrasive cutter may cut the stainless-steel rod smoothly and accurately, minimizing scratches on the pin's surface. After achieving the desired smooth and flat surface, a grinder fitted with 400 grit Silicon Carbide (SiC) grind paper was used to remove the residual scratches.

2.3 Bio-Lubricant Preparation

Lubricants in this study are produced from castor oil and an additive should be used with the Castor oil as a friction modifier to minimize friction. Hyaluronic acid (HA) was used as an addition in this experiment because it has Newtonian behavior and has a clear influence on viscosity decrease as shear rate increases. Three samples of castor oil were mixed with varied HA compositions; Castor oil with 0 ml of HA, Castor oil with 5 ml of HA and Castor oil with 10 ml of HA.

2.4 Tribological Test

The pin-on-disc machine was used to study frictional force, friction coefficient, and wear analysis. Fixed speed and weight circumstances with various bio-lubricant sample compositions were examined. The sensor will measure the friction. At a room temperature of 27 °C, the test lasted 1800 s for each sample.

3 Result and Discussion

3.1 Comparison on Friction Coefficient

Coefficient of friction differs upon sliding time depending on rotational sliding speed and vertical loads applied. The graph fluctuated within the rubbing time for the three compositions of Castor Oil and at the starting point of the experiment, minimal frictional force applied against the pin and disc along with the supplementation of Castor Oil as lubrication.

Figure 1 showed that despite the low applied force, the solid-to-solid contact force can raise the friction coefficient value. In terms of boundary lubrication, pure Castor Oil had a greater coefficient of friction than others, although Castor Oil with 5 ml

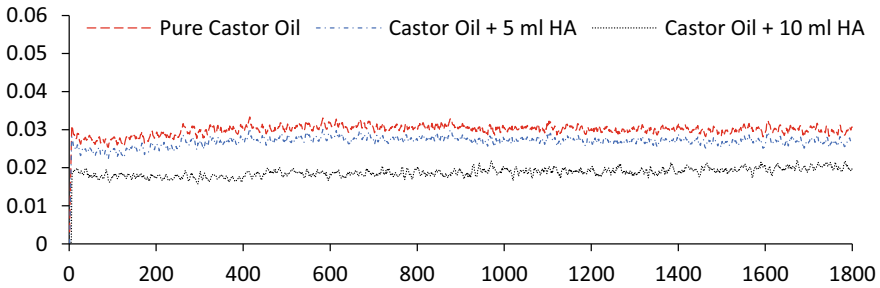


Fig. 1 Relationship of friction coefficient with sliding time at 60 RPM

HA had some- what lower fluctuations in the number of friction coefficients over time. Castor Oil + 10 ml HA, on the other hand, revealed a considerable change in coefficient of friction due to the enough amount of HA to offer improved lubricity to the Castor Oil.

3.2 Comparison on Frictional Force

Due to the first interaction between the pin layer and the PLA disc, the initial magnitude of frictional force is high. The roughness changes dramatically when the primary wear stage is reached.

As the sliding speed dropped, frictional heat reduced material strength and temperature resulting the grip force on the pin increased. There are no discernible variations in the frictional value once the pin reaches a constant vertical force between 1000 and 1800 s. The interaction between the pin and disc can attain a stable state at one point despite a rise in normal load, as seen in Fig. 2. In a short amount of time, the frictional force impacting wear may be plainly visible. This aspect can be addressed by employing a lubricant with a greater lubricity to assist minimise surface roughness.

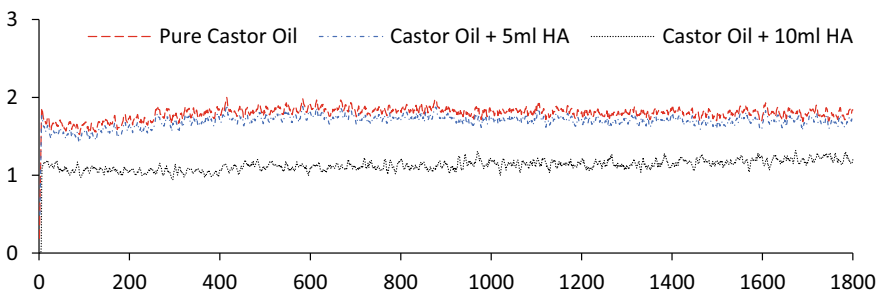


Fig. 2 Relationship of frictional force with sliding time at 60 RPM

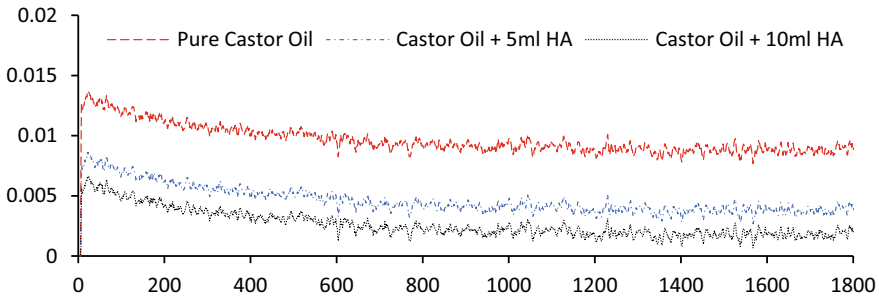


Fig. 3 Relationship of wear with sliding time at 60 RPM

3.3 Comparison on Wear Rates

The wear findings were obtained as the wear performance graph was employed to observe the wear of a PLA disc caused by the sliding of a stainless-steel pin. The greater wear rate data are obtained from pure Castor Oil lubrication, whereas the lower wear rate values are obtained from Castor Oil + 10 ml HA sample. Lubricated sliding condition shown results as in Fig. 3.

The non-Newtonian flow features can be seen as greater HA compositions offer a higher viscosity to Castor Oil at a given speed. The lubricant's molecular weight changed as its concentration changed. The binding interactions between macromolecules influence Castor Oil's sliding movement, resulting in high viscosity solutions. The gliding layers offer smooth lubricated surfaces for the rubbing process, the shear rate can be reduced.

4 Conclusion

Castor Oil resulted in a significant reduction in friction coefficient, wear rates, and frictional force when compared to non-lubricated tests performed by other researchers. The clear decreasing pattern on values for the frictional force, friction coefficient, and wear rates proven the choice of HA as the addition played the most essential role in this experiment. Castor Oil can perform well with the addition of additives to improve viscosity and offer excellent lubrication for artificial joints. Finally, the findings of this study advise that vegetable oils be given further attention by doing additional in vitro, in vivo, and clinical testing before ultimate use.





Acknowledgements The authors would like to acknowledge the School of Engineering, UiTM Shah Alam and Ministry of Higher Education in providing the Fundamental of Research Grant Scheme (FRGS), (435/2019), for the financial support of this research.

References

1. Prekasan D, Saju KK (2016) Review of the tribological characteristics of synovial fluid. *Procedia Technol* 25:1170–1174
2. Alnaimat FA, Shepherd DET, Dearn KD (2016) The effect of synthetic polymer lubricants on the friction between common arthroplasty bearing biomaterials for encapsulated spinal implants. *Tribol Int* 98:20–25
3. Jay GD, Waller KA (2014) The biology of Lubricin: near frictionless joint motion. *Matrix Biol* 39:17–24
4. Myant C, Cann P (2014) On the matter of synovial fluid lubrication: implications for metal-on-metal hip tribology. *J Mech Behav Biomed Mater* 34:338–348
5. Marian M, Shah R, Gashi B, Zhang S, Bhavnani K, Wartzack S, Rosenkranz A (2021) Exploring the lubrication mechanisms of synovial fluids for joint longevity—a perspective. *Colloids Surf B Biointerfaces* 206
6. Salimon J, Salih N, Abdullah BM (2012) Diesters biolubricant base oil: synthesis, optimization, characterization, and physicochemical characteristics. *Int J Chem Eng*
7. Yahaya A, Samion S, Aini N, Ahyam M, Kameil M, Hamid A (2021) Cold extrusion using biodegradable oil as lubricant: experimental and simulation analysis
8. Syahrullail S, Kamitani S, Shakirin A (2013) Performance of vegetable oil as lubricant in extreme pressure condition. *Procedia Eng* 68:172–177
9. More S, Kotiya A, Kotia A, Ghosh SK, Spyrou LA, Sarris IE (2020) Rheological properties of synovial fluid due to viscosupplements: a review for osteoarthritis remedy. *Comput Methods Programs Biomed* 196
10. Quinchia LA, Delgado MA, Reddyhoff T, Gallegos C, Spikes HA (2014) Tribological studies of potential vegetable oil-based lubricants containing environmentally friendly viscosity modifiers. *Tribol Int* 69:110–117
11. Chinchkar DS, Satpute ST, Kumbhar NR (2012) Castor oil as green lubricant: a review. *Int J Eng Res Technol* 1(5)
12. Madankar CS, Pradhan S, Naik SN (2013) Parametric study of reactive extraction of castor seed (*Ricinus communis L.*) for methyl ester production and its potential use as bio lubricant. *Ind Crops Prod* 43(1):283–290
13. Su CY, Chen CC, Huang YL, Chen SW, Fang HW (2017) Optimization of biomolecular additives for a reduction of friction in the artificial joint system. *Tribol Int* 111:220–225
14. Brannan SR, Jerrard DA (2006) Synovial fluid analysis. *J Emerg Med* 30(3):331–339
15. Stachowiak GW, Batchelor AW, Griffiths LJ (1994) Friction and wear changes in synovial joints. *Wear* 171(1–2):135–142
16. Cowman MK, Lee HG, Schwertfeger KL, McCarthy JB, Turley EA (2015) The content and size of hyaluronan in biological fluids and tissues. *Front Immunol* 6

Blast Furnace Slag Cement Clinker Production Using Limestone-Hot Blast Furnace Slag Mixture



Ahmad Abdul Mun'im Ismail, Muhammad Rafiq Haikal Rosdin, Alya Naili Rozhan , Hadi Purwanto, Abd Malek Abdul Hamid, Muhamad Faiz Md. Din , Mohd Fairus Mohd Yasin , and Mohd Hanafi Ani 

Abstract The higher production of steel lead to increase in blast furnace slag (BFS) waste which is the by-product of pig iron production. It is due to the demand of steel and concrete around the world for residential and corporate office. The tapping temperature of BFS waste is 1500 °C, hence the amount of heat exposed to the atmosphere is enormous. Reusing slag and heat waste from hot slag contributes to green economy. Using appropriate mixing composition, BFS and limestone mixture can be used for green cement production. This works explores the potential to convert slag waste into cement clinker using heat recovered from blast furnace of iron production. BFS and limestone was mixed at specific ratio according to their phase diagram for mentioned purpose. The mixing composition of BFS and limestone is varied at weight percentage of 60, 70 and 74% calcium oxide (CaO). The results show the alite and belite phase present in the slag clinker under XRD characterization and the percentage of weight loss increase after annealing process. BET analysis shows the higher addition of CaO results in higher pore volume, which is proving the high percentage of weight loss. It is observed from the annealing process that the final composition of slag clinker changed. This study shows that by heating BFS with limestone has potential to produce cement clinker at the mixing composition of 74% CaO.

Keywords Blast furnace slag · Cement clinker · Waste heat

A. A. M. Ismail · M. R. H. Rosdin · A. N. Rozhan · H. Purwanto · A. M. A. Hamid · M. H. Ani (✉)

Department of Manufacturing and Materials Engineering, Kulliyah of Engineering, International Islamic University Malaysia, 53100 Gombak Selangor, Malaysia
e-mail: mhanafi@iium.edu.my

M. F. Md. Din

Department of Electrical and Electronic Engineering, Faculty of Engineering, National Defence University of Malaysia, Kem Sungai Besi, Kuala Lumpur, Malaysia

M. F. M. Yasin

High Speed Reacting Flow Laboratory, School of Mechanical Engineering, Universiti Teknologi Malaysia, Johor Bahru, Malaysia

1 Introduction

Portland cement is well-known in industry and regularly used as it has the hydraulic binding properties. It consists of Portland cement clinker, 0–5% limestone or granulated BFS, and a small amount of gypsum. The application is very extensive in the construction of buildings and highways as it is a basic component used in concrete. The consumption of cement in construction industry are increasing year by year. According to Müller [1], the production of cement in Malaysia in the year 2013 until 2021 reached about 178.6 million metric tons cumulatively. This trend also applies in the production of Portland cement in United States that approximately produced 70 million metric tons every year from 2013 until 2019 and recorded highest production in 2021 with 92 million metric tons [2]. These data proved the high demand of cement usage.

A survey by United Nation compiled in Commodity Trade Statistics Database shows that the steel and iron industry in Malaysia have produced the highest amount of slag waste which is 103,736,390 kg in 2018. BFS is one of the residues and solid waste from iron–steel metallurgical industry, whose storage does not only occupy a large amount of land resources but also causes environmental pollution to the soil, underground water, and atmosphere [3]. Accounted 25–30% of BFS produced in every iron production. In 2020, world iron slag production was estimated to be between 310 and 380 million tons [4].

The massive amount of slag waste that is generated can be recycled into a variety of applications, the most prevalent of which being cement manufacture. Steel slag or BFS are used to make the cement [5]. Furthermore, steel consumption increases the demand for raw materials like iron ore, scrap, and flux. The raw material extraction resulted in the release of waste slag and gas.

The direct blast furnace cement (BFC) method makes use of the waste heat in the molten slag. The waste heat is used to breakdown limestone, resulting in energy savings in the production of Blast Furnace Cement (BFC). When the thermal exergy from the molten slag is recovered, the overall exergy loss in BFC manufacturing will be reduced by 20% [6]. The temperature used to heat the BFS and limestone is not the same as in the industry due to the furnace's low capability to achieve 1600 °C. This is a restriction in executing the direct blast-furnace-cement experiment procedure. The BFS is also solid, although in real-world applications, the BFS is molten. As a result, the goals of this study are to determine the best blast furnace slag to limestone powder ratio for producing cement clinker and to determine the minimum temperature required for processing limestone and blast furnace slag to make cement clinker.

Table 1 Weight of limestone to be added into BFS

Type of limestone calculation	Desired composition/wt% of CaO	Weight of limestone added/g	Weight of BFS/g
Weight composition calculation	58.3	10.30	
	68.1	44.20	100.00
Ratio of BFS to limestone mixture	74.0	75.00	

2 Materials and Method

Solid BFS and limestone were ball milled to obtain very fine powders of both ingredients. The powder then combined and three samples with varied mixture compositions were made. The CaO-SiO₂ binary phase diagram [7] and the Lea and Parker formula [8] were used to compute the ratio of blast furnace slag to limestone mixture when combining limestone into blast furnace slag. The mixture composition can be seen in Table 1.

All the samples were annealed at minimum temperature of 1338 °C [9] with heating rate of 10 °C/min using high operating temperature furnace. The holding time for the three samples is 30 min for the mixture to mix evenly. Then, the samples were cooled down until room temperature overnight.

XRD and BET were used to characterize the samples. The Bruker D2 Phaser XRD machine was utilized. Every sample was powdered and placed into a mold designed specifically for this XRD device for analysis. The voltage and current levels are maintained at 30 kV and 10 mA throughout the experiment. The scan rate is 0.2 degrees per minute. During X-ray scanning, it is required to obtain more precise information. Profex and Origin software were used to examine the raw data from this instrument for graphical form analysis. Using physical gas adsorption on the sample surface, BET was used to measure the porosity of the solid surface.

3 Results and Discussion

Heating a mixture of BFS and limestone at various weight percentages causes a change in the physical appearance of the samples as well as weight loss. X-Ray Diffraction and BET characterization are used to further characterize the samples.

3.1 Physical Changes of the Sample

BFS and limestone were combined in a high purity alumina crucible before being heated to 1338 °C. Both materials are powders. After the samples were heated to 1338 °C, held at that temperature for 30 min, and cooled to room temperature overnight, there were physical changes in the sample weight. The sample weight loss before and after the annealing procedure is shown in Table 2. The weight loss was due to reaction of free calcium oxide with free silica and aluminium oxide from slag mineral producing gehlenite. Another reaction take place inside the slag-limestone mixture with calcium oxide (CaO) was free silica and aluminium oxide (Al_2O_3) from slag mineral to produce gehlenite ($3Ca_2Al_2SiO_7$). Furthermore, reaction of lime which is calcium oxide (CaO) from the limestone react with quartz which is silicon dioxide (SiO_2) from slag produced dicalcium silicate or known as belite. A half parabolic graph depicting the proportion of weight reduction in all samples was created from the data in Table 2, as shown in Fig. 1.

Table 2 The weight changes before and after annealing process

CaO wt%	Desired composition/wt% of CaO	Weight of limestone added/g	Weight of BFS/g
60.00	27.54	27.01	1.924
70.00	36.03	32.23	10.547
74.00	43.8	38.72	11.598

Fig. 1 Percentage of weight loss at mixture 60, 70 and 74 wt% of CaO

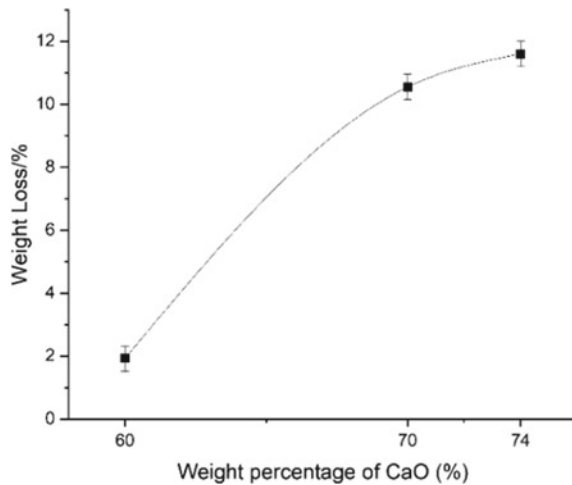
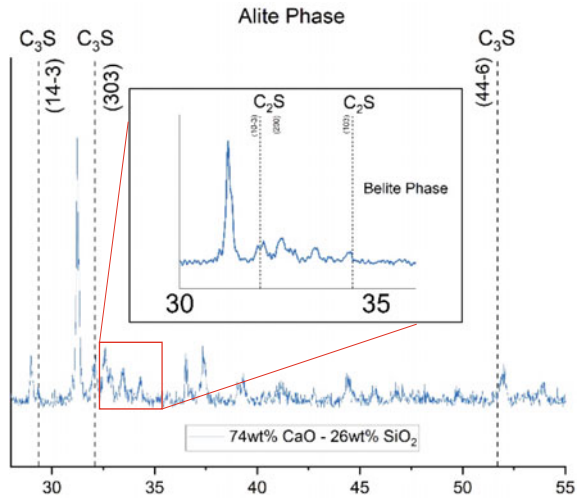


Fig. 2 XRD Spectra of alite phase and belite phase for 74% of CaO composition



3.2 XRD Analysis of the Sample

Tricalcium silicates, Ca_3SiO_5 , and dicalcium silicates, Ca_2SiO_4 , which are alite and belite phases respectively, are the XRD patterns that need to be focused on in this research. Figure 2 show the peaks of alite and belite phase, respectively.

The stated d is the interplanar distance or interplanar spacings of the cementitious materials from the database, and d' is the interplanar distance of the BFS-limestone mixture according to Bragg's Law equation. The equation used is obtained by discarding n and the constant integer '2' from the original equation. As a result, the percentage difference between the two interplanar discrepancies is determined. The equation is

$$d \sin \theta = d' \sin \theta' \tag{1}$$

Table 3 shows the peak of alite and belite from database and BFS-limestone mixture while Table 4 shows the results of d/d' percentage for each peak orientation of the respective phase using equation above.

According to the calculation above, the interplanar distance at each phase at their peak orientation is slightly reduced at 1338 °C. The interplanar distance, d , decreases when CaO from limestone is added to BFS. The angle of the belite and alite peak at all orientations is higher than the database peak. It was discovered that the lattice bears compressive strain, causing the lattice size to shrink. It agrees with the previous computation since the lattice parameter reduces as the interplanar distance, d , decreases [10]. At lattice parameter (10–3) in sample 3, the intensity of the belite phase drops. Furthermore, sample 3 exhibits the largest CaO addition of all the samples, generating the alite phase with an extensive lattice parameter (303).

Table 3 Peak angle of alite and belite phase

Phase	Orientation	Database	As received
Alite	14–3	29.350	29.363
	303	32.100	32.121
	44–6	51.700	51.841
	10–3	32.050	32.070
Belite	200	32.610	32.619
	103	34.400	34.410

Table 4 The d/d' percentage for each peak orientation of the respective phase

	Orientation	d/d' percentage (%)	Average d/d' percentage (%)
Alite	14–3	100.041	
	303	100.065	100.126
	44–6	100.273	
	10–3	100.062	
Belite	200	100.028	100.040
	103	100.029	

4 Conclusion

In conclusion, heating a mixture of BFS and limestone to a minimum temperature of 1338 °C produce clinker containing alite and belite phases confirmed by XRD characterization. Peaks of alite and belite phase formed and grew as the amount of CaO added increased. The optimal BFS-limestone mixture is made with a 1.00–0.75 ratio of blast furnace slag to limestone mixture. Based on this ratio calculation referring to CaO-SiO₂ binary phase diagram, the weight percentage of CaO is 74%. We have concluded that the process of mixing BFS into limestone can produce cement clinker at the temperatures as low as 1338 °C.

Acknowledgements This research was financially supported by Ministry of Higher Education, Malaysia with Grant Number FRGS/1/2019/TK07/UIAM/03/3.

References

1. Joschka M (2021) Malaysia: cement production |Statista, <https://www.statista.com/statistics/719188/cement-production-malaysia/>. Last Accessed 27 Apr 2022
2. Garside M (2021) U.S.: cement production 2021 |Statista. <https://www.statista.com/statistics/219343/cement-production-worldwide/>. Last Accessed 27 Apr 2022
3. Li Y, Liu Y, Gong X, Nie Z, Cui S, Wang Z, Chen W (2016) Environmental impact analysis of blast furnace slag applied to ordinary Portland cement production. *J Clean Prod* 120:221–230
4. Joyce AO (2021) Iron and steel slag, U.S. Geological Survey

5. Gao T, Shen L, Shen M, Liu L, Chen F (2016) Analysis of material flow and consumption in cement production process. *J Clean Prod* 112:553–565
6. Kasai E, Akiyama T, Purwanto H (2010) Process analysis of the effective utilization of molten slag heat by direct blast furnace cement production system. *ISIJ Int* 50(9):1319–1325
7. White JF, Lee J, Hessling O, Glaser B (2017) Reactions between liquid CaO–SiO₂ slags and graphite substrates. *Metall Mater Trans B* 48(1):506–515
8. Kurdowski W (2014) *Cement and concrete chemistry*. Springer, Netherlands
9. Telschow S (2012) *General rights clinker burning kinetics and mechanism*. APA
10. Senkov ON, Chakoumakos BC, Jonas JJ, Froes FH (2001) Effect of temperature and hydrogen concentration on the lattice parameter of beta titanium. *Mater Res Bull* 36:1431–1440

A Quad Band Negative Permittivity Microwave Metamaterial Design for Satellite Applications with Wider Bandwidth



Md. Bellal Hossain, Mohammad Rashed Iqbal Faruque,
and Muhamad Roszaini Roslan

Abstract This study describes a perpendicular arm-based ring resonator quad band negative permittivity microwave metamaterial for satellite applications. The proposed structure comprises of a ring resonator with five perpendicular arm providing quadruple resonance frequency at 5.396, 7.940, 10.028 and 12.580 GHz with magnitude of -22.34 , -26.10 , -25.15 and -20.30 dB, respectively. The metamaterial structure is created on a most familiar FR-4 dielectric material, a thickness of 0.028λ , a dimension of $0.179\lambda \times 0.179\lambda$, λ is calculated at the lowest resonance frequency. The CST microwave studio is employed to calculate the metamaterial properties. The negative real value of the permittivity has been found at the frequency range of 5.396–5.732 GHz, 7.940–8.624 GHz, 10.028–11.180 GHz, and 12.580–13.868 GHz. The operating bandwidth of the structure are 0.48 GHz (5.06–5.54 GHz), 1.12 GHz (7.18–8.3 GHz), 1.11 GHz (9.42–10.53 GHz) and 0.82 GHz (12.15–12.97 GHz) with the transmission coefficient being the lowest -10 dB. The CST results have been verified by HFSS simulator which shows slight discrepancy with each other. The exciting metamaterial behavior with wider bandwidth enable to be used for satellite applications.

Keywords Negative permittivity · Perpendicular arm · Satellite application

1 Introduction

Metamaterials are unnatural composite materials with exotic electromagnetic properties not found in nature that are created by periodically arranging tiny metallic resonating patch. The periodic arrangements of metallic patch on host dielectric materials can be employed to construct a metamaterial unit cell structure [1]. The development of metamaterial research has helped to many applications in microwave and terahertz domains such as antenna design [2, 3], cloaking and light manipulation

Md. B. Hossain · M. R. I. Faruque (✉) · M. R. Roslan
Space Science Centre, Institute of Climate Change, Universiti Kebangsaan Malaysia, UKM,
43600 Bangi, Selangor, Malaysia
e-mail: rashed@ukm.edu.my

[4, 5], specific absorption rate (SAR) reduction [6], metamaterial absorber [7, 8], satellite applications [9, 10], sensors [11] and so on.

In contemporary literature, various structures have been described to acquire double negative (DNG) or single negative (SNG) using a different design. A two-behavior based metamaterial was presented in [12] based on H-shape showing a C-band resonance designed on double substrate material. In [13], an SNG metamaterial was presented that exhibits triple band resonance frequency for microwave applications, fabricated on Rogers RT5880 substrate. A double C shape DNG metamaterial was proposed in [14] that shows triple resonance at 3.36, 5.58, and 11.57 GHz. In [15], a double Z-shape metamaterial has been delineated that reveals a triple band at 7.3, 8.1 and 9.4 GHz with size of $8.5 \times 8.5 \text{ mm}^2$. However, satellite applications with wider bandwidth based multiband metamaterial structure design have yet to be upgraded.

As the metamaterials realize insufficient bandwidth in satellite applications described above, this research is presented to incorporate a perpendicular arm-based ring resonator quad band negative permittivity microwave metamaterial for satellite applications with wider bandwidth. The originality of this study that the proposed design can exhibit an uncommon shape with compact dimension. This unit cell structure has been developed a quad resonance including C, X, and Ku band applications.

2 Metamaterial Structure Design and Simulation

The proposed quad band negative permittivity metamaterial is created on more familiar FR-4 dielectric material with a thickness of 0.028λ , a physical size of $10 \times 10 \text{ mm}^2$ and an electrical dimension of $0.179\lambda \times 0.179\lambda$. The top resonator comprises of a ring resonator with five perpendicular arms shown in Fig. 1.

The front view of the structure constitutes a metallic resonating patch, shown in Fig. 1a, in other ways, the perspective view shows the metallic patch with FR-4 dielectric material which is shown in Fig. 1b. The design parameter of the proposed structure is introduced in Table 1. The simulation geometry is presented in Fig. 1c,

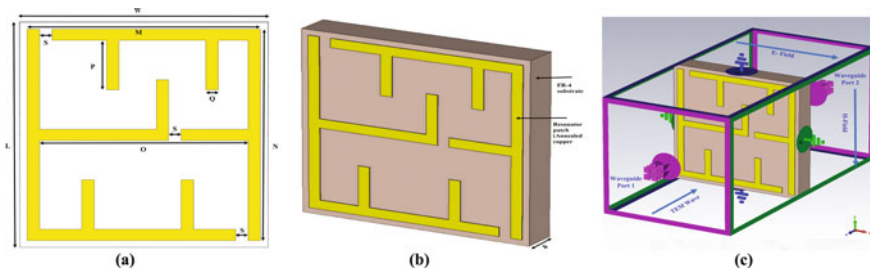


Fig. 1 The figure of **a** front view **b** perspective view **c** simulation view

Table 1 The design parameters

Symbol	Value (mm)	Symbol	Value (mm)
W	10	P	2.2
L	10	Q	0.5
M	9.4	S	0.5
N	9.4	O	8.4

where an incident electromagnetic wave is transmitted through the Z-axis. As shown in Fig. 1c, E-field is applied to X-axis and H-field is concerned to Y-axis for simulation purpose.

3 Parametric Study

Various parametric studies have been performed to explore the impact of the split gap and width of the ring resonator and length of the perpendicular arm.

3.1 Effect of Outer Ring Width on S_{21} Performance

The S_{21} plot for the different outer ring width is introduced in Fig. 2a. As the outer ring width increases, the overall value of the inductance decreases; as a result, the resonance frequency shifts to higher according to the following equation

$$f = \frac{1}{2\pi\sqrt{LC}} \tag{1}$$

The impact of the outer ring width on the S_{21} results has been found that the resonance frequency shifts to higher as increasing the outer ring width.

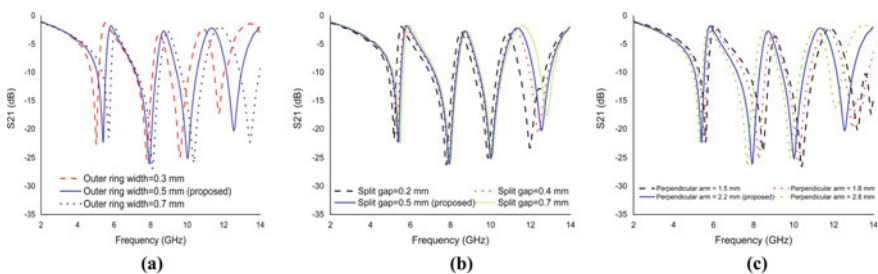


Fig. 2 The graph of S_{21} for varying of **a** outer ring width, **b** split gap, and **c** length of the perpendicular arm

3.2 *Effect of Split Gap of the Ring Resonator on S_{21} Performance*

The transmission coefficient of varying the split gap of the ring are delineated in Fig. 2c. The value of the capacitance decreases as the split gap increases, resonance frequency shifts to higher according to Eq. (1).

3.3 *Effect of Length of the Perpendicular Arm on S_{21} Performance*

The S_{21} plot for the different length of the perpendicular arm are indicated in Fig. 2c. The impact of the length of the perpendicular arm on the S_{21} results has been found that the resonance frequency shifts to lower as increasing the length of the perpendicular arm.

4 Analysis of Surface Current with Electromagnetic Field

The analysis of surface current with electromagnetic field behavior at the frequencies of 5.396, 7.94, 10.028 and 12.55 GHz has been delineated in Fig. 3. At frequency of 5.396 GHz, the upper right corner and lower left corner of the ring resonator contribute most of the current, as indicated in Fig. 3a (i). A good harmony of the surface current and H-field scenario is shown in Fig. 3b (i), which is validated by Ampere's law ($\oint B \cdot dl = \mu_0 I$). The surface current generates a strong H-field at the same location. Higher the value of the H-field in ring resonator in that portion, the higher the value of the E-field in opposite portion of the ring resonator based on Maxwell's law, as shown in Fig. 3c (i). At the resonance frequency of 7.94 GHz, the whole portion of the ring resonator contributed significantly to the flow of surface currents, as the capacitive response of the split gap increased, as shown in Fig. 3a (ii) and Fig. 3b (ii). Meanwhile, the split gap of the proposed structure creates an additional E-field due to form a capacitor, as indicated in Fig. 3c (ii). The same observation held in the rest of the resonance frequency, as shown in Fig. 3 (iii) (iv), where surface current and H-field exhibit same scenario. The strength of the E-field is high where H-field is weak due to the generation of mutual capacitance in the metamaterial unit cell. The scale and axis view are indicated in Fig. 3 (v).

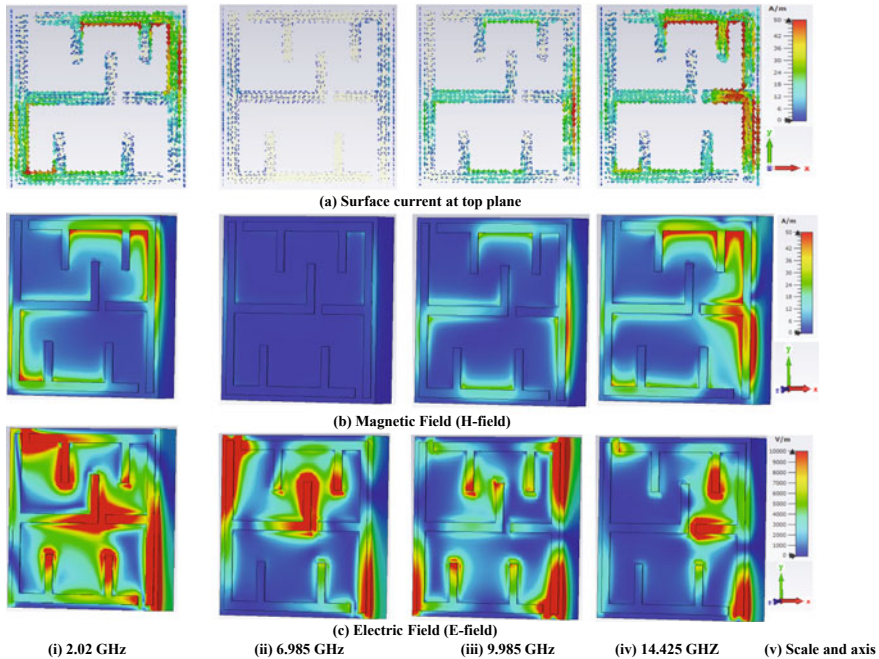


Fig. 3 Electromagnetic field analysis of the proposed structure

5 Results and Discussion

Finite Integration Technique (FIT) based CST simulator was used to simulate the proposed ring resonator unit cell. Figure 4a presents the graph of scattering parameters of proposed structure. The reflection coefficient (S_{11}) of the metamaterial structure provides quad resonances at 5.78, 8.7, 11.35 and 14.5 GHz. The magnitude of the transmission coefficient (S_{21}) are -22.34 , -26.10 , -25.15 and -20.30 dB at 5.396, 7.940, 10.028 and 12.580 GHz. In Fig. 4a, the characteristics of S_{21} have been shown to be suitable for four excellent bandwidths where the S_{21} is less than -10 dB in 0.48 GHz (5.06–5.54 GHz), 1.12 GHz (7.18–8.3 GHz), 1.11 GHz (9.42–10.53 GHz) and 0.82 GHz (12.15–12.97 GHz) including C, X and Ku bands. Numerical simulations were executed using a finite element method (FEM)-based HFSS simulator to validate the CST results. The S-parameters of proposed unit cell using CST and HFSS simulator are delineated in Fig. 4b. It can be seen from Fig. 4b that proposed design revealed quad resonances in CST and HFSS simulator with a slight variation. The effective parameters of the proposed structure depicted in Fig. 5. The permittivity versus frequency graph is presented in Fig. 5a, where negative real value has been found at the resonance frequency. The real and imaginary value of permeability is exhibited in Fig. 5b. The real value of permeability shows nearly zero at all resonance frequency shown in Fig. 5b. The real and imaginary value of η versus f graph is shown

in Fig. 5c, which presents the negative real value of η in the 5.48–5.624 GHz, 8.072–8.48 GHz, 10.172–10.952 and 12.776–13.412 GHz frequency ranges. The real value of impedance shows positive at all resonance frequencies resulting metamaterial structure as a passive medium shown in Fig. 5d.

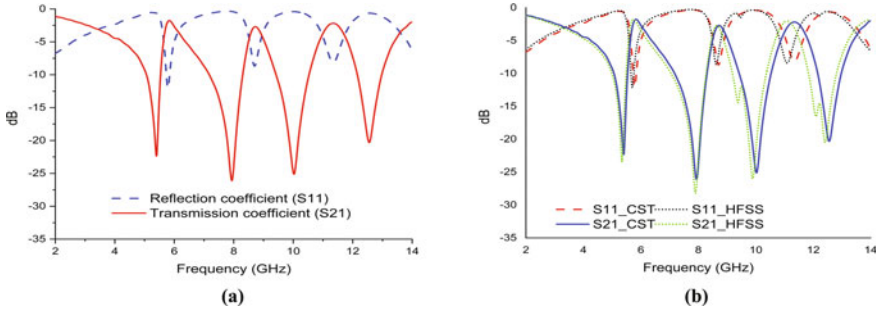


Fig. 4 The graph of **a** S-parameters using CST simulator, **b** S-parameters using CST and HFSS simulator

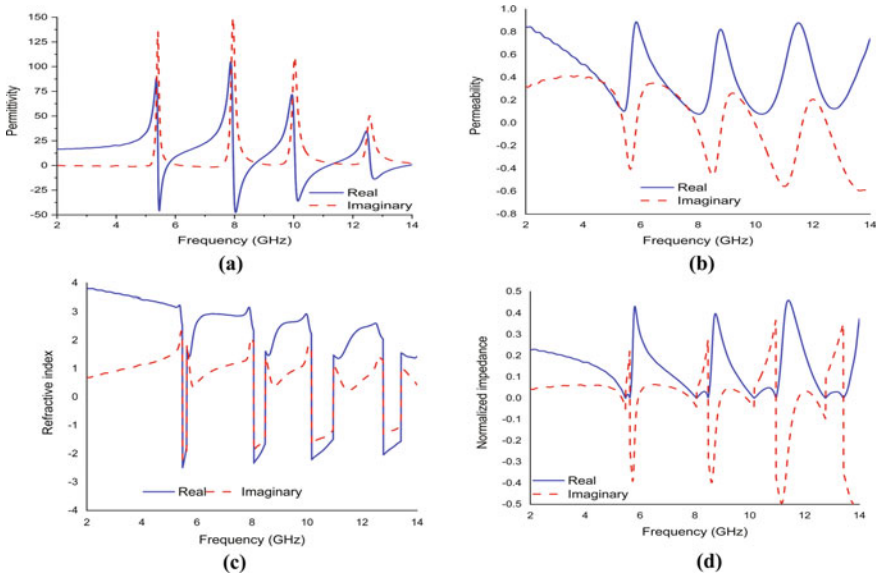


Fig. 5 The plot of **a** ϵ versus **b** μ versus **c** η versus **d** z versus **f**

6 Conclusion

This article presents a quad band negative permittivity metamaterial with wider bandwidth for satellite applications. The scattering parameters of using CST simulator was validated the results with those of the HFSS simulator. The S-parameter response is well consistent with the CST and HFSS simulator results. The surface current with electromagnetic field analysis has been used to investigate the metamaterial performance. Therefore, the proposed structure can be employed for satellite applications. The C-band can be used for commercial satellite communications, the military uses the X-band satellite communications, and the Ku-band can also be applied to satellite TV networks.

Acknowledgements This work was supported by the Research Universiti Grant, Universiti Kebangsaan Malaysia, Dana Impak Perdana (DIP), code: 2020-018.

References

1. Karaaslan M, Bağmancı M, Ünal E, Akgöl O, Sabah C (2017) Microwave energy harvesting based on metamaterial absorbers with multilayered square split rings for wireless communications. *Opt Commun* 392:31–38
2. Islam M, Islam MT, Samsuzzaman M, Faruque MRI (2015) Compact metamaterial antenna for UWB applications. *Electron Lett* 51(16):1222–1224
3. Zhang J, Yan S, Vandenbosch GA (2019) Metamaterial-inspired dual-band frequency reconfigurable antenna with pattern diversity. *Electron Lett* 55(10):573–574
4. Islam SS, Hasan MM, Faruque MRI (2018) A new metamaterial-based wideband rectangular invisibility cloak. *Appl Phys A* 124(2):1–6
5. Guo X, Li B, Fan X, Zhong J, Qi S, Li P, Liu S, Wei B, Zhao J (2021) On-demand light wave manipulation enabled by single-layer dielectric metasurfaces. *APL Photonics* 6(8):086106
6. Faruque MRI, Islam MT, Ali MAM (2013) A new design of metamaterials for SAR reduction. *Measur Sci Rev* 13(2):70
7. Hossain MB, Faruque MRI, Islam MT, Singh M, Jusoh M (2022) Triple band microwave metamaterial absorber based on double E-shaped symmetric split ring resonators for EMI shielding and stealth applications. *J Market Res* 18:1653–1668
8. Afsar MSU, Faruque MRI, Hossain MB, Siddiky AM, Khandaker MU, Alqahtani A, Bradley DA (2022) A new octagonal close ring resonator based dumbbell-shaped tuning fork perfect metamaterial absorber for C- and Ku-band applications. *Micromachines* 13(2):162
9. Faruque MRI, Siddiky AM, Ahamed E, Islam MT, Abdullah S (2021) Parallel LC shaped metamaterial resonator for C and X band satellite applications with wider bandwidth. *Sci Rep* 11(1):1–15
10. Hossain MB, Faruque MRI, Islam SS, Islam MT (2021) Modified double dumbbell-shaped split-ring resonator-based negative permittivity metamaterial for satellite communications with high effective medium ratio. *Sci Rep* 11(1):1–18
11. Dalgaç Ş, Karadağ F, Bakır M, Akgöl O, Ünal E, Karaaslan M (2021) Chiral metamaterial-based sensor applications to determine quality of car lubrication oil. *Trans Inst Meas Control* 43(7):1640–1649
12. Islam SS, Khan MS, Faruque MRI (2019) Design and analysis of modified-split H-shaped DNG metamaterial for microwave application. *Mater Res Express* 6(12):125808

13. Islam MS, Islam MT, Sahar NM, Rmili H, Amin N, Chowdhury ME (2020) A mutual coupled concentric crossed-line split ring resonator (CCSRR) based epsilon negative (ENG) metamaterial for tri-band microwave applications. *Results Phys* 18:103292
14. Hossain MJ, Faruque MRI, Islam MT (2017) Design and analysis of a new composite double negative metamaterial for multiband communication. *Curr Appl Phys* 17(7):931–939
15. Zhou H, Wang C, Peng H (2016) A novel double-incidence and multi-band left-handed metamaterials composed of double Z-shaped structure. *J Mater Sci Mater Electron* 27(3):2534–2544

Fabrication of Plaque Using Hot Press Method for Recycling Plastic Material



Haszeme Bin Abu Kasim, Mohamad Faizuddin Bin Hashim,
Ab Aziz Bin Mohd Yusof, Noor Hafiz Bin Noodin, Hazim Sharudin,
and Mohamad Hussain Bin Ismail

Abstract The study aims to produce plaque using recycling materials. The plaque is manufactured using Compression Moulding (Hot Pressing). The mould design was employed by a computer-aided and fabricated using a CNC milling machine. Three different types of plastic resins were investigated: Poly-ethylene Terephthalate (PET), High-Density Polyethylene (HDPE), and Poly-propylene (PP). The quality of the semi-finished product was examined using Differential Scanning Calorimetry (DSC) and Thermal Gravimetric Analysis (TGA) techniques. The test profiled the outcome in thermal behaviour graphs to represent its behaviours. As a result, the recycling Polyethylene Terephthalate (PET) quality is unsuitable for producing plaque due to its brittle characteristics that introduce crack defects to the final product.

Keywords Hot Pressing · Thermal Analysis Method · Plastic Resins

1 Introduction

Plastic is one of the materials important to people, from food handling and engineering to aerospace applications. Daily consumption of plastic material increases every day, consequently producing more waste. If the current use rate of the natural resources continues and is not handled properly, the community will require more than one planet to sustain the consumption and production patterns [1]. According to a recent poll, most Malaysian residents are unaware of the importance of garbage recycling. Every day, the typical Malaysian tosses away 1.64 kg of plastic garbage. According to a World Bank report, this is 0.44 kg of additional waste produced by the average city dweller at 1.2 kg worldwide. At this rate, the waste increased drastically by 65%, from 10,000 tons per day in 2010 to 17,000 tons per day by 2020 [1, 2].

H. B. A. Kasim · A. A. B. M. Yusof · N. H. B. Noodin · H. Sharudin
College of Engineering (Mechanical), Universiti Teknologi MARA Johor Branch, Pasir Gudang
Campus, Segamat, Malaysia

M. F. B. Hashim · M. H. B. Ismail (✉)
College of Engineering (Mechanical), Universiti Teknologi MARA, Selangor Darul Ehsan, Shah
Alam, Malaysia
e-mail: hussain305@uitm.edu.my

One of the techniques for better management and conserving the environment is the plastic resource needed to recycle waste materials into useful products using Compression Moulding (Hot Pressing) Manufacturing. Compression Moulding plays an important role in the production of certain low-cost products as well as dimensionally precise items [3, 4]. The study’s objective is to fabricate the plaque made from recycled plastic materials using Compression Moulding (Hot Pressing). Plastic recycled material can be divided into two basic groups: thermoplastics and thermosets. By comparison, thermoplastic resins offer advantages in the ability to be repeatedly melted and solidified by heating and cooling. Therefore, thermoplastics are a very popular and versatile material [5, 6]. The scope of this study focused on the difference in plastic polymers: Polyethylene Terephthalate (PET), High-Density Polyethylene (HDPE), and Polypropylene (PP). The fabricated plaque produced an aesthetic and valuable product better for the environment.

2 Methodology

The materials used for the moulds were built from mild steel blocks. Two types of machines were utilized in the manufacturing process Deckel Maho DMU 60 Evo CNC Milling Machine by DMG MORI and Robocut α -CIA Series Wire EDM by FANUC. While the raw material of the plastics is collected from the recycle bin and separated into groups based on the resin number. Only three types of resins were chosen: PET, HDPE, and PP. This research starts with mould preparation shown in Fig. 1.

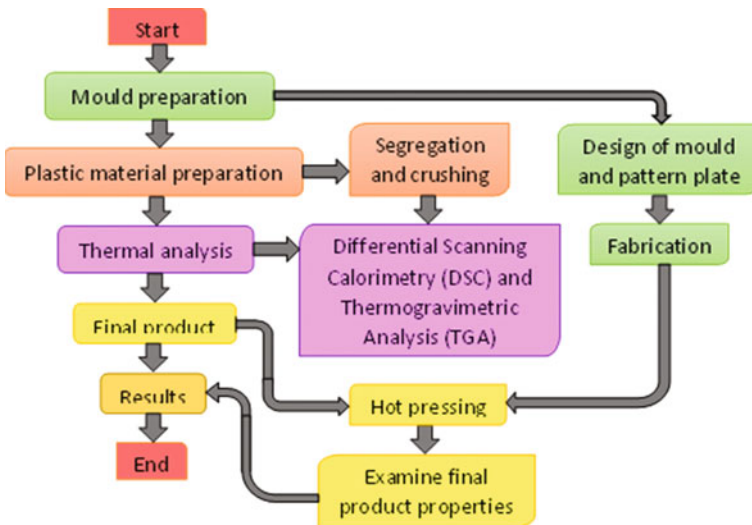


Fig. 1 Process flow

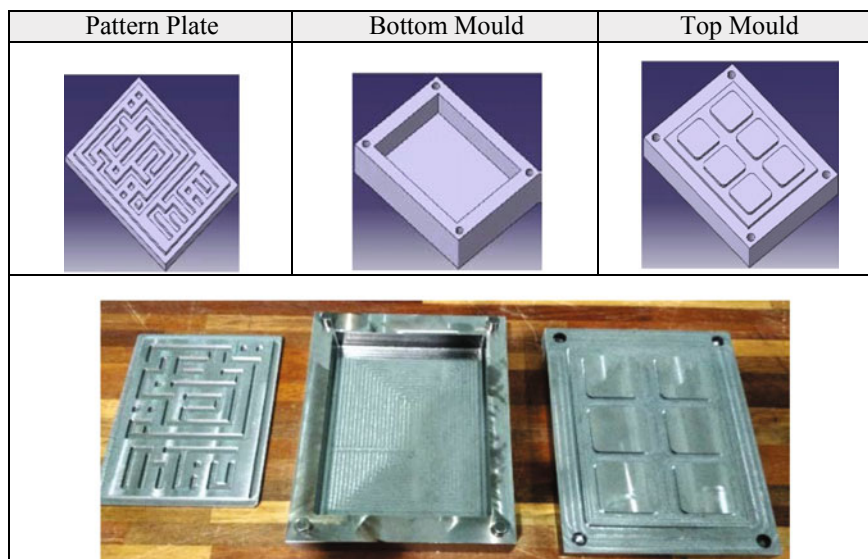


Fig. 2 The moulds were designed using CAD and fabricated using a CNC milling machine

Three parts of the mould; the top, bottom and pattern plate mould need to be fabricated before going to Compression Moulding (Hot Pressing). These parts were designed using Computer-Aided Design (CAD) software, CATIA, before the fabrication process shown in Fig. 2. In the plastic material preparation process, segregation, shredding or crushing become critical stages in recycling plastic into smaller flakes. The washed and sorted plastic is sent through shredding machines where it is ground into smaller pieces of plastic. Hammer Mills Shredder machine was used in this research for each group of plastic resins to pulverise plastics in a rotary drum using swivelling hammers before the final stage of plastic recycling to become small pellets and ready to be used.

To study the thermal behaviour of PET, HDPE and PP, some pellets for each type of polymer were analyzed using the Differential Scanning Calorimetry (DSC) method using NEXTA DSC series machine and Thermogravimetric Analysis (TGA) method using METTLER TOLEDO TGA machine. The Parameter setting for Differential Scanning Calorimetry (DSC) for each group of the polymer starts at a lower temperature range and ends up to 500 °C, the sample of weight between 5 to 10 mg, Gas Flow Rate 50 ml/min and Heating Rate 10 °C/min were used. While the Parameter setting for Thermogravimetric Analysis (TGA) used a maximum temperature of 1600 °C for each group of the polymer, the sample weight was between 10 to 20 mg, Gas Flow Rate 60 ml/min and Heating Rate 20 °C/min will be applied. The different operating temperatures of both DSC & TGA methods will give different results values. Generally, the DSC method is used to measure the energy absorbed/released by a sample as it is heated or cooled for determining the first-order transition (melting) and a second-order endothermic transition (glass transition) with various crystallisation

and melting enthalpies [7, 8]. Meanwhile for TGA method measures the mass of a sample as it is heated, cooled or held at constant temperature in a defined atmosphere. [9, 10]. Lastly, the finished products of plaque (PET, HDPE and PP) were observed on the outer surface to determine the good quality, surface conditions and defects.

3 Results and Discussion

3.1 Thermal Analysis

Differential Scanning Calorimetry (DSC). From the plotted DSC graph in Fig. 3, the total energy absorbed by HDPE released the most heat during the crystallisation phase with total amounts of 1.992 mW/mg and followed by PP with total amounts of 0.553 mW/mg heat during the test. On the other hand, PET recorded the least maximum heat released with only total amounts of 0.104 mW/mg. The release of heat is known as the exothermic reaction. First, HDPE, PP and PET started to crystallize at 103.03 °C, 125.53 °C and 218.58 °C, respectively. Then, at the heating rate of 10 °C/min, HDPE, PP and PET began to melt at 134.15 °C, 164.95 °C and 250.95 °C, respectively. At these points, the polymers were suitable to be shaped as they were in the form of liquid. Therefore, the enthalpy of fusion for HDPE is 144.29 J/g, 76.50 J/g for PP and 31.66 J/g for PET. This fusion enthalpy indicates the heat required for a polymer to transform from a solid to a liquid state.

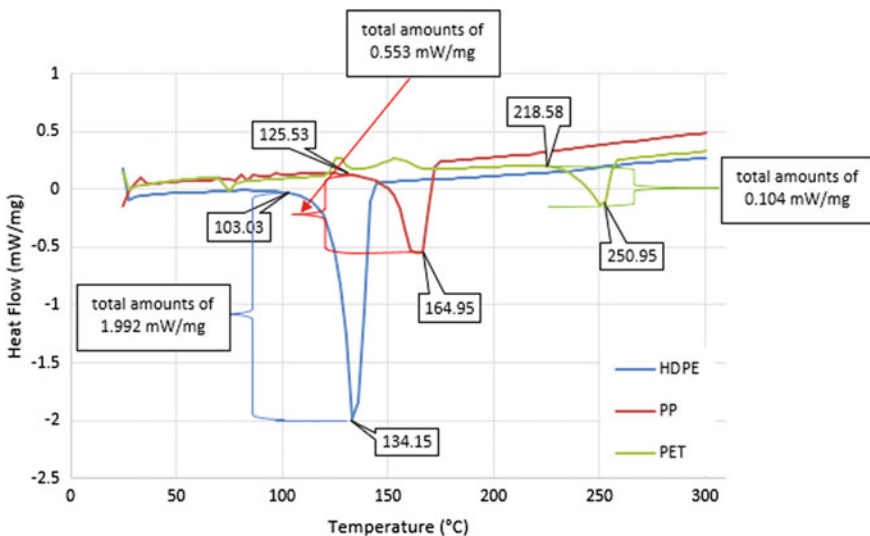


Fig. 3 Graph of heat flow against temperature

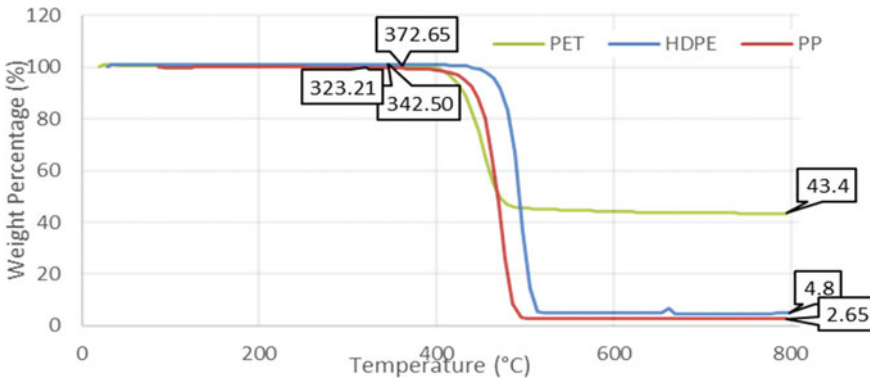


Fig. 4 Graph of weight percentage against temperature

Thermogravimetric Analysis (TGA). PET had the highest residual of 43.4% from the initial weight at the end of the study, according to the displayed TGA graph Fig. 4. On the other hand, PP left the least amount of residual weight inside the crucible with 2.65% only. In the case of HDPE, just 4.8% of the final residue is left. At the heating rate of 20 °C/min, the greatest rate of change on the weight loss curve for PET, PP, and HDPE occurred at 455.40 °C, 472.92 °C, and 495.29 °C, respectively. The decomposition phase started at 323.21 °C for PP, while PET and HDPE began to decompose at 342.50 °C and 372.65 °C, respectively. The decomposition of the HDPE sample ended at a temperature of 606.44 °C, whereas PET and PP stopped decomposing at 636.92 °C and 647.56 °C, respectively. PP, PET and HDPE samples were half decomposed at 468.3 °C, 450.20 °C and 495.29 °C, respectively.

3.2 Final Products of Plaque

The plaque production using the hot-pressing method succeeded, as shown in Fig. 5. The observation was made on the outer surface of the products to determine the good quality, surface conditions and defects to confirm the quality of the process. The mould was also observed after every completed production cycle. To produce the best plaque using PP, PET and HDPE, the correct amount of pellets, the moulding temperature and the heating time play important roles in ensuring that all pellets are fully softened before being pressed. From observation by naked eyes, the plaque using PP had lots of porosity compared to HDPE. Meanwhile, the production of plaque using PET material failed. After hot pressing, it was observed that the material stick to the mould and was very difficult to be taken out. The surface of the plastic also had some cracked lines and was found that PET has brittle properties because due to the high melting temperature of 250.95 °C.

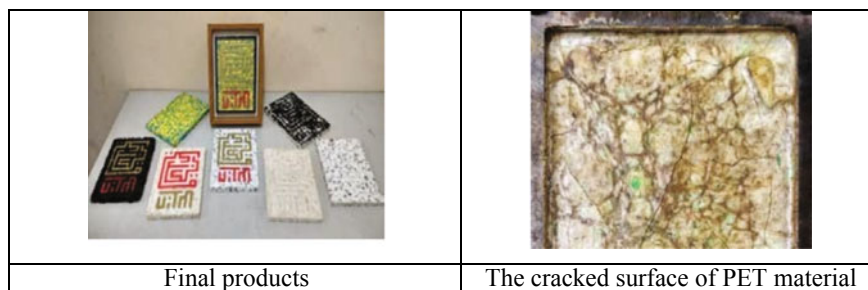


Fig. 5 Finished products

4 Conclusions

The production of plaque using a hot-pressing mould was successfully built from mild steel blocks using multi-functional computer-aided design (CAD) software paired with modern machining technology. Differential Scanning Calorimetry (DSC) and Thermogravimetric Analysis (TGA) thermal studies make determining settings for the hot-pressing process easier. HDPE was the best material for forming the plaque. The plaque using PP was formable, and the quality can be improved by optimizing the processing parameters. However, this plastic production technique was unsuitable for PET. No product can be obtained from this type of polymer as it possesses brittle characteristics.

References

1. Hamid S, Mat Isa CM, Shamer NF, Mustaffa NK (2020) Sustainable management using recycle and reuse of construction waste materials in Malaysia. *ESTEEM Acad J* 16:47–58
2. Wahi N, Joseph C, Tawie R, Ikau R (2016) Critical review on construction waste control practices: legislative and waste management perspective. *Procedia Soc Behav Sci* 224:276–283
3. Wulfsberg J, Herrmann A, Ziegmann G (2014) Combination of carbon fibre sheet moulding compound and prepreg compression moulding in aerospace industry. *Procedia Engineering* 81:1601–1607
4. De Focatiis DSA (2012) Sample preparation: tooling for near net-shape compression moulding of polymer specimens. *Polymer Testing Journal* 31(4):27–34
5. MacDermott CP, Shenoy AV (2020) *Selecting thermoplastics for engineering applications*, 2nd edn. CRC Press
6. Scheutz GM, Lessard JJ, Sims MB, Sumerlin BS (2019) Adaptable crosslinks in polymeric materials: resolving the intersection of thermoplastics and thermosets. *J Am Chem Soc* 141(41):16181–16196
7. Elkordy AA (2013) Applications of calorimetry in a wide context-differential scanning calorimetry, isothermal titration calorimetry and microcalorimetry. *Intech, Croatia*
8. Johnson CM (2013) Differential scanning calorimetry as a tool for protein folding and stability. *Arch Biochem Biophys* 531(2):100–109

9. Cai J, Xu D, Dong Z, Yu X, Yang Y, Banks SW (2018) Processing thermogravimetric analysis data for isoconversional kinetic analysis of lignocellulosic biomass pyrolysis. *Biores Technol* 261:294–330
10. Chong CT, Mong GR, Ng JH, Chong WWF (2019) Pyrolysis characteristics and kinetic studies of horse manure using thermogravimetric analysis. *Energy Convers Manage* 180:1260–1267

A Case Study on Exploring the Benefits and Challenges Influencing the Implementation of Life Cycle Assessment as a Design Tool in an Air Filter Manufacturing Industry



Abu Sadik Billahil Waasi, Atiah Abdullah Sidek, Afiqah Alias, and Muataz Hazza Al Hazza

Abstract In this era of industrialization, environmental impacts from the industries have become a significant concern. Life Cycle Assessment (LCA) is a comprehensive tool that measure the environmental impact of different materials and products throughout different stages in a product lifecycle. This paper aims to explore the benefits and challenges of an air filter manufacturing industry in implementing LCA as a design tool in reducing its environmental impact. An in-depth interview was conducted with the case study industry to explore the opportunities that LCA present in the industry. Based on findings of the study, LCA is found to be an effective design tool for the case study organization where they were successfully able to improve their production process, reduce environmental impact from the product throughout the process lifecycle, established their product in the marketplace and etc. with some challenges to implement in the organization.

Keywords Life cycle assessment · Design tool · Manufacturing industry · Environmental impact

1 Introduction

In today's world, manufacturing industries have become one of the crucial parts of the country's economy. The increase in industrialization globally leads to increased waste production worldwide, posing a significant environmental challenge. As the production rate is multiplying according to consumer needs, the amount of industrial waste is also increasing simultaneously. Subsequently, used products or waste

A. S. B. Waasi · A. A. Sidek (✉) · A. Alias
Department of Manufacturing and Materials Engineering, Faculty of Engineering, International Islamic University Malaysia, 53100 Gombak, Malaysia
e-mail: atiahas@iium.edu.my

M. H. Al Hazza
Department of Mechanical and Industrial Engineering, School of Engineering, American University of Ras Al Khaimah, Ras Al Khaimah, United Arab Emirates

end up in the air, water, or ground, which results in adverse environmental effects [1]. Besides, the manufacturing process is one of the vital parts of the production operation, but not all the processes are equally environmentally friendly. Almost all the raw materials, water, and soil emission in a manufacturing process actively contribute to environmental impact. Therefore, different approaches must be made by the industries and apply appropriately to minimize the harmful effect of waste emission [2].

The awareness of environmental concerns has successfully led the manufacturing industries to be more proactive in improving their management system and designing their current and new products to develop cleaner industrial production processes and avoid more environmental damages. One of the environmental tools, known as LCA, is considered as a well-established analytical technique or design tool to measure the environmental impacts of products, services, or production processes [3, 4]. It has gained a lot of attention from industry and academics alike over the years because it allows the impact of industry processes to be quantified clearly and gives a more complete and precise representation of environmental impacts generated [5, 6] as shown in Fig. 1.

Product development is a process of developing new product from idea stage all the way through marketing and launching the product to the market [7]. The initial stage of the product design and development is a crucial part in a manufacturing industry. At this stage, the industry will have to optimize design considerations of the product's elements, processes and environmental risks that can have a significant impact to the downstream process of the product development and also in creating a better value product to the end users.

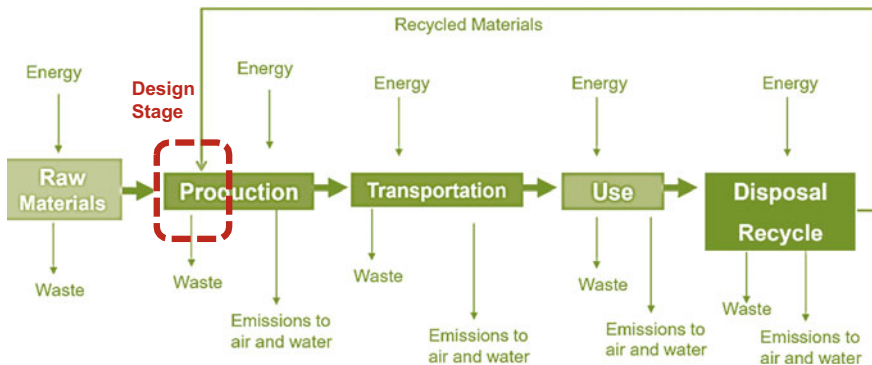


Fig. 1 The product life cycle system in LCA and the focus of this study

2 Methodology

2.1 Study Design

The qualitative research method has been used in this study to collect the primary data from the case study industry. An in-depth interview (IDI) was conducted with an expert from the Department of Quality, Environmental and Safety of an Air Filter Manufacturing industry in order to investigate several aspects related to application of LCA as design tool in the industry. The parent company of the industry is based in Japan but its Asia Pacific branch operates and located in Malaysia. The company mainly exports their product to the global marketplace and a small percentage of the product is sold in Malaysia. The case study industry has obtained ISO 9001 and ISO 14001 (2015) to maintain the environmental impact of its product and has used LCA in their processes.

3 Results and Analysis

The following discussed the findings from the interview analysis based on the focus themes. The first theme discussed about identifying the benefits of LCA as a design tool in the manufacturing industry. The second theme discussed about the effective elimination of the environmental impact by applying LCA in the manufacturing industry and lastly the challenges and remedies to implement LCA are discussed below.

3.1 Theme 1: Identifying the Benefits of Using LCA

LCA is used for assessing the product life cycle during the product planning and designing processes. LCA is one of the important designing tools used in the manufacturing-based industry, which helps the organization take necessary measures in designing technology-based products and other goods manufactured. According to the interviewee's responds of this, *"My team uses Life Cycle Assessment to assess the product life cycle. Based on the assessment report, the company takes necessary corrective measures. Utilizing life cycle assessment helps the company to know where and at which stage their manufactured product is impacting the environment the most and helps them to know to where exactly further improvement measures must be taken. It also helps them to know the type of wastes they produce and how to dispose of them"*. Hence, LCA is an essential design tool that impacts manufacturing effectiveness. The interviewee emphasized on waste management by utilizing LCA that has environmental consequences. The interviewee stated that *"The waste in production can be categorized mainly into raw material-based wastages and finished*

goods wastage". Under these two categories we can divide the waste into a few more groups such as recyclable waste, reusable waste, general waste, schedule waste etc. Once the industry is confirmed about the waste category then they can easily decide on how to dispose of the generated waste. Regarding this, the interviewee has stated, *"We got three types of waste, one we call as a general waste which is under the landfill disposal and then we have recyclable waste, and we also have schedule waste"*. LCA allows the industry to recognize this information and design the product accordingly. The interviewee also added that *"Production will do the segregation. So, the media will throw under the general waste and then the metal part, we throw under the recyclable waste"*.

It further emphasized LCA as one of the essential design tools in any manufacturing-based industry. As stated in the literature review, LCA helps industry to choose suitable material that is environmentally friendly. It helps to compare alternative products and choose a more optimized process for the manufacturing. So, it is easy for the manufacturing industries to pick suitable and environmentally friendly material and the manufacturing process. The case study company utilizes LCA for similar reasons as well. Besides, they follow the design and development requirements from ISO 9001 and ISO 14001 to maintain the quality and environmental impact of the product. The participant mentioned that *"We follow that requirement, and we implement the environmental impact part in the design development"*. Moreover, LCA also helps the manufacturing industry in terms of import and export opportunities by increasing orders and profitability. For example, the case study industry has to follow some specific environmental requirements and concerns by their customers in Singapore. The utilization of LCA in the processes relating to the conventional chemical used showed a potential long-term environmental impact and with the information, the company changed to using water base chemicals which subsequently is a profitable move by the industry and the industry has since received more orders by their Singaporean based customers.

Besides, LCA also helps industries makes better decision making of the type of materials used in throughout their products life cycle that will have minimum environmental risks. So, it allows the industries to decide whether they want to use recyclable materials, reusable materials, or disposable materials as early as at the design stage. Besides better decision-making, it also helps the manufacturing industries make better quality improvements. The participant stated, *"We can have a very good quality product and then we will have a lot of environmental improvements and also include the safety improvements"*.

It is evident that using LCA helps the manufacturing industry in many ways such as making sustainable products, materials and manufacturing process selection, better decision making, export and import matters, profitability, and productivity. So, considering the benefits and added values due to the implementation of the LCA, it surely becomes an effective tool in the manufacturing industry especially at the design stage.

3.2 Theme 2: Reduction of the Environmental Impact by LCA

In this part, the case study industry is accessed on how it can effectively reduce the environmental impact of their manufactured products by utilizing LCA. The discussion is fully based on the case study industry and the steps they are taking to reduce the environmental impacts for their air filter manufacturing. The industry found that there are several materials that they use in their processes to make the air filters that have potential negative impacts to the environment at different stages of its life cycle such as non-recyclable and non-reusable materials, adhesive material used to stick the filter media with the metal part and the dusty filter media. *“Some of the material that we use cannot recycle because of the characteristic of the material and another one is actually the chemical. Because the filter that we are manufacturing usage an adhesive material to stick the media and the frame. So, this really impact to our environment and the media is also very dusty. So, we have air pollution issues in the clean room”*.

Once the environmental risks of above materials and process stage identified using LCA, it is important to take corrective measures to reduce or eliminate the impact. From the interview discussion, it is clear that the industry adopted various process control tests and tools such as Temperature and Environmental Monitoring, Boundary Noise Test to Local Exhaust Ventilation (LEV) and others which helps to control the airborne contaminants effectively and about this, the participant mentioned that *“We are doing some temperature and environmental monitoring. This actually to certify the environment inside the clean room which is one. The second one is the LEV suction. We have LEV suction because some of the area is actually dusty. We do some ducting to suck out all these fumes from the machines. Having these kinds of tools and equipment, there are no air pollution issues for the production or for the manufacturing”*.

So, from the discussion above, it is quite clear that, if the manufacturing industries utilized tools like LCA properly then it is possible to eliminate or at least minimize the environmental impact from their manufactured product or manufacturing process. Beside implementation, it is always important to follow up the process and continuously take feedback and this will help the manufacturing industries to do further improvement. Regarding this the interviewee stated that *“Actually if we have proper tools, we do proper monitoring and do all these life cycle implementations, we actually can reduce the environmental impact. But it must be continuous”*.

3.3 Theme 3: Challenges and Remedies of LCA Implementation

LCA is indeed an effective tool for the manufacturing industries to use at their design stage to reduce environmental impacts from their manufactured products, manufacturing processes or some other factors. However, there are always some

challenges to implement the tool in the industry. The challenges can come from any stages and could be technical or general from the external or internal side. The general challenges to implement LCA or any tool in any industry is the resistance within the organization, and this is a similar scenario faced by the case study industry where it has faced similar initial resistance when implementing LCA on their manufactured products.

Regarding this, the interviewee stated that *“I can implement whatever I want but the continuous improvement, to sustain from different departments is the very challenging part for us. We need to educate them not only on the top higher level but also lower-level people, the down people. Because they need to understand why we do these things, what is the purpose of doing it. These are the challenges that we are currently facing. To make everyone understand, to educate them”*. Also, the participant has mentioned that *“To overcome the issues, the top management’s leadership. It should come first from the top management then it should be continued. I meant top to down. The top already implements or must be taken as an ownership for all these improvements. If the top management or the leadership do not have this kind of commitment, how will you implement it at the down level? This will not work out”*. From this, it is clear that the top management of an industry must be willing to be committed towards implementing the tool and make sure all the employees are aware about the benefits and improvements.

4 Conclusion

To conclude, the study gives some insight on utilization of Life Cycle Assessment (LCA) tool in an air filter manufacturing industry. Based on the findings, the utilization of LCA in the products’ design stage helped the industry significantly to reduce its negative environmental impact of its manufactured products and establish its product in the marketplace. The tool allowed detailed environmental risks layout throughout the production stages from cradle to grave which allowed the industry to make necessary changes early in the production. With increasing concerns about environmental sustainability, LCA can help industries become more environmentally responsible while improving their bottom line.

Acknowledgements The authors would like to thank International Islamic University Malaysia (IIUM) and the Ministry of Higher Education Malaysia for sponsoring this research under FRGS grant.

References

1. Tan Y, Chong C, Subramaniam V, Puah C, Zulkifli H, Halimah M, Ma A, Choo Y (2009) Life cycle assessment—a tool for sustainability and business opportunity. *Oil Palm Bulletin* 58(May):14–36
2. Gaur VK, Sharma P, Sirohi R, Awasthi MK, Dussap CG, Pandey A (2020) Assessing the impact of industrial waste on environment and mitigation strategies: a comprehensive review. *J Hazard Mater* 398
3. Chan CCS, Yu KM, Yung KL (2010) Green product development by using life cycle assessment (LCA), theory of inventive of problems solving (TRIZ). In: *International conference on manufacturing automation 2010*, pp 24–29
4. Jacquemin L, Pontalier PY, Sablayrolles C (2012) Life cycle assessment (LCA) applied to the process industry: a review. *Int J Life Cycle Assess* 17(8):1028–1041
5. Itskos G, Nikolopoulos N, Kourkoumpas DS, Koutsianos A, Violidakis I, Drosatos P, Grammelis P (2016) Energy and the environment. In: *Environment and development: basic principles, human activities, and environmental implications*. Elsevier
6. Yang S, Ma K, Liu Z, Ren J, Man Y (2019) Development and applicability of life cycle impact assessment methodologies. In: *Life cycle sustainability assessment for decision-making: methodologies and case studies*. Elsevier Inc
7. Dieter G, Schmidt L (2021) *Engineering design*, 6th edn. McGraw Hill.

Characterization of Poly(vinyl) Alcohol Based Aerogel Assisted by Cellulose Nanocrystal



Raimi Fariz Nasrudin , Noorasikin Samat ,
and Nurul Sakinah Engliman 

Abstract A versatile and economic synthetic material is successfully prepared using a low-cost polyvinyl alcohol (PVA) and renewable cellulose nanocrystal (CNC) obtained from oil palm biomass through freeze-drying process. The PVA-based aerogels were incorporated with the CNC and glutaraldehyde (GA) which acted as nanofiller and crosslinker, respectively. The properties of fabricated hybrid aerogel samples were measured, and analyzed using compression testing, scanning electron microscope (SEM) and Barrett-Joyner-Halenda (BJH). The presence of CNC and GA crosslinkers have improved the compressive strength of PVA aerogel. The SEM analysis revealed that both materials affects the pore structures in term of its morphology, size and volume. The results of pore volume and volume is supported with the BJH results.

Keywords Poly(vinyl) alcohol (PVA) · Cellulose nanocrystal (CNC) · Hybrid aerogel · Glutaraldehyde (GA) · Crosslinking

1 Introduction

Polyvinyl alcohol (PVA) is a cheap, non-toxic biodegradable polymer with a good biocompatibility. Aerogel-based PVA materials can be fabricated through a freeze-drying process. Freeze-drying is a green energy-saving method compared to super-critical and ambient drying methods [1]. In this process, the solid substance is formed by changing the liquid portion in a wet gel by air without drastically disrupting its network structure. The aerogel material has unique features. It has high porous nanostructures (contains 95–99% of air), ultralow density, high specific surface area, and excellent thermal insulation properties [2–5]. These characteristics makes aerogel

R. F. Nasrudin (✉) · N. Samat
Department of Manufacturing and Materials Engineering, International Islamic University
Malaysia (IIUM), Jalan Gombak, 53100 Kuala Lumpur, Malaysia
e-mail: raiminas94@gmail.com

N. S. Engliman
Department of Biochemical-Biotechnology Engineering, International Islamic University
Malaysia (IIUM), Jalan Gombak, 53100 Kuala Lumpur, Malaysia

© The Author(s), under exclusive license to Springer Nature Singapore Pte Ltd. 2023
Md. A. Maleque et al. (eds.), *Proceeding of 5th International Conference on Advances in Manufacturing and Materials Engineering*, Lecture Notes in Mechanical Engineering,
https://doi.org/10.1007/978-981-19-9509-5_75

571

suitable to be used in various applications including in wastewater treatment [6], aerospace [7], medical [8], catalysis [9], and energy storage [10].

Nanocellulose either the cellulose nanocrystals (CNCs) or cellulose nanofibrils (CNFs) is a new class material which produced from renewable resource. The CNCs and CNFs has high aspect ratio, low density, biodegradable, and non-toxic. Currently, many research works have been reported on the use of CNC and CNF as reinforcing materials in the polymer composite system [11, 12] due to it has high modulus (134–140 GPa) [5]. In Malaysia, the abundant availability of agricultural wastes such as oil palm empty fruit bunch (EFB), pineapple leaves (PALF) and rice husk provide a great source to produce the CNC. The CNCs are also naturally hydrophilic, hence it able to form a strong interaction with PVA through the formation of hydrogen bonding [2]. A work by Nasrudin et al. [13] has produced the CNC from EFB and PALF fibers. Despite the PVA aerogel has great properties but it is also lack in strength [14]. This limits its application in the field of adsorption i.e., dyes, oil, and heavy metal [15–17], respectively. Hence, in this work, the PVA aerogel was hybridized with CNC from EFB, and samples were prepared using freeze-drying process. The content of CNC and glutaraldehyde were varied to evaluate its effect on the mechanical property and pore formation. The fabricated PVA/CNC hybrid aerogel were characterized using compressive testing, scanning electron microscopy (SEM), and Barrett-Joyner-Halenda (BJH) analysis.

2 Experimental Section

2.1 Material

Poly(vinyl) alcohol (PVA) and glutaraldehyde (GA) were purchased from Fisher Scientific Sdn Bhd. The CNCs with an average size of ~ 16.33 nm, was produced from our previous work [13].

2.2 Sample Preparation

PVA solution (10 mL, 0.05 g mL^{-1}) and 10 g of CNC solution (0.25, 0.5, 0.7 wt%) were mixed and stirred for 1 h. Then, the glutaraldehyde solution (80, 120, 160 μL ; 25 wt%) and sulfuric acid (80, 120, 160 μL ; 1.0 vol%) were added to the PVA/CNC solution, and the stirring was continued for another 1 h. The mixture was placed in an ultrasonic bath for 10 min to remove any bubbles. The crosslinking reaction was carried out by placing in a vacuum oven for 3 h at a temperature of 75°C . Finally, the PVA/CNC hybrid aerogels were obtained using a freeze-drying process.

2.3 Characterization

The compression test was conducted using Shimadzu CMT4204 (Kyoto, Japan) with the loading rate of 20%/min. The density was obtained by measuring mass and volume of aerogel. Tristar analyzer (Micrometrics, USA) was used to determine pore distribution of the hybrid aerogels using Barrett-Joyner-Halenda (BJH) model. The morphology of the aerogels was observed through scanning electron microscopy (SEM, JSM 5600, operating at 7 kV).

3 Results and Discussion

3.1 Morphological Analysis

Figure 1 shows the morphology of cross-sectional structure of PVA/CNC aerogels and their aerogel samples, as a function of CNCs and GA content. Most of the hybrid aerogel samples exhibited uniform microporous network structures, which is consistent with morphology characteristic of aerogel material [16, 17]. A closer view in Fig. 1 also noticed that the pore structures in all samples is not similar. For hybrid aerogel with low content of CNC and GA, these samples exhibited a polygonal network porous microstructure Fig. 1a–c. Meanwhile, Fig. 1d–f, reveals that the addition of 0.5 wt% amount of CNCs changed the porous microstructure from polygonal to lamellar or layered network. On the other hand, at higher CNC content (0.7 wt%), the elongated network structure still exists but the pores formation was minimal as seen in Fig. 1h, i. These results suggest that the morphology of PVA aerogel was influenced by the CNC contents which also affects the compressive strength.

The formation of polygonal and lamellar-network microstructure at low CNC content (0.25–0.5 wt%) could also possibly owing to the PVA had a low viscosity, which eased the alignment of PVA's long chain along the ice crystal growth during cooling process [17]. From Fig. 1c, f, h, i, at higher GA content (160 μ L), the existence of porous structure and the pore size decreased significantly. These samples appeared dense with lesser fibrillar network and pores formation. It is likely, the higher amount of GA would promote intense crosslinking reaction with the PVA chains. As a result, the samples were densified and restricted the pores formation during the freeze-drying process. The occurrence of intense crosslinking also caused shrinkage to the hybrid aerogel samples as seen in insert image in Fig. 1c, f, h, i. Moreover, their surface also turned to be rougher than other hybrid aerogel samples (GA < 160 μ L).

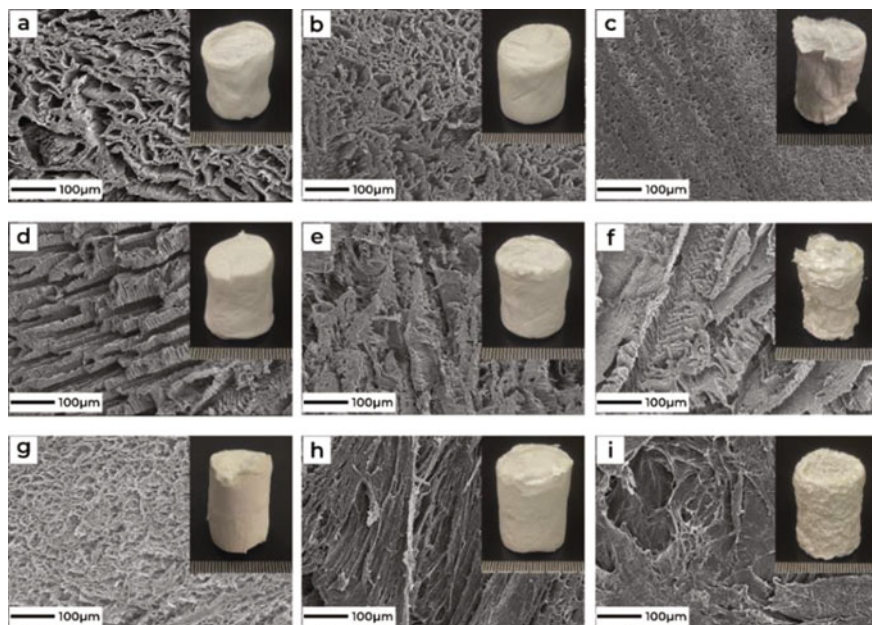


Fig. 1 SEM images of various formulations **a** 0.25 wt%/80 μL , **b** 0.25 wt%/120 μL , **c** 0.25wt%/160 μL , **d** 0.5 wt%/80 μL , **e** 0.5 wt%/120 μL , **f** 0.5 wt%/160 μL , **g** 0.7 wt%/80 μL , **h** 0.7 wt%/120 μL , **i** 0.7 wt%/160 μL

3.2 Compression Test

The compressive stress–strain curve of a series of PVA/CNC hybrid aerogel are shown in Fig. 2a–c. The compression of samples was carried out until 80% of strain. Similar characteristics of compressive curve were observed for different compositions of hybrid aerogels; the linear elastic deformation occurred at a low strain %, followed by a steady increment with increased of stress. A sharp rising of curve was seen at the final stage of deformation which related to the densification of aerogel structures. As observed in Fig. 2a–c, the ultimate compressive stress or compressive strength of neat PVA aerogel was only 0.053 MPa. In contrast, the compressive strength of PVA hybrid aerogel improved substantially. Regardless to the compositions, the increment is more than threefold compared to neat PVA aerogel.

This improvement indicates that: first (1) the CNCs had reinforced the PVA aerogel. Here, the increasing content of CNC would establish more available of free sites for interaction with the PVA via the hydrogen bonding. And second: (2) a successful formation of crosslinking between the PVA and GA crosslinker. Previous studies reported that [3], the formation of crosslinking by GA, assisted in strengthening the 3D network structure of aerogel.

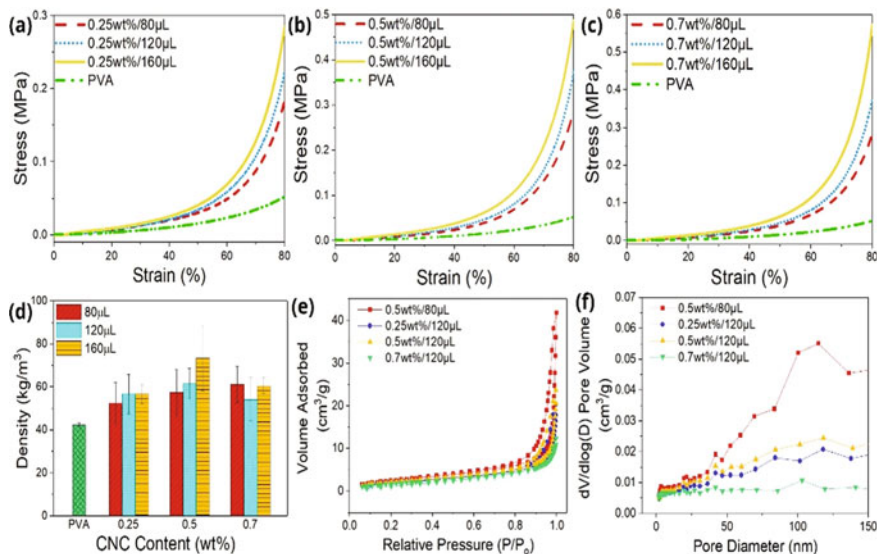


Fig. 2 Stress–strain curve of PVA/CNC aerogels **a** 0.25 wt% **b** 0.5 wt% **c** 0.7 wt%; a comparison with PVA aerogel. **d** Density of neat PVA and PVA/CNC aerogels. **e** Nitrogen adsorption and desorption isotherms and **f** BJH pore size distribution of PVA/CNC hybrid aerogels

3.3 Density

Figure 2d shows the densities of PVA hybrid CNC aerogel samples. All hybrid samples possess higher density than the neat PVA aerogel; ranged from 52 to 73 kg/m³. This is associated with the incorporation of gelatin and CNC, which reduced the volume shrinkage of aerogel during the freeze drying process. As a result the aerogel shape can be retained. The results also signify the existence of good compatibility between the PVA, the CNC from EFB and the GA crosslinker. However, it is noticed for hybrid samples that contain 0.5 and 0.7 wt% of CNC, at higher content of GA crosslinker, their density values dropped slightly. The qualitative observation also found that the higher GA crosslinker percentage had changed the shape of hybrid samples; the aerogel shrank and their surface appear rougher than other samples (refer Fig. 1).

3.4 BJH Pore Distribution Analysis

Figure 2 shows the Barrett-Joyner-Halenda (BJH) model of (e) isothermal adsorption-desorption and (f) pore size distributions on selected samples with respect to their pore shapes; 0.5 wt% 80 μL (polygonal), 0.25 wt% 120 μL (lamellar), 0.5 wt% 120 μL (irregular lamellar), and 0.7 wt% 120 μL (elongated). From Fig. 2e, samples 0.5 wt% 80 μL has the highest volume of gas adsorbed compared to other sample.

This result could be related to its well distributed pores formation. As depicted in Fig. 2f, samples 0.5 wt% 80 μL also showed a prominent pore size; ranged of 90–120 nm, and higher pore volume than the other samples. It is also observed that at higher GA content (0.7 wt%/120 μL), the pore size decreased to around 105 nm and lesser amount of pore volume. These findings is consistent with the observation in SEM results.

4 Conclusion

Based on the results and analysis, the following conclusions can be made:

1. The addition of CNCs increases the density of PVA aerogel.
2. Mechanical strength of the PVA aerogels has been improved by incorporating the CNCs.
3. The variation in the amount of CNCs and crosslinking agent affects the aerogels porous structures as well as the mechanical strength.
4. The intense crosslinking decreases the volume and size of pores of hybrid aerogel.

Acknowledgements The authors wish to thank the Ministry of Higher Education Malaysia (MOHE), for the financial aid under the grant scheme: FRGS/1/2019/TK05/UIAM/02/8, which made this research work possible and International Islamic University Malaysia (IIUM) for their support of this research.

References

1. Huang Y, Zhou T, He S, Xiao H, Dai H, Yuan B, Chen X, Yang X (2019) Flame-retardant polyvinyl alcohol/cellulose nanofibers hybrid carbon aerogel by freeze drying with ultra-low phosphorus. *Appl Surf Sci* 497:143775
2. Javadi A, Zheng Q, Payen F, Altin Y, Cai Z, Sabo R, Gong S (2013) Polyvinyl alcohol-cellulose nanofibrils-graphene oxide hybrid organic aerogels. *ACS Appl Mater Interfaces* 5(13):5969–5975
3. Zheng Q, Javadi A, Sabo R, Cai Z, Gong S (2013) Polyvinyl alcohol (PVA)-cellulose nanofibril (CNF)-multiwalled carbon nanotube (MWCNT) hybrid organic aerogels with superior mechanical properties. *RSC Adv* 3:20816
4. Maleki H, Montes H, Hayati-Roodbari N, Putz F, Huesing N (2018) Compressible, thermally insulating, and fire-retardant aerogels through self-assembling silk fibroin biopolymers inside a silica structure. An approach towards 3D printing of aerogels. *ACS Appl Mater Interf* 10:22718–22730
5. Han J, Yue Y, Wu Q, Huang C, Pan H, Zhan X, Mei C, Xu X (2017) Effects of nanocellulose on the structure and properties of poly(vinyl alcohol)-borax hybrid foams. *Cellulose* 24:4433–4448
6. Xu Z, Jiang X, Zhou H, Li J (2018) Preparation of magnetic hydrophobic polyvinyl alcohol (PVA)-cellulose nanofiber (CNF) aerogels as effective oil absorbents. *Cellulose* 25:1217–1227
7. Randall JP, Meador MAB, Jana SC (2011) Tailoring mechanical properties of aerogels for aerospace applications. *ACS Appl Mater Interfaces* 3:613–626

8. Maleki H, Durães L, García-González CA, del Gaudio P, Portugal A, Mahmoudi M (2016) Synthesis, and biomedical applications of aerogels: possibilities and challenges. *Adv Colloid Interface Sci* 236:1–27
9. Wan W, Zhang R, Ma M, Zhou Y (2018) Monolithic aerogel photocatalysts: a review. *J. Mat. Chem. A* 6:754–775
10. Mao J, Locozzia J, Huang J, Meng K, Lai Y, Lin Z (2018) Graphene aerogels for efficient energy storage and conversion. *Energy Environ Sci* 11:772–799
11. Long LY, Weng YX, Wang YZ (2018) Cellulose aerogels: synthesis, applications, and prospects. *Polymers* 10:623
12. Gopi S, Balakrishnan P, Geethamma VG, Pius A, Thomas S (2018) 4—Applications of cellulose nanofibrils in drug delivery. In: *Applications of nanocomposite materials in drug delivery*. Woodhead Publishing Series in Biomaterials, pp 75–95
13. Samat N, Nasrudin RF, Mokhtar NA, Yacob N (2022) Oil palm empty fruit bunch and pineapple leaf fibre cellulose nanocrystals isolation using double oxidation approach. *Jurnal Teknologi* 84(5):73–81
14. Nita LE, Ghilan A, Rusu AG, Neamtu I, Chiriac AP (2020) New trends in bio-based aerogels. *Pharmaceutics* 12(5):449
15. Martins BF, de Toledo PVO, Petri DFS (2017) Hydroxypropyl methylcellulose-based aerogels: Synthesis, characterization and application as adsorbents for wastewater pollutants. *Carbohydr Polym* 155:173–181
16. Zhou L, Xu Z (2019) Ultralight, highly compressible, hydrophobic, and anisotropic lamellar carbon aerogels from graphene/polyvinyl alcohol/cellulose nanofiber aerogel as oil removing absorbents. *J Hazard Mater*
17. Zheng Q, Cai Z, Gong S (2014) Green Synthesis of polyvinyl alcohol (PVA)—cellulose nanofibril (CNF) hybrid aerogels and their use as superabsorbent. *J Mater Chem A* 2:3110

Perforation Size Effect on Lotus Leaf Based Oil/Water Separator



Muhammad Hariz Ahat, Fethma M. Nor , S. Ramesh ,
and Denni Kurniawan 

Abstract There is increase in risk and actual occurrence of oil leaks and spill due to more drilling, further offshore, and more complex supply chain. Considering environmental pollution and economic damages from oil spills, effective and efficient oil/water separation methods are needed. There is much room for improvement on the existing oil/water separation methods. Filtration method is an alternative, especially when natural-based solution is used. Recent studies showed that softwoods and lotus leaf are some potential candidates to be use for filtration due to their super-hydrophobic nature. This study uses lotus leaf as the material for oil/water separation by filtration, with the objective to identify the effects of perforation size (including gap size) to the oil/water separation performance, in terms of separation efficiency and flux. Perforation of lotus leaf with 0.23, 0.4, 0.75, and 0.9 mm diameter needles were done with gap sizes of 1 mm, 1.5 mm, and 2 mm for separating silicon oil/water mixture. Needle sizes 0.75 and 0.9 mm resulted in low separation efficiency (< 40%) regardless of the gap size between holes, so these sizes were not considered further. The separation efficiency of lotus leaf for perforation sizes of 0.23 and 0.4 mm diameter is within 85–97%, with its value is not affected by the needle diameter size or gap size. Flux increases with needle size and decreases with gap size. The maximum flux of around $62000 \text{ L m}^{-2} \text{ h}^{-1}$ was obtained from 0.23 mm diameter and 1 mm gap size.

Keywords Oil/water separator · Lotus leaf · Perforation size · Flux

M. H. Ahat · S. Ramesh · D. Kurniawan (✉)
Mechanical Engineering Programme Area, Universiti Teknologi Brunei, Gadong BE1410, Brunei Darussalam
e-mail: denni.kurniawan@utb.edu.bn

F. M. Nor
School of Design, Universiti Teknologi Brunei, Gadong BE1410, Brunei Darussalam

Table 1. Previous studies on plant-based oil/water separator

Type of material	Thickness (mm)	Hole diameter (mm)	Gap between holes (mm)	Flux (L/m ² h)	References
Balsa	1	0.34–0.5	1–3	500–375000	[3]
Pine	1	NA	NA	NA	[4]
Lotus leaf	NA	0.21	1–3	190–1500	[5]

1 Introduction

There is a growing number of oil leaks from industrial accidents or the sinking of oil tankers as oil production and shipping grow. Oil spill accidents can cause significant environmental issues and endanger human life [1, 2]. To remedy, the elimination of oil from the water surface is necessary. There are multiple techniques available to separate oil from water. One of the techniques is physical filtering. Specifically, plant based physical filtering is of interest. Being biodegradable material, light weight, and low cost, plant based oil/water separator can be transported to the place where oil spill occurs. Plants which have super wettability and surface energy much lower than the liquid can function as oil/water separator. Balsa wood, pine wood, bamboo, and lotus leaf are among plant based oil/water based separators [3–5]. The effectiveness of the oil/water filter are measured in the forms of the flux of the solution filtered in L/m²h, separation efficiency of the solution, and the durability after few cycles of filtration. The term of cycle indicated to the experiment's repeatability by using the same filter materials. Table 1 shows the current research on plant-based filtration [3–5]. Research on lotus leaf [5] resulted flux of 1500–190 L/m²h with the highest separation efficiency among the plant based separators. Hole diameter of 210 μm with 1–3 mm apart were used for the experiments. They deduced that increasing the gaps between holes reduces flux flow.

Lotus leaf was chosen for this research since it is plentiful, easily accessible in Brunei's ponds, and the method for extracting the material is simpler than balsa and pine wood. In addition, there is very limited previous works on it as plant based oil/water separator. This research aims to identify the effect of hole size, gap size, and thickness of lotus leaf-based oil/water filtration in terms of flux and separation efficiency.

2 Materials and Method

The lotus leaf used in this research is *Nelumbo nucifera* type. The leaf was collected from a pond in Bandar Seri Begawan, Brunei. Custom made test rig was fabricated, as shown in Fig. 1. To fabricate the leaf into an oil/water separator, the leaf was cut into smaller pieces of circular shape. Next, the leaf was stacked as 1, 5 and 9 layers.

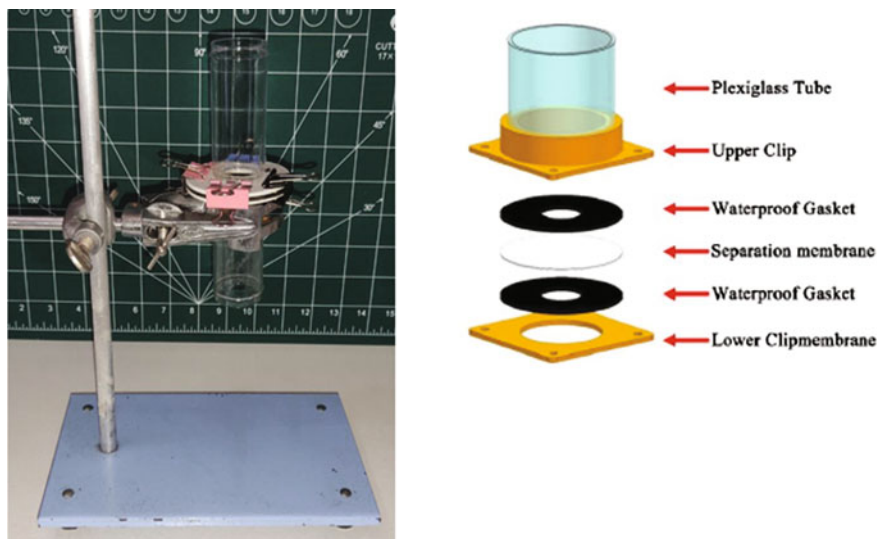


Fig. 1 Custom made test rig of oil/water separation device clamped on a retort stand

Each leaf was perforated using needles of 0.23 mm and 0.4 mm diameter with gap size between the holes of 1 mm to 2 mm. Then, the leaf is placed in between PVC. A flat circular O ring is added to ensure even pressure distribution and proper sealing for the leaf to filter water and oil.

For each cycle of oil/water separation, two measures were taken: separation efficiency and flux. For measuring separation efficiency, a measuring balance were used to measure the weight of the oil/water mixture before and the weight of water and oil after the filtration. The separation efficiency (R) of the filtered oil/water mixture was calculated as in equation (1). For the fluxes, it can be determined by calculating the mass flow of oil/water mixtures passing through the perforated lotus leaf in a given time. The liquid fluxes (F) can be calculated by using the equation (2).

$$R = 1 - \frac{C_s}{C_o} \quad (1)$$

$$F = \frac{V}{S * t} \quad (2)$$

where C_o is the oil concentration of the original oil/water mixture, C_s is the oil concentration of water after oil/water separation, V is the volume of liquid that passes through the perforated leaf, S is the leaf's effective contact area, and t is the testing period.

3 Results and Discussion

The lotus leaf was able to filter the oil/water mixture due to its nature of being both superhydrophilic at the bottom side and superhydrophobic on the top side. When the lotus leaf is being perforated, it only allows either one of the oil or water to pass through, depending on which side of the leaf is being used. When a water droplet is placed on the superhydrophobic side, it slowly moves towards the superhydrophilic side. When the water droplet is introduced on the superhydrophilic side, however, the water droplet spreads on the superhydrophilic surface rather than penetrating into the superhydrophobic side [5].

From Fig. 2, the separation efficiency of the lotus leaf is relatively the same for both 0.23 mm and 0.40 mm hole diameters, ranging from 85 to 97%. The lotus leaf is still able to separate the oil from water effectively regardless of the size gaps. While for the flux flow of the mixture, it decreases linearly with increasing gap. This is due to the lesser amount of holes/area as the gap increases, which leads to lesser holes for the water to flow through. The ratio of flux between 0.40 mm hole and 0.23 mm hole is 6 for gap size of 1 mm and 1.5 mm. Meaning, 0.4 mm hole has 3 times larger hole area than 0.23 mm hole. This is due to the fact that 0.40 mm hole is larger in diameter than the 0.23 mm one. As a result, this results in a 6 times larger flux.

When the gap increases, the number of holes' density per unit area decreases as they move further apart from each other. Hence, fewer holes for the mixture to pass through leads to a decrease in flux. While the 0.24 mm needle was used on the lotus leaf by previous work [5], the flux ratio trend is similar regardless of the material type. However, the 0.23 mm needle has a decreasing flux ratio trend. These may be due to errors on the needle, as it may wobble when perforating and cause a larger size hole than being indented, ranging from 0.35 to 0.45 mm for a 0.40 mm needle. The exact width of the hole is also larger compared to the needle size. Thus, contributing to the flux deviations when it is being used to filter the oil/water mixture.

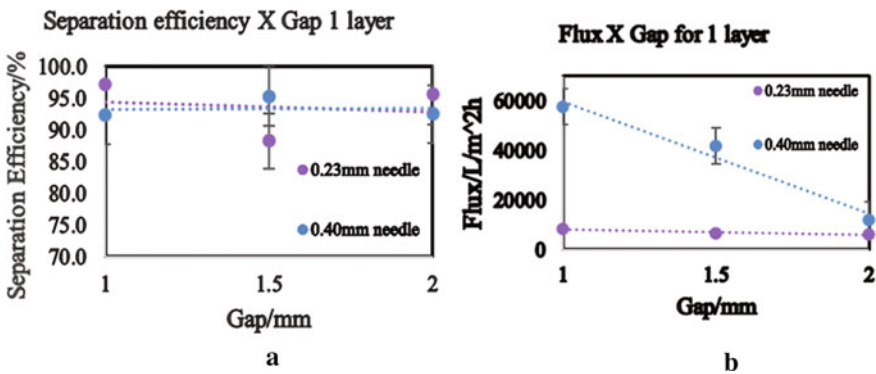


Fig. 2 Separation efficiency **a** and flux **b** at different needle size and gap between holes

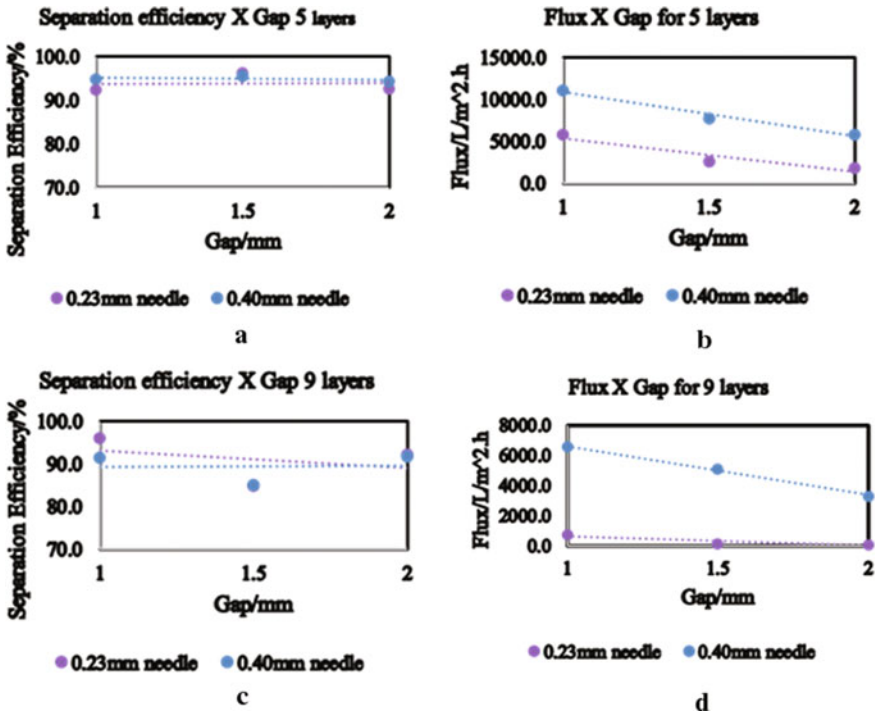


Fig. 3 Separation efficiency and flux at different hole size (needle) and gap between holes for 5 stacks (a and b, respectively) and 9 stacks (c and d, respectively) of lotus leaf

From Fig. 3, for five-layer leaves stacked, the separation efficiency is ranging from 92 to 98%, providing high efficiency separating the mixtures. It has higher separation efficiency in comparison to one layer. However, the high separation efficiency causes the perforated leaves to have a lower flux flow compared to one layer. The oil/water mixture require more time to pass through the thicker leaves when they are stacked against each other. There is no significant difference in separation efficiency between 0.23 and 0.4 mm needles. Similar results were obtained from 9-layer stack of lotus leaf. Both needles have almost similar percentage efficiency in five-layer leaves and nine-layer leaves.

4 Conclusion

In conclusion, the objective of these experiments to identify the optimum hole size, gap size and thickness of lotus leaf in term of flux and separation efficiency is fulfilled. Together with the highest flux flow in comparison with 5 and 9 layered leaves. Even thou the separation efficiencies of 5 and 9 layered leaves are relatively similar with 1

layered leaf, the fluxes were way too low in comparison with 1 layer. Hence, making the 1 layered leaf to become more desirable to be use in real life application as more mixtures can be filtered on a shorter period of time without compromising the separation efficiency.




Acknowledgements The authors gratefully acknowledge the funding by Universiti Teknologi Brunei, Brunei Darussalam and sponsorship by Sarawak Convention Bureau, Malaysia.

References

1. Zhang F, Zhang WB, Shi Z, Wang D, Jin J, Jiang L (2013) Nanowire-haired inorganic membranes with superhydrophilicity and underwater ultralow adhesive superoleophobicity for high-efficiency oil/water separation. *Adv Mater* 25(30):4192–4198
2. Li J, Xu C, Zhang Y, Wang R, Zha F, She H (2016) Robust superhydrophobic attapulgite coated polyurethane sponge for efficient immiscible oil/water mixture and emulsion separation. *J Mater Chem A* 4(40):15546–15553
3. Yong J, Chen F, Huo J, Fang Y, Yang Q, Bian H, Li W, Wei Y, Dai Y, Hou Y (2018) Green, biodegradable, underwater superoleophobic wood sheet for efficient oil/water separation. *ACS Omega* 3(2):1395–1402
4. Luo YQ, Song F, Xu C, Wang XL, Wang YZ (2020) Bioinspired fabrication of asymmetric wood materials for directional liquid manipulation and transport. *Chem Eng J* 383:123168
5. Zhang C, Zhang Y, Xiao X, Guoliang Liu G, Xu Z, Wang B, Yu C, Ras RHA, Jiang L (2019) Efficient separation of immiscible oil/water mixtures using a perforated lotus leaf. *Green Chem* 21(24):6579–6584

Investigation of Chip Formation During Turning of Aluminum Alloys 7075-T651 in Dry and Chilled Air Condition



Muhammad Izzat Amin Bin Rosli, Natasha A. Raof ,
Aishah Najiah Dahnel , Suhaily Mokhtar ,
and Nor Khairusshima Muhamad Khairussaleh 

Abstract Aluminum alloys 7075-T651 is a ductile material which may lead to tool damage and machined surface deterioration due to the formation of built-up-edge (BUE) and adhesion layer during machining especially in dry cutting condition. This paper discusses the chip formation of aluminum alloys 7075-T651 during turning in green environment. Uncoated carbide KW10 cutting tool was used to machine Al7075-T651 in dry and chilled air condition. The cutting speed and feed rate were varied to 450 to 650 m/min and 0.15 mm/rev – 0.05 mm/rev, respectively. The depth of cut was fixed to 0.5 mm. The chip formation was observed and measured in term of chip type, chip thickness and co-efficient of friction. It was found that, among the types of chips produced in turning Al7075-T651 were snarled tubular ribbon, loose arc and long washer-type helical. The thickness of the chip increased as the feed increases by 253% hence increased the friction coefficient by 104.7%. Meanwhile, the chip thickness decreased 5.19% when the cutting speed increased, hence reducing the coefficient of friction by 14.6%. Chilled air machining produced 7.11% thinner chips than dry machining, which lowered the friction coefficient by 19.7%. Therefore, it can be concluded that, machining Al7075-T651 at low feed rate and high cutting speed in chilled air cutting environment may help to improve the lubrication and further enhancing the machining outputs.

Keywords Aluminum alloys 7075-T651 · Chilled air · Chip formation · Coefficient of friction

1 Introduction

Aluminum is one of the commonly available elements which consists of oxygen and others elements to create its natural form [1]. The mixture of aluminum with its alloys produces better properties which enable it to be widely used in many fields from a highly ductile wrapping foil to components for aerospace industries [2].

M. I. A. B. Rosli · N. A. Raof (✉) · A. N. Dahnel · S. Mokhtar · N. K. M. Khairussaleh
Department of Manufacturing and Materials Engineering, Kulliyah of Engineering, International Islamic University Malaysia, Jalan Gombak, 53100 Selangor, Malaysia
e-mail: natashar@iium.edu.my

However, its soft and ductile characteristics may lead to several problems during the manufacturing processes, particularly during machining. Workpiece material, cutting parameters, cutting condition and tool geometry are among the factors that influence the machining outputs, such as tool wear, surface roughness and chip formation [3].

The change in feed rate and cutting speed affect the type of chip formation [4]. Generally, chip thickness decreased with increasing cutting speed but increased with increasing feed. This is because, the increase in cutting speed and decrease in the feed could result in an increasing shear angle, hence producing thinner chip [5].

Dry machining is an alternative to wet machining which improves the effectiveness of metal cutting by cutting the cost of lubricant and saving the environment [6]. Distortion of parts may occur during dry machining due to the high cutting forces and temperatures which affect the quality of machined surface. The effects are caused by the change of metallurgical properties and residual machining stresses [7]. The chip tends to adhere to the tool face then offer more resistance when shearing the chip, hence increase the chip thickness [8].

Chilled air system is another alternative to wet machining for cooling purpose. 7% of temperature was reduced by this system in a test conducted by [9] in machining of Inconel 718. Cutting forces were lowered as the chilled air reduced the work material adhered on the tool surfaces. Applying chilled air cooling during machining improves the heat dissipation in the cutting tool, chip and workpiece.

This research is focusing on the chip formation in regards of its shape, thickness and coefficient of friction in turning aluminum alloy 7075-T651 in dry and chilled air cutting conditions.

2 Methodology

There were four experimental runs carried out in this research by using Bridgeport ROMI Powerpath 15 CNC lathe machine. Table 1 shows the variable and fixed parameters used to setup the experiments. The chips were collected and analyzed by observing and measuring the shape and the thickness, then calculating the coefficient of friction.

Aluminum alloy 7075-T651 was chosen as the workpiece material. The type of cutting tool used in this experiment was KW10 uncoated carbide, held on the

Table 1 Experimental parameters

No. of run	Cutting condition	Cutting speed (m/min)	Feed rate (mm/rev)	Depth of cut (mm)
1	Dry	450	0.15	0.5
2	Dry	650	0.05	0.5
3	Dry	650	0.15	0.5
4	Chilled air	650	0.15	0.5

PTJNR2525M16JETL tool holder, which has -6° rake angle. A vortex tube was used to supply the chilled air with the temperature range in between 8 and 10 °C. The flow rate of air recorded was 15.1 m/s. The nozzle was located near the insert to ensure the cold air could reach the cutting zone during the turning operation.

The chip thickness was measured by using Dino-Lite Edge Digital Microscope. The coefficient of friction, μ was calculated once the thickness of the chip was recorded by using Eq. (1):

$$\mu = \tan \beta \quad (1)$$

where β is the friction angle and can be calculated by using Eq. (2):

$$\beta = 90 + \alpha - 2\emptyset \quad (2)$$

where α is the rake angle, and \emptyset is the shear angle, which can be obtained from Eq. (3):

$$\tan \emptyset = (r \cos \alpha) / (1 - r \sin \alpha) \quad (3)$$

where r is the chip thickness ratio of the uncut chip thickness, t_o and chip thickness after cutting, t_c as shown in Eq. (4):

$$r = t_o / t_c \quad (4)$$

3 Result and Discussion

3.1 Effect of Cutting Parameters on Chip Formation

Close observation of the chips revealed that feed rate has a significant effect on the type of the chip formed during the cutting. Saw tooth edges chip were produced at higher feed rate, meanwhile at low feed rate the saw tooth edges was barely seen as shown in Fig. 1. The temperature rise happens in the separation zone (near the tool tip) during the cutting process and transfers to the chip curl-up side hence induce a waved periodic chip known as saw tooth chip [10]. The thickness of the chip and coefficient of friction increased as the feed rate increased from 0.05 to 0.15 mm/rev as shown in Fig. 2. This is due to the enormous compressive stress on the tool rake at higher feed rate, which result in large volume of material becomes fully plastic which form thick chip [11].

Cutting speed seems to have no effect on the type of chip formed as it was observed that saw tooth edge chips were produced when cutting at different cutting speeds. However, the chip's thickness and coefficient of friction decreased as the cutting

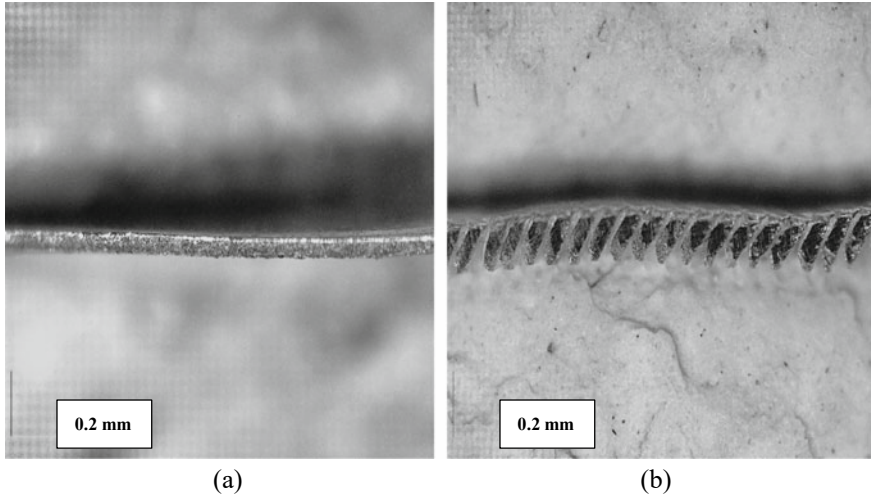


Fig. 1 Magnified view of chip formed at $v = 650$ m/min, $d = 0.5$ mm **a** $f = 0.05$ mm/rev, **b** $f = 0.15$ mm/rev

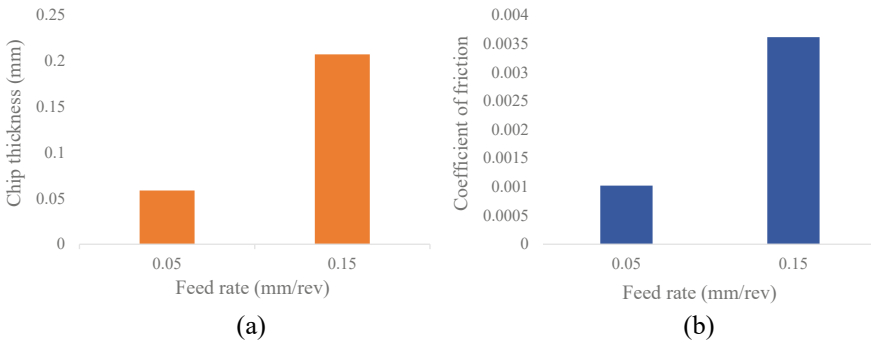


Fig. 2 a Measured chip thickness, and **b** coefficient of friction during turning of aluminum alloys 7075-T651 under different feed rate (dry, $v = 650$ m/min, $d = 0.5$ mm)

speed increased from 450 to 650 m/min as shown in Fig. 3. This happened because the increment in cutting speed cause an increasing the shear angle [12].

3.2 Effect of Cutting Condition on Chip Formation

The chip thickness from chilled air machining was thinner than dry machining as shown in Fig. 4a. Cutting forces were lowered as the chilled air reduced the work material adhered on the tool surfaces, hence resulted in thin chip [9].

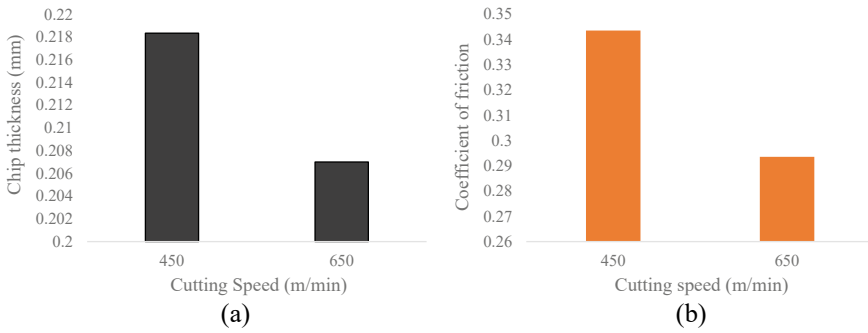


Fig. 3 a Measured chip thickness, and b coefficient of friction during turning of aluminum alloys 7075-T651 under different cutting speed (dry, $f = 0.15$ mm/rev, $d = 0.5$ mm)

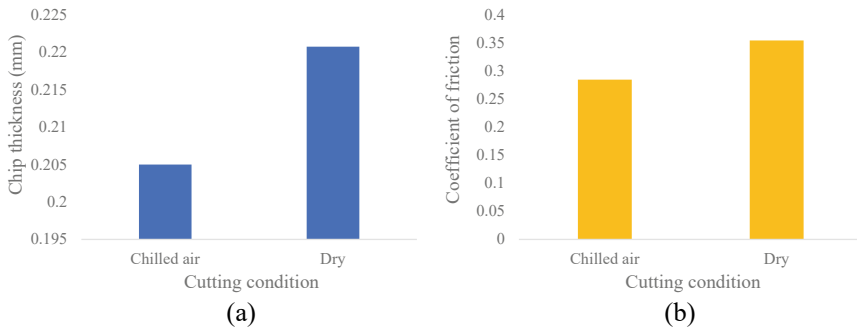


Fig. 4 a Measured chip thickness, and b coefficient of friction during turning of aluminum alloys 7075-T651 under different cutting condition ($v = 650$ m/min, $f = 0.15$ mm/rev, $d = 0.5$ mm)

The calculated coefficient of friction on chilled air machining was lower than dry machining. Figure 4b displays the difference of friction coefficient between both conditions. It recorded that the percentage difference was 19.7% which is quite substantial. Lower temperature of chip-tool interface in chilled air turning assisted in keeping the chip hardness at high level, therefore, the chip was unable to adhere to the tool rake face, eased the chip to slide thus reduced the friction between chip and the cutting tool [13].

4 Conclusion

In this study, aluminum alloys 7075-T651 was machined by uncoated carbide insert at different cutting parameters in dry and chilled air cutting conditions. The following remarks can be concluded:

- Saw tooth edge types of chips were produced in turning the aluminum alloys 7075-T651 in all experimental runs except when cutting at low feed rate value.
- The thickness of the chip increased as the feed increases hence increased the friction coefficient. The thickness of chip decreased when the cutting speed increased hence reduced the coefficient of friction.
- The chip thickness from chilled air machining was thinner than dry machining. The calculated coefficient of friction on chilled air machining was lower than dry machining.
- The lubrication in machining aluminum alloys 7075-T651 was enhanced when machined at low feed rate, high cutting speed, and in chilled air condition.

Acknowledgements This project is supported by Ministry of Higher Education Malaysia and International Islamic University Malaysia under FRGS/1/2018/TK03/UIAM/03/4 (FRGS19-019-0627).

References

1. Santos MC, Machado AR, Sales WF, Barrozo MAS, Ezugwu EO (2016) Machining of aluminum alloys: a review. *Int J Adv Manuf Technol* 86(9–12):3067–3080
2. Kouam J, Songmene V, Balazinski M, Hendrick P (2015) Effects of minimum quantity lubricating (MQL) conditions on machining of 7075–T6 aluminum alloy. *Int J Adv Manuf Technol* 79:1325–1334
3. Wan L, Wang D, Gao Y (2015) Investigations on the effects of different tool edge geometries in the finite element simulation of machining. *J Mech Eng* 61(3):157–166
4. Mgbemena C, Mgbemena C, Etebenumeh G, Ashiedu F (2016) Effect of turning parameters on metal removal and tool wear rates of AISI 1018 low carbon steel. *Niger J Technol* 35(4):847
5. Das SR, Panda A, Dhupal D (2017) Experimental investigation of surface roughness, flank wear, chip morphology and cost estimation during machining of hardened AISI 4340 steel with coated carbide insert. *Mech Adv Mater Mod Process* 3:1–14
6. Zainol A, Yazid MZA (2019) Environmentally friendly approaches assisted machining of aluminum alloy 7075–T6 for automotive applications: a review. *Int J Integr Eng* 6:18–26
7. Andrea LM, James WM, Zhirong L, Alistair S, Jose AR-L, Dragos AA, Mark CH, Clare AT (2021) Surface integrity in metal machining—part II: functional performance. *Int J Mach Tools Manuf* 164
8. Zailani ZA, Mativenga PT (2016) Effects of chilled air on machinability of NiTi shape memory alloy. *Procedia CIRP* 45:207–210
9. Hafiz MSA, Kasim MS, Mohamad WNF, Zainurin NSM, Othman IS, Izamshah R, Akmal M, Mohamed SB, Nawawi MAM (2019) The effects of dry and chilled air on tool wear behavior during face milling of Inconel 718. *Jurnal Tribologi* 21:47–62
10. Chandra BB, Sudarsan GC, Paruchuri VR (2019) Study of saw-tooth chip in machining of Inconel 718 by metallographic technique. *Mach Sci Technol* 23(3):431–454
11. Rodriguez PJM, Carbonell JM, Cante JC, Oliver J, Jonsen P (2018) Generation of segmental chips in metal cutting modeled with the PFEM. *Comput Mech* 61:639–655
12. Moris DA, Sivaprasad PV, Beno T, Eynian M (2020) Predicting continuous chip to segmented chip transition in orthogonal cutting of C45E steel through damage modeling. *Metals* 10(4):519
13. Mia M, Rifat A, Tanvir MF, Gupta MK, Hossain MJ, Goswami A (2018) Multi-objective optimization of chip-tool interaction parameters using Grey-Taguchi method in MQL- assisted turning. *Measur J Int Measur Confederation* 129:156–166

The Influence of Cutting Parameters and Chilled Air on the Tool Wear of Uncoated Solid Carbide Cutting Tool During Milling CFRP



R. Muhammad Nabil , M. K. Nor Khairusshima , R. Siti Fatirah ,
and Sharifah Imihezri Syed Shaharuddin 

Abstract Carbon Fibre Reinforced Plastic (CFRP) has been rising its popularity and demand in automotive and aeronautic industries due to its advantageous properties such as ultra-light, yet have high specific strength, high corrosion resistance and high rigidity. Nonetheless, CFRP is an expensive type of composite which required expensive treatment to manufacture it. Hence, to minimize any additional cost in CFRP's manufacturing, the inconvenient factors such as severe tool wear during its machining, which shorten the tool life and high surface roughness should be minimized. Therefore, various methods have been implemented to overcome the problems. In this study, the effect of cutting temperature on the tool life of an 8 mm solid uncoated carbide cutting tool during milling of CFRP panel with an aid of chilled air is investigated. Chilled air, provided by vortex tube is used to adjust the cutting tool temperature before machining into range of $-14\text{ }^{\circ}\text{C}$ to $14\text{ }^{\circ}\text{C}$. Cutting speed of 3750–6750 rpm and feed rate between 52.19 and 371.81 mm/min have been carried out by using a Computer Numerical Control (CNC) vertical machining center. It has been identified that the tool wear decreases as both cutting speed and feed rate increase during milling CFRP.

Keywords CFRP · Chilled air · Carbide

1 Introduction

Carbon fibre reinforced plastic (CFRP) is a material that characterized by low weight, super strength, and desirable damage tolerance. It has been used tremendously for both low and high technologies engineering applications especially in key load-bearing components such as fuselage of airplane, aircraft skin and stringers for weight and cost reductions [1]. Among other fibre such as glass and aramid fibre, carbon fibre (CF) gives the maximum degree of strength and wear resistance enhancement and boosts the thermal conductivity [2]. In manufacturing of CFRP, prepreg layup

R. Muhammad Nabil · M. K. Nor Khairusshima (✉) · R. Siti Fatirah · S. I. S. Shaharuddin
Department of Manufacturing and Materials Engineering, International Islamic University
Malaysia, Gombak, 53100 Kuala Lumpur, Malaysia
e-mail: norkhairusshima@iium.edu.my

© The Author(s), under exclusive license to Springer Nature Singapore Pte Ltd. 2023
Md. A. Maleque et al. (eds.), *Proceeding of 5th International Conference on Advances in
Manufacturing and Materials Engineering*, Lecture Notes in Mechanical Engineering,
https://doi.org/10.1007/978-981-19-9509-5_78

591

Table 1 Properties of used CFRP panel

Panel	Properties
Fabric type	ABR 1-0006
Yarn type	Toray T300-3K-40A

and autoclave processing are being used for the fabrication of raw CFRP components. This process resulted rough shape, due to the almost-final-shape production process of CFRP composites. Later, CFRP components are then required machining for assembly requirements [3]. Due to high demand of CFRP in industries especially in automotive and aerospace, resulted more investigation conducted including machining methods [1]. During machining CFRP, there are many challenges for manufacturer such as the matrix could soften from too much heat and the fibres does not cut well as they fracture instead of shearing smoothly [2], low thermal conductivity nature of CFRP, and low glass transition temperature of resin matrix have brought great challenges concerning cutting area temperatures for conventional machining of CFRP [3]. Hence, it has been reported that chilled air has been one of the machining methods that could improve both qualities [3]. By depending on variation of cutting speed, feed rate, and temperature, this study is focusing on the effect of cutting temperature on the tool wear of the cutting tool (uncoated carbide) in milling process of CFRP.

2 Methodology

2.1 Workpiece Material

The material used in this project is Carbon Fibre Reinforced Plastic panels with dimensions of $200 \times 300 \times 3$ mm as shown in the Table 1. The panel was fabricated by wet layout method. Figure 1 and Table 1 show the dimensions and the properties of the used CFRP panel in this project respectively.

2.2 Cutting Tool

The cutting tool used is the solid uncoated carbide (N2EM080-U). The diameter of the cutting tool is 8.0 mm, a $20\text{--}24^\circ$ relief angle and a 30° helix angle. Figure 2 shows the used carbide cutting tool while its geometry is tabulated in Table 2.

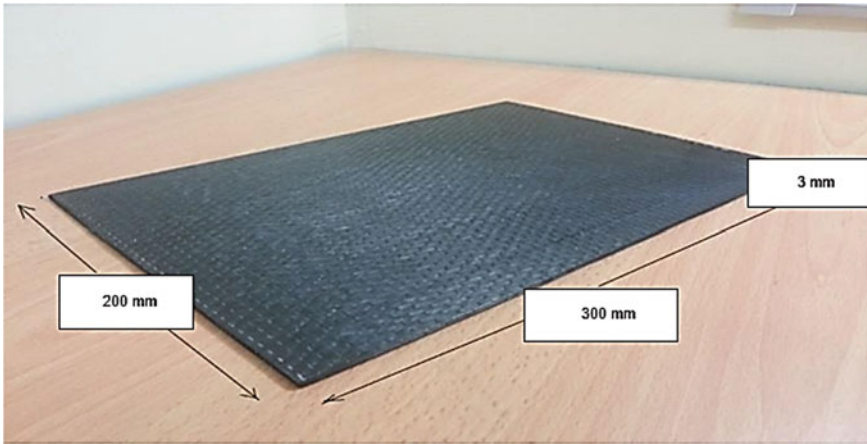


Fig. 1 CFRP panel with dimensions

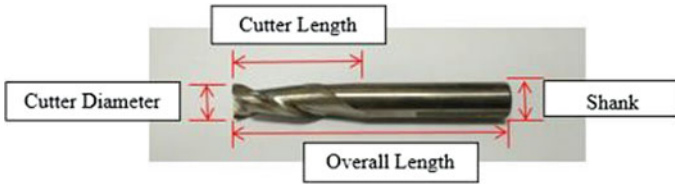


Fig. 2 Carbide cutting tool

Table 2 Geometry values of carbide cutting tool

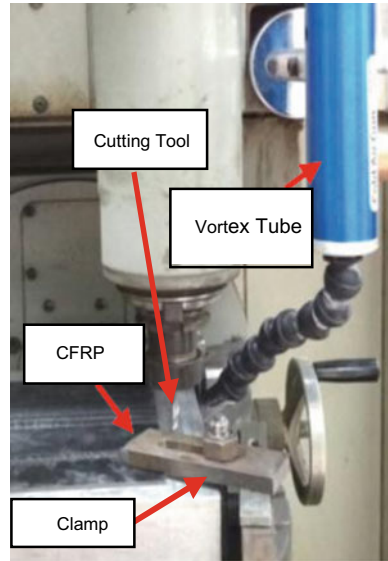
Specification	Diameter (mm)	Shank (mm)	Cutter length (mm)	Overall length (mm)
	8	8	20	60

2.3 Cutting Parameters and Experimental Setup

Vortex tube (VT) which also known as Ranque-Hilsch tube is installed in the CNC milling machining system. The experiment is conducted under chilled air machining condition on CNC milling machine. By using constant depth of cut of 1.5 mm, the range of cutting parameters used are shown in Table 3.

Table 3 Range of cutting parameter

Cutting parameter	Spindle speed (RPM)	Feed rate (mm/min)	Vortex's temperature (°C)
	3750–6750	52.19–371.81	–14.14 to 14.14 °C

Fig. 3 Machining setup

The vortex tube is attached close to the spindle during milling process. Compressed air pressure supplied to the inlet to produce range of $-14.14\text{ }^{\circ}\text{C}$ to $14.14\text{ }^{\circ}\text{C}$ of chilled air. The nozzle is put next to the cutting tool and the distance between the nozzle and the cutting tool is constant throughout the milling process (Fig. 3). The workpiece is clamped to the machine's table properly to avoid any external factors that could affect the surface roughness.

3 Results and Discussion

3.1 Tool Wear

In any machining operation, wear of the cutting tool used is one of the important parts needed to be identified as it could affect the accuracy of the dimension of the final product. In this study, appropriate graph was plotted based on the data collected throughout the experiments. Based on the graph generated, the tool wear trends were analysed and discussed. Figure 4 shows the graph of the tool wear at different spindle speeds at constants feed rate 212 mm/min and temperature of $0\text{ }^{\circ}\text{C}$ respectively. According to the graph, it also shows that the tool wear for every cutting speed increases for every 200 mm machined distance. Furthermore, the graph shows that higher cutting speed gives lower tool wear value. This phenomenon is similar to Nor Khairusshima, et al. [2], as she concluded that the effectiveness of chilled air can be seen at higher cutting speed that resulted with lower tool wear. Thus, higher cutting speed is preferable during chilled air machining. Meanwhile, for the lowest

cutting speed, 3750 rpm, at the beginning of the machining, the tool wear is small compared to the 5250 and 7371 rpm. This happens due to the higher heat generated as the cutting tool begin to cut the material helped to soften the material and reduce the force needed by the tool to remove the workpiece during machining. Thus, the tool wear is small. However, when the tool wear reached 600 mm distance travelled, the tool wear rapidly increasing. At this stage, the heat generated due to the cutting speed started to damage the cutting tool [2]. Figure 5 displays the graph of the tool wear at different feed rate with constants of cutting speed and temperature of 5250 rpm and 0 °C respectively. The graph below shows that the tool wear for each of the feed rate increases as the distance travelled increases. Also, it can be observed that highest feed rate gives lowest tool wear. This trend also agreed with Nor Khairusshima et al. [2] where she found that tool wear is lower at higher feed rate with 31.8% of longer tool life achieved during using chilled air compared to room temperature. Thus, higher feed rate is better during chilled air machining. Meanwhile, for the 212 mm/min feed rate, the tool wear always bigger than 52.19 mm/min feed rate all along the 600 mm distance travelled. Earlier stage of tool wear could show sudden rise in the tool wear as can be seen happened to 212 mm/min feed rate. This happen because the tool wear was still on the earlier stage of tool wear [2]. This is supported by Dervis, et al. [4] where he found that higher feed rate produces bigger tool wear compared to lower feed rate in the earlier stage of tool wear trend, but higher feed rate produces smaller tool wear as the tool wear reached the secondary (break-in) phase.

Graph in Fig. 6 shows the tool wear for temperature at -14 and 14 °C, with constant spindle speed and feed rate. Each of the cutting temperature shows increment in tool wear as the distance machined increases. The graph also shows that -14.14 °C produces lower wear compared to 14.14 °C. Danel et al. [3] found in their study that lower cutting temperature led to shorter tool life. This conclusion agreed with

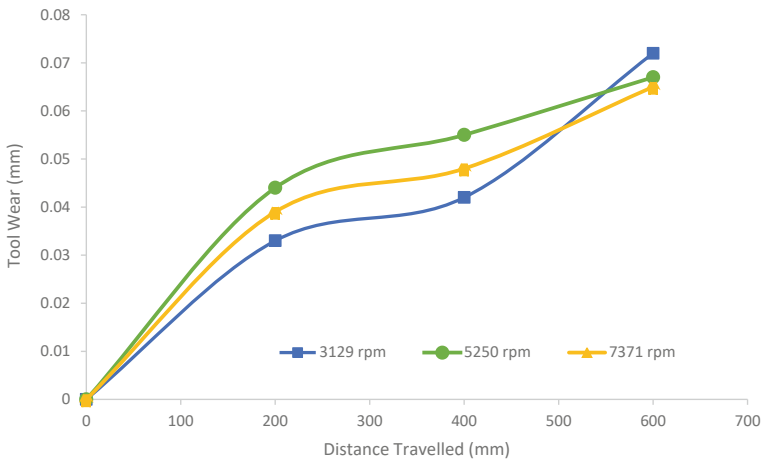


Fig. 4 Comparison of tool wear at different spindle speeds with constant feed rate (212 mm/min) and temperature (T = 0 °C)

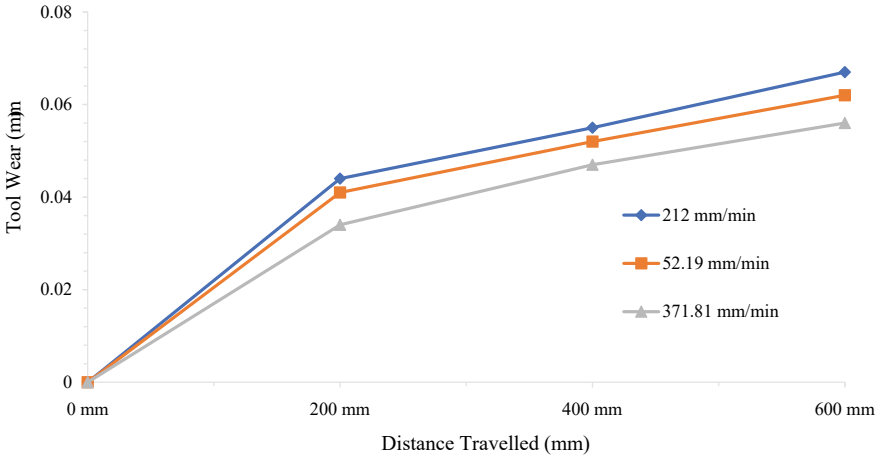


Fig. 5 Comparison of tool wear at different feed rate with constant spindle speed (5250 rpm) and temperature ($T = 0\text{ }^{\circ}\text{C}$)

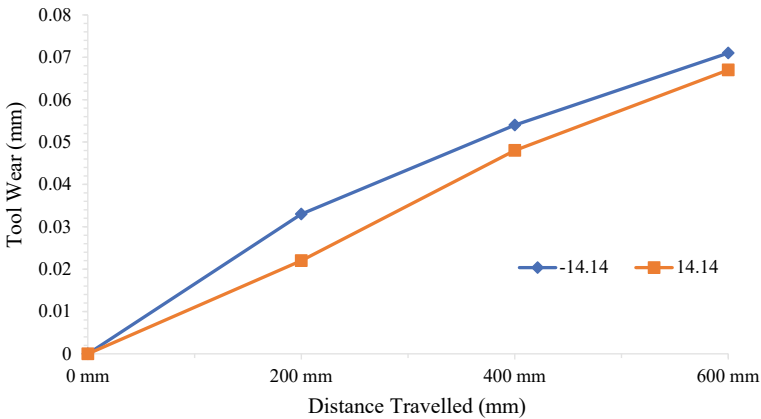


Fig. 6 Comparison of tool wear at different temperature and constant spindle speed (5250 rpm) and feed rate (212 mm/min)

the data shown in the graph below where lower temperature of $-14.14\text{ }^{\circ}\text{C}$ done less tool wear to the cutting tool leading to a longer tool life.

4 Conclusion

This project studies the issue of determining the influence of cutting parameters and chilled air on the tool wear of solid uncoated carbide cutting tool during milling of

CFRP panel. It is found that, at highest cutting speed of 6750 rpm and highest feed rate of 325 mm/min produces lowest tool wear while highest tool wear produced by highest temperature of 14.4 °C and lowest cutting speed of 3750 rpm.

Acknowledgements The authors would like to thank the Government of Malaysia and International Islamic University Malaysia for their financial support under grant number: FRGS/1/2018/TK03/UIAM/03/1.

References

1. Xia T, Kaynak Y, Arvin C, Jawahir IS (2016) Cryogenic cooling-induced process performance and surface integrity in drilling CFRP composite material. *Int J Adv Manuf Technol* (82):605–616
2. Nor Khairusshima MK, Che Hassan CH, Jaharah AG, Amin AKM, Md Idris AN (2013) Effect of chilled air on tool wear and workpiece quality during milling of carbon fibre-reinforced plastic. *Wear* 302(1–2):1113–1123
3. Aishah Najiah D, Barnes S, Bhudwannachai P (2013) Experimental analysis of tool wear when drilling carbon fibre composite (CFC) without cutting fluid, with cutting fluid and with a pre-cryogenically cooled tool. *Appl Mech Mater* 372:512–516
4. Dervis O, Mustafa SG, Hassan G, Karaoglanli AC (2019) The effect of cutting parameters on tool wear during milling of carbon fiber reinforced polymer (CFRP) composites. *Mater Sci J* 25(1)

Study on the Hardness of Uncoated Carbide Cutting Tool at Different Cutting Parameters



K. Muhammad Irfan, M. K. Nor Khairusshima , A. R. Natasha ,
D. Aishah Najiah , and M. Suhaily 

Abstract High hardness is one of properties of carbide cutting tool which make it highly demand in manufacturing sector. The main objective of this project is to study on the effect of cutting parameters (spindle speed, feed rate and depth of cut) in milling machining CFRP on the hardness of carbide cutting tool at three different fiber orientations which are 0° , 45° and 90° . The other objective is to analyze the most influence factor of cutting parameter which responsible in changing the cutting tool hardness during machining CFRP. The 8 mm diameter carbide cutting tool has been used to machine CFRP which has dimension of $200 \times 300 \times 3$ mm at spindle speed of 2000–8700 rpm, feed rate of 500–1000 mm/min and depth of cut 1.0–1.5 mm. Box-Behnken which is one of the tools under Response Surface Methodology (RSM) used to analyze the relationship between the cutting parameters and the hardness of the cutting tool. It has been identified that feed rate was the most influenced factor of affecting the cutting tool hardness with highest F-value (819.6,6565.60 and 7335.85) for all three fiber orientations compared to spindle speed and depth of cut. To conclude, it is recommended to mill machine the CFRP using high spindle speed, low feed rate and high depth of cut.

Keywords Carbide · CFRP · Fiber orientation

1 Introduction

Nowadays, the usage of carbide cutting tools are increasing in a variety of industrial, engineering, and domestic applications. Problem have arisen with machining CFRP as conventional tools cannot applied to machine this material [1]. High hardness, yield and tensile strength, and low thermal conductivity majorly cause frequent tool wear, high cutting force, and poor work surface quality [2]. Hence, there are very limited materials that can be used as cutting tool for CFRP machining [3]. Optimal

K. M. Irfan · M. K. N. Khairusshima (✉) · A. R. Natasha · D. A. Najiah · M. Suhaily
Department of Manufacturing and Materials Engineering, International Islamic University
Malaysia, Gombak, 53100 Kuala Lumpur, Malaysia
e-mail: norkhairusshima@iium.edu.my

cutting parameters such as spindle speed, feed rate and depth of cut are essential to get the best machining outcome and the CFRP surface roughness [4].

Because of the outstanding mechanical and physical properties of solid carbide cutting tool in terms of its hardness, corrosion resistance at high temperatures and low coefficient of thermal expansion, it has been used widely in industrial fields and employed as cutting tool material [5]. However, there are limitations when it involves machining of higher grades of materials such as tool steels, hardened steels, nickel-based alloys, and some composites which are considered as difficult-to-machine (DTM) materials [6]. Machining processes that involve high cutting speed will adversely affect the cutting edges and cause wear problem [7]. The performance of cutting tool is affected by the growth of tool wear mechanisms which causes by cutting parameters. High cutting parameters resulting in high temperature and the hardness of cutting tool decrease as a result in changes in the microstructure. Therefore, choosing the best cutting parameters are important for each of machining process [8]. Thus, it is crucial on investigating the effect of cutting parameters (spindle speed, feed rate and depth of cut) to the hardness of carbide cutting tool and to analyze the most influence factor of changing the cutting tool hardness in machining CFRP.

2 Methodology

In this experiment, hardness of used carbide cutting tool which has cutter diameter (SD) of 8 mm, length of flute (CL) 20 mm and overall length (OVL) 60 mm is studied. Micro Vickers Hardness test is done using the Falcon 400/450 Hardness Testing Instrument. According to the ASTM-E384 (Standard Test Method for Micro indentation Hardness of Materials), micro hardness test uses calibrated machine to force a diamond indenter into the surface of the material being evaluated which the test ranges from 1 to 1000 gf. After indentation, the diagonals are measured with a light microscope after load removal. Furthermore, in micro indentation hardness test, it is assumed that there was no elastic recovery for the indentation after force removal. In terms of forces value used, the hardness number is the same even by the machine with higher test force. For optimum accuracy of measurement, the test should be performed on a surface without any defects that could affect the indentation or diagonal measurement. Minimum recommended distance between an indentation is needed in this project. Thus, with a length of diagonal, d_1 and d_2 are approximately 0.02 mm, distance between indentations should be more than 0.05 mm as suggested by the standard measurements. Following the standard, hardness value was measured at 5 points on the cutting tool with in between distance of 3 mm as in Fig. 1. The hardness value was taken at the critical point (P1) of the cutting tool as there is the point of heat generated while undergo the cutting process. In this project, the carbide cutting tool was used to mill Carbon Fiber Reinforce Plastic (CFRP) with dimensions of 300 mm (length) \times 200 mm (width) \times 3 mm (height). Three fiber orientations are used in the study which are 0° , 45° and 90° . The machining parameters are shown

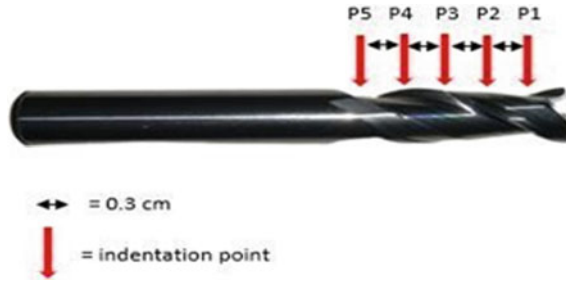


Fig. 1 Indentation points on the cutting tool

Table 1 Process parameters with their values

Factor	Spindle speed (A), rpm	Feed rate (B), mm/min	Depth of cut (C), mm
Low	2000	500	1
High	8700	1000	1.5

in Table 1. Hardness test and mathematical modelling analysis are done to study the effects of machining parameters on the hardness of the cutting tool.

3 Result

3.1 Hardness Test

Figure 2 shows the comparison data on hardness of carbide cutting tool at critical point. The cutting tool is used to mill three different fiber orientation of CFRP at spindle speed of 2000 and 8700 rpm with feed rate of 1000 mm/min and depth of cut 1.25 mm. As spindle speed decreases from 8700 to 2000 rpm, the hardness of the cutting tool is also decreasing in all three fiber orientations. According to [9], this phenomenon is due to less heat generated between the cutting tool and the workpiece. Low temperature did not help in softening the workpiece material hence require high cutting force to mill the CFRP and resulting to higher tool wear [10]. Hardness of carbide cutting tool is lowest during milling 90° fiber orientation at higher spindle speed (8700 rpm) due to dramatical increase in the cutting force for 90° fiber orientation resulting in mechanical properties change into the cutting tool [11]. Figure 3 shows the comparison data on hardness of carbide cutting tool at critical point. The cutting tool is used to mill three different fiber orientation of CFRP at feed rate of 500 and 1000 mm/min, spindle speed of 8700 rpm and depth of cut 1.25 mm. Lower feed rate depicts far better hardness value than higher feed rate at all three fiber orientations. Machining at lower feed rate (500 mm/min) recorded high hardness values which lies within 1693 HV and 1697 HV while higher feed rate

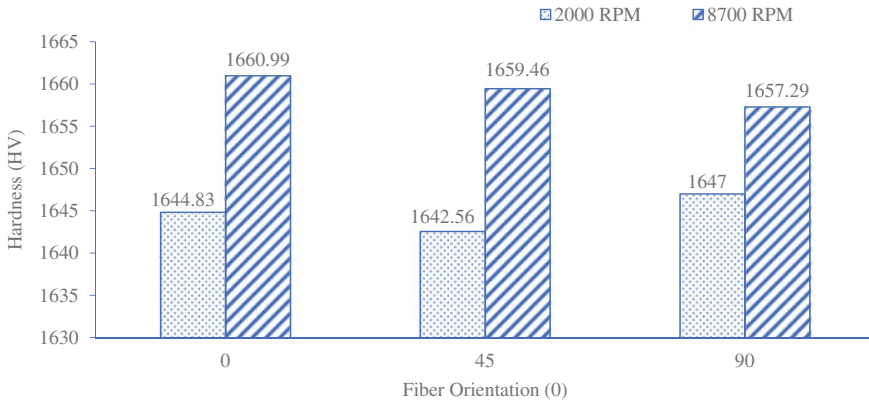


Fig. 2 Cutting tool hardness chart for machining at (8700 rpm) and (2000 rpm) spindle speed with constant feed rate (1000 mm/min) and depth of cut (1.25 mm)

(1000 mm/min) recorded much lower hardness values which lies within 1657–1661 HV. This result is supported by Ho-Cheng and Dharan [12] who mentioned that lower feed rate will produce high temperatures in milling CFRP which is needed to reduce the force in cutting process. Depth of cut. Figure 4 shows the comparison data on hardness of carbide cutting tool at critical point. The cutting tool is used to mill three different fiber orientation of CFRP at depth of cut 1 and 1.5 mm, spindle speed of 8700 rpm and feed rate of 750 mm/min. The hardness value for 0° and 45° orientation shows higher hardness value when machining using 1.5 mm depth of cut while 90° orientation has lower hardness value than using 1.0 mm depth of cut. However, the difference is not much because at higher depth of cut, the contact area between cutting tool and workpiece is bigger, thus the heat generated during the cutting tool started to make a contact with the work- piece is high enough that able to reduce the hardness of CFRP and helped in softening the CFRP hence the tool wear is lower [13].

3.2 Mathematical Modelling

The F-value of fiber orientation 0° , 45° and 90° is 247.32, 1569.07, 1462.73 respectively as the models are significant with a probability of $F < 0.001$. There is only 0.01% that the F-Model is wrong due to noise. The value Prob > F is less than 0.05, indicating the significance of the model terms. In these three-fiber orientation (0° , 45° and 90°), it shows that the factor with the most significant effect on the hardness of the cutting tool is feed rate with F-value that are equal to 819.60, 6565.60, 2922.68 respectively. This is expected as it has been reported by most of the research that feed rate is the primary factor that influences the hardness of cutting tool. The model

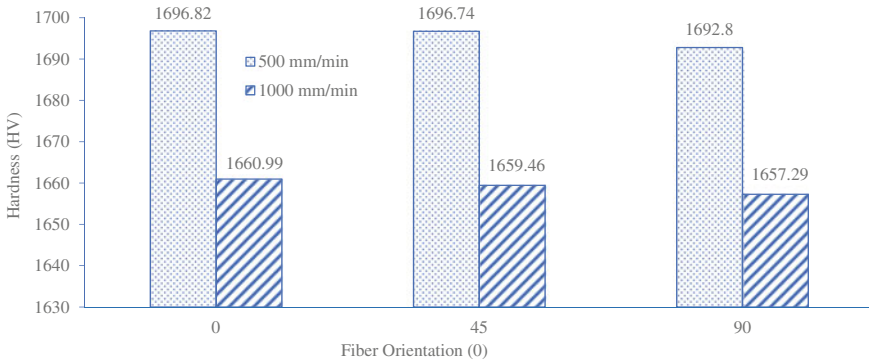


Fig. 3 Cutting tool hardness chart for machining at (500 mm/min) and (1000 mm/min) feed rate with constant spindle speed (8700 rpm) and depth of cut (1.25 mm)

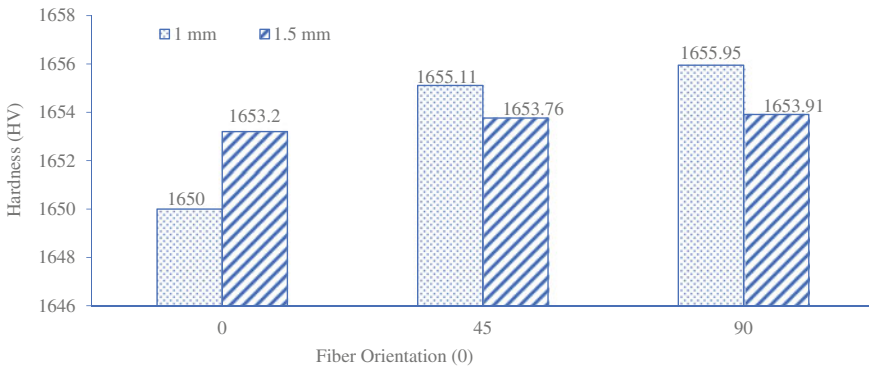


Fig. 4 Cutting tool hardness chart for machining at (1 mm) and (1.5 mm) depth of cut with constant spindle speed (5350 rpm) and feed rate (1000 mm/min)

is a good one as the Lack of Fit are not significant with 13.23% (0° fiber orientation), 5.15% (45° fiber orientation) and 5.93% (90° fiber orientation) relative to the pure error. The R² are 0.988 (0° fiber orientation), 0.9986 (45° fiber orientation) and 0.9863 (90° fiber orientation) which are high and close to 1. A desirable ratio for adequate precision should be greater than 4. In this model, the value of adequate precision is 53.51, 138.140 and 57.006 which are above 4.

4 Conclusion

High spindle speed (8700 rpm) resulted highest value of hardness compared to lower spindle speed (2000 rpm). At higher feed rate (1000 mm/min), cutting tool hardness depicts lower value than using lower feed rate (500 mm/min). As for the depth of

cut, there is no solid trend in the hardness value when varying the parameter as the difference is too small. Thus, for the tool hardness, it has been identified that the tool hardness is higher at higher spindle speed, lower feed rate and high depth of cut for all fiber orientations.

The optimization:

- i. 0° fiber orientation is by using 8698.44 rpm spindle speed, 500.00 mm/min feed rate and 1.50 mm depth of cut.
- ii. 45° fiber orientation, 8700 rpm spindle speed, 500.03 mm/min feed rate and 1.50 mm depth of cut.
- iii. 90° fiber orientation, 8699.98 rpm spindle speed, 500.00 mm/min feed rate and 1.50 mm depth of cut.





Acknowledgements The authors would like to thank the Government of Malaysia and International Islamic University Malaysia for their financial support under grant number: FRGS/1/2018/TK03/UIAM/03/1.

References

1. Karaguzel U, Olgun U, Uysal E, Budak E, Bakkal M (2015) Increasing tool life in machining of difficult-to-cut materials using nonconventional turning processes. *Int J Adv Manuf Technol* 77(9):1993–2004
2. Nurhaniza M, Ariffin MKAM, Mustapha F, Baharudin BTHT (2016) Analyzing the effect of machining parameters setting to the surface roughness during end milling of CFRP-aluminium composite laminates. *Int J Manuf Eng* 206:1–9
3. Hosokawa A, Hirose N, Ueda T, Furumoto T (2014) High-quality machining of CFRP with high helix end mill. *CIRP Ann* 63(1):89–92
4. Mustafa D, Hasan A (2019) The effect of cutting parameters on tool wear during milling of carbon fibre reinforced polymer (CFRP) composites. *Mater Sci* 25:42–46
5. Kishawy HA, Massoom ZF (2019) Prediction of critical thrust force generated at the onset of delamination in machining carbon reinforced composites. *Int J Adv Manuf Technol* 103(5):2751–2759
6. Muhamad Khairussaleh NK, Che Haron C, Ghani AJ (2016) Study on wear mechanism of solid carbide cutting tool in milling CFRP. *J Mater Res* 31(13):1893–1899
7. Sheikh A (2009) Machining of polymer composites. In: Sheikh-Ahmad JY (ed) *Nontraditional machining of FRPs*. In: *Machining of polymer composites*. Springer, Boston, MA
8. Haijin W, Sun J, Zhang D, Guo K, Jianfeng L (2016) The effect of cutting temperature in milling of carbon fiber reinforced polymer composites. *Compos A Appl Sci Manuf* 91(1):380–387
9. Ogedenngbe TS, Okediji AP, Yussouf AA, Aderoba OA, Abiola OA, Alabi IO, Alonge OI (2019) The effects of heat generation on cutting tool and machined. *J Phys* 1378:1–11
10. Zhao LHN, Wang JP, Wu CQ, Zhao YJ, Xu J, Liu X, Zhu WQ (2020) Damage behaviors of unidirectional CFRP in orthogonal cutting: a comparison between single-and multiple-pass strategies. *Composites Part B: Engineering*, vol 185. pp 107774
11. Wang DH, Ramulu M, Arola D (1995) Orthogonal cutting mechanisms of graphite/epoxy composite. Part I: unidirectional laminate. *Int J Mach Tools and Manuf* 35(12):1623–1638
12. Ho-Cheng H, Dharan CKH (1990) Delamination during drilling in composite laminates. *J Eng Indus* 112(2)
13. Prakash R, Krishnaraj V (2014) Experimental study on edge trimming of unidirectional CFRP composites. *Adv Mater Res* 207–213

Cutting Temperatures and Their Effects on Drilling of NFRP Composites Using Taguchi Method



Muhammad ‘Izzudin Mohd Zaid, Suhaily Mokhtar ,
Aishah Najiah Dahnel , Natasha A. Raof ,
and Nor Khairusshima Muhamad Khairussaleh 

Abstract Natural fiber reinforced polymer (NFRP) composites become an interesting topic to be discussed among researchers due to their uniqueness that are different from conventional materials. The nature of this composite that are inhomogeneous and anisotropic becomes the biggest challenges to drill them. The defects such as delamination, rough surface, and fuzzing during drilling will affect the assembly of mechanical components because of the inaccuracy of the holes. These lead to the rejection of the parts and causes the big losses to the manufacturers. In this study, an investigation was done to investigate the influence of drilling parameters to the temperature rising and the quality of the holes. The experiments were conducted in drilling of woven kenaf/epoxy composite by using uncoated carbide twist drill. The results of the experiment were analyzed by using the Taguchi analysis. By using this method, the optimum parameters can be found to obtain minimal surface damages.

Keywords NFRP · Drilling · Temperature · Delamination · Surface roughness · Taguchi

1 Introduction

Natural fiber reinforced polymer (NFRP) composites are defined as the products of combination of the natural fibers with resin, either synthetic or natural in the form of thermoset or thermoplastic [1]. For domestic usage, plants fibers such as hemp, jute, coir, sisal, kenaf, flax and bamboo are widely used due to their availability. Besides of their lower cost and safer to be used, their mechanical strength is comparable to glass fiber reinforced polymer (GFRP) composites [2]. In automotive industry, natural fiber composites have been used for making trim components of cars such as door panels, seatbacks, headliners, and package trays [3]. This is due to the lower weight material can reduce fuel consumption and prevent pollution to be occurred.

M. ‘Izzudin Mohd Zaid · S. Mokhtar (✉) · A. N. Dahnel · N. A. Raof · N. K. M. Khairussaleh
Department Manufacturing and Materials Engineering, Kulliyah of Engineering, International
Islamic University Malaysia, Gombak Selangor, Malaysia
e-mail: suhailymokhtar@iium.edu.my

Drilling of fibrous composites is a challenging task due to their nature that is anisotropic and inhomogeneous. Suhaily et al. [4] stated that drilling of NFRP composites tends to induce material damages such as edge chipping, fuzzing, delamination, burning and spalling. In drilling process, the selection of cutting parameters such as spindle speed, feed rate, and tool geometry should be considered as they contribute to determining the quality of the final product.

Surface roughness is one of the key factors that influence the surface quality of the drilled holes. According to Kumar and Sing [5], surface roughness of the drilled hole is important when the parts are subjected under fatigue load and fastener load. In drilling process, low surface roughness is required to ensure the quality of the holes. According to Jayabal and Gurusideswar [6], the surface roughness of the holes depends on the feed rate and spindle speed adopted during the drilling process. Samy et al. [7] stated that the higher overcut and poor circularity of the drilled holes may increase the surface roughness and produce poor fits. Tan et al. [8] proposed that the lower surface roughness can be achieved when drilling the hybrid carbon/glass composite by adopting 7500 RPM speed and 0.08 mm/rev feed rate. By using high speed and low feed rate, it will cause the high increment in temperature. The high temperature will soften the matrix and will result in finer surface roughness. Sorrentino et al. [9] stated that the drilling temperature will increase by increasing the spindle speed and reducing the feed rate. This is because the lower feed rate causes the longer time where the cutting tool and the workpiece in contact.

From the literature review, it was found that to optimize the cutting parameters is very challenging to minimize the damage and ensure better surface finish. Therefore, this current study is focusing on the investigation of cutting temperature and their effects to the quality of the final product by using woven kenaf/epoxy as a sample.

2 Experimental Procedures

2.1 Material

The material that was used as a specimen in the experiment is a woven kenaf/epoxy composite with thickness of 3 mm. The detail of the composite is tabulated in Tables 1, 2 and 3.

2.2 Procedures

The drilling experiment was conducted by using CNC milling machine model GATE/ECM 1. The holes were made on the specimen by using 6 mm uncoated carbide drill bits with different point angles (118 and 135°). The drilling experiment was done by using L4 array of Taguchi Method and under dry condition. At the same

Table 1 The details of fabrication of woven kenaf/epoxy composites laminates

Items	Descriptions
Fabrication method	Hand lay-up method
Fiber material	Kenaf fibers
Resin used	Epoxy resin
Types of fibers	Woven mat type
Fiber orientation	0 and 90 ° woven

Table 2 Mechanical properties of kenaf fiber

Kenaf properties	Unit
Diameter of fiber (microm)	55.27 (avg)
Density (g/cm ³)	1.222
Tensile modulus (GPa)	51.98
Tensile strength (MPa)	504.78
Specific modulus (m/s) ²	42.5 × 10 ⁶
Specific strength (kNm/kg)	413.1
% elongation at break (%)	9.8

Table 3 Mechanical properties of epoxy resin

Epoxy properties	Unit
Viscosity at 20 degree (mPa.s)	1200
Density (g/cm ³)	1.13
Tensile modulus (GPa)	3.60
Tensile strength (MPa)	67
Specific modulus (m/s) ²	3.18
Specific strength (kNm/kg)	59.3
% elongation at break (%)	6.0

time, a thermal camera was placed near the machine to monitor the temperature rising during the process. Figure 1 shows the diagram of machine setup. The surface roughness (Ra) of the drilled hole was measured by using Alicona Infinite FocusSL.

2.3 Taguchi Method

Taguchi method was used to analyze the two levels of cutting parameters to get the optimum quality of the holes. The factors with their corresponding values of different levels were tabulated in Table 4. The results of experiments based on Taguchi’s L4 Orthogonal Array was shown in Table 5.

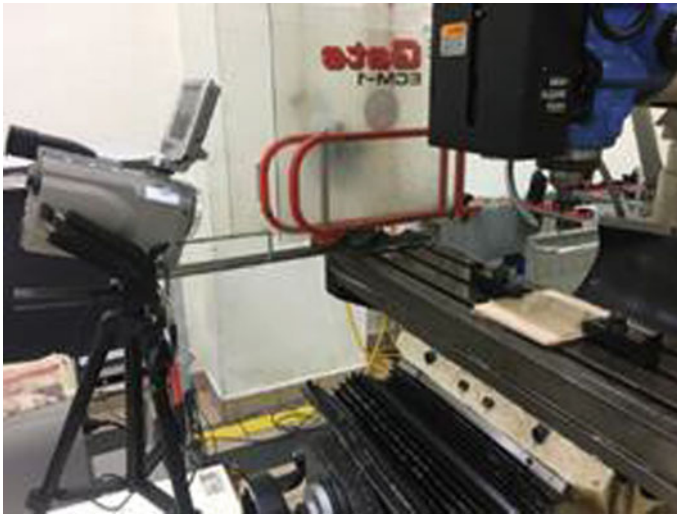


Fig. 1 The position of thermal camera

Table 4 The factors and their levels

Parameters	Levels	
	1	2
Spindle speed (RPM)	500	2500
Feed rate (mm/rev)	0.3	0.5
Point angle (°)	118	135

Table 5 The factors and their levels

No	Spindle speed (RPM)	Feed rate (mm/rev)	Point Angle (°)	Ra (µm)	Temperatures (°)
1	500	0.30	118	2.37	79.4
2	500	0.50	135	1.88	50.9
3	2500	0.30	135	1.06	77.2
4	2500	0.50	118	1.52	65.3

3 Result and Discussion

3.1 Effect of Drilling Parameters on Surface Roughness

According to Table 6, the spindle speed is the major factor that influences the surface roughness, followed by point angle and feed rate. The data of S/N ratios were plotted in the graph as presented in Fig. 2.

Table 6 Response table for S/N ratios of surface roughness

Level	Spindle speed	Feed rate	Point angle
1	-6.48	-3.994	-5.560
2	-2.071	-4.557	-2.991
Delta	4.408	0.562	2.568
Rank	1	3	2

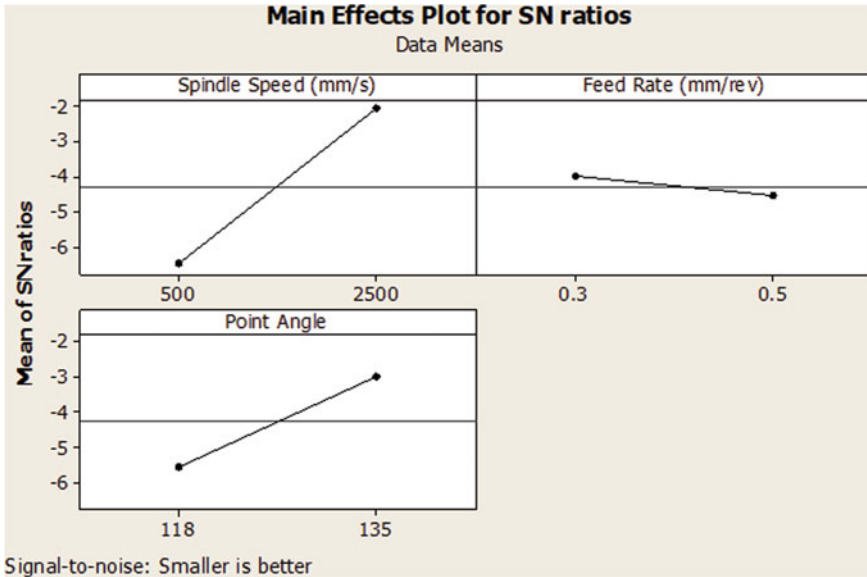


Fig. 2 Main effects plot for S/N ratios of surface roughness

According to the graph, the surface roughness can be minimized by employing high spindle speed. It was clearly presented in the table that 2500 RPM produces the S/N ratio of -2.071 which is 4.408 higher than 500 RPM of spindle speed. The high speed of the spindle increases the heat flow on the workpiece as mentioned by Samy et al. [10]. From the experiment, it was found that the temperature increased until 65.3–77.2 °C when 2500 RPM was employed. This situation is favorable during drilling to minimize the surface roughness as the material enters the ductile deformation zone [11].

The point angle is the second factor that influences the surface roughness. From the S/N ratios data, 135°-point angle of the drill produces -2.991 S/N ratio while 118° was in -5.560 of S/N ratio which is 2.568 lower. The size point angle is a factor that influences the drilling temperature. The higher point angle will increase the drilling temperature as the area of the frictional contact between the cutting tool and workpiece is wider [9]. The wider the frictional area may increase the rate of heat dissipation. During the drilling process, heat tends to accumulate at the tool tip. The accumulated heat at the tool softened the matrix and resulted in lower surface roughness.

Based on the graph, the feed rate is seemed to be not affected much the surface roughness since it has the lowest gradient. However, the lower feed rate should be used to minimize the surface roughness as shown in the graph. It was proven in the data that 0.30 mm/rev of the feed rate was result in the value of S/N ratio to be 0.562 higher than 0.50 mm/rev. From the experiment, lower feed rate is favourable to minimize the surface roughness. According to Sorrentino et al. [9], the higher feed rate reduced the drilling time, thus decreasing the rubbing action between the workpiece and the cutting tool. This situation led to the reduction of drilling temperature. During drilling, it is preferable to be done with high temperature to ensure the smoother surface roughness as agreed by Wang et al. [11].

4 Conclusion

From this study, the heat generated during drilling is dependent on the machining parameters such as spindle speed, feed rate, and point angle. These parameters determine the time consumption during drilling the composites. The higher heat will be generated if the time taken to drill the composite is long. This is because it will be the long time where the cutting tool and composite are in contact. It was found that the combination of 500 RPM spindle speed, 0.3 mm/rev feed rate, and 118 ° point angle has result in the highest temperature which is 79.4 °C with the drilling time of 1.92 s. The higher spindle speed also is the factor that increase the heat generated during drilling. This is because it increases the rate of friction between the cutting tool and the workpiece. It was found that 2500 RPM spindle speed causes the temperature increase until 65.3–77.2 °C.

Acknowledgements Authors would like to thank the International Islamic University Malaysia and Ministry of Education Malaysia for support of this work under the Fundamental Research Grant Scheme (FRGS/1/2018/TK03/UIAM/03/02).

References

1. Mokhtar S et al. (2019) Effects of drilled area temperatures on drilling of NFRP composites : a review. pp 1–5
2. Lau KT, Hung, Yan P, Zhu MH, Huis D (2018) Properties of natural fibre composites for structural engineering applications. In: Composites Part B: engineering vol 136. pp 222–233
3. Hui D (2019) Kenaf fiber composites: a review on synthetic and biodegradable polymer matrix. *J Kejuruter* 31(1):65–76
4. Suhaily M, Hassan CHC, Jaharah AG, Azmi H, Afifah MA, Khairusshima MKN (1957) Study on drilling induced delamination of woven kenaf fiber reinforced epoxy composite using carbide drills. In: AIP conference proceedings, vol 1957
5. Kumar D, Sing KK (2017) Experimental analysis of delmination, thrust force and surface roughness on drilling of glass fiber reinforced polymer composites material using different drills. *Mater Today: Proc* 4(8):7618–7627

6. Jayabal S, Gurusideswar S (2017) Prediction of thrust force and torque using regression model in drilling of natural fibre reinforced composites. In: Proceeding of the national conference on discover real engineers and mechanical simulations
7. Samy GS, Kumaran ST (2017) Measurement and analysis of temperature, thrust force and surface roughness in drilling of AA (6351_B4C composite. *Measurement: J Int Measurem Confederation* 103(6351):1–9
8. Tan CL, Azmi AI, Muhammad N (2016) Delamination and surface roughness analyses in drilling hybrid carbon/glass composite. *Mater Manuf Process* 31(10):1366–1376
9. Sorrentino L, Turchetta S, Bellini C (2017) In process monitoring of cutting temperature during the drilling of FRP laminate. *Compos Struct* 168:549–561
10. Samy GS, Kumaran ST (2017) Measurement and analysis of temperature, thrust force and surface roughness in drilling of AA (6351)-B4C composite. *Meas J Int Meas Confed* 103(6351):1–9
11. Wang H, Zhang X, Duan Y (2018) Effects of drilling area temperature on drilling of carbon fiber reinforced polymer composites due to temperature-dependent properties. *Int J Adv Manuf Technol* 96(5–8):2943–2951

Investigation of Microgels and Double Crosslinked Microgels Containing 2-Carboxyethyl Acrylate (CEA)



Syazwani Mohd Zaki  and Sharan Musa

Abstract In this work, a new pH-responsive microgel (MGs) containing 2-carboxyethyl acrylate (CEA) as a comonomer. MGs were synthesized by emulsion polymerization and denoted as CEAX, whereby X shows different CEA content in MGs. These MGs samples were denoted as CEA14, CEA21 and CEA28. The CEA MGs were vinyl-functionalized with GMA and used to prepare three DX MGs gels denoted as DX CEA21, DX CEA28 and a blended system that contained both CEA21 and CEA28 to observe the effect of a binary system. The latter system is denoted as DX BL-CEA. The z-average diameters (d_z) obtained from DLS measurements for these three systems are 39 nm for CEA14, 84 nm for CEA21 and 255 nm for CEA28. The performance of the gels was further studied by rheology analysis and from rheology, G' values decreased in the order: DX MAA (70.2 kPa) > DX BL-CEA (37.3 kPa) > DX CEA28 (34.5 kPa) > DX CEA21 (4.68 kPa). The MG size increased strongly with increased CEA content used to prepare the MGs. The modulus (E) value of the blend system was remarkably very close to the DX CEA28 gel indicating that CEA28 distributed more stress within these blend gels. The ductility of DX CEA gels was greater than the established DX MAA gels. The data in this study are the first example of DX MGs prepared using a carboxylic acid monomer other than MAA.

Keywords Hydrogels · pH-responsive microgels · CEA · Polymerization

1 Introduction

In general, the CEA molecule is structurally like 2-hydroxyethyl acrylate (HEA) but has COOH groups. CEA contains an ester group and is a vinyl acid monomer. In addition, CEA is a water-soluble monomer, has low toxicity and is frequently used in

S. M. Zaki (✉)

Department of Manufacturing and Materials Engineering, Kuliyyah of Engineering, International Islamic University Malaysia, Gombak, 53100 Kuala Lumpur, Malaysia
e-mail: syazwani_mohdzaki@iium.edu.my

S. Musa

School of Materials and Mineral Resources Engineering, Universiti Sains Malaysia, Nibong Tebal, 14300 Pulau Pinang, Malaysia

the co-polymerization process. This work aims to provide an advanced understanding of the effect of vinyl acid monomer on the enhancement of mechanical properties of MGs and DX MGs. CEA has been selected to determine the effect of the monomer structure on MG particle growth and gel properties. CEA molecule generally is structurally similar to 2-hydroxyethyl acrylate (HEA) but has -COOH groups [1]. This CEA contains an ester group which generates a vinyl acid monomer with two carbonyl groups. In addition, CEA is a water-soluble monomer, has low toxicity and is frequently used in the copolymerization process [1–3]. CEA and MAA differ in their ionization degree, significantly affecting the swelling properties [4]. The rheological properties of the systems at a steady state were strongly influenced by the degree of ionization and thus by the pH [5]. The distribution related to carboxylic acids monomers (CEA or MAA) between water and organic phase are different and the CEA distributions are much closer to AA than MAA [1]. According to the previous literature, tensile strength for CEA-based (water-soluble monomers) is much higher than other water-based monomers [3]. The extra methyl group in MAA makes it significantly more non-polar than AA, even though each is completely water-soluble. When the molecular structures of CEA and AA are compared, CEA has two additional non-polar methylene groups and a polar ester group. So, despite the higher molecular weight of CEA, it appears to have a polarity similar to AA [1]. The distribution behaviour of carboxylic acid groups in CEA in the polymer system (such as emulsion polymerization) depends on the aqueous or organic phase and the pH of those phases [1]. A significant difference between CEA and other carboxylic acids is the flexibility, as poly(CEA) has a low glass transition temperature (T_g) [6]. Besides, CEA was commercially available and had a higher molecular weight than MAA (144 g/mol and 86 g/mol for MAA). Therefore, CEA can be more compatible with other comonomers and may produce a uniform co-polymer when prepared by free-radical copolymerization. The highest pK_a value of CEA is 4.99168. As reported in the literature, pK_a value for MAA and AA are 4.45 and 4.23 [1].

In this work, CEA-based MGs were compared to the MAA-based MGs reported in previous work [1] and should contribute to further understanding of these two systems. The behaviours of the MGs containing different CEA content concerning their particle size, swelling ability, morphology, and mechanical properties as enhancement in the properties were analyzed. The systems undergo functionalized modification with glycidyl methacrylate (GMA) to enable the subsequent formation of DX MGs, DX CEA. Three major systems prepared by emulsion polymerization were CEA14, CEA21 and CEA28, which contained a different amount of CEA. Meanwhile for gels system denoted as DX CEA21 and DX CEA28, refers to DX MGs prepared with 21 mol.% and 28 mol.% of CEA MGs. Here, we invoke the general concept of using a blended system to modulate gel mechanical properties. The blend DX MG is denoted as DX BL-CEA, which comprises functionalized CEA21 and CEA28 MGs. The DX process was started with a mixed dispersion of MGs in latex form. The physical gel was formed by pH-triggered swelling of the MG particles and is termed GM-CEAX, where X is the content of CEA in mol.%. Subsequently, the covalently interlinked gels were achieved by heating in the presence of an initiator (APS), NaOH and accelerator (TEMED), termed DX CEAX. Therefore,

the aims are to determine the effect of CEA on microgels (MG) particle growth and to investigate the mechanical properties of double-crosslinked (DX) microgels.

2 Materials and Method

In this work methyl methacrylate (MMA, 99%), methacrylic acid (MAA 99%), glycidyl methacrylate (GMA 97%), 2-carboxyethyl acrylate (CEA), sodium dodecyl sulphate (SDS), ammonium persulfate (APS, xx%), NaNO₃ (> 99%), NaOH, ethylene glycol dimethacrylate (EGDMA 98%) and N,N,N',N'-tetramethylethylenediamine (TEMED, 99%) were obtained from Sigma-Aldrich and used as received. All aqueous solutions were prepared using high purity deionized water.

MGs were prepared by emulsion polymerization at 80 °C. A brief description of the procedures is given here for MGs containing MMA, CEA and EGDMA. Firstly, SDS (1.214 g) was dissolved in deionized water (240 g) and added to the glass reaction vessel. Before the monomer feed started, APS (0.60 mmol) was dissolved in deionized water and added to the vessel. The monomer feed containing MMA (0.419 mol.), CEA and EGDMA (5.35 mmol) was prepared with mechanical stirring and fed into the reaction vessel at a constant rate of 0.317 ml/min. The masses of CEA used to prepare CEA14, CEA21 and CEA28 were 0.069 mol, 0.113 mol and 0.165 mol, respectively. After the comonomer solution feed was finished, the reaction was continued for 1 h. Finally, the product was purified by extensive dialysis using water for 4 days. The MGs obtained are denoted as CEA14 (14 mol%), CEA21 (21 mol%) and CEA28 (28 mol%). Data for an MG from related work that contained methacrylic acid (MAA) in place of CEA is included for comparison in this study. That MG contained MMA, MAA and EGDMA with MAA concentration of 38 mol%. Table 1 shows the composition of monomers used to prepare CEA MGs. The hydrodynamic diameter measurements of the MGs were carried out using dynamic light scattering (DLS) with a Malvern Nano Zetasizer ZS90 instrument. Dynamic rheology measurements were conducted using a TA Instruments AR-G2 temperature-controlled rheometer equipped with an environmental chamber. A plate geometry of 20 mm diameter was used with a solvent trap to prevent the sample from evaporating. Uniaxial compression measurements were conducted using an Instron series 5569 load frame equipped with a 100 N load cell. SEM images for the gels were recorded using a Philips XL30 FEG-SEM HKL EBSD instrument with an accelerating voltage of 15 kV. TEM images were obtained using a Philips CM20 instrument. All samples were prepared on 400 mesh copper grids, and analysis was operated at 200 keV.

Table 1 Composition of monomers used to prepare CEA MGs

System	CEA (mol.%)	MMA (mol.%)	EGDMA (mol.%)
CEA14	14	85	1
CEA21	21.4	77.7	0.90
CEA28	28	71.14	0.86

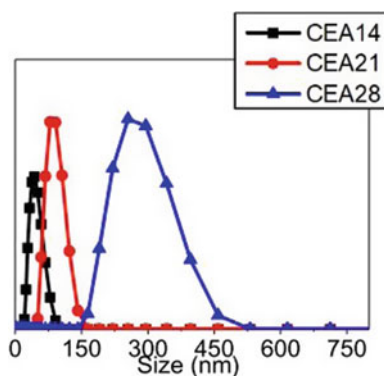
3 Result and Discussion

This section provides the findings of MGs prepared by adding CEA as a comonomer using emulsion polymerization and its effect on particle size. The physical and mechanical properties of these newly synthesized MGs are studied. We also compare the results of MGs and DX MGs containing MAA as comonomer reported by Milani et al. [1]. In addition, DLS measurements were carried out on all samples of microgels to investigate how CEA content and functionalization affected the particle diameters and the swelling ratio.

3.1 Dynamic Light Scattering and Zeta Potential of CEA Microgels

The main monomers used to prepare the microgels were MMA, CEA and EGDMA, while SDS acted as a surfactant, EDGMA as a crosslinker, and APS was an initiator. Four different structures of monomers with various CEA content were prepared to understand the relationship of CEA with particle size and distribution. The DLS size distribution of each system can be seen in Fig. 1. From this graph, it was observed that CEA14 and CEA21 have narrow distributions. compared to CEA28. However, CEA28 still has a low polydispersity of 0.087.

Fig.1 Size distribution obtained from DLS for CEA14, CEA21 and CEA28



3.2 Morphological Studies

Figure 2 depicts SEM morphologies for CEA14, CEA21 and CEA28 systems. From the SEM images, it could be that higher CEA content resulted in bigger particle size. The particle sizes for all systems are homo-dispersed and in spherical shape. Figure 3 shows the morphologies for CEA14, CEA21 and CEA28 obtained by TEM and the particle size obtained is consistent with SEM results. For justification, the MGs were further characterized by DLS and zeta potential. The z-average diameters (d_z) from DLS measurements for these three systems are 39 nm for CEA14, 84 nm for CEA21 and 255 nm for CEA28 at pH 4.0 (collapsed state). These values are larger than the number-average diameters from TEM (see Fig. 3) due to the presence of water in the dispersed particles and their polydispersity. The data obtained showed that the MGs size strongly increased when CEA content increased. In general, surfactant concentration, monomer concentration and initiator are important parameters in determining particle size [9]. Also, it is worth pointing out that monomer's surfactant concentration and molecular weight significantly influence generating smaller particle sizes for dispersion polymerization.

The mechanical properties of the new DX MGs were analysed by rheology technique. Frequency sweep data are shown in Fig. 4. Frequency sweep data show that the storage modulus (G') and loss modulus (G'') values are not dependent on the

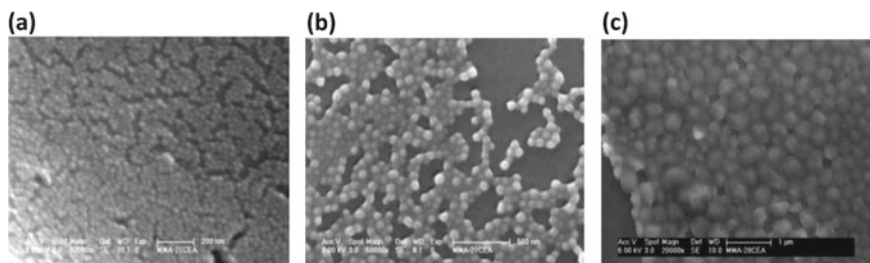


Fig. 2 SEM images for **a** CEA14, **b** CEA21 and **c** CEA28 particles

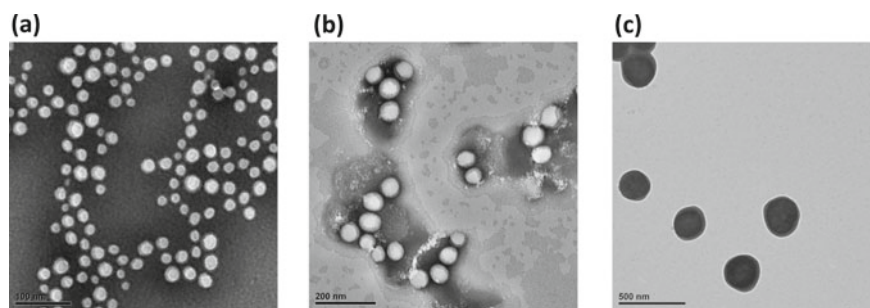


Fig. 3 TEM images for **a** CEA14, **b** CEA21 and **c** CEA28 particles

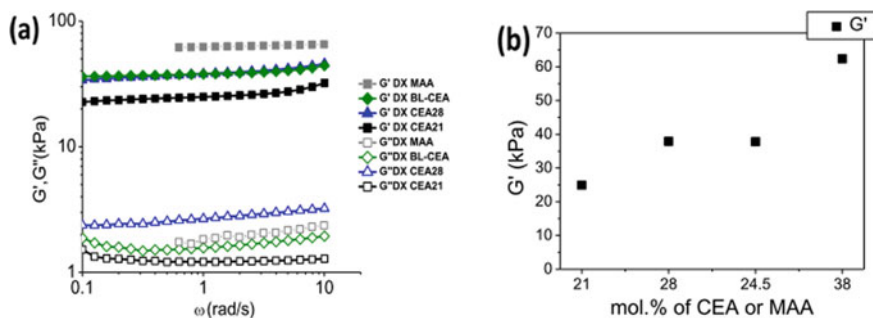


Fig. 4 Dynamic rheology data showing **a** storage modulus (G') and **b** G' value for DX CEA21, DX CEA28, DX BL-CEA and DX MAA gels

frequency, which is indicative of solid-like behaviour. This behaviour was apparently like the G' values shown for DX MAA gel [10, 11]. The values for G' for each system were obtained at angular frequency, $\omega = 1$ rad/s. From the data obtained, the G' values at 10 rad/s decrease in the order: DX MAA (70.2 kPa) > DX BL-CEA (37.3 kPa) > DX CEA28 (34.5 kPa) > DX CEA21 (4.68 kPa). This indicates that the crosslinking was strongest in the DX MAA gels and least in the DX CEA21 gels. Further analysis for the gel transition was obtained from the values of $\tan \delta$ ($= G'' / G'$) demonstrated low-frequency dependency, indicating the gels were low viscous and mostly elastic [12]. For DX CEA28 gel, the $\tan \delta$ values increased as ω increased, indicating energy dissipation by intermolecular friction. In DX CEA28, more ionic groups were present compared to DX CEA21 gel.

4 Conclusion

In this study, we have investigated the effects of adding CEA as a co-monomer during emulsion polymerization on MG and DX MG properties. We concluded that the MG size increased strongly with increased CEA content to prepare the MGs. An improvement in the ductility was evident when compared to the established DX MAA gels, which may favour biomaterial applications. The effect of blends of MGs on the properties of the DX CEA gels was also studied. The modulus (E) value of the blend system was remarkably close to the DX CEA28 gel, indicating that CEA28 distributed more stress within these blend gels. The data in this study are the first example of DX MGs prepared using a carboxylic acid monomer other than MAA.

Acknowledgements This work was supported by the University of Manchester and International Islamic University Malaysia.

References

1. Tripathi AK, Vossoughi J, Sundberg DC (2015) Partitioning of 2-carboxyethyl acrylate between water and vinyl monomer phases applied to emulsion polymerization: comparisons with hydroxy acrylate and other vinyl acid functional monomers. *Ind Eng Chem Res* 54(9):2447–2452
2. Tripathi AK, Sundberg DC (2013) Partitioning of functional monomers in emulsion polymerization: distribution of carboxylic acid monomers between water and monomer phases. *Ind Eng Chem Res* 52(9):3306–3314
3. Pietrzak E, Wicinska P, Szafran M (2016) 2-carboxyethyl acrylate as a new monomer preventing negative effect of oxygen inhibition in gel casting of alumina. *Ceram Int* 42(12):13682–13688
4. Swift T, Swanson L, Geoghegan M, Rimmer S (2016) The pH-responsive behaviour of poly(acrylic acid) in aqueous solution is dependent on molar mass. *Soft Matter* 12(9):2542–2549
5. Charbonneau C, Chassenieux C, Colombani O, Nicolai T (2012) Progressive freezing-in of the junctions in self-assembled triblock copolymer hydrogels during aging. *Macromolecules* 45(2):1025–1030
6. Milani AH, Bramhill J, Freemont AJ, Saunders BR (2015) Swelling and mechanical properties of hydrogels composed of binary blends of inter-linked pH-responsive microgel particles. *Soft Matter* 11(13):2586–2595
7. Suzuki D, Horigome K (2011) Binary mixtures of cationic and anionic microgels. *Langmuir* 27(20):12368–12374
8. Milani AH, Fielding LA, Greensmith P, Saunders BR, Adlam DJ, Freemont AJ, Hoyland JA, Hodson NW, Elsayy MA, Miller AF, Ratcliffe LPD, Mykhaylyk OO, Armes SP (2017) Anisotropic pH-responsive hydrogels containing soft or hard rod-like particles assembled using low shear. *Chem Mater* 29(7):3100–3110
9. Zhu M, Lu D, Wu S, Lian Q, Wang W, Milani AH, Cui Z, Nguyen NT, Chen M, Lyon LA, Adlam DJ, Freemont AJ, Hoyland JA, Saunders BR (2017) Responsive nanogel probe for ratiometric fluorescent sensing of pH and strain in hydrogels. *ACS Macro Lett* 6(11):1245–1250
10. Liu R, Milani AH, Saunders JM, Freemont TJ, Saunders BR (2011) Tuning the swelling and mechanical properties of pH-responsive doubly crosslinked microgels using particle composition. *Soft Matter* 7(19):9297–9306
11. Cui Z, Wang W, Obeng M, Chen M, Wu S, Kinloch I, Saunders BR (2016) Using intra-microgel crosslinking to control the mechanical properties of doubly crosslinked microgels. *Soft Matter* 12(33):6985–6994
12. Milani AH, Freemont AJ, Hoyland JA, Adlam DJ, Saunders BR (2012) Injectable doubly cross-linked microgels for improving the mechanical properties of degenerated intervertebral discs. *Biomacromol* 13(9):2793–2801

Magnetic Properties of High Entropy Alloys as Electromagnetic Wave Absorber



Ain Najwa Md Saupi, Norhuda Hidayah Nordin, Nur Azam Abdullah, and Muhammad Hanafi Azami

Abstract High entropy alloys (HEAs) feature several unique properties in terms of physical, mechanical, and chemical compared to conventional alloys. As a functional material, some HEAs show superior soft magnetic characteristics as well as superior mechanical properties. This paper reported the magnetic properties of $\text{FeCoNi}(\text{B}_x\text{Al}_{1-x})_{0.1}\text{Si}_{0.1}$ ($x = 0, 0.2, 0.4, 0.5, 0.9, 1.0$). The HEAs were characterized under optical microscopic and X-ray diffraction. The morphology of HEA samples shows some lamellar patterns that were produced during the solidification process. The X-ray diffraction result of the B0.4 and B1.0 shows the existence of Fe_2B intermetallic phase and primary face-centered cubic FCC simple solid solution phase and a minor body-centered cubic BCC phase that forms due to the entropy effect. A Vibrating Sample Magnetometer (VSM) was used to study the magnetic properties of the sample at different boron content. The result obtained in this study will be used as a preliminary study for the utilization of $\text{FeCoNi}(\text{B}_x\text{Al}_{1-x})_{0.1}\text{Si}_{0.1}$ as electromagnetic wave absorbance material.

Keywords Electromagnetic wave absorbance · FeNiCo alloy · High entropy alloys (HEAs) · Magnetic properties

1 Introduction

The Internet of Things (IOT) is transforming our lifestyle as we enter the 5G era. While we appreciate the ease that modern technologies provide, we should not overlook the negative consequences [1]. The widespread usage of electronic technologies and wireless gadgets such as cell phones, local area networks, and satellite airing systems has been discovered to disrupt its surroundings [2]. It also has caused serious

A. N. M. Saupi · N. H. Nordin
Department of Manufacturing and Materials Engineering, International Islamic University
Malaysia, Jalan Gombak, 53100 Kuala Lumpur, Malaysia

N. A. Abdullah · M. H. Azami (✉)
Department of Mechanical and Aerospace Engineering, International Islamic University
Malaysia, Jalan Gombak, 53100 Kuala Lumpur, Malaysia
e-mail: hanafiazami@iium.edu.my

© The Author(s), under exclusive license to Springer Nature Singapore Pte Ltd. 2023
Md. A. Maleque et al. (eds.), *Proceeding of 5th International Conference on Advances in Manufacturing and Materials Engineering*, Lecture Notes in Mechanical Engineering,
https://doi.org/10.1007/978-981-19-9509-5_82

pollution on environment and threatened human health through emitted electromagnetic (EM) waves [2, 3]. As a result, EM wave absorption materials have gotten a lot of interest among researchers as promising materials for reducing EM wave pollution [4].

Numerous studies have stated that high entropy alloys (HEAs) have shown outstanding properties in term of physical, mechanical, and chemical compared to conventional alloys. Thanks to its versatile features of high entropy alloys (HEAs) including numerous principles alloying elements, nowadays HEAs attracting a lot of interest in developing new alloy designs [5]. However, most of the developed HEA nowadays are focusing on mechanical properties [6, 7] only.

According to Yeh [8] and Fu et al. [9], the high entropy core effect in HEA plays a most important role in simplifying the microstructures, which are mostly made up of simple solid solution (SS) phases with body centered cubic (BCC) and face centered cubic (FCC) structures. Because of their strong entropy influence, most HEAs are found to have simple crystal structures such as solid solution phases that do not include the intermetallic phases [10]. The formation of simple structures from the equiatomic multiple component elements contributes to the uniqueness of HEAs, including great hardness and strength, and high stability in thermal, unique electrical characteristics, remarkable properties of magnetism, and strong corrosion resistance [11–13]. Traditional alloys, on the other hand, have drawbacks for instance poor mechanical behavior, and lower electrical resistivity of alloys. Several HEAs, on the other hand, exhibit good quality soft magnetic properties and outstanding mechanical qualities [14, 15].

$\text{FeCoNi}(\text{B}_x \text{Al}_{1-x})_{0.1}\text{Si}_{0.1}$ composition with additional of boron [10] is chosen here because research has shown that the addition of boron reduces the stability of the disordered BCC solid solution and encourages the production of secondary phases. The replacement of aluminum with additional of boron was since both elements belong to the same group in the periodic table. Therefore, their valence electrons, chemical compositions, and mixing entropies will be the same [10] and due to few understandings of how boron addition affects the microstructure and magnetic characteristics of Fe-Al alloys [11].

Overall, these studies concentrate on the understanding of the magnetic properties of $\text{FeCoNi}(\text{B}_x \text{Al}_{1-x})_{0.1}\text{Si}_{0.1}$ HEA. The characterizations and magnetic properties of $\text{FeCoNi}(\text{B}_x \text{Al}_{1-x})_{0.1}\text{Si}_{0.1}$ HEAs were also determined in order to know its performance as electromagnetic wave absorbance material.

2 Materials and Method

High purity starting materials were used to create the alloys as described in [10] with measurements of 3 mm in diameter and 60 mm in length. Optical microscope (OM), X-ray diffraction (XRD) and Vibrating Sample Magnetometer (VSM) were used to characterize the $\text{FeCoNi}(\text{B}_x \text{Al}_{1-x})_{0.1}\text{Si}_{0.1}$ HEAs where ($x = 0, 0.2, 0.4, 0.5, 0.9$), later will be described as B0, B0.2, B0.4, B0.5 and B0.9 respectively in this paper. The

morphology of the $\text{FeCoNi}(\text{B}_{0.2}\text{Al}_{0.8})_{0.1}\text{Si}_{0.1}$ was observed under the visible light of Olympus BX41M Optical Microscope. To determine the phase composition, crystallographic of $\text{FeCoNi}(\text{B}_x\text{Al}_{1-x})_{0.1}\text{Si}_{0.1}$ ($x = 0.4, 1.0$), the x-ray diffraction peak of the sample is observed using XRD. By referring to similar paperwork, the diffraction angle 2θ was set to $20\text{--}80^\circ$ and the step size of the increment was set to 0.01° . VSM is a method used to determine the magnetic properties of $\text{FeCoNi}(\text{B}_x\text{Al}_{1-x})_{0.1}\text{Si}_{0.1}$ HEAs. To magnetize the sample, the sample are be placed inside a uniform magnetic field. The HEA is then physically vibrated in a sinusoidal pattern, frequently using a piezoelectric material. The hysteresis curve of the samples was plotted from the data obtained.

2.1 Characterizations of the HEAs

Figure 1 shows the optical microscope image of $\text{FeCoNi}(\text{B}_{0.2}\text{Al}_{0.8})_{0.1}\text{Si}_{0.1}$, at magnification of $20\times$, and $50\times$ respectively. The OM image shows a typical polycrystalline structure with the grain size of the sample around $50\text{--}100\ \mu\text{m}$. The existence of lamellar-like pattern was observed in the sample morphology. The lamellar pattern is produced due to the segregation of intermetallic phases (Fe_2B) that formed during the solidification process while intermetallic phases exist because of the Al and Fe content in the $\text{FeCoNi}(\text{B}_x\text{Al}_{1-x})_{0.1}\text{Si}_{0.1}$ HEAs. When Al and Fe-based alloys are mixed and heated to a specific temperature, an intermetallic phases formed [16]. The existence of Fe_2B phase later will be observe under XRD analysis.

To obtain the information on the crystalline structure of $\text{FeCoNi}(\text{B}_x\text{Al}_{1-x})_{0.1}\text{Si}_{0.1}$ after addition of boron content, the $\text{FeCoNi}(\text{B}_x\text{Al}_{1-x})_{0.1}\text{Si}_{0.1}$ ($x = 0.4, 1.0$) crystal structure were observed in the X-ray diffraction pattern in Fig. 2.

From Fig. 2, it can be seen that the addition of boron changed the crystal structure of the $\text{FeCoNi}(\text{B}_x\text{Al}_{1-x})_{0.1}\text{Si}_{0.1}$. For boron content B0.4, at the diffraction peak ($2\theta = 43^\circ$), indicated that the peak is a face-centered cubic phase FCC. At the same peak for B1.0, the difference after addition of boron contents can be seen here when there is additional boron element which is AlBNi and others diffraction peak too when some weak diffraction peaks appear. Those diffraction peaks are at ($2\theta = 24^\circ, 35^\circ, 45^\circ$ and 6°), additional of high content of boron has the peak of $(\text{FeNi})\text{B}$ to appear. At the highest diffraction peak at ($2\theta = 45^\circ$) of B0.4 shows the presence of $\text{FeSi}/\text{Fe}_2\text{B}$ that has overlapped at the same diffraction peak. The additional boron content in B1.0 has at the same diffraction peak angle has convert $\text{FeSi}/\text{Fe}_2\text{B}$ peak to become Fe_2B diffraction peak. CoB peak also resurface after addition on boron content at diffraction peak at ($2\theta = 47^\circ$). According to the XRD data, the HEAs have a primary face-centered cubic FCC phase and a minor body-centered cubic BCC phase that form because of the mixture of Fe, Co and Ni element [13].

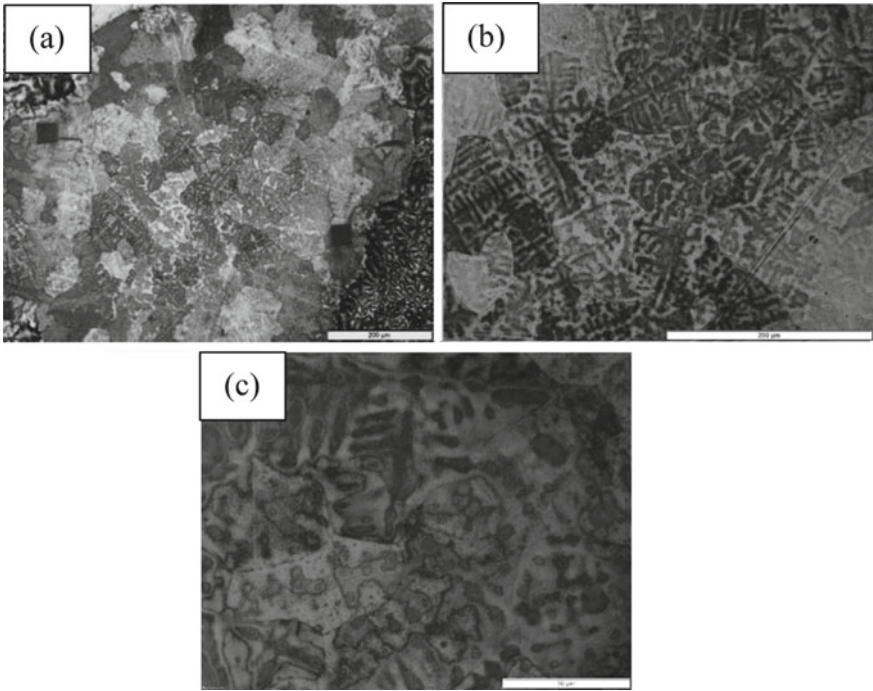


Fig. 1 Morphology of FeCoNi(B_{0.2}Al_{0.8})_{0.1}Si_{0.1} at magnification **a** 10x, **b** 20 and **c** 50 × shows a lamellar-like pattern of the HEAs

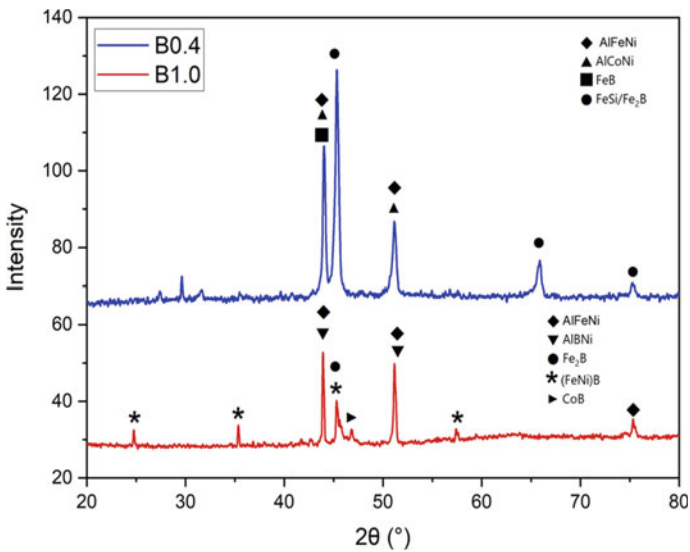


Fig. 2 XRD pattern of samples B0.4 and B1.0

2.2 Magnetic Properties

Magnetic properties of $\text{FeCoNi}(\text{B}_x\text{Al}_{1-x})_{0.1}\text{Si}_{0.1}$ obtained using VSM were illustrated in the Fig. 3 in the form of hysteresis loop. The sample that was tested were B0, B0.2, B0.4, B0.5 and B0.9. From the result obtained, the B0 exhibit highest magnetic saturation followed by B0.2, B0.4, B0.5 and B0.9. B0 is having 122.32 emu/g value of magnetic saturation while B0.9 is 93.67 emu/g. The magnetic saturation of the sample is decreased as the boron content increase. This is because the aluminum content decreases respectively with the addition of boron according to $\text{FeCoNi}(\text{B}_x\text{Al}_{1-x})_{0.1}\text{Si}_{0.1}$ composition. The addition of boron and the reduction of aluminum content has increased the magnetic saturation value of $\text{FeCoNi}(\text{B}_x\text{Al}_{1-x})_{0.1}\text{Si}_{0.1}$ samples [12]. It is because Al is a non-magnetic material while boron is also paramagnetic material due to unpaired electrons. Therefore, as the amount of non-magnetic components in the FeCoNi base alloy increases, the saturation magnetization of the sample would decrease [5].

Table 1 shows the value of magnetic saturation and coercivity of the $\text{FeCoNi}(\text{B}_x\text{Al}_{1-x})_{0.1}\text{Si}_{0.1}$. The result shows increases in the values of the coercivity and the decreases in the values of magnetic saturation as the boron content increases. The ability of ferromagnetic material to endure an external magnetic field without getting demagnetized is measured by coercivity. Therefore, it can be stated that B0.9 exhibit hard magnetic and hard to magnetized and demagnetized compared to B0 due to boron element that consist of domain that weakly aligned with the applied magnetic field. From the result it can be concluded that the equiatomic FeCoNiAl alloy exhibits relatively soft magnetic behavior with high permeability and low coercivity compared to other conventional alloys [13].

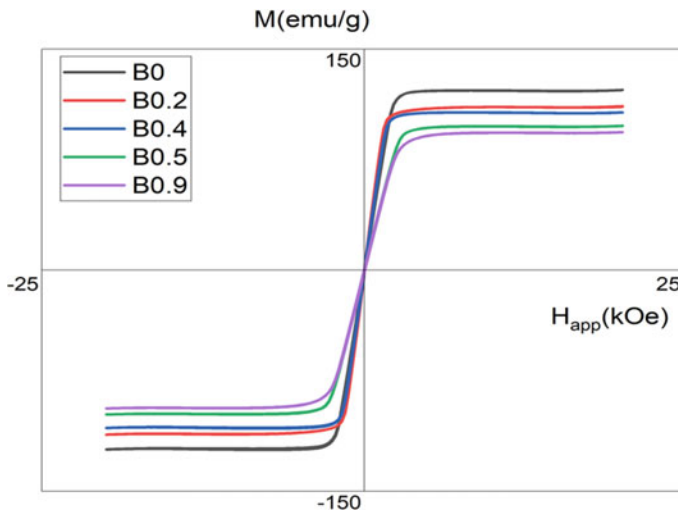


Fig. 3 Hysteresis loop of sample B0, B0.2, B0.4, B0.5, B0.9

Table 1 Magnetic value of the samples

Sample	Max magnetic saturation, Ms (emu/g)	Coercivity, Hs (kOe)
B0	122.32	0.39333
B0.2	111.24	-0.24064
B0.4	107.04	0.27211
B0.5	97.96	0.28293
B0.9	93.67	0.84167

3 Conclusion

In conclusion, the characterizations and magnetic properties of $\text{FeCoNi}(\text{B}_x\text{Al}_{1-x})_{0.1}\text{Si}_{0.1}$ where ($x = 0, 0.2, 0.4, 0.5, 0.9$) was determined. The morphology shows the lamellar-like pattern that was produced because of the segregation which formed intermetallic phases (Fe_2B) formed during the solidification process. The X-ray diffraction result of the samples shows the existence of Fe_2B with a primary face-centered cubic (FCC) phase and a minor body-centered cubic (BCC) phase. As boron content increases, the saturation magnetization of the HEAs decreases while the coercivity value increases. This shows that samples with a higher value of boron have hard magnetic behavior while samples with low boron content show soft magnetic properties.

Acknowledgements Financial support from Malaysian of Higher Education (MoHE) grant no. (FRGS/1/2019/TK05/UIAM/03/3) and Asian Office of Aerospace R&D (AOARD) grant no. (SP 121-112-0112).

References

1. Wu H, Lan D, Li B, Zhang L, Fu Y, Zhang Y, Xing H (2019) High-entropy alloy@ air@ Ni–NiO core-shell microspheres for electromagnetic absorption applications. *Compos B Eng* 179:107524
2. Liu C, Yu D, Kirk DW, Xu Y (2017) Electromagnetic wave absorption of silicon carbide based materials. *RSC Adv* 7(2):595–605
3. Gao C, He X, Ye F, Wang S, Zhang G (2021) Electromagnetic wave absorption and mechanical properties of CNTs@ GN@ Fe₃O₄/PU multilayer composite foam. *Materials* 14(23):7244
4. Zhang L, Jia J, Liang H, Chen G (2021) Facile synthesis of adjustable high-entropy alloy/polypyrrole electromagnetic wave absorber. *J Mater Sci: Mater Electron* 32(21):26074–26085
5. Na SM, Yoo JH, Lambert PK, Jones NJ (2018) Room-temperature ferromagnetic transitions and the temperature dependence of magnetic behaviors in FeCoNiCr-based high-entropy alloys. *AIP Adv* 8(5):056412
6. Egilmez M, Abuzaid W (2021) Magnetic, electrical and mechanical properties of Fe₄₀Mn₄₀Co₁₀Cr₁₀ high entropy alloy. *Sci Rep* 11(1):1–12

7. Huang EW, Hung GY, Lee SY, Jain J, Chang KP, Chou JJ, Yang WC, Liaw PK (2020) Mechanical and magnetic properties of the high-entropy alloys for combinatorial approaches. *Curr Comput-Aided Drug Des* 10(3):200
8. Jien-Wei YEH (2006) Recent progress in high entropy alloys. *Ann Chim Sci Mat* 31(6):633–648
9. Fu M, Ma X, Zhao K, Li X, Su D (2021) High-entropy materials for energy-related applications. *Iscience* 24(3):102177
10. Nordin NH, Zhaoyuan L, Goodall R, Todd I (2022) Theoretical critical metastability temperature to interpret phase formation in a lamellar-like-structured high entropy alloy. *J Market Res* 18:2519–2530
11. Gharsallah HI, Makhoulf T, Saurina J, Escoda L, Suñol JJ, Llorca-Isern N, Khitouni M (2016) Effect of boron addition on structural and magnetic properties of nanostructured Fe₇₅Al₂₅ alloy prepared by high energy ball milling. *Mater Lett* 181:21–24
12. Lan D, Zhao Z, Gao Z, Kou K, Wu G, Wu H (2020) Porous high entropy alloys for electromagnetic wave absorption. *J Magn Magn Mater* 512:167065
13. Na SM, Lambert PK, Jones NJ (2021) Hard magnetic properties of FeCoNiAlCuXTiX based high entropy alloys. *AIP Adv* 11(1):015210
14. Mishra RK, Shahi RR (2018) Magnetic characteristics of high entropy alloys. *Magn Magn Mater* 67–80
15. Yu PF, Zhang LJ, Cheng H, Zhang H, Ma MZ, Li YC, Li G, Liaw PK, Liu RP (2016) The high-entropy alloys with high hardness and soft magnetic property prepared by mechanical alloying and high-pressure sintering. *Intermetallics* 70:82–87
16. Liu B, Yang Q, Wang Y (2019) Intereaction and intermetallic phase formation between aluminum and stainless steel. *Results Phys* 12:514–524. <https://doi.org/10.1016/j.rinp.2018.11.076>

The Latching Performance of Soy Wax/Beeswax Prints in Alkaline Dye Solution and Heated Water



Sharifah Imihezri Syed Shaharuddin , Muhammad Rizal bin Saidi ,
Norhashimah Shaffiar , M. K. Nor Khairusshima ,
and Hazlina Md. Yusof 

Abstract Presently the main resist materials or waxes used in the batik industry are made of a blend of beeswax, dammar, resin, paraffin, and microcrystalline wax. Increasing environmental concerns over textile wastewater have led to the search for ‘greener’ batik wax compositions for the batik industry. Thus, plant-based wax such as soy wax is seen to be a promising candidate to replace the use of petrol-based waxes such as paraffin and microcrystalline wax. In this study, an in-house design melt extrusion system was used to print various soy wax/beeswax blends onto the surface of cotton fabric. The effect of beeswax additions on soy wax was evaluated based on the mass loss (%) upon immersion in the following solutions: alkaline dye solution at room temperature and tap water at 100 °C for 30 min and 5 min respectively. The immersion process of the cotton fabric in the alkaline dye solution or mercerization resulted in a mass increment of approximately 4% due to the effect of water absorption by the natural cotton fiber. Further immersion of the fabrics in hot water showed decreasing mass loss trend from 10.3 to 5.1%. It was inferred from this result that additions of beeswax had improved the latching property and resilience of the soy wax blends. The results of this study established the potential of using soy wax/beeswax blends as sustainable alternative resist materials in the batik industry.

Keywords Batik · Extruder · Mass-loss

1 Introduction

Hand-drawn batik is a technique that utilizes a pen-like tool known as *tjanting* which consists of a copper wax container with a small nozzle attached to a wooden handle. Over the years, the traditional *tjanting* has been modified to maintain the stability of

S. I. S. Shaharuddin (✉) · M. R. Saidi · N. Shaffiar · M. K. Nor Khairusshima
Department of Manufacturing and Materials Engineering, Kuliyyah of Engineering, International Islamic University Malaysia, 53100 Kuala Lumpur, Malaysia
e-mail: shaimihezri@iium.edu.my

H. Md. Yusof
Department of Mechatronics Engineering, Kuliyyah of Engineering, International Islamic University Malaysia, 53100 Kuala Lumpur, Malaysia

© The Author(s), under exclusive license to Springer Nature Singapore Pte Ltd. 2023
Md. A. Maleque et al. (eds.), *Proceeding of 5th International Conference on Advances in Manufacturing and Materials Engineering*, Lecture Notes in Mechanical Engineering,
https://doi.org/10.1007/978-981-19-9509-5_83

wax temperature and ease the waxing process [1, 2]. Technologically driven changes were also observed with the development of automated batik plotting or wax extrusion systems to replace the time-consuming and labor-intensive batik waxing process [3, 4]. Hussin et al. [5] recommend the utilization of computer-aided machines for the mass printing of batik in the future.

The batik waxes used in Malaysia often consist of a mixture of naturally sourced materials such as beeswax, dammar, and resin as well as synthetically derived materials such as paraffin and microcrystalline wax. Beeswax is often blended with both microcrystalline and paraffin and imparts the crackling effect on the batik motif. However, the use of these petrol-based waxes has raised environmental concerns due to their non-sustainable and non-biodegradable nature.

Recently, soy wax has been studied as a biodegradable and renewable option for paraffin wax [6]. In this study, beeswax was incrementally added to compensate for the lack of adhesiveness quality of soy wax. Kudiya et al. [7] defined the quality of batik wax based on several criteria such as resistance to alkaline, ease of removal and resistance towards wetness penetration, and non-sticky. Apart from Bowen [8], the performance of soy-based wax as potential batik resist material based on the quality requirements mentioned above has not been empirically documented.

In this work, an in-house temperature-controlled extruder system was used to print the soy wax/beeswax blends onto the surface of the cotton fabric. The main aim of this study was to determine the effects of beeswax additions on the latching performance of soy wax in the alkaline dye solution and hot water.

2 Methodology

2.1 Material Preparation and Extrusion

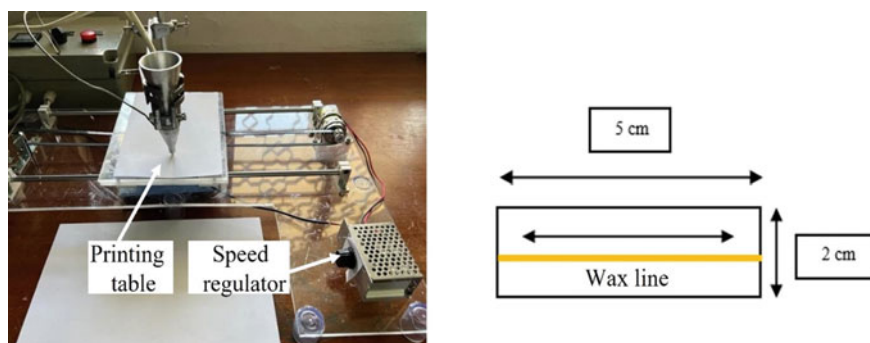
The ratios of beeswax (Global Sdn Bhd, Malaysia) and soy wax (Jargeous Sdn Bhd, Malaysia) were weighed according to the wt% ratios. Each component was melted in a pan in the order of decreasing melting temperature as follows; beeswax (melting point = 70 °C), and finally soy wax (melting point = 55 °C). The prepared batik wax blends were then left to solidify for 48 h before being re-melted for the printing process.

2.2 Wax Extrusion and Latching Performance Test

The sample code and melt extrusion temperature used to print the wax blends via the in-house design extruder system are enumerated in Table 1. The in-house designed wax extrusion system is shown in Fig. 1a. The cotton fabric was hand-washed and then dried for 24 h before being used. In the latching performance test, six rectangular

Table 1 Sample codes and extrusion temperatures for the soy wax/beeswax blends

Sample code	Soy wax (wt%)	Beeswax (wt%)	Extrusion temperature
			(°C)
Neat soy wax	100	–	60
Soy80bees20	80	20	60
Soy60bees40	60	40	65
Soy40bees60	40	60	65
Soy20bees80	20	80	70
Neat beeswax	–	100	75

**Fig. 1** a The in-house designed wax extrusion system. b Sample dimension for the latching test

cotton samples with the dimension of 5×2 cm were prepared for each composition as shown in Fig. 1b. Each wax blend was printed in a straight line of 5 cm at a printing table speed of 0.04 m/s-0.08 m/s. The initial mass (M_i) of each cotton fabric sample was then recorded.

The dye alkaline solution was prepared by dissolving 6.2 g of soda ash and 4 g of blue dye into 200 ml of water. Each cotton fabric specimen was soaked in the alkaline solution at room temperature for 30 min and then dried for 24 h. The mass (M_{f1}) of each cotton fabric specimen was then weighed. These samples were then soaked in water at 100 °C for 5 min and left to dry for 24 h. The final mass (M_{f2}) of each cotton fabric specimen was measured again.

The mean mass loss (%) was measured by using the equations below:

$$\text{Mass loss in alkaline solution} = [(M_i - M_{f1}) / M_i] \times 100 \quad (1)$$

$$\text{Mass loss in water } 100^\circ\text{C} = [(M_{f1} - M_{f2}) / M_{f1}] \times 100 \quad (2)$$

3 Results and Discussions

In this study, each wax blend was successfully printed with consistent linewidth on the cotton fabric via the in-house designed wax extrusion system. In the textile industry, immersion in an alkaline dye solution or mercerization is used for cellulosic and cotton fibers to increase the pH of the dye water. This process encourages the cellulose anion of the natural fiber to chemically react with the dye and create a strong permanent bond for long-lasting coloration. Figure 2 shows the resultant wax-printed cotton fabrics after the alkaline treatment. It was observed that there were no perceptible differences between each wax line in Fig. 2a–f as most of the wax was still present on the cotton fabric after being soaked in the alkaline dye solution. Generally, wax does not dissolve in water due to the difference in the bonding structures of the water molecule and the wax. However, it is possible to degrade in mediums at high temperatures for a longer duration.

Figure 3a shows a consistent mass increment in the range of 3.8–3.6% after being soaked in the alkaline dye solution attributed to the water uptake or absorption of the cotton fiber. John and Anandjiwala [9] also reported that cotton fabric that

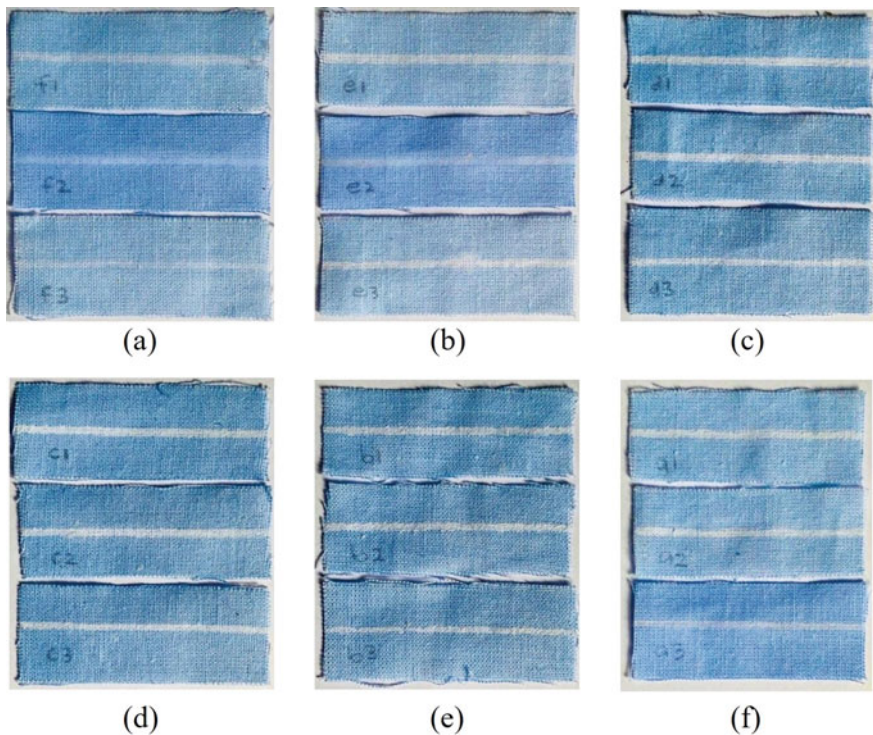


Fig. 2 Resultant cotton fabric samples **a** neat soy wax **b** Soy80bees20 **c** Soy60bees40 **d** Soy40bees60 **e** Soy20bees80 **f** neat beeswax after immersion in an alkaline dye solution

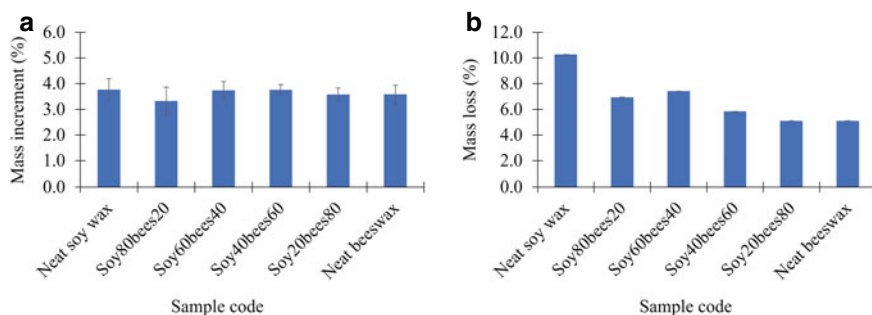


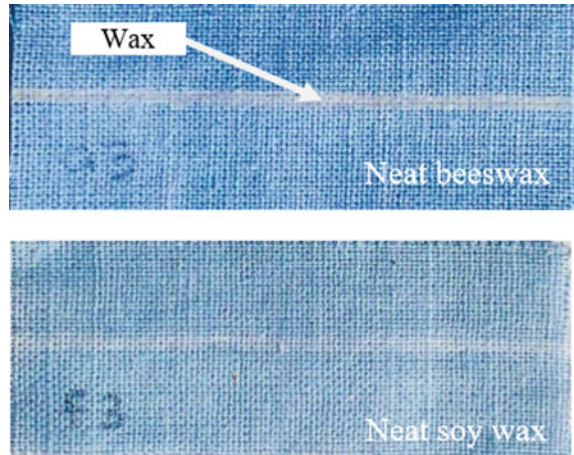
Fig. 3 **a** Mass increment after immersion in alkaline dye solution. **b** Mass loss after immersion in water at 100 °C

was mercerized had greater strength, luster, absorbency, and a greater capacity to soak up dye compared to untreated cotton fabric. Figure 3b shows the mass loss trend of the wax-printed cotton upon immersion in 100 °C water after the alkaline treatment. It was noted that increasing the amount of beeswax (wt%) in the blend resulted in a decreasing mass loss trend from 10.3 to 5.1%. It was also observed that neat beeswax was still latched to the cotton fabric in comparison to the neat soy wax as shown in Fig. 4. The mass loss trend obtained agrees with a prior study by Rasid [10] for similar soy wax/beeswax compositions where the soy wax blends were rendered on cotton fabric using the *tjanting* tool. This study concluded that the addition of beeswax had improved the latching property and resilience of the soy wax blends against dissolution in hot water. The latching performance of the waxes has an inverse relationship with the ease of removal. As the latching (measured from the mass loss (wt%)) of the waxes increases, the ease of removal decreases. Several factors contribute to the latching or ease of removal of soy wax/beeswax blends in this study. Neat beeswax was not easily removed in hot water as it has a higher melting temperature than neat soy wax. In addition, Shen et al. [11] observed that beeswax had a slightly higher apparent contact angle (162°) compared to soy wax (159°) indicating that beeswax offers better durability against wettability or wetness penetration.

4 Conclusion

In this study cotton fabric was successfully printed with soy wax/beeswax blends via an in-house design melt extrusion system without any over extrusion or under extrusion issues. It was evident in this study that the increase in mass loss of the wax printed samples after immersion in alkaline dye solution was linked to the water uptake by the natural cotton fibers. The decreasing mass loss trend observed after immersion in hot water reflected that beeswax had indeed improved the latching

Fig. 4 A comparison between neat beeswax and neat soy wax printed on cotton fabric



properties of the soy wax. The results of this study can be used to initiate sustainable resources and raw material management for the batik industry.

Acknowledgements This work was fully supported by International Islamic University Malaysia and funded by the Ministry of Higher Education Malaysia (FRGS/1/2018/TK03/UIAM/02/3). The authors would like to express their deepest gratitude for the support from all co-researchers.

References

- Ikawanty BA, Rifa'i M, Patma TS (2015) Otomatisasi canting listrik untuk pembuatan batik tulis Probolinggo. *Sentia* 7:111–116
- Affanti TB, Hidayat SR (2019) Batik innovations in Surakarta Indonesia. *Adv Soc Sci Educ Humanit Res* 207:138–141
- Hitchcock M, Nuryanti W (2016) *Building on batik: the globalization of a craft community*, 1st edn. Routledge, New York
- Akhmad S, Arendra A, Mu' Alim Winarso K, Hidayat R (2020) Design of the mBatik, textile hot wax applicator to emulate hand drawn batik using CNC plotter machine and characterization of wax plotting parameters. *J Phys Conf Ser* 1569
- Hussin H, Husain K, Pilus AM, Hasan H, Cheong KM, Yaacob Yaacob NM (2016) Innovation of Malaysian batik craft in arts: a reflection for vocational education. *Soc Sci* 11:2983–2986
- Rezaei K, Wang T, Johnson LA (2002) Hydrogenated vegetable oils as candle wax. *J Amer Oil Chemist' Soc* 79:1241–1247
- Kudiya K, Sumintono B, Sabana S, Sachari A (2016) Batik artisans' judgment of batik wax quality and its criteria: an application of the many-facets Rasch model. In: *Pacific rim objective measurement symposium 2016*, Springer, Singapore, pp 27–37
- Bowen DB (2005) Soy wax : an alternative resist. In: *Kuala Lumpur international Batik convention*. Yayasan Budi Penyayang Malaysia, Kuala Lumpur, pp 1–12
- John MJ, Anandjiwala RD (2009) *Surface modification and preparation techniques for textile materials*. Woodhead Publishing, United Kingdom

10. Rasid MA (2021) Technical report—thermal degradation and ease of wax removal of various soy wax /beeswax blends. International Islamic University Malaysia, Gombak
11. Shen T, Fan S, Li Y, Xu G, Fan W (2020) Preparation of edible non-wettable coating with soybean wax for repelling liquid foods with little residue. *Materials* 13(15):1–11

Analysis and Optimum Machining Parameters on Surface Roughness and Material Removal Rate for Titanium Alloy in Milling Machining with MQL



Siti Haryani Tomadi, Nor Farah Huda Abd Halim, H. Mas Ayu, R. Daud, and Muhammad Ariff Zakaria

Abstract Proper cutting parameters are needed to produce lower surface roughness of titanium alloy machined material. The high temperature in the cutting zone is always happened due to high friction between the tool and the workpiece and will cause dimensional error and poor surface roughness. Therefore, the main objectives of this research were to investigate and compare the surface roughness and material removal rate (MRR) of Ti-6Al-4 V alloy under the dry and minimum quantity lubrication (MQL) technique. The effect of cutting parameters towards surface roughness was investigated and the optimum cutting parameters was studied to obtain lower surface roughness and higher MRR. From ANOVA, spindle speed has been identified as the most significant parameter that affects the surface roughness and MRR. In this paper, the optimum cutting parameters that give the low surface roughness and high MRR was 1500 rpm (spindle speed), 0.4 mm/tooth (feed per tooth), and 0.4 mm (depth of cut). From this study, it can be concluded that in this milling of Ti-6Al-4 V alloy, higher spindle speed, feed per tooth, and depth of cut are preferable to achieve the better surface quality of Ti-6Al-4 V alloy.

Keywords Optimization · Surface roughness · MRR · Titanium Alloy · MQL

S. H. Tomadi (✉) · N. F. H. A. Halim · M. A. Zakaria
Department of Manufacturing and Materials Engineering, International Islamic University
Malaysia, Kuala Lumpur, Malaysia
e-mail: sharyani@iium.edu.my

H. Mas Ayu
Faculty of Manufacturing and Mechatronic Engineering Technology, Universiti Malaysia Pahang,
26600 Pekan, Pahang, Malaysia

R. Daud
Faculty of Mechanical and Automotive Engineering Technology, Universiti Malaysia Pahang,
26600 Pekan, Pahang, Malaysia

1 Introduction

Titanium alloy (Ti-6Al-4 V) is a low-density element and nonmagnetic metal which is approximately 60% comes from the density of steel [1]. More than 50% of titanium alloy has been produced in titanium industry and has found wide applications in aerospace, sub marine industries and others [2]. In addition, titanium alloy which made up of 90% of titanium, 6% of aluminum and 4% of vanadium has unique mechanical properties such as high hardness and good fracture toughness [3]. Machining of titanium alloy is very popular and highly recommended for the aerospace and any engineering field due to its properties such as high temperature-strength and good corrosion resistance. However, low thermal conductivity and high chemical reactivity make the titanium alloy is hard to cut or machine. The heat cannot be dissipated away quickly thus chemical reaction in cutting tool material will produce high temperature. To enhance machining productivity, MQL is used to remove heat and chips from the cutting zone and acts as lubricant to reduce the friction between tool and the chip [2].

Cutting fluids have a major role in improving the performance and productivity of machining [4]. Minimum quantity lubrication (MQL) has proved a suitable replacement for conventional cooling methods, as they meet the sustainability criteria and are able to reduce waste of the coolant. The MQL technique also has proved to be acceptable as it meets “green” machining requirements. There are two advantages by using MQL which are enhance the machining process performance and obtain more sustainable process as the system applies an optimal amount of oil compared to the flood coolant strategy [4].

Sustainable machining can be obtained by the implementation of cutting fluids due to its significant impact on the machining quality characteristics. For that reason, minimum quantity lubrication (MQL) is the alternative to reduce the environmental pollution unhealthy operators and at the same time reduce the manufacturing cost [5]. Thus, vegetable-oil-based cutting fluid is used due to the good lubrication and produce high strength film between the surface of cutting tool and machined material [4].

Therefore, the aims of this research are; to investigate the surface roughness and material removal rate (MRR) of Ti-6AL-4 V alloy by using dry and MQL technique, to compare the surface roughness between dry and MQL technique of Ti-6AL-4 V machined material, and to optimize cutting parameters to obtain lower surface roughness and higher MRR.

Table 1 Taguchi's orthogonal array L4

No. of runs	Spindle speed, S(rpm)	Feed per tooth, f(mm/tooth)	Depth of cut, D(mm)
1	500	0.2	0.3
2	500	0.4	0.4
3	1500	0.2	0.4
4	1500	0.4	0.3

2 Methodology

2.1 Experimental Procedure

There were two (2) different cutting conditions in milling process that were used in this project which were dry and Minimum Quantity Lubrication (MQL) technique by using vegetable-based oil. Lubricant was applied by spraying it between the cutting tool and the workpiece. Process was done by using Accu-lube MQL machine. The data for surface roughness and material removal rate (MRR) was compared between dry and MQL. The optimization of cutting parameter was done by using Taguchi method L4 in Minitab software. Based on Table 1, cutting parameters were assigned as the inputs while surface roughness and MRR were the responses.

2.2 Workpiece and Cutting Tool

The workpiece used in this project was titanium alloy (Ti-6Al-4 V). Table 2 shows the chemical composition of titanium alloy.

Figure 1 shows the workpiece, tool holder and insert which for the workpiece is titanium alloy; the length is 160 mm, width is 110 mm and the height is 50 mm. For the cutting tool, coated carbide titanium alloy nitride with 12 mm diameter, 2 number of flutes and 60 mm overall length was used in this experiment to increase the tool life and obtain better wear resistance.

Table 2 Chemical composition of titanium alloy

Element	Al	V	Fe	H2	O2 + N2	Ti
Weight (%)	5.5–6.75	3.5–4.5	0.03	0.0125	0.25	88.48

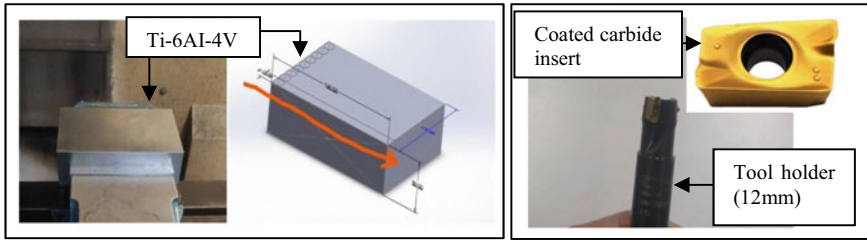


Fig. 1 Workpiece and cutting tool

2.3 Surface Roughness and MRR Measurement

The surface roughness was measured using surface roughness tester and the 3D Profiler; Alicona optical microscope. Meanwhile, Material removal rate (MRR) can be calculated by using formula below (Company, 2021).

$$MRR(mm^3/min) = W \times D \times F \quad (1)$$

W = Width of cut (mm), D = Depth of cut (mm), F = Feed rate (mm/min).

3 Results/Discussion

3.1 Surface Roughness for Dry and MQL Condition and Material Removal Rate (MRR)

Table 3 shows the surface roughness value for dry and MQL cutting condition. For dry condition; at cutting parameter ($f = 0.4$ mm/tooth, $D = 0.3$ mm) with spindle speed 1500 rpm, lower surface roughness was obtained which was $0.19 \mu\text{m}$. For MQL; at cutting parameter ($f = 0.4$ mm/tooth, $D = 0.3$ mm) with spindle speed also 1500 rpm, lower surface roughness was also obtained which was $0.18 \mu\text{m}$. Meanwhile, Fig. 2 shows the example of surface topography for experiment 1 ($S = 500$ rpm, $f = 0.2$ mm/tooth, $D = 0.3$ mm). From the results, it shows that surface roughness is strongly depends on the spindle speed followed by the feed rate [6]. Therefore, high spindle speeds resulting in lower surface roughness because spindle speed gives more significant factor and gives most contribution to the surface roughness. This is due to the occurrence of Built-Up Edge (BUE) when machining titanium alloy at lower spindle speed [1]. As a comparison between dry and MQL, it shows that using MQL will improve the cutting fluid's ability to penetrate the cutting zone, improve surface roughness and reduce the usage of cutting fluid [5]. The tool and the workpiece will generate high temperature during machining process [7]. This will shorten the tool life and create poor surface quality on workpiece.

Table 3 Surface roughness (Ra value) for dry and MQL

No. of experiment	Spindle speed, S(rpm)	Feed per tooth, f(mm/tooth)	Depth of cut, D(mm)	Surface roughness, Ra(μm)		Percentage of improvement (%)
				Dry	MQL	
1	500	0.2	0.3	0.56	0.35	37.50
2	500	0.4	0.4	0.36	0.27	25.00
3	1500	0.2	0.4	0.25	0.22	12.00
4	1500	0.4	0.3	0.19	0.18	5.26

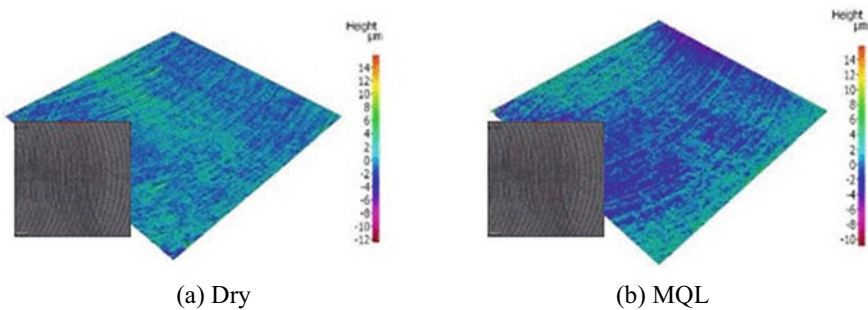


Fig. 2 Surface topography for Experiment 1 **a** dry and **b** MQL condition

ANOVA was used to conduct an analysis in order to confirm the factors that affect most of the Ra values. Table 4 shows the signal to noise ratio using Taguchi method. Spindle speed was ranked as the most significant factor that influence the Ra value, followed by feed per tooth and depth of cut at last. It is because the occurrence of Built-Up Edge (BUE) when machining multiphase materials at lower spindle speeds [8]. It generates large burr quantity on the machined surface thus poor surface finish was obtained [8].

From the Eq. (1), it can be seen that, the higher the feed rate, the higher the MRR. A high machining rate is always desirable because it is directly related to productivity [9]. The higher the MRR, the better productivity will be obtained. Table 5 shows the signal to noise ratio for MRR. From the analysis, spindle speed was seen as the most

Table 4 Response table for signal to noise ratios for surface roughness

Level	Spindle speed	Feed per tooth	Depth of cut
1	6.955	8.539	9.731
2	13.233	11.649	10.458
Delta	6.278	3.111	0.727
Rank	1	2	3

Table 5 Response table for signal to noise ratios for MRR

Level	Spindle speed	Feed PER tooth	Depth of cut
1	-55.39	-57.15	-58.91
2	-64.93	-63.17	-61.41
Delta	9.54	6.02	2.50
Rank	1	2	3

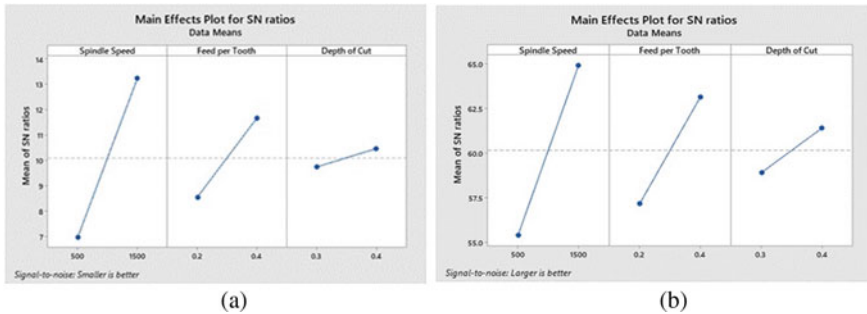


Fig. 3 Main effects plot for SN ratio for **a** surface roughness and **b** MRR

significant parameter that affects the MRR and ranked as the most significant factor that influence the MRR value, followed by feed per tooth and depth of cut.

3.2 Optimization of Machining Parameter for Lower Surface Roughness and Better MRR

In Taguchi method, the highest value of SN ratio for each parameter shows the optimum value in obtaining better response. Figure 3 shows the main effects plot for SN ratio; spindle speed, feed per tooth and depth of cut for (a) Surface roughness and (b) MRR. In this study, the $S = 1500$ rpm $f = 0.4$ mm/tooth and $D = 0.4$ mm gives the lowest Ra values and highest MRR.

4 Conclusion

Based on the result that obtained by surface roughness tester, experiment 4 (Spindle speed 1500 rpm, feed per tooth 0.4 mm/tooth and depth of cut 0.3 mm) recorded lower surface roughness compared to other experiment; for dry ($0.19 \mu\text{m}$) and MQL ($0.18 \mu\text{m}$). In addition, experiment 4 also recorded higher MRR compared to other experiment for both conditions ($2160 \text{ mm}^3/\text{min}$). The higher the MRR value, the higher the productivity obtained. Based on this result, it can be concluded that spindle

speed is the most important factor, contributing the lower surface roughness and higher MRR. From the experiment, the MQL experiment experienced good surface roughness compared to dry cutting experiment. The higher percentage of improvement (37.5%) is recorded during experiment 1 (Spindle speed 500 rpm, feed per tooth 0.2 mm/tooth and depth of cut 0.3 mm). Based on this result, it can be concluded that MQL improves surface finish during machining of titanium alloy. Thus, the optimum parameters in obtaining lower surface roughness and higher MRR is 1500 rpm for spindle speed, 0.4 mm/tooth for feed per tooth and 0.4 mm for depth of cut.

Acknowledgements The authors greatly acknowledge the financial assistance under the Research Management Centre Grant 2020 (RMCG20-019-0019), International Islamic University Malaysia (IIUM).

References

1. Kumar U, Senthil P (2019) A comparative machinability study on titanium alloy Ti- 6Al-4V during dry turning by cryogenic treated and untreated condition of uncoated WC inserts. *Mater Today: Proc* 27(3):2324–2328
2. Abbasi SA, Pingfa F (2015) Evaluating the effectiveness of various coating layers applied on k-grade cemented carbide cutting tools on machinability of titanium alloy Ti-6Al-4V in high speed end milling. In: *Proceedings of 2015 12th international Bhurban conference on applied sciences and technology, IBCAST 2015*, pp 14–19
3. Du Q, Chen X, Zhang K (2006) Study on high speed cutting machinability of medical titanium alloy Ti-6Al-4V. In: *IET conference publications*, vol 524. pp 263–266
4. Rao PN, Srikant RR (2015) Sustainable machining utilizing vegetable oil based nanofluids. *May*, pp 664–672
5. Hegab H, Kishawy HA, Darras B (2019) Sustainable cooling and lubrication strategies in machining processes: a comparative study. *Proc Manuf* 33:786–793
6. Pradeep Kumar J, Thirumurugan K (2012) Optimization of machining parameters for milling titanium using taguchi method. *Int J Adv Eng Technol* 3(2). E-ISSN 0976-3945 IJAET
7. Sudin I, Prof A, Ripin A, Azrul M, Mat H, No VOT (2009) Feasibility study of using vegetable oil as a cutting lubricant through the use of minimum quantity lubrication during machining
8. Anand N, Kumar AS, Paul S (2019) Effect of cutting fluids applied in MQCL mode on machinability of Ti-6Al-4V. *J Manuf Process* 43(May):154–163
9. Jahan MP, Rahman M, Wong YS (2014) Micro-electrical discharge machining (Micro-EDM): processes, varieties, and applications, *comprehensive materials processing*, vol 11. pp 333–371

Thermoelectric Properties of B-FeSi₂ Thermoelectric Module Utilizing Cast-Iron Scrap Chips



Assayidatul Laila Nor Hairin, Muhammad Haziq Hakmal Jailani, and Megat Muhammad Ikhsan Megat Hasnan

Abstract Semiconducting β -FeSi₂ has been considered one of the most promising thermoelectric materials among numerous innovative thermoelectric materials due to its inexpensive cost and exceptional oxidation resistance up to 900 °C. Thermoelectric generation modules consisting of pairs of p-type 0.94C.I.-0.06Co-1.86Si and n-type 0.92C.I.-0.08Mn-1.86Si have been fabricated using Cu sheets as electrodes and Ag paste as bonding material. In an experiment, the maximum power density is measured by using a variable resistor range of 10 Ω —10 kohm. Two different temperatures that are tested in this project are 40 and 60 °C. A rectangle and a trapezoid as the thermoelectric leg shape geometry are compared. The percentage difference for voltage is around 21% while the power shows a 41 and 65% difference depending on the temperature difference. The latter percentage difference is possessed by higher T. Based on the comparison with the reference, thermoelectric module from cast iron scrap chips was comparable and better than the reference. Trapezoid shows better geometry than rectangular shape in terms of thermoelectric power density. At 40 °C, the maximum power output are 21.89 and 21.91 μ W whilst the maximum power for 60 °C are 28.13 μ W and 28.42 μ W for rectangle and trapezoid respectively.

Keywords β -FeSi₂ thermoelectric module · Cast-iron scrap chips · Power density

1 Introduction

Thermoelectric module (TEM) is built in the presence of two unique semiconductor material are linked together, electrically in series and thermally in parallel while sandwiched between the ceramics plate act as an electrical insulator. Due to current flow, a temperature differential is generated across the junctions of two semiconductors

A. L. N. Hairin (✉) · M. H. H. Jailani
Department of Manufacturing and Materials Engineering, Kulliyah of Engineering, International Islamic University Malaysia, Kuala Lumpur, Malaysia
e-mail: assayidatul_laila@iium.edu.my

M. M. I. M. Hasnan
Faculty of Engineering, University Malaysia Sabah, Sabah, Malaysia

when input is delivered at their free ends [1]. Nowadays, thermoelectric has much potential in leading the new technologies towards a greener and more environmentally friendly energy. Many international automakers, such as Renault, Honda, and Ford, have developed TEG-based systems to collect exhaust heat [2–4]. For an ideal thermoelectric generator (TEG), this is the equation in determining the maximum heat-to-power efficiency (η_{max}) [5]:

$$\eta_{max} = \left(\frac{T_H - T_C}{T_H} \right) \left(\frac{\sqrt{1 + ZT} - 1}{\sqrt{1 + ZT} + \frac{T_C}{T_H}} \right). \quad (1)$$

where the conversion efficiency (η_{max}) is given as the ratio of temperature gradient between hot (T_H) and cold (T_C) reservoirs and the figure of merit (ZT). Figure of merit limit how efficiently a TE material can convert between the energies. The efficiency with which a TE material may convert between thermal to electrical energy is limited by its figure of merit (ZT) and expressed as:

$$ZT = \frac{(\alpha^2 \sigma T)}{k} \quad (2)$$

where α , σ , T and k are the Seebeck coefficient ($\mu\text{V/K}$), electrical conductivity (S/cm), absolute temperature (K) and thermal conductivity (W/mK). There is also power factor (PF) in the formula which is $\alpha^2 \sigma$. Thermoelectric materials ZT will be higher when the thermal conductivity (k) is low and the electrical conductivity (σ) and Seebeck coefficient (α) are high [6].

Semiconducting $\beta\text{-FeSi}_2$ has been regarded one of the most promising thermoelectric materials among many novel thermoelectric materials because of its low cost and outstanding oxidation resistance up to 900°C [7]. It has been discovered that by substituting appropriate elements for iron and silicon, it is feasible to dope FeSi_2 in both n-type and p-type. Doping is used to change the electrical, optical, and structural characteristics of a material. For n-type doping, the element must have five electrons in the outermost shell or valence electrons. As for p-type, the elements must have 3 valence electrons [8]. There are few doping elements that has been used in the previous research which are Cobalt (Co), Phosphorus (P), Manganese (Mn), Aluminium (Al) etc. [9, 10]. In order to fabricate $\beta\text{-FeSi}_2$, the starting materials are generally pure Fe with a purity of 99.99% and Si with a purity of 99.9%. Some combination of processes like arc melting based on ingot metallurgy, mechanical alloying and sintering can be used to fabricate $\beta\text{-FeSi}_2$ [10]. There are numerous methods of manufacturing $\beta\text{-FeSi}_2$ using Hot Pressing Sintering (HPS) and Spark Plasma Sintering (SPS) [11].

Cast iron is one of the family of ferrous alloys. It is an iron alloy with composition of more than 2% carbon (C), and silicon (Si) in the range of 1–3% [12]. Presence of small amounts of manganese (Mn) and some impurities like sulphur (S) and phosphorus (P) also can be detected. The amount of alloying and accompanying regulation of the heat and cooling process may provide different grades of cast iron

a wide range of qualities which are gray iron, white iron, ductile iron, malleable iron and compacted graphite iron. Cast iron is being used to making water conduit pipes, packer parts, boilers, valve bodies and valve parts [12].

The purpose of this project is to fabricate different thermoelectric module shape geometry using β -FeSi₂ from cast iron scrap chips and test their performance in order to compare them with the previous Fe-based thermoelectric module in terms of power density and internal resistance under applied temperature difference. From this fundamental study, the benchmark of waste material (cast-iron scrap chips) as thermoelectric is highlighted for future development in terms of shape design to be comparable with conventional thermoelectric material.

1.1 Methodology

The fabricated thermocouple pair is consisting of 0.94C.I.-0.06Co-1.86Si (C.I.-Co0.06) for n-type and 0.92C.I.-0.08Mn-1.86Si (C.I.-Mn0.08) for p-type [11]. For the rectangular, the dimension will be 2 mm × 3 mm × 4 mm (width × length × height). Trapezoidal legs dimension will be the same with rectangular but with shorter base with around 1 mm length. For assemble part, the additional materials that are needed are silver paste and copper sheets. These copper sheets or strips acted as the electrode connecting the cold and hot side to the thermoelectric module. Copper sheets are cut to smaller pieces with dimension of 3 × 6 mm (width × length) and connected to the thermoelectric legs via silver (Ag) paste. The SEM and EDX are used to characterize the junction between the electrode and thermoelectric leg. The thermoelectric module is sandwiched between the cold and hot side to create a temperature difference. In this testing, the hot side is hot plate and the cold side is ice. The setup is shown in Fig. 1c. After completed the setup, the resistance is measured for this entire testing setup.

For the thermoelectric power generation measurement, the thermoelectric module is connected to the load resistor that parallel to voltmeter. The voltage output that under load resistor is measured using Ohm’s law as shown in Eq. (3), where V is the

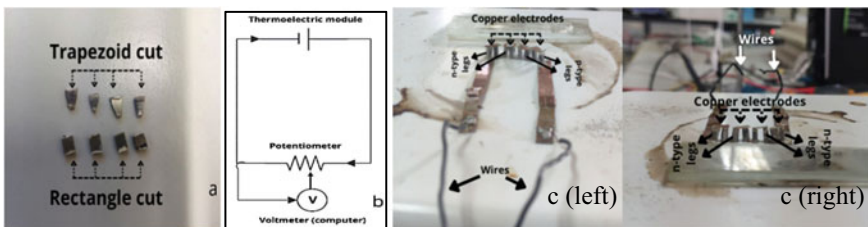


Fig. 1 a Trapezoidal and rectangular cut thermoelectric legs and the cut dimension, b circuit diagram for the setup and c β -FeSi₂ thermoelectric module using rectangle (left) and trapezoid (right) legs

voltage and R is the resistance. The power density is calculated based on thermoelectric module area, A as shown in Eq. (4). Variable resistor range from $10\ \Omega$ - $10\ \text{K}\ \Omega$ is tested using electrical connection of parallel thermoelectric modul with variable resistor and voltmeter which as illustarted in Fig. 1b in order to identify maximum power density. From power density analysis, the performance of the thermoelectric module is compared for the best shape and temperature diffrence.

$$P = \frac{V^2}{R} \quad (3)$$

$$P_d = \frac{P}{A} \quad (4)$$

2 Experimental Results

As shown in Fig. 1a is the rectangular leg, the dimension was $2 \times 3 \times 4\ \text{mm}$ (width \times length \times height) and trapezoidal legs dimension was the same with rectangular but with shorter base with around $1\ \text{mm}$ length. The purpose of this project is to develop a thermoelectric module that can be functional towards different temperature difference (ΔT). As shown in Fig. 1b is the circuit diagram for the setup and Fig. 1c is $\beta\text{-FeSi}_2$ thermoelectric module using rectangle (left) and trapezoid (right) legs. SEM image and EDX elemental mapping result of the connection of thermoelectric leg (p-type) and electrode using silver (Ag) paste are shown in Fig. 2 and Table 1. Therefore, the thermoelectric modules are put in between hot side and cold side to obtain two temperature difference $40\ ^\circ\text{C}$ and $60\ ^\circ\text{C}$.

First, total resistance of the fabricated modul is measured to identify internal modul resistance as shown in Table 2. It is found that trapezoidal has lower resistance value

Fig. 2 SEM images of the connection of thermoelectric leg (p-type) and electrode using silver (Ag) paste

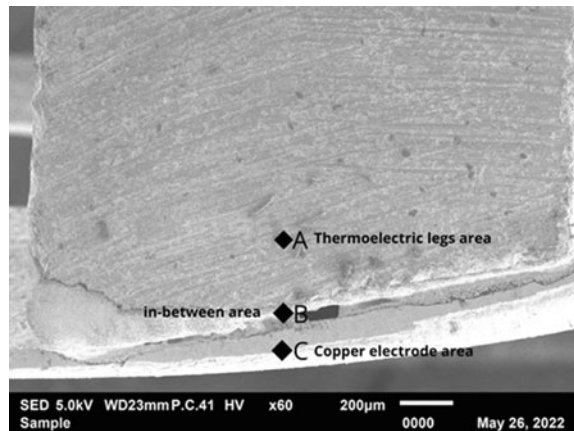


Table 1 EDX elemental mapping result for point A, B and C

Point	Fe (wt%)	Si (wt%)	Mn (wt%)	Ag (wt%)	Cu (wt%)
A	52.4	43.5	4.1	–	–
B	40.8	30.2	3.0	23.8	2.2
C	–	–	–	70.6	29.4

than rectangular shape. Then, open circuit voltage for the thermoelectric module is measured under no load. Table 2 shows that, the voltage generated for 60 °C is higher than 40 °C by ± 30 mV for both shape. This proves that higher temperature difference will produce higher open circuit voltage. Figure 3 shows the the voltage and power versus variation of load resistance. The maximum power peaks found at 40 °C were 21.89 and 21.91 μW for rectangle and trapezoid respectively. At 60 °C, the maximum power values of rectangle and trapezoid were 28.13 μW and 28.42 μW respectively.

Table 3 shows the calculated power density. The obtained power density is compared with the previous β-FeSi₂ study that having different compositions which p-type of Fe_{0.91}Mn_{0.09}Si₂ and n-type of Fe_{0.98}Co_{0.02}Si₂ [13] whilsy, this project used 0.94C.I.-0.06Co-1.86Si for n-type and 0.92C.I.-0.08Mn-1.86Si for p-type [11]. Based on the performance comparison between this study with the previous work, the performance of this work which using waste product as thermoelectric source material is comparable with conventional method. The shape has influence the power density to mach the previous work performance that having difrent atomic composition. This study inferred that the shape affect the power density by the internal resistance value of the modul where the power density of trapezoidal is the highest due to its lowest internal resistance. Hence, the optimisation of the thermoelectric module

Table 2 Total electrical resistance and voltage open circuit for triangular and trapezoidal leg module

Module	Total resistance, R_T	Voltage open circuit, v_{oc}	
		40 °C (mV)	60 °C (mV)
Rectangular	184.1Ω	61.2	90.8
Trapezoidal	167.4Ω	62.5	92.3

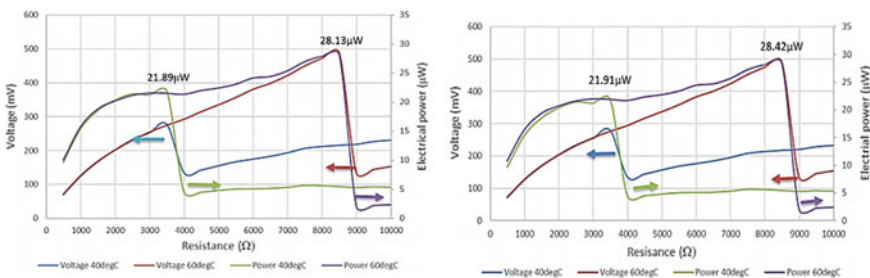


Fig. 3 Voltage versus Resistance graph and Power curve for rectangular (top) and trapezoidal (bottom) legs module

Table 3 Power density performance between experimental data and reference

	Research paper (Nogi et al. [13])		Experimental			
			Rectangular		Trapezoid	
	40 °C	60 °C	40 °C	60 °C	40 °C	60 °C
Power density (W/mm ²)	0.26	0.39	0.19	0.25	0.26	0.34

shape is highlighted as smart strategy to optimise thermoelectric power density for future work.

3 Conclusion

To conclude, the purpose of this project is to design and fabricate a β -FeSi₂ thermoelectric module made from cast iron scrap chips, as well as demonstrates the thermoelectric module properties experimentally to function as thermoelectric generator. The thermoelectric performance on two different leg geometries (rectangle and trapezoid) is tested in two-temperature difference, ΔT . The effect of these two variables is investigated on voltage, v and maximum power, P . According to the findings in the investigation, we can conclude that by increasing the temperature difference, ΔT on the module will also increase the voltage and power produced by the module. These effects caused by the electrons flow when temperature difference exists that will generate current. Higher ΔT will excites electrons faster and current also increase. When current increase, the voltage and power also will increase due to the directly proportional relationship.

References

1. Patidar S (2018) Applications of thermoelectric energy: a review. *Int J Res Appl Sci Eng Technol* 6(5):1992–1996
2. Espinosa N, Lazard M, Aixala L, Scherrer H (2010) Modeling a thermoelectric generator applied to diesel automotive heat recovery. *J Electron Mater* 39(9):1446–1455
3. Mori M, Yamagami T, Sorazawa M, Miyabe T, Takahashi S, Haraguchi T (2011) Simulation of fuel economy effectiveness of exhaust heat recovery system using thermoelectric generator in a series hybrid. *SAE Int J Mater Manuf* 4(1):1268–1276
4. Hussain QE, Brigham DR, Maranville CW (2009) Thermoelectric exhaust heat recovery for hybrid vehicles. *SAE Int J Engines* 2(1):1132–1142
5. He R, Schierning G, Nielsch K (2018) Thermoelectric devices: thermoelectric devices: a review of devices, architectures, and contact optimization (adv. mater. technol. 4/2018). *Adv Mater Technol* 3(4):1870016
6. Soleimani Z, Zoras S, Ceranic B, Shahzad S, Cui Y (2020) A review on recent developments of thermoelectric materials for room-temperature applications. *Sustain Energy Technol Assess* 37:100604

7. Zhao XB, Zhu TJ, Hu SH, Zhou BC, Wu ZT (2000) Transport properties of rapid solidified Fe–Si–Mn–Cu thermoelectric alloys. *J Alloy Compd* 306(1–2):303–306
8. Granath E, James L (2021) Understanding the difference between N- and p-type semiconductors. *Power and Beyond*, November 19. Retrieved December 16, 2021, from <https://www.power-and-beyond.com/understanding-the-difference-between-n-and-p-type-semiconductors-a-905805/>
9. Dąbrowski F, Ciupiński Ł, Zdunek J, Kruszewski J, Zybala R, Michalski A, Jan Kurzydłowski K (2019) Microstructure and thermoelectric properties of P and N type doped β-fesi2 fabricated by mechanical alloying and Pulse Plasma Sintering. *Mater Today: Proc* 8:531–539
10. Umemoto M (1995) Preparation of Thermoelectric β-fesi2 doped with Al and Mn by mechanical alloying (overview). *Mater Trans, JIM* 36(2):373–383
11. Laila A, Nanko M, Takeda M (2014) Upgrade recycling of cast iron scrap chips towards β-fesi2 thermoelectric materials. *Materials* 7(9):6304–6316
12. Singh R (2012) Cast iron. *Appl Welding Eng* 57–64
13. Nogi K, Kita T, Yan X-Q (2001) Production of iron-disilicide thermoelectric devices and thermoelectric module by the slip casting method. *Mater Sci Eng, A* 307(1–2):129–133

Mechanical Properties of Magnesium Hydroxide/Halloysite Nanotubes Reinforced Polyamide 11 Nanocomposites



Nur Najma Athirah Azahari, Hazleen Anuar, Azman Hassan, Mohammed Jawaid, Zahurin Halim, and Sani Amril Samsudin

Abstract In this study, polyamide 11 (PA 11) and halloysite nanotubes (HNTs) with varying magnesium hydroxide (MH) contents were prepared using a twin-screw extruder and injection moulding process. The mechanical properties of nanocomposites were investigated. The nanocomposites are made up of 100 phr of PA 11 and 4 phr of HNTs, with three different MH loadings of 10, 20 and 30 phr. Tensile and flexural strength showed slightly increase while Young's and flexural modulus continuously increased with addition of MH. Meanwhile, the impact strength and elongation at break decreases.

Keywords Polyamide · Halloysite nanotubes · Magnesium hydroxide · Nanocomposites · Mechanical properties

1 Introduction

Recent advancements in polymer nanocomposite technology are facilitating metal replacement in a variety of applications, particularly in the offshore and automotive industries. PA 11 is widely used as an engineering thermoplastic materials in a wide range of high performance applications due to its excellent impact strength, chemical resistance, low water absorption, excellent to stress cracking, ageing, resistance to wear, low coefficient of friction and ability to withstand high filler loads [1]. However,

N. N. A. Azahari (✉) · H. Anuar · Z. Halim

Department of Manufacturing and Materials Engineering, Kulliyyah of Engineering, International Islamic University Malaysia, 53100 Gombak, Kuala Lumpur, Malaysia
e-mail: najmatyraazahari@gmail.com

A. Hassan · S. A. Samsudin

School of Bioprocess and Polymer Engineering, Faculty of Chemical and Energy Engineering, Universiti Teknologi Malaysia, 81310 Skudai, Johor Darul Takzim, Malaysia

M. Jawaid

Department of Biocomposite Technology Lab, Institute of Tropical Forestry and Forest Product, Universiti Putra Malaysia, 43400 Serdang, Selangor Darul Ehsan, Malaysia

because of its high flammability and extended dripping during combustion, neat PA 11 cannot satisfy some of its applications [2].

The addition of a small amount of nanofillers to multifunctional polymer systems is gaining popularity [3]. The high interest in polymer nanocomposites stems from the nanofiller's large surface area and the good interaction between the matrix and the nanofillers, which improves their properties when compared to neat polymers that accept a high filler content [4]. There are many different types of nanofillers, and HNTs are one of them. HNTs are aluminosilicates clay minerals that contain oxygen, silicon, aluminium and hydrogen and the chemical composition is $\text{Al}_2\text{Si}_2\text{O}_5(\text{OH})_4 \cdot n\text{H}_2\text{O}$ [5]. HNTs is an environmentally friendly nanotubes that is relatively inexpensive materials than other nanotubes. HNTs are effective at improving the thermal stability, mechanical properties, and flame retardancy of thermoplastics and are easily processed [6]. Using HNTs to improve flame retardant is an intriguing approach because it does not reduce mechanical strength [7].

Inorganic flame retardants have been widely used in polymers due to significant advantages such as low cost, excellent smoke control performance, ecological and physical nan-toxicity, and recent worldwide development of halogen-free flame retardants [8]. The flame retardant for PA 11 was a halogen-free flame retardant such MH with chemical formula $\text{Mg}(\text{OH})_2$. At 340 °C, MH's flame retardant mechanism us an endothermic decomposition into water and magnesium oxide [9]. On one hand, the MH particles cover the surface of the combustion material and act as an excellent refractory barrier, preventing additional combustion. The vapors, on the other hand, can effectively lower the temperature of the fire and dilute the concentration of fuel gas and oxygen. The obvious disadvantages of MH are the system's compatibility with most polymers. As a result, dispersing MH in polymer resin is difficult, and workability is significantly reduced [8]. Furthermore, because of the relatively low flame retardancy efficiency, the expected flame retardancy generally necessitates a high load level (20% by weight or more), significantly reducing mechanical properties and flame retardancy [10].

Although HNTs are used to enhance some polymer systems, there are very few reports on the use of HNTs to add MH as flame retardants additives to form enhanced PA 11 nanocomposites. The goals of this study were to see how flame retardants affected the mechanical properties of PA 11/HNTs nanocomposites.

2 Experimental

2.1 Materials and Sample Preparation

Arkema Inc. created PA 11, an injection moulding grade Rilsan® BMN G8 TLDA resin made from a renewable source (Lacq, France). The HNTs known as Dragonite were obtained from Applied Minerals in New York. Its specific gravity is 2.53. HNTs have an average diameter of 80 nm, a length of about 1.2 μm and a density

of 2.5 g/cm³. MH with product name of Zerogen® 50 SP was supplied by Huber Corporations.

The materials were dried in an oven at 80 °C for about 8 h to remove moisture. The prepared nanocomposites are made up of 100 phr of PA 11, 4 phr of HNTs, and 10, 20, and 30 phr of MH. All materials were manually premixed in the container before being fed into the Brabender counter-rotating twin-screw extruder with speed was set to 60 rpm and temperature range from 220–235 °C. The extruded sample was cooled and cut into pellets using a laboratory scale pelletizer. The pellets were oven dried at 80 °C for about 5 h before being injection moulded on a JSW 80-ton injection molding machine. The temperature from the hopper to the nozzle was in the 220–235 °C range, and the water-cooling system kept the mould temperature at 25 °C. The holding pressure and screw speed were 300 bar and 100 rpm, respectively, with a throughput of 50 cm³s⁻¹.

2.2 Characterization on Mechanical Properties of PA 11/HNTs/MH Nanocomposites

Tensile Testing

Tensile testing of the samples was performed according to ASTM D638 using an Instron universal testing machine, Shimadzu Autograph AGS-X series with a crossed speed of 50 mm/min and a 50kN load cell. At 25 ± 2 °C and 50 ± 5% relative humidity, samples with a gauge length of 25 mm were injection moulded and tested to determine nanocomposite tensile strength, modulus, and elongation at break. Each formulation's five samples were tested and averaged.

Flexural Testing

Flexural properties of the samples were determined using an Instron Universal Testing machine that was compliant with ASTM D790, a three-point bending system method. The sample was tested at 10 mm/min crosshead speed and 100 mm span. The flexural tests yielded flexural strength and modulus values. The average of five samples of each formulation was reported.

Impact Testing

Impact strength was measured on the injected sample using an ASTM D256 Charpy impact machine (Dynisco Polymer Test, Advance Pendulum Impact (API)) equipped with a 7.5 J hammer. The injected sample was notched before the test using Dynisco Polymer Test, Automatic Sample Notcher (ASN). Five duplicates of each formulation were prepared for impact testing, and average impact strength values were reported in kJ/m².

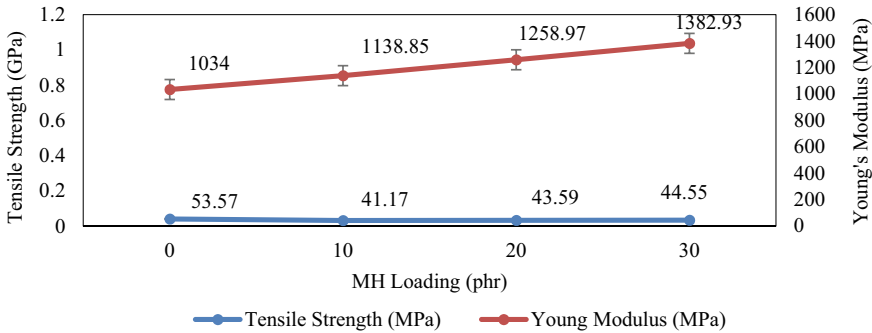


Fig. 1 The effect of MH contents on the tensile strength and Young's modulus of PA 11/HNTs/MH nanocomposites

3 Results and Discussion

3.1 Mechanical Properties

Figure 1 depicts the tensile strength and Young's modulus of neat PA 11/HNTs and PA 11/HNTs/MH nanocomposites. The tensile strength of the nanocomposites decreased with the addition of MH due to a decrease in crystallinity. Furthermore, the MH may not interact or adhere well with the matrix polymer, reducing the nanocomposites' tensile strength. These findings agree with those of Hao et al. [11] who studied the effect of flame retardant (FR) additives on the tensile strength properties of PA11/HNTs nanocomposites. They found that as the crystallinity of the PA 11/HNTs decreased, so did the tensile strength of the nanocomposites. However, as the MH loading increased, the tensile strength remained constant. In their study on the effect of FR content on the mechanical properties of PA 11/HNTs nanocomposites, Wu et al. [12] reported similar results. They found that the tensile strength did not change with different flame-retardant concentrations.

The effect of MH content in the Young's modulus of PA 11/HNTs nanocomposites is shown in Fig. 1. With increasing MH load, the young's modulus gradually increased. The addition of 10 phr MH increased the young's modulus of the PA 11/HNTs nanocomposite by 10.1% at first. Lao et al. [13] made similar observations on the effect of flame-retardant additives on the Young's modulus of PA 11 nanocomposites. They increased stiffness of the PA 11 nanocomposites was discovered to be due to the small particle size of MH and the good distribution between the FR and PA 11 nanocomposites.

The effect of MH content on the flexural strength of PA 11/HNTs nanocomposites is shown in Fig. 2. The addition of MH reduced the flexural strength of PA 11/HNTs and slightly increased it with increasing MH content. This is similar to the tensile strength tendency. According to Balakrishnan et al. [14] the decrease in flexural

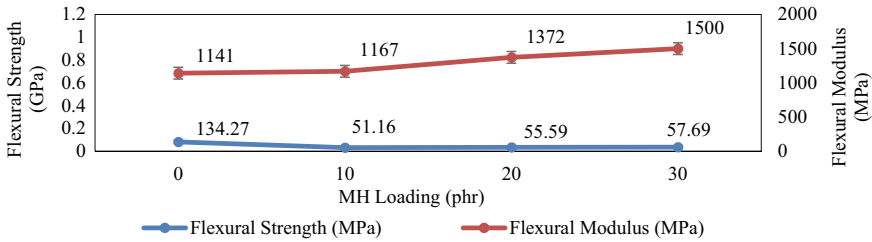


Fig. 2 The effect of MH contents on the flexural strength and flexural modulus of PA 11/HNTs/MH nanocomposites

strength is caused by the presence of MH additives in the PA 11/HNTs nanocomposites, which reduces crystallinity. The increase in flexural strength with increasing MH load could be attributed to the good MH dispersion in the PA 11/HNTs nanocomposite. Balakrishnan et al. [14] reported similar results on the flexural strength of PA 11/HNTs with MH added. They reported that the increasing flexural strength may be due to the compatibility of MH in nanocomposites.

Flexural modulus of PA 11/HNTs nanocomposites as a function of MH content is also shown in Fig. 2. The addition of MH to the PA 11/HNTs nanocomposite increased the flexural modulus value. A similar increasing trend was observed for Young’s modulus. The significant effect of MH on PA 11/HNTs nanocomposites accounts for the incremental flexural modulus. Lao et al. [13] made similar observations in their study on the effect of MH on the mechanical properties of PA 11 nanocomposites. They discovered that the increase in flexural modulus was due to the nanocomposite’s excellent distribution of FR additives dispersion.

Figure 3 shows the effect of MH content on impact strength of PA 11/HNTs nanocomposites. The impact strength significantly decreased with the presence of MH. This decrease is due to the reduction in the crystallinity of the nanocomposites. Similar findings was reported by Hao et al. [11] on the influence of FR additives on impact strength of PA 11/HNTs nanocomposites. They reported that the greater FR loadings tend to lead to lower impact strength with the same HNTs loadings that refers to 30 phr composition.

The effect of MH content on elongation at break of PA 11/HNTs is shown in Fig. 3. The addition of 10 phr MH decreased the elongation at break by 73% compared to neat PA 11/HNTs nanocomposites. It can be seen that all MH drop the value of elongation at break compared to neat PA 11/HNTs nanocomposites. similar results were found by Hao et al. [11] on the effect of FR on elongation at break of PA 11/HNTs nanocomposites. They reported that elongation at break of the nanocomposites decreases with increasing FR loading due to the decreased degree crystallinity, the PA 11 nanocomposites become more brittle with the addition of FR.

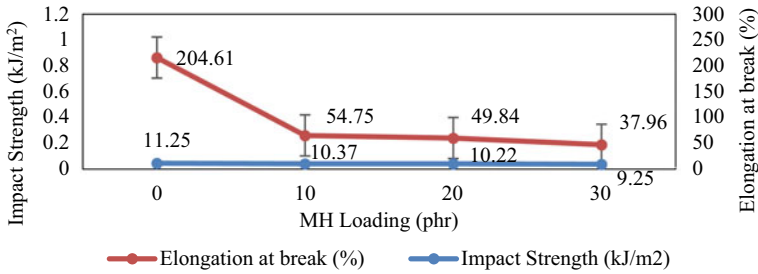


Fig. 3 The effect of MH contents on the impact strength and elongation at break of PA 11/HNTs/MH nanocomposites

4 Conclusion

This study showed that the Young's and flexural modulus of PA 11/HNTs were generally improved by the incorporation of MH, with a maximum recorded at 30 phr. However, it was found that the tensile strength and flexural strength of PA 11/HNTs did not change with further addition of MH content. A decrease in impact strength was observed as the MH content increased. As the MH content increases, the elongation at break decreases.

Acknowledgements The authors would like to thank IIUM, Universiti UTM, UPM and the Ministry of Higher Education Malaysia under Collaborative Research Initiative Grant Scheme (C-RIGS20-007-0013) and (RJ130000-7351-48524) for the financial support.

References

- Androsch R, Jariyavidyanont K, Schick C (2019) Enthalpy relaxation of polyamide 11 of different morphology far below the glass transition temperature. *Entropy* 21(10):984
- Mandlekar N, Malucelli G, Cayla A, Rault F, Giraud S, Salaün F, Guan J (2018) Fire retardant action of zinc phosphinate and polyamide 11 blend containing lignin as a carbon source. *Polym Degrad Stab* 153:63–74
- Fu S, Sun Z, Huang P, Li Y, Hu N (2019) Some basic aspects of polymer nanocomposites: a critical review. *Nano Mater Sci* 1(1):2–30
- Bidsorkhi HC, Adelnia H, Heidar Pour R, Soheilmoghaddam M (2015) Preparation and characterization of ethylene-vinyl acetate/halloysite nanotube nanocomposites. *J Mater Sci* 50(8):3237–3245
- Arman N, Tekay E, Şen S (2020) Preparation of high-strength SEBS nanocomposites reinforced with halloysite nanotube: Effect of SEBS-g-MA compatibilizer. *J Thermoplast Compos Mater* 33(10):1336–1357
- Marset D, Dolza C, Fages E, Gonga E, Gutiérrez O, Gomez-Caturra J, Ivorra-Martinez J, Sanchez-Nacher L, Quiles-Carrillo L (2020) The effect of halloysite nanotubes on the fire retardancy properties of partially biobased polyamide 610. *Polymers* 12(12):1–21
- Kovačević Z, Flinčec Grgac S, Bischof S (2021) Progress in biodegradable flame retardant nano-biocomposites. *Polymers* 13(5):1–30

8. Fei G, Liu Y, Wang Q (2008) Synergistic effects of novolac-based char former with magnesium hydroxide in flame retardant polyamide-6. *Polym Degrad Stab* 93(7):1351–1356
9. Liu Y, Li J, Wang Q (2008) Solid state shear milling to prepare magnesium hydroxide flame-retardant polyamide 6 with high performance. *Mater Manuf Processes* 23(3):284–288
10. Arjmandi R, Balakrishnan H, Hassan A, Jawaid M, Othman AY (2018) Enhanced flame retardancy, thermal and mechanical properties of hybrid magnesium Hydroxide/Montmorillonite reinforced polyamide 6/Polypropylene Nanocomposites. *Fibers and Polym* 19(4):914–926
11. Hao A, Wong I, Wu H, Lisco B, Ong B, Sallean A, Butler S, Londa M, Koo JH (2014) Mechanical, thermal, and flame-retardant performance of polyamide 11–halloysite nanotube nanocomposites. *J Mater Sci* 50:157–167
12. Wu H, Ortiz R, Koo JH (2018) Rubber toughened flame retardant (FR) polyamide 11 nanocomposites Part 1: the effect of SEBS-g-MA elastomer and nanoclay. *Flame Retardancy and Thermal Stab of Mater* 1(1):25–38
13. Lao SC, Yong W, Nguyen K, Moon TJ, Koo JH, Pilato L, Wissler G (2010) Flame-retardant polyamide 11 and 12 nanocomposites: processing, morphology, and mechanical properties. *J Compos Mater* 44(25):2933–2951
14. Balakrishnan H, Hassan A, Isitman NA, Kaynak C (2012) On the use of magnesium hydroxide towards halogen-free flame-retarded polyamide-6/polypropylene blends. *Polym Degrad Stab* 97(8):1447–1457

Two-Stage Sintering of Zirconia Toughened Alumina Composite (ZTA) Doped with Copper Oxide



S. Sivakumar, C. H. C. Alexander, H. L. Teow, M. Yeakub Ali, and S. Ramesh

Abstract Zirconia-toughened alumina (ZTA) has been widely studied owing to their excellent strength and toughness for mechanical applications. However, to realise these excellent properties, ZTA is often sintered at high temperatures ($>1550\text{ }^{\circ}\text{C}$) which may be uneconomical. This study aims to aid the sintering of ZTA composite containing zirconia content (up to 20 vol%) by the addition of 0.6 vol% copper oxide (CuO) and sintered via two-stage sintering process. The result revealed that ZTA containing 10 vol% zirconia and when sintered at $T_1 = 1450\text{ }^{\circ}\text{C}$ and $T_2 = 1350\text{ }^{\circ}\text{C}$ with a soaking time of 6 h were found to exhibit the best mechanical properties (i.e. Vickers hardness, elastic modulus and fracture toughness of 18.5 GPa, 409 GPa and $8.1\text{ MPam}^{1/2}$, respectively). In addition, the ZTA grain size was reduced by more than 10% without compromising on the relative density of above 99%. The study concluded that ZTA could be sintered at low temperatures by controlling the sintering profiles and the use of CuO as sintering additive.

Keywords Zirconia · ZTA · Y-TZP · Copper oxide · Two-stage sintering

S. Sivakumar (✉) · C. H. C. Alexander
School of Engineering, Asia Pacific University Technology and Innovation, Jalan Teknologi 5,
Taman Teknologi Malaysia, 57000 Kuala Lumpur, Malaysia
e-mail: siva.kumar@staffemail.apu.edu.my

H. L. Teow
Taylor's University, No.1, Jalan Taylors, 47500 Subang Jaya, Selangor, Malaysia

M. Y. Ali · S. Ramesh
Faculty of Engineering, Universiti Teknologi Brunei, Tungku Highway, Gadong BE1410, Brunei Darussalam

S. Ramesh
Center of Advanced Manufacturing and Materials Processing, Department of Mechanical Engineering, Faculty of Engineering, University of Malaya, 50603 Kuala Lumpur, Malaysia

1 Introduction

ZTA or Zirconia Toughened Alumina Composite is an advanced ceramic material used in various industries [1]. This composite was developed to mitigate the lower fracture toughness of alumina and the low-temperature degradation of Y-TZP when exposed to humid environment [2]. ZTA exhibits excellent hardness and high fracture toughness, thus making the composite of significant importance in the biomedical field [3]. Many researchers have investigated the fracture toughness enhancement of ZTA composite and concluded that with the presence of tetragonal zirconia grains in the composite matrix promote stress-induced transformation toughening in the presences of an advancing crack [4] and other toughening mechanisms such as residual stresses and microcracking [5]. As the microstructure, grain size and grain boundaries have been frequently found to play a role in governing the properties of various material [6–12], there is a need to ensure that these parameters are finely controlled during processing [13–18] to tailor the material properties to meet the application requirements. In the case of ceramics composites, these microstructural parameters, particularly grain coarsening during sintering must be controlled to prevent microcracks from forming and restraining the tetragonal zirconia grains from transforming to the monoclinic symmetry on cooling to room temperature [19–21]. Several authors [22, 23] suggested that a two-stage sintering (TSS) method were beneficial in enhancing the densification and successfully prevented grain growth of ceramics. The strategy in two-stage sintering is to raise the temperature to a high value of T_1 and hold for a short period of time (< 1 h) to allow particle rearrangement to proceed quickly and then reduce the sintering temperature to a lower value of T_2 to allow surface diffusion and particle consolidation to take place without incurring grain growth as it would be the case if the sample would have been sintered at T_1 . Other researchers have also reported that through manipulation of sintering conditions and the incorporation of sintering additives are viable strategies in controlling the properties of ceramics and composites, enable microstructure modification during joining or welding, and in the tailoring of suitable microstructure-properties for a host of applications [12–17]. In this study, the microstructural and mechanical properties of ZTA composites doped with 0.6 vol% CuO was investigated by using the two-stage sintering.

2 Methodology

The starting powders used were commercially available alumina (Al_2O_3), copper oxide (CuO) and yttria-stabilised tetragonal zirconia (Y-TZP). The amount used to prepare the ZTA varied between 0 (pure alumina) to 20 vol% Y-TZP, and the CuO content was fixed at 0.6 vol%. The mixing was accomplished by ball milling and green samples consisting of disc (20 mm diameter) and rectangular bars ($5 \times 5 \times 15$ mm), were prepared by powder compaction, followed with cold-isostatic press at about 200 MPa. In this work, different two-stage sintering profiles (i.e. by varying the T_1 , holding time and keeping T_2 constant at 1350 °C) were investigated as summarized in Table 1.

Table 1 Different TSS profiles used in the present work

Sintering profile	Heating rate (°C/min)	1st stage sintering temp., T1 (°C)	2nd stage sintering temp., T2 (°C)	Holding time (h)
TSS 1	10	1400	1350	6
TSS 2	20	1400		12
TSS 3	10	1450		6
TSS 4	20	1450		12
TSS 5	10	1500		6
TSS 6	20	1500		12

All the sintered samples were polished using the diamond paste to obtain a reflective surface for clear SEM images. The bulk density was measured using the Archimedes method, and the hardness was measured using the Vickers Indentation method. Young's modulus was measured based on ASTM C769 standard, and the fracture toughness was determined using the Niihara's equation [24]. The average grain size was determined from the line intercept method on SEM micrographs.

3 Results and Discussion

The densification curve in Fig. 1a shows that samples containing 10 vol% Y-TZP sintered via TSS 3 exhibited relative density above 99%. The TSS 3 and TSS 4 samples had better densification than the ATZ sintered at other sintering profiles. Other researchers had also observed that 10 vol% Y-TZP [23, 25] was found as the optimum amount. It is not well understood the reason for the optimum Y-TZP content being at 10 vol%, however it is believed that the large amounts of zirconia particles may increase the difference between the thermal expansion mismatched between the zirconia and alumina grains, and this could hinder densification of the composites.

The effect of two-stage sintering on the Vickers hardness is shown in Fig. 1b. It was found that ZTA composed of 10 vol% Y-TZP attained Vickers hardness up to 18.5 GPa when sintered at TSS 3. When the zirconia content increases to 15 vol% and above, a reduction in Vickers hardness was observed mainly for samples sintered at TSS 1, TSS 5 and TSS 6. On the contrary, the maximum value of Young's modulus recorded was 409 GPa (see Fig. 2) for ZTA having 10 vol% Y-TZP sintered using TSS 3 profile. A decreasing hardness and modulus trend was observed when the zirconia content increases beyond 10 vol% for all samples and this could be associated with the reduction in bulk density as depicted in Fig. 1a. A similar observation with decreasing mechanical properties in ceramics with decreasing bulk density was also reported by other researchers [19, 21]. It was suggested in the literatures that the higher the bulk density, the more difficult would be for dislocation to move with

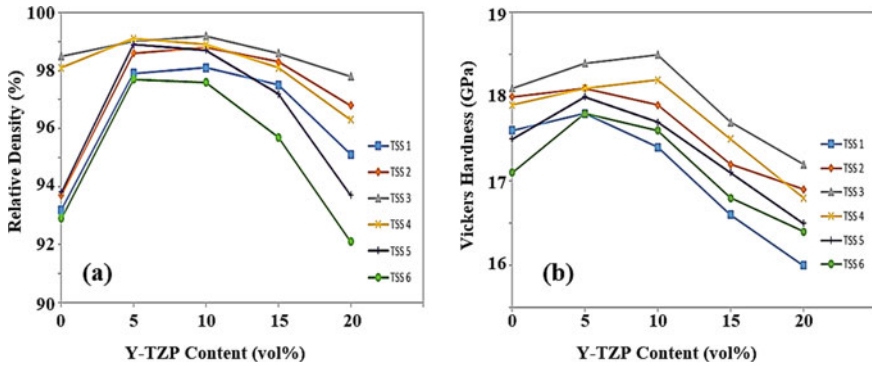


Fig. 1 a Relative density and b Vickers hardness variation of ZTA as a function of Y-TZP content sintered at different TSS profiles

the matrix and this has an effect of enhancing the mechanical properties since more energy would be required to bring about plastic deformation [1, 19, 23].

The average grain sizes of all ZTA samples are given in Table 2 and the fracture toughness of the ZTA variation with zirconia content is shown in Fig. 3

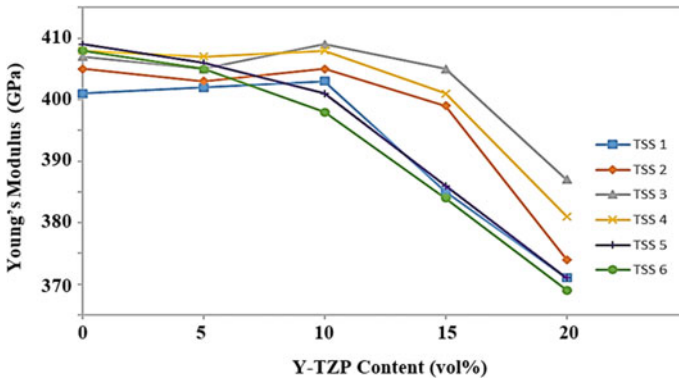


Fig. 2 Variation in young's modulus with TSS profiles

Table 2 Average grain size of sintered samples at varying sintering profile

Y-TZP (vol%)	TSS 1	TSS 2	TSS 3	TSS 4	TSS 5	TSS 6
0	0.76	0.80	0.82	0.89	0.93	0.97
5	0.36	0.39	0.40	0.45	0.51	0.54
10	0.43	0.45	0.48	0.49	0.54	0.56
15	0.51	0.52	0.53	0.55	0.58	0.61
20	0.52	0.55	0.57	0.64	0.63	0.66

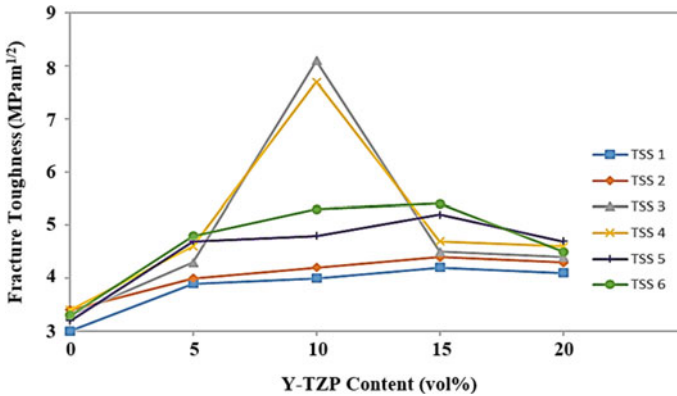


Fig. 3 Variation in fracture toughness of ZTA as a function of Y-TZP content

It was found that the grain size of ZTA decreases to a low value at 5 vol% Y-TZP before increasing with further addition of zirconia content. This trend seemed to be in good agreement with that reported by other researchers [23] although the mechanism involved is not well understood. Further work is in progress to elucidate this behaviour.

The fracture toughness was found to fluctuate between 3 and 3.4 $\text{MPa}\cdot\text{m}^{1/2}$ as depicted in Fig. 3. One striking observation was that at 10 vol% Y-TZP, the fracture toughness was significantly higher i.e. $8.1 \text{ MPa}\cdot\text{m}^{1/2}$ and $7.7 \text{ MPa}\cdot\text{m}^{1/2}$ when sintered at TSS 3 and TSS 4, respectively.

4 Conclusions

In this work, the properties of ZTA composites containing up to 20 vol% Y-TZP and doped with 0.6 vol% CuO consolidated by two-stage sintering (TSS) was investigated. It was found the addition of 10 vol% Y-TZP subjected to TSS 3 sintering profile ($T_1 = 1450 \text{ }^\circ\text{C}$, heating rate of $10 \text{ }^\circ\text{C}/\text{min}$, $T_2 = 1350 \text{ }^\circ\text{C}$, and 6 h holding time) exhibited the overall best properties with samples having Vickers hardness of 18.5 GPa, Young's modulus of 409 GPa and toughness of $8.1 \text{ MPa}\cdot\text{m}^{1/2}$.

References

1. Fan J, Lin T, Hu F, Yu Y, Ibrahim M, Zheng R, Huang S, Ma J (2017) Effect of sintering temperature on microstructure and mechanical properties of zirconia-toughened alumina machinable dental ceramics. *Ceram Int* 43(4):3647–3653
2. Aragón-Duarte MC, Nevarez-Rascón A, Esparza-Ponce HE, Nevarez-Rascón MM, Talamantes RP, Ornelas C, Mendez-Nonell J, González-Hernández J, Yacamán MJ, Hurtado-Macías A

- (2017) Nanomechanical properties of zirconia-yttria and alumina zirconia-yttria biomedical ceramics, subjected to low temperature aging. *Ceram Int* 43(5):3931–3939
3. Ghalme SG, Mankar A, Bhalerao Y (2016) Biomaterials in hip joint replacement. *Int J Mater Sci Eng* 4(2):113–125
 4. Sommer F, Landfried R, Kern F, Gadow R (2012) Mechanical properties of zirconia toughened alumina with 10–24 vol.% 1Y-TZP reinforcement. *J Europ Ceramic Soc* 32(16):4177–4184
 5. Zhu T, Xie Z, Han Y, Li S (2018) Microstructure and mechanical properties of ZTA composites fabricated by oscillatory pressure sintering. *Ceram Int* 44(1):505–510
 6. Ramesh S, Sara Lee KY, Tan CY (2018) A review on the hydrothermal ageing behaviour of Y-TZP ceramics. *Ceram Int* 44:20620–20634
 7. Duraisamy N, Numan A, Ramesh K, Choi K-H, Ramesh S, Ramesh S (2015) Investigation on structural and electrochemical properties of binder free nanostructured nickel oxide thin film. *Mater Lett* 161:694–697
 8. Manladan SM, Yusof F, Ramesh S, Zhang Y, Luo Z, Ling Z (2017) Microstructure and mechanical properties of resistance spot welded in welding-brazing mode and resistance element welded magnesium alloy/austenitic stainless steel joints. *J Mater Process Technol* 250:45–54
 9. Sampath Udeni Gunathilake TM, Ching YC, Chuah CH, Illias HA, Ching KY, Singh R, Nai-Shang L (2018) Influence of a nonionic surfactant on curcumin delivery of nanocellulose reinforced chitosan hydrogel. *Int J Biol Macromolecules* 118:1055–1064
 10. Francis KA, Liew C-W, Ramesh S, Ramesh K, Ramesh S (2016) Ionic liquid enhanced magnesium-based polymer electrolytes for electrical double-layer capacitors. *Ionics* 22:919–925
 11. Ramesh S, Amiriyani M, Meenaloshini S, Tolouei R, Hamdi M, Purboloksono J, Teng WD (2011) Densification behaviour and properties of manganese oxide doped Y-TZP ceramics. *Ceram Int* 37:3583–3590
 12. Azim Jais A, Muhammed Ali SA, Anwar M, Rao SM, Mughtar A, Wan Isahak WNR, Tan CY, Singh R, Brandon NP (2017) Enhanced ionic conductivity of scandia-ceria-stabilized-zirconia (10Sc1CeSZ) electrolyte synthesized by the microwave-assisted glycine nitrate process. *Ceramics Int* 43:8119–8125
 13. Misran H, Singh R, Yarmo MA (2008) Nonsurfactant route of fatty alcohols decomposition for templating of mesoporous silica. *Microporous Mesoporous Mater* 112:243–253
 14. Barzani MM, Sarhan AAD, Farahany S, Ramesh S, Maher I (2015) Investigating the machinability of Al-Si-Cu cast alloy containing bismuth and antimony using coated carbide insert. *Measurement* 62:170–178
 15. Yeo WH, Fry AT, Purboloksono J, Ramesh S, Inayat-Hussain JI, Liew HL, Hamdi M (2014) Oxide scale growth and presumed exfoliation in a 700°C or higher steam condition: a simulation study for future operations of ultra-supercritical power plants. *J Supercrit Fluids* 92:215–222
 16. Ching YC, Gunathilake TMSU, Chuah CH, Ching KY, Ramesh S, Liou N-S (2019) Curcumin/Tween 20-incorporated cellulose nanoparticles with enhanced curcumin solubility for nano-drug delivery: characterization and in vitro evaluation. *Cellulose* 26:5467–5481
 17. Yee YY, Ching YC, Rozali S, Hashim NA, Ramesh S (2016) Preparation and characterization of poly(lactic acid)-based composite reinforced with oil palm empty fruit bunch fiber and nanosilica. *BioResources* 11(1):2269–2286
 18. Bowen C, Ramesh S, Gill C, Lawson S (1998) Impedance spectroscopy of CuO-doped Y-TZP ceramics. *J Mater Sci* 33:5103–5110
 19. Ramesh S, Zulkifli N, Tan CY, Wong YH, Tarlochan F, Ramesh S, Teng WD, Sopyan I, Bang LT, Sarhan AAD (2018) Comparison between microwave and conventional sintering on the properties and microstructural evolution of tetragonal zirconia. *Ceram Int* 44:8922–8927
 20. Ramesh S, Gill C (2001) Environmental degradation of CuO-doped Y-TZP ceramics. *Ceram Int* 27(6):705–711
 21. Ramesh S, Sara Lee KY, Tan CY, Wong YH, Alengaram UJ, Tarlochan F, Teng WD, Sutharsini U, Sarhan AAD (2018) Effect of microwave sintering on the properties of copper oxide doped Y-TZP ceramics. *Ceramics Int* 44(16):19639–19645

22. Chen IW, Wang XH (2000) Sintering dense nanocrystalline ceramics without final-stage grain growth. *Nature* 404(6774):168
23. Sivanesan S, Loong TH, Namasivayam S, Fouladi MH (2019) Two-stage sintering of alumina-Y-TZP ($\text{Al}_2\text{O}_3/\text{Y-TZP}$) composites. *Key Eng Mater* 814:12–18
24. Niihara K (1983) A fracture mechanics analysis of indentation-induced Palmqvist crack in ceramics. *J Mater Sci Lett* 2(5):221–223
25. Meunier C, Zuo F, Peillon N, Saunier S, Marinel S, Goeriot D (2017) In situ study on microwave sintering of ZTA ceramic: effect of ZrO_2 content on densification, hardness, and toughness. *J Am Ceram Soc* 100(3):929–936